



**HAL**  
open science

# Localized protein-assisted self-assembly : from mechanism to applications

Jennifer Rodon Fores

► **To cite this version:**

Jennifer Rodon Fores. Localized protein-assisted self-assembly : from mechanism to applications. Other. Université de Strasbourg, 2019. English. NNT : 2019STRAE017 . tel-02494094

**HAL Id: tel-02494094**

**<https://theses.hal.science/tel-02494094>**

Submitted on 28 Feb 2020

**HAL** is a multi-disciplinary open access archive for the deposit and dissemination of scientific research documents, whether they are published or not. The documents may come from teaching and research institutions in France or abroad, or from public or private research centers.

L'archive ouverte pluridisciplinaire **HAL**, est destinée au dépôt et à la diffusion de documents scientifiques de niveau recherche, publiés ou non, émanant des établissements d'enseignement et de recherche français ou étrangers, des laboratoires publics ou privés.

**ÉCOLE DOCTORALE DE PHYSIQUE ET CHIMIE PHYSIQUE**

**CNRS- Institut Charles Sadron UPR 22**

**THÈSE** présentée par :

**Jennifer RODON FORES**

Soutenue le : **20 Septembre 2019**

pour obtenir le grade de : **Docteur de l'Université de Strasbourg**

Discipline/ Spécialité : Chimie / Biomatériaux

**Auto-assemblages localisés assistés par des protéines : du mécanisme aux applications**

*Localized protein-assisted self-assembly: from mechanism to applications*

**THÈSE dirigée par :**  
Pr. **JIERRY Loïc**

Professeur, Université de Strasbourg

**RAPPORTEURS :**

Pr. **WOISEL Patrice**

Professeur, Université de Lille

Pr. **AUZELY-VELTY Rachel**

Professeur, Université Grenoble Alpes

**EXAMINATEURS :**

Pr. **HOSSEINI Mir Wais**

Professeur, Université de Strasbourg

**MEMBRES INVITES :**

Dr. **BALLY-LE GALL Florence**

Maître de Conférences, Institut de Science des Matériaux de Mulhouse

Pr. **SCHAAF Pierre**

Professeur, Université de Strasbourg



*« L'imagination est plus importante que la connaissance. La connaissance est limitée, l'imagination encercle le monde. »*

**Albert Einstein**



## — REMERCIEMENTS —

Je souhaite tout d'abord remercier ma famille qui m'a soutenue tout au long de ces trois années et qui sont mes soutiens de la première heure, toujours présent dans les bons comme dans les mauvais moments, de vos mots toujours réconfortants qui m'ont porté tout au long de mon cursus.

Je tiens ensuite à exprimer ma profonde reconnaissance à mon directeur de thèse, le Professeur Loïc Jierry, Professeur à l'ECPM et chercheur à l'Institut Charles Sadron, grâce à qui j'ai pu travailler dans d'excellentes conditions, qui m'a poussé à me surpasser chaque jours et a rendu mon expérience de doctorat aussi riche et complète que possible. Loïc, merci pour ton encadrement, ta disponibilité, ton enthousiasme et surtout tes précieux conseils.

Je souhaite adresser un grand merci au Docteur Fouzia Boulmedais, Directrice de recherches à l'ICS, pour ta pédagogie, ta sagesse et tous tes conseils pendant ces trois années. Et surtout un grand merci pour ton pouvoir canalisateur sur Pierre. Les réunions en ta compagnie ont toujours été les plus drôles et constructives. Et au Professeur Pierre Schaaf, Directeur de l'Unité INSERM 1121, pour votre confiance, votre bienveillance et pour toutes ces discussions scientifiques passionnantes et riches d'enseignements de ces trois années.

J'adresse tous mes remerciements aux membres de mon jury, la Professeure Rachel Auzely-Velty, Professeur à l'Université de Grenoble-Alpes, au Docteur Florence Bally-Le-Gall, Maître de conférence à l'institut de science des matériaux de Mulhouse, au Professeur Patrice Woisel, Professeur à l'Université de Lille et au président de mon jury, le Professeur Mir Wais Hosseini, Professeur à l'université de Strasbourg pour avoir gentiment accepté de juger mon travail de thèse.

J'aimerais tout spécialement remercier mon colocataire de bureau et meilleur ami Miguel pour ta gentillesse, et ta patience pendant ma rédaction et surtout pour tous les bons moments que nous avons passés ensemble que se soit quand tu étais mon stagiaire ou après pour ta thèse.

Un grand merci à mes collègues de l'équipe PECMAT, Janwa, Miryam, Sarah, Lionel, Déborah, Xiyu, Haseeb, Julien, Nicolas, Agata et Rémy sans qui ces trois années n'auraient pas été les mêmes. Pour toutes nos discussions et sorties, tous ces bon moments qui ont fait de mon expérience de thèse une expérience sans pareil.

Un merci particulier aussi pour mes stagiaires, Miguel, Xiyu, Camille, Mathilde, Maëlle C., Maëlle Q., Claire et Assane dont j'ai eu le plaisir d'encadrer et de partager tous ces projets et discussions scientifiques.

Je souhaite finalement adresser un grand merci à toutes les personnes qui ont contribué à la réalisation de mes travaux et qui m'ont conseillé au cours de ces trois années. Merci au Docteur Morgane Rabineau, Ingénieure de recherche à l'unité INSERM 1121, pour les formations sur les appareils, tes conseils scientifiques et ta

patience. Merci au Docteur Marc Schmutz, Docteur Christian Blanck et au Docteur Alain Carvalho, responsable et membres de la plateforme de microscopie de l'ICS, pour votre aide dans mes différents projets et de m'avoir formé en microscopie ainsi que pour votre pédagogie, toutes les discussions scientifiques et vos conseils. Merci au Docteur Ludovic Richert, ingénieur de recherche à la faculté de pharmacie de Strasbourg, pour les expériences de FCS, pour ta disponibilité et ton optimisme. Merci au Docteur Alain Chaumont, enseignant chercheur à l'institut de chimie de Strasbourg, pour ses travaux de simulations numériques qui ont enrichi notre raisonnement. Enfin, merci aux Docteurs Jean-François Lutz, Directeur de recherche CNRS à l'ICS, et Vincent Ritleng, maître de conférence à l'ECPM, d'avoir évalué mon travail à mi-parcours et prodiguer de précieux conseils pour ma troisième année.

Et je remercie également le centre international de recherche exploratoire en chimie (Labex CSC, numéro de projet PSC-016) pour la bourse qui m'a permis de réaliser cette thèse.



## Introduction

L'humanité s'est toujours demandé comment la vie a émergé ? Quels sont les mécanismes contrôlant le comportement des cellules et comment celles-ci agissent ensemble pour former des espèces hautement évoluées. Une des hypothèses sur l'origine de la vie est que nous venons tous d'une seule cellule. Cette cellule a dû se diviser pour que la vie puisse s'épanouir. Ensuite, elle s'est adaptée à son environnement. Pour y parvenir, les cellules ont développé de nombreuses stratégies, l'une d'entre elles consistant à contrôler les processus d'auto-assemblage. Ces processus sont des mécanismes dans lesquels les composants cellulaires interagissent spontanément les uns avec les autres pour former des structures organisées et fonctionnelles.

Malgré son apparente spontanéité, la nature a dû mettre au point des méthodes pour contrôler l'auto-assemblage de protéines ou de peptides afin que ceux-ci s'initient à des emplacements spécifiques et à un moment bien défini : c'est ce qu'on appelle le contrôle spatio-temporel. Un exemple de ces processus est la formation des fibres d'actine qui sont formées par auto-assemblage de protéines globulaires appelées actine, qui s'auto-assemblent sous l'action d'une enzyme, la phosphatase alcaline. Cette enzyme élimine un groupement phosphate de l'actine, qui s'auto-assemble ensuite en fibres. La particularité de l'auto-assemblage des fibres d'actine réside dans le fait que les phosphatases alcalines sont localisées à la surface de la membrane cellulaire, ce qui permet de localiser la



génération des fibres (Figure 1). Cette localisation est essentielle pour la motilité cellulaire, car les fibres d'actine lorsqu'elles se forment exercent une pression sur la membrane cellulaire, ce qui conduit à un mouvement de la cellule. De tels mouvements sont nécessaires pour que la cellule s'adapte à son environnement mécanique et chimique. Cela illustre l'importance des processus d'auto-assemblages et en particulier leur contrôle spatio-temporel dans le comportement cellulaire.

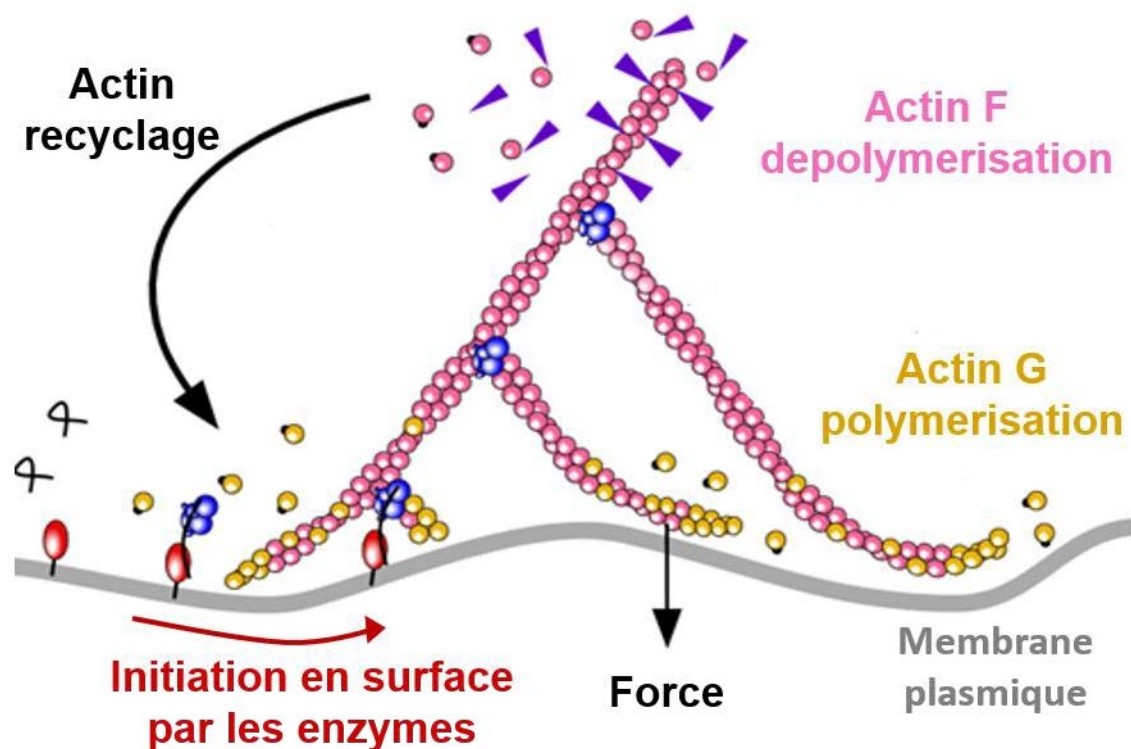


Figure 1: Exemple de contrôle spatio-temporel de l'auto-assemblage de protéines conduisant à la motilité cellulaire: l'auto-assemblage de la protéine globulaire d'actine se produit lorsque cela est nécessaire dans la vie de la cellule et ne se produit pas partout mais il est localisé près de la membrane plasmique interne. Ce contrôle spatio-temporel est assuré par la présence de phosphatase transmembranaire. (I2BC.paris-saclay.fr/02/02-14-17).

En s'appuyant sur des liaisons non covalentes et donc réversibles, les réseaux auto-assemblés répondent de manière dynamique aux divers stimuli externes. Dans la quête actuelle de matériaux intelligents dotés de caractéristiques de performance élevées similaires à celles de la matière vivante, les hydrogels supramoléculaires apparaissent

comme un outil prometteur, en raison notamment de leur caractère non covalent, ils peuvent s'adapter à leur environnement immédiat. Dans ce contexte, l'utilisation d'enzymes pour déclencher l'auto-assemblage localisé de peptides est extrêmement prometteuse. Comme l'illustre la figure 2, les enzymes peuvent catalyser la transformation de précurseurs non groupés, en entités capables de se reconnaître et de s'auto-assembler rapidement, conduisant à la formation d'un hydrogel exclusivement à partir de l'endroit où les enzymes sont localisées.

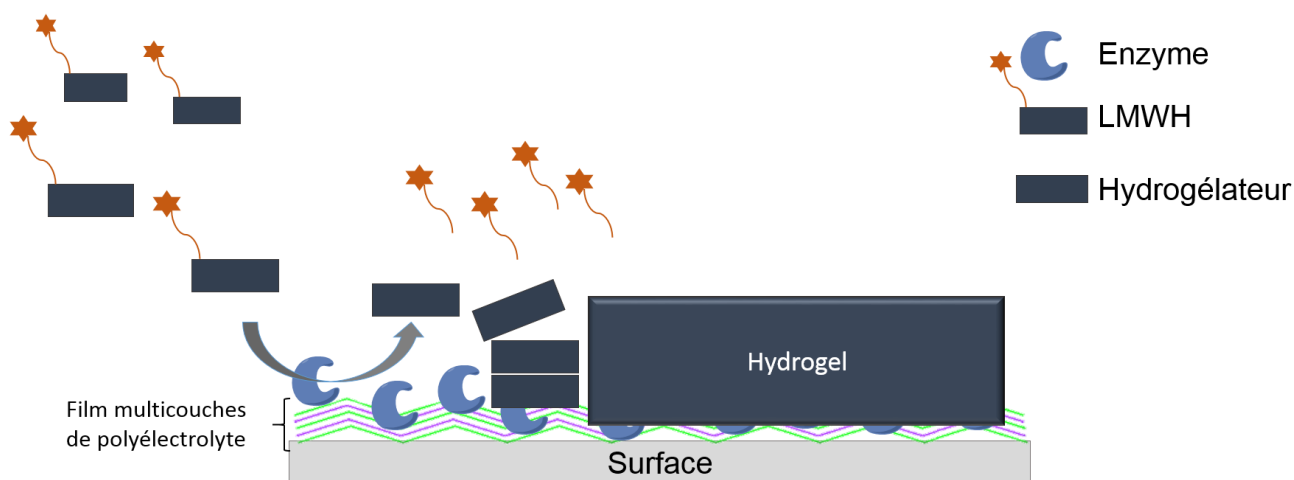


Figure 2: Schéma du principe de l'auto-assemblage localisé assisté par enzyme

Depuis 2011, le groupe de recherche Ingénierie Macromoléculaire aux interfaces (IMI) de l'Institut Charles Sadron a conçu une stratégie «one pot» pour construire des films à base de polyelectrolytes exclusivement à partir de surfaces, en utilisant tout d'abord un stimulus électrique. Des gradients électrochimiques de catalyseurs générés à la surface des électrodes (ions métalliques, protons ou composés organiques) ont été utilisés pour induire des auto-constructions de nanofilms constitués d'oligomères, de polymères ou de petites molécules localisées à la surface de ces électrodes. Par analogie avec le développement des tissus biologiques, ces catalyseurs ont été appelés morphogènes. Cette approche représente un moyen pratique de fonctionnaliser des surfaces en utilisant

tous les constituants présents simultanément en solution et permettant un contrôle précis de la formation du film de manière ascendante à partir de la surface de l'électrode productrice du gradient.

En 2015, une doctorante du groupe IMI, Cécile Vigier-Carrière, a introduit l'auto-assemblage localisé assisté par enzyme. En adsorbant des enzymes sur des films multicouches de polyélectrolytes et en mettant ces films en contact avec des solutions de peptides réagissant avec les enzymes, elle a pu diriger l'auto-assemblage des peptides pour obtenir des couches micrométriques d'hydrogels supramoléculaires spécifiquement situées sur en surface où les enzymes étaient déposées. En plus de représenter un processus *one-pot* qui conduit à une accumulation d'hydrogel localisée sans utiliser de stimulus externe, il donne lieu à la croissance d'architectures nanofibreuses organisées de bas en haut. Elle a développé deux approches pour illustrer le concept de l'auto-assemblage localisée assistée par enzyme (LEASA). Dans la première, l'auto-assemblage du peptide était assisté par l' $\alpha$ -chymotrypsine, qui catalyse la condensation de dipeptides pour former des oligomères. Ces oligopeptides sont progressivement libérés de la surface puis assemblés automatiquement en nanofibres poussant à partir de la surface. La largeur et la cinétique de l'auto-assemblage des oligopeptides ont été ajustées en fonction de la concentration initiale en dipeptides en solution et de la densité d' $\alpha$ -chymotrypsine en surface. Dans la seconde approche, elle a déposé un film mince favorisant à la fois la production enzymatique d'hydrogélateurs et la nucléation de l'auto-assemblage de l'hydrogélateur à la surface. Cela a été réalisé en utilisant un film multicouche bioactif comprenant la phosphatase alcaline et présentant des hydrogélateurs peptidiques correspond à ceux constituant l'auto-assemblage.

L'objectif initial de mon doctorat était de concevoir des hydrogels

supramoléculaires formés à partir de surfaces et capables de catalyser leur propre formation par un processus autonome. Pour atteindre cet objectif, la première étape a consisté à obtenir une architecture auto-assemblée catalytique pouvant être générée à partir d'une surface en utilisant l'approche LEASA. Ensuite, ce système a été adapté pour pouvoir produire ses propres blocs de construction en fonction de son activité catalytique inhérente et cela de manière autonome. Cette stratégie est le plan de travail que j'ai adopté lors de mon doctorat.

## État de l'art

La recherche sur l'auto-assemblage moléculaire est centrée sur l'auto-assemblage de biomacromolécules (i.e. protéines, acides nucléiques, acides aminés et polysaccharides) et de leurs mimes principalement dans l'eau. Ce domaine de recherche s'inscrit aussi bien dans la recherche fondamentale qu'appliquée dans des domaines comme l'ingénierie tissulaire, le développement de biomatériaux ou encore de biocapteurs.

L'une des conséquences habituelles de l'auto-assemblage de petites molécules est la formation d'un gel, ce qui leur a donné l'appellation de « gélifiants ». En fonction des solvants dans lesquels elles s'auto-assemblent, ces petites molécules sont en outre classées en tant qu'hydrogélateurs (utilisant l'eau comme phase liquide) ou organogélateurs (utilisant un «solvant» organique comme phase liquide). Le cas qui m'a intéressé pendant ma thèse est celui des hydrogélateurs supramoléculaire, car ils s'assemblent spontanément dans l'eau pour former des réseaux supramoléculaires tridimensionnels qui encapsulent une grande quantité d'eau pour former un mélange aqueux. Le mélange aqueux est un hydrogel car il présente la viscoélasticité d'un gel,

autrement dit, il est incapable de s'écouler sans force de cisaillement. Contrairement aux hydrogels polymères classiques qui reposent principalement sur des réseaux de polymères réticulés de manière covalentes, les réseaux d'hydrogels supramoléculaires sont formés *via* des interactions non covalentes (électrostatique, hydrogène, van der Waals, etc.) entre les hydrogélateurs (Figure 3). Comme l'eau est le solvant maintenant les formes de vie sur Terre, il n'est pas surprenant que les applications des hydrogels en sciences de la vie aient progressé de la manière la plus significative.

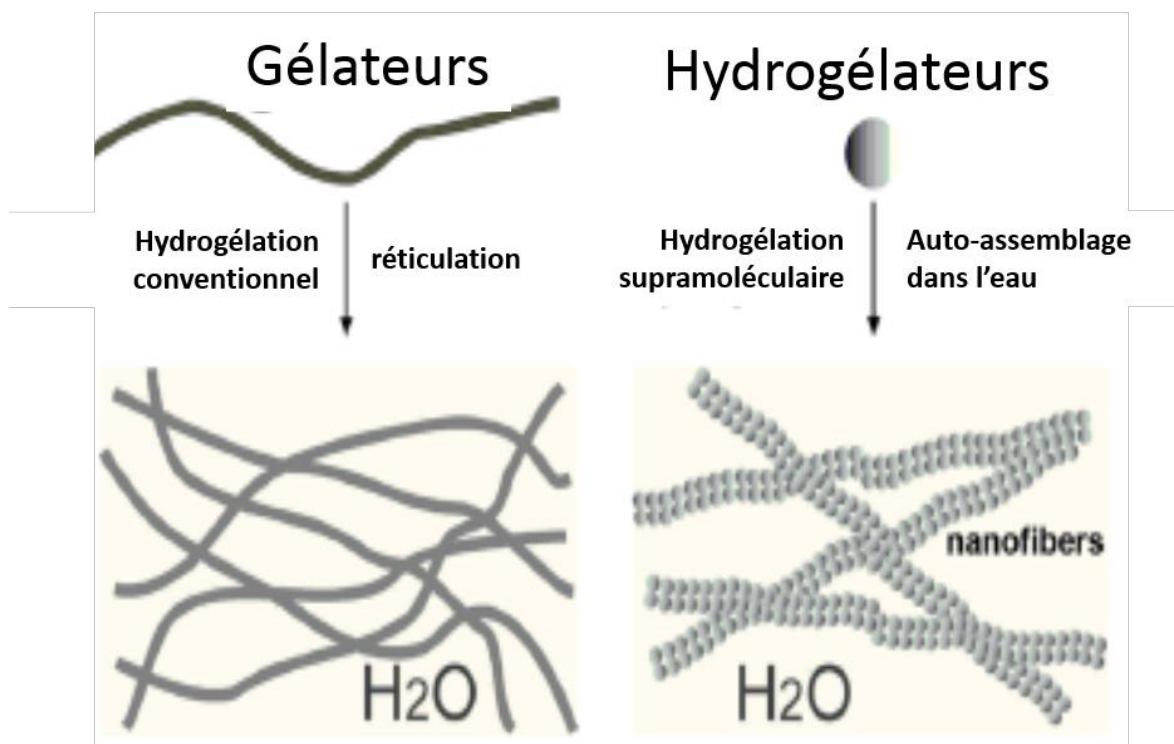


Figure 3: Illustration du processus de création d'hydrogels polymères par réticulation (à gauche) ou par la formation d'hydrogels supramoléculaires via un auto-assemblage initié par une perturbation chimique ou physique (à droite).

Des exemples bien connus d'hydrogels sont des hydrogels constitués de polypeptides, tels que le collagène, la poly-L-Lysine, de polysaccharides tels que l'acide alginique, l'acide hyaluronique et l'agarose ou encore de polymères synthétiques tels que l'alcool polyvinylique (PVA) et le polyéthylène glycol (PEG). Les PEG sont couramment utilisés pour former des réseaux macromoléculaires réticulés gonflés dans l'eau. Bien qu'ils

partagent un aspect et des propriétés communes avec les hydrogels polymères, les hydrogels supramoléculaires diffèrent des hydrogels polymères de nombreuses subtiles manières. Une différence essentielle réside dans le fait que les hydrogels supramoléculaires, contrairement aux hydrogels polymères issus d'un réseau réticulé de manière aléatoire constitué de liaisons covalentes fortes, sont la conséquence d'auto-assemblages moléculaires entraînés par de faibles interactions non covalentes entre les hydrogélateurs dans l'eau. Cette différence, subtile mais fondamentale, non seulement rend les arrangements moléculaires plus ordonnés dans les hydrogels supramoléculaires, mais se manifeste également dans le processus d'hydrogélation. Alors qu'un simple gonflement confère généralement un hydrogel polymère, un stimulus ou une force de déclenchement est nécessaire pour biaiser l'équilibre thermodynamique afin d'initier le processus d'auto-assemblage ou la transition de phase pour obtenir un hydrogel supramoléculaire. Par conséquent, il existe de nombreuses formes de stimuli ou de déclencheurs pour manipuler les interactions faibles, qui peuvent être obtenues par des méthodes physiques (par exemple, modification de la température, application d'ultrasons ou modulation de la force ionique), des méthodes chimiques (par exemple, changement de pH ou une modification chimique), ou encore par des réactions photochimiques, d'oxydoréduction et de catalyse (Figure 3).

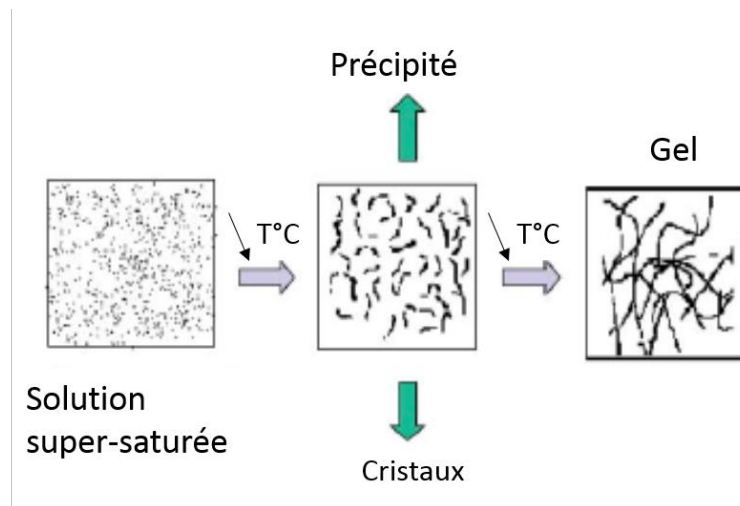


Figure 4: Représentation schématique des différentes voies possibles conduisant à la précipitation, à la cristallisation ou à la formation d'un gel à partir d'une solution saturée en molécules.

Dans ce manuscrit, je me suis concentrée sur l'utilisation de petites molécules, de simples acides aminés ou de courts peptides (entre 2 et 8 acides aminés), afin de générer des hydrogels.

Les hydrogels supramoléculaires issus de peptides peuvent adopter différentes structures secondaires (bobines, hélices, ou en feuillets) et conduire à une large gamme d'objets à l'échelle nanométrique: fibres, tubes, sphères ou feuillets (Figure 5) à partir d'interactions non covalentes se produisant pendant la formation de l'auto-assemblage.

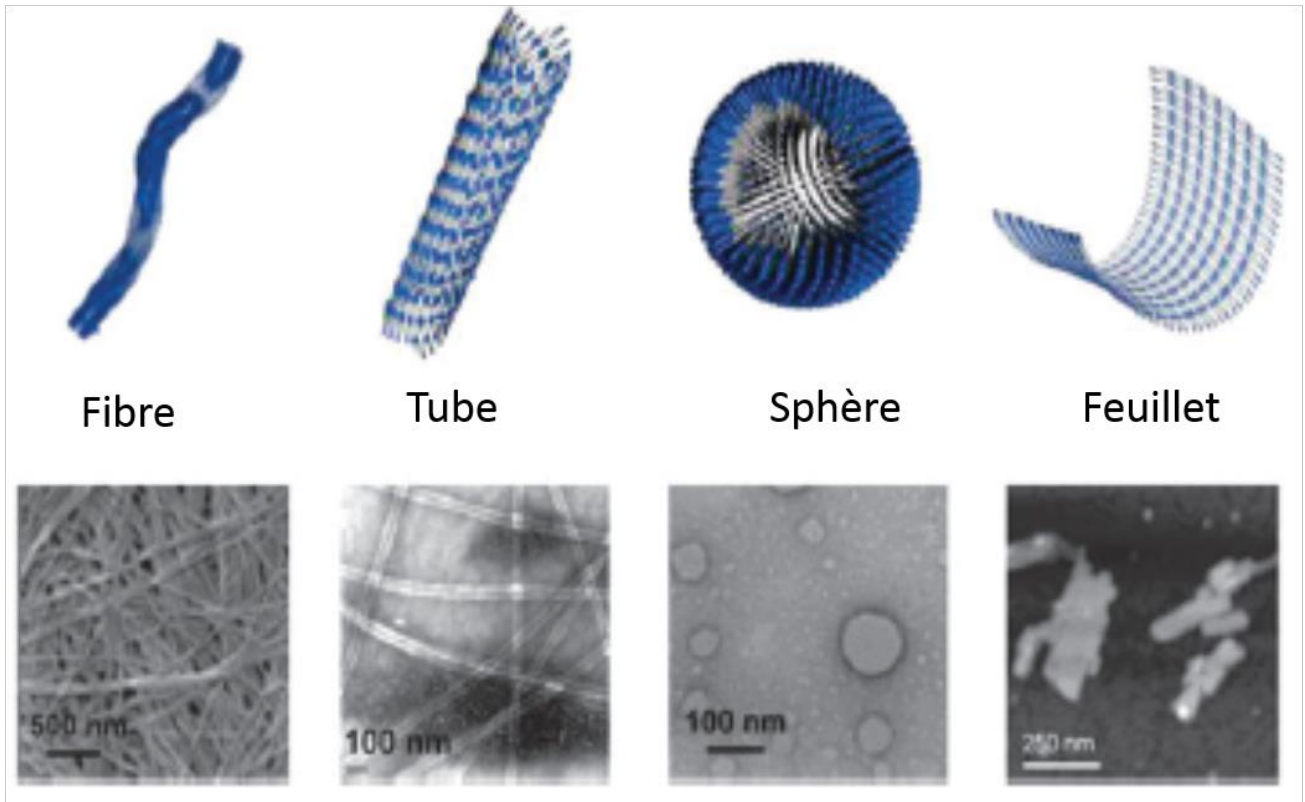


Figure 5 : Structures supramoléculaires accessibles via l'auto-assemblage peptidique.

Depuis le milieu du siècle dernier, la fonctionnalisation de surface est apparue comme une méthode pratique pour contrôler les interactions entre un matériau et son environnement. De nombreuses approches efficaces ont été développées pour couvrir un large éventail d'applications permettant de modifier les surfaces afin de leur conférer des propriétés variées en fonction des molécules et des stimuli utilisés. La principale question qui se pose pour la fonctionnalisation de surface est de savoir comment diriger l'accumulation de nanostructures exclusivement à partir d'une surface ou sur une surface.

Pour relever ce défi, les surfaces ont été considérées comme des supports précieux pour contrôler et structurer les assemblages ascendants de d'hydrogélateur à faible poids moléculaire (LMWH) dans l'espace et dans le temps. Deux principales approches ont été développées pour répondre à cette question. La première approche



consiste à générer des points de nucléation sur la surface en liant des LMWH sur la surface. Cette approche conduit à une augmentation de la concentration locale de LMWH, favorisant la formation de l'auto-assemblage. La seconde approche consiste à générer à la surface des espèces, appelées morphogènes, qui induiront la formation locale des LMWH. La Figure 6 présente les différentes stratégies de modification de surface permettant la croissance d'auto-assemblages localisés sur la surface ou à partir de la surface.

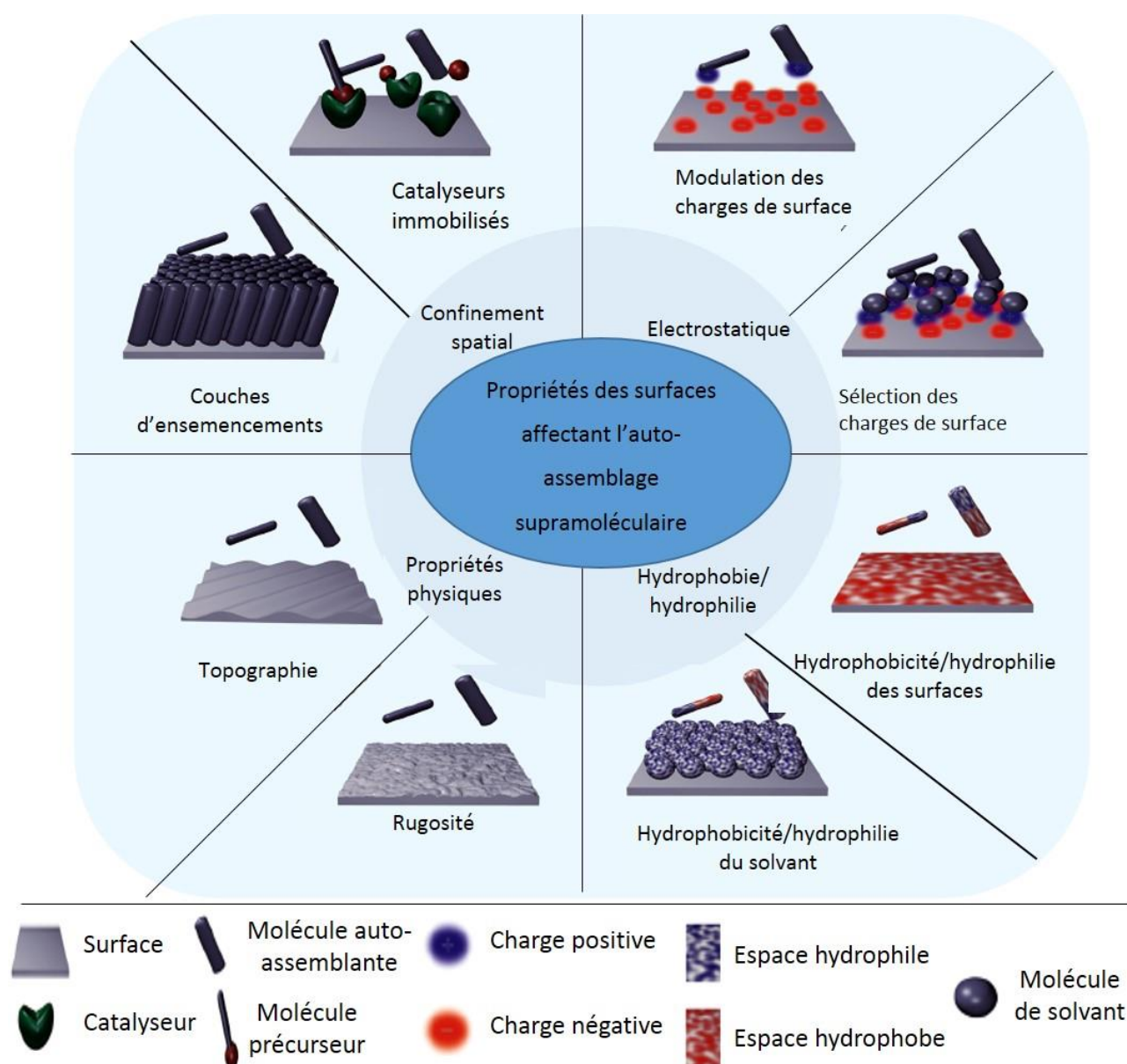


Figure 6 : Vue d'ensemble des propriétés de surface impliquées dans le processus de localisation d'auto-assemblage en surface

Ces travaux ont fait l'objet de deux revues publiées récemment. La première en 2017 par Vigier-carrière *et al.* et la seconde en 2018 par Yang *et al.* Dans ce manuscrit, je présente de manière succincte les principaux points mis en évidence par ces revues et les articles publiés par la suite sont également décrits.

## 1) Localisation de l'auto-assemblage de LMWH par interactions électrostatiques avec la surface

L'hydrogélotion localisée induite en surface de LMWH à des concentrations bien inférieures à la concentration critique de gélification (CGC) a été observée pour la première fois par Bing Xu en 2002 sur la membrane de cellules et démontrée par J.C. Tiller en 2003. Un moyen facile d'induire la formation localisée d'un hydrogel supramoléculaire consiste à ajuster la balance hydrophilie / hydrophobie ou la charge de la surface afin de favoriser l'absorption non spécifique des molécules d'hydrogélatrice sur la surface par le biais d'interactions faibles. La concentration élevée de molécules d'hydrogélatrice adsorbées favorise ensuite l'auto-assemblage et la formation de l'hydrogel sur la surface. Le système chimique utilisé par Tiller était basé sur cette stratégie. À pH acide, la surface sélectionnée était chargée positivement en raison de la présence d'un groupe ammonium ( $-\text{NH}_3^+$ ), alors que l'hydrogélateur était chargé négativement. Par interaction électrostatique, l'hydrogélateur a pu se lier à la surface. Cela a entraîné une augmentation locale de la concentration de l'hydrogélateur au niveau de la surface entraînant son auto-assemblage avec d'autres hydrogélateurs. La structure de l'auto-assemblage obtenu est semblable à celle d'un brocoli localisée à l'interface liquide-solide (Figure 7).

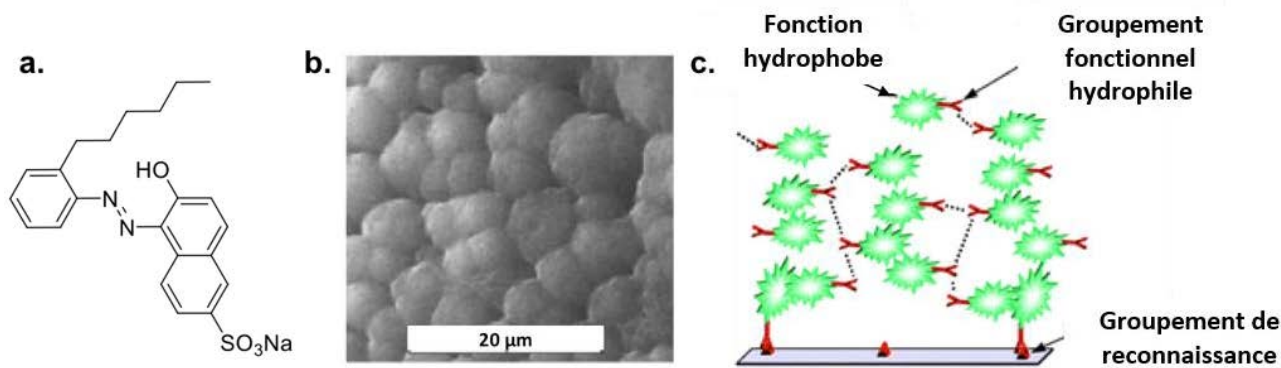


Figure 7: a) Structure chimique de l'hydrogélateur anionique, b) structure semblable à un brocoli de l'auto-assemblage formé sur la surface du verre modifié observée par SEM, c) modèle proposé par les auteurs pour expliquer la gélification localisée à la surface

## 2) Localisation de l'auto-assemblage de LMWH par liaison covalente de catalyseurs sur la surface

La deuxième stratégie décrite pour contrôler l'auto-assemblage d'hydrogélateurs exclusivement à une interface liquide/surface est basée sur la génération de LMWH directement à la surface ou près de la surface. La génération d'hydrogélateurs près de la surface peut être obtenue en produisant des espèces chimiques, appelées morphogènes, qui diffusent de la surface vers la solution et qui commutent les molécules présentes dans la solution d'un état de non-assemblage (précurseur) à un état d'auto-assemblage (hydrogélateur) (Figure 8). Dans le cas des LMWH, les systèmes rapportés utilisent des protons en tant que morphogènes et les LMWH présentant des groupes acides faibles. Un flux de proton diffuse de la surface vers la solution et protone les LMWH conduisant à la modification de leurs équilibre hydrophile / hydrophobe, générant alors un auto-assemblage.

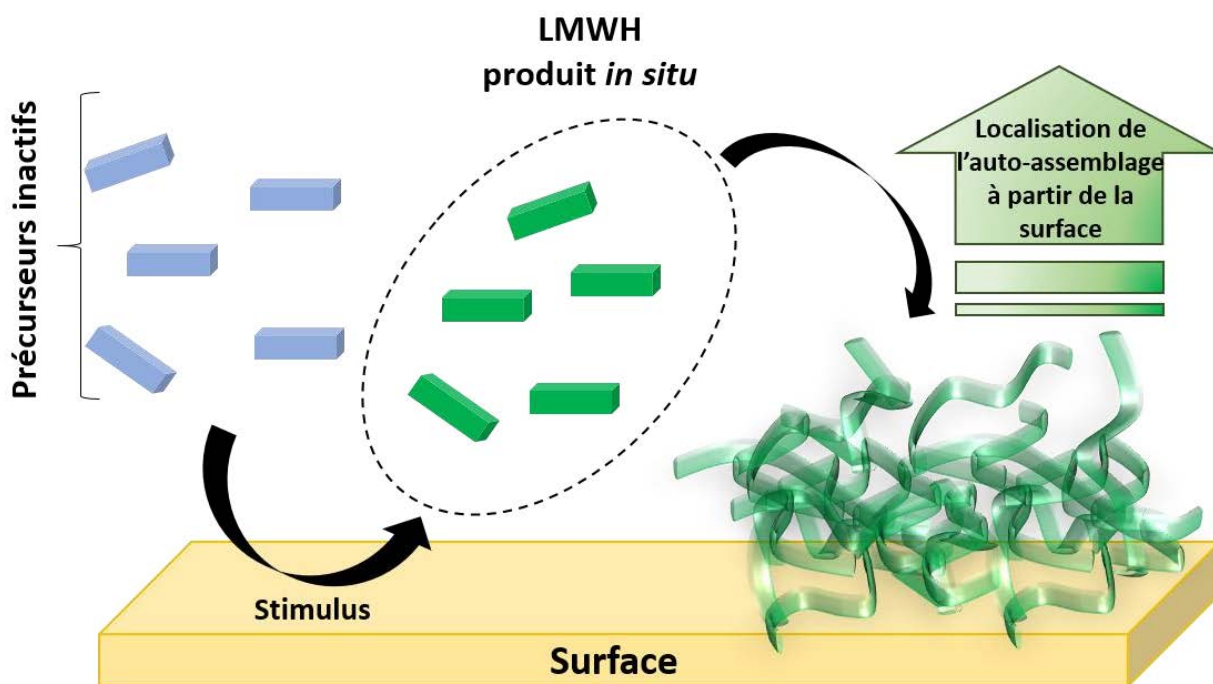


Figure 8: La surface catalytiquement active transforme les précurseurs inactifs en LMWH efficaces. L'accumulation locale de ce dernier au voisinage immédiat de la surface induit la formation d'un auto-assemblage dirigé.

En 2014, van Esch *et al.* ont rapporté une procédure permettant à l'aide de protons, de catalyser la transformation de LMWH en hydrogélateur *in situ*. Ils ont développé un moyen ingénieux de générer un hydrogel supramoléculaire de manière localisée en utilisant un catalyseur à micro-motifs sur une surface. Différentes formes de micro-motifs de catalyseurs ont été réalisées (lignes, cercles, carrés, etc.). Les auteurs ont observé que la forme de l'hydrogel suit de près le motif du catalyseur situé en dessous. Cette observation a été suivie par microscopie à fluorescence confocale *via* une sonde fluorescente ajoutée au mélange. Cette méthode permet d'obtenir une organisation de nanofibres sur plusieurs niveaux, ce qui est très prometteur pour des développements ultérieurs.

### 3) Déclenchement électrochimique de l'auto-assemblage de peptides sensible au pH

Une autre manière de produire *in situ* des hydrogélateurs est par voie électrochimique. Cette approche est l'une des plus utilisées pour la génération localisée d'auto-assemblage sur une surface. Le groupe de Cameron a mis au point, en 2010, une méthode pratique pour diriger l'auto-assemblage d'un peptide amphiphile aromatique (PA), Fmoc-LG-OH (L = leucine, G = glycine), dans une membrane d'hydrogel ultra-mince sur une électrode. L'auto-assemblage de l'hydrogélateur a été déclenché par une diminution du pH généré à l'électrode par oxydation électrochimique de l'hydroquinone en 1,4-benzoquinone, permettant la libération de deux protons. L'ajustement de l'intensité du courant affecte le pH près de la surface et a donc un impact sur l'auto-assemblage Fmoc-LG-OH, permettant ainsi un contrôle précis de la croissance du réseau fibreux.

Finalement, une dernière approche mettant en jeu la catalyse enzymatique a vu le jour en 2004 et permet elle aussi de localiser la formation d'auto-assemblages peptidiques à partir d'une surface. C'est cette dernière approche qui a fait l'objet de mes travaux de thèse et dont le principe est expliqué ici.

### 4) Auto-assemblage localisé de peptides assisté par des enzymes (LEASA)

Depuis 2004, la catalyse enzymatique est apparue comme un moyen efficace de déclencher l'auto-assemblage d'hydrogélateur à partir de LMWH à partir d'une surface. Même si l'auto-assemblage assisté par enzyme est largement répandu dans la nature pour permettre un contrôle spatial d'architectures complexes, l'immobilisation d'enzymes sur une surface pour produire localement des hydrogélateurs et obtenir une croissance localisée d'hydrogel en surface est un domaine qui a émergé récemment. Les enzymes utilisées

comme catalyseurs assurent une surface catalytique active permanente qui, en présence de précurseurs, conduit à une génération continue de molécules s'auto-assemblant. Ce contrôle autonome du taux de formation d'hydrogélateurs confiné à la surface peut contribuer au développement de surfaces intelligentes capables de diriger l'organisation de la matière dans l'espace et dans le temps.

Dans ce manuscrit, deux utilisations du LEASA sont décrites, à partir de surface plane et de surface non-planariaire.

#### 4.1. Auto-assemblage localisé assisté par enzyme (LEASA) sur surfaces planes

Il existe deux approches différentes pour créer des processus LEASA sur des surfaces planes: l'une en greffant de manière covalente l'enzyme sur la surface et l'autre en les adsorbants de manière électrostatiques.

##### 4.1.1. LEASA par liaison covalente des enzymes

En 2009, Ulijn a été le premier à immobiliser une enzyme, la thermolysine, liée de manière covalente sur une surface afin d'induire l'auto-assemblage localisé d'un mélange composé de Fmoc-L-OH et de LL-OH (Figure 9). La thermolysine est capable de catalyser à la fois la réaction de couplage entre Fmoc-L-OH et LL-OH et l'hydrolyse des liaisons amides entre les différents amino acids, conduisant à une distribution statistique des oligopeptides Fmoc-(L)<sub>n</sub>-OH. Les peptides résultants s'auto-assemblent et forment un réseau fibrillaire. Au cours des premières étapes du processus d'auto-assemblage, la formation des nanofibres a été observée à partir des agrégats d'enzymes présents sur la surface. Ce travail pionnier a montré que le confinement d'enzymes sur une surface

constitue une stratégie efficace pour générer et orienter localement la croissance de réseau fibrillaire d'hydrogélateurs à l'interface liquide/surface.

Plus récemment, le même groupe a montré l'effet de la force d'ancrage d'une enzyme à la surface sur le processus d'auto-assemblage. En utilisant à nouveau la thermolysine et le système Fmoc-T-OH / F-NH<sub>2</sub> (T = thréonine, F-NH<sub>2</sub> = phénylalanine avec un groupe carboxamide en position C-terminale), formant *in situ* l'hydrogélateur Fmoc-TF-NH<sub>2</sub>, ils ont montré qu'ils pouvaient diriger l'auto-assemblage à partir d'une surface en liant de manière covalente l'enzyme mais également en l'adsorbant. Lorsque les enzymes sont liées de manière covalente à la surface, l'hydrogel résultant est plus mince que lorsque les enzymes ne sont qu'adsorbées. L'hypothèse postulée est que, lorsqu'elles ne sont qu'adsorbées en surface, les enzymes se désorbent pendant le processus d'auto-assemblage, ce qui conduit à une formation plus épaisse d'hydrogel (figure 9).

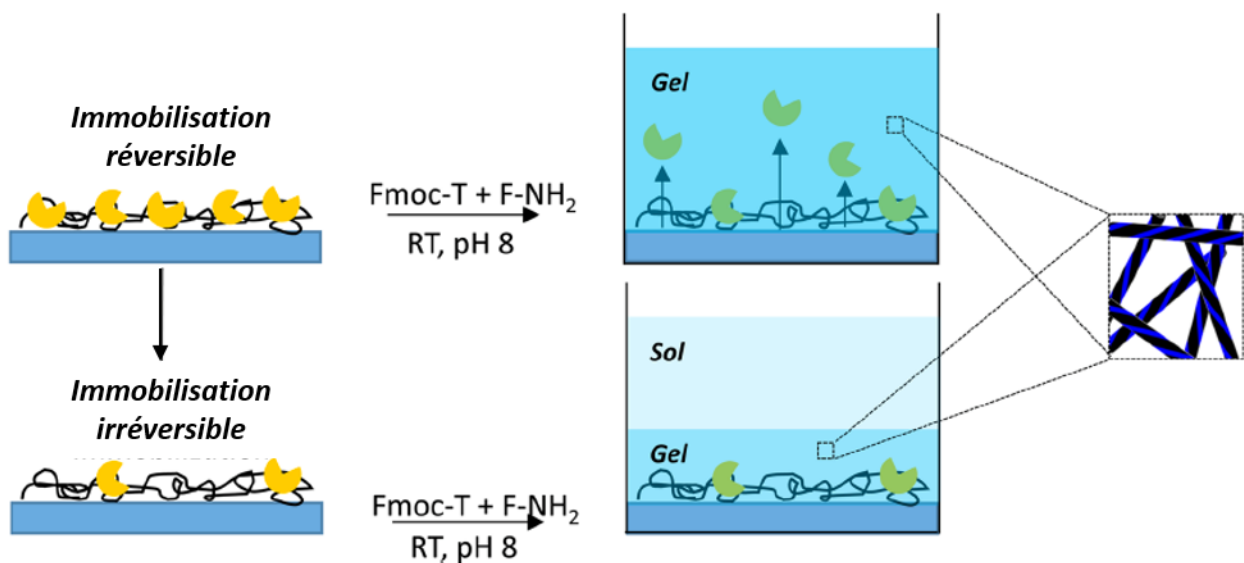


Figure 9 : Représentation schématique de l'immobilisation d'enzymes de manière réversible et irréversible sur des surfaces pour la génération de LEASA

#### 4.1.2. LEASA par adsorption des enzymes sur la surface

En 2011, Williams *et al.* ont rapporté la localisation de l'auto-assemblage de l'hydrogélateur Fmoc-L<sub>3</sub> en adsorbant de la thermolysine sur un substrat de verre. Lorsqu'une solution contenant les deux précurseurs Fmoc-L-OH et LL-OH avec une protéine de poisson, la laminine, était déposée sur le substrat de verre modifié, les auteurs étaient en mesure de diriger l'auto-assemblage depuis la surface, mais aussi de piéger la laminine dans le réseau fibreux résultant. Les auteurs ont également montré la possibilité d'injecter l'hydrogel contenant la laminine chez le poisson zèbre dans une zone de tissu touchée par une maladie détruisant la matrice extracellulaire. Cette approche est intéressante pour traiter les maladies génétiques impliquant la famille des gènes de la laminine.

En 2017, Vigier-Carrière *et al.* ont établi que l' $\alpha$ -chymotrypsine confinée sur une surface est capable d'oligomériser les dipeptides d'ester éthylique KL-OEt (K = lysine, OEt = groupe éthyle ester en position C-terminale) et de produire des oligopeptides (KL)<sub>n</sub>-OEt, en surface. La croissance du réseau d'auto-assemblage commence après un temps de latence qui peut facilement être réglé en faisant varier la densité d' $\alpha$ -chymotrypsine en surface et la concentration de KL-OEt en solution. L'épaisseur du réseau de fibres formé peut atteindre environ 10  $\mu$ m. Les images *Cryo*-SEM montrent que le réseau de gel est plus dense à l'interface que loin de l'interface (Figure 10), ce qui confirme que la concentration d'hydrogélateurs est plus dense près de la surface. En ce qui concerne l'épaisseur atteinte, ce résultat confirme les travaux du groupe d'Ulijn sur la désorption des enzymes. Cependant, la quantité désorbée doit être inférieure à celle de la surface pour observer une telle densification près de l'interface.



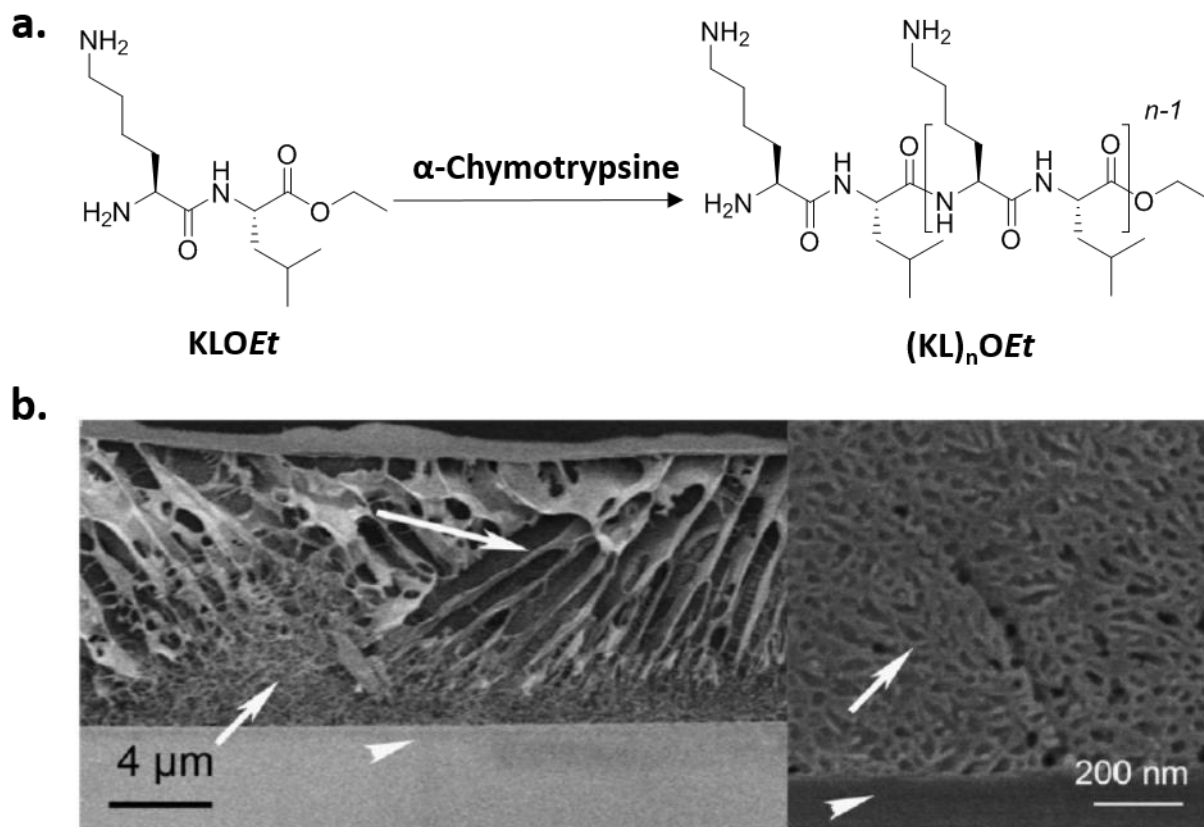


Figure 10: Oligomérisation de KL-OEt en (KL)<sub>n</sub>-OEt catalysée par l' $\alpha$ -chymotrypsine, b) Images Cryo-SEM de l'hydrogel à base de (KL)<sub>n</sub>-OEt en section z.

Néanmoins, lorsqu'une concentration initiale de précurseurs trop faible est présente près de la surface active, aucun gel ne se forme. En utilisant le peptide Fmoc-FFY (PO<sub>4</sub><sup>2-</sup>)-OH (molécule 12), Vigier-Carrière *et al.* pour contourner cette difficulté ont modifié la surface avec un film mince nano-architecturé comprenant de la phosphatase alcaline et une couche de polyélectrolytes portant des peptides Fmoc-FFC, C (qui représentant la cystéine) a été utilisé comme agent de liaison entre l'hydrogélateur, Fmoc-FFY (13) et le polyélectrolyte. Le polyélectrolyte modifié ainsi obtenu joue le rôle de couche d'ensemencement (figure 10.b). Ensuite, lorsque AP déphosphoryle 12 en 13, l'auto-assemblage se produit à une concentration inférieure à la concentration de gélification critique, ce qui conduit à un hydrogel reposant sur un réseau de nanofibres (figure 10.c). La

variation de la densité d'enzymes dans le nanofilm ou de la densité de surface des peptides d'ensemencement à la surface a fourni différents types d'architectures de nanofibres (Figure 10.c).

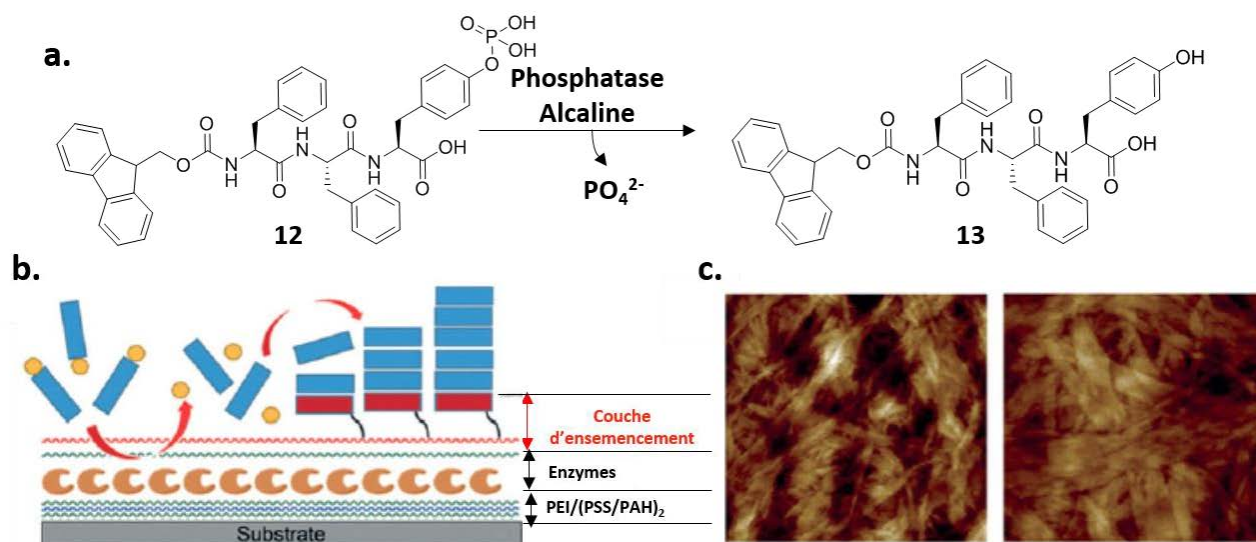


Figure 11: a) Structures chimiques des molécules 12 et 13, b) Représentation schématique du film nanoarchitecturé sur une surface, permettant l'auto-assemblage localisé assisté par enzymes basé sur une couche d'ensemencement, c) Images AFM de l'hydrogel formé à partir de la surface.

En résumé, ces deux approches, la liaison covalente et non covalente d'enzymes en surface pour générer des auto-assemblages localisés, constituent de puissants outils pour réaliser un auto-assemblage contrôlé à partir de surfaces. Les épaisseurs atteintes sont différentes selon l'approche choisie, comme l'a souligné le groupe d'Uljin. Pour faciliter la formation de l'auto-assemblage, l'utilisation d'une couche d'ensemencement bioactive est utile et permet de contrôler à la fois la cinétique du réseau de formation et les morphologies des fibres.

Plus récemment, l'utilisation de LEASA a également été décrite pour initier un auto-assemblage à partir de surfaces non planes.

## 4.2. Auto-assemblage localisé assisté par enzyme (LEASA) sur surfaces non-planaires (surface de nanoparticules)

Dirigé un LEASA à partir d'une surface non plane n'avait pas encore été rapporté lorsque j'ai commencé mon doctorat. Cependant, je vais présenter cette approche qui présente un intérêt en ce qui concerne l'intérêt de la localisation d'auto-assemblage à partir de surface. En 2018, c'est le groupe d'Uljin qui a décrit pour la première fois dans la littérature l'immobilisation d'enzymes, *via* des liaisons covalentes avec la surface, sur des nanoparticules magnétiques (NP) afin de localiser spatialement l'initiation de l'auto-assemblage de peptides en nano-fibres autour des NPs. Les auteurs ont généralisé le concept sur tout type de surfaces et ils ont démontrés qu'il été applicable à un système biocatalytique à l'équilibre formant des hydrogels stables comme à un système n'atteignant jamais un équilibre, possédant une durée de vie prédéfinie. Le système 1 est le système à l'équilibre, thermodynamiquement stable, qui utilise la thermolysine pour la condensation enzymatique réversible des précurseurs peptidiques (Fmoc-T et F-NH<sub>2</sub>) afin de former l'hydrogélature Fmoc-TF-NH<sub>2</sub> (Figure 12). Le système 2 est le système n'atteignant pas d'équilibre thermodynamique, contrôle cinétique, qui utilise la chymotrypsine afin de générer l'association mais aussi la dissociation des hydrogélature par le biais de réactions d'acylation et d'hydrolyse concurrentes. Les précurseurs du système 2 sont le DF-OMe et le F-NH<sub>2</sub> conduisant à l'hydrogélature DFF-NH<sub>2</sub>. Pour les deux systèmes, ils ont obtenu des réseaux de fibres stables à la surface des NP (Figure 13). Ensuite, en utilisant les propriétés magnétiques de leurs NPs, ils ont montré que le processus d'hydrogélature peut être inhibé ou activé en fonction de la position d'un aimant et donc de la répartition des NPs dans le milieu.

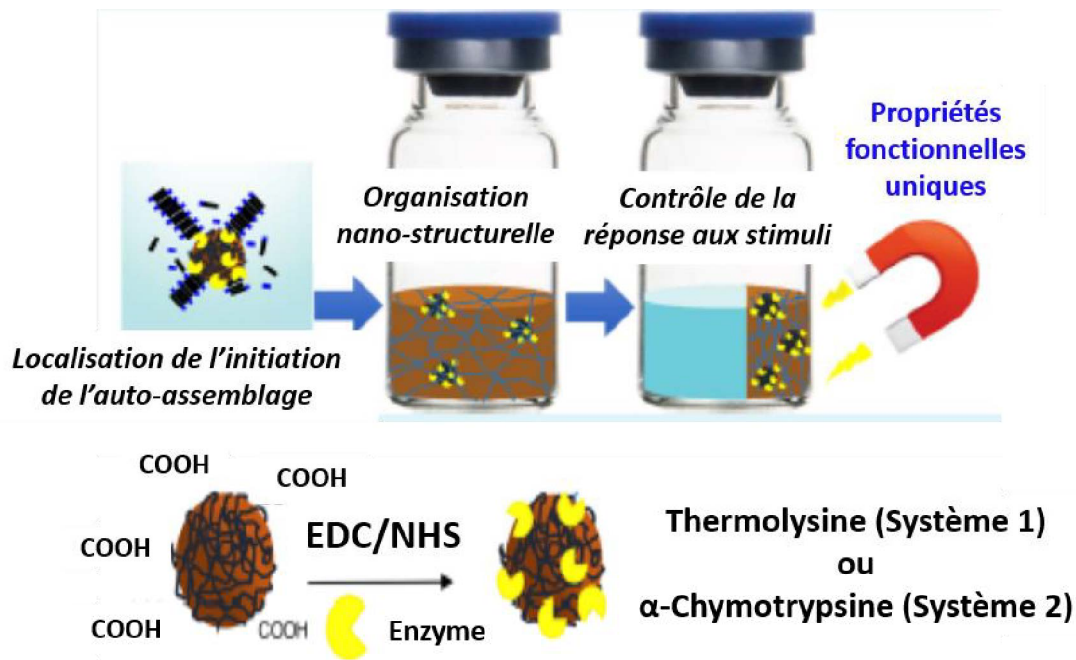


Figure 12: Représentation schématique de l'initiation localisée de l'auto-assemblage sur les NPs magnétiques et de la manipulation externe de l'hydrogel formé avec un aimant, permise par l'immobilisation de l'enzyme sur les NPs utilisées pour les systèmes 1 et 2.

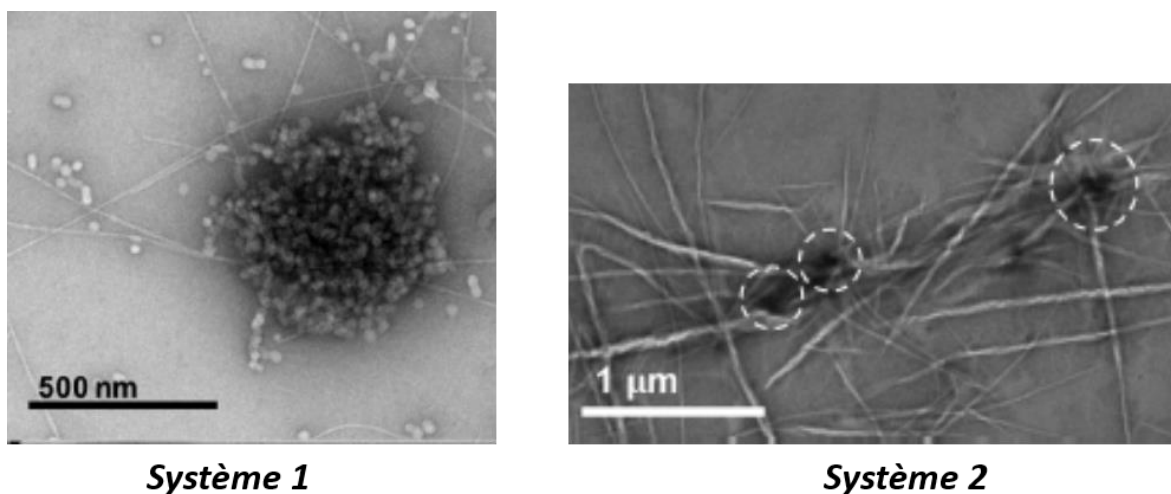


Figure 13: Images TEM du réseau de fibres initié à partir de la surface des NPs pour le système 1 (gauche) et le système 2 (droite).

Wang *et al.* ont démontré récemment (2018) la formation d'un nano-hydrogel de type core-shell, formé par catalyse enzymatique et dont l'épaisseur de l'enveloppe externe est ajustable par contrôle sur l'auto-assemblage d'hydrogélateurs à la surface de

nanoparticules de silicium (core). Les nano-hydrogels qu'ils ont conçus agissent comme des supports biocompatibles pour l'administration de médicaments. Ils ont testé cette capacité en utilisant un médicament modèle, le chlorhydrate de doxorubicine (DOX), un inhibiteur bien connu de la prolifération cellulaire, soluble dans l'eau, qui leur a permis de la piéger pendant la formation de l'auto-assemblage. L'auto-assemblage est destructible par l'action enzymatique de la protéinase K libérée par les cellules. En effet, lors des tests sur cellules, les auteurs ont observé que le nano-hydrogel était localisé principalement dans les cellules cancéreuses contrairement au médicament libre (Figure 14). Cela s'explique par une absorption sélective des nano-hydrogels par les cellules tumorales, permettant une administration du médicament plus spécifique. Néanmoins, l'expérience avec la DOX libre conduit à une meilleure mortalité des cellules cancéreuses (viabilité de 28,7%) par rapport aux nano-hydrogels chargés de DOX (viabilité: 46,2%). Cette publication montre que l'utilisation de LEASA est très prometteuse dans des applications en médecine.

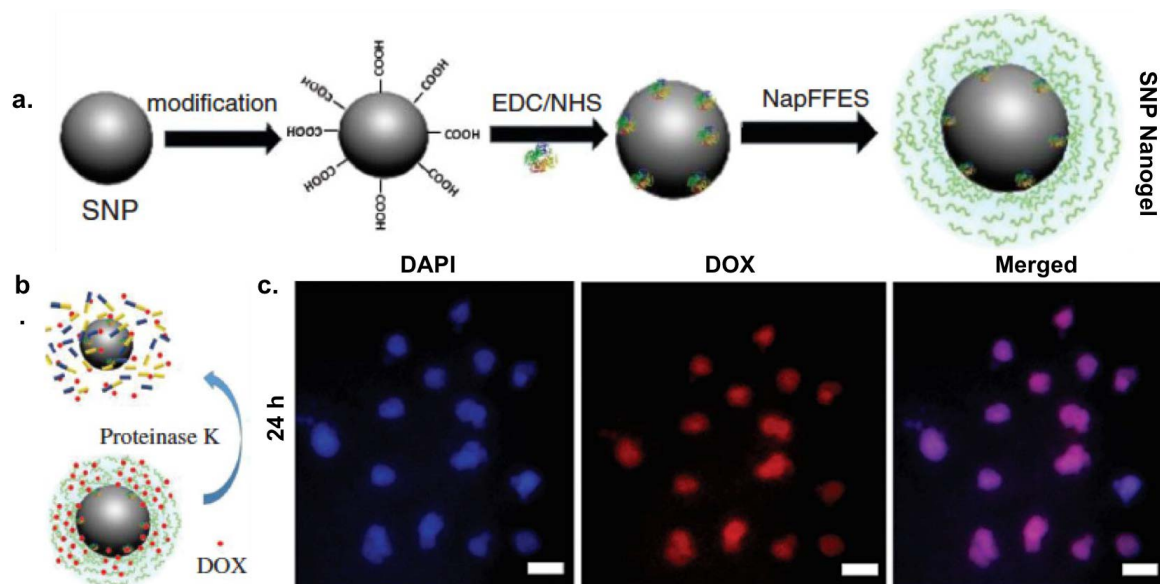


Figure 14: a) Représentation schématique de la préparation des nanogels « core-shell » par l'hydrogel supramoléculaire localisé sur des nanoparticules de SiO<sub>2</sub> (SNP), b) Représentation schématique de la libération de DOX par des nanogels chargés de DOX à 37 ° C dans du PBS et en présence de protéinase K, c) Images confocales de cellules HeLa incubées avec les nanogels chargés de DOX pendant 24 h. Les images de gauche à droite affichent les noyaux des cellules colorés avec DAPI (bleu), la fluorescence DOX dans les cellules (rouge) et leur chevauchement. Barres d'échelle = 10 µm.

En résumé, en immobilisant des (bio)-catalyseurs sur des nanoparticules, il est possible en localisant la nucléation de l'auto-assemblage de localiser la formation des nanofibres. Cette localisation permet d'améliorer non seulement les propriétés mécaniques d'un réseau d'hydrogel nanofibreux et de contrôler le moment de sa formation et de sa durée de vie mais aussi de conférer une réponse nanostructure auto-assemblée à des stimuli ouvrant le champ des applications possibles de tels systèmes. Ces matériaux apportent des avancées supplémentaires dans la science des matériaux pour trouver d'autres applications potentielles, telles que la conception de systèmes de propulsion, la fabrication de nanodispositifs, l'administration de médicaments de manière localisé et spécifique ou encore pour le traitement de cancer ou la réparation ciblée d'organes ou de tissus.

#### 4.2. LEASA localisé sur la membrane des cellules

Une autre approche qui est de plus en plus utilisée est le LEASA dans un environnement cellulaire. Les cellules contiennent des enzymes situées à l'intérieur et sur leur membrane. Cette localisation des enzymes, de manière intrinsèque aux besoins de la cellule, a été étudiée comme une autre approche LEASA menant à des applications biologiques telles que le piégeage de cellules tumorales.

Le groupe du professeur Bing Xu a rapporté le premier exemple de LEASA à la surface de cellules en 2014. L'auto-assemblage a été généré par la transformation du précurseur Nap-D-Phe-D-Phe-D-p-tyr (DDD-1P) en un hydrogélateur, le Nap-D -Phe-D-Phe-D-Tyr (DDD), par la phosphatase alcaline présente sur la membrane cellulaire. L'auto-assemblage généré par l'AP a permis de piéger la cellule, entraînant sa mort. Les cellules cancéreuses sur-expriment les phosphatases par rapport aux cellules normales, ce qui

conduit à une sélectivité plus élevée des cellules cancéreuses pour la formation de l'hydrogel (Figure 15.a). D'autres exemples sont présents dans la littérature utilisant le LEASA pour induire la mort cellulaire en localisant la formation d'auto-assemblage autour des cellules ou à l'intérieur de celle-ci (Figure 15.b).

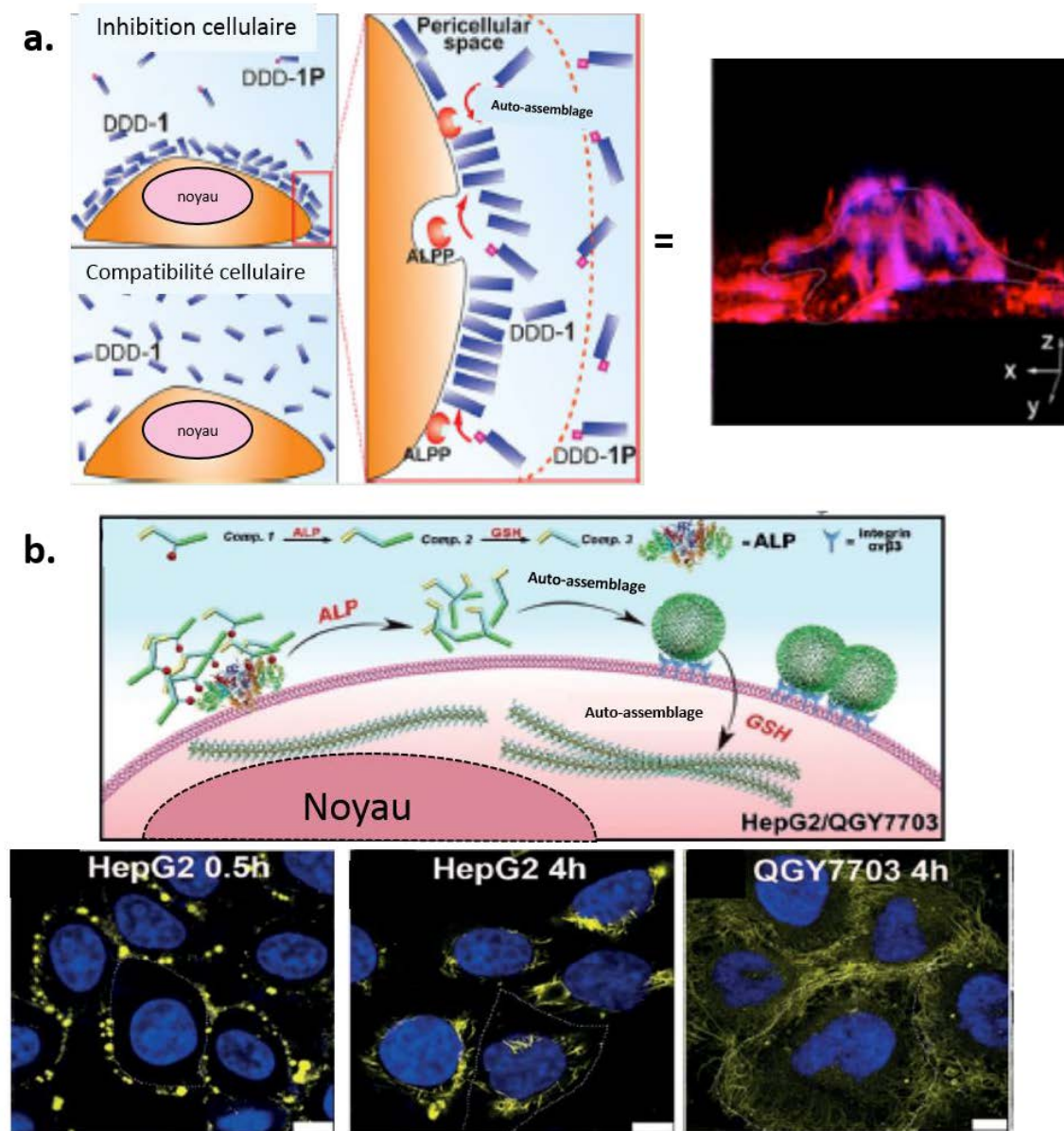


Figure 15: a) Schéma du principe de LEASA à la surface des cellules conduisant au piégeage des cellules HeLa par le réseau fibreux étiqueté en rouge Congo représenté sur l'image confocale.115. Copyright © 2014 American Chemical Society. b) Mode proposé d'un auto-assemblage moléculaire en tandem dans l'environnement extracellulaire et intracellulaire de cellules cancéreuses du foie soutenu par les images de microscopie confocale fusionnées (la fluorescence bleue de Hoechst 33342 et la fluorescence jaune de NBD représentent respectivement le noyau et le peptide de NBD) de cellules HepG2 et QGY7703 incubées avec le précurseur pendant différentes périodes. Barres d'échelle = 10  $\mu$ m. La ligne pointillée blanche indique la limite d'une cellule.

Les recherches sur les auto-assemblages supramoléculaires ont connu une croissance rapide au cours de la dernière décennie, comme en témoigne le fait que le nombre d'ouvrages publiés sur l'auto-assemblage supramoléculaire en 2019 est environ 10 fois celui de 2004, selon le site web of science. Comme l'illustrent les auto-assemblages supramoléculaires présentés dans cet état de l'art, les recherches dans ce domaine vont de la simple curiosité envers un type intrigant de matière molle au développement rationnel de biomatériaux moléculaires aux applications multiples. En particulier, l'auto-assemblage assisté par enzyme localisée est une approche attrayante pour déclencher des processus d'hydrogélotion. La catalyse enzymatique est hautement sélective, capable de transformer en continu des molécules précurseurs en hydrogéloteurs. Ce contrôle autonome du taux de formation d'hydrogéloteurs qui peut être confiné aux surfaces contribue au développement de surfaces intelligentes capables de diriger l'organisation de la matière dans l'espace et dans le temps.

Parmi toutes les stratégies décrites dans ce manuscrit, les peptides aromatiques ou les acides aminés protégés sont les plus utiles pour les processus d'auto-assemblage assisté en surface. Cet état de l'art a mis en évidence trois stratégies principales mises en œuvre à cet effet. Premièrement, des surfaces greffées avec des entités chimiques ont été utilisées afin de créer de nouveaux environnements d'interactions pour de petits blocs de construction situés à proximité de la surface. Dans une deuxième stratégie, des hydrogels sensibles au pH à partir d'une surface ont été intensément développés pour la formation *in situ* de blocs de construction à assemblage autonome. La diminution du pH est confinée au voisinage de la surface par un signal électrique ou une lithographie de molécules spécifiques. Enfin, dans une troisième stratégie, des enzymes naturelles ont été utilisées comme stimuli hautement sélectifs et efficaces, capables de catalyser la formation de blocs de construction auto-assemblés sur des surfaces planes ou non planes.



Cette dernière approche a été publiée pour la première fois en 2009 et a été appliquée aux systèmes biologiques plus récemment (en 2014). Durant les trois années de mon doctorat, mes travaux de recherche étaient basés sur cette troisième stratégie afin de concevoir des surfaces sophistiquées présentant des propriétés catalytiques ou présentant un intérêt biologique.

## De l'étude du mécanisme ...

L'idée initiale du projet décrit dans cette partie était de réguler de manière dynamique la croissance de nanofibres auto-assemblées en utilisant deux enzymes ayant des activités antagonistes. Un peptide précurseur contenant un pont disulfure a été préparé, conduisant à un hydrogélateur contenant un thiol lorsque la liaison SS est réduite. Le couple d'enzymes choisies était la glutathion réductase et la glutathion peroxydase capable de «casser» et de «reformer» le pont disulfure du peptide, respectivement. Les activités enzymatiques de ce couple peuvent à la fois assurer la formation des hydrogélateurs disponibles et la croissance / désassemblage des nanofibres obtenues (Figure 16).

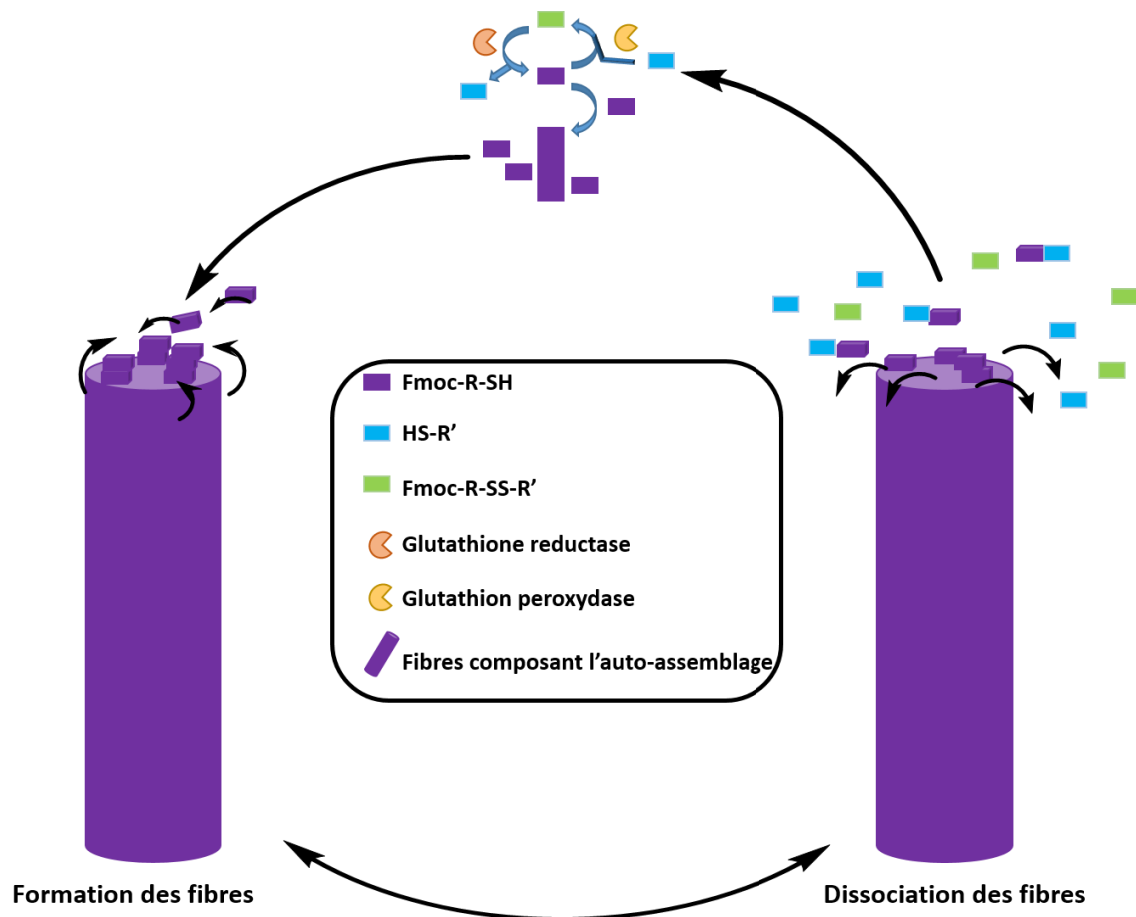


Figure 16: Schéma de la formation et de la dissociation des nanofibres auto-assemblées en présence du couple d'enzymes antagonistes.

Cependant, nous avons observé que lorsque le peptide précurseur contenant le pont disulfure est en présence de protéines catalytiquement non actives (expérience de contrôle négatif), un hydrogel se forme spontanément comme observé en présence de glutathion réductase. Ce résultat n'était pas attendu. Cela nous intriguait particulièrement et nous avons donc décidé de chercher plus loin pour répondre aux questions suivantes: quel est le mécanisme de ce nouveau type de processus d'auto-assemblage assisté par protéine? Quel est le rôle de la protéine dans l'initiation de l'auto-assemblage? Comment une protéine non catalytiquement active réduit-elle un pont disulfure?

Dans le chapitre 3 de ce manuscrit, je propose quelques réponses possibles à ces questions, en introduisant une nouvelle stratégie pour contrôler les processus d'auto-

assemblage de manière spatio-temporel. Elle repose sur la présence simultanée de protéines possédant ou non une activité catalytique, de LMWH et son précurseur, tous deux en équilibre dynamique via une liaison réversible (ici une liaison disulfure). L'interaction du précurseur avec la protéine déclenche un processus d'auto-assemblage qui conduit à l'établissement d'un cycle auto-entretenu dans lequel une génération continue d'hydrogélateurs induite par le processus d'auto-assemblage lui-même. Cette approche semble étroitement liée au concept de la chimie dynamique combinatoire.

Le peptide utilisé est un peptide original, le Fmoc-GFFYE-NH- $(\text{CH}_2)_2$ -SH, appelé Fmoc-**A**-SH, inspiré de la littérature. Le groupe protecteur N-Fluorénylméthoxycarbonyl (Fmoc) a été ajouté à la position N-terminale pour améliorer la capacité de l'hydrogélateur correspondant Fmoc-**A**-SH à s'auto-assembler. Lorsque le groupe thiol de ce peptide est protégé par un pont disulfure, le Fmoc-**A**-SS-**B** résultant (Fmoc-GFFYE-NH- $(\text{CH}_2)_2$ -SS- $(\text{CH}_2)_2$ -NHCO- $(\text{CH}_2)_2$ -CO-EE-OH) n'est pas capable de s'auto-assembler en raison de la séquence B fortement chargée négativement. Lorsque 10 mg/mL (7,3 mmol) de Fmoc-**A**-SS-**B** sont dissous dans du tampon PBS (pH 7,4) à 25 °C, aucune hydrogel ne se forme, même après 48 heures, comme prévu. Les chromatogrammes de HPLC contrôlant la composition chimique de cette solution dans le temps montrent qu'un équilibre thermodynamique entre Fmoc-**A**-SS-**B** et Fmoc-**A**-SH est rapidement établi (moins de 2 minutes). À l'équilibre, 10% de Fmoc-**A**-SH sont présents et 90% de Fmoc-**A**-SS-**B** constituent le composé principal. Bien entendu, Fmoc-**A**-SS-**A**-Fmoc et **B**-SS-**B** sont également présents dans le mélange: Fmoc-**A**-SS-**A**-Fmoc est présent au niveau de trace et **B**-SS-**B** n'est pas détectable par notre détecteur UV.

Pour obtenir un hydrogel supramoléculaire à partir d'une solution de Fmoc-**A**-SS-**B** (10 mg/mL), le pont disulfure doit être réduit et la glutathion réductase (GR, 1 mg/mL) a été choisie pour jouer ce rôle. Étant donné que l'initiation de la formation de l'hydrogel devrait

dépendre de la production suffisante de Fmoc-**A**-SH (pour atteindre sa concentration critique de gélation), nous avons suivi sa formation par HPLC dès l'introduction de GR dans le flacon. La formation de l'hydrogel est qualitativement observée par un simple test d'inversion de flacon. Fmoc-**A**-SS-**B** disparaît au cours des premières minutes et corrélativement la formation de Fmoc-**A**-SH est observée. Environ deux minutes après l'addition de GR, il se forme 100% de l'hydrogélisateur Fmoc-**A**-SH et on obtient un gel possédant un module d'élasticité  $G_0$  proche de 1 kPa.

Pour démontrer le rôle catalytique de l'enzyme dans le processus de gélation, une autre enzyme incapable de scinder le pont disulfure du Fmoc-**A**-SS-**B**, la phosphatase alcaline (AP), a été utilisée à la place de la protéine GR et la même étude par HPLC a été réalisée. Comme prévu, aucun gel ne s'est formé même 60 minutes après l'addition de AP (1 mg/mL) dans la solution de Fmoc-**A**-SS-**B** (10 mg/mL). Cependant, le suivi par HPLC a révélé la formation de Fmoc-**A**-SH, plus lentement qu'avec GR, mais atteignant néanmoins une transformation chimique complète (à partir de Fmoc-**A**-SS-**B**) après une heure. Afin de vérifier si ce résultat inattendu peut être étendu à d'autres protéines que l'AP, nous avons mis une solution de Fmoc-**A**-SS-**B** fraîchement préparée en contact avec de l'albumine provenant de sérum bovin (BSA, 1 mg/mL). En dépit d'une cinétique plus lente de la formation de Fmoc-**A**-SH que de celle de l'AP, Fmoc-**A**-SS-**B** a finalement presque complètement disparu au bout d'une heure, mesurée par HPLC, mais aucun gel ne s'est formé même 24 heures plus tard. La réduction plus rapide de Fmoc-**A**-SS-**B** catalysée par GR étant peut-être impliquée dans l'efficacité du processus de gélation, 1 équivalent de l'agent réducteur (tris (2-carboxyéthyl) phosphine) (TCEP) a été ajouté à une solution de Fmoc-**A**-SS-**B** pour vérifier cette hypothèse: la HPLC met en évidence une conversion complète instantanée en Fmoc-**A**-SH mais aucune gélation n'a été observée, même après une heure. Une conversion complète en Fmoc-**A**-SH a également été observée par HPLC

quand 1 équivalent molaire de dithiothréitol (DTT) ou de glutathion (GSH) était utilisé à la place du TCEP sans formation de gel comme pour le TCEP. Le système a donc été étudié de manière plus approfondi et les résultats ainsi que l'hypothèse émise sur le mécanisme de l'auto-assemblage sont décrit en détails dans le chapitre 3.

## ... aux applications

Il y a neuf ans, mon groupe d'accueil a introduit un nouveau concept sur l'accumulation de film localisé sur la surface d'électrode basé la formation d'un gradient électrochimique de catalyseurs. Le catalyseur  $\text{Cu}^+$  a été produit par la réduction de  $\text{Cu}^{2+}$ , permettant de catalyser la réticulation covalente de polymères par chimie clic. La réticulation des polymères conduit à la formation d'un nanofilm mince sur l'électrode (Figure 17 à gauche). La formation contrôlée de manière spatiale de ce catalyseur est responsable de la localisation de la formation du film polymère. Par analogie avec le terme utilisé dans le domaine du développement de la biologie, ce catalyseur a été appelé «morphogène». Cette stratégie a été étendue à d'autres types de morphogènes: (i) en utilisant des composés bis-quinones générés à partir de dérivés de bis-catéchol oxydés *in situ* à la surface d'une électrode conduisant à l'accumulation de film mince de polymères recouvrant la surface de l'électrode par réticulation de polyamines (Figure 17 milieu). (ii) En utilisant l'oxydation du  $\text{Fe}^{2+}$  en  $\text{Fe}^{3+}$  par un courant anodique, il est également possible de créer une couche organométallique sur l'électrode par complexation du Fer (III) avec de l'acide tannique (Figure 17, à droite). (iii) Enfin, la production de protons à partir d'une électrode par oxydation à l'hydroquinone a permis la constitution de films à base de polyélectrolytes à l'aide de polymères à transfert de charge.

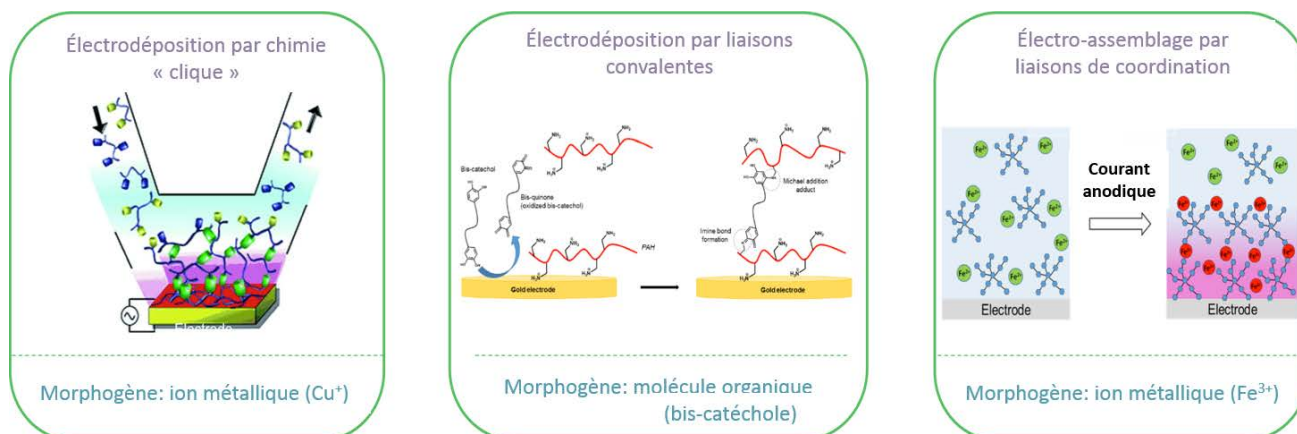


Figure 17 : Stratégies développées pour initier un auto-assemblage localisé d'un film polymère par électrochimie

L'inconvénient principal de l'utilisation d'une électrode pour initier la localisation de l'auto-assemblage de films mince est la nécessité d'un matériau conducteur pour produire le gradient de morphogènes. Cela réduit considérablement le champ d'application de cette stratégie. Pour surmonter l'utilisation de surfaces conductrices, mon objectif était de développer un film multicouche enzymatiquement actif capable de générer un gradient de morphogènes.

Dans le chapitre 4 de ce manuscrit, je présente un moyen pratique de produire un gradient de proton à partir d'une surface non conductrice en utilisant un film multicouche enzymatiquement actif.

L'auto-assemblage décrit est celui d'un dipeptide initié par un gradient continu de protons produits par voie enzymatique à partir d'une surface non conductrice. Notre système modèle est composé de (i) du dipeptide Fmoc-AA-OH, un LMWH déjà décrit comme un hydrogélateur en conditions acides et (ii) de la glucose oxydase (GOx), une enzyme produisant des protons par la transformation de glucose en acide gluconique en présence d'oxygène. L'immobilisation de la GOx en surface dans un film multicouche permet la production de protons en présence de glucose. Lorsque le dipeptide Fmoc-AA-

OH diffuse vers l'interface, son groupe carboxylate C-terminal est protoné, ce qui induit spontanément son auto-assemblage, uniquement à l'interface. La modification de la surface par le film multicouche contenant la GOx et l'évolution du processus d'auto-assemblage dans le temps ont été suivies à la fois par microbalance à cristal de quartz (QCM-D) et par spectroscopie infrarouge à transformée de Fourier (ATR-FTIR). La morphologie des architectures auto-assemblées a été étudiée par microscopie à force atomique (AFM), microscopie électronique à balayage (MEB) et *cryo*-MEB.

Dans le chapitre 5, l'approche LEASA a été utilisée pour la conception de réacteurs pour des processus de chimie en flux. En effet, les hydrogels supramoléculaires fabriqués à partir de LMWH sont des matériaux mécaniquement fragiles. Il semble donc difficilement envisageable de les envisager pour des transformations chimiques à grande échelle. Si l'hydrogel supramoléculaire est supporté par un matériau plus robuste, il devient plus facile à manipuler et ce problème peut ainsi être contourné. Dans ce chapitre, cet aspect est décrit mais également une autre propriété des hydrogels supramoléculaires: les propriétés catalytiques émergent de l'assemblage d'hydrogélateurs peptidiques appropriés. Cela donne lieu à une fonctionnalité au matériau résultant.

Dans la deuxième partie de ce chapitre, je présente les résultats préliminaires prometteurs obtenus dans la conception de la croissance autonome d'hydrogel par les propriétés d'autocatalyse de l'hydrogel. Ce développement est basé sur les réalisations de la première partie du chapitre.

Pour offrir une robustesse mécanique à des matériaux très mous tels que les hydrogels, l'utilisation de mousses polymères comme squelette interne pour rigidifier la matière est une approche intéressante. Dans le cas des hydrogels à base de peptides, un

premier problème technologique à résoudre est le problème spatial. La localisation de la croissance de l'hydrogel à partir de la surface de la mousse de polymère afin de lier l'hydrogel au polymère. Ceci peut être réalisé en immobilisant un (bio) catalyseur sur la surface de la mousse. Dans ce projet, nous avons utilisé l'approche par LEASA. Le confinement des blocs de construction à l'interface matériau-eau induit la croissance de nanofibres ancrées à la surface et supportant l'hydrogel.

Le développement d'un CASH supporté repose sur le choix approprié du précurseur devant remplir deux conditions essentielles: (i) générer des dérivés auto-assembleurs en présence d'une enzyme adéquate et (ii) donner un hydrogel supramoléculaire présentant une activité catalytique. Jusqu'à présent, aucun précurseur de ce type d'hydrogélateur de faible poids moléculaire (LMWH) n'a été décrit.

La chimie en flux continu semble particulièrement bien adaptée aux applications CASH puisque le flux à travers l'hydrogel catalytique compense le faible taux de diffusion des substrats dans des conditions statiques (réduisant ainsi le temps de réaction) et fournit également un moyen de séparation facile entre les produits et la phase catalytique. Ces caractéristiques ne sont pas évidentes car les hydrogels supramoléculaires sont des gels physiques résultant de l'auto-assemblage de petites molécules et, par conséquent, un décollement progressif du CASH par la contrainte de cisaillement induite par l'écoulement est un scénario impossible à exclure à première vue. Pourtant, un CASH supporté sur une mousse s'est révélé stable en termes de débit et dans le temps et le processus catalytique pouvait être répété plusieurs fois sans aucune perte catalytique. Le CASH-supporté que nous avons conçu donne naissance à un hydrogel de type estérase efficace, actif vis-à-vis des esters activés mais également vis-à-vis d'un large éventail de substrats inactivés tels que les classes d'ester méthylique, primaire, secondaire et tertiaire, caractéristique qui n'a jamais été rapportée, ce qui accroît son intérêt pour le chimiste. Dernier point mais non le



moindre, notre CASH supporté montre également une capacité de résolution cinétique permettant d'isoler une quantité quantitative d'acides carboxyliques énantiopurs à partir d'esters inactivés racémiques ou énanti-enrichis. Ainsi, nous pensons que cette découverte peut trouver un écho dans diverses communautés de chimistes allant de la chimie de synthèse à la science des matériaux et au génie chimique.

Dans le dernier chapitre de ce manuscrit, l'étude visait à concevoir de nouveaux hydrogels composites en combinant un auto-assemblage peptidique avec les propriétés biologiques favorables de l'acide hyaluronique naturel afin d'obtenir une gamme de propriétés morphologiques convenant aux biologistes pour les utiliser comme substrat de culture cellulaire et pour comprendre les interactions entre les différents composants. Au fur et à mesure que la quantité de HA dans les hydrogels composites augmente, la dureté des matériaux résultants diminue et la viabilité des cellules de fibroblastes NIH 3T3 diminue également. En microscopie CD, FT-IR, fluorescence, confocale et SEM, nous avons démontré que l'HA interagit avec l'auto-assemblage du peptide au niveau moléculaire, même si les deux molécules sont chargées négativement. Nous avons également compris que le milieu dans lequel se forment les hydrogels composites revêt une importance capitale pour leurs propriétés. Cette affirmation semble évidente, mais dans la plupart des publications, les hydrogels sont formés dans un tampon, puis la culture cellulaire est effectuée avec un autre milieu au-dessus de celui-ci. Cependant, l'engagement d'échange de milieux effectué lors de la culture cellulaire n'est pas mentionné même si, comme nous le montrons, il représente un point critique car il influence les propriétés telles que les propriétés mécaniques de l'hydrogel. En raison de la possibilité d'ajuster finement de nombreux paramètres et des applications étendues en biomédecine et en biotechnologie, nous pensons que notre contribution peut trouver un écho dans diverses communautés de chimistes et de biologistes allant de la science des matériaux à la bio-ingénierie.

En conclusion, ma contribution au cours des trois dernières années dans ce domaine peut être divisée en quatre axes:

1. Le renforcement des propriétés mécaniques des hydrogels supramoléculaires basés sur le concept LEASA pour des applications dans des réacteurs catalytiques en flux continu.

Grâce à la localisation spatiale du procédé EASA, la prise en charge des hydrogels supramoléculaires permet de les manipuler, condition *sine qua non* pour prévoir de nouveaux développements à partir d'une mousse polymère à cellules ouvertes. Un hydrogel catalytique sur supporté a été conçu, affichant une activité de type estérase efficace vis-à-vis de toutes les classes d'esters et une excellente résolution cinétique. Des applications dans la conception de cartouches catalytiques pour des réacteurs à flux continu sont actuellement à l'étude pour être brevetées par un bureau de transfert de technologie (SATT Conectus Alsace).

2. Vers la croissance auto catalytique d'un auto-assemblage peptidique selon le concept de LEASA.

L'auto-assemblage catalytique décrit dans le chapitre 5 partie 1 a été la première étape sur la voie de la conception d'un autre capable de catalyser sa propre formation. J'ai conçu et synthétisé un peptide précurseur prometteur sensible à l'hydrogel supramoléculaire de type estérase évoqué ci-dessus. Le précurseur peptidique a été transformé en hydrogélateur lorsqu'il est en contact avec l'hydrogel catalytique. J'ai prouvé que cette couche d'hydrogel formée sur une surface peut catalyser sa propre croissance.

### 3. Démonstration d'une méthode alternative à la production électrochimique de protons pour diriger l'auto-assemblage de peptides et la formation de revêtements d'hydrogel à travers un film multicouche enzymatiquement actif.

J'ai conçu la première surface non conductrice capable de produire un gradient de proton afin de localiser la formation d'hydrogel supramoléculaire en la modifiant avec une multicouche enzymatiquement active utilisant deux enzymes, l'une est GOx, produisant des protons à partir de l'oxydation du glucose. J'ai optimisé la production de proton et surmonté le besoin en oxygène du système en introduisant une deuxième enzyme, la peroxydase de raifort. Cette enzyme est capable de produire l'O<sub>2</sub> nécessaire à la GOx, à partir du H<sub>2</sub>O<sub>2</sub> libéré par la GOx, ce qui conduit à un système autonome. L'efficacité des réactions enzymatiques en tandem a été obtenue en adaptant la position entre les deux enzymes de la multicouche. Ce revêtement peut être formé sur n'importe quel type de surface, ce qui ouvre le champ d'application de ce type de matériaux.

### 4. Les protéines dépourvues d'activité catalytique peuvent initier l'hydrogélification supramoléculaire localisée.

Cette découverte était une découverte fortuite et n'était donc pas prévue initialement dans le programme de travail de mon doctorat. J'ai montré que l'absence d'activité catalytique des protéines joue le rôle de point de nucléation principalement par le biais d'interactions électrostatiques entre protéines et peptides précurseurs. Ceci est une découverte cruciale dans l'élaboration des nanostructures auto-assemblées de peptides. Grâce à un équilibre dynamique entre le précurseur et son hydrogélateur correspondant, cette étape de nucléation induit un déplacement d'équilibre conduisant à la consommation totale du précurseur vers la formation de l'hydrogélateur menant à la croissance de nanofibres auto-assemblées. Cette découverte est un changement de paradigme dans la définition de l'EASA, car l'initiation de l'auto-assemblage ne nécessite plus de transformation enzymatique du précurseur en hydrogélateur.

De ces différents projets ont émergé de nouvelles questions qui trouveront réponses à plus ou moins court terme. Lors de la conception de nouveaux biomatériaux destinés aux applications de culture cellulaire de EASA et de LEASA, il serait intéressant de 1) réaliser une culture de cellules et de pouvoir conserver les cellules dans un matériau poreux revêtu d'un hydrogel approprié, comme dans le chapitre 5. Cela aurait un grand intérêt pour de grands problèmes cliniques de la médecine régénérative notamment pour la réparation de dommages graves subis par les os. Malgré leur capacité de régénération innée, les os ne peuvent combler l'espace généré par de petits défauts (épaisseur de l'espace inférieure à 2 mm). Si un matériau poreux biocompatible contenant des ostéoblastes peut être attaché à de gros défauts osseux, il peut aider les os à guérir complètement en favorisant l'ostéogenèse dans un milieu qui le rend souvent hostile en endommageant les tissus mous environnants et le système vasculaire. 2) Toujours dans le domaine de la biomédecine, insérer des cellules à l'intérieur d'un hydrogel biocompatible et pouvoir former l'hydrogel en présence des cellules permettra d'injecter le matériau contenant les cellules en endommageant le corps. Comme le matériau est un hydrogel physique, les cellules pourraient avoir la possibilité de s'y déplacer sans endommager l'hydrogel de manière irréversible. L'hydrogel pourra relier les limites du dommage et favoriser la cicatrisation, car les réseaux fibreux d'hydrogels imitent la nature fibreuse de la matrice extracellulaire et pourra également permettre distributions de médicaments directement à l'endroit de la pathologie.

Pour atteindre les différentes perspectives dans les domaines applicatifs, il est important de caractériser plus en profondeur les surfaces couvertes d'enzymes (concentration en surface, répartition d'enzymes à la surface et activité enzymatique à la surface) pour comprendre comment les structures auto-assemblées interagissent avec la surface, les mécanismes derrière la formation de l'auto-assemblage. Dans l'objectif de

concevoir, par exemple, un système de propulsion en initiant un mouvement d'un côté des nanoparticules de Janus, comme le filament d'actine sur la membrane cellulaire conduisant à la motilité cellulaire, ce qui peut conduire à des applications en ingénierie.

D'un point de vue personnel, ces trois années d'expérience professionnelle en gestion de projets ont été très enrichissantes.

Elles m'ont permis de mieux comprendre le monde de la recherche et le monde professionnel de manière générale. Cette expérience a été l'occasion d'approfondir mes connaissances et mes compétences dans mon domaine de spécialité et d'en développer de nouvelles au travers de mes différents projets et collaborations. En effet, tout au long de ma thèse j'ai pu m'exprimer en public en français et en anglais lors de réunions, séminaires, congrès et de formations transversales comme lors de ma thèse en 180 secondes ; de révéler ma créativité, notamment lors de la création d'une des couvertures du journal *Chemical Science*, et mon leadership lors de travaux en équipe et de l'encadrement de stagiaires. Ces trois années m'ont aussi permis d'élargir mon réseau grâce aux différentes rencontres pendant les congrès mais aussi lors des collaborations que j'ai pu mettre en place. Et finalement, j'ai également appris à mieux me connaître pendant ces trois années, pendant lesquelles j'ai appris à renforcer ma persévérance et mon mental en restant enthousiaste face aux différentes difficultés et épreuves rencontrées.





~ Thesis ~





# – Table of Contents –

List of abbreviations .....	i
Definitions .....	iv
General Introduction.....	1
<b>Chapter 1: State of the art .....</b>	<b>9</b>
Definition of gelator.....	12
A little history .....	13
1.1. Supramolecular hydrogels of Low Molecular Weight Hydrogelator (LMWH) ...	14
1.1.1. Principles.....	14
1.1.2. Enzymatic trigger for hydrogelation .....	15
1.2. Surface-assisted self-assembly of LMWH.....	17
1.2.1. Surface seeding of LMWH self-assembly.....	18
1.2.2. Covalently bond catalysts on surfaces induced self-assembly of LMWH .	20
1.2.3. Electrochemical trigger of pH-responsive self-assembly of peptides.....	22
1.3. Localized Enzyme Assisted Self-Assembly of peptides (LEASA).....	26
1.3.1. Localized Enzyme Assisted Self-Assembly (LEASA) on planar surfaces.	27
1.3.1.1. LEASA by covalently bonding enzymes .....	27
1.3.1.2. LEASA by non-covalently bonding enzymes .....	28
1.3.2. LEASA on non-planar surfaces (i.e. nanoparticles surface) .....	30
1.3.3. Localized self-assembly in a host hydrogel .....	33
1.3.4. LEASA on cell surfaces .....	34
CONCLUSION.....	36
REFERENCES .....	37
<b>Chapter 2: Materials &amp; Methods .....</b>	<b>45</b>
2.1. Materials .....	48
2.1.1. Buffer solutions.....	48
2.1.2. Polymers and enzymes .....	48

2.1.3. Peptides .....	49
2.2. Synthesis procedure, characterization and samples preparation .....	51
2.2.1. Peptide synthesis .....	51
2.2.2. Protocol of the synthesis and HPLC monitoring of the Fmoc-Y( <i>Succ</i> ) (molecule from chapter 5 part 5.2) .....	52
2.2.3. Characterization of the Fmoc-GFFY( <i>Succ</i> )GHY( <i>Succ</i> ) (molecule from chapter 5 part 5.2) .....	53
2.2.4. Preparation of peptide solution and hydrogel formation .....	53
2.2.5. Multilayer film preparation and localized hydrogel formation at the interface liquid-solid .....	54
2.3. Methods: Physical-chemical characterizations .....	55
2.3.1. Quartz Crystal Microbalance with Dissipation (QCM-D) .....	55
2.3.2. Atomic Force Microscopy (AFM) .....	57
2.3.3. Fourier Transform Infrared spectroscopy (FTIR) .....	59
2.3.4. Scanning Electron Microscopy (SEM) and Cryo-SEM .....	64
2.3.5. Analytic High-Performance Liquid Chromatography (HPLC) .....	67
2.3.6. Dynamic Light Scattering (DLS) .....	70
2.3.7. Circular Dichroism spectroscopy (CD) .....	72
2.3.8. Ultraviolet-Visible spectroscopy (UV-Visible) .....	76
2.3.9. Fluorescence spectroscopy .....	78
2.3.10. Rheology .....	79
REFERENCES .....	82

## Chapter 3: Protein-induced low molecular weight hydrogelator self-assembly through a self-sustaining process.....83

Context .....	87
3.1. Abstract .....	88
3.2. Introduction .....	89
3.3. Results and discussion .....	91
3.4. Conclusion .....	98

Current continuation of the project.....	99
3.5. Additional Figures.....	101
3.6. Experimental section .....	118
3.6.1. Materials.....	118
3.6.2. Hydrogel preparation in bulk and upside-down vial tests .....	119
3.6.3. Multilayer film preparation and hydrogel self-assembly .....	120
3.6.4. Quartz Crystal Microbalance with Dissipation monitoring.....	120
3.6.5. Infrared spectroscopy .....	120
3.6.6. Scanning Electron Microscopy and cryo-SEM.....	121
3.6.7. Transmission Electronic Microscopy (TEM) .....	121
3.6.8. Analytical High-Performance Liquid Chromatography .....	121
3.6.9. Dynamic Light Scattering .....	122
3.6.10. Fluorescence emission spectroscopy.....	122
3.6.11. Rheology measurements .....	122
3.6.12. Nuclear Magnetic Resonance (NMR).....	122
3.6.13. Circular Dichroism .....	125
3.6.14. High Resolution Mass Spectroscopy (HRMS).....	125
3.6.15. Syntheses of Fmoc- <i>A-SS-B</i> and <i>A-SS-B</i> .....	126
REFERENCES .....	127

## Chapter 4: Localized supramolecular peptide self-assembly directed by enzyme-induced proton-gradients ..... 129

Context .....	130
4.1. Abstract .....	134
4.2. Introduction.....	135
4.3. Results and discussion.....	136
4.4. Conclusion.....	141
4.5. Additional Figures.....	143
4.6. Experimental section .....	152
4.6.1. Materials.....	152

4.6.2. Preparation of Fmoc-AA-OH .....	153
4.6.3. Multilayer film preparation and hydrogel self-assembly .....	153
4.6.4. Quartz crystal microbalance with dissipation monitoring .....	153
4.6.5. O-dianisidine assay .....	154
4.6.6. Atomic force microscopy .....	154
4.6.7. Infrared spectroscopy .....	154
4.6.8. Scanning electron microscopy and <i>cryo</i> -SEM .....	155
REFERENCES .....	156

## Chapter 5: Supported catalytically-active supramolecular hydrogels for continuous flow chemistry. *Towards the design of a self-sustained hydrogel growth*..... 159

5.1. Supported catalytically-active supramolecular hydrogels for continuous flow chemistry .....	164
5.1.1. Abstract .....	164
5.1.2. Introduction.....	165
5.1.3. Results and discussion.....	166
5.1.4. Conclusion.....	173
5.2. Towards the design of a self-sustained hydrogel growth .....	175
5.2.1. Introduction.....	175
5.2.2. Design of an adequate precursor peptide.....	176
5.2.3. Synthesis of the precursor Fmoc-GFFY( <i>Succ</i> )GHY( <i>Succ</i> ).....	178
5.2.4. Gelation tests of Fmoc-GFFY( <i>Succ</i> )GHY( <i>Succ</i> ) in vials.....	179
5.2.5. Characterization of the autocatalytic hydrogel by FT-IR and Fluorescence microscopy .....	182
5.2.6. Surface-localization of the autocatalytic hydrogel.....	184
5.2.6.1. Monitoring of the mass deposition onto a surface by QCM-D .....	184
5.2.6.2. Morphological characterization of the hydrogel grew from an auto-catalytic process and generated from a surface.....	186
5.2.7. Conclusion .....	187
GENERAL CONCLUSION OF CHAPTER 5.....	187
5.3. ESI of the part 5.1 of this chapter .....	189

5.3.1. Additional Figures.....	189
5.3.2 Experimental section .....	197
5.3.2.1. Materials.....	197
5.3.2.2. Synthesis and characterization of Fmoc-GFFYGHY, Fmoc-GFF $\rho$ YGHY, Fmoc-GFFYGH $\rho$ Y and Fmoc-GFF $\rho$ YGH $\rho$ Y .....	198
5.3.2.3. Preparation of peptide solution and hydrogel formation .....	210
5.3.2.4. Multilayer film preparation and localized hydrogel formation at the liquid-solid interface .....	211
5.3.2.5. Quartz crystal microbalance with dissipation monitoring (QCM-D).....	211
5.3.2.6. Atomic force microscopy (AFM) .....	212
5.3.2.7. Infrared spectroscopy .....	212
5.3.2.8. Scanning Electron Microscopy (SEM) and <i>cryo</i> -SEM .....	212
5.3.2.9. Transmission Electronic Microscopy (TEM) .....	213
5.3.2.10. Analytic High-Performance Liquid Chromatography (HPLC).....	213
5.3.2.11. Nuclear Magnetic Resonance (NMR).....	214
5.3.2.12. Circular Dichroism (CD) .....	214
5.3.2.13. High Resolution Mass Spectroscopy (HRMS).....	214
5.3.2.14. Esterase-like activity assays.....	215
5.3.2.15. Esterase-like activity of the supported-CASH onto a glass substrate	216
5.3.2.16. Esterase-like activity and kinetic resolution of the supported CASH in the continuous flow reactor .....	216
5.3.2.17. Determination of the proportion of peptides involved in the catalytic process.....	217
5.3.2.18. Experimental determination of $K_m$ , $V_{max}$ and $k_{cat}$ using methyl ester 9 and the Michaelis-Menten equation .....	217
5.3.2.19. Molecular simulation.....	219
REFERENCES .....	220

## Chapter 6: Morphological, mechanical and biological study of a composite hydrogel based on self-assembled peptides and hyaluronic acid.....223

6.1. Introduction.....	226
6.2. State of the art.....	226
6.3. Results and Discussion .....	228
6.3.1. Preliminary hydrogelation upside-down vial test assays .....	229
6.3.2. Mechanical properties of the composite hydrogels.....	231
6.3.3. Morphological study of the fibrous network composing the composite hydrogels.....	233
6.3.4. Molecular study of the interactions between HA and the self-assembly of Fmoc-FFY .....	238
6.3.5. LEASA of the composite hydrogels on a surface .....	245
6.3.6. Cell culture with NIH 3T3 Fibroblasts .....	249
6.4. Conclusion.....	252
6.5. Experimental section .....	253
6.5.1. Materials.....	253
6.5.2. Synthesis and characterization of Fmoc-FFpY.....	254
6.5.3. Multilayer film preparation and hydrogel self-assembly.....	256
6.5.4. Upside-down hydrogel test in Bulk .....	257
6.5.5. Quartz crystal microbalance with dissipation monitoring .....	257
6.5.6. Atomic force microscopy .....	258
6.5.7. Infrared spectroscopy.....	258
6.5.8. Scanning electron microscopy and cryo-SEM.....	258
6.5.9. Transmission Electronic Microscopy .....	259
6.5.10. Fluorescence emission spectroscopy.....	259
6.5.11. Circular Dichroism .....	260
6.5.12. Rheology .....	260
6.5.13. <sup>1</sup> H and <sup>31</sup> P NMR .....	260
6.5.14. Epifluorescence microscopy and confocal laser scanning microscopy	261
6.5.15. Cells assays on Fibroblast NIH 3T3 .....	262

ANNEXES .....	267
REFERENCES.....	270
General conclusion & Outlooks .....	273
Annexes .....	279





## List of abbreviations

### A

AFM	Atomic force microscopy
AP	Alkaline phosphatase (= ALP)
ATR	Attenuated total reflection

### B

BSA	Bovine serum albumin
BTA	Benzene-1,3,5-tricarboxamide

### C

CD	Circular dichroism
Cryo-TEM	Cryo transmission electron microscopy
Cryo-SEM	Cryo scanning electron microscopy
CASH	Catalytically-active supramolecular hydrogel
CGC	Critical gelation concentration
CBT	Cyanobenzothiazole
2-CTC	Resin 2-chlorotriyl chloride
CLSM	Confocal laser scanning microscopy

### D

DIEA	Diisopropylethylamine
DMF	Dimethylformamide
DCM	Dichloromethane
DLS	Dynamic Light Scattering
DMEM	Dulbecco's modified institute medium
DTT	Dithiothreitol

### E

EASA	Enzyme-assisted self-assembly
E-COLI	Escherichia coli
EDC	2-ethyl-3-(3-dimethylaminopropyl)carbodiimide hydrochloride
ECM	Extracellular matrix

### F

FITC	Fluorescein isothiocyanate
Fmoc	Fluorenylmethoxycarbonyl
FT-IR	Fourier transform infrared spectroscopy
FBS	Fetal bovine serum

**G**

GOx	Glucose oxidase
GR	Glutathione reductase
GSH	Glutathione

**H**

HA	Hyaluronic acid
HOBt	hydroxybenzotriazole
HBTU	(2-(1 H-benzotriazol-1-yl)-1,1,3,3-tetramethyluronium hexafluorophosphate
HRP	Horseradish peroxidase
HRMS	High resolution mass spectrometry
HPLC	High performance liquid chromatography
HDF	Human dermal fibroblast

**L**

LbL	Layer-by-layer
LEASA	Localized enzymatic assisted self-assembly
LMWH	Low molecular weight hydrogelator
LDH	Lactate dehydrogenase

**M**

MALDI-TOF	Matrix assisted laser desorption/ionization time-of flight
MMP-9	Matrix metalloproteinase-9
MTGase	Microbial transglutaminase
MH	Gelose Mueller-Hinton

**N**

Nap	Naphtalene
NMR	Nuclear magnetic resonance
NPs	Nanoparticles
NCNPs	Negatively charged nanoparticles
NHS	N-hydroxysuccinimide
NBD	Nitrobenzoxadiazole

**P**

PAH	Poly (allylamine hydrochloride)
PEG	Poly (ethylene glycol)
PEO	Poly (oxiethylene)
PEI	Poly (ethyleneimine)
<i>p</i> -NPA	<i>para</i> -Nitrophenyl acetate (= PNA)
<i>p</i> -NP	<i>para</i> -Nitrophenol

PSS	Poly (styrene sulfonate)
PVA	Poly (vinyl alcohol)
PDMS	Poly (dimethylsiloxane)
PA	Peptide amphiphile
PBS	Phosphate buffered saline
PLL	Poly-L-Lysine
PGA	Poly-L-Glutamic acid

## **Q**

QCM-D	Quartz crystal microbalance with dissipation monitoring
-------	---

## **R**

Rho	Rhodamine B
Rho-AP	Alkaline phosphatase labeled with rhodamine B
RPMI	Roswell park memorial institute medium

## **S**

SEM	Scanning electron microscopy
SAH	S-adenosyl-homocysteine

## **T**

TEM	Transmission electron microscopy
TIPS	Triisopropylsilyle
TFA	Trifluoroacetic acid
TCEP	Tris-(2-carboxyethyl) phosphine

## **U**

UV-vis	Ultraviolet-Visible spectroscopy
--------	----------------------------------



## Definitions

The definition of scientific concepts and the words which carry them can vary according to the fields considered or/and can also change over time. Because my Ph.D. project is multidisciplinary by essence, it appeared important to provide herein the meaning of some words/concepts used in my manuscript.

**Composite** Hydrogel composite, refer to a hydrogel composed of at least two components of different nature, like a polysaccharide and a peptide. It do not refer to a mixture of different peptides.

**EASA** *Enzyme-Assisted Self-Assembly*  
This concept proposed by Xu Bing and coworkers in 2004 in his seminal work<sup>1</sup> means that the self-assembly process of low molecular weight hydrogelator (LMWH) is triggered by the presence of an adequate enzyme. There is no specification of the localization in the EASA concept. EASA is also in opposition to the physical triggers such as temperature and ultrasounds because it induces a chemical transformation of a precursor, by the formation or the cleavage of a bond, into a hydrogelator.

**Hydrogelator** Refers to a small molecule (amino acids or peptides ≠ Polymers), obtained after the application of an enzymatic stimulus, which can self-assemble (e.g. same as LMWH).

**LEASA** *Localized Enzymatic Assisted Self-Assembly:*  
Means that the enzyme is fixed on a surface and will trigger the self-assembly from that place leading to the localization of the self-assembly.

**LMWH** *Low Molecular Weight Hydrogelator.*  
Corresponds to small molecules such as amino acids or peptides (< 50 AAs)<sup>2</sup>, which can self-assemble after transformation of a precursor by an enzyme.

**Precursor** Molecule, which needs to be activated by a trigger to become a hydrogelator. Triggers can be pH, enzymes, etc.

**Substrate** It exists different meanings depending on the field  
1) Refers to the substrate of an enzyme (e.g. precursors).  
2) Refers to the surface on which the experiments are performed.  
3) In chapter 5, it refers to the ester used for the catalytic assays in solution or in the reactor.

---

<sup>1</sup> Yang, Z., et al., *Enzymatic formation of supramolecular hydrogels*, *Adv. Mater.*, **2004**,16, 1440.

<sup>2</sup> Sabokkhiz, M., et al., *Study on antiviral activity of two recombinant antimicrobial peptides against tobacco mosaic virus*, *Probiotics and antimicrobial proteins*, 2019, DOI: 10.1007/s12602-019-09539-4.

**System**

1) Generally in the manuscript system will refer to the modified-surface with the enzyme and precursor/hydrogelator combination. In analogy of complex systems defined below:

*“Systems composed of many components which may interact with each other (e.g. Living cell, an ecosystem, etc.) and whose behavior is intrinsically difficult to model due to the huge number of different interactions between the different components composing it”.*<sup>3</sup>

2) If specified “enzymatic system”, it will refer only to the couple enzyme/substrate, where the substrate is the precursor.

---

<sup>3</sup> Yaneer, B.-Y., *General Features of Complex Systems, Encyclopedia of Life Support Systems, 2002.*



# **General Introduction**







Mankind always wondered how life emerged and still tries to understand the mechanisms controlling cell behavior and how cells work together to form highly evolved species. One theory about the origin of life is that we all come from a single cell. This cell had to divide itself so that life could blossom. Then it had to respond to its environment. To achieve this, cells have developed numerous strategies, one of them being the control over self-assembly processes. Such processes are mechanisms in which cellular components interact spontaneously one with each other to form organized and functional structures.

Despite its spontaneous appearance, nature developed methods to control the self-assembly of proteins or peptides at specific locations and according to a well-defined timing: this is called *the spatiotemporal control*. For example, actin fibers are created by self-assembly of globular proteins called actin, which self-assemble under the action of an enzyme, alkaline phosphatase. This enzyme removes a phosphate group from actin, which then self-assembles in fibers. The particularity of the self-assembly of actin fibers is that alkaline phosphatase enzymes are localized at the surface of the cell membrane which enable the localization of the fiber generation (Figure 1). This localization is essential for cell motility because actin fibers that self-assemble will exert a pressure over the cell membrane, which ultimately leads to the movement of the cell. Such movements are required for the cell to adapt to its mechanical and chemical environment. This illustrates the importance of self-assembly processes and especially their control over space and time in cell behavior.

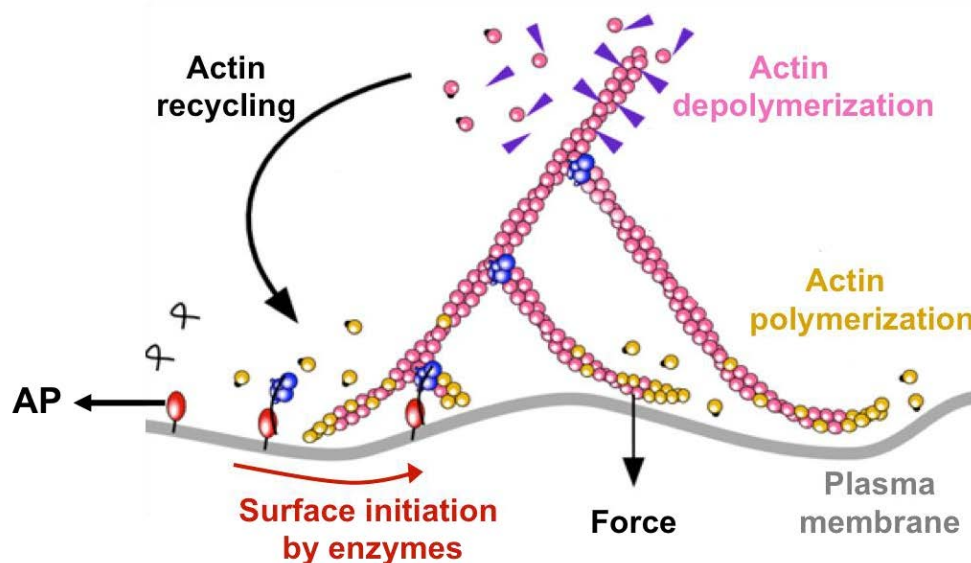


Figure 1: Example of spatiotemporal control of protein self-assembly leading to cell motility: the self-assembly of globular actin protein occurs when it is needed in the cell's life and happens not everywhere but it is localized near the internal plasma membrane. This spatiotemporal control is ensured by the presence of transmembrane phosphatase (12BC.paris-saclay.fr/02-14-17).

By relying on non-covalent and thus reversible bonds, self-assembled networks respond dynamically to various external stimuli. In the current quest for smart materials design with high performance characteristics similar to those found in living matter, supramolecular hydrogels appear as a promising tool, in particular because of their non-covalent character, they can adapt to their immediate environment. In this context, the use

of enzymes to trigger the localized self-assembly of peptides is extremely promising. As illustrated in Figure 2, enzymes can catalyze the transformation of ungrouped precursors into entities able to recognize themselves and to self-assemble quickly, leading to the formation of a hydrogel exclusively from where the enzymes are localized.

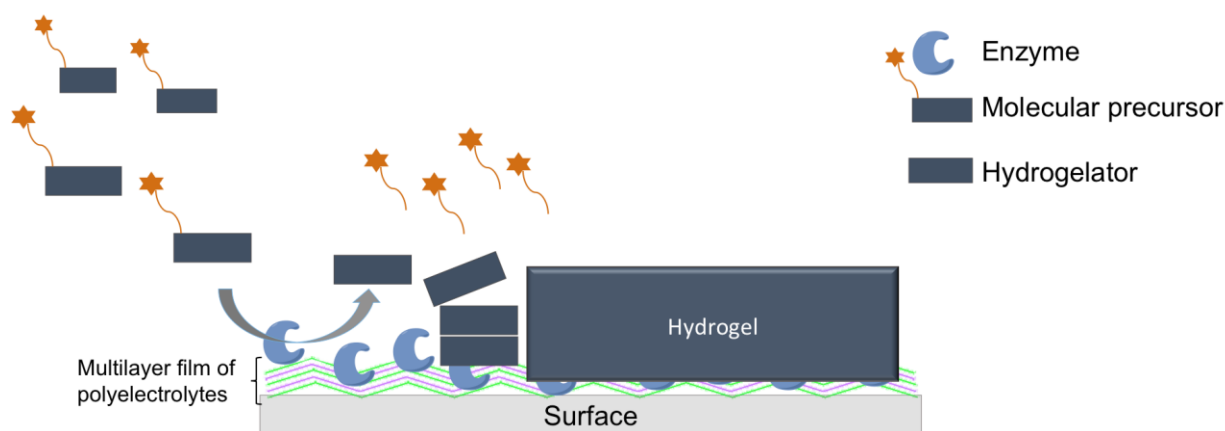


Figure 2: Schematic of the principle of the localized enzyme-assisted self-assembly

Since 2011, the research group *Ingénierie Macromoléculaire aux Interfaces* (IMI) from the Charles Sadron Institute designed a one-pot strategy to build polyelectrolyte-based films exclusively from surfaces, first using an electrical stimulus. Electrochemical gradients of catalysts generated at electrode surfaces (metallic ions, protons or organic compounds) were used to induce self-constructions of nanofilms constituted of oligomers, polymers or small molecules localized at these electrode surfaces. By analogy with biological tissue development these catalysts were called *morphogens*. This approach represents a convenient way of surface functionalization using all the constituents simultaneously present in solution and allowing a high control of bottom-up film buildup through the electrochemical setup.

In 2015, a Ph.D. student of the IMI group, Cécile Vigier-Carrière, introduced localized enzyme assisted self-assembly. By adsorbing enzymes on polyelectrolyte multilayer films and bringing these films in contact with solutions of peptides that react with the enzymes, she could direct self-assembly of peptides to get micrometric layers of supramolecular hydrogels specifically located on the surfaces where the enzymes were deposited. In addition to represent a one-pot process that leads to localized hydrogel buildup without using an external stimulus, it gives rise to the growth of nanofibrous architectures organized from the bottom to the top. She developed two approaches to illustrate the concept of Localized Enzyme-Assisted Self-Assembly (LEASA). In the first one, the peptide self-assembly was assisted by  $\alpha$ -chymotrypsin, which catalyzed the condensation of dipeptides to form oligomers. These oligopeptides are gradually released from the surface and then self-assemble into nanofibers growing from the surface. The width and the kinetic of oligopeptide self-assembly were tuned by the initial concentration of dipeptides in solution and by the surface density of  $\alpha$ -chymotrypsin. In a second approach, she deposited a thin film promoting both the enzymatic production of hydrogelators and the nucleation of the hydrogelator self-assembly at the surface. This was achieved by using a bioactive multilayer film embedding alkaline phosphatase and exhibiting self-assembly peptide precursors.

The initial objective of my Ph.D. was to design supramolecular hydrogels formed on surfaces and able to catalyze their own formation through a self-sustaining process. To achieve this goal, the first step was to get a catalytic self-assembled architecture that can be generated from a surface using the LEASA approach. Then, this system had to be adapted to get the ability to produce its own building blocks based on its inherent catalytic activity in an autonomous way. This is the work plan I have adopted during my Ph.D.

I first investigated LEASA processes leading to catalytically active self-assembled films (esterase-like films). Yet the resulting supramolecular hydrogels are fragile materials which hampers their widespread use. By localizing the self-assembly process on surfaces of adequate materials, it might thus be possible to circumvent this drawback. Along this line, I have investigated the LEASA approach of my catalytically active films in porous materials and explored the possibility to get flow reactors presenting esterase-like activity. This was done by supporting the catalytically-active supramolecular hydrogel by polymer foams. This should represent a real breakthrough in the field of low molecular weight hydrogelator self-assemblies.

Previous Ph.D. students from my host group have directed the self-construction of polyelectrolyte-based films from an electrode surface using localized morphogen gradient, as already mentioned. According to the literature, the electrochemical generation of protons has also proved to be highly efficient to localize the self-assembly of peptides giving rise to the growth of a fibrous network at an electrode. Immobilization of a proton-producing enzymes at a surface may allow to direct the pH-sensitive self-assembly of peptides (or others molecules) not only from conductive material but also on almost any kind of material. This extends the possible applications of this approach and also extends to possible systems to be used in order to get autonomous peptide self-assembly systems. I thus also focused on this project, working mainly on the most suitable enzymatically-active multilayer film design to initiate the self-assembly of peptides from the surface through the generation of protons.

In quest of autonomous peptide self-assemblies I came to investigate glutathione reductase and precursor disulfide-containing peptides. I have tried to show that this enzyme can initiate the self-assembly of hydrogelator's peptides when the disulfide bridge of the precursor is enzymatically reduced in thiol group. Through control experiments, I have noticed that proteins lacking catalytic activity (such as albumin) can also induce the formation of the expected supramolecular hydrogel using another mechanism. The full study of this discovery and its understanding is described in the Chapter 3.

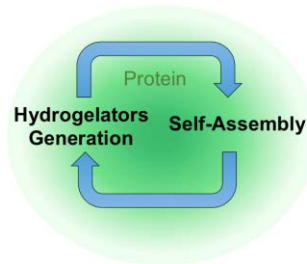
Finally in the field of biomaterials, the search for very soft biocompatible hydrogels is a hot topic for 2D and 3D cell experiments. Supported supramolecular hydrogels generated in a biological culture media from a glass substrate have been investigated because they could represent a convenient way to manipulate soft cell substrates. Even if this subject is not directly related to my initial goal, it represents an interesting possible application of the peptides I developed. Thus, I focused on the influence of a polysaccharide, *i.e.* hyaluronic acid, present during the growth of the hydrogel on the morphology of the resulting self-assembled peptide nanofibers, the mechanical properties of the hydrogel and the biological cell adhesion response.

The manuscript of my Ph.D. is constituted of six chapters. Chapter 1 is devoted to the description of the bibliographic context of the enzyme-assisted self-assembly concept. All scientific results obtained from the different projects described just above are gathered in Chapters 3 to 6 as depicted in Figure 3 below. Chapters 3 and 4 correspond to two publications and Chapter 5 is a submitted draft. Chapter 2 presents the materials and methods common to all chapters. All chapters are independent one from each other which means that each chapter has its own references list. Of course, the manuscript ends with a general conclusion summarizing my Ph.D. work and provides an outlook.

During my Ph.D., I had the opportunity to collaborate with a post doctorate, Miryam Criado-Gonzalez, on several projects aiming on the generation of peptide self-assemblies initiated at nanoparticles or in host gel. For all these projects, I participated by producing the peptides needed for the studies, in the discussions and interpretations of the results. Publications related to these works are in the Annexes part of this manuscript.

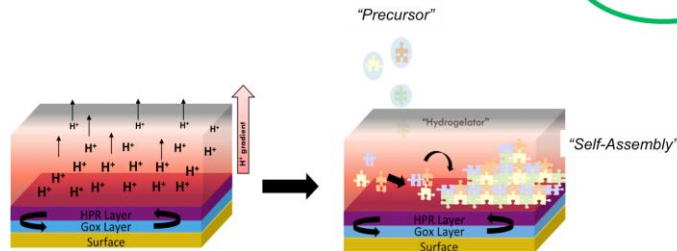
2016

Chapter 3



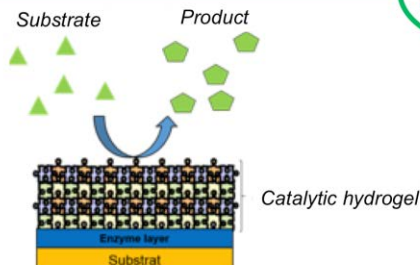
Protein-induced low molecular weight hydrogelator self-assembly through a self-sustaining process

Chapter 4



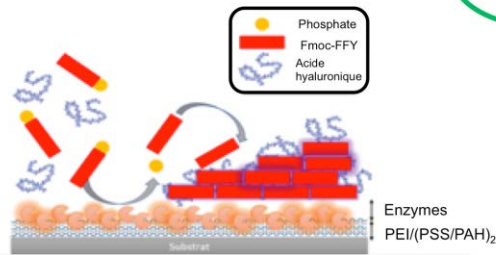
Localized supramolecular peptide self-assembly directed by enzyme-induced proton-gradients

Chapter 5



Supported catalytically-active supramolecular hydrogels for continuous flow chemistry  
Towards the design of a self-sustaining hydrogel

Chapter 6



Morphological, mechanical and biological study of a composite hydrogel based on self-assembled peptides and hyaluronic acid

2019

Figure 3: List of the different chapters of the manuscript.





# **Chapter 1**



## **State of the art**

**Localized Enzyme-Assisted Self-Assembly strategy  
from planar surfaces to non-planar surfaces**





## Summary

Definition of gelator .....	12
A little history.....	13
1.1. Supramolecular hydrogels of Low Molecular Weight Hydrogelator (LMWH) .....	14
1.1.1. Principles .....	14
1.1.2. Enzymatic trigger for hydrogelation.....	15
1.2. Surface-assisted self-assembly of LMWH .....	17
1.2.1. Surface seeding of LMWH self-assembly .....	18
1.2.2. Covalently bond catalysts on surfaces induced self-assembly of LMWH .....	20
1.2.3. Electrochemical trigger of pH-responsive self-assembly of peptides ...	22
1.3. Localized Enzyme Assisted Self-Assembly of peptides (LEASA).....	26
1.3.1. Localized Enzyme Assisted Self-Assembly (LEASA) on planar surfaces .....	27
1.3.1.1. LEASA by covalently bonding enzymes .....	27
1.3.1.2. LEASA by non-covalently bonding enzymes .....	28
1.3.2. LEASA on non-planar surfaces (i.e. nanoparticles surface).....	30
1.3.3. Localized self-assembly in a host hydrogel.....	33
1.3.4. LEASA on cell surfaces .....	34
<b>CONCLUSION.....</b>	<b>36</b>
<b>REFERENCES .....</b>	<b>37</b>

## Definition of gelator

Molecular self-assembly is an ubiquitous process in nature and is also believed to play an essential role in the emergence, maintenance and advancement of life.<sup>1-3</sup> While the primary focus of the research on molecular self-assembly centers on the biomacromolecules (proteins, nucleic acids and polysaccharides) or their mimics, the self-assembly of small molecules in water (or organic solvent) also has profound implications from fundamental science to practical applications. Because one usual consequence of the self-assembly of the small molecules is the formation of a gel (or gelation), a subset of the small molecules is called gelators. Depending on the solvents in which they form gels, these small molecules are further classified as hydrogelators<sup>4</sup> (using water as the liquid phase) or organogelators<sup>5</sup> (using an organic “solvent” as the liquid phase). More precisely, hydrogelators self-assemble in water to form three-dimensional supramolecular networks that encapsulate a large amount of water to afford an aqueous mixture. The aqueous mixture is a hydrogel because it exhibits viscoelasticity of a gel, in other words is unable to flow without shear force. Unlike the conventional polymeric hydrogels that are mainly based on covalent cross-linked networks of polymers, the networks in supramolecular hydrogels are formed due to noncovalent interactions between the hydrogelators (Figure 1).<sup>6</sup> As water is the unique solvent to maintain life forms on earth, it is not surprising that applications of hydrogels in life science have advanced most significantly.

Thus, in this chapter I mainly focus on works devoted to the properties and applications of supramolecular hydrogels in biomedical science.

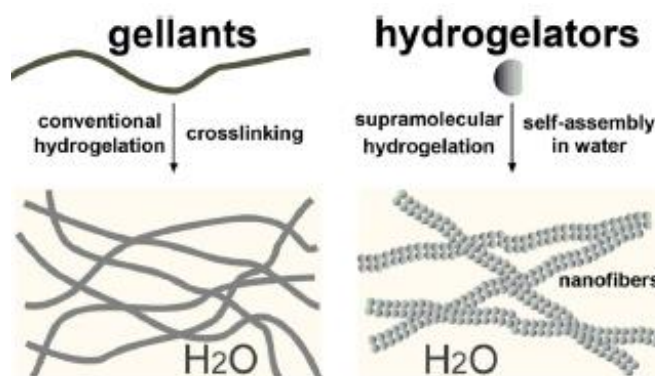


Figure 1<sup>128</sup>: Illustration of the process for creating polymeric hydrogels via crosslinking (left), or formation of supramolecular hydrogels via a chemical or physical perturbation initiated self-assembly (right)<sup>6</sup>. Copyright© 2015 American Chemical Society.

## A little history

In 1892, Brenzinger reported the formation of the first hydrogelator of the history, the dibenzoyl-L-cystine (**1**) (Figure 2).<sup>7</sup> This molecule was then reported again 29 years later by Hoffman which stipulated that **1** is able to form “a gel of 0.1% concentration [which] was rigid enough to hold its shape for a minute or more when the beaker containing the gel was inverted”.<sup>8</sup> We had to wait until 2000, that Menger *et al.* use modern physical methods in chemistry, X-ray crystallography, light and electron microscopy, rheology, and calorimetry to examine the hydrogel of **1** and provide invaluable molecular details that reveal many fundamental design principles for creating effective hydrogelators made of small molecules.<sup>9</sup> Impressively, among the 14 aroyl-L-cystine derivatives studied by Menger in his seminal work, the best hydrogelator (**2**) (Figure 2) obtained, is able to self-assemble and rigidify aqueous solutions at 0.25 mM, ca. 0.01 wt % in less than 30 s, which probably still holds the record in terms of the lowest concentration of hydrogelators and the fastest rate for gelation.<sup>10</sup> One of the most revealing design principles in the study of **1** is that aromatic moieties are highly effective for enhancing intermolecular interactions in water. This principle is largely responsible for the successful use of aromatic-aromatic interactions to design hydrogelators of small peptides.<sup>11,12</sup> Not surprisingly, nature has already used aromatic-aromatic interactions to evolve proteins.<sup>13</sup> These facts imply that the use of aromatic-aromatic interactions is an effective and biomimetic way to enhance hydrogen bonds and other interactions in water for molecular self-assembly in water that usually lead to supramolecular hydrogels.<sup>12</sup> A notable example of this principle is that a small dipeptide derivative (**3**: Fmoc-FF (Figure 2)) is capable of enabling many other molecular motifs to self-assemble in water to form supramolecular hydrogels.<sup>14</sup> More surprising is that even a single amino acid (**4**: Fmoc-Tyr (Figure 2)) is able to self-assemble and leads to the formation of a hydrogel.<sup>15</sup>

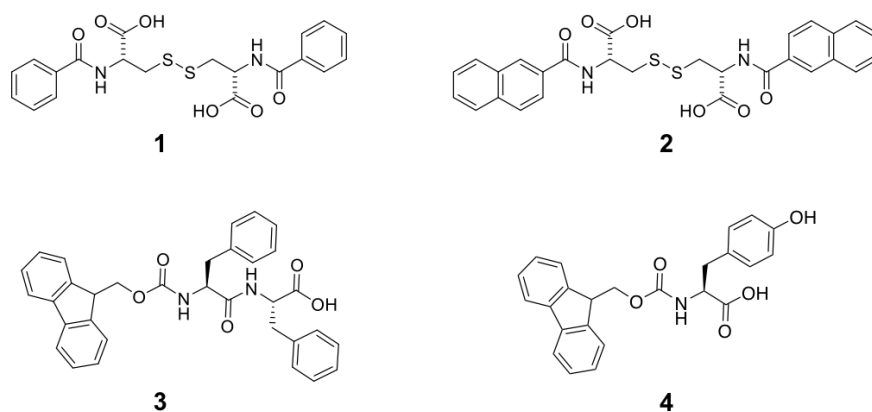


Figure 2: Molecular structures of 1, 2, 3 and 4.

Despite the above seemingly obvious general principle of supramolecular hydrogelation, one common theme mentioned by the researchers who study hydrogelators, intriguingly, is that their work on gelators started from an accidental discovery of a particular molecule that forms a gel in a solvent. For example, the first small molecule hydrogelator reported by Brenzinger unlikely was the intended goal. Therefore, the exploration of supramolecular hydrogels unlikely will be fruitless, and

the applications of supramolecular hydrogelators will have a more profound impact than a mere serendipitous observations, as I intend to illustrate in this chapter.

## 1.1. Supramolecular hydrogels of Low Molecular Weight Hydrogelator (LMWH)

### 1.1.1. Principles

Hydrogels can be formed from macromolecules or small molecules. Most of hydrogels used for medical applications are formed from natural polymers often assembled through physical interactions, chemical covalent cross-linking or both. Well-known examples are polypeptides, such as collagen<sup>16,17</sup>, poly-L-Lysine<sup>18</sup> and polysaccharides such as alginic acid<sup>19</sup>, hyaluronic acid<sup>20</sup> and agarose.<sup>21</sup> Synthetic polymers such as poly(vinyl alcohol) (PVA) and poly(ethylene glycol) (PEG) are commonly used to form water swollen crosslinked macromolecular networks.<sup>22</sup> Despite the fact that they share a common appearance and properties (e.g., soft and wet) with polymeric hydrogels, supramolecular hydrogels differ from polymeric hydrogels in many subtle ways. One essential difference is that supramolecular hydrogels, unlike the polymeric hydrogels that originate from a randomly cross-linked network made of strong covalent bonds, are the consequence of molecular self-assemblies driven by weak, noncovalent interactions among hydrogelators in water. This subtle but yet fundamental difference not only renders molecular arrangements more ordered in supramolecular hydrogels, but also manifests itself in the process of hydrogelation. While simple swelling usually confers a polymeric hydrogel, a stimulus or a triggering force is necessary to *bias* thermodynamic equilibrium for initiating the self-assembly process or phase transition to obtain a supramolecular hydrogel. Therefore, there are many forms of stimuli or triggers for manipulating the weak interactions, which can be achieved by either physical methods (e.g., changing the temperature, applying ultrasound, or modulating the ionic strength) or chemical methods (e.g., pH change, chemical or photochemical reactions, redox, and catalysis) (Figure 3).

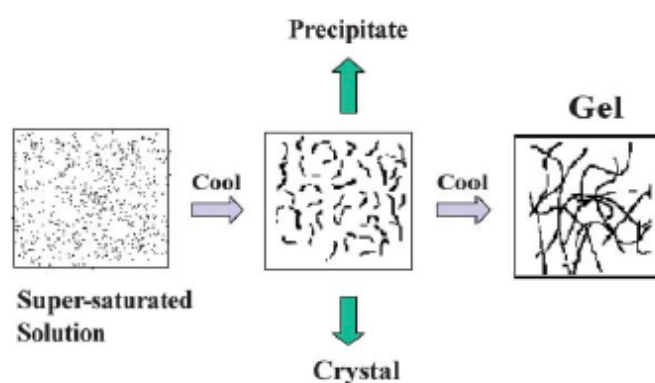


Figure 3: Schematic representation of different possible pathways leading to precipitate, crystal or gel from supersaturated solution of molecules<sup>128, 130</sup>. Copyright © 2018 Wiley.

In this chapter I focus on small molecules, which can be peptides or single amino acids, based hydrogels.

Supramolecular hydrogels from peptides<sup>23-25</sup> can adopt different secondary structures (coils, helices,  $\beta$ -sheets) and lead to a large range of nanoscale objects: fibers, tubes, spheres or sheets (Figure 4) from non-covalent interactions occurring during the formation of self-assembly.

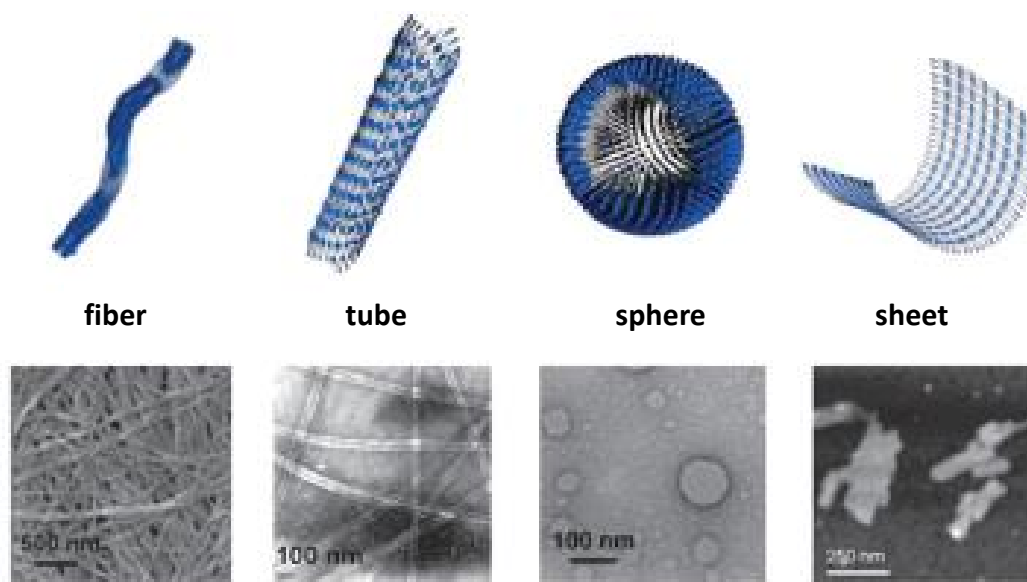


Figure 4: Supramolecular structures accessible via peptide self-assembly<sup>131</sup>. Copyright © 2010 Reproduced from ref (131) with permission of The Royal Society of Chemistry

Due to their inherent biological compatibility, peptides are considered as valuable building blocks for production of biomaterials used in regenerative medicine<sup>26</sup>, drug delivery<sup>27</sup>, 3D cell-culture<sup>28</sup>, or enzyme immobilization for biosensing.<sup>29</sup> In order to create such functional materials, properties of peptide-based hydrogels can be tailored through suitable hierarchical assemblies of small molecules.

### 1.1.2. Enzymatic trigger for hydrogelation

Enzymatic reactions are undoubtedly a prominent dynamic feature of life, and they are tailored to most of the self-assemblies occurring in cells. Today, the reports of catalytic control over self-assembly processes mostly deal with biocatalytic formation of hydrogels that is called the enzyme-assisted hydrogelation.<sup>6,30-34</sup> However, we are still far from achieving directed self-assembly by catalytic action in a fully synthetic system. The pivotal importance of enzymes in a variety of cellular processes justifies the exploration of enzymatic supramolecular hydrogelation. Although the application of enzymes to cross-linked covalent polymers is an effective process for generating hydrogels<sup>35</sup>, the use of enzymes to prepare supramolecular hydrogels has several distinct advantages, such as the opportunity to achieve sophisticated secondary structures, adaptability to structural modifications, excellent accessibility to enzymes both *in vitro* and *in vivo* due to the fast diffusion of small

molecules and, most importantly, the possibility to adsorb enzymes on a surface to localize the self-assembly.

Despite the huge diversity of enzymes, so far only a handful of enzymes have been explored for catalyzing hydrogelation. These enzymes are phosphatase,<sup>15,36-46, 94</sup>  $\beta$ -lactamase,<sup>47</sup> esterase,<sup>48</sup> matrix metalloproteinase-9 (MMP-9),<sup>49,50</sup>  $\alpha$ -chymotrypsin,<sup>51,95</sup> thrombin,<sup>52</sup> chymotrypsin,<sup>52</sup> and  $\beta$ -galactosidase<sup>53</sup> for catalyzing bond cleavage reaction; lipase,<sup>54</sup> microbial transglutaminase (MTGase),<sup>55</sup> and thermolysin,<sup>56-59</sup> for catalyzing bond-forming reactions; and some other enzymes such as glucose oxidase for proton formation,<sup>60, 61</sup> peroxidase for oxygen production,<sup>62-64</sup> and tyrosinase for the oxidation of phenol and in particular tyrosine.<sup>65</sup> Regardless of the types of reactions or enzymes, the essential feature for enzymatic hydrogelation of small molecules involves the enzymatic conversion of a precursor into a hydrogelator (normally *via* bond cleavage or bond formation but not only). The self-assembly of the hydrogelators to form supramolecular hydrogels leads to the formation of nanostructures, which are usually nanofibers and their entanglement afford the matrixes of the hydrogels. The most reported enzymatic formation of supramolecular hydrogels is by using alkaline phosphatase<sup>46</sup> to dephosphorylate a precursor. One can for example use Fmoc-tyrosine phosphate (**5**) under slightly basic conditions which transforms into Fmoc-tyrosine to self-assemble and form a supramolecular hydrogel (Figure 5).<sup>15</sup> Besides providing a new methodology for the creation of hydrogels *in situ*, this process also builds up a platform for screening enzyme inhibitors<sup>46,47</sup> and detecting the presence of an enzyme.<sup>47</sup>

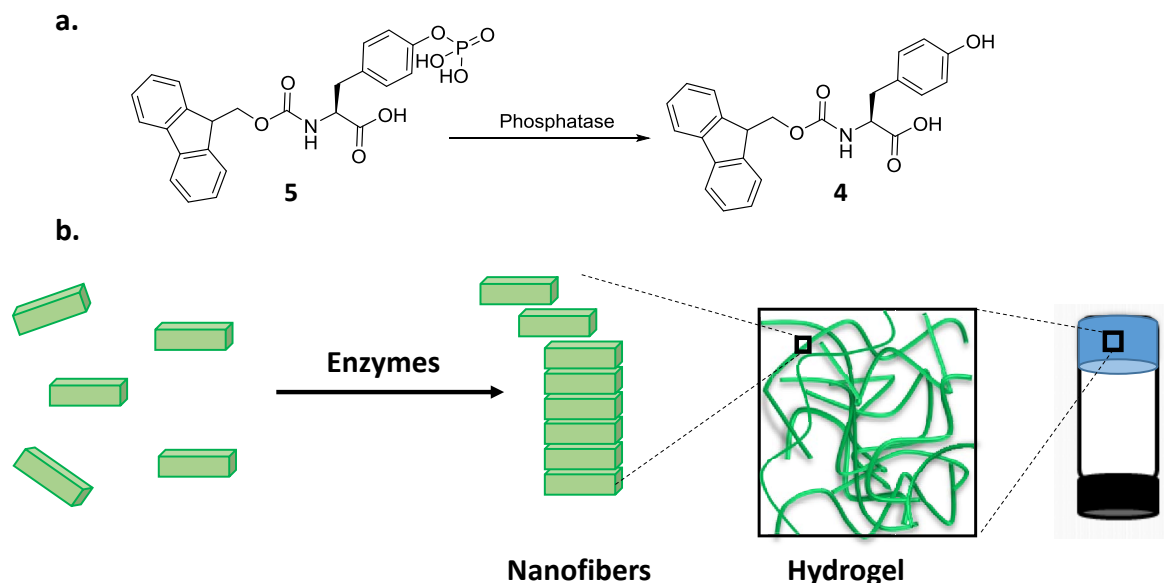


Figure 5: a) Representative molecular structures of precursor (**5**) and hydrogelator (**4**) to form hydrogels on the basis of catalysis and b) Schematic representation of the gelation triggered by enzymatic catalysis. This initiation induces the self-assembly of the LMWG in the whole solution and leads to the formation of a fibrous network self-supporting the hydrogel<sup>15</sup>.

Instead of catalytically breaking bonds for supramolecular hydrogelation, Ulijn *et al.* took a different approach by triggering the self-assembly of peptide hydrogels *via* reverse hydrolysis using thermolysin.<sup>58</sup> Utilizing the fact that certain proteases can thermodynamically favor the formation of peptide bonds, they used thermolysin to catalyze the coupling of two amino acid precursors to form a hydrogel. A major

advantage of employing reverse hydrolysis is that no byproducts except water are formed, although the use of hydrophobic precursors may be problematic in water.

The demonstration of enzymatic supramolecular hydrogelation has sparked relatively active research on bioresponsive materials (Figure 5b). For example, McNeil *et al.* recently developed a modular system for detecting protease activity.<sup>52</sup> They designed and developed a precursor (molecule **6** (Figure 6)), which is unable to form a hydrogel under most conditions, but turned into a translucent gel upon the treatment of a protease (thrombin).

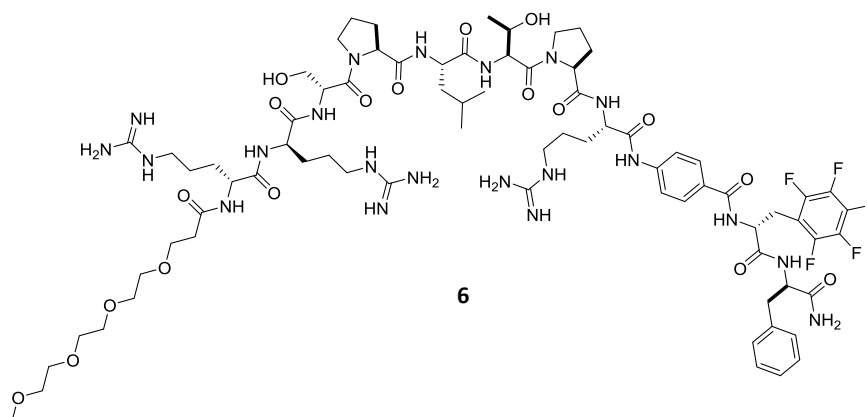


Figure 6: Representative molecular structure of precursor 6<sup>52</sup>

The past decade has witnessed a considerable success in preparation of supramolecular hydrogels using enzymatic transformation and by recognizing enzyme-assisted self-assembly as a common process in nature to achieve spatial control over structure formation. Localizing the self-assembly is the next challenge that researchers have to address to create systems as evolved as cells.

Along this line during the last 10 years, several publications, reported examples of Localized Enzyme-Assisted Self-Assembly (LEASA) of precursors. So, in the second part of this chapter, I will review the strategies developed towards the design of surface-assisted self-assembly of LMWH.

## 1.2. Surface-assisted self-assembly of LMWH

Since the middle of the last century, functionalization of surfaces has emerged as a convenient method for controlling interactions between a material and its surrounding environment.<sup>66</sup> Many effective approaches were developed covering a large spectrum of applications to modify surfaces to confer them properties to respond to different stimuli.<sup>67-68</sup> The main question is, how to direct a nanostructure buildup exclusively from or on a surface? To address this challenge, surfaces were considered as valuable supports to control and pattern bottom-up assemblies of LMWH over space and time. Two main approaches were reported to answer this question. One approach makes use of a seed-layer on the surface, which means depositing the LMWH on the surface. This will lead to an increase of the local concentration favoring the formation of the self-assembly. The second approach



consists in generating species on the surface, called morphogens, which will induce the local formation of LMWHs (Figure 7).

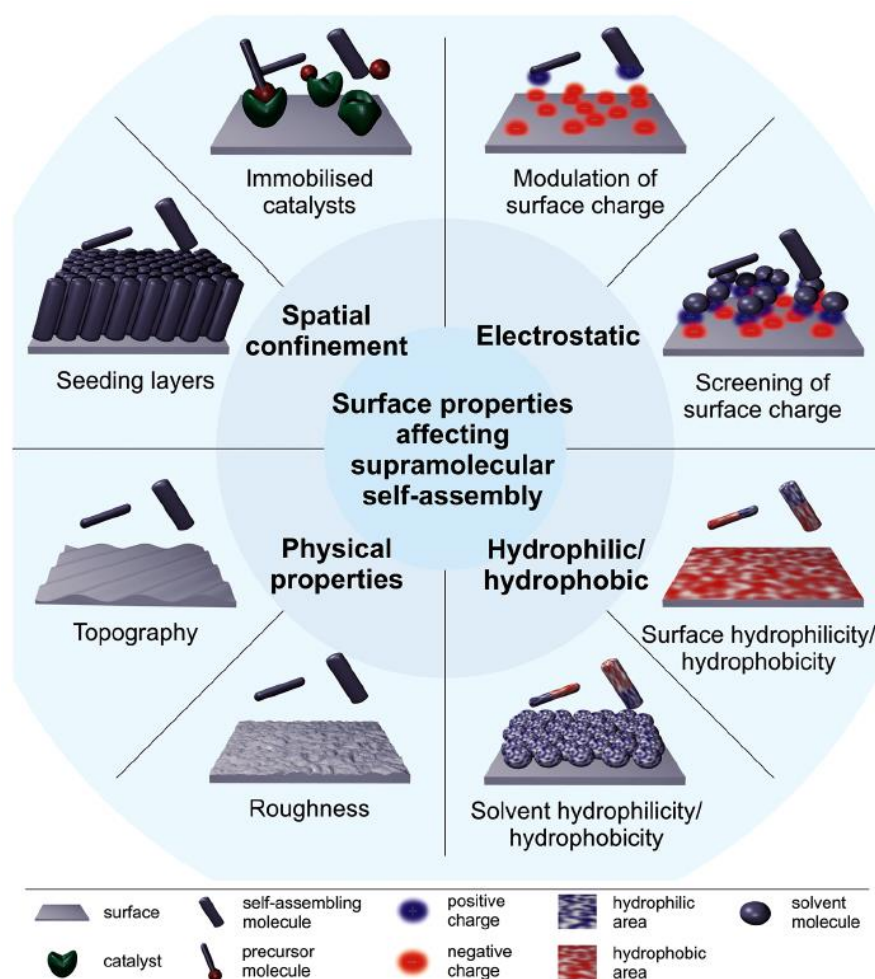


Figure 7: Overview of the surface properties that have been implicated in surface-mediated self-assembly processes<sup>69</sup>.  
Copyright © 2018 American Chemical Society

These works were the object of two reviews published recently. The first one in 2017 by Vigier-carrière *et al.*<sup>130</sup> and the second one in 2018 by Yang *et al.*<sup>69</sup> Here we will be rapidly describing the main points highlighted by these reviews and articles published afterwards will be described too.

### 1.2.1. Surface seeding of LMWH self-assembly

The surface-induced localized gelation of LMWH at concentrations far below the critical gelation concentration (CGC) was first observed by B. Xu in 2002 on cells<sup>70</sup> and demonstrated by J.C. Tiller in 2003.<sup>71,72</sup> One easy way to induce localized formation of a supramolecular hydrogel is to adjust the hydrophilicity/hydrophobicity balance or the charge of the surface in order to favor nonspecific adsorption of the hydrogelator molecules onto the surface through weak interactions. The high concentration of adsorbed hydrogelator molecules then favors self-assembly and gel formation at the substrate. The chemical system used by Tiller was based on this strategy. At acidic pH, the selected surface was positively charged because of the

presence of ammonium group ( $-\text{NH}_3^+$ ), while the hydrogelator was negatively charge. This allowed them to interact by electrostatic bonding. The hydrogelator bound to the surface self-assembled with other hydrogelators present near the surface by the local increase of the concentration of hydrogelator. This led to the generation of broccoli-like structure localized at the liquid-solid interface (Figure 8).

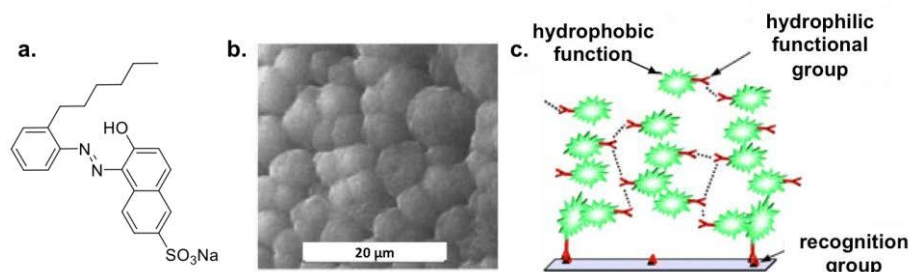


Figure 8: a) Chemical structure of the anionic hydrogelator, b) broccoli-like structure of the self-assembly formed on modified-glass surface observed by SEM, c) model proposed by the authors to explain the localized gelation on surface through electrostatic attraction of hydrogelator onto a surface.<sup>72</sup> Reproduced from ref (72) with permission of The Royal Society of Chemistry.

Two others examples were described, one using grafting of phenyl or  $-\text{OH}$  groups onto the surface to favor the interaction of a specific hydrogelator with the surface (Figure 9).<sup>73,76</sup> Another example to obtain a more specific interaction between the surface and the hydrogelator, grafted directly the hydrogelator onto the surface to increase the propensity of LMWH to self-assemble into hydrogels (Figure 10).<sup>74,75</sup> What was observed is that the way used to locally generate the hydrogels from the surface influences the shape and the mechanical properties of the hydrogel.<sup>73</sup>

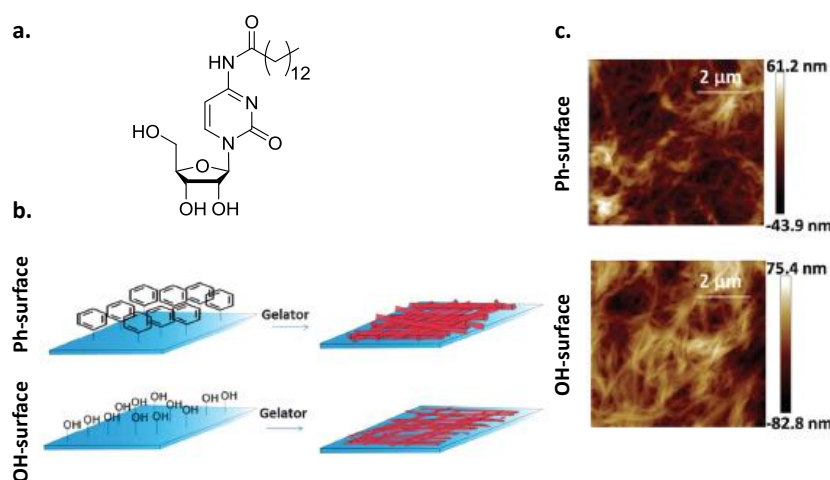


Figure 9: a) Chemical structure of the hydrogelator  $\text{C}_{14}$ -cytidine, b) schematic representation of the two glass surfaces studied exhibiting either a hydrophobic or a hydrophilic property and used as substrates for hydrogel formation, c) AFM images observed when both substrates are brought in contact with  $\text{C}_{14}$ -cytidine solution, distinct fibrillary network are induced in each case.<sup>73</sup> Copyright © 2016 Reproduced from ref (73) with permission of The Royal Society of Chemistry.

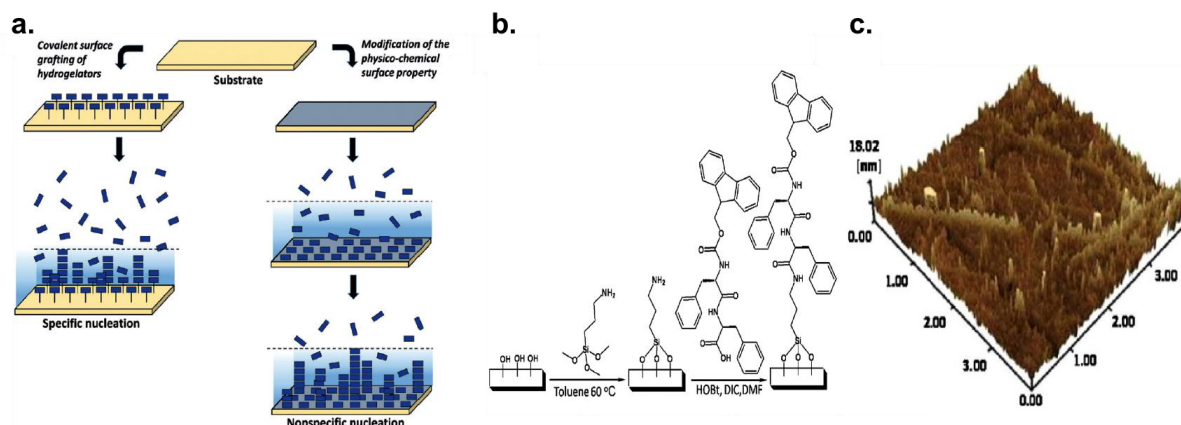


Figure 10: (a) Schematic representation of surface modifications that lead to the localized self-assembly of LMWH in the close vicinity of the surface.<sup>130</sup> Copyright © 2018 Wiley. b) The surface modification of silica wafers with the hydrogelator FmocNH-FF-COOH, b) three-dimensional AFM images (4 μm x 4 μm) of Fmoc-FF-OH modified silica wafers after self-assembly in aqueous solution of FmocNH-FF-COOH (0.8 mg/mL) and a rinsing step with aqueous acidic solutions (pH 4).<sup>74</sup> Copyright © 2011 Elsevier B.V.

### 1.2.2. Covalently bond catalysts on surfaces induced self-assembly of LMWH

The second strategy reported to control the self-assembly of hydrogelators exclusively at an interface is based on generating the LMWH directly at or near the surface (Figure 10a right). Generating hydrogelators near the surface can be achieved by producing chemical species, called morphogens, that diffuse from the surface towards the bulk and which switch molecules present in solution from a non-self-assembling state (precursor) into a self-assembling one (hydrogelator) (Figure 11). In the case of LMWH, the reported systems use protons as morphogens and LMWH presenting weak acid groups. An acidic flow diffuses from the surface towards the solution and protonates the LMWH by changing its hydrophilicity/hydrophobicity balance. This then induces self-assembly.

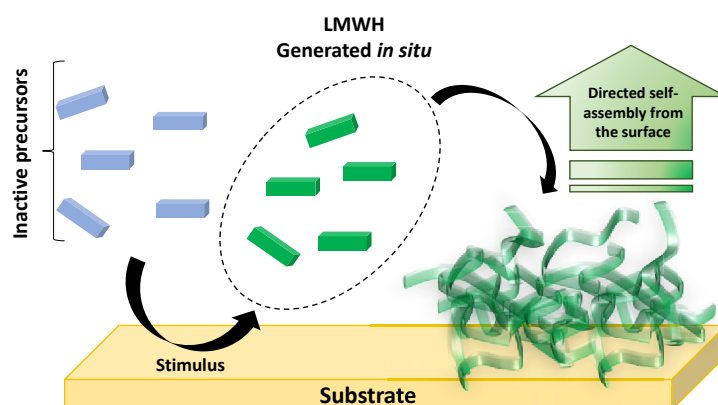


Figure 11: Catalytically active surface transforms inactive precursors in solution into efficient LMWHs. The local accumulation of the latter in the close vicinity of the surface induces the directed self-assembly<sup>130</sup>.

In 2014, van Esch *et al.*<sup>77</sup> reported a procedure for the preparation of LMWH by using protons, which catalyzes the *in situ* formation of hydrogelators. They developed an ingenious way to generate a spatially controlled supramolecular

hydrogel using a micropatterned catalyst on a surface (Figure 12.1).<sup>78-79</sup> Different shapes of catalyst micropatterns were realized (lines, circles, squares, etc.) (Figure 12.2). The authors observed that the hydrogel pattern closely follows the catalyst pattern underneath. This observation was followed by confocal fluorescence microscopy *via* a fluorescent probe added to the mixture. This method can achieve multilevel organization among the nanofibers, which is very promising for further development.

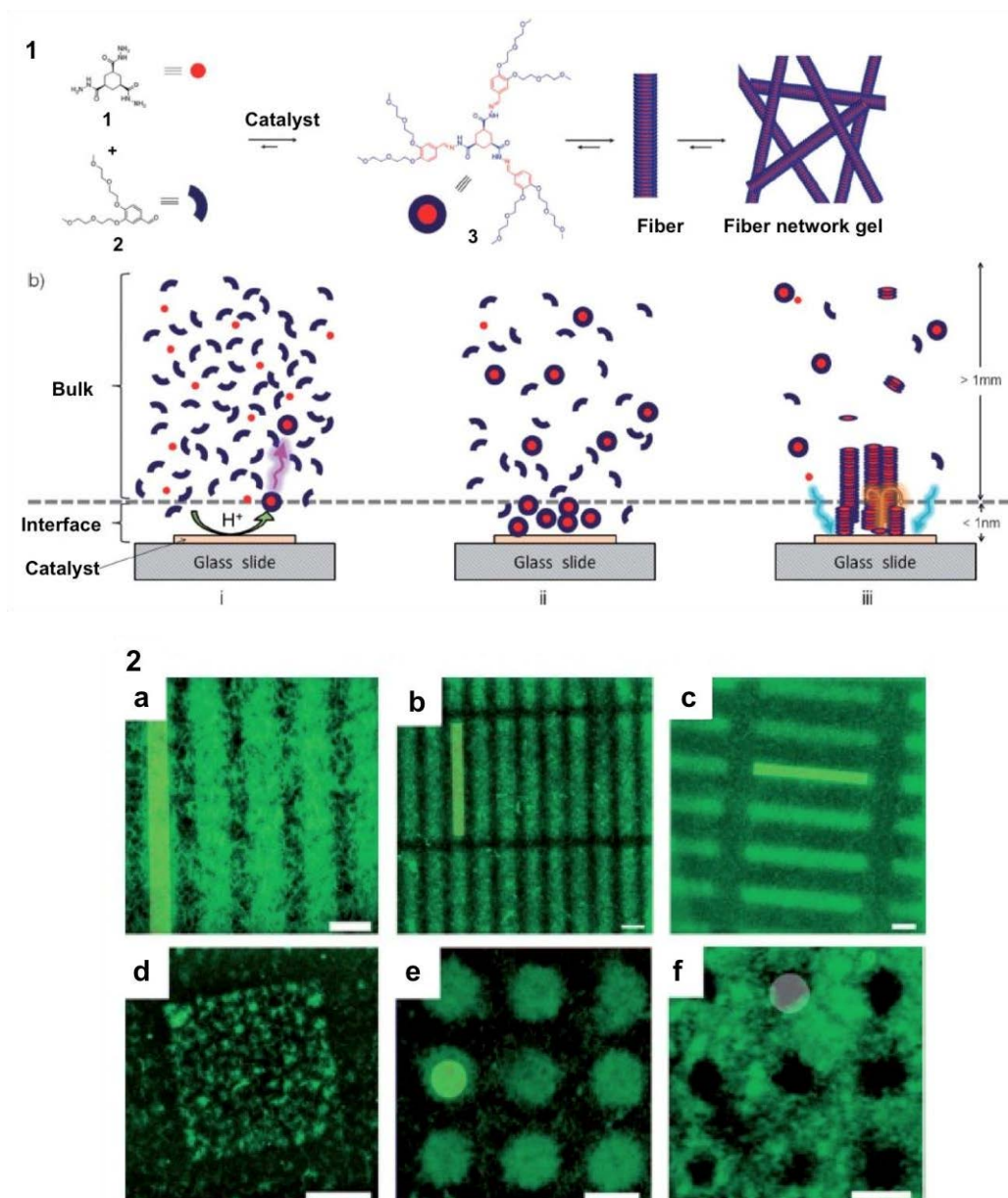


Figure 12: 1) Schematic of the molecules involved in the self-assembly and the localization of the self-assembly. 2) Confocal microscopy images of patterns composed of self-assembled fibers, which reflect the previously stamped catalytic pattern shown by the green areas on the images. a) Lines: 10 μm width with 15 μm spacing, b) rectangle: 10 x 100 μm with 10 μm spacing, c) 10 x 100 μm rectangles with 25 μm spacing, d) square of 50 x 50 μm, e) discs with 15 μm diameter and 20 μm spacing, f) negative image of (e). Scale bars: 20 μm.<sup>79</sup> Copyright © 2014 Wiley.

### 1.2.3. Electrochemical trigger of pH-responsive self-assembly of peptides

Another way to produce *in situ* hydrogelators is by using electrochemistry. This strategy is one of the most used to localized self-assembly on a surface. Cameron's group developed, in 2010, a convenient method to direct the self-assembly of an aromatic peptide amphiphile (PA), Fmoc-LG-OH (L=leucine, G=glycine), into an ultrathin hydrogel membrane on an electrode (Figure 13a).<sup>80</sup> The self-assembly of the dipeptide hydrogelator was triggered by a decrease of pH generated at the electrode through the electrochemical oxidation of hydroquinone into 1,4-benzoquinone, releasing two protons per oxidized hydroquinone (Figure 13b). The adjustment of the current intensity affects the pH near the surface and thus impacts the Fmoc-LG-OH self-assembly, allowing for a precise control of the growth of a fibrous network (Figure 13c,d).

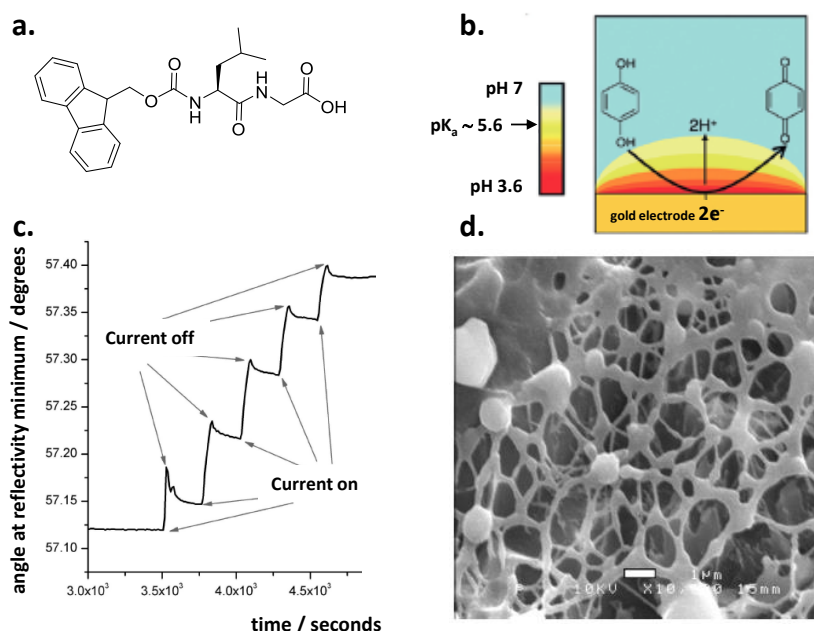


Figure 13: a) Chemical structure of the aromatic PA, Fmoc-LG-OH, b) electrochemical oxidation of 1,4-hydroquinone to generate a gradient of protons going from the bottom to the top, c) SPR experiment showing the stepwise growth of the dipeptide Fmoc-LG-OH hydrogel with each 60 s current pulse, d) Cryo-SEM image of the top surface of an electrically grown gel film. Scale bar = 1 μm<sup>80</sup>. Copyright © 2010, American Chemical Society.

In another contribution, the same authors first produced the protons electrochemically in the presence of the peptides until a hydrogel of 80–100 nm thickness was reached. They then stopped the electrochemical stimulus still in the presence of the Fmoc peptides and observed that the gel continues to grow slowly at least over 48 h<sup>81</sup>. It was suggested that the initial electro-stimulated gel on the surface played the role of a seed layer for the continuation of the gelation process observed without continuing to apply a stimulus (Figure 14).<sup>81</sup>

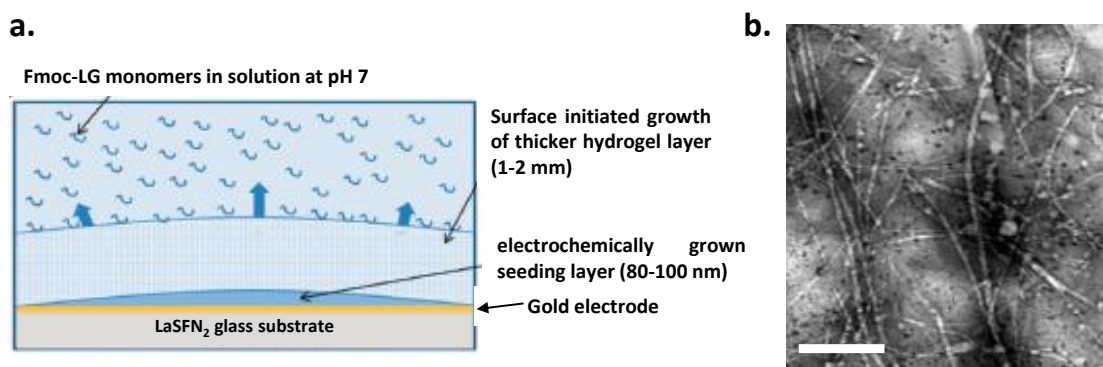


Figure 14: a) Schematic representation of the surface initiated growth of an Fmoc-LG film, b) Shows a TEM image of the development of fibrous structures after the seeding layer was left in contact with Fmoc-LG-OH in solution for 48 h. Scale bar = 200 nm<sup>81</sup>. Copyright © 2013 Reproduced from ref (81) with permission of The Royal Society of Chemistry.

This electrochemically generated pH decrease generated from a surface also allowed the spatially resolved self-assembly of carbazole-protected amino-acids.<sup>82</sup> The self-assembly of another hydrogelator initiated locally by the electrochemical oxidation of hydroquinone was recently investigated using patterned electrodes.<sup>83</sup> By using the N-protected phenylalanine with an Fmoc group, Fmoc-F-OH (**7**) (Figure 15), Payne extended the electrochemical control over LMWH self-assembly by studying the reversibility of the assembly/disassembly process of hydrogelators. The hydrogel disassembled in response to a cathodic current that increased the pH in the proximity of the electrode surface. When simultaneous cathodic and anodic currents were addressed to adjacent electrodes, spatially specific assembly and disassembly of Fmoc-F-OH were observed on the same chip. This spatial and temporal control over the proton gradient is the key process to pattern reversibly assembly and disassembly of aromatic N-protected amino acids. This represents a new step towards further control of self-assembly.

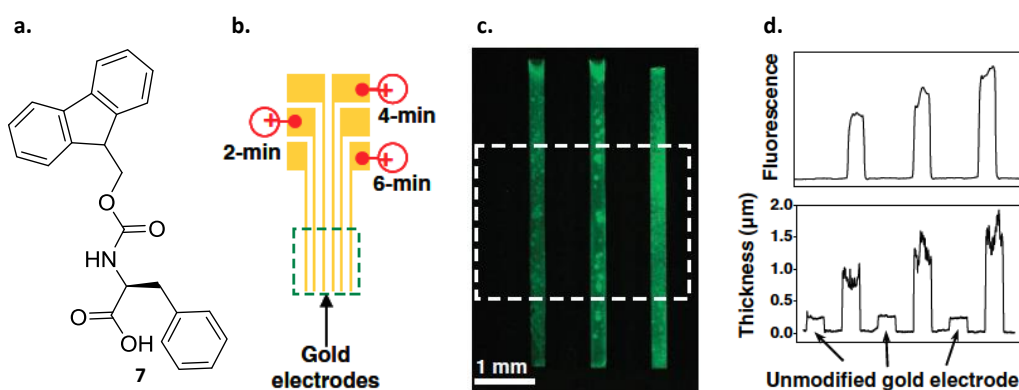


Figure 15: a) Chemical structure of the Fmoc-F-OH, b) Spatial-selectivity of Fmoc-F-OH electrodeposition. A chip with patterned gold electrodes (250 μm wide gold lines patterned onto silicon wafer), c) demonstrates spatial selectivity of electrodeposition of 10 mM Fmoc-F-OH (0.005 M fluorescein-labeled dextran was included for visualization), d) Thicknesses of the deposited self-assemblies on the electrodes of c)<sup>84</sup>. Copyright © 2011 Wiley.

In 2014 Adams and Cameron took up another challenge; they proposed to electrochemically produce protons with hydroquinone to trigger spatially and temporally resolved multi-component hydrogels.<sup>84</sup> By using different aromatic peptides present simultaneously in solution, the chemical constitution of a gel could be controlled. By changing the electrochemical parameters controlling the oxidation of hydroquinone, they tuned the production of protons and thus the self-assembly

propensity of peptides presenting different pKa values to self-assemble. Fine adjustment of the pH near the electrode surface permitted reaching pKa<sub>8</sub> (pKa of compound **8**) in the first place. LMWH **8** self-assembled to form a 3D network of fibers entrapping both water and the second non-self-assembling LMWH **9** (Figure 16). Then, a continuous decrease of pH initiated the self-assembly of LMWH **9** to finally form an interpenetrated multi-component hydrogel. The chemical composition of the gel could be controlled temporally and spatially through the fine adjustment of electrical inputs.

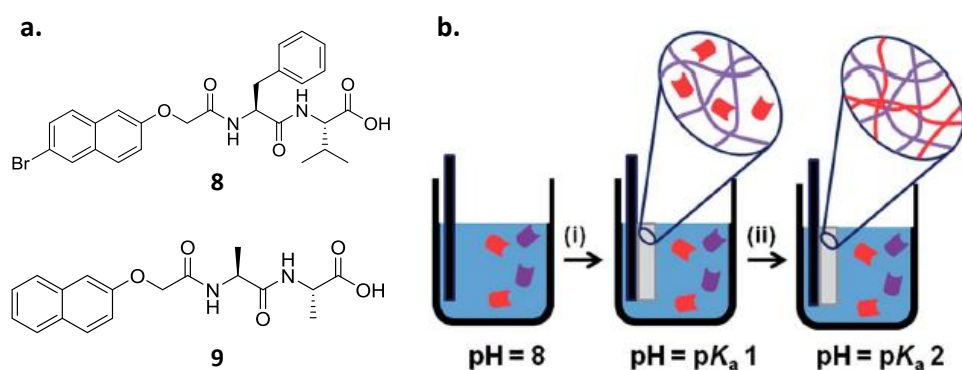


Figure 16: a) Chemical structures of dipeptide-based LMWH **8** and **9**; b) schematic showing the sequential assembly of two LMWH **8** and **9** in a multicomponent system<sup>84</sup>. Copyright © 2014 Reproduced from ref (84) with permission of The Royal Society of Chemistry.

Other studies, by Hermans *et al.*, used the production of protons to control the localization of hydrogels formations in a microfluidic device.<sup>85</sup> They described a pH-regulated self-assembly of an amphiphilic C<sub>3</sub>-symmetric benzene-1,3,5-tricarboxamide peptide conjugate (BTA-1, Figure 17a), and showed how surface-assisted assembly is controlled inside microfluidic devices and from the surface of elastomer cubes.<sup>86</sup> When a 5-10 mm<sup>3</sup> cubes of poly(dimethylsiloxane) (PDMS) was soaked in concentrated HCl<sub>aq</sub> for 96 h, they were able to observe a propagating front of supramolecular polymerization/gelation (Figure 17c). After few minutes, when the protons started to diffuse out of the PDMS, BTA-1 monomers became activated and started to self-assemble at the surface forming a growing hydrogel layer on the PDMS cube (Figure 17b). But the authors observed that the proton diffusion from PDMS is rate-limiting and the fiber bundling/gel started to stop growing. To investigate the early stages of gelation, they printed two microfluidic channels on the PDMS. One was filled with a solution of BTA-1 and the second one with a pH 4 potassium hydrogen phthalate buffer (Figure 17d,e). After 5 min, the diffusion of proton started through the PDMS and the fluorescence intensity in the channel containing BTA-1 gradually increased, which indicates that the self-assembly is occurring. The time of diffusion in this experiment is more in the order of water diffusion in PDMS (10<sup>-9</sup> m<sup>2</sup>s<sup>-1</sup>)<sup>87</sup> instead of proton diffusion in water (9 x 10<sup>-9</sup> m<sup>2</sup>s<sup>-1</sup>)<sup>88</sup> and it enabled the formation of supramolecular polymer structure formation close to the surface which grew gradually outwards.

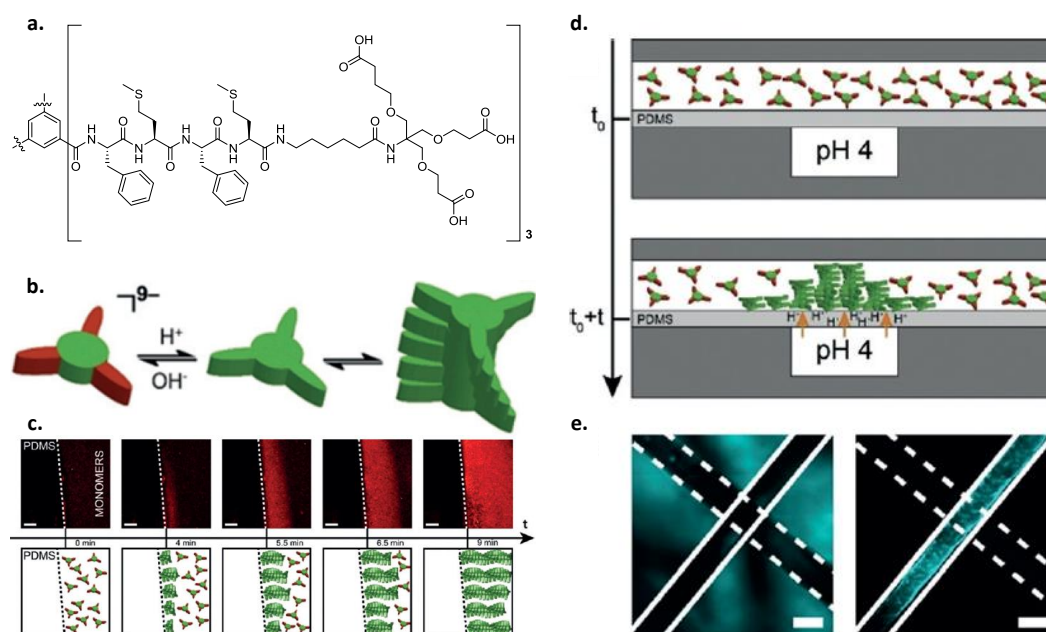
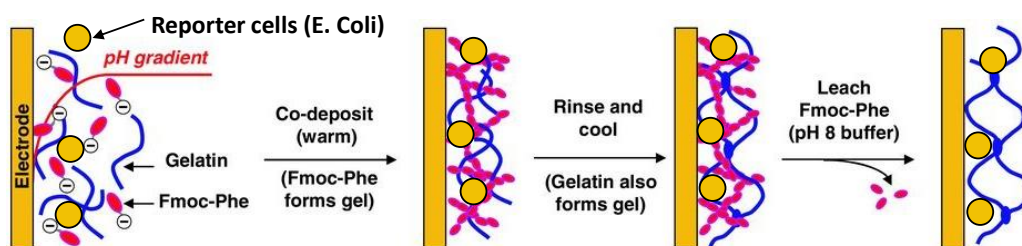


Figure 17: a) Structure of BTA-1, b) Schematic representation showing that the tricarboxylic acid moieties can be protonated and deprotonated as a function of the pH. At high pH ( $pH > 5.6$ ), the monomer has 9 negative charges, and the resulting electrostatic repulsion between monomers prevents self-assembly, c) surface-assisted self-assembly from a PDMS cube. Confocal microscopy of a  $5 \text{ mm}^3$  PDMS cube soaked in saturated HCl solution for 96 hours and subsequently dropped in a  $160 \mu\text{M}$  BTA-1 solution at pH 7.4 (monomers). After 4 min, a thin hydrogel layer is seen to emerge from the PDMS block, followed by a propagating front of polymerization. Nile Red at  $5 \mu\text{M}$  is used as a dye. Scale bar =  $200 \mu\text{m}$ ., d) Side view of the microfluidic device. It consists of two perpendicular channels on top of each other and separated by a  $100 \mu\text{m}$  PDMS membrane. The bottom channel is filled with a pH 4 buffer and the top is filled with  $160 \mu\text{M}$  BTA-1 solution at pH 7.4 (monomers). At  $t=t_0$ , one starts the flow of the buffer channel at  $500 \mu\text{L}\cdot\text{min}^{-1}$  while the monomer channel is at rest (that is, no flow). The protons start diffusing through the membrane and eventually reach the other channel, activating the monomers in solution that starts growing on the membrane. The self-assembly occurs at the intersection of the two channels., e) Transmitted light (left) and fluorescence image (right) of the intersection between the two channels taken after the experiment. Only the top channel shows fluorescence intensity, which indicates that BTA-1 monomers self-assemble in response to the pH-gradient. Scale bar =  $500 \mu\text{m}$ <sup>86</sup>. Copyright © 2018 Wiley.

The strategy to produce electrochemically a proton gradient to localize self-assembly gives rise to different applications. One example is the creation of an efficient biosensor by Payne *et al.* in 2012. The biosensor is based on the encapsulation of bacteria by using the molecule **7** (Fmoc-Phe) as hydrogelator.<sup>29</sup> The aim of this study was to develop a multi-component matrix able to detect the presence of S-adenosyl-homocysteine (SAH) in the surrounding solution, used as a model substrate. The fabrication of this sensitive matrix was achieved in two steps (Figure 18): first, self-assembly of **7** was triggered through the application of an anodic current generating a localized proton gradient. This gelation was realized with a warm solution containing the hydrogelator of course, but also gelatin and cells (*E. Coli*) leading to their entrapment into the self-assembled structure. When the system was cooled down, an interpenetrated network formed, due to the assembly of gelatin chains. This hybrid network was viable for *E. Coli*. Then, the peptide-based scaffold was dissolved thanks to a simple addition of a basic buffer ( $pH=8$ ) providing a gelatin matrix embedded with cells.



### 1. Electrochemical self-assembly



### 2. Enzymatic covalent crosslink

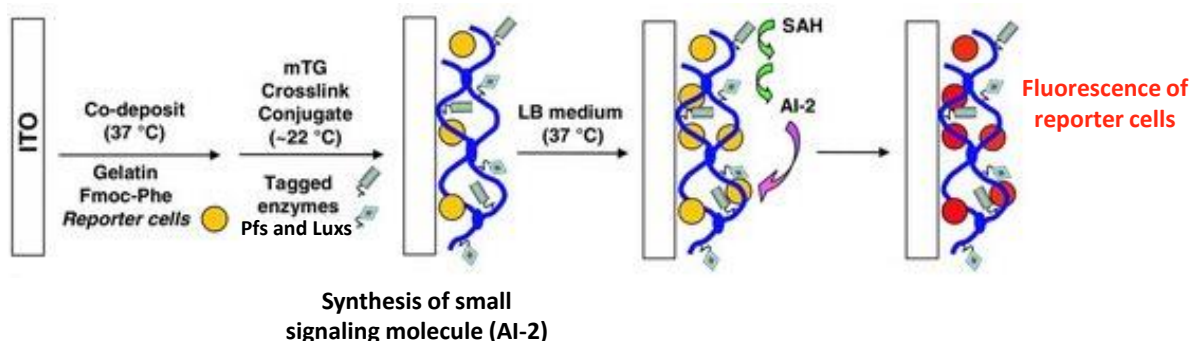


Figure 18: Experimental pathway for the co-deposition of gelatin and Fmoc-Phe. Multifunctional gelatin based matrix is capable of in situ synthesis and detection of a bacterial quorum sensing signaling molecules<sup>29</sup>. Copyright © 2012 Wiley.

In conclusion, using an electrochemical trigger to direct and control the formation of pH-responsive self-assembly of peptides is a really powerful way to do localized self-assembly formation. But the use of an electrode to realize it reduces considerably the scope of applications. That is why, another strategy was born to direct and control the generation of self-assembly by localizing enzymes on all kind of surfaces.

### 1.3. Localized Enzyme Assisted Self-Assembly of peptides (LEASA)

Since 2004, enzyme catalysis emerged as a valuable trigger to spontaneously and selectively transform non-assembling precursors into efficient LMWH in the bulk.<sup>89</sup> Despite the fact that enzyme-assisted self-assembly is widespread in nature to achieve spatial control over complex architectures, the immobilization of enzymes onto a surface to produce LMWH locally and achieve surface-localized hydrogel growth is a field that emerged recently (Figure 19). Enzymes used as catalysts ensure a permanent catalytic active surface that, in the presence of precursors, leads to a continuous generation of self-assembling molecules. This autonomous control over the rate of LMWH formation confined to the surface can contribute to the development of smart surfaces that are able to direct the organization of matter in space and time.

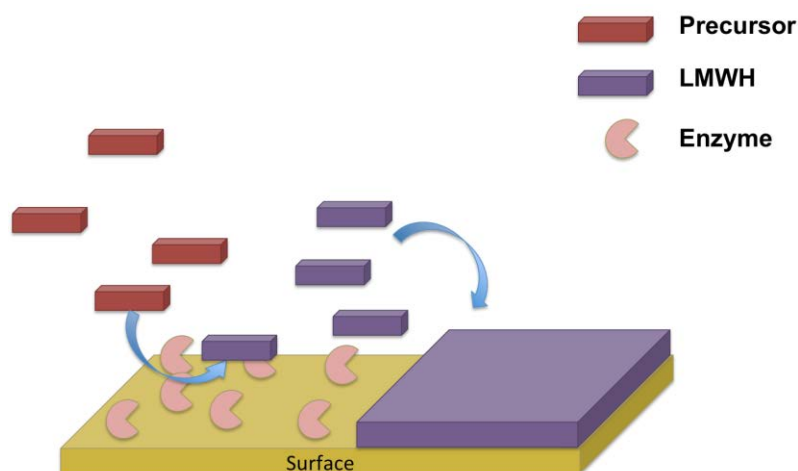


Figure 19: Schematic of the principle of LEASA.

### 1.3.1. Localized Enzyme Assisted Self-Assembly (LEASA) on planar surfaces

Two different approaches exist to create LEASA processes on planar surfaces: one by grafting covalently the enzyme onto the surface and the second by adsorbing it by electrostatic interactions.

#### 1.3.1.1. LEASA by covalently bonding enzymes

In 2009, Ulijn was the first to immobilize an enzyme, thermolysin, covalently linked on a surface in order to induce local self-assembly of a mixture composed of Fmoc-L-OH (**10**) and the diamino acids LL-OH (**11**) (Figure 20a).<sup>90</sup> Thermolysin is able to both catalyze the coupling reaction between **10** and **11** and hydrolyze amide bonds, leading to a statistical distribution of oligopeptides Fmoc-L<sub>n</sub>-OH. These resulting aromatic peptides self-assemble to form fibers. During the early stages of the self-assembly process, nanofibers starting from the expected aggregates of enzymes were observed (Figure 20b). This pioneer work has shown that the confinement of enzymes onto a surface can be a fine strategy to locally nucleate and direct LMWH-fibers growth at the interface.

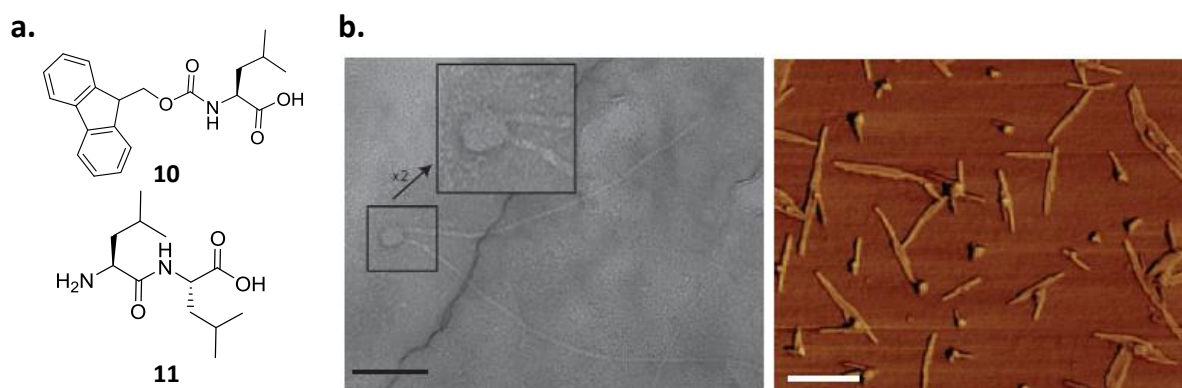


Figure 20: a) Chemical structures of molecules **10** and **11**, b) TEM image observed with fiber propagation, demonstrating confined fiber growth from unidentified spherical structures (left, scale bar = 100 nm) and the same process visualized by AFM phase imaging (right, scale bar = 250 nm)<sup>90</sup>. Copyright © 2008, Springer Nature.

More recently, the same group showed the effect of the anchoring strength of an enzyme on the surface on the self-assembly process.<sup>91</sup> Using again thermolysin and the system Fmoc-T-OH/ F-NH<sub>2</sub> (T=threonine, F-NH<sub>2</sub> = phenylalanine with a carboxamide group at C-terminal position), forming the hydrogelator Fmoc-TF-NH<sub>2</sub> *in situ*, they showed that they can direct the self-assembly from a surface by covalently bonding the enzyme but also by adsorbing it. When the enzymes are covalently bonded to the surface, the resulting hydrogel is thinner than when the enzymes are only adsorbed. The postulated hypothesis is that, when only adsorbed on the surface, the enzymes are desorbed during the self-assembly process, leading to a thicker hydrogel formation (Figure 21).

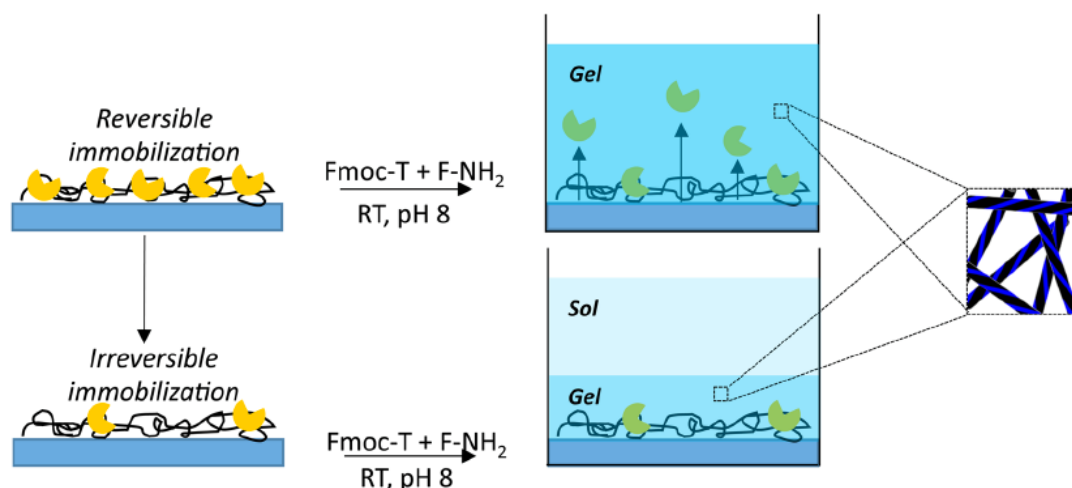


Figure 21: Schematic representation of reversible and irreversible enzyme immobilization on modified surfaces for generation of LEASA<sup>91</sup>. Copyright © 2017 American Chemical Society

### 1.3.1.2. LEASA by non-covalently bonding enzymes

In 2011 Williams *et al.* reported the localization of the self-assembly of the hydrogelator Fmoc-L<sub>3</sub> by adsorbing thermolysin on a glass substrate. When a solution containing the two precursors 10 and 11 with a fish ECM protein, laminin, was dropped off onto the modified glass substrate the authors were able to direct the self-assembly from the surface but also to entrap laminin in the resulting fibrous network.<sup>92</sup> The authors showed also the possibility to inject the hydrogel containing the laminin in zebrafish to an area of tissue affected by ECM disease. This approach could be of interest to treat genetic diseases involving the laminin gene family.

In 2017, Vigier-Carrière *et al.* established that  $\alpha$ -chymotrypsin confined on a surface is able to oligomerize ethyl ester dipeptides KL-OEt (K = lysine, OEt = ethyl ester group at C-terminal position) and produce oligopeptides (KL)<sub>n</sub>-OEt, which are efficient LMWHs at the surface.<sup>93</sup> The growth of the self-assembly network starts after a lag time that can easily be tuned by varying the surface density of  $\alpha$ -chymotrypsin and the concentration of KL-OEt in solution. The thickness of the fiber

network formed can reach up to around 10  $\mu\text{m}$ . Cryo-SEM images show that the gel network is denser at the interface than far from the interface (Figure 22), which confirms that the concentration of hydrogelators is denser near the surface. Regarding the thickness reached, this result confirmed the work of Ulijn's group about the desorption of enzymes. However, the amount desorbed must be lower than the one on the surface to observe such densification near the interface.

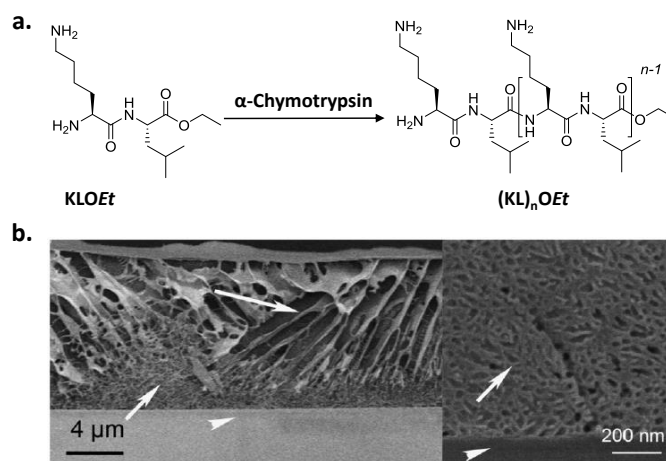


Figure 22: a) Oligomerization of KL-OEt into  $(\text{KL})_n\text{OEt}$  catalyzed by  $\alpha$ -chymotrypsin, b) Cryo-SEM images of the  $(\text{KL})_n\text{OEt}$ -based hydrogel in z-section<sup>93</sup>. Copyright © 2017, American Chemical Society.

Nevertheless, when a too-low initial concentration of precursors is present near the active surface, no gel forms. Using the Fmoc-FFY( $\text{PO}_4^{2-}$ )-OH peptide (molecule **12**), Vigier-Carière *et al.* circumvented this difficulty by modifying the surface with a thin nano-architected film including alkaline phosphatase and a layer of polyelectrolytes bearing Fmoc-FFC peptides, C (which stand for cysteine) was used as a linker between the hydrogelator, Fmoc-FFY (**13**), and the polyelectrolyte. The resulting modified polyelectrolyte played the role of a seed layer (Figure 23a).<sup>94</sup> Then, when AP dephosphorylates **12** into **13** the self-assembly occurs at a concentration lower than the critical gelation concentration, leading to a hydrogel underpinned by a nanofiber network that evolved over time (Figure 23b). Varying the density of enzymes in the nanofilm or the surface density of the seeding peptides on the surface provided different kinds of nanofiber architectures (Figure 23c).

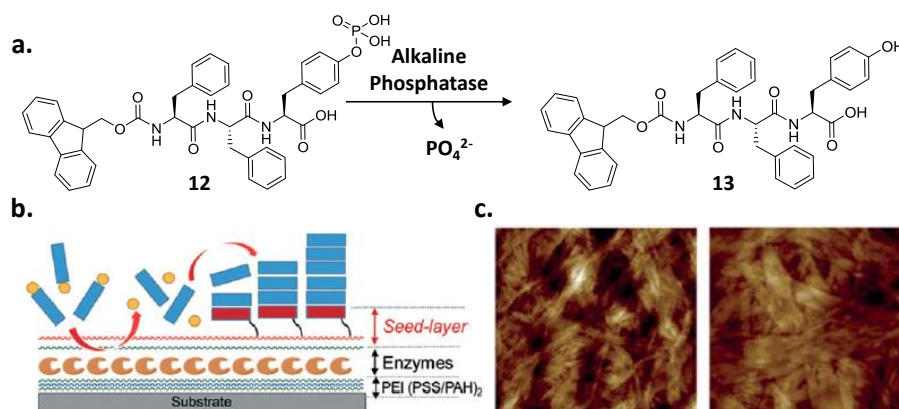


Figure 23: a) Chemical structures of molecules **12** and **13**, b) Schematic representation of the nanoarchitected film on a surface, allowing the localized enzyme-assisted self-assembly based on a seed layer, c) AFM images of the hydrogel formed from the surface at 120 min and 12 h.<sup>94</sup> Copyright © 2015, Wiley.

To sum up, these two approaches, covalent and non-covalent bonding of enzymes to direct self-assembly, are powerful tools for achieving controlled self-assembly directed from planar surfaces. They lead to different thicknesses depending on the chosen approach as highlighted by Ulijn's group. To help the self-assembly formation, the use of a bioactive seed-layer is useful and will allow to control and tune both the kinetic of the formation network and the fiber morphologies.

More recently, the use of LEASA was also described to initiate self-assembly from non-planar surfaces.

### 1.3.2. LEASA on non-planar surfaces (i.e. nanoparticles surface)

LEASA directed on non-planar surface was not yet described when I started my Ph.D. but I will present this part which is of interest regarding the Localized-Assisted Self-Assembly strategy. In 2018, for the first time in the literature, Ulijn *et al.* reported the covalently bonding enzymes immobilization onto magnetic nanoparticles (NPs) to spatially localize the initiation of peptide self-assembly into nanofibers around NPs.<sup>95</sup> They generalized the concept for both an equilibrium biocatalytic system that forms stable hydrogels and a non-equilibrium system that normally has a preset lifetime. The system 1 is the equilibrium system, thermodynamically controlled that exploits thermolysin for reversible enzymatic condensation of peptide precursors (Fmoc-T and F-NH<sub>2</sub>) to form self-assembling hydrogelators (Fmoc-TF-NH<sub>2</sub>) (Figure 24a,b,c).<sup>96</sup> The system 2 is the non-equilibrium, kinetically controlled system using chymotrypsin that has the potential to both generate self-assembly building blocks and break them down through competing acylation and hydrolysis reactions (Figure 24a,b,c).<sup>97</sup> The precursors of system 2 are DF-OMe and F-NH<sub>2</sub> leading to the hydrogelator DFF-NH<sub>2</sub>. For both systems they obtained stable fibrous networks on the NPs surface (Figure 25a). Then, by using magnetic NPs, they showed that the hydrogelation process can be inhibited or activated depending of the position of a magnet and thus the positions of the NPs.

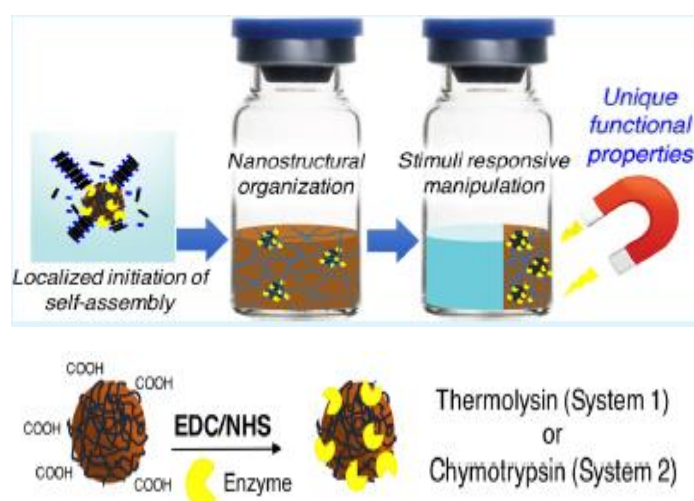
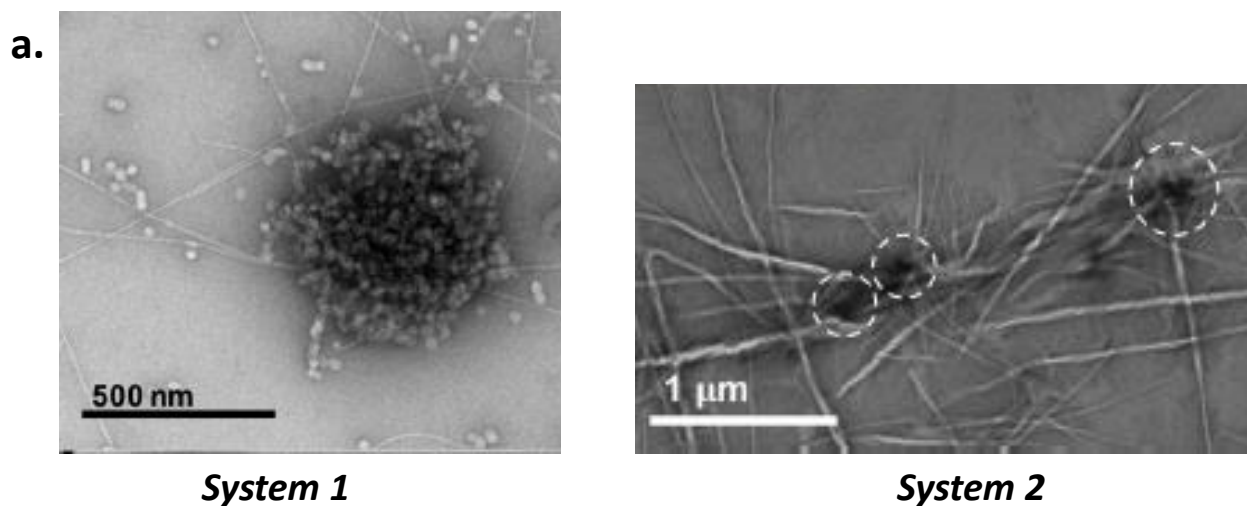


Figure 24: Schematic representation of the localized initiation of the self-assembly onto the magnetic NPs and external manipulation of the formed hydrogel with a magnet, allowed by the enzyme immobilization on the NPs used for the systems 1 and 2. <sup>9</sup>. Copyright © 2018, American Chemical Society.



b. *Figure 25: TEM images of the fibrous network initiated from the NPs surfaces for the system 1 (left) and system 2 (right).<sup>95</sup> Copyright © 2018, American Chemical Society.*

Recently, van Esch *et al.* demonstrated that growth of supramolecular hydrogel fibers can be spatially directed at the nanoscale by catalytic negatively charged nanoparticles (NCNPs).<sup>98</sup> Here, enzymes are not used as stimulus for the self-assembly generation but the approach is interesting and shows similarities with LEASA explaining why it is described in this manuscript. The NCNPs used as model present poly(acylic acid) chains on the NPs surface, which will lead, depending on the pH of the buffer, to deprotonate the acid groups. This generates negatively charged NPs and releases protons in the medium. This proton release promotes the interaction of two precursors **1** and **2** with each other leading to the formation of hydrogelator **3** (Figure 26). Then, the self-assembly is initiated thanks to the negative charged of the NPs by electrostatic interaction with the hydrogelator (Figure 26). Moreover, when they kept the hydrogelator concentration below the critical gelation concentration, the NCNPs, in a mixture of different nanoparticles (negatively charged or neutral), could be selectively trapped and precipitated out from other non-catalytic nanoparticles (Figure 27). This new approach shows a possibility to use directed molecular self-assembly to selectively trap target nano-objects, which may find applications in therapies, such as virus infection prevention, or engineering applications, like water treatment.

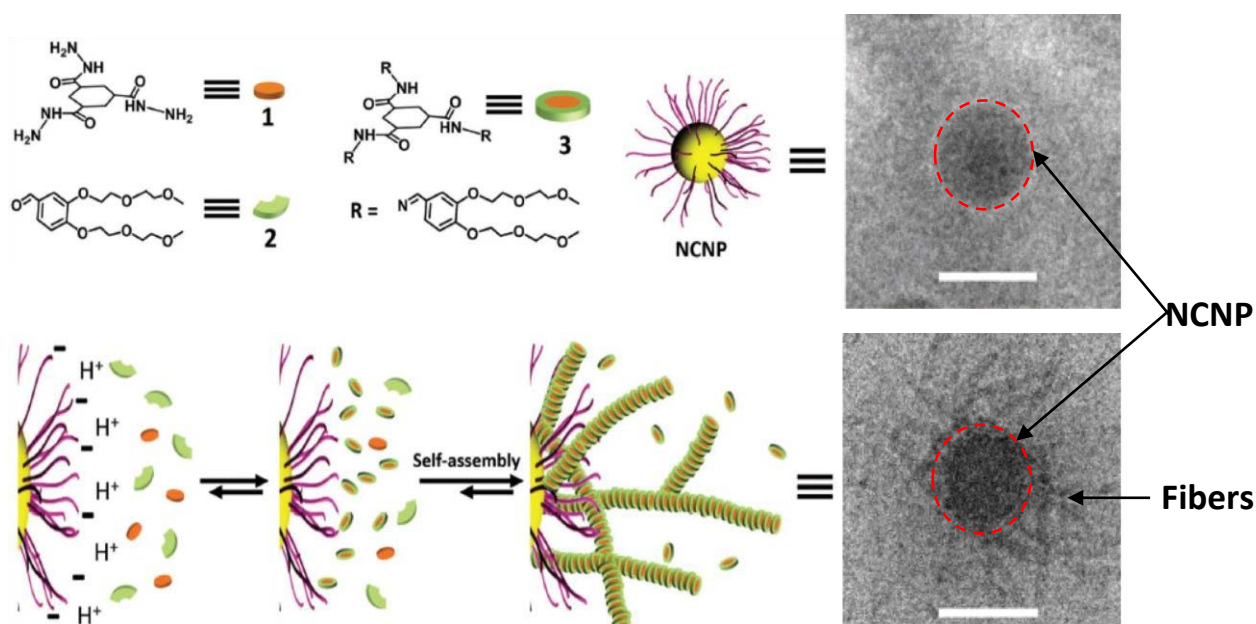


Figure 26: NCNPs directed hydrazone-based gel fibers formation. The formation of hydrazone hydrogelator 3 is catalyzed by protons near the surface of the NCNPs, ultimately leading to self-assembly of 3 into fibers in the vicinity of the NCNPs. Scale bars in the cryo-TEM images are 100 nm.<sup>98</sup> Copyright © 2018 Wiley.

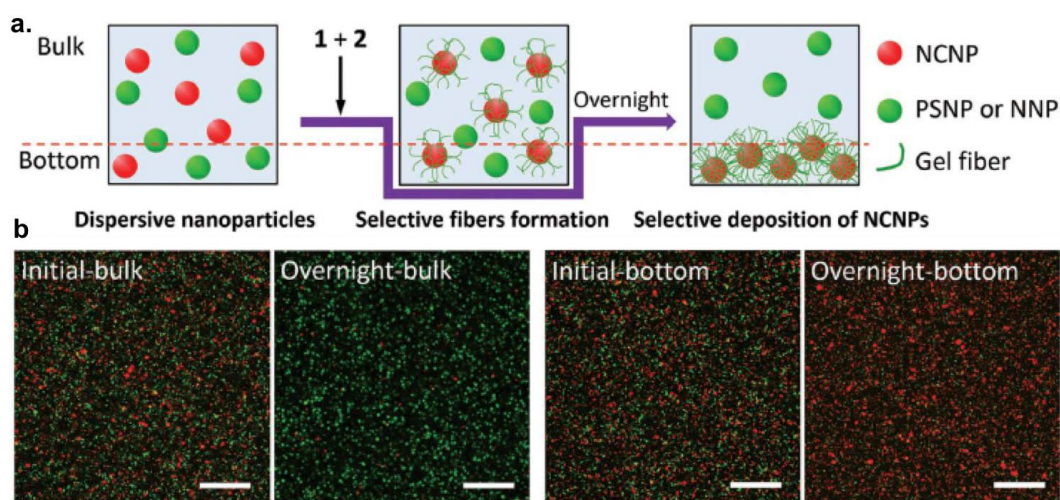


Figure 27: Selective trapping of NCNPs from the mixture suspensions with non-catalytic nanoparticles. a) illustration of local formation of fibers around NCNPs for selective trapping of NCNPs from the nanoparticles mixture, b) CLSM images of the suspension of NCNPs and PSNPs (positively charged NPs) with the addition of hydrogelator precursors 1 and 2, and generated hydrazone fibers.<sup>98</sup> Copyright © 2018 Wiley.

Wang *et al.* reported recently (2018) an enzyme-responsive core-shell nanogel with tunable thickness *via* the assembly of hydrogelators at the surface of silicon nanoparticles.<sup>99</sup> The covalently immobilized carboxylesterase at the surface of NPs can catalyze precursors (Nap-FFES) into hydrogelators (Nap-FFE) (Figure 28a), self-assembling around the surface of the NPs owing to its surface confinement effect. The nanogels that they designed act as biocompatible carriers for drug delivery. They tested this ability by using a model drug, doxorubicin hydrochloride (DOX), well known water-soluble inhibitor of cell proliferation, which enabled them to entrap it during the self-assembly formation. The self-assembly could be destroyed by the proteinase K released by cells. Indeed, during the cells assays they demonstrated that the DOX-loaded nanogel can be better taken compared to the free DOX due to

its selective uptake by tumor cells and the enzyme-specific drug delivery. Nevertheless, the free DOX experiment leads to a better cancer cell death (viability of 28.7 %) compared to DOX-loaded nanogels (viability: 46.2 %). This publication shows the great promise for the use of LEASA on NPs surfaces, specifically by the generation of core-shell hybrid nanogels as drug delivery systems and for tumor therapy.

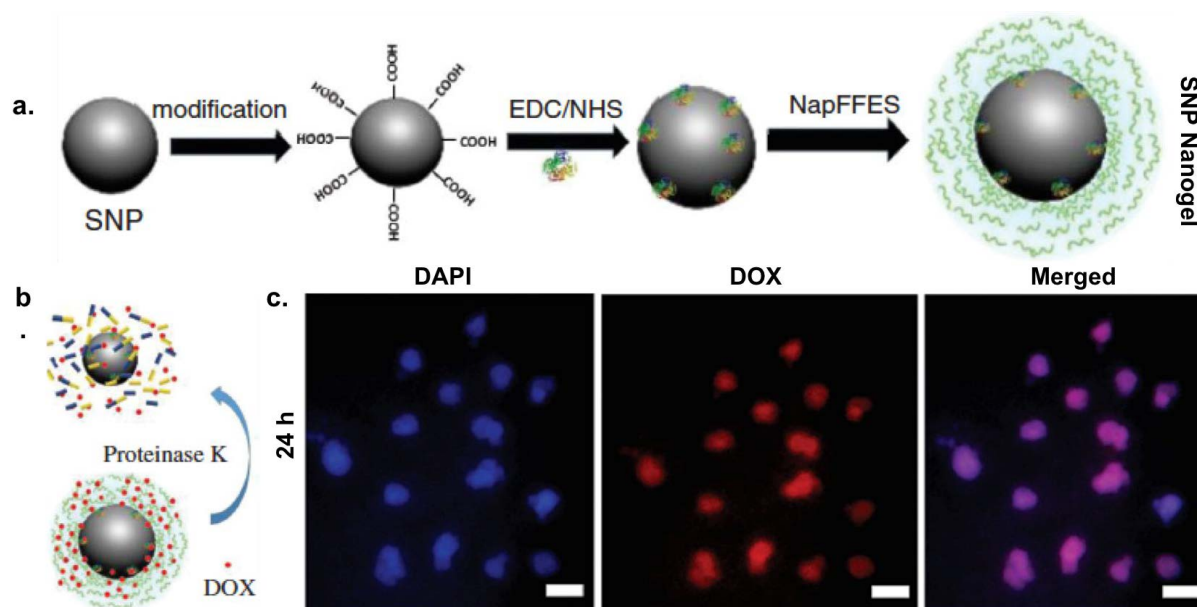


Figure 28: a) Schematic representation of the preparation of the core-shell nanogels by localized supramolecular hydrogel on  $\text{SiO}_2$  nanoparticles (SNP), b) Schematic representation of the DOX release from DOX-loaded nanogels at 37 °C in PBS and in presence of proteinase K, c) Confocal images of HeLa cells incubated with the DOX-loaded nanogels for 24 h. The images from left to right display cell nuclei stained using DAPI (blue), DOX fluorescence in cells (red) and their overlap. Scale bars = 10  $\mu\text{m}$ .<sup>99</sup> Copyright © 2018 American Scientific Publishers.

In summary, by immobilizing (bio)catalysts on NPs, hence localizing the nucleation of nanofiber self-assembly, it is possible not only to enhance the mechanical properties of a nanofibrous hydrogel networks but also to control the timing of its formation and lifetime, as well as to confer stimuli-responsiveness to the self-assembled nanostructure. Such materials afford further advances in materials science for finding more potential applications, such as designing propulsion systems<sup>100,101</sup>, fabricating nanodevices<sup>102,103</sup>, drug delivery and cancer therapy<sup>104</sup> or targeting repair of organs or tissues.<sup>105</sup>

### 1.3.3. Localized self-assembly in a host hydrogel

The pioneer work of the localization of self-assembly inside a host hydrogel was performed by Van Esch *et al.*, in 2017.<sup>106</sup> This work does not present a LEASA, because the stimulus is not an enzyme but an agar hydrogel matrix, which plays not only the role of stimulus as it is formed at acidic pH but also as host hydrogel. During my Ph.D. I collaborated in a project, which use LEASA in a host hydrogel. The article and its brief description are presented in the Annexes part of the manuscript. Nevertheless, this work is the first to report self-assembly triggered inside a host gel and this is why it is presented here. Then two solutions containing the two precursors

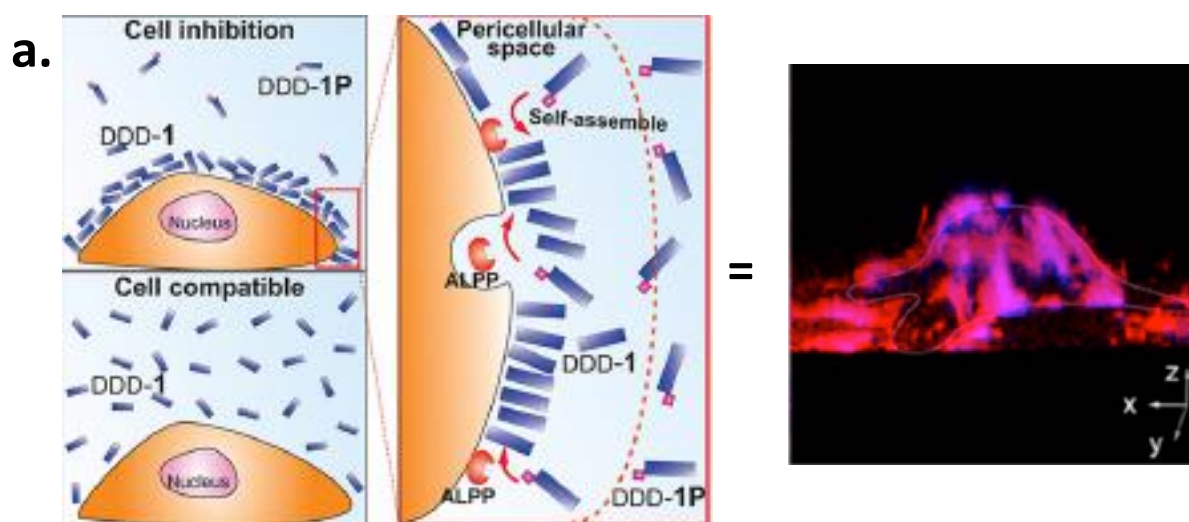


separately, a hydrazide (**H**) and an aldehyde (**A**), were dropped off at the opposite sides one from each other. Then, the two precursors diffused inside the agar matrix. When they met, under the acidic condition of the matrix, a hydrogelator, the trishydrazone (**HA<sub>3</sub>**), was generated which self-assembled, leading to a second network entrapped with the first one. With this approach, they achieved to give different forms to their second network such as triangles, coils and stars. This highlights the control that can be achieved over the formation of the self-assembly in space.

### 1.3.4. LEASA on cell surfaces

Another approach described is the LEASA in a cellular environment. Cells contain enzymes that are located inside of them and on their membrane. This localization of enzymes was investigated as another LEASA approach leading to biological applications like the entrapment of tumor cells for example.<sup>107-117</sup>

Xu *et al.* reported the first example of LEASA on cell surfaces in 2014. The self-assembly was generated by the transformation of the precursor, Nap-D-Phe-D-Phe-D-pTyr (DDD-1P) into the hydrogelator, Nap-D-Phe-D-Phe-D-Tyr (DDD) by alkaline phosphatase present on the cell membrane. The self-assembly entrapped the cell, which led to cell death. Cancer cells overexpress phosphatases compared to normal cells, which leads to a higher selectivity for cancer cells for the hydrogel formation<sup>115</sup> (Figure 31a). Other examples are present in the literature using LEASA for inducing cell death by localizing the self-assembly formation around the cell<sup>116-122, 123-125</sup> or inside it (Figure 31b).<sup>114,122,126 and 127</sup>



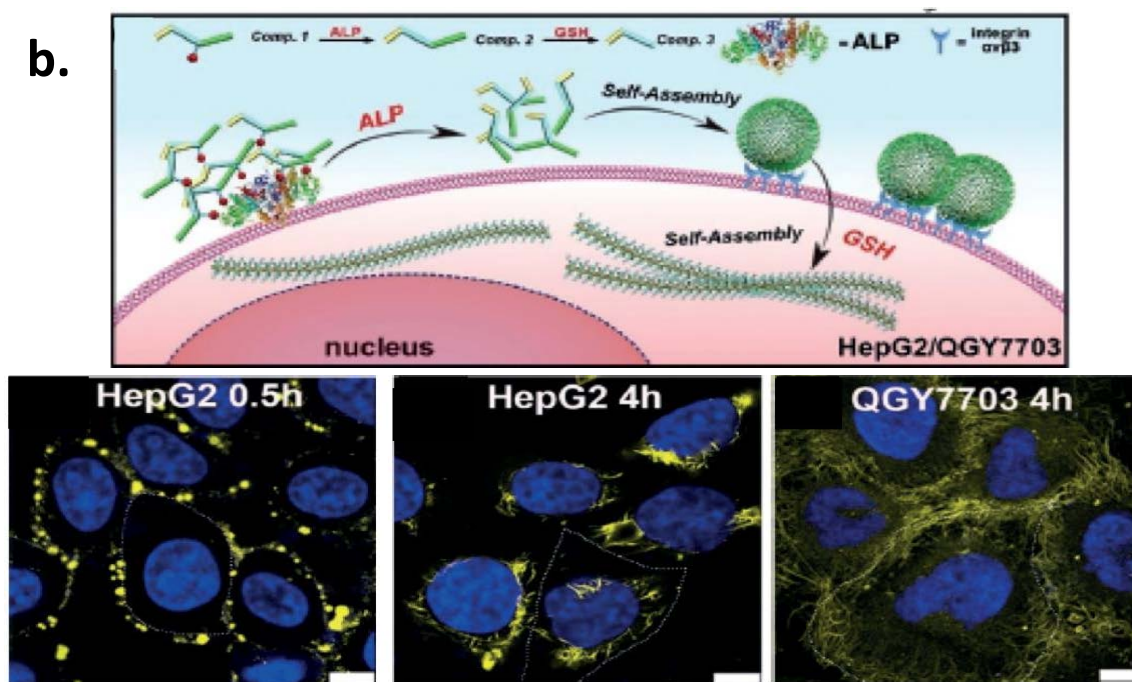


Figure 29: a) Scheme of the principle of LEASA on cell surface leading to the entrapment of HeLa cells by the fibrous network labelled by Congo red shown in the confocal image.<sup>115</sup> Copyright © 2014 American Chemical Society. b) Proposed mode of a tandem molecular self-assembly in the extra- and intra-cellular environment of liver cancer cells supported by the merged confocal microscopy images (blue fluorescence from Hoechst 33342 and yellow fluorescence from NBD represent the nucleus and NBD peptide, respectively) of HepG2 and QGY7703 cells incubated with the precursor for different periods of time. Scale bars = 10  $\mu\text{m}$ . The white dashed line indicates the boundary of a cell.<sup>126</sup> Copyright © 2018 Wiley.

## CONCLUSION

The research on supramolecular self-assembly has experienced rapid growth, over the past decade, as evidenced by the fact that the numbers of published works on the supramolecular self-assembly in 2019 is about 10 times that in 2004, according to the web of science. As illustrated by the supramolecular self-assemblies in this chapter, the research focuses are expanding from the curiosity towards an intriguing type of soft matter to the rational development of molecular biomaterials with a wide scope of applications. Specifically, Localized Enzyme-Assisted Self-Assembly is an attractive approach to trigger hydrogelation processes. Enzymatic catalysis is highly selective, able to transform continuously precursor molecules into LMWHs. This autonomous control over the rate of LMWH formation that can be confined to surfaces contributes to the development of smart surfaces able to direct organization of matter in space and time.

Among all strategies reported, aromatic peptides or protected single amino acids are the most useful for surface-assisted self-assembly processes. This chapter highlighted three main strategies implemented for this purpose. First, surfaces grafted with chemical entities were used in order to create new environments of interactions for small building blocks at proximity of the surface. In a second strategy, pH responsive hydrogelations from a surface have been intensively developed for *in situ* formation of self-assembling building blocks. The decrease of pH is confined at the vicinity of the surface by electrical signal or soft lithography of specific moieties. Finally, in a third strategy, natural enzymes were used as highly selective and efficient stimuli able to catalyze the formation of self-assembling building blocks on planar or non-planar surfaces.

This last approach was first published in 2009 and was applied to biological systems more recently (in 2014). During the three years of my Ph.D., my research work was based on this third strategy in order to design sophisticated surfaces displaying catalytic properties or being of biological interest.

## REFERENCES

1. Lehn, J.-M., Perspectives in supramolecular chemistry – from molecular recognition towards molecular information-processing and self-organization. *Angew. Chem., Int. Ed.*, **1990**, *29*, 1304.
2. Whitesides, G., *et al.*, Molecular self-assembly and nanochemistry - a chemical strategy for the synthesis of nanostructures, *Science*, **1991**, *254*, 1312.
3. Luisi, P., Chemistry constraints on the origin of life, *Isr. J. Chem.*, **2015**, *55*, 906.
4. Estroff, L., and Hamilton, A., Water gelation by small organic molecules, *Chem. Rev.*, **2004**, *104*, 1201.
5. Terech, P., and Weiss, R., Low molecular mass gelators of organic liquids and the properties of their gels, *Chem. Rev.*, **1997**, *97*, 3133.
6. Yang, Z., and Xu, B., Using enzymes to control molecular hydrogelation, *Adv. Mater.*, **2006**, *18*, 3043.
7. Brenzinger, Z., *Physiol. Chem.*, **1892**, *16*, 537.
8. Cortner, R., and Hoffman, W., An interesting colloid gel, *J. Am. Chem. Soc.*, **1921**, *43*, 2199.
9. Menger, F., and Caran, K., Anatomy of a gel. Amino acid derivatives that rigidify water at submillimolar concentrations, *J. Am. Chem. Soc.*, **2000**, *122*, 11679.
10. Shi, J., *et al.*, Exceptionally small supramolecular hydrogelators based on aromatic-aromatic interactions, *Beilstein J. Org. Chem.*, **2011**, *7*, 167.
11. Zhang, Y., *et al.* Supramolecular hydrogels respond to ligand-receptor interaction, *J. Am. Chem. Soc.*, **2003**, *125*, 13680.
12. Ma, M., *et al.*, Aromatic- aromatic interactions induce the self-assembly of pentapeptidic derivatives in water to form nanofibers and supramolecular hydrogels, *J. Am. Chem. Soc.*, **2010**, *132*, 2719.
13. Burley, S., and Petsko, G., Aromatic-aromatic interaction – a mechanism of protein-structure stabilization, *Science*, **1985**, *229*, 23.
14. Zhang, Y., *et al.*, Versatile small-molecule motifs for self-assembly in water and the formation of biofunctional supramolecular hydrogels, *Langmuir*, **2011**, *27*, 529.
15. Yang, Z., *et al.*, Enzymatic formation of supramolecular hydrogels, *Adv. Mater.*, **2004**, *16*, 1440.
16. Tuttolomondo, M., *et al.*, Dye-collagen interactions. Mechanism, kinetic and thermodynamic analysis, *RSC Adv.*, **2015**, *5*, 57395.
17. Eglin, D., *et al.*, In vitro apatite forming ability of type I collagen hydrogels containing bioactive glass and silica sol-gel particles, *J. Mat. Sci.: Materials in Medicine*, **2006**, *17*, 161.
18. Chen, L., *et al.*, Synthesis of nonspherical microcapsules through controlled polyelectrolyte coating of hydrogel templates, *Langmuir*, **2015**, *31*, 9228.
19. Augst, A., *et al.*, Alginate hydrogels as biomaterials, *Macromol. Biosci.*, **2006**, *6*, 623.
20. Ranga, A., *et al.*, Hyaluronic acid hydrogels formed in situ by transglutaminase-catalyzed reaction, *biomacromolecules*, **2016**, *17*, 1553.
21. Priya, M., *et al.*, Injectable amorphous chitin-agarose composite hydrogels for biomedical applications, *J. Funct. Biomater.*, **2015**, *6*, 849.

22. Buwalda, S., *et al.*, Hydrogels in a historical perspective: from simple networks to smart materials, *J. control. release*, **2014**, *190*, 254.
23. Li, X., *et al.*, Supramolecular nanofibers and hydrogels of nucleopeptides, *Angew. Chem., Int. Ed.*, **2011**, *50*, 9365.
24. Chen, Q., *et al.*, Cysteine and pH-responsive hydrogel based on a saccharide derivative with an aldehyde group, *Langmuir*, **2010**, *26*, 3165.
25. Hsu, L.-H., *et al.*, Nanofibrous hydrogels self-assembled from naphthalene diimide (NDI)/amino acid conjugates, *RSC Adv.*, **2015**, *5*, 20410.
26. Ravichandran, R., *et al.*, Applications of self-assembling peptide scaffolds in regenerative medicine: the way to the clinic, *J. Mater. Chem. B*, **2014**, *2*, 8466.
27. Bhuniya, S., *et al.*, (S)-(+)-ibuprofen-based hydrogelators: an approach toward anti-inflammatory drug delivery, *Tetrahedron letters*, **2006**, *47*, 7153.
28. Jayawarna, V., *et al.*, Nanostructured hydrogels for three-dimensional cell culture through self-assembly of fluorenylmethoxycarbonyl-dipeptides, *Adv. Mater.*, **2006**, *18*, 611.
29. Liu, Y., *et al.*, Biofabricating multifunctional soft matter with enzymes and stimuli-responsive materials, *Adv. Funct. Mater.*, **2012**, *22*, 3004.
30. Yang, Z., *et al.*, Enzymatic hydrogelation of small molecules, *Acc. Chem. Res.*, **2008**, *41*, 315.
31. Ulijn, R. V., Enzyme-responsive materials: A new class of smart biomaterials, *J. Mater. Chem.*, **2006**, *16*, 2217.
32. Yang, Z., and Xu, B., Supramolecular hydrogels based on biofunctional nanofibers of self-assembled small molecules, *J. Mater. Chem.*, **2007**, *17*, 2385.
33. Yang, Z., *et al.*, Enzymatic control of the self-assembly of small molecules: A new way to generate supramolecular hydrogels, *Soft Matter*, **2007**, *3*, 515.
34. Hahn, M., and Gianneschi, N., Enzyme-directed assembly and manipulation of organic nanomaterials, *Chem. Commun.*, **2011**, *47*, 11814.
35. Hu, B.-H., and Messersmith, P., Rational design of transglutaminase substrate peptides for rapid enzymatic formation of hydrogels, *J. Am. Chem. Soc.*, **2003**, *125*, 14298.
36. Gao, J., *et al.*, Dual enzymes regulate the molecular self-assembly of tetra-peptide derivatives, *Soft Matter*, **2011**, *7*, 10443.
37. Thornton, K., *et al.*, Controlling stiffness in nanostructured hydrogels produced by enzymatic dephosphorylation, *Biochem. Soc. Trans.*, **2009**, *37*, 660.
38. Wang, W., *et al.*, Using magnetic resonance imaging to study enzymatic hydrogelation, *Anal. Chem.*, **2014**, *86*, 5955.
39. Li, J., *et al.*, Dephosphorylation of D-Peptide derivatives to form biofunctional, supramolecular nanofibers/hydrogels and their potential applications for intracellular imaging and intratumoral chemotherapy, *J. Am. Chem. Soc.*, **2013**, *135*, 9907.
40. Li, J., *et al.*, The conjugation of nonsteroidal anti-inflammatory drugs (Nsaid) to small peptides for generating multifunctional supramolecular nanofibers/hydrogels, *Beilstein J. Org. Chem.*, **2013**, *9*, 908.
41. Zhou, J., *et al.*, Aromatic-aromatic interactions enhance interfiber contacts for enzymatic formation of a spontaneously aligned supramolecular hydrogel, *J. Am. Chem. Soc.*, **2014**, *136*, 2970.

42. Wang, Q., *et al.*, Enzymatic hydrogelation to immobilize an enzyme for high activity and stability, *Soft Matter*, **2008**, 4, 550.
43. Gao, Y., *et al.*, Enzyme-instructed molecular self-assembly confers nanofibers and a supramolecular hydrogel of taxol derivative, *J. Am. Chem. Soc.*, **2009**, 131, 13576.
44. Gao, Y., *et al.*, Imaging enzyme-triggered self-assembly of small molecules inside live cells, *Nat. Commun.*, **2012**, 3, 1033.
45. Gao, J., *et al.*, Enzyme promotes the hydrogelation from a hydrophobic small molecule, *J. Am. Chem. Soc.*, **2009**, 131, 11286.
46. Yang, Z., and Xu, B., A simple visual assay based on small molecule hydrogels for detecting inhibitors of enzymes, *Chem. Commun.*, **2004**, 2424.
47. Yang, Z., *et al.*, Using beta-lactamase to trigger supramolecular hydrogelation, *J. Am. Chem. Soc.*, **2007**, 129, 266.
48. Yang, Z., *et al.*, Intracellular enzymatic formation of nanofibers results in hydrogelation and regulated cell death, *Adv. Mater.*, **2007**, 19, 3152.
49. Yang, Z., *et al.*, Using matrix metalloprotease-9 (mmp-9) to trigger supramolecular hydrogelation, *Soft Matter*, **2009**, 5, 2546.
50. Bremmer, S., *et al.*, Enzyme-triggered gelation: targeting proteases with internal cleavage sites, *Chem. Commun.*, **2014**, 50, 1691.
51. Qin, X., *et al.*, Enzyme-triggered hydrogelation via self-assembly of alternating peptides, *Chem. Commun.*, **2013**, 49, 4839.
52. Bremmer, S., *et al.*, A general method for detecting protease activity via gelation and its application to artificial clotting, *Chem. Commun.*, **2012**, 48, 5482.
53. Zhao, F., *et al.*, Beta-galactosidase-instructed formation of molecular nanofibers and a hydrogel, *Nanoscale*, **2011**, 3, 2859.
54. Chronopoulou, L., *et al.*, Lipase-supported synthesis of peptidic hydrogels, *Soft Matter*, **2010**, 6, 2525.
55. Song, F., and Zhang, L.-M., Enzyme-catalyzed formation and structure characteristics of a protein-based hydrogel, *J. Phys. Chem. B*, **2008**, 112, 13749.
56. Das, A., *et al.*, Exploiting enzymatic (reversed) hydrolysis in directed self-assembly of peptide nanostructures, *Small*, **2008**, 4, 279.
57. Williams, R., *et al.*, Monitoring the early stage self-assembly of enzyme-assisted peptide hydrogels, *Aust. J. Chem.*, **2013**, 66, 572.
58. Toledano, S., *et al.*, Enzyme-triggered self-assembly of peptide hydrogels via reversed hydrolysis, *J. Am. Chem. Soc.*, **2006**, 128, 1070.
59. Guilbaud, J., *et al.*, Enzymatic catalyzed synthesis and triggered gelation of ionic peptides, *Langmuir*, **2010**, 26, 11297.
60. Liu, Y., *et al.*, Glucose oxidase-mediated gelation: a simple test to detect glucose in food products, *J. Agric. Food Chem.*, **2012**, 60, 8963.
61. Rodon Fores, J., *et al.*, Localized supramolecular peptide self-assembly directed by enzyme-induced proton gradients, *Angew. Chem., Int. Ed.*, **2017**, 56, 15984.
62. Sakai, S., *et al.*, Glucose-triggered co-enzymatic hydrogelation of aqueous polymer solutions, *RSC Adv.*, **2012**, 2, 1502.

63. Ogushi, Y., *et al.*, Synthesis of enzymatically-gellable carboxymethylcellulose for biomedical applications, *J. Biosci. Bioeng.*, **2007**, *104*, 30.
64. Sakai, S., *et al.*, Enzymatically crosslinked carboxymethylcellulose-tyramine conjugate hydrogel: cellular adhesiveness and feasibility for cell sheet technology, *Acta Biomater.*, **2009**, *5*, 554.
65. Choi, Y., *et al.*, Human gelatin tissue-adhesive hydrogels prepared by enzyme-mediated biosynthesis of dopa and Fe<sup>3+</sup> ion crosslinking, *J. Mater. Chem. B*, **2014**, *2*, 201.
66. Lodish, H., *et al.*, Molecular cell biology, *7th ed.*, W. H. Freeman: New York, **2013**.
67. Stuart, M., *et al.*, Emerging applications of stimuli-responsive polymer materials, *Nat. Mater.*, **2010**, *9*, 101.
68. Ariga, K., *et al.*, Nanoarchitectonics: a new materials horizon for nanotechnology, *Mater. Horiz.*, **2015**, *2*, 406.
69. Yang, B., *et al.*, Surface-mediated supramolecular self-assembly of protein, peptide, and nucleoside derivatives: from surface design to the underlying mechanism and tailored functions, *Langmuir*, **2018**, *34*, 15109.
70. Xing, B., *et al.*, Hydrophobic interaction and hydrogen bonding cooperatively confer a vancomycin hydrogel: a potential candidate for biomaterials, *J. Am. Chem. Soc.*, **2002**, *124*, 14846.
71. Tiller, J., Increasing the local concentration of drugs by hydrogel formation, *Angew. Chem., Int. Ed.*, **2003**, *42*, 3072.
72. Bieser, A., and Tiller, J., Surface-induced hydrogelation, *Chem. Commun.*, **2005**, 3942.
73. Angelerou, M., *et al.*, Surface-directed modulation of supramolecular gel properties, *Chem. Commun.*, **2016**, *52*, 4298.
74. Liu, Y., *et al.*, Surface self-assembly of N-fluorenyl-9-methoxycarbonyl diphenylalanine on silica wafer, *Colloids Surf. B*, **2011**, *87*, 192.
75. Reches, M., and Gazit, E., Controlled patterning of aligned self-assembled peptide nanotubes, *Nat. Nanotechnol.*, **2006**, *1*, 3, 195.
76. Demirel, G., and Buyukserin, F., Surface-induced self-assembly of dipeptides onto nanotextured surfaces, *Langmuir*, **2011**, *27*, 12533.
77. Olive, A., *et al.*, Spatial and directional control over self-assembly using catalytic micropatterned surfaces, *Angew. Chem., Int. Ed.*, **2014**, *53*, 4132.
78. Poolman, J., *et al.*, Variable gelation time and stiffness of low-molecular-weight hydrogels through catalytic control over self-assembly, *Nat. Protoc.*, **2014**, *9*, 977.
79. Boekhoven, J., *et al.*, Catalytic control over supramolecular gel formation, *Nat. Chem.*, **2013**, *5*, 433.
80. Johnson, E., *et al.*, Directed self-assembly of dipeptides to form ultrathin hydrogel membranes, *J. Am. Chem. Soc.*, **2010**, *132*, 5130.
81. Johnson, E., *et al.*, Surface nucleated growth of dipeptide fibres, *Chem. Commun.*, **2013**, *49*, 8698.
82. Kubiak, P., *et al.*, Polymerization of low molecular weight hydrogelators to form electrochromic polymers, *Chem. Commun.*, **2015**, *51*, 10427.
83. Liu, Y., *et al.*, Reversible electroaddressing of self-assembling amino-acid conjugates, *Adv. Funct. Mater.*, **2011**, *21*, 1575.


84. Raeburn, J., *et al.*, Electrochemically-triggered spatially and temporally resolved multi-component gels, *Mater. Horiz.*, **2014**, *1*, 241.
85. Seibt, S., *et al.*, Hydrogelation kinetics measured in a microfluidic device with in situ X-ray and fluorescence detection, *Langmuir*, **2018**, *34*, 5535.
86. Spitzer, D., *et al.*, Surface-assisted self-assembly of a hydrogel by proton diffusion, *Angew. Chem., Int. Ed.*, **2018**, *57*, 11349.
87. Watson, J., and Baron, M., The behaviour of water in poly(dimethylsiloxane), *J. Membr. Sci.*, **1996**, *110*, 47.
88. Lide, D., Handbook of chemistry and physics, *CRC, Boca Raton, FL*, **2003**.
89. Yang, Z., *et al.*, Novel anisotropic supramolecular hydrogel with high stability over a wide pH range, *Adv. Mater.*, **2004**, *16*, 1440.
90. Williams, R., *et al.*, Enzyme-assisted self-assembly under thermodynamic control, *Nat. Nanotechnol.*, **2009**, *4*, 19.
91. Conte, M., *et al.*, Biocatalytic self-assembly using reversible and irreversible enzyme immobilization, *ACS Appl. Mater. Interf.*, **2017**, *9*, 3266.
92. Williams, R., *et al.*, The in vivo performance of an enzyme-assisted self-assembled peptide/protein hydrogel, *Biomaterials*, **2011**, *32*, 5304.
93. Vigier-Carrière, C., *et al.*, Bioactive seed layer for surface-confined self-assembly of peptides, *Angew. Chem., Int. Ed.*, **2015**, *54*, 10198.
94. Vigier-Carrière, C., *et al.*, Control of surface-localized, enzyme-assisted self-assembly of peptides through catalyzed oligomerization, *Langmuir*, **2017**, *33*, 8267.
95. Conte, M., *et al.*, Biocatalytic self-assembly on magnetic nanoparticles, *App. Mater. & Interfaces*, **2018**, *10*, 3069.
96. Sasselli, I., *et al.*, Using experimental and computational energy equilibration to understand hierarchical self-assembly of fmoc-dipeptide amphiphiles, *Soft Matter*, **2016**, *12*, 8307.
97. Pappas, C., *et al.*, Biocatalytic Pathway Selection in Transient Tripeptide Nanostructures, *Angew. Chem., Int. Ed.*, **2015**, *54*, 8119.
98. Wang, Y., *et al.*, Directed nanoscale self-assembly of low molecular weight hydrogelators using catalytic nanoparticles, *Adv. Mater.*, **2018**, *30*, 1707408.
99. Wu, C., *et al.*, Controllable growth of core-shell nanogels via esterase-induced self-assembly of peptides for drug delivery, *J. Bio. Nanotechnol.*, **2018**, *14*, 354.
100. Gao, W., *et al.*, Organized self-assembly of janus micromotors with hydrophobic hemispheres, *J. Am. Chem. Soc.*, **2013**, *135*, 998.
101. Torelli, E., *et al.*, A DNA origami nanorobot controlled by nucleic acid hybridization, *Small*, **2014**, *10*, 2918.
102. Carlson, A., *et al.*, Transfer printing techniques for materials assembly and micro/nanodevice fabrication, *Adv. Mater.*, **2012**, *24*, 5284,
103. Hu, L., *et al.*, Oil-water interfacial self-assembly: a novel strategy for nanofilm and nanodevice fabrication, *Chem. Soc. Rev.*, **2012**, *41*, 1350.
104. Oh, J., *et al.*, The development of microgels/nanogels for drug delivery applications, *Prog. Polym. Sci.*, **2008**, *33*, 448.




105. Guo, X., *et al.*, Synthesis of spherical polyelectrolyte brushes by photoemulsion polymerization with different photoinitiators, *Macromolecules*, **1999**, 32, 6043.
106. Lovrak, M., *et al.*, Free-standing supramolecular hydrogel objects by reaction-diffusion, *Nature commun.*, **2017**, 8, 15317.
107. Richardson, P., *et al.*, Ectoenzymes control adenosine modulation of immunisolated cholinergic synapses, *Nature*, **1987**, 327, 232.
108. Yegutkin, G., Nucleotide- and nucleoside-nonverting ectoenzymes: important modulators of purinergic signalling cascade, *Biochim. Biophys. Acta, Mol. Cell Res.*, **2008**, 1783, 673.
109. Netzel-Arnett, S., *et al.*, Membrane Anchored Serine Proteases: A Rapidly expanding group of cell surface proteolytic enzymes with potential roles in cancer, *Cancer Metastasis Rev.*, **2003**, 22, 237.
110. Pospisil, P., *et al.*, A combined approach to data mining of textual and structured data to identify cancer-related targets, *BMC Bioinf.*, **2006**, 7, 354.
111. Kuang, Y., *et al.*, Pericellular hydrogel/nanonets inhibit cancer cells, *Angew. Chem., Int. Ed.*, **2014**, 53, 8104.
112. Du, X., *et al.*, Enzymatic transformation of phosphate decorated magnetic nanoparticles for selectively sorting and inhibiting cancer cells, *Bioconjugate Chem.*, **2014**, 25, 2129.
113. Du, X., *et al.*, Ectoenzyme switches the surface of magnetic nanoparticles for selective binding of cancer cells, *J. Coll. Interf. Sci.*, **2015**, 447, 273.
114. Tanaka, A., *et al.*, Cancer cell death induced by the intracellular self-assembly of an enzyme-responsive supramolecular gelator, *J. Am. Chem. Soc.*, **2015**, 137, 770.
115. Shi, J., *et al.*, D-amino acids modulate the cellular response of enzymatic-instructed supramolecular nanofibers of small peptides, *Biomacromolecules*, **2014**, 15, 3559.
116. Wu, D., *et al.*, The first Cd73-instructed supramolecular hydrogel, *J. Coll. Interf. Sci.*, **2015**, 447, 269.
117. Pires, R., *et al.*, Controlling cancer cell fate using localized biocatalytic self-assembly of an aromatic carbohydrate amphiphile, *J. Am. Chem. Soc.*, **2015**, 137, 576.
118. Fishman, W., *et al.*, Immunology and biochemistry of regan isoenzyme of alkaline phosphatase in human cancer, *Nature*, **1968**, 219, 697.
119. Zheng, W., *et al.*, Surface-induced hydrogelation inhibits platelet aggregation, *J. Am. Chem. Soc.*, **2013**, 135, 266.
120. Yang, Z., *et al.*, Intracellular hydrogelation of small molecules inhibits bacterial growth, *Angew. Chem., Int. Ed.*, **2007**, 46, 8216.
121. a) Yang, Z., *et al.*, Intracellular enzymatic formation of nanofibers results in hydrogelation and regulated cell death, *Adv. Mater.*, **2007**, 19, 3152. b) Gao, Y., *et al.*, Imaging self-assembly dependent spatial distribution of small molecules in a cellular environment, *Langmuir*, **2013**, 29, 15191.
122. Zhou, R., and Xu, B., Insight of the cytotoxicity of the aggregates of peptides or aberrant proteins: a meta-analysis, *PLoS One*, **2014**, 9, e95759.
123. Zheng, P., *et al.*, Cell environment-differentiated self-assembly of nanofibers, *J. Am. Chem. Soc.*, **2016**, 138, 11128.

- 124.** Yao, Q., *et al.*, Enzyme-instructed supramolecular self-assembly with anticancer activity, *Adv. Mater.*, **2018**, 1804814.
- 125.** Zhan, J., *et al.*, Tandem molecular self-assembly in liver cancer cells, *Angew. Chem., Int. Ed.*, **2018**, 57,1813.
- 126.** Du, X., *et al.*, Supramolecular hydrogelators and hydrogels : from soft matter to molecular biomaterials, *Chem. Rev.*, **2015**, 115, 13165.
- 127.** Sangeetha, N., *et al.*, Supramolecular gels : functions and uses, *Chem. Soc. Rev.*, **2005**, 34, 821.
- 128.** Vigier-Carrière, C., *et al.*, Surface-assisted self-assembly strategies leading to supramolecular hydrogels, *Angew. Chem., Int. ed.*, **2018**, 57, 1448.
- 129.** Zelzer, M., and Ulijn, R., Next-generation peptide nanomaterials: molecular networks, interfaces and supramolecular functionality, *Chem. Soc. Rev.*, **2010**, 39, 3351.





# **Chapter 2**



## **Materials & Methods**

*This second chapter is dedicated to the description of the different materials and methods used to perform the experiments described in chapter 3,4,5 and 6. The principles of the different techniques common to all chapters from articles are presented. Techniques specific to one chapter will be described in the material and method of the chapter in question. This will be the case of confocal laser scanning microscopy and biology assays in chapter 6. Transmission electron microscopy and mass analysis was held by platforms, so they will not be described in this chapter but the samples preparations are present in the ESI of each chapter using them. General protocols for sample preparation are described for each technique. A more detailed protocol is present at the ESI of each chapter.*

## Summary

2.1. Materials .....	48
2.1.1. Buffer solutions.....	48
2.1.2. Polymers and enzymes .....	48
2.1.3. Peptides .....	49
2.2. Synthesis procedure, characterization and samples preparation .....	51
2.2.1. Peptide synthesis .....	51
2.2.2. Protocol of the synthesis and HPLC monitoring of the Fmoc-Y( <i>Succ</i> ) (molecule from chapter 5 part 5.2) .....	52
2.2.3. Characterization of the Fmoc-GFFY( <i>Succ</i> )GHY( <i>Succ</i> ) (molecule from chapter 5 part 5.2).....	53
2.2.4. Preparation of peptide solution and hydrogel formation .....	53
2.2.5. Multilayer film preparation and localized hydrogel formation at the interface liquid-solid .....	54
2.3. Methods: Physical-chemical characterizations .....	55
2.3.1. Quartz Crystal Microbalance with Dissipation (QCM-D).....	55
2.3.2. Atomic Force Microscopy (AFM) .....	57
2.3.3. Fourier Transform Infrared spectroscopy (FTIR).....	59
2.3.4. Scanning Electron Microscopy (SEM) and Cryo-SEM.....	64
2.3.5. Analytic High-Performance Liquid Chromatography (HPLC).....	67
2.3.6. Dynamic Light Scattering (DLS) .....	70
2.3.7. Circular Dichroism spectroscopy (CD) .....	72
2.3.8. Ultraviolet-Visible spectroscopy (UV-Visible).....	76
2.3.9. Fluorescence spectroscopy.....	78
2.3.10. Rheology .....	79
<b>REFERENCES</b> .....	<b>82</b>

## 2.1. Materials

### 2.1.1. Buffer solutions

All buffer and aqueous solutions were prepared in Milli-Q ultrapure water (Milli-Q Plus system, Millipore, Billerica, MA) that has a resistivity of 18.2  $\Omega$ . pH of buffer solutions was monitored with pH/mV meter (HANNA instruments) and adjusted by dropwise addition of HCl<sub>(aq)</sub> (0.1 M) and/or NaOH<sub>(aq)</sub> (0.1 M).

Buffer	Formula	Suppliers	Mw (g/mol)	Concentration (mol/L)
<b>Borax, pH = 9.5</b>	Na <sub>2</sub> B <sub>4</sub> O <sub>7</sub>	Acros organics	201.22	25 mM
<b>Sodium Phosphate, pH = 7.4</b>	NaH <sub>2</sub> PO <sub>4</sub>	Sigma Aldrich	142.1	1.76
	Na <sub>2</sub> HPO <sub>4</sub>		120	10
	NaCl		58.44	137
	KCl		74.55	2.7

Table 1: Buffer solution used for the buildup of precursor layer and enzymatic responsive hydrogelations.

To prepare 200 mL of Borax buffer at 25 mM and pH 9.5, 1 g of sodium tetraborate, anhydrous, in 200 mL of ultra-pure water. The pH is checked by pH-meter and adjusted if needed as describe above.

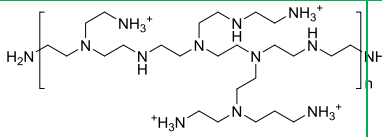
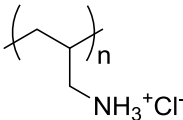
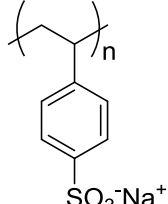
To prepare 200 mL of PBS buffer at 7.4, one tablet of phosphate buffered saline (containing 0.01 M phosphate buffer, 0.0027 M potassium chloride and 0.137 M sodium chloride) in 200 mL of ultra-pure water. The pH is checked by pH-meter and adjusted if needed as describe above.

All buffer solutions were stored at room temperature for one week maximum.

### 2.1.2. Polymers and enzymes

#### Polyelectrolytes

All commercial polyelectrolytes are presented in the table below.

Polymers	Nature	Structure	Suppliers	Mw (g/mol)
<b>Poly(ethylenimine) (PEI)</b>	Polycation		Sigma Aldrich	750 000 (50% wt. In water)
<b>Poly(allylamine hydrochloride) (PAH)</b>	Polycation		Sigma Aldrich	15 000
<b>Poly(styrene sulfonate) (PSS)</b>	Polyanion		Sigma Aldrich	70 000

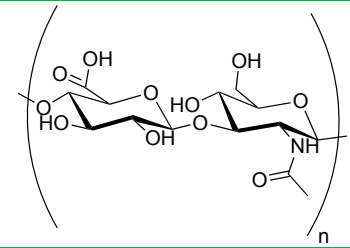
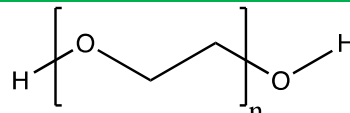
<b>Hyaluronic acid (HA)</b>	Polyanion		Primalhyal 400	472 000
<b>Poly(oxiethylene) (PEO)</b>	Polyanion		Seebio biotech	435 000 – 480 000

Table 2: Polyelectrolytes used for the buildup of multilayer films.

## Enzymes

All commercial proteins are presented in the table below.

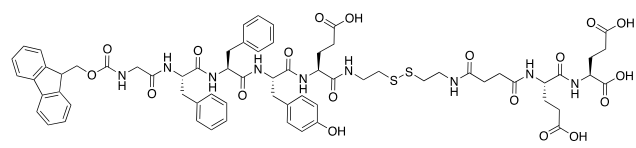
Enzymes	Mw (g/mol)	Pi	Suppliers
<b>Glutathion Reductase (GR) from Baker's yeast</b>	124 000	4.9-5.9	Sigma Aldrich
<b>Albumine, bovine serum (BSA) &gt; 99, essentially globulin free</b>	66 000	4.7	Sigma Aldrich
<b>Alkaline Phosphatase (AP), from bovine intestinal mucosa</b>	150 000	4.4-5.8	Sigma Aldrich
<b>Glucose Oxidase (GOx), from Aspergillus niger</b>	160 000	4.2	Sigma Aldrich
<b>Peroxidase from horseradish (HRP), 150 U/mg</b>	40 000	3.0-9.0	Sigma Aldrich

Table 3: Proteins used to initiate hydrogel formation

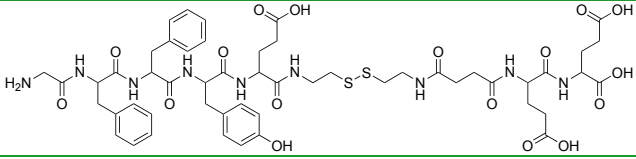
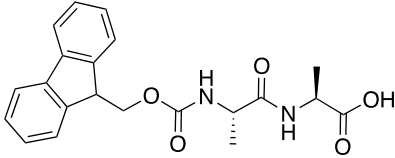
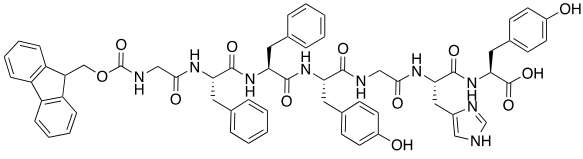
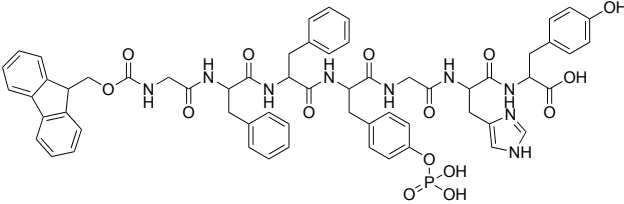
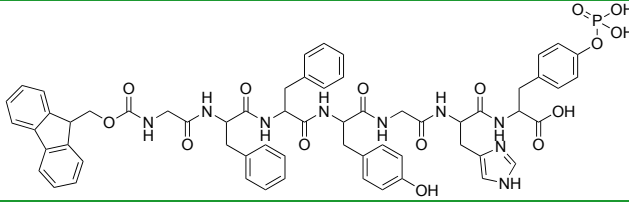
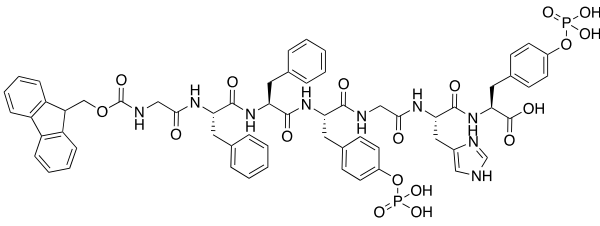
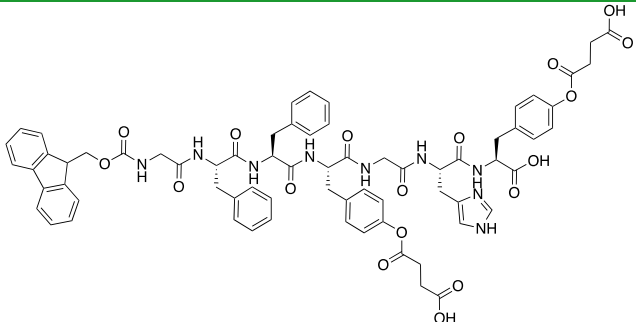
All the proteins for all projects were dissolved in one of the buffer solution mentioned just above in point 2.1.1., at a concentration of 1 mg/mL which means 15  $\mu$ M for BSA, 6.7  $\mu$ M for AP, 8  $\mu$ M for GR, 6.25  $\mu$ M for GOx and 25  $\mu$ M for HRP. All solutions were just prepared before each experiment.

### 2.1.3. Peptides

I designed and synthesized all peptides used in this thesis, except for the peptide used in chapter 6 which was already used before in the group but I synthesized all the batches that I used for the project. General synthesis protocol is described in this chapter in point 2.2.1, but specific synthesis protocols are present in the ESI of each chapter.

Name	Structure	Mw (g/mol)	ESI in Chapter
<b>Fmoc-A-SS-B</b>		1375.48	<b>3</b> <i>p: 17-18 and 26-29</i>



<b>A-SS-B</b>		1153.41	<b>3</b> <i>p: 17-18 and 26-29</i>
<b>Fmoc-AA-OH</b>		382.15	<b>4</b> <i>p:8</i>
<b>Fmoc-GFFYGHY</b>		1111.44	<b>5</b>
<b>Fmoc-GFFpGHY</b>		1191.41	<b>5</b>
<b>Fmoc-GFFYGHpY</b>		1191.41	<b>5</b>
<b>Fmoc-GFFpYGHpY</b>		1271.38	<b>5</b>
<b>Fmoc-GFFY(succ)G HY(succ)</b>		1311.48	<b>5</b>

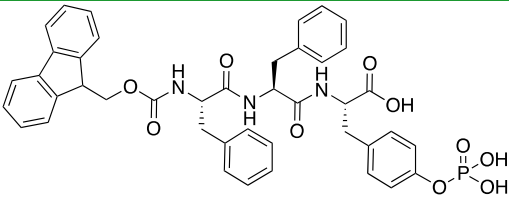
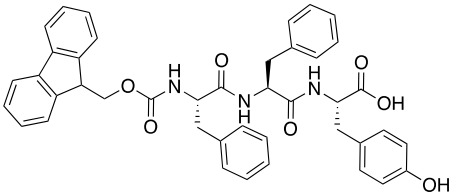
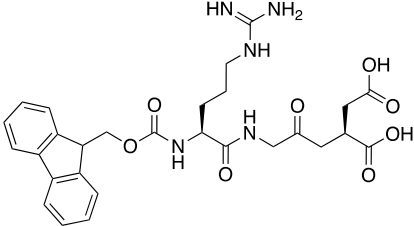
<b>Fmoc-FFpY</b>		777.25	<b>6</b> <i>p: 12-14</i>
<b>Fmoc-FFY</b>		713.31	<b>6</b> Mentioned but not described
<b>Fmoc-RGD</b>		567.23	<b>6</b> Mentioned in the conclusion but not described

Table 4: Peptides used in the different projects

*N.B.* Other peptides were synthesized during my Ph.D. but only the one mentioned in the publications are presented in the list above.

## 2.2. Synthesis procedure, characterization and samples preparation

### 2.2.1. Peptide synthesis

All peptides were prepared using solid support chemistry. The “Fmoc strategy” was used based on 2-CTC resin.<sup>1</sup> The following synthetic pathway is given in the scheme below.

General procedure:

- **Step a:** loading of the resin. Addition of 3 eq/r of the first Fmoc protected amino acid + 6 eq/r of DIEA in 3 mL of DMF for 300 mg of resin. The solution in contact with the resin is stirred at RT for 2 h. Then, the solution is removed and a solution of MeOH is added at RT for 1 h.
- **Step b:** Fmoc group deprotection: 3 mL of a 20% of piperidine in DMF solution is added and stirred at RT for 15 min.
- **Step c:** Coupling step: 3eq/r of Fmoc-amino acid + 3 eq/r of HOBt + 3 eq/r of HBTU + 6 eq/r of DIEA are added in 3 mL of DMF and let in contact with the resin at RT for 30 min.
- **Step d:** Cleavage of the resin and lateral chains deprotection: addition of 3 mL of a solution containing 95% TFA + 2.5 % H<sub>2</sub>O + 2.5 % triisopropylsilane it's stirred at RT for 2 h. Then the solution is filter. The solvent is then removed. Finally the product is precipitate by using a small amount of cold ether.

- Between each step **a**, **b**, **c** and **d**, a rinsing stage is executed by using 5 times 3 mL of DMF and then a Kaiser test is made to confirm the achievement of the coupling or deprotection steps.

**Protocol for Kaiser Test (Ninhydrin Test):** one drop of the following solutions A, B and C is added in a test tube containing 10 beads of the resin. The test tube is heated at 100 °C and the color of the beads is observed

♣ Solution A:

- Dissolve 16.5 mg of KCN in 25 mL of distilled water.
- Dilute 1.0 mL of above solution with 49 mL of pyridine.
- Pour it into a small reagent bottle and label it "A"

♣ Solution B:

- Dissolve 1.0 g of ninhydrin in 20 mL of n-butanol.
- Pour into a small reagent bottle and label it as "B".

♣ Solution C:

- Dissolve 40 g of phenol in 20 mL of n-butanol.
- pour it into a small reagent bottle and label it "C".
- *When the Kaiser test is positive*, the beads and the solution takes a blue coloration. This indicates the presence of free amine that means that the Fmoc-deprotection step succeed or coupling step failed.
- *When the Kaiser test is negative*, the beads and solution stays yellow. This indicates that the coupling step is completed or the Fmoc-deprotection failed.

In the case of a Fmoc deprotection or a coupling step failed, it is repeated until it work with in between each a rinsing step is performed.

### **2.2.2. Protocol of the synthesis and HPLC monitoring of the Fmoc-Y(Succ) (molecule from chapter 5 part 5.2)**

In a 50 mL one neck ballon, the 250 mg of Fmoc-GFFYGHY is solubilized in 10 mL of DCM. Then, 2.5 eq of succinic anhydride is added. Then solution is stirred for 24 h at room temperature. The ester formation is followed by HPLC at 15 min, 30 min, 45 min, 1h, 2h, 3h, 4h, 6h, 12h and 24h. The HPLC method used is in isocratic condition of 80/20 (ACN/water) with a run of 20 min at a flow rate of 1 mL/min. The column used is a Supelcosil ABZ + Plus with the following dimensions 15 cm × 4.6 mm, 3 µm. The sample is prepared by diluting 20 µL of the reaction mixture in 480 µL of ACN/water (80/20). Then, 20 µL of the sample is injected inside the analytical HPLC.

### 2.2.3. Characterization of the Fmoc-GFFY(Succ)GHY(Succ) (molecule from chapter 5 part 5.2)

$^1\text{H}$  NMR (400 MHz, DMSO- $d_6$ )  $\delta$  2.65-2.82 (m, 5H), 2.88-2.99 (m, 6H), 3.04-3.09 (dd, 1H,  $J=5.6, 17.7$  Hz), 3.46-3.51 (dd, 1H,  $J=5.6, 17.7$  Hz), 3.58-3.63 (dd, 2H,  $J=5.5, 17.7$  Hz), 3.65-3.70 (m, 2H), 4.31-4.37 (m, 3H), 4.42-4.50 (m, 5H), 4.65-4.67 (m, 2H), 6.63-6.66 (m, 4H), 6.97-7.04 (dd, 7.9, 15.9 Hz), 7.14-7.21 (m, 11H), 7.29-7.35 (m, 5H), 7.39-7.42 (dd, 2H, 8.7, 8.8 Hz), 7.46-7.48 (t, 1H, 5.4 Hz), 7.67-7.69 (d, 2H, 7.6 Hz), 7.87-7.88 (d, 2H, 7.5 Hz), 7.95-7.97 (d, 1H, 7.7 Hz), 8.08-8.09 (m, 2H), 8.15-8.21 (m, 3H), 8.94 (s, 1H), 14.09 (s, 2H); MALDI-TOF (ESI/Q-TOF)  $m/z$ :  $[\text{M} + \text{NA}]^+$  Calcd for  $\text{C}_{61}\text{H}_{62}\text{N}_9\text{NaO}_{12}$  1333.48; Found 1333.99; UV-VIS spectra: max Abs: 290 nm. IR spectra:  $\nu_{\text{OH}}= 3520 \text{ cm}^{-1}$ ;  $\nu_{\text{C=O acid}}= 1739 \text{ cm}^{-1}$ ;  $\nu_{\text{C=O amide}}= 1674 \text{ cm}^{-1}$ ;  $\nu_{\text{N-H}}= 1640 \text{ cm}^{-1}$  and  $1547$ ;  $\nu_{\text{C-O}}= 1395 \text{ cm}^{-1}$  and  $1200 \text{ cm}^{-1}$ . HPLC analytic (Column C18 SUPULCOSIL ABZ +, ACN/H $_2$ O (50/50)\_isocratic\_20 min\_flow: 1 mL/min\_22°C) : rt : 4.0 min

### 2.2.4. Preparation of peptide solution and hydrogel formation

All hydrogels were prepared from buffer solution of peptides (PBS, Borax) or in ultrapure water. All buffers were prepared the day of the hydrogel preparation.

#### *General preparation of peptide solution*

An adequate amount of peptide was dissolved inside a buffer solution to get the suitable concentration (usually 1 or 10 mg/mL but the concentration depends of the peptide and the methods used). This solution is vortexed 2-5 minutes and sonicated in an ultrasound bath during 1 minute. The resulting peptide solution was thus used for all kind of analyses described in ESI of chapter 3, 4, 5 and 6.

#### *General preparation for the upside-down vial test demonstrating the hydrogel formation.*

Upside-down vial tests with peptides for the hydrogelation assays. Hydrogels were obtained from peptide by heating for Fmoc-GFFYGHY and by enzymatic reaction for all the other peptides (hydrogelators). First, the peptide is solubilized as described above but at a concentration where we obtain a hydrogel. Then, the stimulus (usually here the enzyme) is added at a concentration of 1 mg/mL and the all mixture is vortexed 10 seconds to homogenized the solution. Finally, the upside-down vial test is done after the time needed for the hydrogel to form. This time can vary between 1 minute to more than 5 hours.

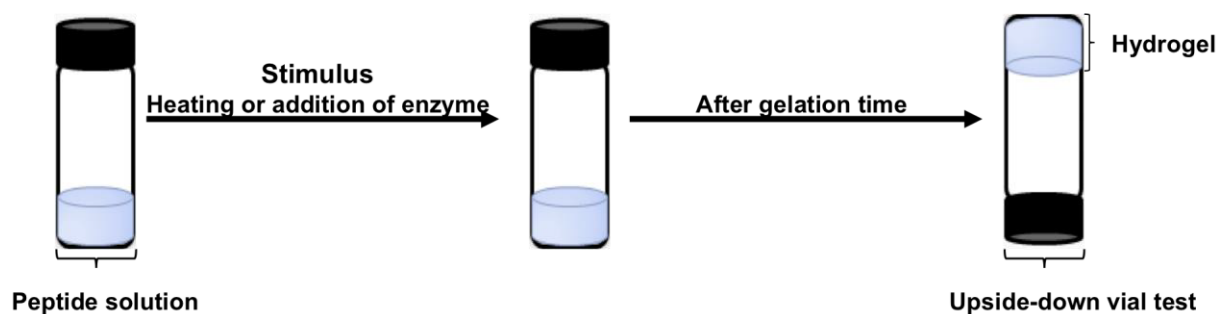


Figure 1: Schematic of the upside-down vial test principle.

### 2.2.5. Multilayer film preparation and localized hydrogel formation at the interface liquid-solid

All polyelectrolytes (1 mg/mL), proteins (1 mg/mL), and peptides solutions (1 mg/mL) were freshly prepared in a buffer. Different solid substrates were used depending on the characterization techniques investigated: gold coated quartz crystal for QCM-D monitoring, ZnSe crystal for ATR-FTIR experiments, glass slide and silica wafer for Cryo-SEM analyses, glass slide for fluorescence emission assays (using a multiplate reader (FLX-Xenius®, SAFAS, Monaco)) and melamine foam (from Foam Partner industry) for activity assays in the continuous flow reactor experiments.

The growth of the supramolecular hydrogel from the chosen substrate was done as following: after the deposition of a PEI (1 mg/mL) precursor layer on the chosen surface by dipping (10 minutes in the PEI solution), the multilayer film was built up by alternately exposing the surface to PSS (1 mg/mL inside buffer solution) and PEI or PAH (1 mg/mL inside buffer solution) solutions for 10 minutes with an intermediate rinsing step with the buffer solution for 5 minutes. Protein (1 mg/mL) are prepared in an adequate buffer, which was put in contact with the multilayer during 20 minutes followed by 5 minutes of rinsing step with the buffer. Finally, the peptide solution (1 mg/mL inside buffer solution) was let in contact with the modified surface for 12 hours. The volume of each solution brought in contact with the substrate was 1 mL except for the QCM-D experiment where it was 700  $\mu$ L. All steps were done at 20°C.

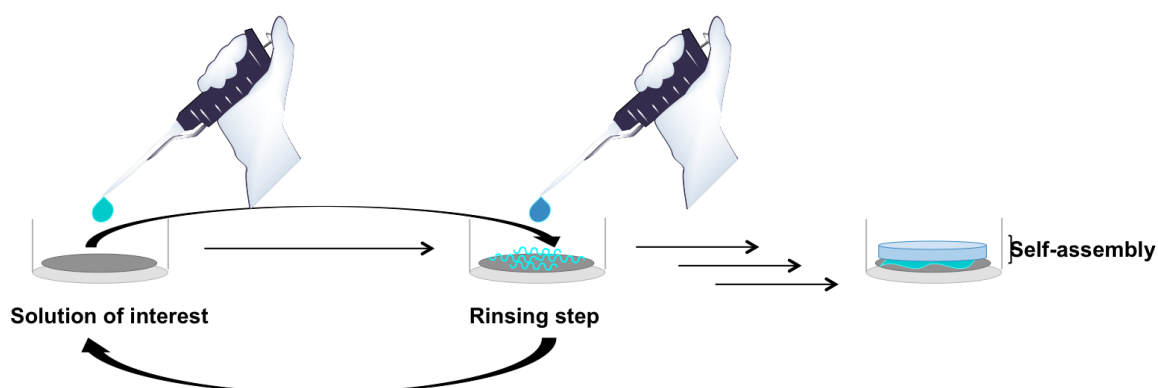


Figure 2: Schematic of the multilayer film preparation and localized self-assembly formation at an interface liquid-solid.

## 2.3. Methods: Physical-chemical characterizations

### 2.3.1. Quartz Crystal Microbalance with Dissipation (QCM-D)

Quartz crystal microbalance (QCM-D) with dissipation is an acoustic device used to monitor in situ mass deposition of molecules or macromolecules. This sensitive technique is suitable to follow real-time buildup of enzymatic films and hydrogels assembly.

#### Principle

The fundamental principle of quartz crystal microbalance was developed by G. Sauerbrey in 1959.<sup>2</sup> This technique relies on piezoelectric properties of quartz, deformed when an electrical potential is applied to it.

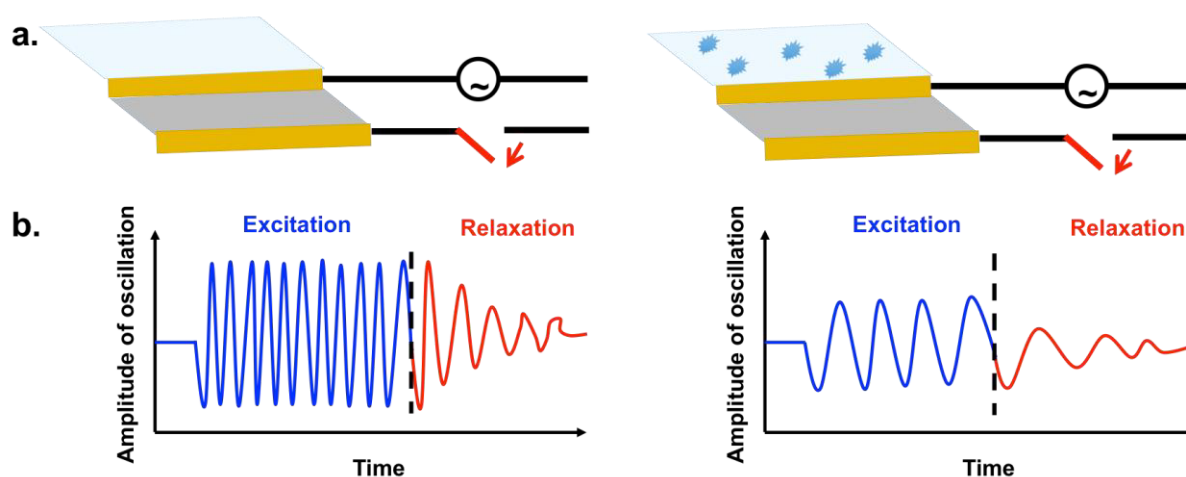


Figure 3: a) Schematic representation of a coated gold QCM-D crystal and its driving circuit during the adsorption of molecules, b) the crystal oscillates at its fundamental frequency and its harmonics: the blue curve corresponds to the oscillation signal during the excitation phase and the red curve corresponds to the signal during relaxation phase. A shift of the frequency is obtained when molecules are adsorbed on the surface of the QCM crystal.

The QCM device uses a quartz crystal coated on both sides with gold electrodes (figure 3a). The application of an electrical potential between the two electrodes induces a shear movement of the quartz crystal. By fixing the lower side of the crystal on a stationary support, the upper side undergoes a horizontal translational movement resulting in mechanical oscillations at its fundamental frequency and its harmonics (Figure 3b). The system behaves as a harmonic oscillator that can be characterized by its resonance frequency  $f_r$  (Hz):

$$f_r = \frac{1}{2\pi} \sqrt{\frac{k}{M}} \quad (1)$$

$M$  is the oscillator mass and  $k$  the spring constant (N/m).

When a mass  $m$  (ng/cm<sup>2</sup>) is deposited on the surface of the crystal ( $m \ll M$ ), the total mass of the resonator changes and a new resonance frequency  $f$  is associated:

$$f = \frac{1}{2\pi} \sqrt{\frac{k}{M+m}} \approx fr \left(1 - \frac{m}{2M}\right) \quad (2)$$

The resonance frequency shift  $\Delta f$  induced by the mass deposition  $m$  on the crystal can be written as following:

$$\Delta f = f - fr = -\frac{mfr}{2M} = -\frac{m}{C} \quad (3)$$

$C$ , called Sauerbrey constant, is a constant ( $17.7 \text{ ng.cm}^{-2}.\text{Hz}^{-1}$ ) that depends only on the thickness and on the inherent properties of the quartz crystal.  $C$  is defined as:

$$C = \frac{2M}{fr} \quad (4)$$

By measuring the resonance frequency shift of the system during an experiment, QCM gives access to the deposited mass per surface unit on the crystal as a function of time. It is also possible to determine the frequencies of all odd harmonics of the fundamental resonance frequency and to follow their shifts during an experiment. The Sauerbrey equation can be written as following:

$$m = -C \frac{\Delta f \nu}{\nu} \quad (5)$$

Where  $\nu$  is the overtone number.

In order to evaluate the viscoelastic properties of the material deposited on the crystal, the QCM-D device measures the dissipation factor ( $D$ ).  $D$  is experimentally determined by exciting the quartz crystal at its fundamental frequency and measuring the relaxation time of the system as the resonator energy is dissipated in the crystal, in the deposited material and in the liquid in contact of the system and allows the determination of the dissipation factor  $D$ . This parameter is defined by the proportion of dissipated energy at each oscillation with respect to the total stored energy as following:

$$D = \frac{E_{dissipated}}{2\pi E_{stocked}} \quad (6)$$

If the deposited material is stiff, the relaxation time is short and the dissipation value is small. On the contrary, a soft and viscous material will display a longer relaxation time with high values of dissipation.

### Experimental Setup

The QCM-D experiments were performed on a Q-Sense E1 or E4 apparatus (Q-Sense AB, Göteborg, Sweden) by monitoring the resonance frequencies of gold coated crystals, as well as the dissipation factors at four frequencies the fundamental frequency: at 5 MHz ( $\nu = 3, 5$  and  $7$ ) at 15, 25 and 35 MHz). The apparatus is equipped with one measurement cell (volume of about 100  $\mu\text{L}$ ). The cell, set at 22  $^{\circ}\text{C}$ , allows the “in” and “out” fluxes of the solutions in contact with 1.4 cm of diameter and 0.3 mm of thickness. Before each experiment, the quartz crystal was clean under

UV-Ozone for 10-15 minutes. Placed into the cell, the crystal is exposed to the experimental buffer and left to stabilize for around 30 min. The multilayer films were built *in situ* by the layer-by-layer method on the crystal surface. Each deposited layer was obtained exposing the substrate to 700  $\mu\text{L}$  of solution for 5 min alternated 700  $\mu\text{L}$  of buffer for 5 min as a rinsing step. At the end of the experiment, the crystal is cleaned *in situ* with a 2 % Hellmanex solution for 10 min, then with a 0.1 M NaOH solution for 10 min and finally with 0.1 M HCl solution for 10 min. The crystal is then rinsed with water and dried under compressed air.

### 2.3.2. Atomic Force Microscopy (AFM)

Atomic force microscopy is a type of scanning probe microscopy designed to study topography and local surface properties of samples at the nanoscale. Indeed, in this powerful microscopy technology, information are gathered by “feeling” the surface with a mechanical probe and images are obtained by the detection of inter-atomic interaction forces between the nanometric tip of this mechanical probe and the surface. Versatile and allowing high resolution images (down to the angstrom scale), this method has become the reference analysis technique to characterize the surface physicochemical and mechanical properties of samples in several domains including soft matter science and molecular biology.

#### Principle

This near-field microscopy technique was first elaborated in the 1980's by Billig, *et al.*<sup>3</sup> following on from their developments on scanning tunneling microscope based on the detection of an electrons flow between a conductive surface and an adapted probe. Allowing for the characterization of conductive as well as non-conductive surfaces, AFM uses a very sharp tip attached at the end of a cantilever with a specific spring constant  $k$  to scan over a sample surface and then detects the interactions (van der Waals, electrostatic forces, ionic forces...) between this tip and the studied surface (Figure 4). These interactions depend on the physicochemical characteristics of the tip and the surface, but also on the distance between them. In fact, as the tip approaches the surface, attractive forces between the surface and the tip dominate and cause the cantilever to deflect towards the surface. However, as the cantilever is brought even closer to the surface, such that the tip makes contact with it, increasingly repulsive forces take over and cause the cantilever to deflect away from the surface. Cantilever deflections ( $\Delta z$ ) towards or away from the surface are detected thanks to a laser beam sent in direction of the flat top of the cantilever and reflected by the cantilever toward a position sensitive photo-diode. Indeed, when the cantilever is deflected, the direction of the reflected beam changes and this modification is tracked by the position sensitive photo diode, which generates electrical signals then converted into displacement values in nanometer by a suitable software (Figure 4).



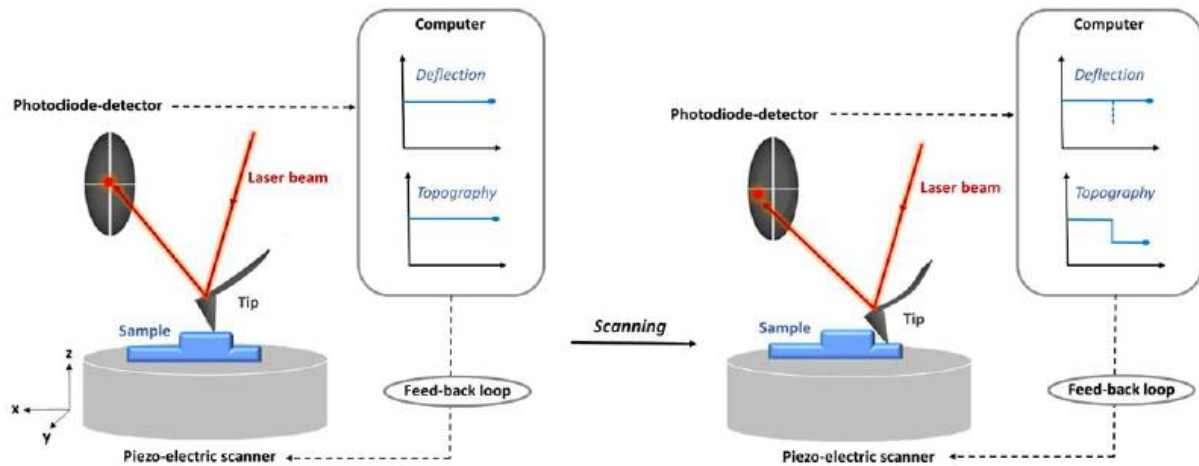


Figure 4: Schematic representation of Atomic Force Microscopy (AFM) principle. The sample is fixed on a piezo-electric scanner. The cantilever is approached to the surface. During the scanning process interactions between the tip and the surface generate a deflection ( $\Delta z$ ) of the cantilever. This deflection is monitored by analyzing the reflection direction change of a laser beam directed toward the cantilever thanks to a photodiode detector connected to an adapted software.

In this way, an accurate topographic map of the sample surface can be obtained since the raised and lowered features on the sample surface influence the deflection of the cantilever. This detection mode is called contact mode (Figure 5a) and is controlled by a feedback loop between the photodiode detector and the piezoelectric table on which the sample is deposited. This feedback loop allows to maintain a constant contact force  $F_c$  on the surface. Contact mode enables also to determine the interaction force  $F_i$  between the tip and the sample relying on the Hook's law:

$$F_i = k \cdot \Delta z \quad (7)$$

Where  $k$  is the spring constant of the cantilever and  $\Delta z$  corresponds to the deflection of the cantilever.

Several other types of characterization can be achieved with this detection mode, as for example friction forces measurements. However maintaining a contact between the tip and the surface can present a drawback: close to the surface of the sample, attractive forces can be quite strong and can cause the tip to damage the surface after a certain scanning duration. To overcome this possible limitation, dynamic detection modes have been developed and are based on the detection of oscillations instead of deflection of the cantilever. Indeed, in these modes, the cantilever is oscillated and changes in its resonant frequency or amplitude are recorded since interaction between the tip and the sample dampen the oscillations. In the non-contact mode (Figure 5b), the cantilever is oscillated above the sample without touching it. Relying on attractive forces only, this mode is not widely used because it requires a low noise environment, which is often difficult to achieve experimentally. Tapping mode (Figure 5c) is a more common dynamic detection mode. In this mode, attractive and repulsive forces are involved in the response since the tip is oscillated closer to the surface than in the non-contact mode and touches intermittently the surface. Monitoring of the oscillations changes thus allows to obtain

phase images revealing surface heterogeneities non observable in the topography images recorded with the contact mode.

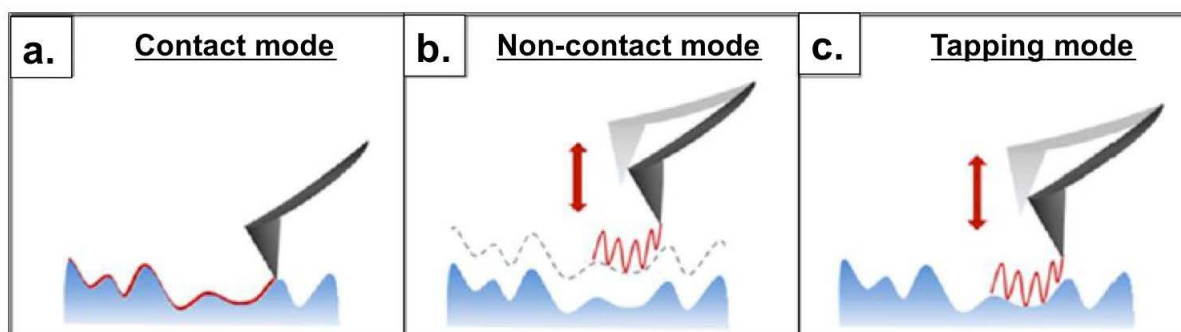


Figure 5: Schematic representation of the main detection modes for AFM imaging. In the contact mode (a), the tip touches the surface and the photodiode detects the deflection of the cantilever. In the non-contact mode (b), the cantilever oscillates above the surface without touching it, whereas in the tapping mode (c), it oscillates at such a distance of the surface that it touches it intermittently. In these both dynamic modes, the photodiode perceives changes in cantilever's oscillations frequency and amplitude.

### Experimental Setup

Atomic force microscopy (AFM) was carried out with a BioScope Catalyst (Bruker corp., Santa Barbara, CA, USA). Micrographs from different interaction stages of hydrogelators with the enzymatic film were recorded in contact mode by using silicon tips mounted on nitride levers. All samples were observed in dry state with triangular cantilevers having a spring constant of 0.4 N/m and a nominal tip radius of 2 nm. Selected AFM images were treated with the nanoscope analysis software (Bruker corp., Santa Barbara, CA, USA). Multilayer films were assembled on gold-coated quartz crystal from QCM-D experiments or on glass slide by the dipping method as described above in point 2.2.3.

### 2.3.3. Fourier Transform Infrared spectroscopy (FTIR)

Infrared spectroscopy is a suitable method to identify and to collect information about chemical compound. In the context of this thesis, the device allowed us to monitor *in situ* supramolecular self-assembly of peptides.

#### Principle of infrared spectroscopy

Infrared spectroscopy technique is based on the measurements of energetic transitions between fundamental states and excited states of vibrational levels. These transitions are observable after absorption or emission of energetic quanta. The total energy of a molecule is described as the sum of four contributions (Figure 6): the electron energy ( $E_e$ ), the vibrational energy ( $E_v$ ), the rotational energy ( $E_r$ ) and translational energy ( $E_t$ ).

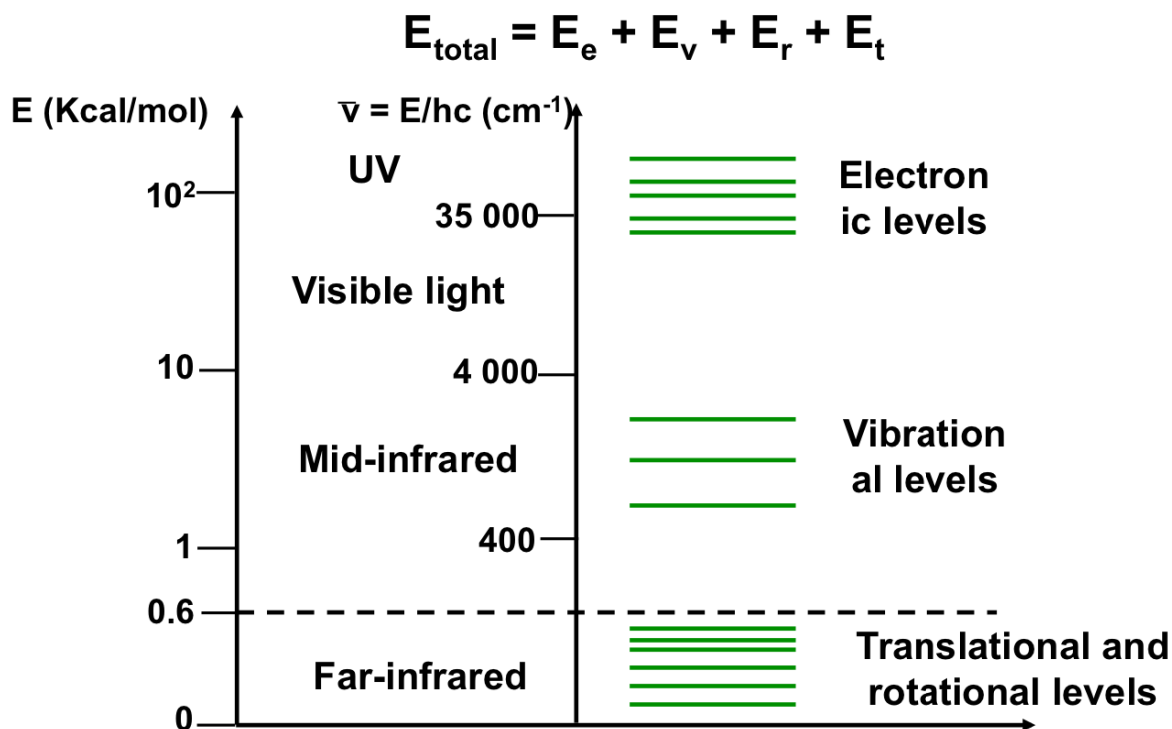


Figure 6: Respective values of electronic, vibrational, rotational and translational contributions to total energy of one molecule<sup>4</sup>.

Radiations of a molecule in the mid-infrared (400-4000  $\text{cm}^{-1}$ ) have an effect on the vibrational energy  $E_v$ . The variation of the vibrational energy is given by the equation of Bohr :

$$\Delta E = E_2 - E_1 = hf = hcv \quad (8)$$

With  $E_1$  the initial energy,  $E_2$  the final energy,  $h$  Planck's constant,  $c$  celerity of light,  $f$  the vibration frequency ( $\text{s}^{-1}$ ) and  $\nu$  the wavenumber ( $\text{cm}^{-1}$ ). Due to the proportional relation between the frequency  $f$  and the wavenumber  $\nu$ , we will describe infrared radiations with  $\nu$  ( $\text{cm}^{-1}$ ).

At a bond scale, absorption and emission in the mid-infrared is transduced in different kinds of vibration mode (Figure 7). Polyatomic molecules composed of  $N$  atoms present  $3N-6$  normal modes of vibrations and  $3N-5$  modes if the molecules is linear. Each vibration mode presents a characteristic frequency.

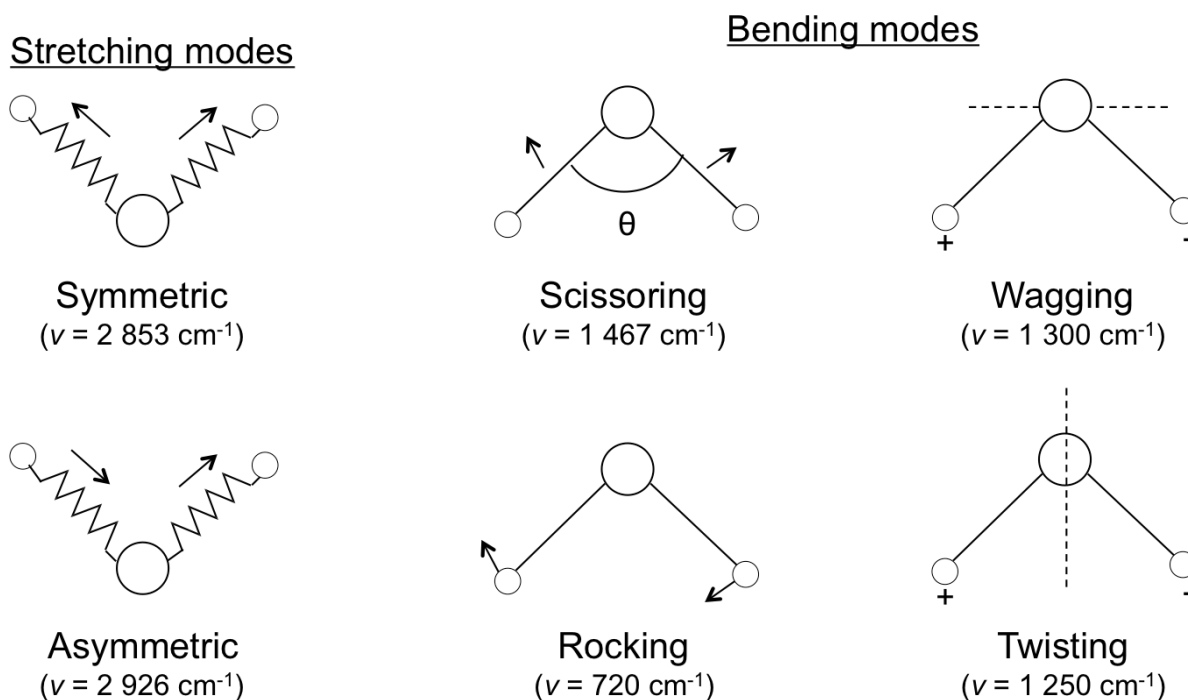


Figure 7: Representation of vibration modes localized on  $-\text{CH}_2-$ .<sup>4</sup>

The infrared spectra of one chemical compound can give valuable information's about its composition, conformation and environment. Infrared spectroscopy can characterize chemical functions regardless molecule's crude formula. For instance, methylene group ( $-\text{CH}_2$ ) shows a characteristic band at  $2850\ \text{cm}^{-1}$  specific to methylene symmetric stretching mode of vibration. However, interactions of molecules with their environment affects this characterization. Non covalent interactions as hydrogen bonds change vibrations of covalent bonds. Consequently, alteration of vibration transitions due to intra or extra molecular interactions might shift the chemical characteristic band in infrared spectroscopy is thus a convenient method to determine supramolecular assembly of molecules and secondary structures of macromolecules as proteins.

### *Principle of Fourier transform infrared spectroscopy (FTIR)*

This infrared device requires the use of Michaelson interferometer (Figure 8). Michaelson interferometer is made of two perpendicular mirrors, one fixed ( $M_f$ ), the other mobile ( $M_m$ ) and one semi-reflective blade (S). The beam emitted by an infrared (IR) source is passing through the semi-reflective blade made of KBr coated with germanium and positioned at  $45^\circ$ . When the laser reaches S after it reflection, half of it is reflected by the fixed mirror, whereas the other half is reflected by the mobile mirror. The IR beam reaches back again the semi-reflective blade to be gathered in one and cross the chemical sample with absorbing properties related to its structure.

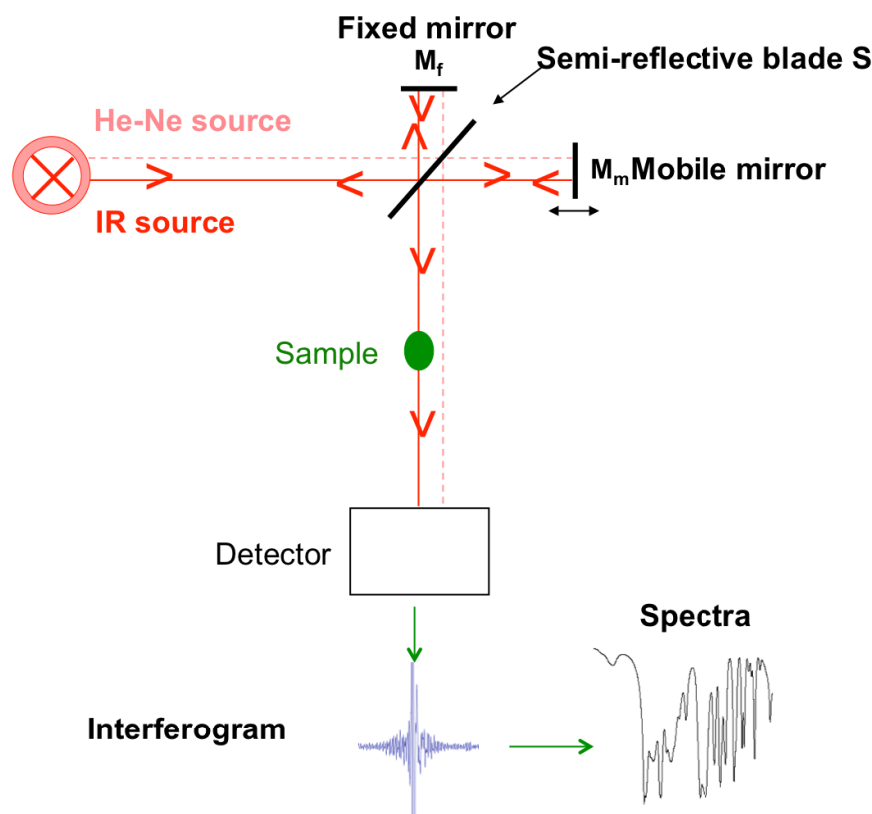


Figure 8: Schematic representation of a Michelson interferometer used in infrared spectroscopy.

If both mirrors  $M_m$  and  $M_f$  are equidistant from the semi-reflective blade both beams follow the same optical trajectory and are emitted in phase. Modification of the  $M_m$  position increases the optical trajectory of one of the beams. As a result, the two beams will have a phase difference. The intensity of the combined optical signals with tunable phase is called the interferogram. Finally, the interferogram is analyzed by the detector and converted with Fourier transformation to give the infrared spectra corresponding to the sample.

### FTIR attenuated total reflection

FTIR attenuated total reflection method (ATR) was used to monitor *in situ* adsorption of polyelectrolytes, enzymes and peptide supramolecular self-assembly. As we mentioned previously, FTIR technique allows to characterize intermolecular interactions and to determine secondary structures of proteins or peptides. This technique in ATR mode is suitable to follow *in situ* the self-assembly of peptides.

### Principle

The principle of ATR was described by Harrick<sup>5</sup> and its applications in the biological field by Fringeli and Gunthard.<sup>6</sup> In our study, we use a trapezoid crystal made of ZnSe (Figure 9).

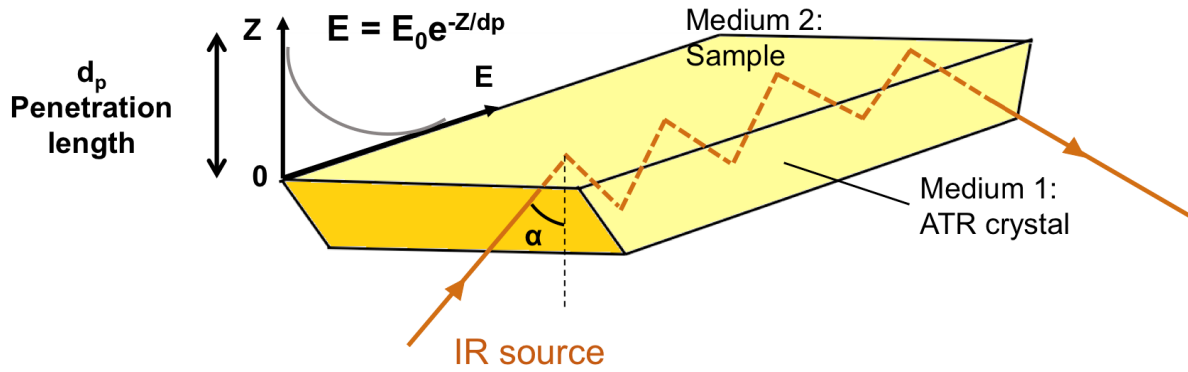


Figure 9: Schematic representation of the infrared source crossing a ZnSe trapezoidal crystal. The incident IR beam usually penetrates into the crystal with a critical angle  $\alpha = 45^\circ$ , and strikes the interface between the crystal (medium 1) and the sample (medium 2). It creates an evanescent wave in medium 2 above the crystal of ATR. The beam is thus reflected several times before to reach a detector at the other side of the crystal.

The IR beam coming out from the Michaelson interferometer is guided toward one face of a trapezoidal crystal of ZnSe (Figure 9). The infrared incident source then arrives at the interface between the ATR crystal (medium 1) and the aqueous solution above the crystal (medium 2). In this case if the  $\alpha$  angle of the incident beam is more important than the critical angle  $\alpha_c$ , the IR source is totally reflected within the crystal. The critical angle is defined by :

$$\alpha_c = \sin^{-1} \left( \frac{n_2}{n_1} \right) \quad (9)$$

With  $n_1$  the refractive index of ATR crystal (medium 1) and  $n_2$  the refractive index of the sample (medium 2). By taking into account value of the refractive index of ZnSe  $n_1 = 2.42$  (at  $1550 \text{ cm}^{-1}$ ) and protein solution  $n_2 = 2.5$  (at  $1550 \text{ cm}^{-1}$ ) is possible to set the critical angle value at  $38.8^\circ$ . Using the ZnSe crystal (GRASEBY-SPECAC, England) with a size of  $72 \times 10 \times 6 \text{ mm}^3$ , the incident angle is of  $45^\circ$  and 6 reflections are occurring at the interface of medium 1 and medium 2. For each reflection, an evanescent wave spreads in medium 2. The intensity  $E$  of this wave decreases exponentially with the increase of the distance  $z$  from the crystal (considering  $z = 0$  as the surface of ZnSe crystal). Intensity  $E$  can be calculated with :

$$E = E_0 e^{-z/d_p} \quad (10)$$

With  $E_0$  corresponding to the intensity at the crystal surface ( $z = 0$ ) and  $d_p$  the wavelength penetration depth that can be determined with:

$$d_p = \frac{\lambda}{2\pi n_1 \sqrt{\sin^2 \theta - \left(\frac{n_2}{n_1}\right)^2}} \quad (11)$$

With  $\lambda$  the wavelength of incident light. For example the penetration depth for the adsorption of protein solutions onto the ZnSe crystal is  $d_p = 1.26 \mu\text{m}$  at  $1550 \text{ cm}^{-1}$ .

### Experimental setup

The Fourier Transform Infrared (FTIR) experiments were performed on a Vertex 70 spectrometer (Bruker, Germany) using DTGS detector. Spectra, for the surface analysis, were recorded in the Attenuated Total Reflection (ATR) mode using a 45° trapezoidal ZnSe (internal reflection element) crystal (6 reflections, dimensions 72 × 10 × 6 mm<sup>3</sup>) in ATR cell (GRASEBY-SPECAC, England). Reference (bare ZnSe crystal in contact with ultrapure water) and sample spectra were taken by collecting 128 interferograms between 800 and 4000 cm<sup>-1</sup> at 2 cm<sup>-1</sup> resolution, using Blackman-Harris three-term apodization and the standard Bruker OPUS/IR software (version 7.5). Multilayer films were assembled on ZnSe crystal by the dipping method as described above. PEI, PSS, PAH, Enzymes, or Peptides solutions were prepared as described previously (section 4, just above) but in deuterated buffer to avoid the water signal in the amide I region.

Spectrums of the hydrogels made in solution were recorded in ATR mode using a diamond. All the hydrogels were formed in deuterated buffer.

### 2.3.4. Scanning Electron Microscopy (SEM) and Cryo-SEM

A scanning electron microscope scans a focused high-energy electron beam to generate a variety of signals at the surface of solid specimens. The signals that derive from electron-sample interactions reveal information about the sample including external morphology (texture), chemical composition, and crystalline structure and orientation of materials making up the sample.

#### Principle

Accelerated electrons in an SEM carry significant amounts of kinetic energy, and this energy is dissipated as a variety of signals produced by electron-sample interactions when the incident electrons are decelerated in the solid sample. These signals include secondary electrons (which produce SEM images), backscattered electrons (BSE), diffracted backscattered electrons (DBSE that are used to determine crystal structures and orientations of minerals), photons (characteristic X-rays that are used for elemental analysis and continuum X-rays), visible light (cathodoluminescence), and heat (Figure 10).<sup>7</sup> Secondary electrons and backscattered electrons are most valuable for illustrating contrasts in composition in multiphase samples. The electron beam is scanned in a raster scan pattern, and the position of the beam is combined with the intensity of the detected signal to produce an image. The number of secondary electrons that can be detected, and thus the signal intensity, depends, among other things, on specimen topography. SEM can achieve resolution better than one nanometer depending of the sample. Specimens are observed in high vacuum in conventional SEM, or in low vacuum or wet conditions in variable pressure or environmental SEM, and at a wide range of cryogenic or elevated temperatures with specialized instruments. SEM analysis is considered to be « non-destructive », which means that the signals generated by

electron interactions do not lead to a volume loss of the sample, and thus make possible to analyze the same sample repeatedly.

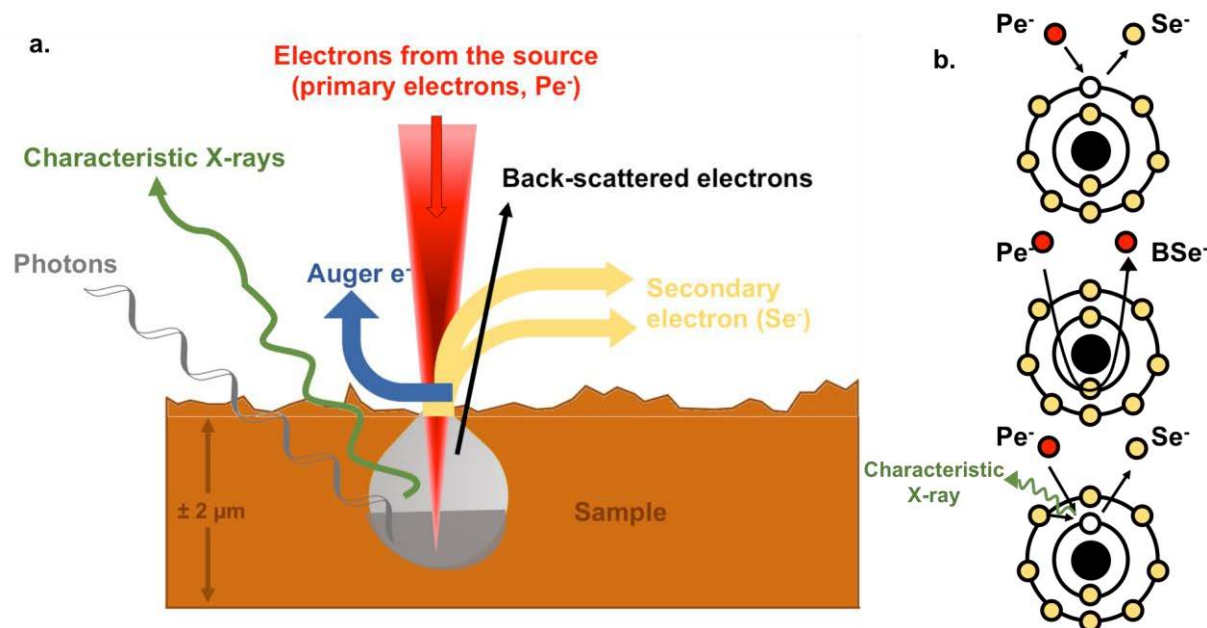


Figure 10 : a) Schematic of the source of radiation from an electron microscope, b) mechanisms of emission of secondary electrons, backscattered electrons, and characteristic X-rays from atoms of the sample.

In a typical SEM, an electron beam is thermionically emitted from an electron gun fitted with a tungsten filament cathode. Tungsten is normally used in thermionic electron guns because it has the highest melting point and lowest vapor pressure of all metals, thereby allowing it to be electrically heated for electron emission, and because of its low cost. The electron beam, which typically has an energy ranging from 0.2 keV to 40 keV, is focused by one or two condenser lenses to a spot about 0.4 nm to 5 nm in diameter. The beam passes through pairs of scanning coils or pairs of deflector plates in the electron column, typically in the final lens, which deflect the beam in the x and y axes so that it scans in a raster fashion over a rectangular area of the sample surface (Figure 11).<sup>8</sup> When the primary electron beam interacts with the sample, the electrons lose energy by repeated random scattering and absorption within a teardrop-shaped volume of the specimen known as the interaction volume, which extends from less than 100 nm to approximately 2  $\mu\text{m}$  into the surface (Figure 10). The size of the interaction volume depends on the electron's landing energy, the atomic number of the specimen and the specimen's density. The energy exchange between the electron beam and the sample results in the reflection of high-energy electrons by elastic scattering, emission of secondary electrons by inelastic scattering and the emission of electromagnetic radiation, each of which can be detected by specialized detectors. The beam current absorbed by the specimen can also be detected and used to create images of the distribution of specimen current. Electronic amplifiers of various types are used to amplify the signals, which are displayed as variations in brightness on a computer monitor (or, for vintage models, on a cathode ray tube). Each pixel of computer video memory is synchronized with the position of the beam on the specimen in the microscope, and the resulting image is, therefore, a



distribution map of the intensity of the signal being emitted from the scanned area of the specimen. Older microscopes captured images on film, but most modern instrument collect digital images.

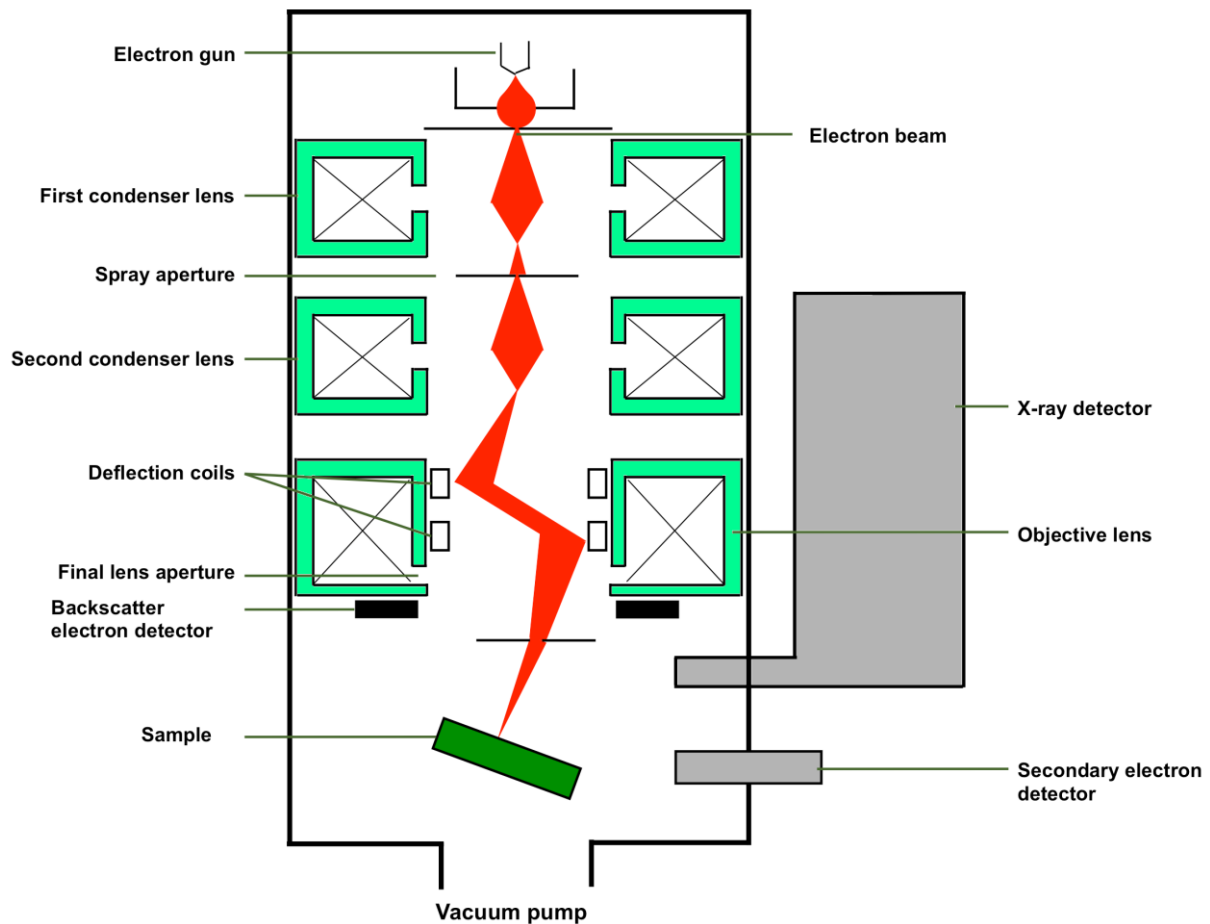


Figure 11: Schematic of the principle of the fonctionnement of a SEM

### Experimental Setup

To observe cross-sectioned gels, a specific cryo-holder was designed and manufactured by the mechanical facility of the Charles Sadron Institute (see Figure 12). The glass slide, covered by enzymatic precursor film and the self-assembled gel, was inserted vertically in the jaws of the vise. The sample is plunged rapidly into liquid ethane and then fixed into the holder, which was previously place inside nitrogen slush. Finally, the holder with the sample is placed inside the cryo preparation chamber of the Quorum PT 3010 machine. As the sample is free standing over the holder, during the plunging, the sample is rapidly frozen by direct contact with the liquid ethane. The sample is then transferred under vacuum into the chamber attached to the microscope and fractured with a razor blade. First, a sputtering step is realized (10 mA for 30s), and then the surface is fracture. A slight etching at  $-90^{\circ}\text{C}$  for 2 min is performed to render the fibers more visible followed by the deposition of a thin Pt layer (metallization step, 5 mA for 20s). The sample is then transferred in the FEG-cryoSEM (Hitachi SU8010) and observed at 1kV at  $-170^{\circ}\text{C}$ .

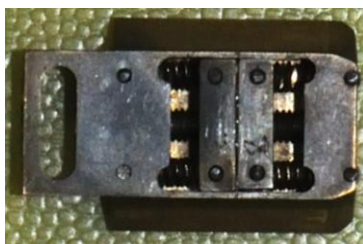


Figure 12: Picture of the specific cryo-holder designed and built for the preparation of cross-sections. The “cross-section” holder is a vise like holder with two movable jaws. A screw compressing/uncompressing two springs moves the jaws forwards and backwards. By design the center of the holder is invariable as the two jaws can be displaced independently to adjust to the sample thickness by screws and springs. In that way, the sample will be in the optical axis of the SEM after introduction in the microscope and easily found under the beam.

### 2.3.5. Analytic High-Performance Liquid Chromatography (HPLC)

HPLC is a type of liquid chromatography where the sample is forced through a column that is packed with a stationary phase composed of irregularly or spherically shaped particles, a porous monolithic layer, or a porous membrane by a liquid (mobile phase) at high pressure to achieve the separation of the different molecules present inside the sample.

#### Principle

HPLC is characterized by the use of high pressure to push a mobile phase solution through a column of stationary phase allowing separation of complex mixtures with high resolution.

Analytical HPLC instruments consist of a reservoir of mobile phase, a pump, an injector, a pre-column, a separation column, and a detector. The pre-column serves to protect the analytical column. The pre-column is usually packed with the same material as the main column and serves to trap particulate matter (including septum material) and high molecular weight sample constituents. After passing the pre-column, the different component of the mixture pass through the column at different time due to differences in their interactions between the mobile phase and the stationary phase.<sup>9</sup> The principle of separation in the two main phase mode (normal and reverse phase mode) is adsorption. When a mixture of components are introduced into a HPLC column, they travel according to their relative affinities towards the stationary phase. The component which has more affinity towards the adsorbent, travels slower. The component which has less affinity towards the stationary phase travels faster. Since no two components have the same affinity towards the stationary phase, the components are separated.

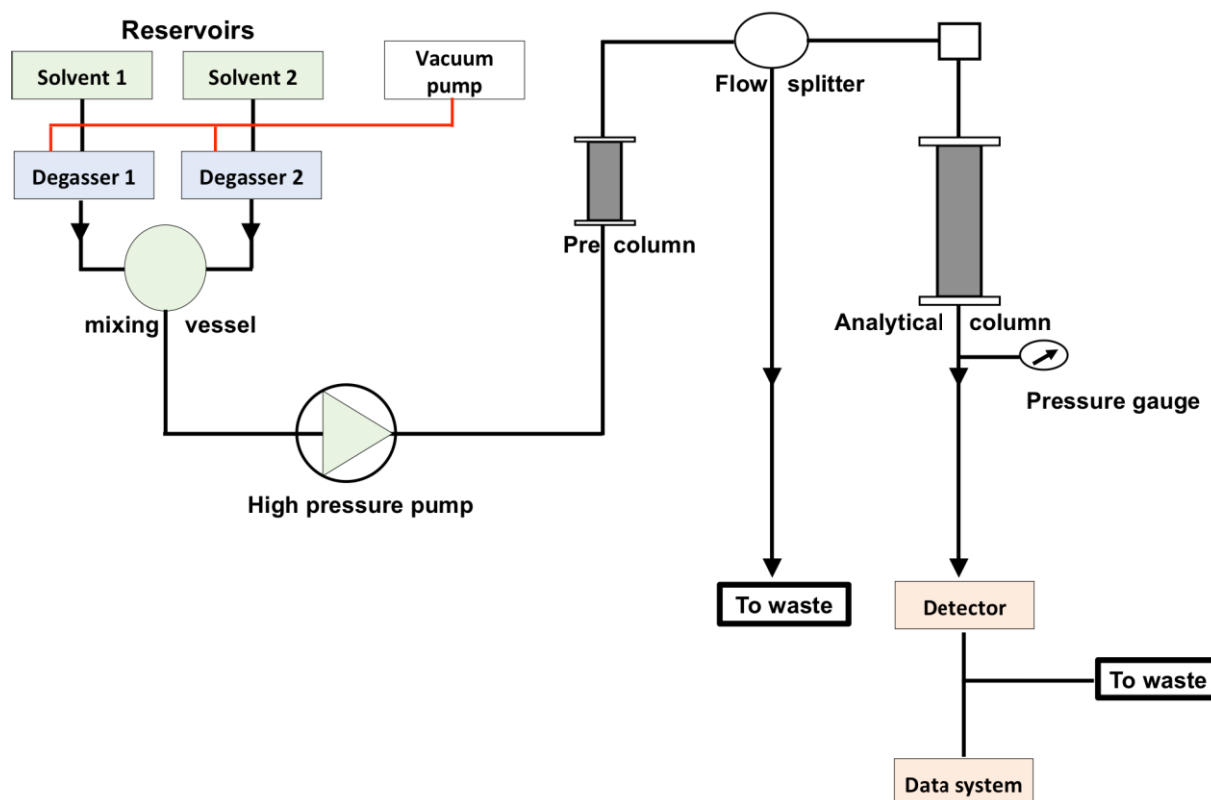


Figure 13: Schematic of an analytical HPLC system.<sup>10</sup>

The principle of HPLC are based on Van Deemter equation which relates the efficiency of the chromatographic column to the particle size of the column, molecular diffusion and thickness of stationary phase. The Van Deemter Equation is given as:<sup>11</sup>

$$H \text{ or } HETP = A + \frac{B}{v} + Cv \quad (12)$$

Where, A = Eddy diffusion, B = Molecular diffusion, C= Rate of mass transfer and v = Flow rate

HPLC modes: the normal phase mode is a adsorption mode where the stationary phase is polar, most of times contituted of a silica gel, and a non-polar mobile phase (only organic solvents), where the less polar sample will be the fastest and the separation between two molecules is based on the difference between polarities.

In the reversed phase mode, the stationary phase is non-polar, with a C18 phase (Octadecyl Silyl), and the mobile phase is polar, with a mixture of aqueous and organic solvent. The more polar sample will be the fastest and the separation is based on the difference in the hydrocarbon content. The stationary can have lot of different functional groups for the interaction with the sample. Most of the stationary phase are chemically bonded to the silica.

The choice of mobile phase is very importante in HPLC and the eluting power of the mobile phase is determined by its overall polarity, the polarity of the stationary phase and the nature of the sample components. The solvents or mobile phases used must be passed through the column at high pressure at about 1000 to 3000 psi.

This is because of the small size of the particle of the stationary phase (3-10  $\mu\text{m}$ ), which make the resistance to the solvent's flow high. Two kind of mobile phase mode can be used, the isocratic mode and the gradient mode. In an isocratic separation, the mobile phase is prepared by using the same mixture of solvents for whole time of a method, and by consequence the eluting power or polarity will be unchange. But in gradient elution technique, the polarity of the mobile phase is gradually increased and hance the solvent composition has to be changed during the run. The control over the gradient speed can be achieved by the starting and final ratio between solvents and the time of the run.

Finally, when the different molecules exit the main column, they are detected by the detector. In HPLC, different detectors can be used depending of the kind of detection needed. The most common detector is the UV-vis detector because it is the better compromise between price and efficiency in detection. But others detectors exist as refractive index detector, fluorescence detector, or mass detector.

### *Experimental Setup*

Analytic High-Performance Liquid chromatography (HPLC) was carried out with a 1100 Series from Agilent technologies.

**For characterization of the different peptides and the catalytic assays:** the column is a Supelcosil ABZ + Plus with the following dimensions 15 cm  $\times$  4.6 mm, 3  $\mu\text{m}$ . The eluent used for all analyses was acetonitrile/deionized water in different ratio depending on the experiment. Ratio 80/10 in isocratic conditions, at 1 mL/min for the first catalytic assays but a ratio 50/50 in isocratic conditions, at 1 mL/min for the peptide characterization.

**For the racemic discrimination assays:** the column is a chiral column is a cosmosil 3B with the following dimensions 4.6 mm I.D.  $\times$  250 mm. The eluent used for all analyses was n-Hexane/ isopropanol in ratio 90/10 in isocratic conditions, at 1 mL/min except for the racemic solution of methyl-3-(4-methoxyphenyl) oxirane-2-carboxylate where the ratio was 97.5/2.5 in isocratic conditions at 1 mL/min.

Chromatograms were recorded by the software OpenLab Agilent 1100. All samples were observed in solution in diluted conditions (ten times under the gelation condition (1 mg/mL of peptides).

### 2.3.6. Dynamic Light Scattering (DLS)

Dynamic light scattering also known as Photon Correlation Spectroscopy (PCS) or quasi-elastic light scattering (QELS) is a non-destructive spectroscopic analysis technique that can be used to determine the size distribution profile of small particles in suspension or polymers in solution.<sup>12</sup>

#### Principle

A monochromatic light source, usually a laser, is shot through a polarizer and into a sample. The scattered light then goes through a second polarizer where it is collected by a photomultiplier and the resulting image is projected onto a screen. This is known as a speckle pattern (Figure 14a).<sup>13</sup> All molecules in the solution are being hit with the light and all diffract the light in all directions. The diffracted light can either interfere constructively (light regions) or destructively (dark regions). This process is repeated at short time intervals and the resulting set of speckle patterns are analyzed by an autocorrelator that compares the intensity of light at each spot over time. The polarizers can be set up in two geometrical configurations. One is a vertical/vertical (VV) geometry, where the second polarizer allows light through that is in the same direction as the primary polarizer. In vertical/horizontal (VH) geometry the second polarizer allows light not in same direction as the incident light.

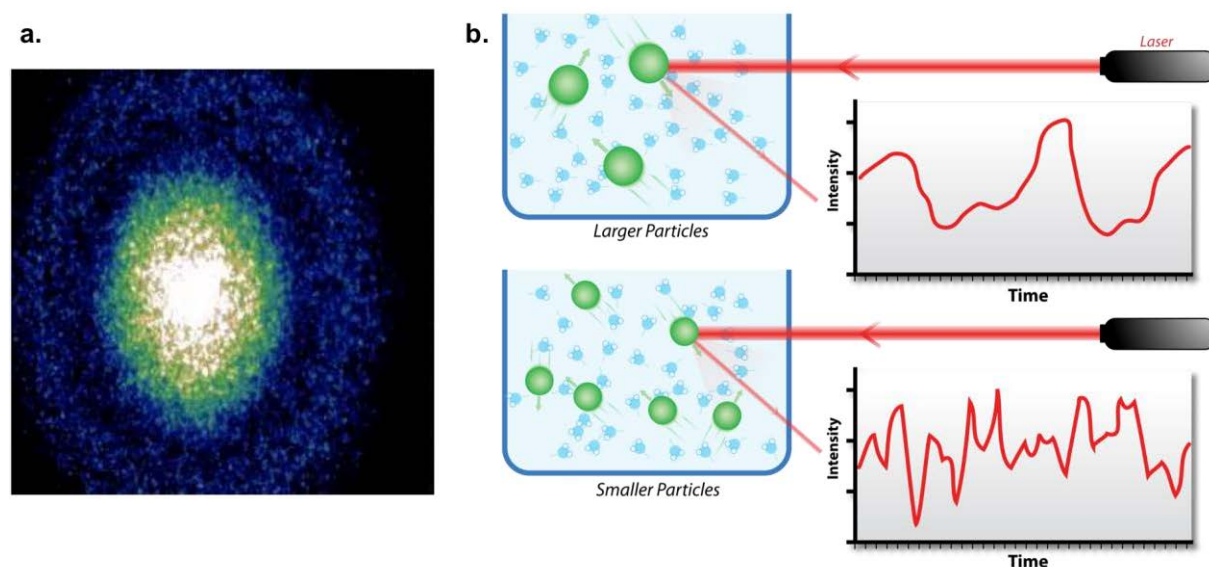


Figure 14: a) Typical speckle pattern, b) Hypothetical dynamic light scattering of two samples: larger particles on the top and smaller particles on the bottom.

The schematic representation of a typical instrument of DLS (Figure 15)<sup>14</sup> contains a cell containing the sample of particles dispersed in a liquid. The cell is fixed on a sample holder which integrates temperature control systems and the mechanical stability of the solution. The particles in the sample are illuminated by a coherent beam of light (laser) of constant intensity. In a given direction, the intensity of the scattered light is measured by a photodetector. In some instruments, the photodetector is carried on a goniometer to allow to vary the angle of observation. The instrument comprises a set of optical elements (lenses, openings, etc.) for

conditioning the beam of the incident light and the collection of scattered light. The section of the cell containing the sample can take different forms (round, square, etc.). In the case of using a square cell, the light scattered by the particles refracts when it passes through the walls of the cell. The scattering angle is different from the detection angle (the angle between the detector and the incident light axis). The advantage of using a round cell is that there is no refraction by the walls of the cell and thus the scattering angle is the same as the angle of detection.

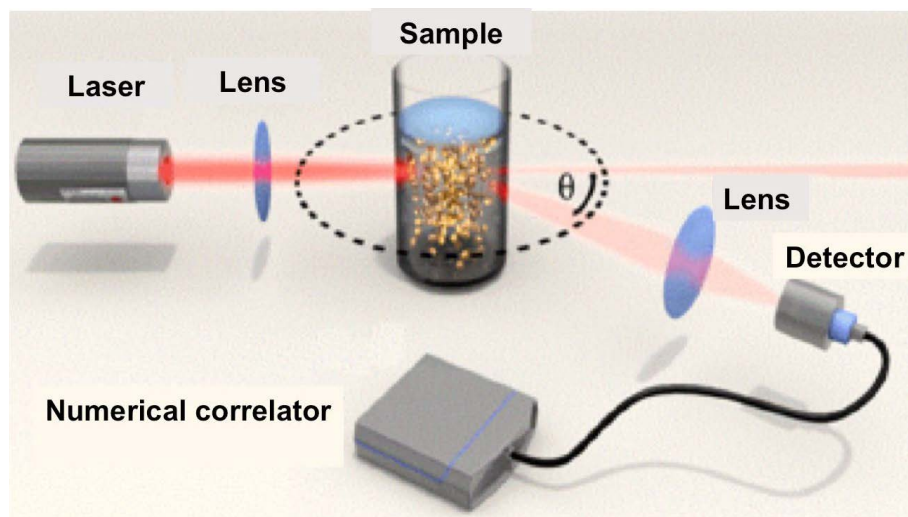


Figure 15: Schematic of the DLS instrument principle.

The DLS technique is based on the analysis of fluctuations over time of the intensity of the light scattered by the particles. These fluctuations in intensity are caused by incessant changes of the relative positions of the particles subjected to random motions of translation and rotation. These movements are essentially Brownian movements. Brownian motion depends on the viscosity of the surrounding environment, its temperature, and particle size.<sup>16</sup> The distances traveled by the waves scattered by the particles towards the detector vary with time as a function of the movements of the particles. The phase of the light scattered by each particle also varies with time. Due to the interference of the waves scattered by the particles, the total intensity fluctuates with time. Figure 14b illustrates fluctuations in the intensity of light scattered by particles of small sizes and large sizes. Because of particle motions, the frequency of scattered light is slightly different from that of incident light. The frequency difference varies from a few Hertz to a few hundred Hertz. This is why the light scattering in these conditions is called quasi-elastic. The analysis of the variations of the intensity of the scattered light can provide information on the motions of the particles. Some characteristics of particles, such as their size, can thus be revealed.

### Experimental Setup

Dynamic Light Scattering (DLS) experiments were carried out with a Zetasizer from Malvern. The experiments were done in diluted system, which means that the concentration of peptide is at 1 mg/mL with a concentration of enzyme at 1 mg/mL too. The kinetics is followed every 10 min. All solutions were freshly prepared in PBS buffer and filtrated with a PTFE 0.2  $\mu\text{m}$  filter before each experiment.

### 2.3.7. Circular Dichroism spectroscopy (CD)

Circular dichroism measurement is a spectroscopy technique based on the unequal absorbance by studied molecules of left and right handed circularly polarized light generated by a spectropolarimeter. Extensively used to study chiral molecules of all types and sizes, it has a wide range of applications in many fields, but it finds its most extended applications in the study of large biomolecules. Indeed, able of accurate measurements in the middle and far-UV (between 170 and 300 nm), it is a powerful tool for a rapid determination of the secondary structure and folding properties of peptides, proteins and polypeptides.

#### Principle

An electromagnetic radiation such as light consists of an electric and magnetic fields that oscillate perpendicular to one another and to the propagating direction. The polarization of electromagnetic waves refers to the oscillations of the electric field. Linear polarization (Figure 16a) occurs when electric field vector oscillates only in one direction, whereas circular polarization appears when the electric field vector rotates around its propagation direction while keeping a constant norm (Figure 16b).

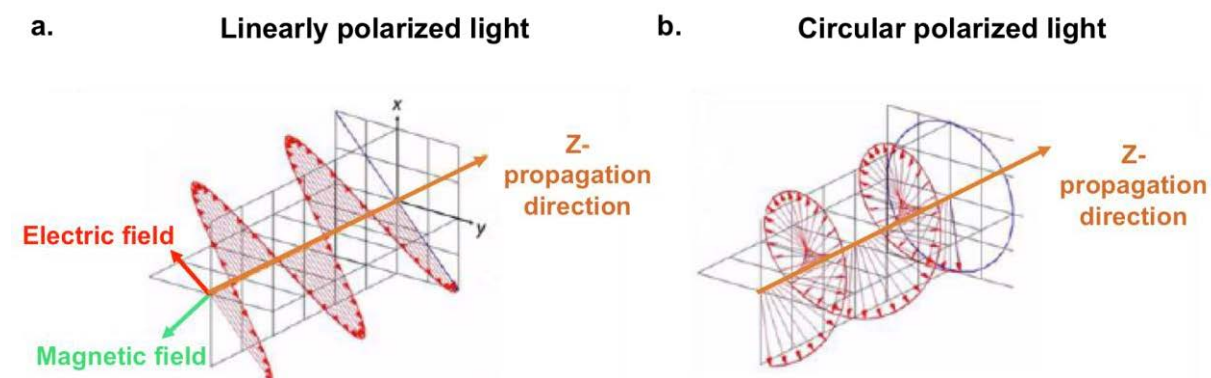


Figure 16: Light polarization. a) Linearly polarized light by 45 ° toward the propagation direction, b) circularly polarized light rotating clockwise around the propagation direction.

Linear polarized wave can be described as the superposition of two opposite circular polarized waves of same amplitudes rotating in two opposite directions: clockwise (Right Circularly Polarized-RCP) and counterclockwise (Left Circularly Polarized (LCP)). A projection of the combined amplitudes perpendicular to the propagation direction thus yields a line (Figure 17). When this linear polarized wave passes through certain optically active molecules, its left and right-handed components are unequally absorbed at certain wavelengths:

$$\Delta A = A_L - A_R \quad (19)$$

With  $A_L$  the absorbance of the LCP and  $A_R$  the absorbance of the RCP for a given wavelength.

This difference of absorbance thus leads to a difference of amplitudes between the two absorbed oppositely polarized components: the amplitude of the more absorbed component is smaller than that of the less absorbed one. The consequence is that a projection of the resulting amplitudes now yields an ellipse instead of the usual line (Figure 17). The occurrence of this ellipticity is called circular dichroism.<sup>17-18</sup>

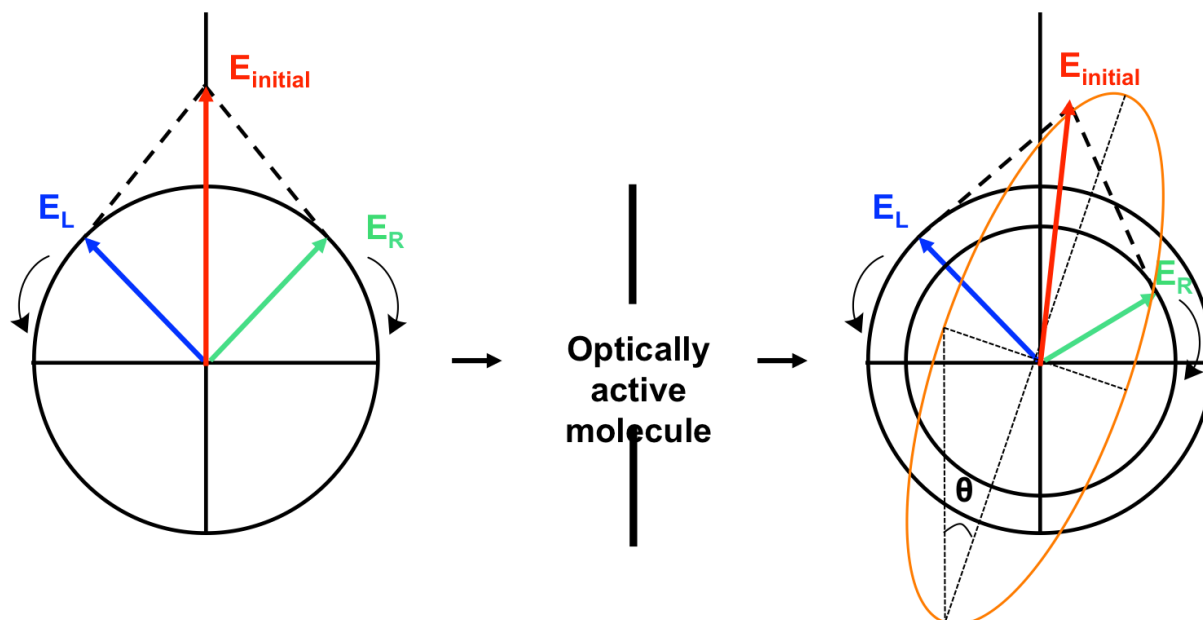


Figure 17: Projections of polarized waves (oscillations of the electric field  $E$ ): when the initially linearly polarized light, which is a superposition of two circularly polarized waves, passes through an optically active molecule, left ( $E_L$ ) and right ( $E_R$ ) components are unequally absorbed then resulting in an elliptic polarization.

When measured with a spectropolarimeter, the wavelength-dependent difference of absorption results in a circular dichroism spectrum characteristic of the sample representing the ellipticity ( $\theta$ ) expressed in degrees as a function of wavelength. So circular dichroism is generally reported in terms of ellipticity  $\theta$  for a given wavelength:

$$\theta = \tan^{-1} b/a \quad (20)$$

Where  $b$  and  $a$  represent the minor and major axes of the resulting ellipse (Figure 17). But different other relations exist and are often used to express circular dichroism. Indeed, relying on the Beer-Lambert's law previously exposed when describing UV-visible spectroscopy measurements, it is possible to deduce the molar circular dichroism  $\Delta\varepsilon$  ( $\text{L}\cdot\text{mol}^{-1}\cdot\text{cm}^{-1}$ ):

$$\Delta\varepsilon = \varepsilon_L - \varepsilon_R = \frac{\Delta A}{c \cdot l} \quad (21)$$

With  $l$  (cm) and  $c$  ( $\text{mol}\cdot\text{L}^{-1}$ ) and  $\varepsilon$  ( $\text{L}\cdot\text{mol}^{-1}\cdot\text{cm}^{-1}$ ) the length and the molar concentration of the studied sample, and  $\varepsilon_L$  and  $\varepsilon_R$  the molar extinction coefficients of LCP and RCP respectively. The molar ellipticity  $[\theta]$  ( $\text{deg}\cdot\text{cm}^2\cdot\text{dmol}$ ) can also be derived from these relationships and is approximated as follows:

$$[\theta] \approx \frac{100 \cdot \theta}{c \cdot l} \approx 3298.2 \cdot \Delta\varepsilon \quad (22)$$



When studying polymers, peptides or proteins  $[\theta]$  can also be converted into a normalized value called mean residue ellipticity by being divided by the number of monomer units (residues) in the molecule.

*How do circularly polarized light interact with matter and why are chiral molecules specifically sensitive to this kind of polarization?*

As previously exposed for UV-spectroscopy, the interaction of matter with a light beam induces electronic displacements: the electric field of a light beam causes a linear displacement of charge when interacting with a molecule (electric dipole), whereas its magnetic field causes a circulation of charge (magnetic dipole). By calculating the scalar product of the vectors of these two motions, the rotational strength can be deduced. This value, which can be linked to the molar circular dichroism is an indicator of the behavior of the studied molecule toward circularly polarized light. Indeed, when electric and magnetic dipoles are perpendicular, which is the case in symmetric molecules, the rotational strength is equal to zero and thus the studied molecules exhibit no circular dichroism. However an asymmetric disposition of dipoles leads to a non-zero circular dichroism. Circular dichroism can thus be observed for molecules presenting intrinsic asymmetries as chiral centers on specific chromophores or global chirality imposed by the macromolecular spatial arrangement. In the case of global chirality, the optical activity depends on the interaction of the dipoles of different chromophores and is thus strongly influenced by the spatial relative position of these chromophores. In this way, by studying circular dichroism in different spectral regions, one can obtain information on the global structure of the macromolecule.

The principal chromophores contributing to the circular dichroism signals in biomacromolecules like proteins and polypeptides, are: *i*) the peptide bond with a contribution at wavelengths below 240 nm (in particular at 190 and 208 nm ( $\pi\pi^*$  transition) and at 222 nm ( $n\pi^*$ ), *ii*) the amino acid side chains which absorb below 260 and 320 nm and *iii*) disulfide bridges presenting a wide absorption band at 260 nm. Three basic conformations (helix, sheet and random coil) showing each a characteristic circular dichroism spectrum (Figure 18) can be observed in different proportions in proteins and polypeptides, that is why the circular dichroism spectrum of a biomacromolecule is often described in first approximation as a linear combination of the circular spectra of these three basic spatial arrangements:

$$\theta_T = x_1 \cdot \theta_h + x_2 \cdot \theta_s + x_3 \cdot \theta_{rc} \quad (25)$$

With  $\theta_T$  the total ellipticity at each wavelength expressed as a sum of the helix ( $\theta_h$ ), the sheet ( $\theta_s$ ) and the random coil ( $\theta_{rc}$ ) contributions weighted by  $x_n$  fractions.

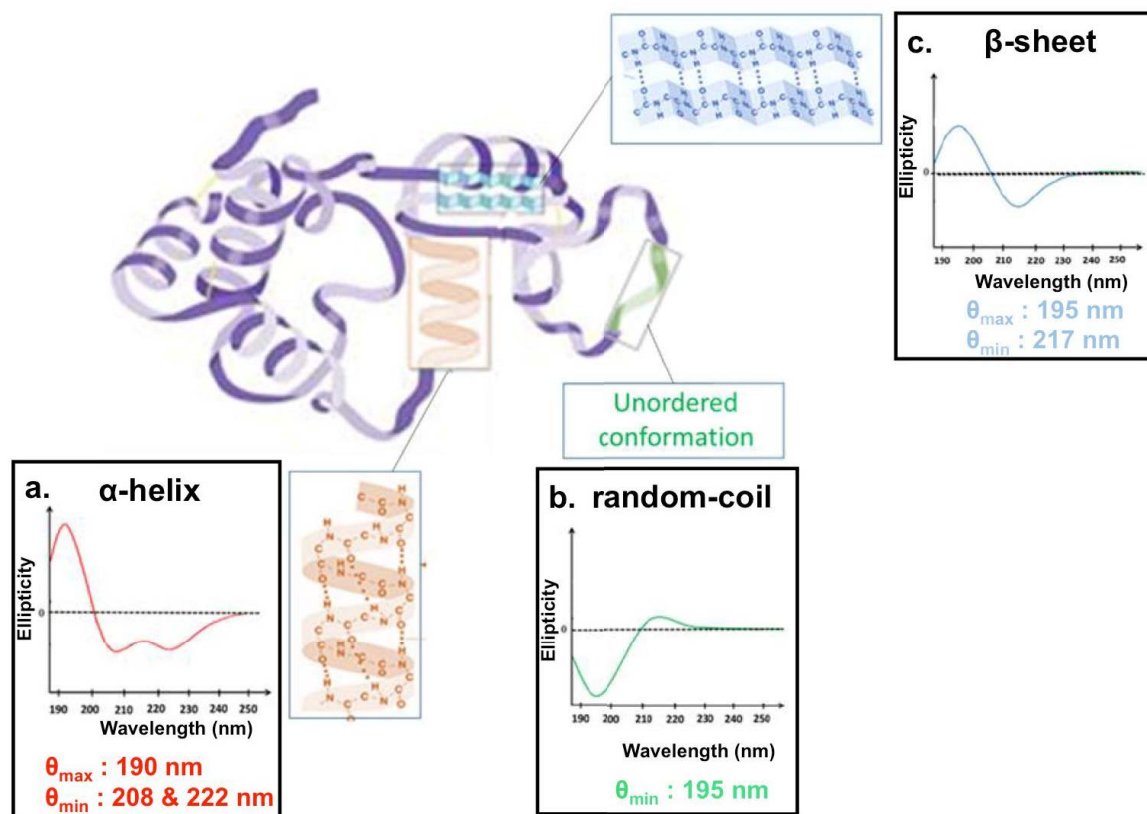


Figure 18: Examples of basic conformations and their relative circular dichroism spectra, a)  $\alpha$ -helix, b) unordered conformation (random-coil), c)  $\beta$ -sheet.

As other less common conformations can also be adopted, the previous expression can be generalized as follows:<sup>19</sup>

$$\theta_{T\lambda} = \sum x_i \cdot \theta_{i\lambda} + \text{noise} \quad (26)$$

with  $\theta_{T\lambda}$  the total ellipticity at wavelength  $\lambda$  expressed as a sum of  $\theta_{i\lambda}$ , ellipticities at each wavelength of each  $i^{\text{th}}$  secondary structural elements weighted by  $x_i$  fractions. Based on this relation, specialized software relying on protein databases have been developed to analyze experimental circular dichroism spectra by estimating the proportion of each type of secondary structural elements.<sup>19</sup>

### Experimental Setup

Circular dichroism (CD) spectra were recorded between 190 and 400 nm using a Jasco J-1100 spectropolarimeter with a data pitch of 1 nm on the light wavelength in a continuous scanning mode, at a scanning speed of 100 nm/min and with a data integration time (D.I.T) of 1 s. The CD spectra show the ellipticity expressed as an angle as a function of the wavelength. Liquid samples were inserted in a quartz cell of path length 1 mm. Solutions were maintained at 25 °C using a peltier apparatus (Jasco-PTC-423S) with an accuracy of  $\pm 0.2$  °C. A blank value was measured with the buffer solution (usually PBS, pH 7.4) before each series of measurements.

### 2.3.8. Ultraviolet-Visible spectroscopy (UV-Visible)

UV-visible spectroscopy is a technique allowing assessing the ability of a sample to absorb radiations in the ultraviolet-visible region of the electromagnetic spectrum. The intensity of the absorption of a given sample varies as a function of wavelength and this wavelength dependent behavior recorded by a spectrophotometer results in an absorption spectrum characteristic of the studied sample. This technique is thus often used as analytical tool to detect the presence or to monitor the appearance of a particular substance in a sample and to quantify the amount of this substance in the studied sample.

#### Principle

An electromagnetic wave is associated with energy dependent on its wavelength and carried by photons. The energies of electromagnetic waves in the UV-visible regions are sufficient to excite electrons of a molecule and to favor their transition from the ground state to the excited state. The principle of UV-visible spectroscopy relies on this ability of molecules bearing light-sensitive groups (chromophores) to undergo electronic transitions. Indeed, as illustrated in Figure 19, when a molecule containing  $\pi$ -electrons or non-bonding electrons is exposed to light having an energy that matches a possible electronic transition within the molecule, some of the light energy (photons) will be absorbed and will trigger the displacement of the electron from the highest occupied molecular orbital (HOMO) toward the lowest unoccupied molecular orbital (LUMO). According to the type of chromophores, which are sensitive to specific excitation energies and so to specific wavelengths, different types of transitions can be observed ( $n\text{-}\pi^*$  (Figure 19),  $\pi\text{-}\pi^*$ ,  $n\text{-}\sigma^*$ ,  $\sigma\text{-}\sigma^*$ ) thus resulting in different absorption profiles. An optical spectrophotometer records the wavelengths at which absorption occurs for a given sample, together with the degree of absorption at each wavelength, thus resulting in a spectrum presenting the evolution of absorbance ( $A$ ) as a function of wavelength. The obtained absorbance can be related to the sample concentration by the Beer-Lambert's law:

$$A = -\log\left(\frac{I}{I_0}\right) = \varepsilon \cdot l \cdot c \quad (27)$$

With  $I_0$  and  $I$  the intensities of incident and transmitted radiations respectively,  $l$  (cm),  $c$  ( $\text{mol}\cdot\text{L}^{-1}$ ) and  $\varepsilon$  ( $\text{L}\cdot\text{mol}^{-1}\cdot\text{cm}^{-1}$ ) the length, the molar concentration and the molar extinction coefficient of the studied sample.

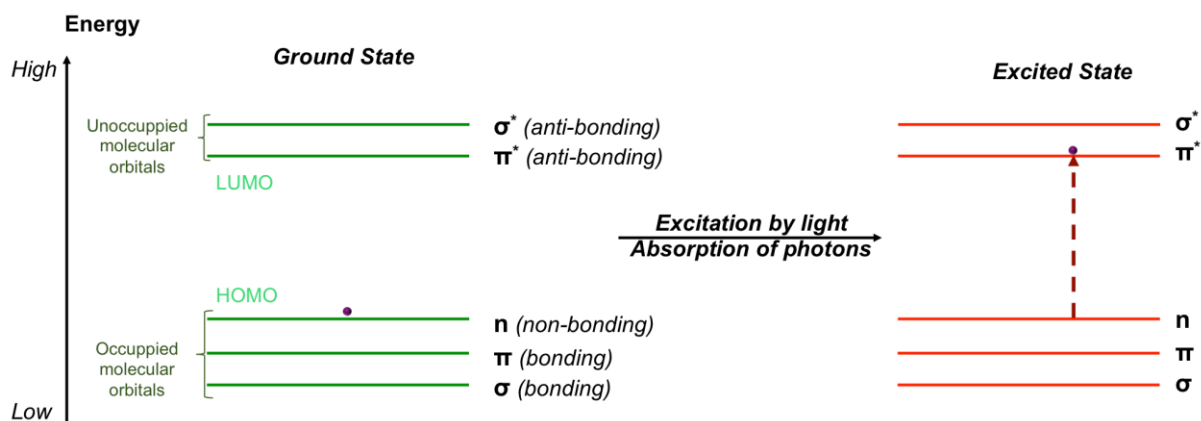


Figure 19: Example of an electronic transition ( $n-\pi^*$ ) induced by the absorption of a photon by a chromophore-bearing molecule exposed to UV-Visible light.

### Experimental Setup

Microplate reader UV spectroscopy (FLX-Xenius<sup>®</sup>, SAFAS, Monaco) using SP<sub>2000</sub>V<sub>7</sub> software was the main device entailed in characterization of UV-Vis spectra of all synthesized molecules and esterase-like activity measurement. For UV-Vis spectra recorded, a 96 corning well-plate was used with a 200  $\mu$ L of sample's solution solubilized in milliQ water or in methanol. A blank (air) was done before each series of measurement and the spectrum of the solvent was done in the same conditions as the sample. UV-Vis analysis of hydrogel formed in the bulk was done in 96 corning well plate like for the solutions. UV-Vis analysis of hydrogel generated from a surface was realized in 24 corning well-plate where glass slide ( $\Phi = 14$  mm) were deposited at the bottom of the wells. Then, the multilayer was build-up inside the well by alternating the addition of solution of polyelectrolytes and buffer alone for the rinsing step. Finally, the enzyme layer is adsorbed on the polyelectrolyte multilayer and then the peptide solution is added and the self-assembly is let to grow for 12 h.

Esterase-like activity was recorded for the activated ester para-nitrophenyl acetate (p-NPA) and followed at 405 nm.

### 2.3.9. Fluorescence spectroscopy

Fluorescence spectroscopy is a spectroscopy technique based on the fluorescent properties of a sample. It allows to measure the intensity of photons emitted from a sample after this sample has absorbed photons. Due to its sensitivity and selectivity, it is an important investigation tool in many areas of analytical science, in particular for detection and quantification of specific compounds in a sample.

#### Principle

As previously explained for the other spectroscopy techniques, energies (photons) associated with electromagnetic waves are sufficient to excite electrons in light-sensitive molecules. Fluorescent groups are called fluorophores and have the ability, when excited by light, to absorb a photon at a specific wavelength and to re-emit it at longer wavelength. Indeed, when submitted to a specific wavelength ( $\lambda_{\text{ex}}$ ), a fluorophore absorbs a photon, which triggers a transition from the ground electronic state ( $S_0$ ) to one of the various vibrational levels in the excited electronic state ( $S_1'$ ) (Figure 20). Collisions with surrounding molecules cause the excited fluorophore to lose vibrational energy until it reaches the lowest vibrational state of the excited electronic state ( $S_1''$ ). The fluorophore then drops down again to one of the various vibrational levels of the ground electronic state ( $S_0$ ), thus leading to the emission of a photon. This emitted photon is characterized by a lower energy than the initially absorbed one corresponding, according to Planck's law expressed below, to a higher emission wavelength ( $\lambda_{\text{em}}$ ) than excitation-wavelength ( $\lambda_{\text{ex}}$ ):

$$E = h \cdot \nu = \frac{h \cdot c}{\lambda} \quad (28)$$

Where E is the energy of the photon,  $\lambda$  and  $\nu$  represent respectively the wavelength and the frequency of the electromagnetic wave and h and c correspond respectively to the Planck constant and the speed of light.

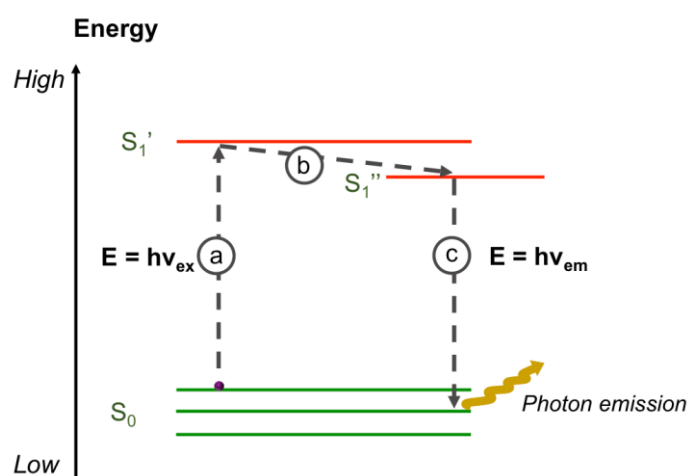


Figure 20: Jablonski diagram : when a fluorophore is subject to light, the absorption of a photon (a) triggers the transition of an electron from the ground state  $S_0$  to excited level  $S_1'$ , this electron is then de-energized toward  $S_1''$  level (b), to then drop back to level  $S_0$  level by emitting a photon (c).

This difference of energy between the absorbed and the emitted photon is called Stokes shift and it is a characteristic of the studied fluorophore. In fact, as several vibrational levels exist in the ground electronic state  $S_0$ , the emitted photon can have different energies (corresponding to different emissions-wavelengths) depending on the type of fluorophore. It is therefore possible to characterize a fluorophore by determining its excitation and emission spectra (intensity as a function of wavelength) with a spectrofluorimeter and to quantify its amount by measuring the intensity of the emitted light when this fluorophore is excited at a precise wavelength.

### *Experimental Setup*

Fluorescence measurements were carried out with a microplate reader, multi-detector SAFAS spectrofluorimeter (FLX-Xenius®, SAFAS, Monaco) using SP2000V7 software was the main device entailed in the fluorescence measurement of the  $\pi$ -stacking involved in the peptides self-assembly in the different chapters of this thesis. To follow the  $\pi$ -stacking of the Fmoc group, we excite our molecule at 280 nm and take our spectrum in the range 300-600 nm. The fluorescence assays were done for hydrogels in solution (peptide (3.6, 5 or 10 mg/mL), enzyme (1 mg/mL)), diluted solutions (peptide and enzyme at 1 mg/mL) and in surface by adding the glass slide at the bottom of the well (peptide and enzyme at 1 mg/mL).

### **2.3.10. Rheology**

Rheology is the study of the flow of matter, primarily in a liquid state, but also as “soft solids” or solids under conditions in which they respond with plastic flow rather than deforming elastically in response to an applied force. It applies to substances that have a complex microstructure, such as muds, sludges, suspensions, polymers, as well as to biological materials or soft matter (hydrogels).

#### *Principle*

The main purpose of a rheometer is to give a relation between stress and strain applied to a material. Numerous devices exist to achieve this objective, allowing either a simple viscosity measurement (e.g., measurement of the falling time of beads in a fluid) or exploring more unusual scales (e.g., micro-rheology); in our case, we will specifically use a “rotational” rheometer in order to characterize the different phenomena specific to “soft matter”.<sup>20</sup> A rotating motor is responsible for transmitting the stress to the material via a specific geometry; the resulting displacement or torque is then recorded. There are two kinds of rheometers of this type (Figure 21): imposed constraint or imposed deformation. The first ones are controlled natively by means of the requested torque to the motor. The second commonly include a strain sensor uncoupled from the motor responsible for imposing rotation.

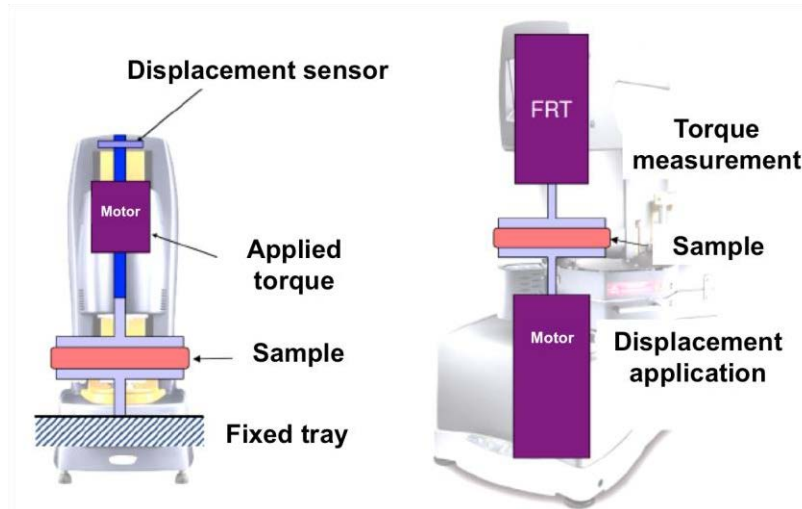


Figure 21: different type of rheometer : imposed constraint (right) and imposed deformation (left)

The engine of a rheometer can impose only two stresses: a torque or a displacement of the mobile in contact with the sample. The relationship between these magnitudes and the stress or strain applied to our materials can be expressed through the following relationships:

$$\tau = K_{\tau}C \quad (29) \quad \text{et} \quad \dot{\gamma} = K_{\dot{\gamma}}\dot{\theta} \quad (30)$$

Where  $C$  is the couple applied to the machine (N.m),  $\dot{\theta}$  is the rotation speed (rad/s), and  $K_{\tau}$  (Pa/(N.m)) and  $K_{\dot{\gamma}}$  (rad<sup>-1</sup>) are the geometrical factors respectively binding torque with stress and rotational speed with shear rate. These factors depend on the geometry used for the measurement. They can either be calculated precisely (for given geometries), or be derived from a calibration process.<sup>21</sup> The choice of geometry is based on the measurements. A fairly fluid material will need to be sheared over a large area so that a sufficient torque can be recorded by the rheometer (depends on the device). The thickness of the sample can also be adapted ("gap"); the weaker it is, the more important shear is imposed at the same speed of rotation. In our case, we use a plane-plane geometry in an imposed constraint rheometer, which seems the best solution for characterizing supramolecular hydrogels.

This instrument imposes a specific stress field or deformation to the fluid, and monitors the resultant deformation or stress to determine constants, which permits to characterize the mechanical properties of fluids and materials. These constants are the Young's modulus of elasticity ( $E$ ), the shear modulus ( $G$ ) and Poisson's ratio ( $\nu$ ). Young's modulus of elasticity is defined as the constant that relates the tensile or compressive stress (force per unit area) applied to a material and the beginning of its deformation. The shear modulus ( $G$ ) establishes a ratio similar to that between tension and deformation. It rather applies to a material subjected to shear stresses.  $G = G' + iG''$ , where  $G'$  is the real part of  $G$ , which characterizes the elastic behavior of the material (the energy conserved and totally restored by the material) and  $G''$  the imaginary part of  $G$ , called the loss modulus or dissipation modulus, which characterizes the viscous behavior (dissipated energy).

$$\tan \delta = G''/G' \quad (31)$$

Finally, Poisson's ratio makes it possible to characterize the contraction of the material perpendicular to the direction of the applied force.

The ratio between the shear stress applied to a material and the resulting deformation (a relative elongation) is constant, as long as this deformation remains small and the yield strength of the material is not reached. The law of elasticity is Hooke's law:

$$\sigma = E\varepsilon \quad (32)$$

Where  $\sigma$  is the shear (Pa),  $E$  is the Young modulus (Pa) and  $\varepsilon$  is the relative elongation or deformation ( $\varepsilon = \frac{l-l_0}{l_0}$  (33)).

Mechanical properties of a material can be characterized by Young's modulus, which is the mechanical stress that would result in an elongation of 100 % of the initial length of a material. It would therefore double in length, if it could actually be applied. In fact, the material is deformed irreversibly, or breaks, long before this value is reached. The Young modulus is the initial slope of the strain-strain curve and can be related to the shear modulus by the following equation:

$$G = \frac{E}{2(1+\nu)} \quad (34)$$

In our case, we are interested by characterizing supramolecular hydrogels. Gelation can be considered as a connective transition and described by a model percolating of bonds: initially, the monomers are evenly distributed. The interaction between monomers is modeled by a random connection, by bonds, of neighboring monomers. The fraction of bonds formed at each moment of the reaction (or progress of the reaction) will be designated by  $p$ ,  $p$  varying from 0 to 1: when all the links are formed and all the monomers are connected in a macroscopic network, the reaction is total ( $p = 1$ ). When  $p = 0$ , the gel is a viscoelastic liquid (polymer solution). So we have  $G'' \gg G'$ . When  $p = 1$ , the gel is formed and then has a strong elastic character, so  $G' \gg G''$ . The more "perfect" a network is, the more important this difference will be. Indeed, in the case of a network with defects (hanging chains in particular), the relaxations of these pendants structures increase the  $G''$ .

### Experimental Setup

Rheological properties were measured on a Kinexus Malvern rheometer (plane-plane geometry) using a plate geometry of 20 mm diameter and a gap of 0.5 mm. Gelation process was followed at a fixed frequency of 0.3 Hz and 0.06 % strain for 30 min until a plateau was reached. Subsequently, strain measurements were carried out from 0.01% to 100% at 0.3Hz and frequency sweeps were performed from 0.01 Hz to 10 Hz at a fixed strain of 0.06%. Samples were prepared in two different ways depending of the system (Enzyme/peptide) used. In the first case, the hydrogel is formed directly on the plate of the rheometer and in the second case, the hydrogel is formed 24h before measurement inside a PTFE mould at the rheometer plate dimension.



## REFERENCES

1. Kreutzer, A., Salvesson, P., Standard practices for Fmoc-based solid-phase peptide synthesis in the Nowick laboratory, **2018**, *version 1.6.3*
2. Sauerbrey, G., Verwendung von schwingquartzen zur wägung dünner schichten und zur mikrowägung., *Z. Phys.*, **1959**, *155*, 206.
3. Billig, G., *et al.*, Atomic Force Microscope, *Phys. Rev. Lett.*, **1986**, *56*, 930.
4. Dalibart, M., Servant, L., Spectroscopie dans l'infrarouge, *In techniques de l'ingénieur*, Paris, P2845, **2000**, PP1.
5. Harricks, N., Internal reflection spectroscopy, *Wiley interscience*, **1967**.
6. Fringeli, U., IR membrane spectroscopy, *Berlin: Springer*, **1981**.
7. Stokes, D., Principles and practice of variable pressure environmental scanning electron microscopy (VP-ESEM), *Chichester: John Wiley & Sons*, **2008**, ISBN 978-0470758748.
8. Knoll, M., "Aufladepotential und sekundäremission elektronenbestrahlter Körper", *Zeitschrift für Technische Physik*, **1935**, *16*,467.
9. Introduction to HPLC-agilent technologies
10. HPLC instrumentation-agilent technologies
11. Wilson, K., Walter, J., Principles and technique of biochemistry and molecular biology, *Cambridge University press*, **2010**, *13<sup>th</sup> Ed.*, ISBN-13: 978-0521731676
12. Berne, B., Pecora, R., Dynamic Light Scattering, *Courier Dover Publications*, **2000**, ISBN 0-486-41155-9
13. Chu, B., "Laser light scattering", *Annual Review of Physical Chemistry*, **1970**, *21*, 145.
14. Pecora, R., "Doppler shifts in light scattering from pure liquids and polymer solutions". *The Journal of Chemical Physics*, 1964, *40*, 1604. .
15. Goodman, J., (1976). "Some fundamental properties of speckle", *J. Opt. Soc. Am.*, **1976**, *66*, 1145.
16. Einstein, A., Investigations on the theory of the brownian movement, *Dover Books on Physics Series*, **1956**, *Dover Publications*
17. Kelly, S., *et al.*, How to study proteins by circular dichroism, *Biochim. Biophys. Acta*, **2005**, *1751*, 119.
18. Martin, S., Schilstra, M., Circular dichroism and its application to the study of biomolecules, *Methods Cell Biol.*, **2008**, *84*, 263.
19. Greenfield, N., Using circular dichroism spectra to estimate protein secondary structure, *Nature Protocol*, **2006**, *1*, 2876.
20. Chen, D., *et al.*, Rheology of soft materials, *Annual Review of Condensed Matter Physics*, **2010**, *1*, 301.
21. Ait-Kadi, A., *et al.*, Quantitative analysis of mixer-type rheometers using the coquette analogy, *Canadian Journal of Chemical Engineering*, **2002**, *80*, 1166.



## **Chapter 3**



**Protein-induced low molecular weight hydrogelator  
self-assembly through a self-sustaining process**



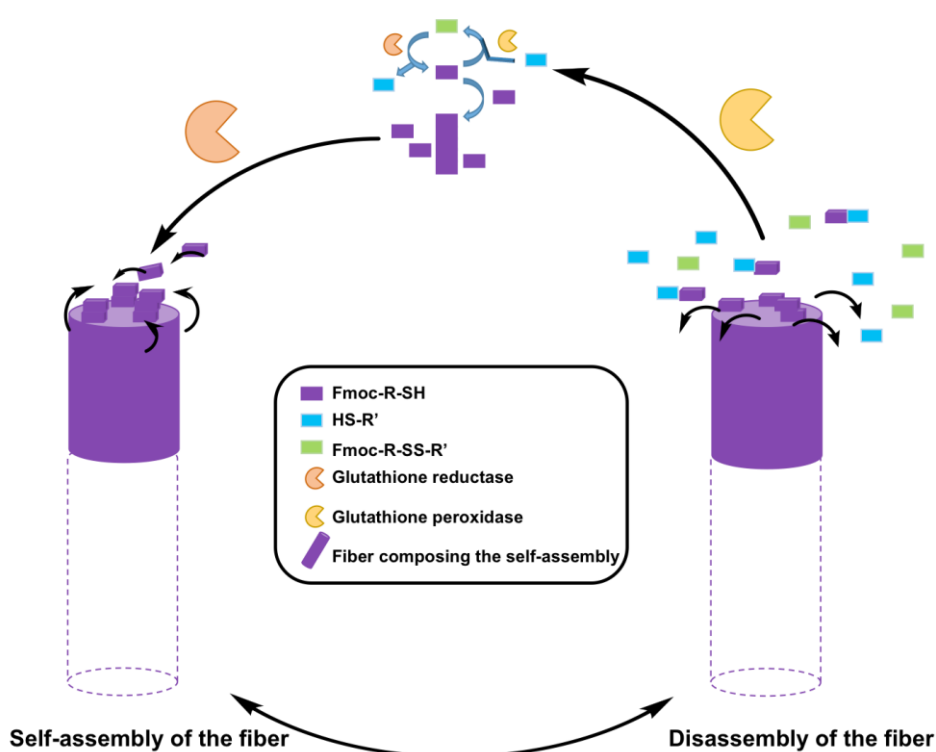
## Summary

<b>Context</b> .....	<b>87</b>
3.1. Abstract .....	88
3.2. Introduction .....	89
3.3. Results and discussion .....	91
3.4. Conclusion .....	98
<b>CURRENT CONTINUATION OF THIS PROJECT</b> .....	<b>99</b>
3.5. Additional Figures .....	101
3.6. Experimental section .....	118
3.6.1. Materials .....	118
3.6.2. Hydrogel preparation in bulk and upside-down vial tests .....	119
3.6.3. Multilayer film preparation and hydrogel self-assembly .....	120
3.6.4. Quartz Crystal Microbalance with Dissipation monitoring .....	120
3.6.5. Infrared spectroscopy .....	120
3.6.6. Scanning Electron Microscopy and cryo-SEM .....	121
3.6.7. Transmission Electronic Microscopy (TEM) .....	121
3.6.8. Analytical High-Performance Liquid Chromatography .....	121
3.6.9. Dynamic Light Scattering .....	122
3.6.10. Fluorescence emission spectroscopy .....	122
3.6.11. Rheology measurements .....	122
3.6.12. Nuclear Magnetic Resonance (NMR) .....	122
3.6.13. Circular Dichroism .....	125
3.6.14. High Resolution Mass Spectroscopy (HRMS) .....	125
3.6.15. Syntheses of Fmoc-A-SS-B and A-SS-B .....	126
<b>REFERENCES</b> .....	<b>127</b>



## Context

The initial idea of the project described in this chapter was to regulate dynamically the growth of self-assembled nanofibers by using two enzymes having antagonist activities. A precursor peptide containing a disulfide bridge was prepared, leading to a thiol-containing hydrogelator when the SS bond is reduced. The couple of enzymes chosen was glutathione reductase/ glutathione peroxidase able to “break” and “reform” the disulfide bridge of the peptide, respectively. The enzymatic activities of this couple can both ensure the proportion of hydrogelators available and the growth/disassembly of the resulting nanofibers (Scheme 1).



Scheme 1: Schematic of the self-assembled nanofiber's growth and disassembly in presence of the couple of antagonist enzymes.

However, we observed that when the disulfide-containing precursor peptide is in the presence of catalytically non-active proteins (negative control experiment), a hydrogel formed spontaneously as observed in presence of glutathione reductase. This result was not expected. We were particularly intrigued to get this and thus decided to look further to answer the following questions: what is the mechanism of this new kind of protein-assisted self-assembly process? What is the role of the protein in the self-assembly initiation? How a non-catalytically-active protein reduce a disulfide bridge?

In this chapter, I provide some possible answers to these questions.

**- Published article - RCS, *Chemical Science*, 2019, 10, 4761-4766**

Jennifer Rodon Fores, Miryam Criado-Gonzalez, Marc Schmutz, Christian Blanck, Pierre Schaaf, Fouzia Boulmedais, and Loïc Jierry

---

### **3.1. Abstract**

Controlling how, when and where a self-assembly process occurs is essential for the design of the next generation of smart materials. Along this route, enzyme-assisted self-assembly is a powerful tool developed during the last decade. Here we introduce another strategy allowing for spatiotemporal control over peptide self-assemblies. We use a Fmoc-peptide precursor in dynamic equilibrium with its low molecular weight hydrogelator (LMWH) through a reversible disulfide bond. In the absence of proteins, no self-assembly of the hydrogelator is observed. In the presence of proteins, their interactions with the precursor initiate a self-assembly process of the hydrogelator around them. This self-assembly displaces the equilibrium between precursor and LMWH according to Le Chatelier's principle, producing new hydrogelators available to pursue the self-assembly growth. One thus establishes a self-sustaining cycle fuelled by the self-assembly itself until full consumption of the LMWH. For proteins in solutions this process can lead to a supramolecular hydrogel whereas for proteins deposited on a surface, the gel growth is initiated exclusively from the surface.

## 3.2. Introduction

Self-assembly processes are the heart of supramolecular chemistry. Relying on reversible non-covalent bonds, they allow the emergence of new types of materials with dynamic responses towards external stimuli and thus able to adapt to the surrounding environment.<sup>1</sup> In the quest to design materials possessing high performance features similar to those found in biological tissues, an absolute prerequisite for success is to control self-assembly processes both spatially and temporally.<sup>2</sup> Within this framework, the use of (bio)catalysts to trigger the localization of the self-assembly of low molecular weight hydrogelators (LMWH) has proven to be highly interesting.<sup>3</sup> Indeed, enzymes can catalyse the transformation of non-assembling entities into self-assembling ones, rapidly and with high specificity.<sup>4</sup> This approach called enzyme-assisted self-assembly (EASA) was introduced by Xu<sup>5</sup> and extended by Ulijn and others<sup>6,7</sup> and a large number of reports describing the use of EASA based on a short list of enzymes able to produce hydrogelators mainly through bond cleavage or bond formation have been published. Another approach based on a dynamic covalent library of peptides has also been developed thanks to enzymes such as thermolysin, able to both condense amino acids and hydrolyse the resulting peptides.<sup>8,3a</sup> Compared to other triggers that modify the environment (pH, temperature or ionic strength for instance), enzymes appear up to now as the only tool capable to both control and direct the self-assembly process in an efficient way thanks to a range of methods to localize enzymes precisely in space. In spite of the lack of works dedicated to the elucidation of the self-assembly initiation step, it is well established that hydrogelators self-assemble leading to nanofibers: their resulting entanglement (or others nanostructures) affords the architectures of the supramolecular hydrogel that have been already carried out to a large scope of promising applications. Here, we introduce a new strategy to control spatiotemporally self-assembling processes. It is based on the simultaneous presence of proteins possessing or not catalytic activity, LMWH and its precursor, both being in dynamic equilibrium through a reversible bond (here a disulfide bond). The interaction of the precursor with the protein initiates a self-assembly process which leads to the establishment of a self-sustaining cycle where continuous hydrogelator generation is induced by the self-assembly process itself (Figure 1a). This approach appears closely related to 2D dynamic covalent chemistry where adsorption of a product out of a combinatorial library displaces chemical reactions by harvesting a final product otherwise present in small amounts.<sup>9</sup>



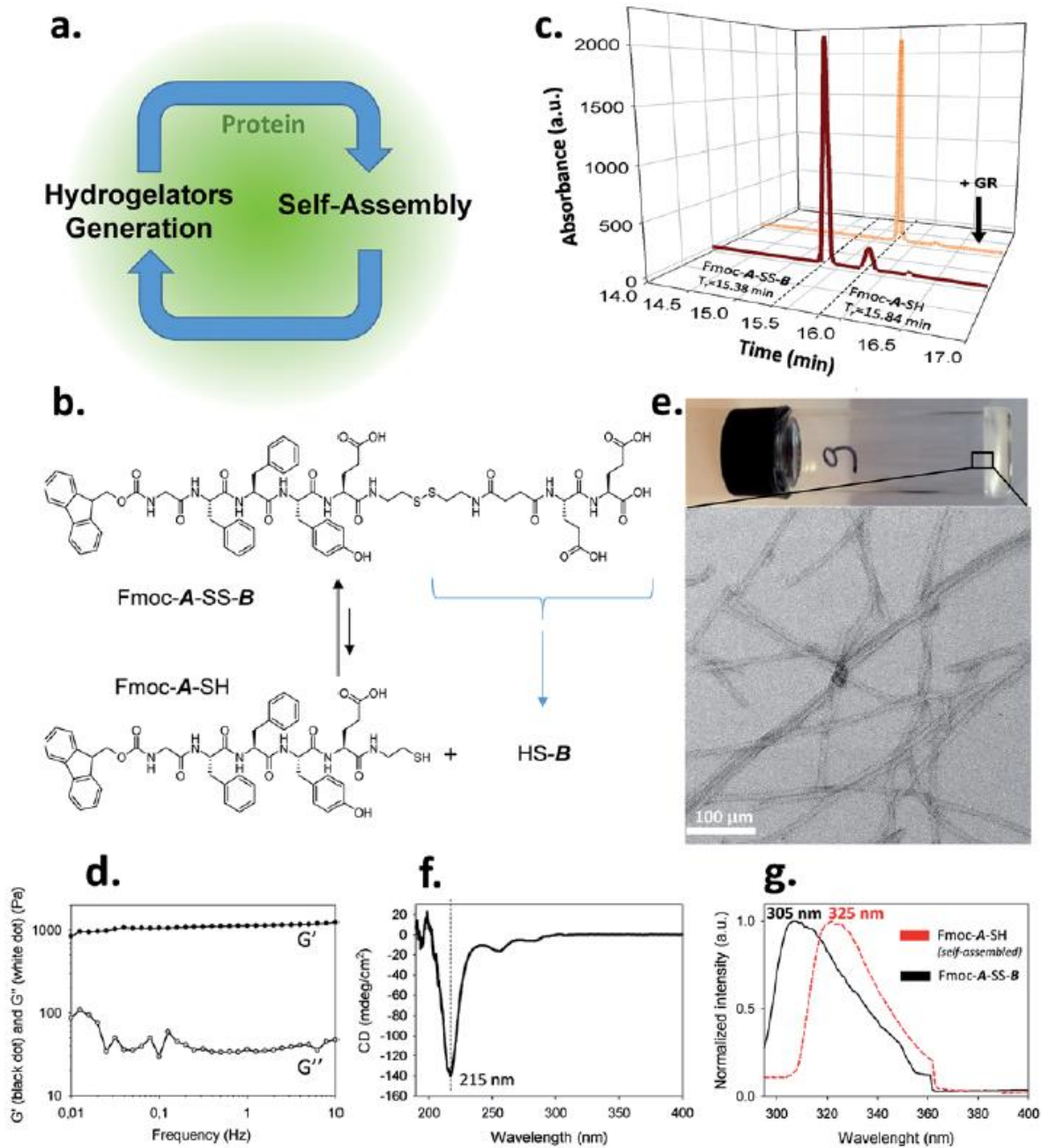


Figure 1: (a) Protein-assisted self-assembly's concept; (b) Chemical equilibrium between Fmoc-A-SS-B and Fmoc-A-SH; (c) HPLC analysis of a solution of Fmoc-A-SS-B before (black curve) and after the addition of GR (orange curve); (d)  $G'$  and  $G''$  measurements, (e) TEM image, (f) CD spectra and (g) normalized emission of fluorescence excimer intensity of Fmoc groups from Fmoc-A-SH based hydrogel.

### 3.3. Results and discussion

We use an original peptide as LMWH, Fmoc-GFFYE-NH-(CH<sub>2</sub>)<sub>2</sub>-SH, called Fmoc-**A**-SH, inspired from literature (Figure 1b).<sup>10</sup> The Fluorenylmethoxycarbonyl (Fmoc) N-protected group has been added at the N-terminal position to enhance the ability of the corresponding hydrogelator Fmoc-**A**-SH to self-assemble.<sup>4,11</sup> When the thiol group of this peptide is protected through a disulfide bridge, the resulting Fmoc-**A**-SS-**B** (Fmoc-GFFYE-NH-(CH<sub>2</sub>)<sub>2</sub>-S-S-(CH<sub>2</sub>)<sub>2</sub>-NHCO-(CH<sub>2</sub>)<sub>2</sub>-CO-EE-OH) is not able to self-assemble because of the highly negatively charged B sequence. When 10 mg/mL (7.3 mmol) of Fmoc-**A**-SS-**B** is dissolved in PBS buffer (pH 7.4) at 25 °C, no gelation occurs, even after 48 hours, as expected. High performance liquid chromatography monitoring the chemical composition of this solution over time shows that a thermodynamic equilibrium between Fmoc-**A**-SS-**B** and Fmoc-**A**-SH is quickly established (less than 2 minutes). At equilibrium, 10% of Fmoc-**A**-SH is present and 90% of Fmoc-**A**-SS-**B** constitutes the major compound (Figure 1c). Of course, Fmoc-**A**-SS-**A**-Fmoc and **B**-SS-**B** are also both present in the mixture: Fmoc-**A**-SS-**A**-Fmoc is present at trace-level and **B**-SS-**B** is not measured through our HPLC's UV-detector.

To get a supramolecular gel from a Fmoc-**A**-SS-**B** solution (10 mg/mL), the disulfide bridge must be reduced and glutathione reductase (GR, 1 mg/mL) was selected to play this role. Because the initiation of gelation should depend on the sufficient production of Fmoc-**A**-SH (to reach its critical gelation concentration), we followed its formation by HPLC as soon as GR was introduced in the vial. Gelation is qualitatively observed by a simple vial inversion test. Fmoc-**A**-SS-**B** disappears over the first minutes and correlatively Fmoc-**A**-SH forms (Figure 1c). Roughly two minutes after addition of GR, 100% of the hydrogelator Fmoc-**A**-SH is formed and a gel is obtained having an elastic modulus  $G_0$  close to 1 kPa (Figure 1d and S1 in ESI). The gel is underpinned by a network of entangled nanofibers ( $\varnothing = 15$  nm) as observed by transmission electron microscopy (TEM) after negative staining (Figure 1e and S2 in ESI). Circular dichroism shows a  $\beta$ -sheet peptide assembly from Fmoc-**A**-SH (Figure 1f) in which Fmoc groups are stacking one another, thus exhibiting a characteristic fluorescence emission of excimers at 325 nm when excited at 280 nm (Figure 1g).

To demonstrate the catalytic role of GR in the gelation process, another enzyme unable to cleave the disulfide bridge of Fmoc-**A**-SS-**B**, alkaline phosphatase (AP), was used instead of GR and the same HPLC monitoring study was realized. As anticipated, no gel was formed even after 60 minutes following the addition of AP (1 mg/mL) in the Fmoc-**A**-SS-**B** solution (10 mg/mL). Yet, the HPLC monitoring revealed the formation of Fmoc-**A**-SH, more slowly than with GR, but reaching nevertheless a full chemical transformation (from Fmoc-**A**-SS-**B**) after one hour (Figure S3 in ESI). In order to verify if this unexpected result can be extended to other proteins than AP, we brought a freshly prepared Fmoc-**A**-SS-**B** solution in contact with bovine serum albumin (BSA, 1mg/mL). In spite of a slower kinetic of Fmoc-**A**-SH formation than for AP, Fmoc-**A**-SS-**B** ultimately almost fully disappeared after 1 h as measured by HPLC but no gel formed even 24 hours later (Figure S3 in ESI). The faster reduction of Fmoc-**A**-SS-**B** catalyzed by GR being perhaps involved in the efficiency of the

gelation process, 1 equivalent of the strong reductive agent (tris(2-carboxyethyl)phosphine) (TCEP) was added to a Fmoc-**A-SS-B** solution to check this hypothesis: HPLC highlights an instantaneous full conversion into Fmoc-**A-SH** (Figure S3 in ESI) but no gelation was observed, even after one hour. A complete conversion into Fmoc-**A-SH** has also been observed by HPLC when 1 molar equivalent of dithiothreitol (DTT) or glutathione (GSH) was used instead of TCEP without gel formation as for TCEP (Figure S4 in ESI). Using higher Fmoc-**A-SS-B** and protein concentrations (both 30 mg/mL) a gel was formed in the presence of BSA or AP whereas no gel was formed in contact with TCEP (Fig. S4 in ESI).

Of course, self-assembly of Fmoc-**A-SH** may occur in solution without leading to hydrogel formation. Thus, to check whether self-assembly takes place in the four experiments described above, we used complementary analytical tools: TEM, fluorescence emission and infrared spectroscopies, CD, nuclear magnetic resonance and dynamic light scattering. For all these studies, lower concentrations of peptide and protein were used: solutions of 1 mg/mL of Fmoc-**A-SS-B** and 1 mg/mL of one of the three proteins (GR, AP or BSA) were used except for DLS measurements where concentrations of protein were lower. At such small concentrations, no gelation from the Fmoc-**A-SS-B** solution occurs even in presence of GR (1 mg/mL). TEM analysis of each four solutions mixing Fmoc-**A-SS-B** and GR (sol. 1), AP (sol. 2), BSA (sol. 3) and TCEP (sol. 4) showed nanostructures formation except for sol. 4 when TCEP was added. Typical images can be found in Figure 2. GR and AP lead to counter clockwise twisted nanofibers: in the presence of GR, fibers are slightly twisted and their diameters are typically 15 nm whereas AP leads to highly twisted fibers that are 5 nm in diameter. Nanofibers are several hundred micrometers long in both cases (sol. 1 and 2). For BSA (sol. 3), wide platelets, several hundreds of nanometers long, are typically observed. Therefore, despite full conversion of Fmoc-**A-SS-B** in Fmoc-**A-SH** (confirmed by HPLC analysis) in all four solutions, the self-assembly of Fmoc-**A-SH** starts only in the presence of one of the three proteins GR, AP and BSA. In addition, we thus find that depending on the initial self-assembly conditions, the resulting self-assembled nanostructure can have various morphologies.<sup>12</sup> Investigating the origin of these different morphologies is out of the scope of this article.

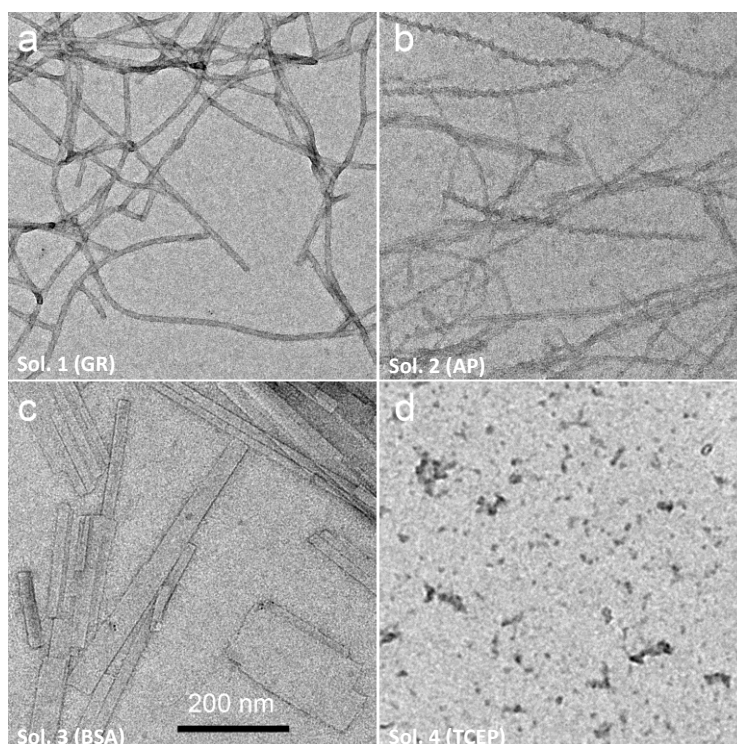


Figure 2: TEM analysis of Fmoc-**A-SS-B** solution (1 mg/mL) after the addition of (a) GR (Sol. 1), (b) AP (Sol. 2), (c) BSA (Sol. 3) to reach 1 mg/mL of biomacromolecule's final concentration or (d) 1 equivalent of TCEP (Sol. 4).

Conclusions from TEM analysis have been confirmed by fluorescence emission measurements done on sol. 1, 2, 3 and 4 when excited at 280 nm. This wavelength allows to observe the fluorescence emission band of the Fmoc groups at 305 nm when Fmoc-**A-SS-B** is dissolved in solution (1 mg/mL) and then to follow its shifting evolution to 320–325 nm over 60 minutes (Figure 3). This shift is only noticed for sol. 1, 2 and 3 and is the characteristic signature of the Fmoc excimer formation found in the Fmoc-containing peptides stacked through  $\pi$ - $\pi$  interactions.<sup>3d,11</sup> The absence of shift for sol. 4 proves also the absence of self-assembled structures in this case. CD and IR measurements confirmed the presence of  $\beta$ -sheets resulting from Fmoc-**A-SH** self-assembly in sol. 1, 2 and 3 exclusively (when a protein is present) and not in sol. 4 (Figure S5 in ESI). The necessary participation of GR, AP or BSA in the self-assembly initiation of Fmoc-**A-SH** was also examined through DLS when each of these proteins was brought in contact with Fmoc-**A-SS-B** (1 mg/mL). In the absence of Fmoc-**A-SS-B**, the size of each protein is close to 1 nm. One minute after the addition of Fmoc-**A-SS-B** (1 mg/mL), the apparent size of the scattering species increases rapidly. Indeed, as shown in Table S1 and Figure S6, one observes a shift of the scattering peak towards higher diameters. It must be noticed that the given sizes are obtained by applying the models of a Brownian sphere and should not be taken as representing physically the size of the scattering object. They reflect their average hydrodynamic size. They nevertheless show that the self-assembly leads to a continuous increase of this size starting from that of the enzymes. This indicates that the self-assembly process should start at the enzymes. When 1 equivalent of TCEP was added to Fmoc-**A-SS-B**, no diffusive species were

measured, even after one hour.

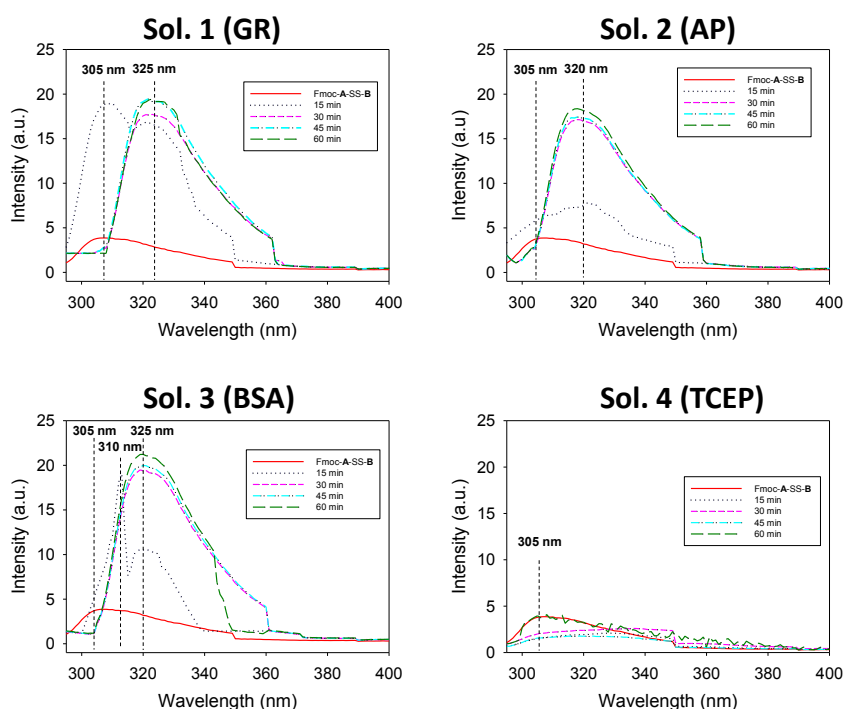


Figure 3: Evolution over 60 minutes of the emission fluorescence intensity of Fmoc-**A-SS-B** solution (1 mg/mL) in presence of 1 mg/mL of GR (Sol. 1), AP (Sol. 2), BSA (Sol. 3) or 1 equivalent of TCEP (Sol. 4) when the solution is excited at 280 nm.

From this set of experiments one concludes that (i) the self-assembly process of Fmoc-**A-SH** peptides is initiated from Fmoc-**A-SS-B** only in the presence of a protein or an enzyme even if this later does not play a catalytic role in the disulfide reduction; (ii) the equilibrium reaction between Fmoc-**A-SS-B** and Fmoc-**A-SH** is totally shifted towards Fmoc-**A-SH** only in the presence of one of the investigated proteins. Therefore one can propose the following self-assembly mechanism schematically represented in Figure 4a: in the presence of proteins such as BSA or AP, Fmoc-**A-SS-B** or Fmoc-**A-SH** interact with them and initiate the self-assembly of Fmoc-**A-SH**, thus reducing the concentration of free Fmoc-**A-SH** in solution. This consumption of free Fmoc-**A-SH** disturbs the equilibrium, which counteracts by providing Fmoc-**A-SH** from Fmoc-**A-SS-B** according to Le Chatelier's principle. Of course, because the self-assembly process of Fmoc-**A-SH** continues over time, a total displacement of the equilibrium takes place leading to the growth of nanofibers underpinning a supramolecular hydrogel (at high Fmoc-**A-SS-B** concentration, i.e. 30 mg/mL).

In order to prove that it is the self-assembly process that is at the origin of the total equilibrium displacement in favor of Fmoc-**A-SH** we dissolved the lacking-Fmoc disulfide peptide **A-SS-B** in water (10 mg/mL). This peptide is unable to self-assemble because of the absence of the Fmoc group. The thermodynamic equilibrium (disulphide/thiol) is established in a few minutes with 95% of **A-SS-B** and 5% of **A-SH** according to HPLC analysis. Addition of BSA or AP (1 mg/mL) to this

solution does not change the initial **A-SS-B/A-SH** ratio, thus proving our case (Figure S7 in ESI). On the other hand, addition of GR (1 mg/mL) to this solution yields to an entire production of **A-SH** with no gel formation as expected, even 1 hour later.

What remains to be understood is how the self-assembly process is initiated by the presence of the protein and in particular if initiation takes place through interactions between the proteins with Fmoc-**A-SH** or Fmoc-**A-SS-B**. Indeed, the Fmoc group in Fmoc-**A-SS-B** (or Fmoc-**A-SH**) is an N-protecting group known to interact with proteins<sup>13</sup> and to be involved in the self-assembly of a large number of LMWH thanks to hydrophobic effects.<sup>4,11</sup> In addition, the peptide sequence **B** (Figure 1b) is a highly negatively charged group that could also be able to interact with proteins. We brought a Fmoc-**A-SS-B** solution (10 mg/mL) in contact with 1 equivalent of TCEP to generate 100% of Fmoc-**A-SH** that do not self-assemble as described before. When BSA (1 mg/mL) was added to this Fmoc-**A-SH** solution, a gel was obtained but only one hour after the addition of BSA. To understand why the hydrogel formation takes one hour instead of being immediate, we monitored by HPLC the establishment of the natural thiol/disulphide equilibrium between Fmoc-**A-SH** and Fmoc-**A-SS-B** over time and in parallel we followed the fluorescence emission evolution of this mixture when excited at 280 nm. Both were tracked after the addition of BSA in the 100% Fmoc-**A-SH** solution (generated using TCEP) freshly prepared (Figure 4b). We observe that 25 minutes after the addition of TCEP (and thus also BSA), the proportion of Fmoc-**A-SH** starts to decrease concomitantly with the growing formation of Fmoc-**A-SS-B**. This is due to the re-equilibration between these two species, thanks to the presence of dissolved oxygen in the solution. This evolution is reversed 25 minutes later ( $t = 50$  min) leading to full disappearance of Fmoc-**A-SS-B**. Almost at the same time (50 minutes after the addition of TCEP), the shift of the fluorescence emission band of the Fmoc group from 305 nm to 325 nm is observed, proving the stacking of Fmoc-**A-SH**. The replacement of BSA by AP or GR in this experiment shows the same scenario (Figure S8 in ESI). One can thus conclude that the presence of Fmoc-**A-SH** is necessary but not sufficient to get the hydrogel formation. Both a few amount of Fmoc-**A-SS-B** and the presence of a protein are required to initiate the self-assembly process. The expected electrostatic interaction between the negatively charged **B** sequence of Fmoc-**A-SS-B** and positively charged patches onto proteins can be verified through the addition of a competitive negatively charged compounds. To mimic the three negative charges of **B** sequence due to the two glutamic acid residues and the carboxylic acid in C-terminal position, we used sodium citrate. Thus, 1, 10 and 100 equivalents of citrate were added into Fmoc-**A-SS-B** (30 mg/mL) solutions before the addition of BSA (30 mg/mL). In presence of 10 equivalent of sodium citrate, only a viscous liquid is obtained. When 100 equivalents are added, the gelation process is inhibited, due to the competitive interaction between sodium citrate and Fmoc-**A-SS-B** with BSA (Figure S9). This simple test highlights the necessary interaction between Fmoc-**A-SS-B** and proteins involving the carboxylate groups present in the **B** sequence of the peptide, to allow the hydrogelation process to start.

As reported recently by Martin, Thordarson and coworkers, hydrophobic N-terminal capping groups on short peptide hydrogelators are involved in the formation of pre-assembled structures present in solution.<sup>14</sup> Because of the Fmoc group present in Fmoc-**A-SS-B** peptide, <sup>1</sup>H NMR analysis of this peptide in D<sub>2</sub>O was investigated (Figure S10). These analyses confirm that Fmoc-**A-SS-B** is in a pre-aggregated state, probably in fast equilibrium with discrete molecules. This aggregation involved phenylalanine and tyrosine residues of Fmoc-**A-SS-B** but not the Fmoc group, which is in agreement with the absence of fluorescence excimer measurements (that appears from Fmoc stacking), as mentioned above. <sup>1</sup>H NMR (D<sub>2</sub>O) monitoring of Fmoc-**A-SH** generated in situ from Fmoc-**A-SS-B** in presence of TCEP shows that Fmoc-**A-SH** is maintained in an aggregated state, despite the reduction of the disulfide bridge (Figure S11). The introduction of a protein such as BSA into the aqueous solution of Fmoc-**A-SS-B** leads to a full disappearance of all <sup>1</sup>H NMR spectra signals (Figure S12), suggesting that all Fmoc-**A-SH** peptide are involved in supramolecular assembly.<sup>15</sup>

The design of complex chemical systems controlling their nanoarchitecture at the molecular scale through a bottom up approach<sup>16</sup> can be envisaged using our self-assembly process: thanks to the initiator role of the protein, it is possible to spatially control the self-assembly process and thus the gelation buildup localization near surfaces. We thus covered surfaces by BSA or AP using an adequate polyelectrolyte multilayer<sup>3d,e,17</sup> and brought these modified surfaces in contact with Fmoc-**A-SS-B** solutions. The spatially localized self-assembly process can be followed by quartz crystal microbalance with dissipation. Contact of these surfaces covered by BSA or AP with Fmoc-**A-SS-B** solutions leads to a huge and rapid decrease of the different measured frequencies and concomitantly an increase of the corresponding dissipation (Figure 4c and S13 in ESI). Such QCM-D signal evolutions are typical of the formation of highly hydrated gels exceeding several micrometers in thickness.<sup>3d,e</sup> Cryo-SEM analysis of the peptide self-assemblies grown up on surfaces covered by BSA or AP were performed (Figure 4d and S14 in ESI). In both cases, one observes a fibrillar network that grows exclusively from the surface, with fibers oriented perpendicularly to the surface from the bottom (surface) to the top of the gel.<sup>3c</sup> The self-assembly appears thus the same for BSA and AP. The assembly of Fmoc-**A-SH** located on surfaces was also monitored by fluorescence emission spectroscopy, following the characteristic excimer emission of Fmoc group at 325 nm (when excited at 280 nm) and the  $\beta$ -sheet secondary structure adopted in the peptide assembly was confirmed by IR spectroscopy in ATR mode (Figure S15 in ESI). Similar results were obtained when the surface was covered by GR instead of BSA and AP (Figure S16 in ESI). To check the hypothesis discussed previously that Fmoc-**A-SS-B** interacts first onto positive patches of proteins to initiate the self-assembly process, we have used positively charged multilayer ended by the polycation, poly-L-lysine (PLL), and a negatively charged multilayer ended by the polyanion, poly-L-glutamic acid (PGA).

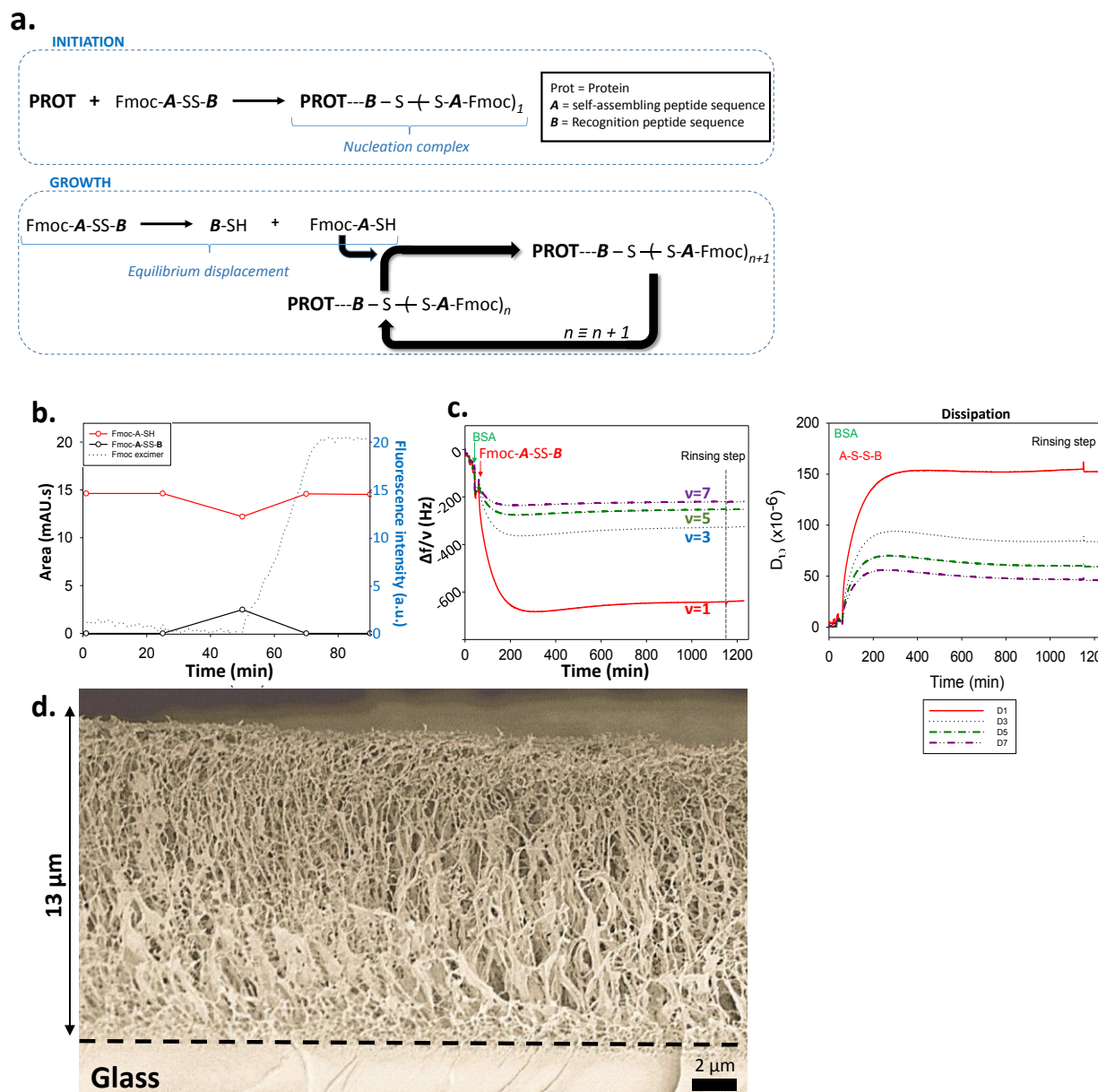


Figure 4: (a) Mechanism proposed for the protein-assisted self-assembly's concept; (b) HPLC monitoring and fluorescence emission intensity measurement at 320 nm ( $\lambda_{ex}=280\text{nm}$ ) of Fmoc-A-SH solution after the addition of BSA; (c) QCM-D monitoring of the self-assembly growth initiated from a substrate modified with AP; (d) Cryo-SEM image of a cross sectioned supramolecular hydrogel formed from a AP layer adsorbed onto a glass slide.

The QCM-D monitoring shows clearly that an important mass is adsorbed strongly onto a polycationic polypeptide layer and does not adsorb on a polyanionic layer when brought in contact with Fmoc-A-SS-B (Figure S17). The frequency decrease observed with poly-L-lysine deposited on surface is similar to those observed using proteins (Figure 4c, S13 and S16). This means that the presence of the polypeptide cationic layer can allow the initiation of the whole self-assembly process. The absence of tertiary structure in poly-L-lysine suggests also that the electrostatic interaction is the *sine qua none* condition for Fmoc-A-SS-B to interact with proteins/polypeptides.



### 3.4. Conclusion

We have found a chemical pair “LMWH-precursor” where both partners are in dynamic equilibrium. Interestingly, the self-assembly of the LMWH (hydrogelator) takes place only when it is initiated by the interaction between the protein and the precursor. This aspect can be exploited upon for the spatial localization of the self-assembly process by specific localization of proteins as demonstrated herein. From the mechanistic point of view, the interaction between the precursor and the protein leads to a self-assembly that acts as a scavenging process of the hydrogelator, displacing thus the “LMWH-precursor” equilibrium towards the full generation of the LMWH. Our study also highlights that adsorption of hydrogelators on enzymes (in the case GR) is a *sine qua non* step required to initiate the self-assembly. Despite many reports in enzyme-assisted self-assembly's field, this aspect was not yet unambiguously demonstrated. Chemical equilibrium generating a combinatorial library of peptides thanks to the use of an enzyme able to catalyze both peptides formation and peptides hydrolysis has been already reported<sup>3a,8</sup> but is singularly different from the approach described here. Indeed, here it is the self-assembly itself that displaces the dynamic equilibrium without the action of the protein, this later being necessary to initiate the self-assembly through its interaction with the precursor of the LMWH. In the field of complex functional nanoarchitectures design which is typically based on bottom up bio-inspired strategies, we are convinced that this new self-assembly process of LMWH initiated by proteins will echo to the chemical research community and beyond, for instance in medicine and biology in which localized supramolecular hydrogelation in living systems shows currently a remarkable development.

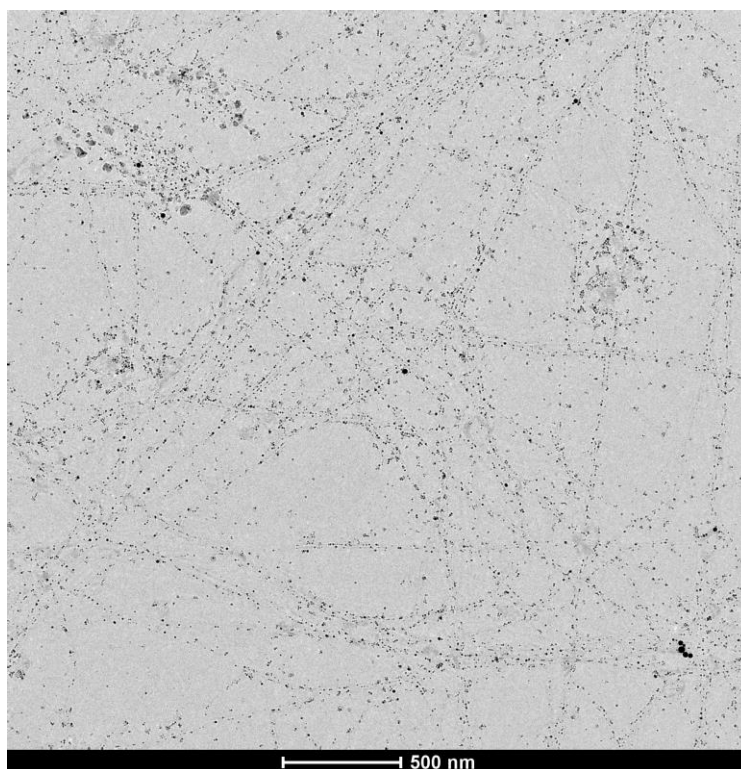
---

#### \*Copyright information

Texts and figures of Part 3.1 have been reprinted with permission from [Rodon Fores, J., *et al.*, Protein-induced low molecular weight hydrogelator self-assembly through a self-sustaining process, *RSC Chemical Science*, **2019**, *10*, 4761-4766.], Copyright 2019, Published by The Royal Society of Chemistry (RSC).

## CURRENT CONTINUATION OF THIS PROJECT

To go further in the understanding of the protein's role in the self-assembly process, we have investigated two techniques: TEM and the Fluorescence Correlation Spectroscopy (FCS) in collaboration with Dr. Ludovic Richert (Faculty of pharmacy – Strasbourg University). Using the FCS, we want to confirm that the peptide self-assembly nucleates from the surface of the protein. This information can be obtained indirectly through the measurement of the coefficient of diffusion of the protein over time, once in presence of the peptide. Using TEM, our goal is to localize the presence of the protein when the self-assembled nanofibers are formed. To do that, we are using commercially available silver nanoparticles modified with an antibody directed toward the suitable protein. Very recently, we have prepared a supramolecular hydrogel from the tripeptide Fmoc-FF $\rho$ Y in presence of alkaline phosphatase (AP). When nanoparticles modified with an antibody anti-AP is brought in contact with the internal fibrous network of the hydrogel, we observed by TEM the decoration all along the fibers with nanoparticles (Figure 5). This results shows that AP produce the hydrogelator Fmoc-FF $\rho$ Y from Fmoc-FF $\rho$ Y but also may participate to the fiber constitution.



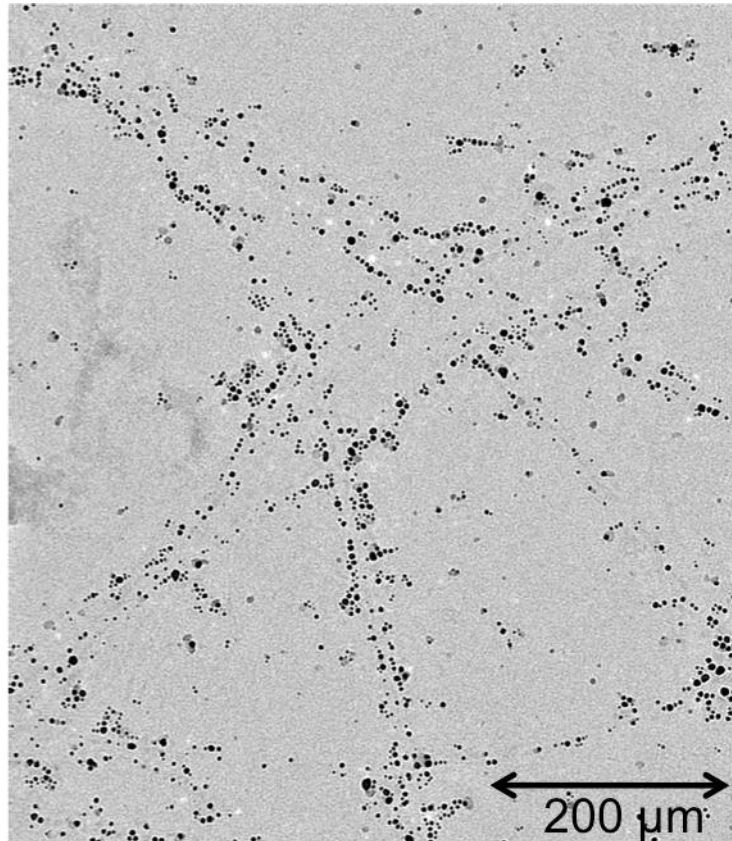


Figure 5: TEM image of silver nanoparticles labelled with an antibody anti-AP decorating exclusively the fibers formed from Fmoc-FFpY and AP solution.

## Highlights of the chapter

- ✓ Not only enzymes can initiate self-assembly but also proteins.
- ✓ The *sine qua non* step of the self-assembly is the interaction between the hydrogelator and the surface of the proteins by electrostatic and hydrophobic interaction.
- ✓ Self-assembly can be achieved by a chemical equilibrium displacement, where the self-assembly itself displaces the dynamic equilibrium without the action of the protein, which leads to a self-sustaining process.

### 3.5. Additional Figures

#### Synthesis scheme and characterization of the peptides Fmoc-A-SS-B and A-SS-B

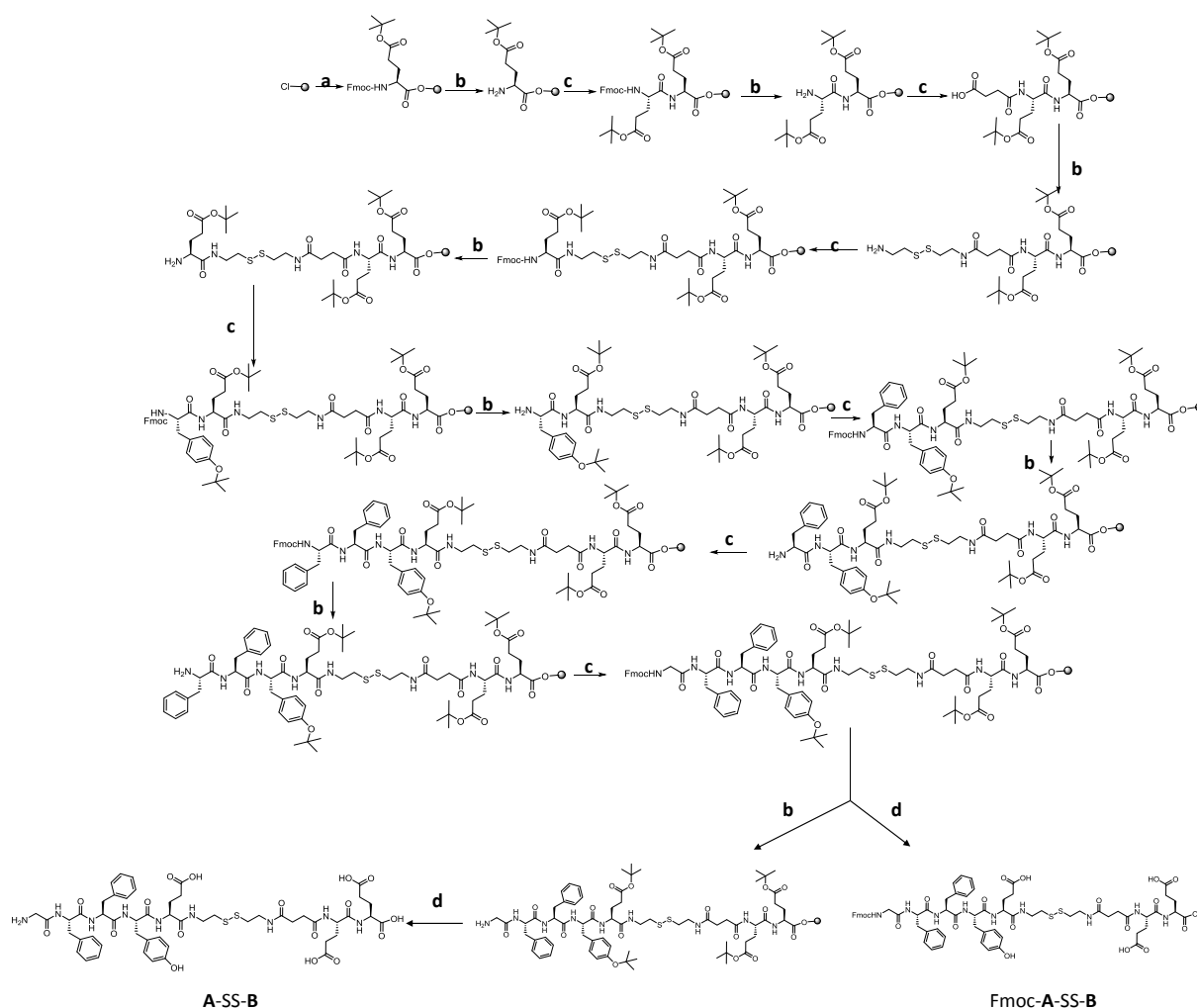


Figure 6: Scheme of the peptides synthesis on solid support

#### Fmoc-A-SS-B:

$^1\text{H NMR}$  (400 MHz,  $\text{DMSO-}d_6$ ):  $\delta$  1.92-2.02 (*m*, 12H), 2.15-2.64 (*m*, 12H), 2.67-2.81 (*m*, 5H), 2.90-3.04 (*m*, 8H), 4.06-4.12 (*m*, 8H), 4.18-4.28 (*m*, 3H), 6.63-6.65 (*d*, 2H,  $^3J=8.5$  Hz), 7.02-7.04 (*d*, 2H,  $^3J=8.5$  Hz), 7.09-7.25 (*m*, 10H), 7.29-7.33 (*dd*, 2H,  $^3J=^3J=7.5$  Hz), 7.39-7.44 (*dd*, 2H,  $^3J=^3J=7.5$  Hz), 7.46-7.48 (*dd*, 1H,  $^3J=^3J=6.5$  Hz), 7.68-7.70 (*d*, 2H,  $^3J=7.5$  Hz), 7.88-7.90 (*d*, 2H,  $^3J=7.6$  Hz), 7.97 (*s*, 1H), 8.06-8.20 (*m*, 8H); HRMS (ESI/microTOF-Q)  $m/z$ :  $[\text{M} + \text{H}]^+$  Calcd for  $\text{C}_{62}\text{H}_{67}\text{N}_9\text{O}_{19}\text{S}_2$ : 1310.3317; Found 1310.3398; HPLC (ACN/Water=80/20): retention time (rt): Fmoc-A-SS-B (15.43 min, 90%, 10% Fmoc-A-SH, rt: 15.63 min). UV-VIS spectra: max Abs: 280 nm. IR spectra:  $\nu_{\text{OH}}=3521\text{ cm}^{-1}$ ;  $\nu_{\text{C=O acid}}=1721\text{ cm}^{-1}$ ;  $\nu_{\text{C=O amide}}=1679\text{ cm}^{-1}$ ;  $\nu_{\text{N-H}}=1648\text{ cm}^{-1}$ ;  $\nu_{\text{C-O}}=1195\text{ cm}^{-1}$  and  $1013\text{ cm}^{-1}$ .

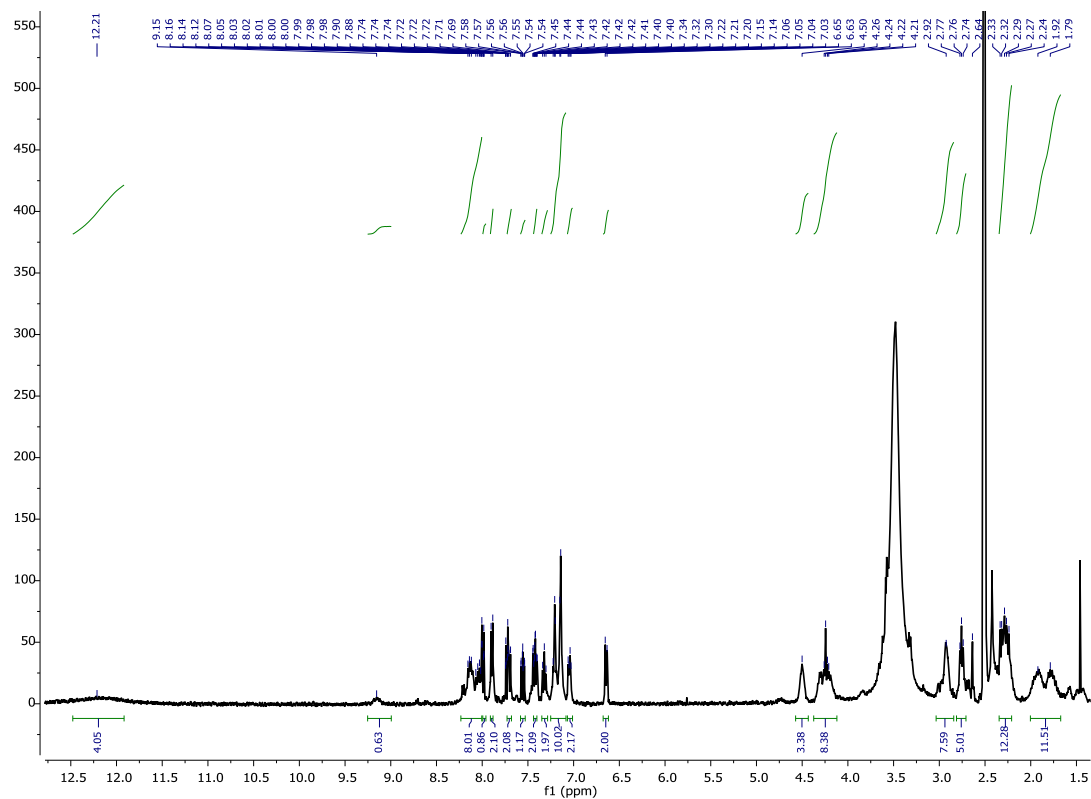


Figure 7:  $^1\text{H}$  NMR spectrum of Fmoc-A-SS-B

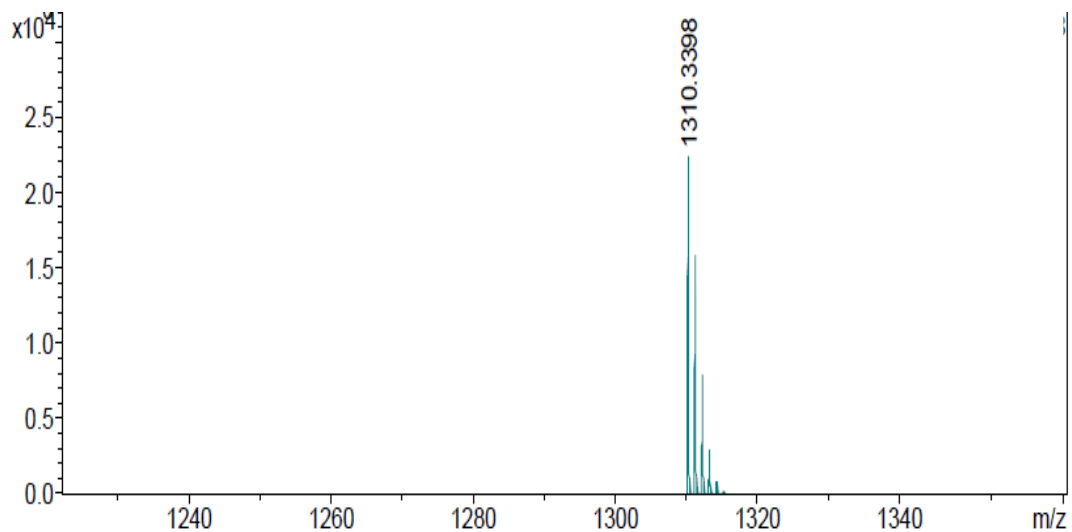
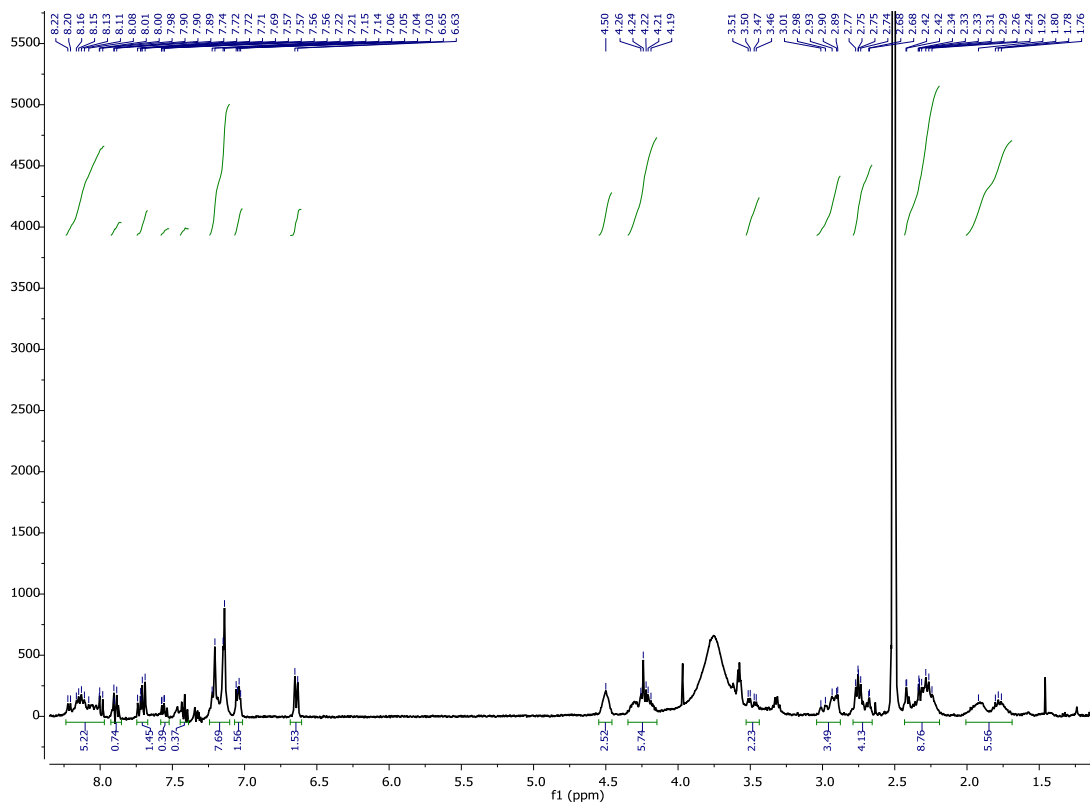
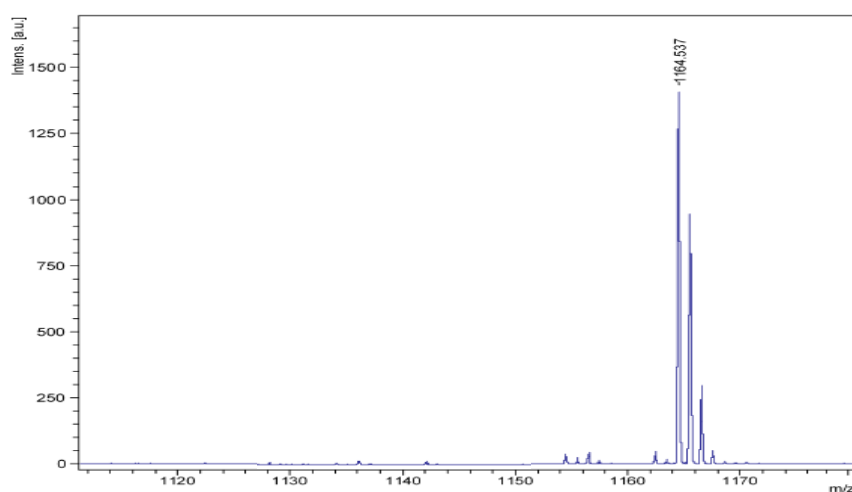


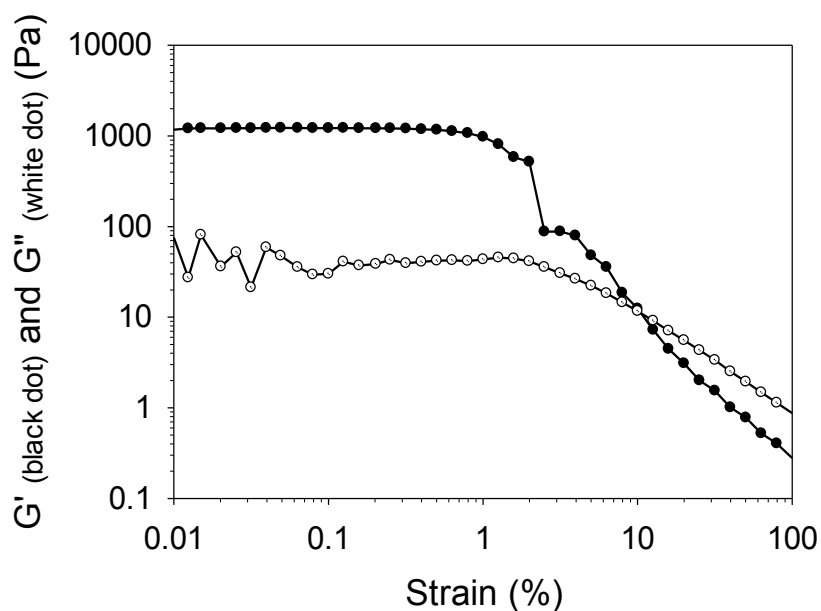
Figure 8: HRMS mass spectrum of Fmoc-A-SS-B

**A-SS-B:**

$^1\text{H}$  NMR (400 MHz,  $\text{DMSO-}d_6$ ):  $\delta$  2.21-2.42 (m, 7H), 2.65-2.79 (m, 11H), 2.90-3.04 (m, 10H), 4.06-4.28 (m, 8H), 4.50 (m, 3H), 6.63-6.65 (d, 2H,  $^2J=8.5$  Hz), 7.02-7.04 (d, 2H,  $^2J=8.5$  Hz), 7.14-7.22 (m, 10H), 7.74 (m, 2H), 7.93 (m, 1H), 8.06-8.20 (m, 7H); HRMS (ESI/Q-TOF) m/z:  $[\text{M} + \text{H}]^+$  Calcd for  $\text{C}_{52}\text{H}_{67}\text{N}_9\text{Na}_1\text{O}_{17}\text{S}_2$ : 1164.470; Found 1164.537; HPLC (80/20= ACN/Water): retention time (rt): **A-SS-B** (1.39 min, 98%, 5% A-SH, rt: 6.55 min).

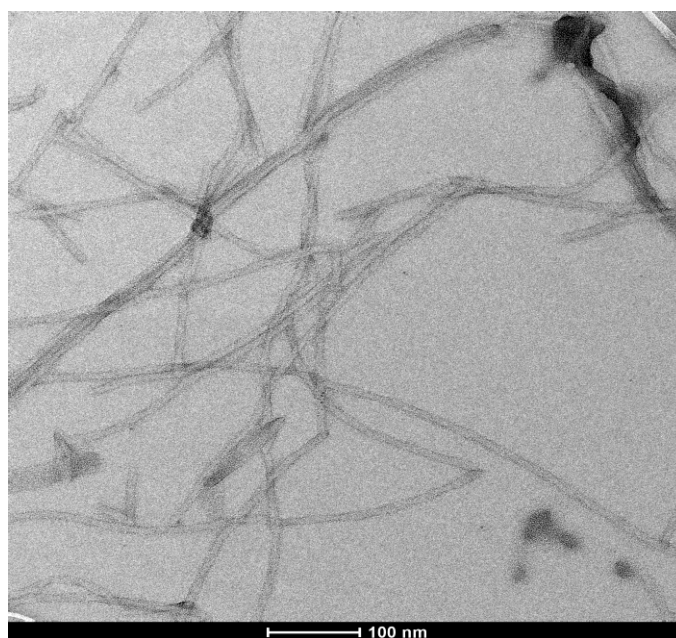
Figure 9:  $^1\text{H}$  NMR spectrum of **A-SS-B**Figure 10: HRMS mass spectrum of **A-SS-B**

## Mechanical properties of the hydrogel formed with the Glutathione Reductase



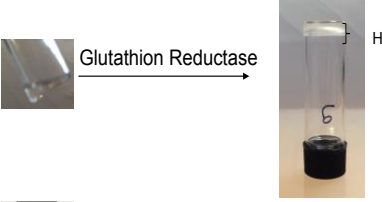
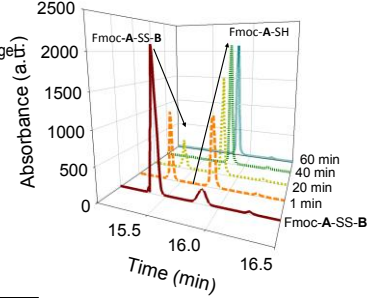
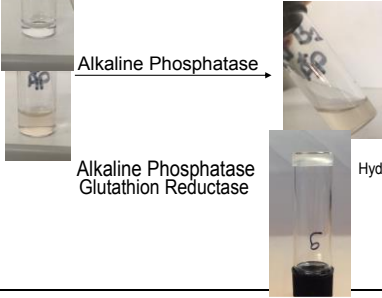
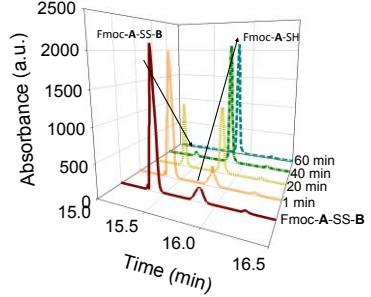
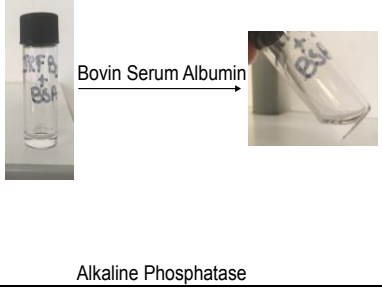
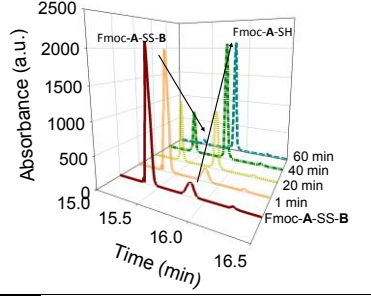
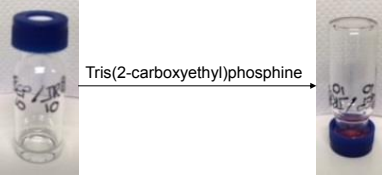
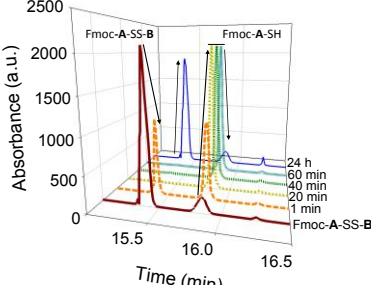
**Figure S1:** Rheology measurement of the *Fmoc-A-SS-B* (10 mg/mL) hydrogel in presence of GR (20  $\mu$ L/mL). The gelation process is monitored at a fixed strain (0.06%) and fixed frequency (0.3 Hz).

## Magnification of a TEM image from Figure 1e



**Figure S2:** Magnification of Figure 1e given in the manuscript. This image highlights nanofibers constituting the hydrogel formed from the addition of GR in *Fmoc-A-SS-B* solution (10 mg/mL).

### Characterization of the hydrogel formation by visual observation and HPLC monitoring with the different triggers (GR, AP, BSA, TCEP)

Addition at t = 0	Solution	Observations at t = 60 minutes	HPLC monitoring over time
GR (1 mg/mL)	Sol.1	 <p>Glutathion Reductase</p> <p>Bovin Serum Albumin</p>	 <p>Absorbance (a.u.)</p> <p>Time (min)</p> <p>Fmoc-A-SS-B</p> <p>Fmoc-A-SH</p> <p>60 min 40 min 20 min 1 min</p>
AP (1 mg/mL)	Sol.2	 <p>Alkaline Phosphatase</p> <p>Alkaline Phosphatase Glutathion Reductase</p>	 <p>Absorbance (a.u.)</p> <p>Time (min)</p> <p>Fmoc-A-SS-B</p> <p>Fmoc-A-SH</p> <p>60 min 40 min 20 min 1 min</p>
BSA (1 mg/mL)	Sol.3	 <p>Bovin Serum Albumin</p> <p>Alkaline Phosphatase</p>	 <p>Absorbance (a.u.)</p> <p>Time (min)</p> <p>Fmoc-A-SS-B</p> <p>Fmoc-A-SH</p> <p>60 min 40 min 20 min 1 min</p>
TCEP (1 equiv.)	Sol.4	 <p>Tris(2-carboxyethyl)phosphine</p>	 <p>Absorbance (a.u.)</p> <p>Time (min)</p> <p>Fmoc-A-SS-B</p> <p>Fmoc-A-SH</p> <p>24 h 60 min 40 min 20 min 1 min</p>

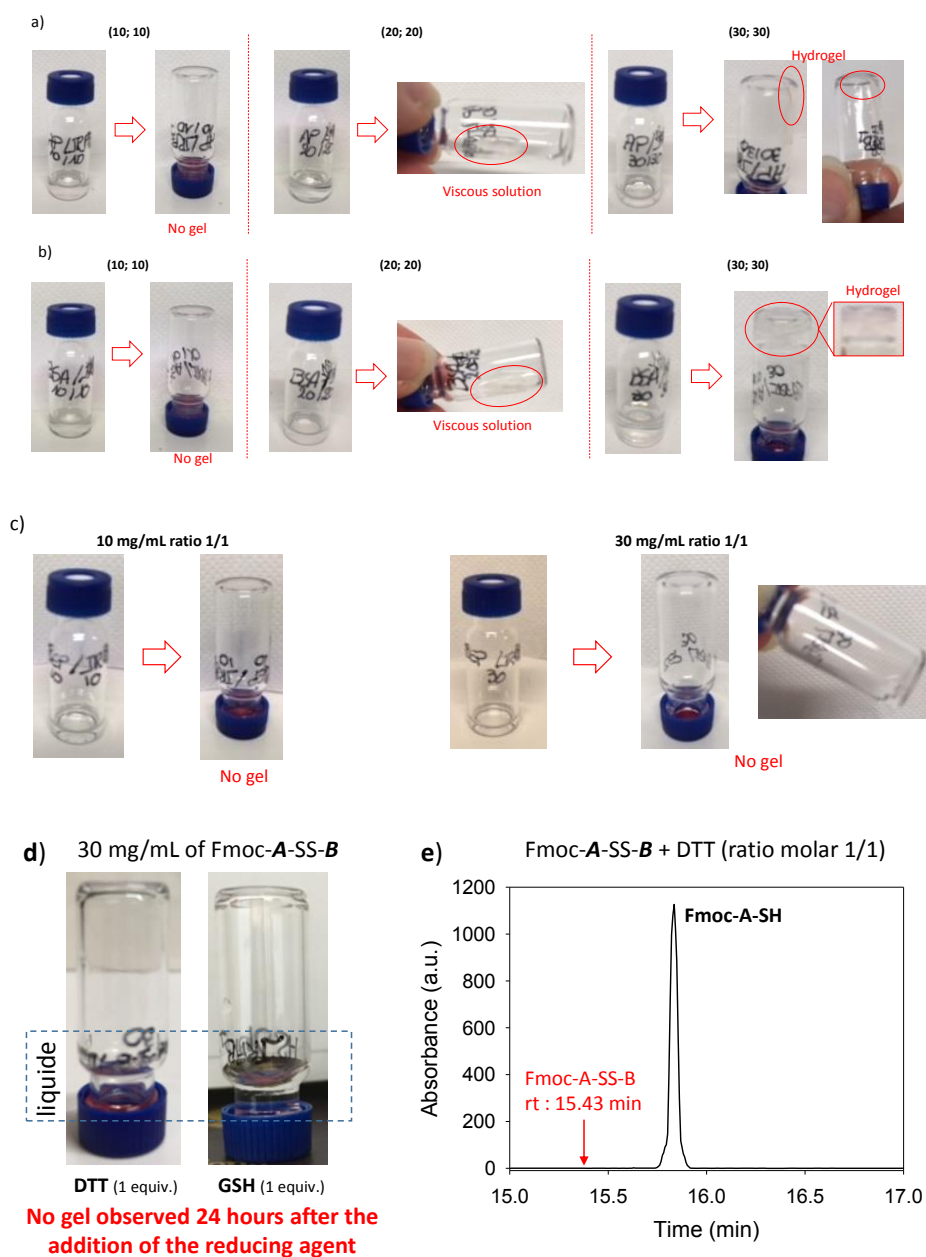
**Figure S3:** Observations and HPLC monitoring of the evolution overtime of the Fmoc-A-SS-B solution (10 mg/mL) when a biomacromolecule or TCEP is added: GR (Sol.1), AP (Sol.2), GR (Sol.3) and TCEP (Sol.4).

### Determination of the Hydrogel formation conditions in the bulk

Observations of macroscopic hydrogel formation using the inversion tube test according to the concentration of Fmoc-A-SS-B and biomacromolecules used: 10, 20 and 30 mg/mL for both Fmoc-A-SS-B and the biomacromolecule. This ratio is mentioned (X; X) for X mg/mL of Fmoc-A-SS-B and biomacromolecule concentration.

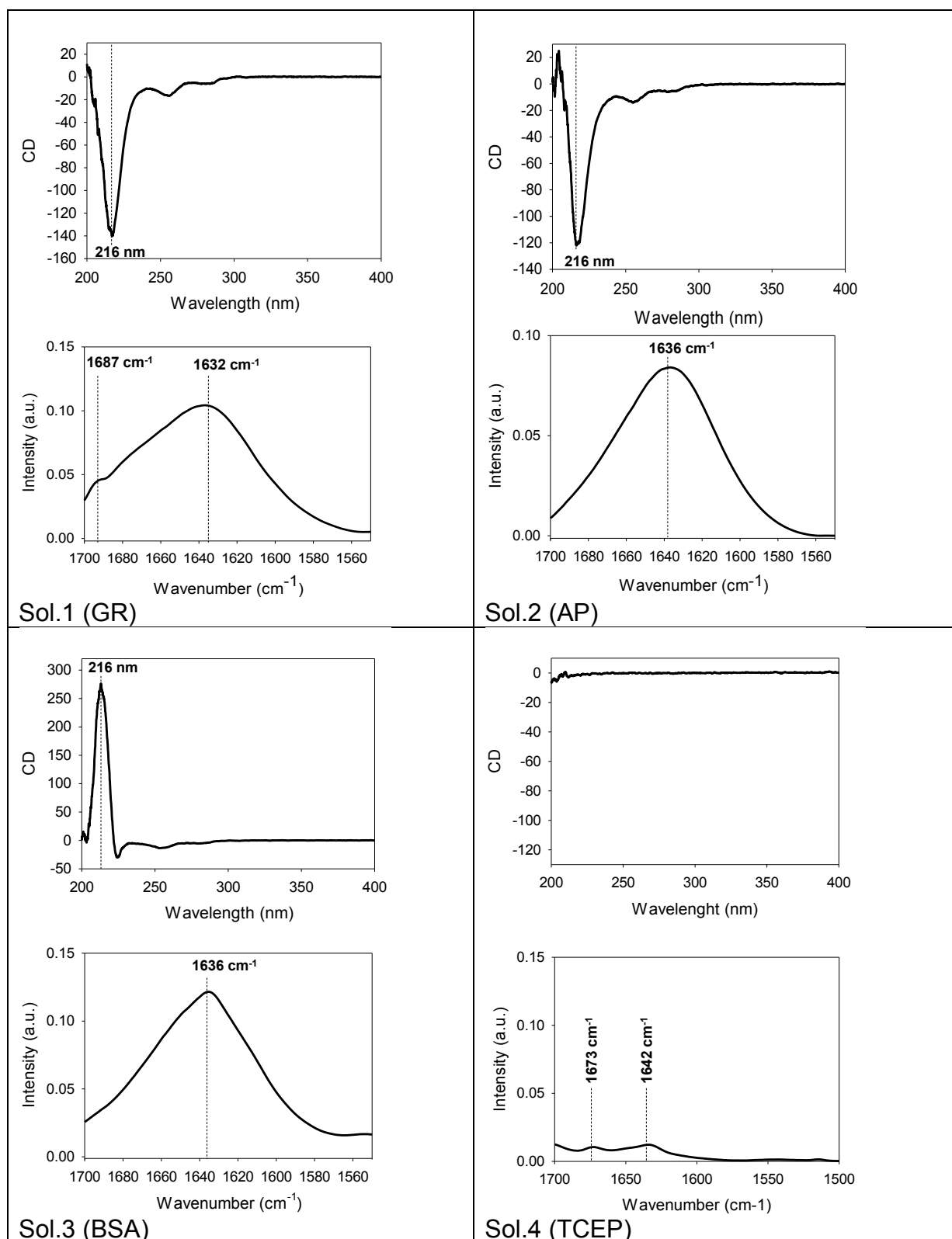


In case of solutions containing TCEP, 10 or 30 mg/mL of Fmoc-**A-SS-B** were used involving 1 equivalent of TCEP in both cases. The supramolecular hydrogel formation is potentially observed after the addition of the biomacromolecule or TCEP into the vial. In case of solution containing DTT or GSH, 30 mg/mL of Fmoc-**A-SS-B** were used involving 1 molar equivalent of the reducing agent in both cases.



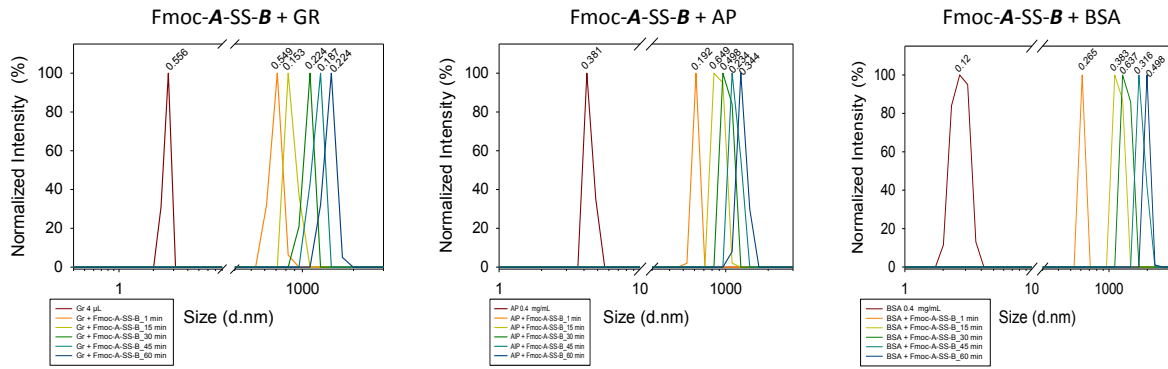
**Figure S4 :** (a) Upside-down vial test in presence of (AP; Fmoc-**A-SS-B**) = (10;10), (20;20) or (30;30); (b) Upside-down vial test in presence of (BSA; Fmoc-**A-SS-B**) = (10;10), (20;20) or (30;30) and (c) upside-down vial test of Fmoc-**A-SS-B** solution (10 and 30 mg/mL) in presence of 1 equivalent of TCEP; (d) Picture of the 30 mg.mL<sup>-1</sup> of Fmoc-**A-SS-B** solution, 24 hours after the addition of 1 molar equivalent of DTT or GSH; (e) HPLC analysis of the mixture few minutes after the addition of 1 molar equivalent of DTT.

## CD and FTIR-ATR spectra of the self-assembly formed with the different triggers



**Figure S5:** CD and IR spectra of Fmoc-A-SS-B solution (1 mg/mL) in presence of 1 mg/mL of GR (Sol.1), AP (Sol.2), BSA (Sol.3) or 1 equivalent TCEP (Sol.4) after 60 min.

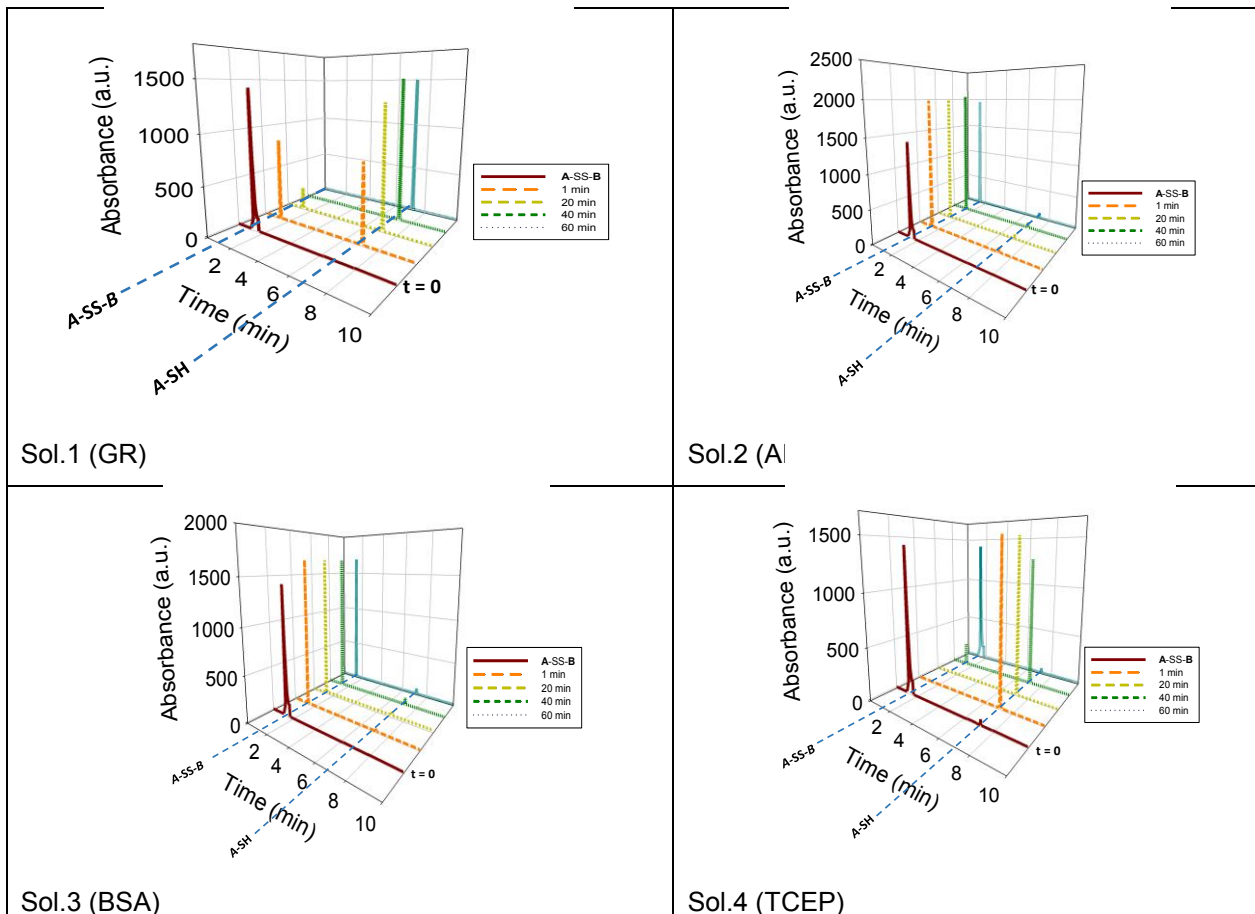
DSL spectra highlighting enzyme growing dimension



**Figure S6:** DLS spectra evolution of the hydrodynamic diameter over time of GR (4  $\mu\text{L/mL}$ ), AP (0.4 mg/mL) and BSA (0.4 mg/mL) in presence of Fmoc-A-SS-B (1 mg/mL). Values between brackets up to each peak give the PDI. It must be take into account that the values herein reported are not accurate and only the trends in the evolution has to be considered.

HPLC

SS-B in presence of different TCEP



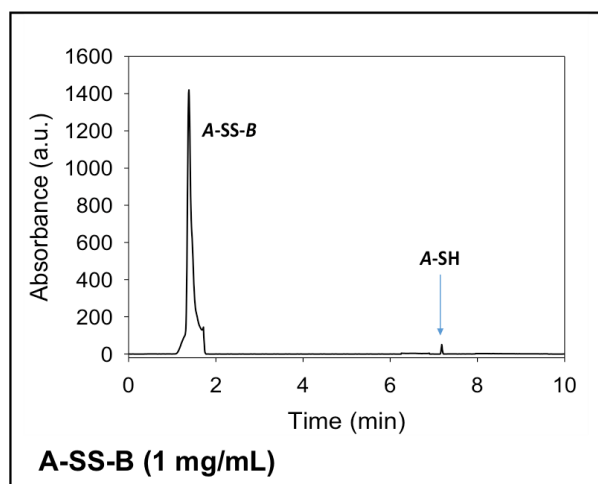
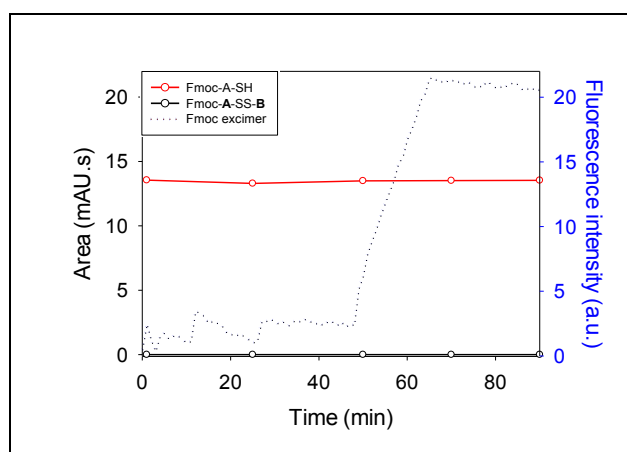


**Figure S7:** HPLC monitoring of **A-SS-B** solution (1 mg/mL) in presence of 1mg/mL of GR (Sol.1), AP (Sol.2), BSA (Sol.3) or 1 equivalent of TCEP (Sol.4).

HPLC monitoring of the Fmoc-**A-SS-B**/Fmoc-**A-SH** evolution when protein and TCEP are present together

GR



AP

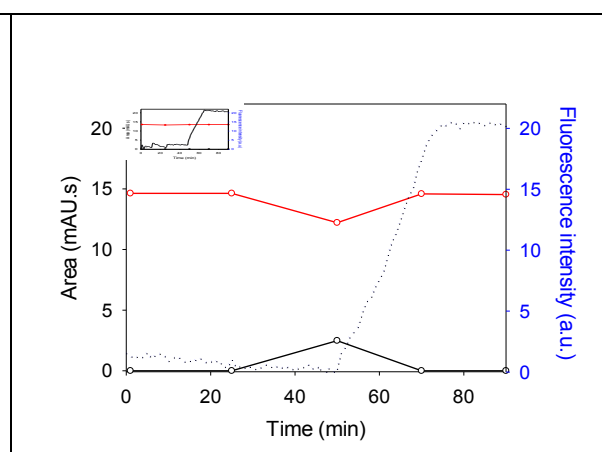


**Figure S8:** HPLC monitoring and fluorescence emission intensity measured at 325 nm over time ( $\lambda_{ex} = 280\text{nm}$ ) of a freshly prepared 100% Fmoc-**A-SH** solution (generated from the following mixture: Fmoc-**A-SS-B** + 1 equivalent of TCEP) after the addition of GR or AP.

### Influence of the presence of sodium citrate on the gelation process in solution

Initial solution: Fmoc-**A-SS-B** (30 mg/mL) + BSA (30 mg/mL)

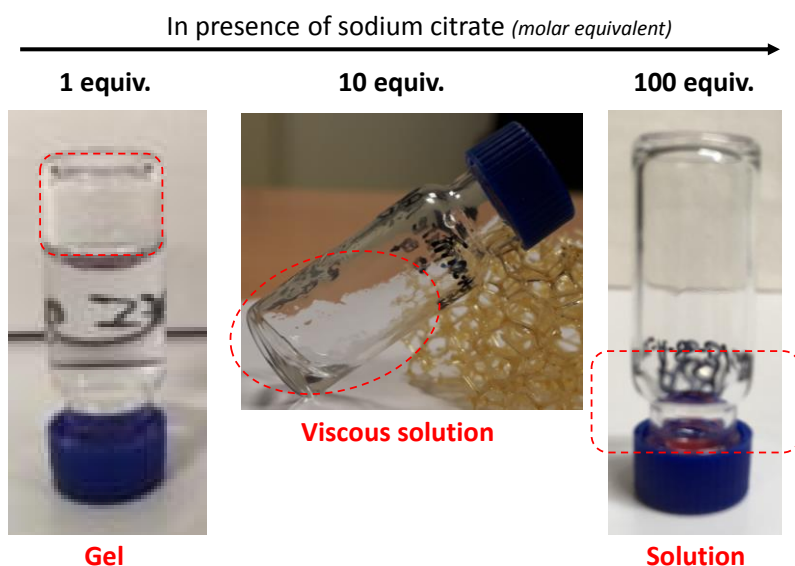


**Figure S9:** Pictures of the Fmoc-**A-SS-B** (30 mg.mL<sup>-1</sup>) in presence of 1, 10 or 100 equivalents of sodium citrate, 24 hours after the addition of BSA (30 mg.mL<sup>-1</sup>).

### RMN study of the pre-aggregation of the peptide

As reported recently by Martin, Thordarson and coworkers, hydrophobic N-terminal capping groups on short peptide hydrogelator are involved in the formation of pre-assembled structures present in solution.<sup>5</sup> Because of the Fmoc group present in Fmoc-**A-SS-B** peptide, <sup>1</sup>H NMR analysis of this peptide in D<sub>2</sub>O was investigated and compared to the spectra recorded in DMSO-*d*<sub>6</sub>. All aliphatic signals are present but in the aromatic area of the <sup>1</sup>H NMR, those corresponding to protons from phenylalanine and tyrosine residues are missing. Only the signals of the Fmoc group are present. By adding progressively a disturbing agent of supramolecular interaction such as DMSO-*d*<sub>6</sub> into the D<sub>2</sub>O solution of Fmoc-**A-SS-B**, the aromatic missing signals appear. This simple NMR analysis shows that Fmoc-**A-SS-B** peptide is already pre-assembled before the introduction of a protein, an association that does not involve the Fmoc group. This observation is in agreement with the absence of fluorescence excimer measurements (that appears from Fmoc stacking), as mentioned above. These aggregates can be in dynamic equilibrium with isolated peptides as reported in other systems.

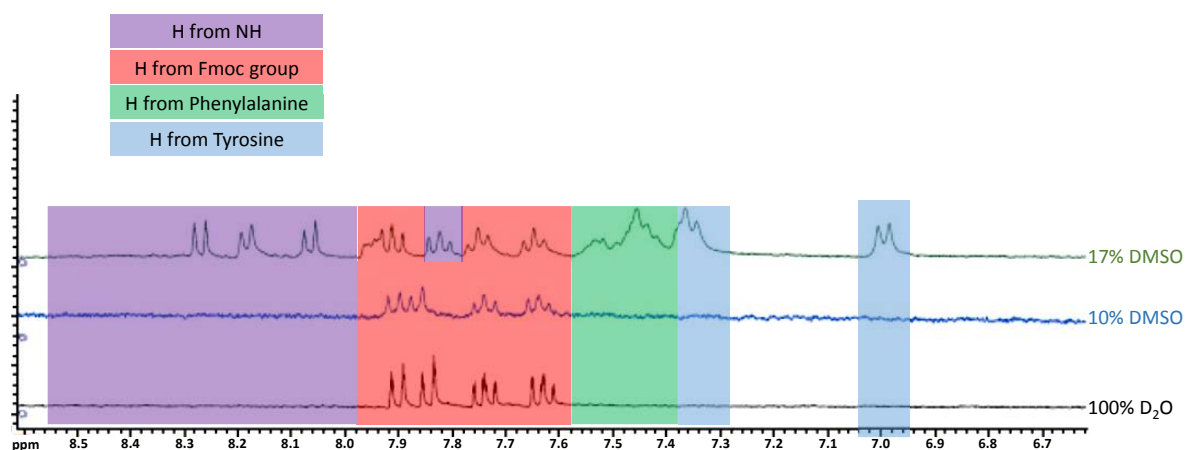


**Figure S 10:**  $^1\text{H}$  NMR spectra of the aromatic region corresponding to Fmoc-**A-SS-B** in 100%  $\text{D}_2\text{O}$  (black spectra), 90%  $\text{D}_2\text{O}/10\%$  (blue spectra)  $\text{DMSO-d}_6$  and 83%  $\text{D}_2\text{O}/17\%$   $\text{DMSO-d}_6$  (green spectra).

TCEP (1 equiv. molar) was added into a  $\text{D}_2\text{O}$  solution of Fmoc-**A-SS-B** and  $^1\text{H}$  NMR monitoring was carried out. The 2 minutes time to record the  $^1\text{H}$  NMR spectra after the addition of TCEP is enough to cleave entirely the disulfide bridge of Fmoc-**A-SS-B** as confirmed by HPLC. Particular attention was paid to the aromatic region of the  $^1\text{H}$  NMR spectra. Before TCEP addition, Fmoc-**A-SS-B** is pre-aggregated in  $\text{D}_2\text{O}$  and only the aromatic signals corresponding to the Fmoc groups can be observed. When 1 equivalent molar of TCEP is added into the  $\text{D}_2\text{O}$  solution only signals of protons in  $\alpha$  and  $\beta$  positions of the sulfur atom are changing. The aromatic region does not change, and thus there is no appearance of the protons corresponding to Phe or Tyr residues. This means that despite the reduction of the disulfide bridge by TCEP, the resulting Fmoc-**A-SH** is maintained aggregated.

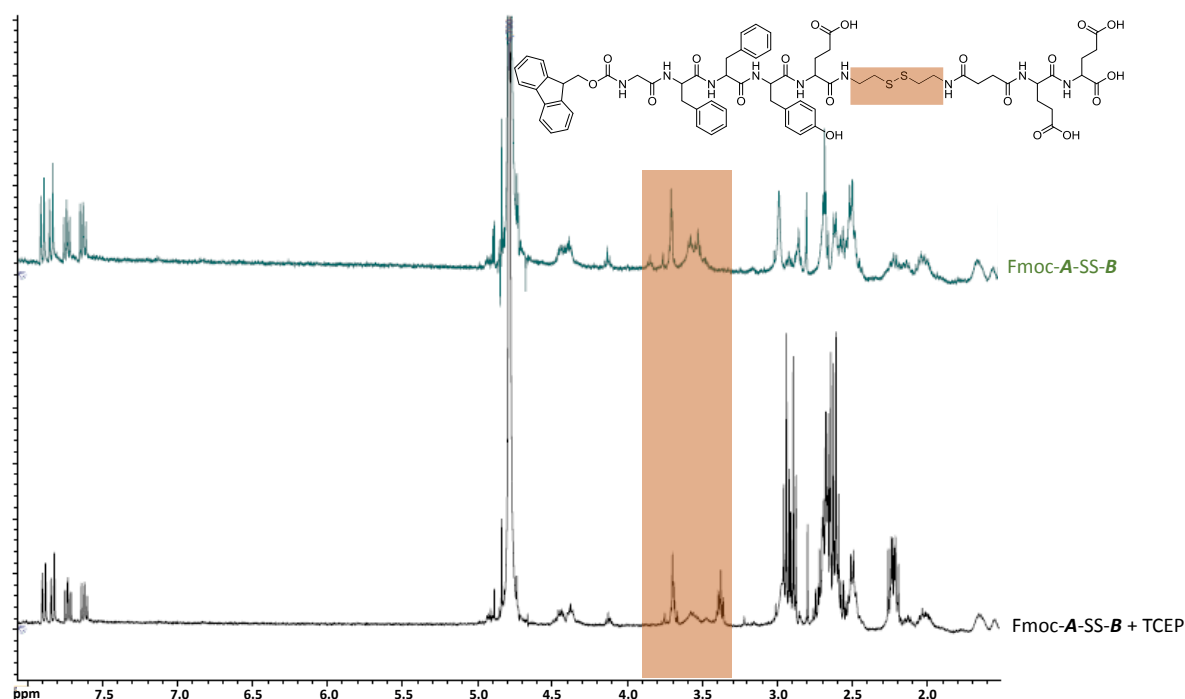


**Figure S11:**  $^1\text{H}$  NMR spectra of Fmoc-A-SS-B in  $\text{D}_2\text{O}$  before (up) and after (down) the addition of 1 equivalent molar of TCEP.

After the dissolution of Fmoc-A-SS-B ( $10 \text{ mg.mL}^{-1}$ ) and the record of the NMR spectra, BSA ( $1 \text{ mg.mL}^{-1}$ ) was introduced into the NMR tube and spectra were immediately recorded.

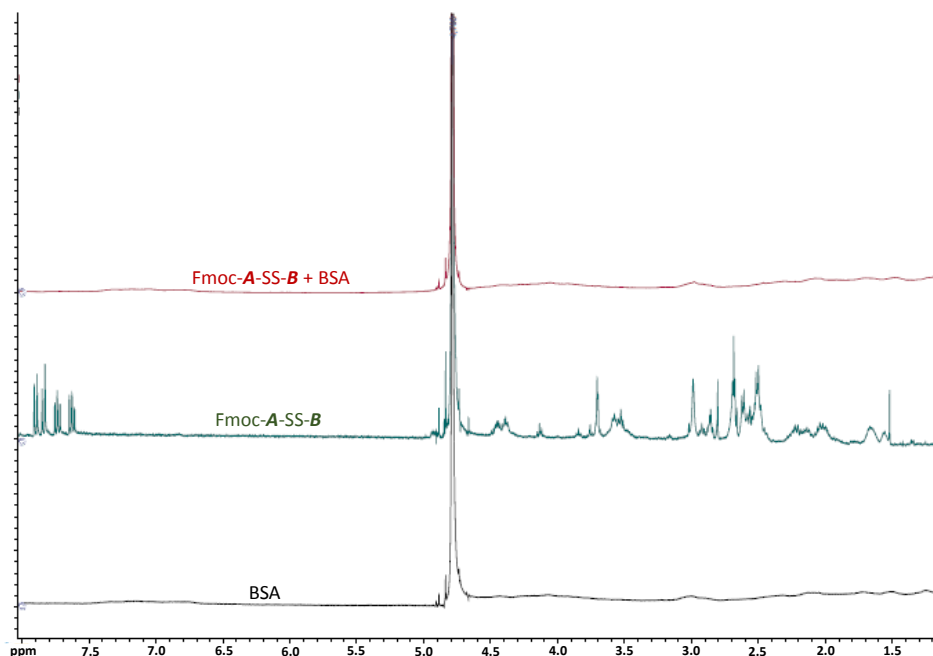
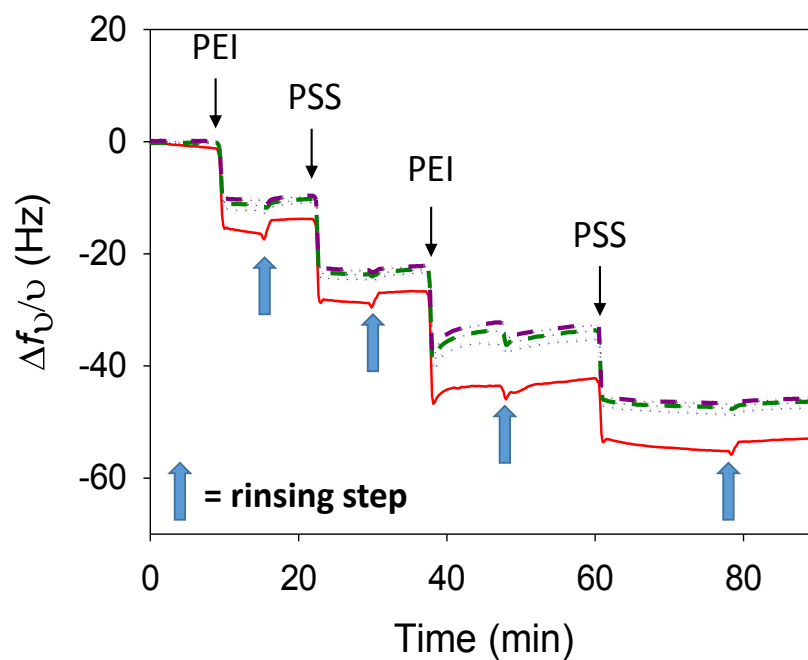


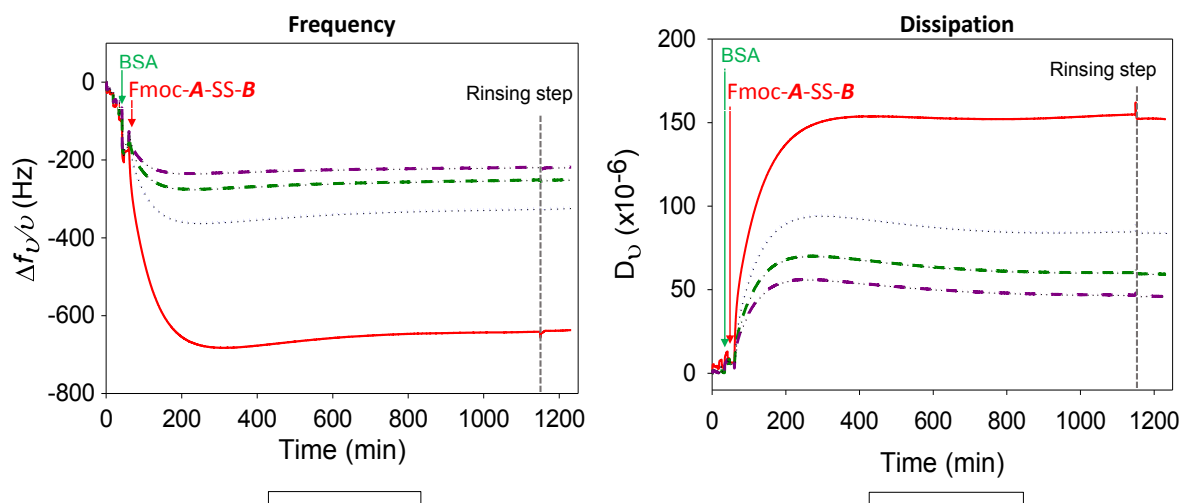
**Figure S12:**  $^1\text{H}$  NMR (in  $\text{D}_2\text{O}$ ) spectra of BSA (black curve), Fmoc-A-SS-B (green curve) and Fmoc-A-SS-B after the addition of BSA (red curve).

### QCM-D monitoring of the multilayer and the self-assembly growing

- Multilayer film  $(\text{PEI/PSS})_2$  buildup monitored by QCM-D: Frequency shift (F1 – red curve, F3 – dotted blue, F5 – dotted green and F7 – dotted purple) measurements overtime:



- Adsorption of BSA on (PEI/PSS)<sub>2</sub> multilayer film followed by the contact with the Fmoc-**A-SS-B** solution (1 mg/mL): Frequency shifts (F1 – red curve, F3 – blue curve, F5 – green curve and F7 – purple curve) and corresponding dissipation factors measurements overtime:





- Adsorption of AP on (PEI/PSS)<sub>2</sub> multilayer film followed by the contact with the Fmoc-A-SS-B solution (1 mg/mL): Frequency shifts (F1 – red curve, F3 – blue curve, F5 – green curve and F7 – purple curve) and corresponding dissipation factors measurements overtime:

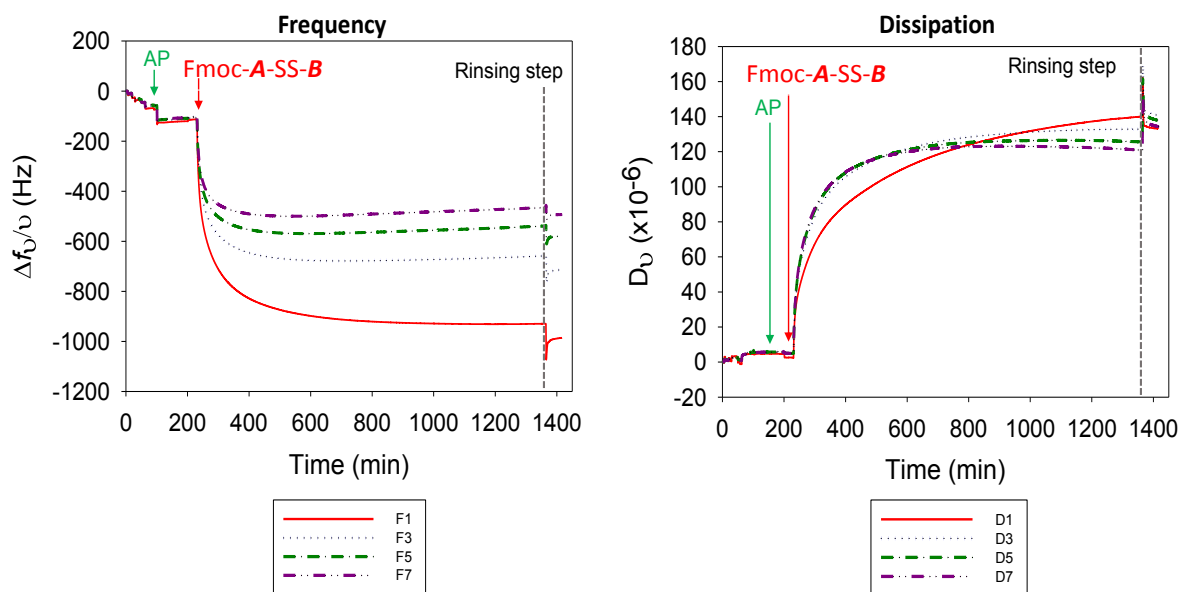


**Figure S13:** QCM-D monitoring of the multilayer film buildup followed by the biomacromolecule adsorption, and the localized peptide self-assembly from this modified surface.

### Cryo-SEM characterization of the morphology of the self-assembly generated from a surface

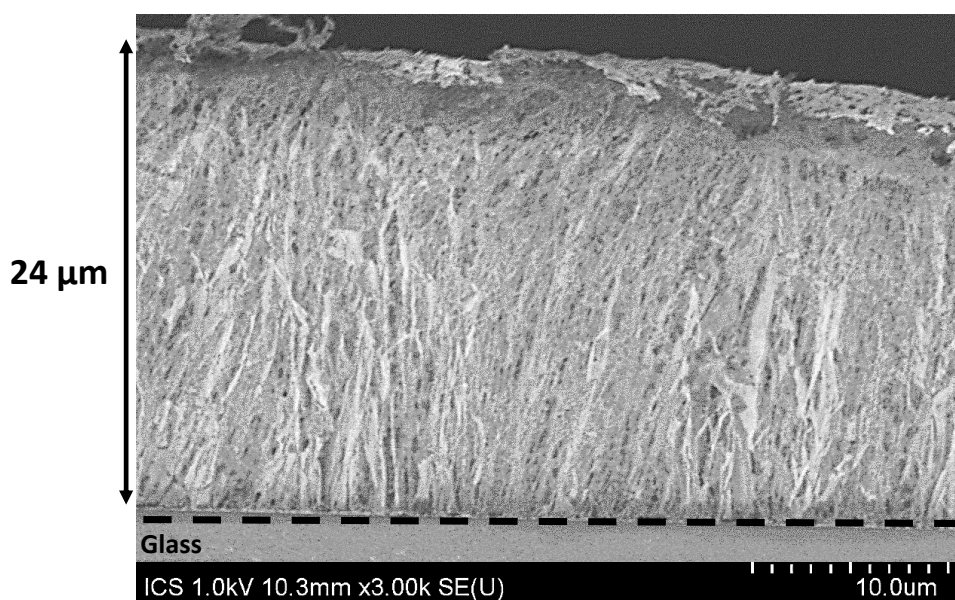


**Figure S14:** Cryo-SEM image (z cross section) of the supramolecular hydrogel formed from a BSA layer adsorbed on a suitable multilayer supported on a glass substrate in contact with a Fmoc-A-SS-B solution (1 mg/mL).

## Characterization of the self-assembly generated from the surface

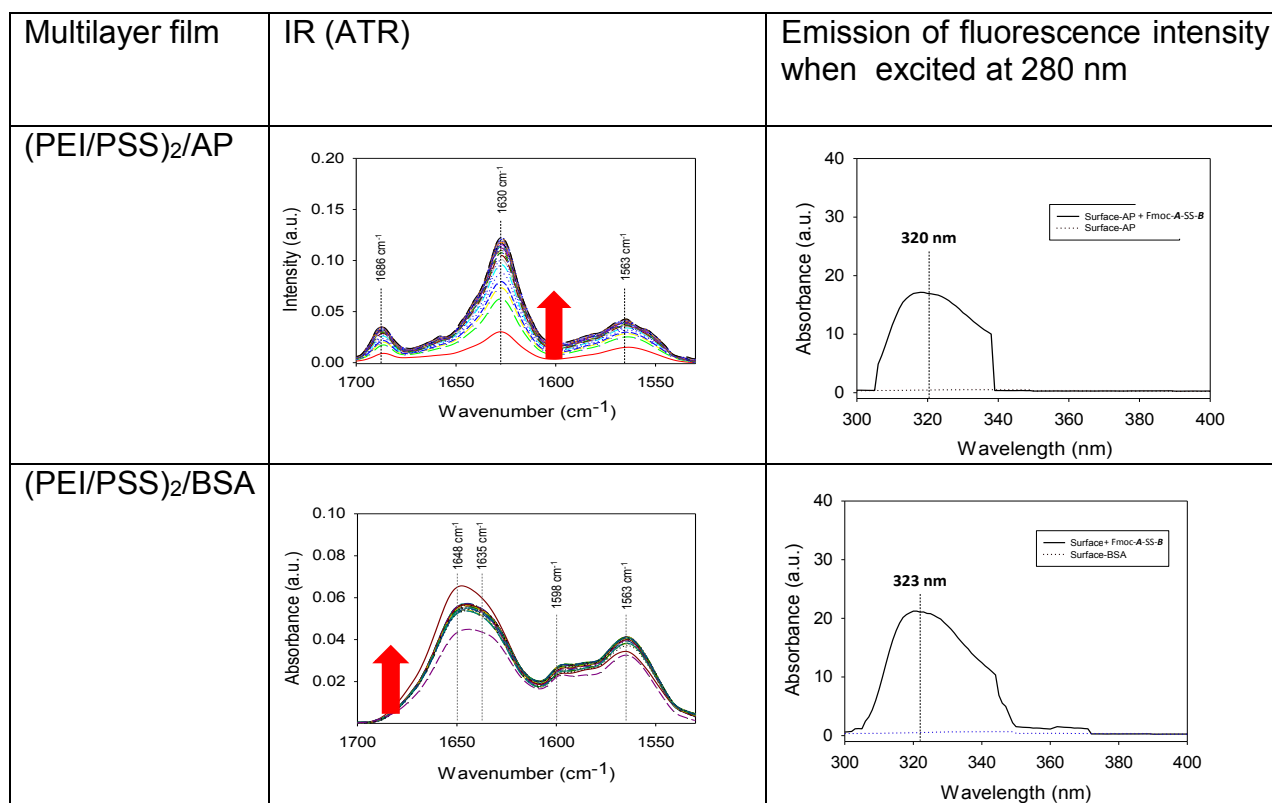


**Figure S15:** IR and fluorescence emission intensity measurements monitored on the supramolecular hydrogels grew from BSA or AP modified substrate in presence of Fmoc-A-SS-B solution (1 mg/mL). The red arrow indicates the evolution of the IR spectra (ATR) recorded at different time from  $t=1$  minute to  $t=12$  hours.

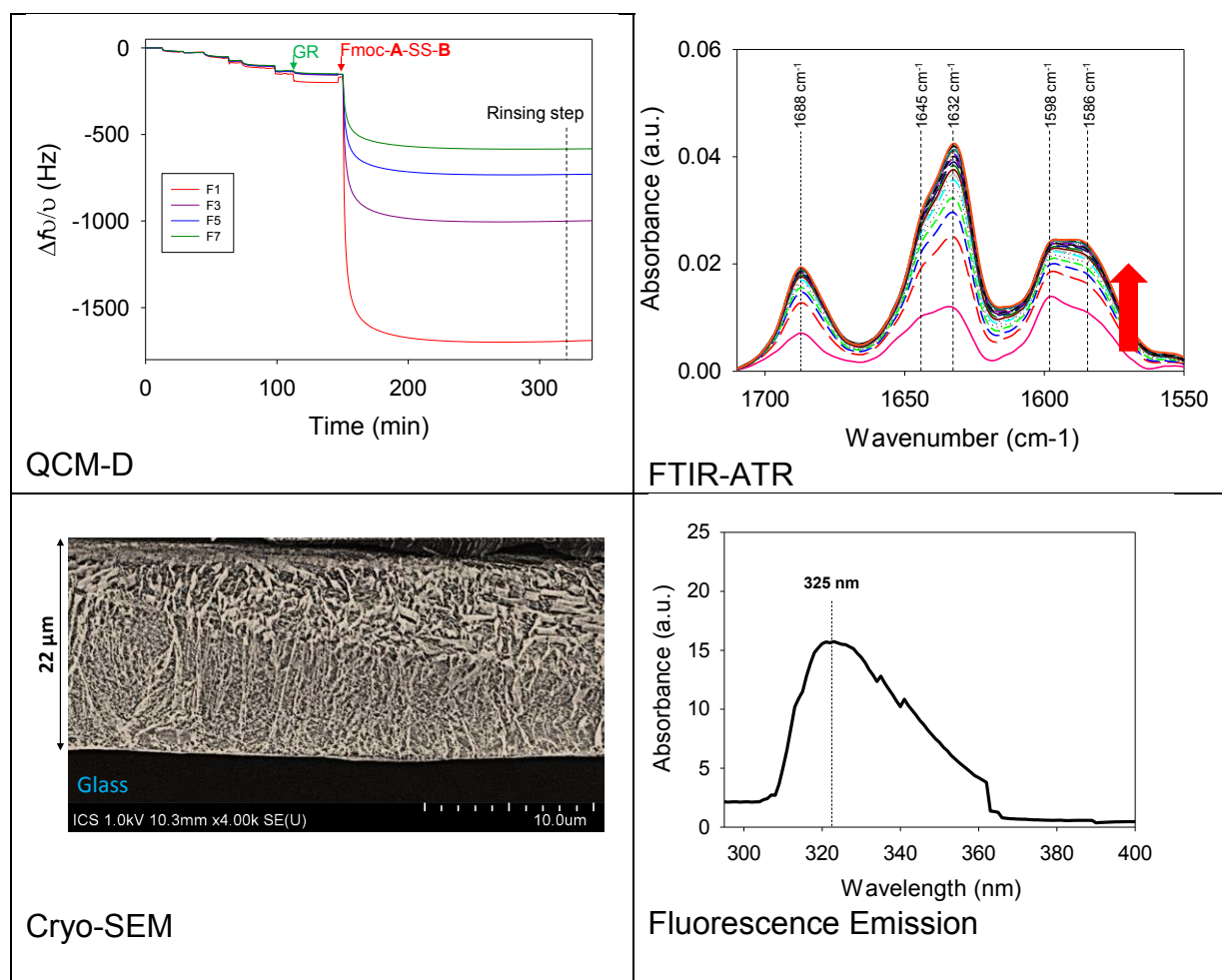


**Figure S16:** QCM-D, IR, cryo-SEM and fluorescence emission intensity ( $\lambda_{ex}=280$  nm) analyses of the supramolecular hydrogels grew from GR modified substrate in presence of Fmoc-A-SS-B solution (1 mg/mL). The red arrow indicates the evolution of the IR spectra recorded at different time from  $t=1$  minute to  $t=12$  hours.

Thus, to highlight the electrostatic interaction of the negatively charged peptide Fmoc-A-SS-B (mainly due to the **B** sequence which contains two glutamic acid residues and the carboxylate group at the C-term position), we have modified the surface of a first substrate with poly-L-Lysine (PLL) and a second substrate with poly-L-glutamic acid (PGA). We brought each of them in contact with Fmoc-A-SS-B solution freshly prepared. This has been monitored by quartz crystal microbalance with dissipation (QCM-D), which is an adequate tool to bring to light this kind of interaction. The surface modification of the QCM quartz substrate was done using the multilayer film strategy (as described in the submitted manuscript). Positively and negatively charged films were obtained through the buildup of the following multilayer architectures (and their effective structure monitored and confirmed by QCM-D):

- Positively charged film (**P-Film**): PEI/(PSS/PLL)<sub>2</sub>
- Negatively charged film (**N-Film**): PEI/PGA/PEI/PGA

(Polycations: PEI=poly(ethylene imine), PLL=poly-L-lysine; Polyanions: PSS=poly(styrene sulfonate), PGA=poly-L-glutamic acid).

P-Film and N-Film are ended by poly-L-lysine (polycation) and poly-L-glutamic acid (polyanion) respectively, mimicking so protein charged patches of each electrostatic charge.

When N-Film is put in contact with a freshly prepared solution of Fmoc-**A-SS-B** ( $1 \text{ mg}\cdot\text{mL}^{-1}$ ), almost no decrease of the normalized frequency shift ( $\nu=3$ ) from the quartz crystal is measured, meaning that no significant mass is adsorbed onto the N-Film, suggesting that no interaction occurs between Fmoc-**A-SS-B** and the negatively charged polypeptide adsorbed onto the surface, even after several hours. When the P-film is put in contact with a freshly prepared solution of Fmoc-**A-SS-B** ( $1 \text{ mg}\cdot\text{mL}^{-1}$ ), a decrease of the normalized frequency shift ( $\nu=3$ ) is measured. This decrease occurs immediately after contact between the Fmoc-**A-SS-B** solution and the positively charged polypeptide layer. Despite a rinsing step, Fmoc-**A-SS-B** stays onto the top of the P-film.

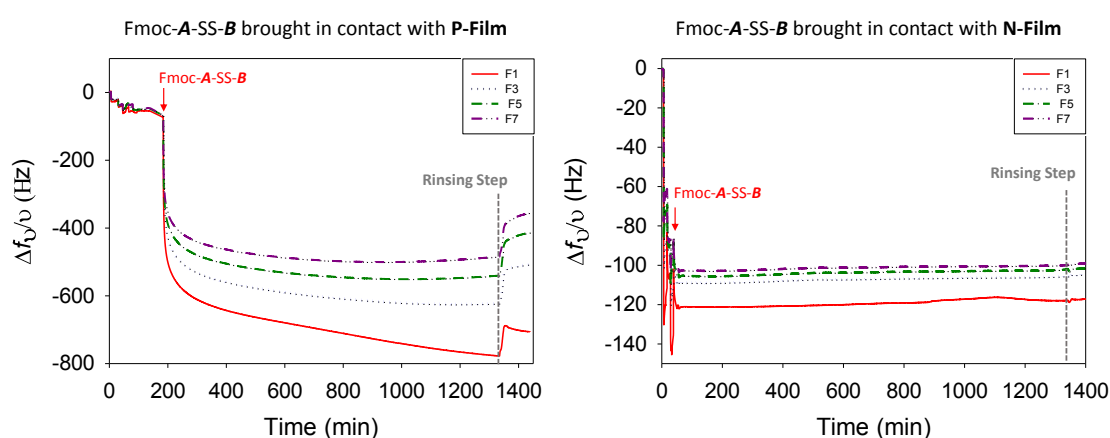


**Figure S17:** QCM monitoring (evolution of the 3<sup>rd</sup> harmonic  $\nu=3$ ) when Fmoc-**A-SS-B** ( $1 \text{ mg/mL}$ ) solution is brought in contact with P-film (green curve) and N-Film (red curve) at  $t=0$ .

[Protein]	GR	AP	BSA
Time (min)	Hydrodynamic diameter (nm) (PDI)		
1	734.9 (0.549)	616 (0.192)	615 (0.265)
15	873.6 (0.153)	894 (0.649)	1187 (0.383)
30	1065 (0.224)	1032 (0.498)	1314 (0.637)
45	1356 (0.187)	1154 (0.234)	1796 (0.316)
60	1405 (0.224)	1251 (0.344)	1924 (0.498)

**Table 1:** Evolution the hydrodynamic diameter over time measured by DLS of GR ( $4 \mu\text{L/mL}$ ), AP ( $0.4 \text{ mg/mL}$ ) and BSA ( $0.4 \text{ mg/mL}$ ) in presence of Fmoc-**A-SS-B** ( $1 \text{ mg/mL}$ ). Values between brackets give the PDI. It must be take into account that the values herein reported are not accurate and only the trends in the evolution has to be considered.

### 3.6. Experimental section

#### 3.6.1. Materials

All reagents and solvents were purchased at the top commercial quality and used without further purification.

Name, acronym (abbreviation)	MW (g.mol <sup>-1</sup> )	Supplier	CAS number
Bovine serum albumin (BSA)	66 000	Sigma-Aldrich	9048-46-8
Poly(ethylene imine) (PEI)	750 000	Alfa Aesar	9002-98-6
Poly(styrene sulfonate) (PSS)	70 000	Sigma Aldrich	25704-18-1
Deuterated Water (D <sub>2</sub> O)	20.03	Sigma Aldrich	7789-20-0
Dimethylformamide (DMF)	73.09	Acros Organics	68-12-2
Dichloromethane (DCM)	84.93	Acros Organics	75-09-2
Trifluoroacetic acid (TFA)	114.02	Alfa Aesar	76-05-1
Deuterated DMSO (DMSO-d <sub>6</sub> )	84.17	SDS	2206-27-1
N-Ethyl-diisopropylamine (DIEA)	129.25	Alfa Aesar	7087-68-5
Alkaline Phosphatase from bovine intestinal mucosa (AP)	170 000	Sigma Aldrich	9001-78-9
Fmoc-L-phenylalanine (Fmoc-F-OH)	387.43	Iris biotech	35661-40-6
Fmoc- L-Tyrosine 5- <i>tert</i> -butyl ester (Fmoc-Y(tBu)-OH)	483.41	Bachem	147762-53-6
Fmoc-L-Glycine (Fmoc-G-OH)	297.31	Iris biotech	29022-11-5
Fmoc-L-glutamic acid 5- <i>tert</i> -butyl ester (Fmoc-E(tBu)-OH)	619.71	Iris biotech	109425-51-6
Glutathion reductase from baker's yeast ( <i>S. cerevisiae</i> ) (GR)	124 000	Sigma Aldrich	9001-48-3
Cystamine dihydrochloride	225.20	Sigma Aldrich	56-17-7
Triisopropylsilane (TIPS)	158.36	Sigma Aldrich	6485-79-6
Resin 2-chlorotriyl chloride (2-CTC)	-	Sigma Aldrich	42074-68-0
1-Hydroxybenzotriazole hydrate (HOBt)	135.12	Sigma Aldrich	123333-53-9
N,N,N',N'-Tetramethyl-o-(1H-benzotriazol-1-yl)uranium hexafluorophosphate (HBTU)	379.24	Alfa Aesar	94790-37-1
Diethyl ether	74.12	Acros Organics	60-29-7
Succinic acid	118.09	Sigma Aldrich	110-15-6
Poly-L-Lysine (PLL)	52 000	Sigma Aldrich	26124-78-7
Poly-L-Glutamic acid (PGA)	41 400	Sigma Aldrich	26247-79-0
Dithiothreitol (DTT)	154.25	Sigma Aldrich	3483-12-3
Glutathione	307.32	Sigma Aldrich	70-18-8

### 3.6.2. Hydrogel preparation in bulk and upside-down vial tests

All hydrogels were prepared in PBS buffer (pH 7.4). The PBS buffer is prepared the day of the hydrogel preparation.

**General preparation of Fmoc-A-SS-B solution:** the suitable amount of Fmoc-A-SS-B was dissolved in PBS to get the suitable concentration (usually 1, 10 or 30 mg/mL). This solution is vortexed 2 – 5 minutes and sonicated in an ultrasound bath during 1 minute. The resulting Fmoc-A-SS-B solution was thus used for all kind of analyses.

**PBS Buffer (pH 7.4):** one tablet of commercially available PBS (P4417 from Sigma Aldrich) was dissolved in 200 mL of ultrapure water (Milli-Q Plus system, Millipore, Billerica, MA) leading to 0.01 M phosphate buffer, 0.0027 M potassium chloride and 0.137 M sodium chloride. If necessary, the pH of this buffer is adjusted to 7.4 value by addition of few drops of HCl (0.01 M) or NaOH (0.01 M) solution. The pH value is monitored using a pH meter.

**Hydrogel formation triggered with GR** was obtained by dissolving Fmoc-A-SS-B (10 mg/mL) in PBS buffer. This solution was vortexed during 2 min and then dipped into an ultrasound bath during 1 minute. 20  $\mu$ L of commercial GR (G3664 from Sigma Aldrich) was added. The resulting hydrogel was obtained immediately.

**Hydrogel formation triggered by BSA or AP:** peptide solution was prepared by dissolving Fmoc-A-SS-B in PBS buffer to get a concentration of 30 mg/mL. This solution was vortexed during 5 min and then dipped in an ultrasound bath during 5 min. BSA or AP was added to the Fmoc-A-SS-B solution to get a concentration of 30 mg/mL and the resulting mixture was vortexed 10 seconds. The hydrogel is obtained in 20 min for both proteins.

**Upside-down vial test of TCEP and Fmoc-A-SS-B solution:** Fmoc-A-SS-B (30 mg/mL) was dissolved into a freshly prepared solution in PBS buffer. This mixture was vortexed (5 min) and then dipped in an ultrasound bath (5 min). Then 1 equivalent molar of TCEP was added as a single solid portion into the mixture. This solution was vortexed 10 seconds. The inverted vial test was done 5 and 20 minute later.

**Upside-down vial test of Fmoc-A-SS-B and BSA mixture in presence of sodium citrate:** the peptide solution was prepared by dissolving Fmoc-A-SS-B (30 mg/mL) in PBS buffer. This solution was vortexed (5 min) and then dipped in an ultrasound bath (5 min). Then 1, 10 or 100 molar equivalents of sodium citrate were added and the mixture was vortexed during 30 seconds. Finally, BSA solution was added in PBS to get a concentration of 30 mg/mL) and the mixture was vortexed during 1 min. The inverted vial test was done 5 minute later.

**Upside-down vial test of GR and A-SS-B mixture:** the peptide solution was prepared by dissolving A-SS-B in PBS buffer. The solution was vortexed (2 min) and then dipped in an ultrasound bath (1 min). Then 20  $\mu$ L of the commercial solution of GR was added to get a concentration of 10 mg/mL and the resulting mixture was vortexed during 10 seconds. The inverted vial test was done 5 minute later.

**Upside-down vial test of BSA or AP and A-SS-B mixture:** the peptide solution was prepared by dissolving A-SS-B (30 mg/mL) in PBS buffer. The solution was vortexed (2 min) and then dipped in an ultrasound bath (1 min). Then BSA or AP was added as a solid portion into to A-SS-B solution to get a concentration of 30 mg/mL. The resulting mixture was vortexed 10 seconds. The inverted vial test was done 20 minute later.

### **3.6.3. Multilayer film preparation and hydrogel self-assembly**

All polyelectrolytes (1 mg/mL), enzymes (Gr 10  $\mu$ L/mL; AP 1 mg/mL) and proteins (1 mg/mL) were prepared in PBS buffer freshly prepared as described in section 3.6.2. Different surfaces were used depending on the characterization techniques investigated: Gold coated quartz crystal for QCM-D, ZnSe crystal for ATR-FTIR experiments and glass slide for Cryo-SEM and Fluorescence emission assays (in SAFAS instrument) experiments.

The preparation of the hydrogel on surface was done as following: after the deposition of a PEI (1 mg/mL) precursor layer on the chosen surface by dipping, the multilayer film was built up by alternately exposing the surface to PSS (1 mg/mL in PBS buffer) and PEI (1 mg/mL in PBS buffer) solutions for 10 min with an intermediate rinsing step with PBS buffer during 5 min. AP (1 mg/mL), BSA (1 mg/mL) and GR (10  $\mu$ L/mL), all prepared in PBS, were put in contact during 20 min followed by 5 min of rinsing step with PBS buffer. Finally, the peptide Fmoc-**A-SS-B** solution (1 mg/mL in PBS buffer) was let in contact with the modified surface overnight. The volume of each solution used brought in contact with the substrate was 700  $\mu$ L.

### **3.6.4. Quartz Crystal Microbalance with Dissipation monitoring**

QCM-D experiments were performed on a Q-Sense E1 apparatus (Q-Sense AB, Göteborg, Sweden) by monitoring the resonance frequencies of gold coated crystals, as well as the dissipation factors at four frequencies: the fundamental frequency at 5 MHz ( $\nu = 1$ ) and the 3<sup>rd</sup>, 5<sup>th</sup>, and 7<sup>th</sup> harmonics ( $\nu = 3, 5$  and  $7$  at 15, 25, and 35 MHz respectively). The QCM-D results give information on the adsorption process, as well as on viscoelastic properties of the adsorbed film<sup>18</sup>. Preparation of the multilayer film and formation of the hydrogel layer are described in point 3.1.3.3 just above.

### **3.6.5. Infrared spectroscopy**

The Fourier Transform Infrared (FTIR) experiments were performed on a Vertex 70 spectrometer (Bruker, Germany) using a DTGS detector. Spectra, for the surface analysis, were recorded in the Attenuated Total Reflection (ATR) mode using a 45° trapezoidal ZnSe (internal reflection element) crystal (6 reflections, dimensions 72  $\mu$ m  $\times$  10  $\mu$ m  $\times$  6 mm<sup>3</sup>) in ATR cell (GRASEBY-SPECAC, England). Reference (bare ZnSe crystal in contact with ultrapure water) and sample spectra were taken by collecting 128 interferograms between 800 and 4000  $\text{cm}^{-1}$  at 2  $\text{cm}^{-1}$  resolution, using Blackman-Harris three-term apodization and the standard Bruker OPUS/IR software (version 7.5). Multilayer films were assembled on ZnSe crystal by the dipping method as described above. PEI, PSS, AP, BSA, GR or Fmoc-**A-SS-B** solutions were prepared as described previously (section 3.6.3., just above) but in deuterated PBS buffer to avoid the water signal in the amide I region.

Spectrums of the hydrogels made in solution were recorded in ATR mode using a diamond. All the hydrogels were formed in deuterated PBS buffer.

### 3.6.6. Scanning Electron Microscopy and cryo-SEM

To observe cross-sectioned gels, a specific cryo-holder was designed and manufactured by the mechanical facility of the Charles Sadron Institute (see Figure below). The glass slide, covered by enzymatic precursor film and the self-assembled gel, was inserted vertically in the jaws of the vise. The sample is plunged rapidly into liquid ethane and then fixed into the holder, which was previously placed inside nitrogen slush. Finally, the holder with the sample is placed inside the cryo preparation chamber of the Quorum PT 3010 machine. As the sample is free standing over the holder, during the plunging, the sample is rapidly frozen by direct contact with the liquid ethane. The sample is then transferred under vacuum into the chamber attached to the microscope and fractured with a razor blade. First, a sputtering step is realized (10 mA for 30s), and then the surface is fractured. A slight etching at  $-90^{\circ}\text{C}$  for 2 min is performed to render the fibers more visible followed by the deposition of a thin Pt layer (metallization step, 5 mA for 20s). The sample is then transferred in the FEG-cryoSEM (Hitachi SU8010) and observed at 1kV at  $-170^{\circ}\text{C}$ .



Picture of the specific cryo-holder designed and built for the preparation of cross-sections. The “cross-section” holder is a vise like holder with two movable jaws. A screw compressing/uncompressing two springs moves the jaws forwards and backwards. By design the center of the holder is invariable as the two jaws can be displaced independently to adjust to the sample thickness by screws and springs. In that way, the sample will be in the optical axis of the SEM after introduction in the microscope and easily found under the beam.

### 3.6.7. Transmission Electronic Microscopy (TEM)

The TEM images were performed with sample prepared in liquid (diluted solutions (1 mg/mL of Fmoc-**A-SS-B**) or hydrogels (10 mg/mL of Fmoc-**A-SS-B**)). To make the observations 20  $\mu\text{L}$  of the sample is dropped off on a shelf. Then, the sample is observed by a TEM Technai G2 machine in negative coloration. To make the observations, 5 microliters of the different hydrogels are deposited onto a freshly glow discharged carbon-covered grid (400 mesh). The hydrogel is left for 2 minutes and the grid is negatively stained with 5 microliters uranyl acetate (2% in water) for another minute and finally dried using a filter paper. The grids were observed at 200kV with a Tecnai G2 (FEI) microscope. Images were acquired with a camera Eagle 2k (FEI) sCCD camera.

### 3.6.8. Analytical High-Performance Liquid Chromatography

Analytic High-Performance Liquid chromatography (HPLC) was carried out with a 1100 Series from Agilent technologies. The column is a Supelcosil ABZ + Plus with the following dimensions 15 cm  $\times$  4.6 mm, 3  $\mu\text{m}$ . The eluent used for all analyses was acetonitrile/deionized water in ratio 80/10 in isocratic conditions, at 1 mL/min. Chromatograms were recorded by the software OpenLab Agilent 1100. All samples were observed in solution in diluted conditions (ten times under the gelation condition (1 mg/mL of Fmoc-**A-SS-B**)).

Note: For the assays using 1 equivalent of TCEP in presence of Fmoc-**A-SS-B** (1 mg/mL), the peptide is first solubilized then the TCEP is added. The 100% formation of Fmoc-**A-SH** peptide is checked by HPLC before the addition in this reaction mixture of the chosen protein



(ALP or BSA). Solutions were prepared in the eluent ratio of ACN and water. All solutions were filtrated with a PTFE 0.2  $\mu\text{m}$  filter before each injection.

### **3.6.9. Dynamic Light Scattering**

Dynamic Light Scattering (DLS) experiments were carried out with a Zetasizer from Malvern. The experiments were done in diluted system, which means the concentration of peptide is at 1 mg/mL with a concentration of enzyme at 1 mg/mL too and the concentration of TCEP is done for a 1/1 ratio between TCEP and Fmoc-**A-SS-B**. The kinetics is followed every 10 min. For the assays using a 1/1 ratio of TCEP with peptide, the peptide is solubilized first then the TCEP is added and after 1 min, the protein is added to be sure that the Fmoc-**A-SS-B** is totally converted into Fmoc-**A-SH** before the addition of the protein. All solutions were freshly prepared in PBS buffer and filtrated with a PTFE 0.2  $\mu\text{m}$  filter before each experiment.

### **3.6.10. Fluorescence emission spectroscopy**

Microplate reader UV spectroscopy (FLX-Xenius®, SAFAS, Monaco) using SP2000V7 software was the main device entailed in the fluorescence measurement of the  $\pi$ -stacking. To follow the  $\pi$ -stacking of the Fmoc group, we excite our molecule at 280 nm and take our spectrum in the range 300-600 nm. The fluorescence assays were done for hydrogels in solution (Fmoc-**A-SS-B** (10 mg/mL with GR and 30 mg/mL for AP and BSA), enzymes (20  $\mu\text{L}$ /mL for GR and 30 mg/mL for BSA and AP) and TCEP in ratio 1/1 with the peptide), diluted solutions (peptide and enzymes at 1 mg/mL) and in surface by adding the glass slide at the bottom of the well and following the protocol describe in section 3.6.3. For the assays using a 1/1 ratio of TCEP with peptide, the peptide is solubilized first then the TCEP is added and after 1 min, the protein is added to be sure that the Fmoc-**A-SS-B** is totally converted into Fmoc-**A-SH** before the addition of the protein.

### **3.6.11. Rheology measurements**

Rheological properties were measured in a Kinexus Malvern rheometer using a plate geometry of 20 mm diameter and a gap of 0.5 mm. Firstly, 380  $\mu\text{L}$  of Fmoc-**A-SS-B** (10 mg/mL) were mixed with 20  $\mu\text{L}$  (20  $\mu\text{L}$ /mL) of GR directly over the plate of the rheometer and the gelation process was followed at a fixed frequency of 0.3 Hz and 0.06 % strain for 30 min until a plateau was reached. Subsequently, strain measurements were carried out from 0.01% to 100% at 0.3Hz and frequency sweeps were performed from 0.01 Hz to 10 Hz at a fixed strain of 0.06%.

### **3.6.12. Nuclear Magnetic Resonance (NMR)**

#### *Principle*

NMR spectroscopy consists in observing the transitions between two energy levels very close to a core subjected to a magnetic field. When a hydrogen nucleus is subjected to a  $H_0$  field, the nuclei will align with the magnetic field (i.e. their magnetic spin moment  $\mu$ ). Their magnetic quantum number of spin will have either  $m_s = \frac{1}{2}$  value, the most stable state

in the same direction as  $H_0$ , i.e.  $m_s = -1/2$  as opposed to  $H_0$  and minority (valid for spin -1 number nuclei =  $1/2$ ) (Figure 11). The ratio between the two populations is close to 1. This results in a slight magnetization denoted  $M_0$ <sup>19</sup>.

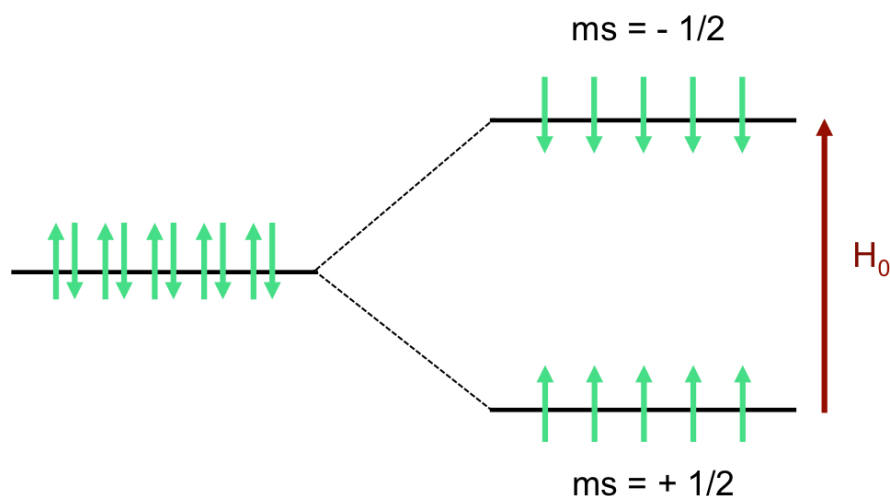


Figure 11: Nucleus under a magnetic field

When the nucleus is subjected to  $H_0$ , it aligns itself on the field but also enters precession (following its movement of rotation on itself). The magnetic moment takes an angular velocity proportional to  $H_0$ :  $\omega_0 = \gamma B_0$  (Figure 12, left).

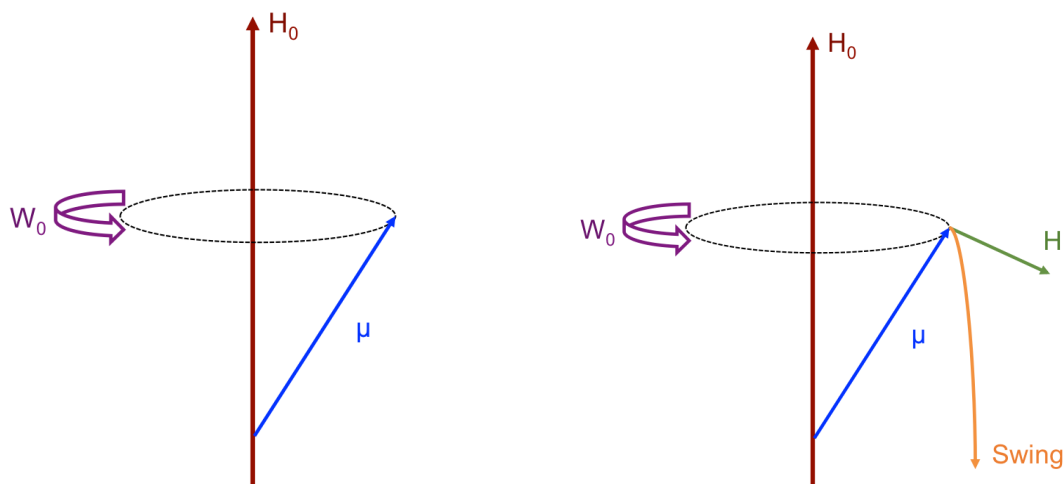


Figure 12: The nucleus when subjected to  $H_0$  (left) and when subjected to a field  $H_1$  (right).

For tilting, it is necessary to apply a field  $H_1$  perpendicular to  $\mu$  so that the generated force flips  $\mu$  (rule of Lorentz) (Figure 12, right)<sup>20</sup>.

If the field  $H_1$  is fixed the condition is filled only once per rotation, hence the obligation to create a rotating field  $H_1$ . Concretely, a rotating field is simulated using a solenoid and an alternating current. The simulated rotation speed  $\omega_1$  must be equal to  $\omega_0$ . The conditions for a switchover are thus always fulfilled. When the Larmor frequency is reached, there is resonance and tilting of the magnetization  $M_0$ . The technique using a fixed frequency and a field sweep is abandoned for the pulsed NMR because many precise:  $H_0$  remains fixed, and sends a "flash" radio frequency sweeping the frequency area of interest. One thus excites all the nuclei of a blow.

The chemical shift makes it possible to determine the relative position of the absorption frequencies. The reference used is tetramethylsilane (TMS).

The chemical shift denoted  $\delta$ , in ppm (parts per million). It is determined using the following relationship:

$$\delta = \frac{\nu_H - \nu_{TMS}}{\nu_{TMS}}$$

TMS is used as a reference because it has a high screen constant, is volatile, soluble in organic solvents, chemically inert and used in small amounts. If the signal is emitted near the TMS we speak of strong field: there is shielding. If the signal is emitted far from the TMS (weak field) there is clearing. The chemical shift varies from 0 to 15 ppm.

In NMR, not all nuclei perceive the same magnetic field, this effect is called the screen effect. It is necessary to consider the field received by the proton (the nucleus). In the absence of electrons, the perceived field  $H$  is equal to the field of the magnet  $H_0$  (Figure 13a). The conditions of the fundamental relationship of the NMR are fulfilled and there can be resonance. But the presence of electron will oppose the field  $H_0$ . The effect will be more or less strong depending on the surrounding electronic density. Conditions are no longer fulfilled for there to be resonance. Thus, it will be necessary to increase the field  $H_0$  so that the effective field perceived by the atom  $H$  (Figure 13b) is effectively equal to  $H_0$  in the absence of electron. This does not translate the relation:  $H_{\text{effective}} = H_0 + \sigma H_0$  with  $\sigma$  the screen constant.

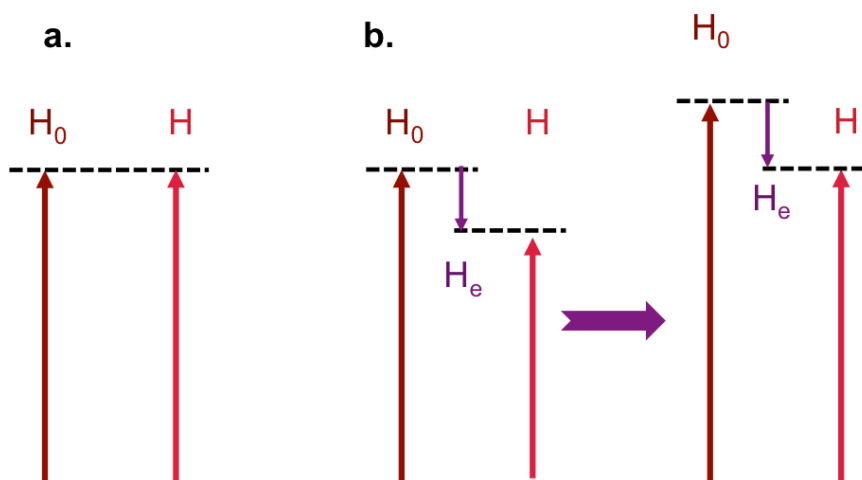


Figure 13: a) In absence of electron, b) in presence of electron, increase of the  $H_0$  to reach the resonance.

Depending on the electronegativity of atoms close to the hydrogen, it will be shielded or unshielded. If the surrounding environment is very electronegative, it will attract the electrons towards it (O atom for example). The electron density will be lower at the hydrogen level. The resonance will be at a weaker magnetic field than if the surrounding atoms had no influence. It is said that there is a clearing. If not, we say that there is shielding. In practice TMS (tetramethylsilane) is used as reference because it has a strong shielding due to silicon.

The screen effect comes from 3 factors:

**Diamagnetic contribution:** it is related to the circulation of the electrons of the atom considered. The electrons will create an induced magnetic field that opposes the applied magnetic field

**Paramagnetic contribution:** very low, it depends on the possibility that a nucleus to provide an excited state or not.

**Anisotropic contribution:** this is the main contribution. It is due to the electronic circulation of neighboring groups.

### *Experimental Setup*

$^1\text{H}$ -NMR spectra were recorded on a Bruker Avance 400 spectrometer at 400 MHz in the specified solvent at 25°C. The spectra were internally referenced to the residual solvent signal. The chemical shifts are given in ppm and coupling constants  $J$  are listed in Hz. The following notation is used for the  $^1\text{H}$ -NMR spectral: singlet (s), doublet (d), triplet (t), multiplet (m).  $^1\text{H}$  NMR is used to characterize peptide synthesis, but also to determine if the peptide pre-aggregates itself. In NMR, if the peptide pre-aggregates, the signals corresponding to the part of the peptide involved in the aggregation will disappear.

**Experimental set-up concerning the  $^1\text{H}$  NMR measurement in D<sub>2</sub>O:** Fmoc-**A-SS-B** (30 mg) was dissolved in 1 mL of deuterated water, vortexed 5 min and treated in an ultrasound bath during 5 min. Then the solution was added to the NMR tube. BSA (30 mg/mL) or TCEP (1 molar equivalent) was added directly in the 30 mg/mL of Fmoc-**A-SS-B** solution. The mixture was vortexed before transferred inside an NMR tube for analysis. The  $^1\text{H}$  NMR spectrum of solely BSA was recorded as following: 30 mg of BSA was solubilized in 1 mL of deuterated water and vortexed. Then, the  $^1\text{H}$  NMR spectra were recorded. Addition of DMSO in D<sub>2</sub>O and  $^1\text{H}$  NMR analysis was done as following: 5 mg of Fmoc-**A-SS-B** was solubilized in 1 mL D<sub>2</sub>O in a vial, vortexed during 1 min and finally dipped in an ultrasound bath during 2 min. Then the solution is transferred into a NMR tube. The first spectrum is taken. Then we added inside the NMR tube 10  $\mu\text{L}$  per 10  $\mu\text{L}$  of DMSO (in D<sub>2</sub>O). The solution is homogenized by turning the NMR tube upside-down 3 times before  $^1\text{H}$  NMR recording.

### **3.6.13. Circular Dichroism**

Circular dichroism (CD) spectra were recorded using a Jasco J-1100 spectropolarimeter with a data pitch of 1 nm on the light wavelength. The CD spectra show the ellipticity expressed as an angle as a function of the wavelength. Liquid samples were inserted in a quartz cell of path length 1 mm. Solutions were maintained at 25°C using a Peltier apparatus with an accuracy of  $\pm 0.2$  °C.

### **3.6.14. High Resolution Mass Spectroscopy (HRMS)**

All spectra were done by a platform from the Laboratoire de spectrométrie de masse Bio-organique (Département des sciences analytiques, Institut Pluridisciplinaire Hubert Curien, UMR 7178 (CNRS-UdS) ECPM, 25 rue Becquerel F67087-Strasbourg-Cedex 2). For doing the mass analysis they performed them on a microTOF-Q mass spectrometer (Bruker Daltonics GmbH, Bremen, Germany). This instrument was used at a maximum accelerating potential of 20 kV in positive mode and was operated in linear mode at 19 kV. The delay extraction was fixed at 80 ns and the frequency of the laser (nitrogen 337 nm) was set at 5 Hz. Each raw spectrum was opened with flexAnalysis 2.4 build 11 (Bruker Daltonics GmbH, Bremen, Germany) software.

### **3.6.15. Syntheses of Fmoc-A-SS-B and A-SS-B**

Both peptides Fmoc-A-SS-B and A-SS-B were prepared using solid support chemistry.

The “Fmoc strategy” was used based on 2-CTC resin.<sup>21</sup> The following synthetic pathway is given in the scheme below.

General procedure:

- Step a: loading of the resin. Addition of 3 eq/r of Fmoc-Glu(OtBu)-OH + 6 eq/r of DIEA in 3 mL of DMF for 300 mg of resin. The solution in contact with the resin is stirred at RT for 2 h. Then, the solution is removed and a solution of MeOH is added at RT for 1 h.
  - Step b: Fmoc group deprotection: 3 mL of a 20% of piperidine in DMF solution is added and stirred at RT for 15 min.
  - Step c: Coupling step: 3 eq/r of Fmoc-amino acid + 3 eq/r of HOBt + 3 eq/r of HBTU + 6 eq/r of DIEA are added in 3 mL of DMF and let in contact with the resin at RT for 30 min.
  - Step d: Cleavage of the resin and lateral chains deprotection: addition of 3 mL of a solution containing 95 % TFA + 2.5 % H<sub>2</sub>O + 2.5 % triisopropylsilane it's stirred at RT for 2 h. Then the solution is filter. The solvent is then removed. Finally the product is precipitate by using a small amount of cold ether.
- Between each step a, b, c and d, a rinsing stage is executed by using 5 times 3 mL of DMF and then a Kaiser test is made to confirm the achievement of the coupling or deprotection steps.

## REFERENCES

1. a) Lehn, J.-M., *Supramolecular chemistry: concepts and perspectives*, in *Supramolecular Chemistry*, Wiley-VCH, Weinheim, **1995**, b) Aida, T., *et al.*, Functional supramolecular polymers, *Science*, **2012**, 335, 813, c) Mattia, E., and Otto, S., Supramolecular systems chemistry, *Nat. Nanotechnol.*, **2015**, 10, 111., d) Lehn, J.-M., Perspectives in chemistry-aspects of adaptive chemistry and materials, *Angew. Chem., Int. Ed.*, **2015**, 54, 3276.
2. a) Mann, S., Life as a nanoscale phenomenon, *Angew. Chem., Int. Ed.*, **2008**, 47, 5306., b) Barral, J., and Epstein, H., Protein machines and self-assembly in muscle organization, *BioEssays*, **1999**, 21, 813., c) Li, R., and Albertini, D., The road to maturation: somatic cell interaction and self-organization of the mammalian oocyte, *Nat. Rev. Mol. Cell Biol.*, **2013**, 14, 141.
3. a) Williams, R., *et al.*, Enzyme-assisted self-assembly under thermodynamic control, *Nat. Nanotechnol.*, **2009**, 4, 19., b) Williams, R., *et al.*, The in vivo performance of an enzyme-assisted self-assembled peptide/protein hydrogel, *Biomaterials*, **2011**, 32, 5304., c) Olive, A., *et al.*, Spatial and directional control over self-assembly using catalytic micropatterned surfaces, *Angew. Chem., Int. Ed.*, **2014**, 53, 4132., d) Vigier-Carrière, C., *et al.*, Bioactive seed layer for surface-confined self-assembly of peptides, *Angew. Chem., Int. Ed.*, **2015**, 54, 10198., e) Rodon Fores, J., *et al.*, Localized supramolecular peptide self-assembly directed by enzyme-induced proton gradients, *Angew. Chem., Int. Ed.*, **2017**, 56, 15984., f) Spitzer, D., *et al.*, Surface-assisted self-assembly of a hydrogel by proton diffusion, *Angew. Chem., Int. Ed.*, **2018**, 57, 11349.
4. Du, X., *et al.*, Supramolecular hydrogelators and hydrogels: from soft matter to molecular biomaterials, *Chem. Rev.*, **2015**, 115, 13165.
5. a) Yang, Z., *et al.*, Enzymatic formation of supramolecular hydrogels, *Adv. Mater.*, **2004**, 16, 1440., b) Yang, Z., and Xu, B., Using enzymes to control molecular hydrogelation, *Adv. Mater.*, **2006**, 18, 3043.
6. a) Toledano, S., *et al.*, Enzyme-triggered self-assembly of peptide hydrogels via reversed hydrolysis, *J. Am. Chem. Soc.*, **2006**, 128, 1070., b) Thornton, K., *et al.*, Controlling stiffness in nanostructured hydrogels produced by enzymatic dephosphorylation, *Biochem. Soc. Trans.*, **2009**, 37, 660., c) Williams, *et al.*, Exploiting biocatalysis in peptide self-assembly, *Biopolymers*, **2010**, 94, 107.
7. a) Qin, X., *et al.*, Enzyme-triggered hydrogelation via self-assembly of alternating peptides, *Chem. Commun.*, **2013**, 49, 4839., b) Hu, B.-H., and Messersmith, P., Rational design of transglutaminase substrate peptides for rapid enzymatic formation of hydrogels, *J. Am. Chem. Soc.*, **2003**, 125, 14298., c) Bremmer, S., *et al.*, Enzyme-triggered gelation: targeting proteases with internal cleavage sites, *Chem. Commun.*, **2014**, 50, 1691., d) Chronopoulou, L., *et al.*, Lipase-supported synthesis of peptidic hydrogels, *So Matter*, **2010**, 6, 2525., e) Liu, Y., *et al.*, Glucose oxidase-mediated gelation: a simple test to detect glucose in food products, *J. Agric. Food Chem.*, **2012**, 60, 8963.
8. a) Pappas, C., *et al.*, Dynamic peptide libraries for the discovery of supramolecular nanomaterials, *Nat. Nanotechnol.*, **2016**, 11, 960., b) Debnath, S., *et al.*, Peptide nanofibers with dynamic instability through non-equilibrium biocatalytic assembly, *J. Am. Chem. Soc.*, **2013**, 135, 16789., c) Nalluri, S., and Ulijn, R., Discovery of energy transfer nanostructures using gelation-driven dynamic combinatorial libraries, *Chem. Sci.*, **2013**, 4, 3699., d) Rasale, D., *et al.*, Chemical reactions directed peptide self-assembly, *RSC Adv.*, **2015**, 5, 1529.
9. a) Plas, J., *et al.*, Insights into dynamic covalent chemistry at surfaces, *Chem. Commun.*, **2015**, 51, 16338., b) Bartolec, B., *et al.*, Dynamic combinatorial evolution within self-replicating supramolecular assemblies, *Chem. Commun.*, **2018**, 54, 13096.
10. Yang, C., *et al.*, Molecular hydrogels with esterase-like activity, *Chin. J. Chem.*, **2013**, 31, 494.
11. Smith, A., *et al.*, Fmoc-diphenylalanine self assembles to a hydrogel via a novel architecture based on  $\pi$ - $\pi$  interlocked  $\beta$ -sheets, *Adv. Mater.*, **2008**, 20, 37.
12. a) Marti-Centelles, R., and Escuder, B., Protein-induced low molecular weight hydrogelator self-assembly through a self-sustaining process, *Chem. Nano Mat.*, **2018**, 4, 798., b) Draper,

- E., *et al.*, Opening a can of worm (-like micelle): the effect of temperature of solutions of functionalized dipeptides, *Angew. Chem., Int. Ed.*, **2017**, *129*, 10603., c) Colquhoun, C., *et al.*, Controlling the network type in self-assembled dipeptide hydrogels, *So Matter*, **2017**, *13*, 1914., d) Morris, K., *et al.*, Structural determinants in a library of low molecular weight gelators, *So Matter*, **2015**, *11*, 1174., e) Raeburn, J., *et al.*, The effect of solvent choice on the gelation and final hydrogel properties of Fmoc-diphenylalanine, *So Matter*, **2015**, *11*, 927.
13. Javid, N., *et al.*, Cooperative self-assembly of peptide gelators and proteins, *Biomacromolecules*, **2013**, *14*, 4368.
  14. Martin, A., Controlling self-assembly of diphenylalanine peptides at high pH using heterocyclic capping groups, *Sci. Rep.*, **2017**, 43947.
  15. a) Reches, M., and Gazit, E., Controlled patterning of aligned self-assembled peptide nanotubes, *Nat. Nanotechnol.*, **2006**, *1*, 195., b) Ariga, K., *et al.*, Nanoarchitectonics: a new materials horizon for nanotechnology, *Mater. Horiz.*, **2015**, *2*, 406., c) Yang, B., *et al.*, Surface-mediated supramolecular self-assembly of protein, peptide, and nucleoside derivatives: from surface design to the underlying mechanism and tailored functions, *Langmuir*, **2018**, *34*, 15109.
  16. Decher, G., Fuzzy nanoassemblies: toward layered polymeric multicomposites, *Science*, **1997**, *277*, 1232.
  17. Martin, A., *et al.*, Controlling self-assembly of diphenylalanine peptides at high pH using heterocyclic capping groups, *Sci. Rep.*, **2017**, 43947.
  18. a) Sauerbrey, G., Verwendung von schwingquarzen zur wägung dünner schichten und zur mikrowägung, *Z. Phys.*, **1959**, *155*, 206., b) Voinova, M., *et al.*, Viscoelastic acoustic response of layered polymer films at fluid-solid interfaces: continuum mechanics approach, *Phys. Scr.*, **1999**, *59*, 391., c) Höök, F. *et al.*, Variation in coupled water, viscoelastic properties, and film thickness of a mefp-1 protein film during adsorption and cross-linking: a quartz crystal microbalance with dissipation monitoring, ellipsometry, and surface plasmon resonance study, *Anal. Chem.*, **2001**, *73*, 5796.
  19. [www.lachimie.fr](http://www.lachimie.fr), Résonance magnétique nucléaire. Cours théorique de RMN, 01/05/2019.
  20. Olivier Lequin, cours sur la Résonance magnétique nucléaire, UPMC.
  21. Kreutzer, A., and Salveson, P., Standard practices for Fmoc-based solid-phase peptide synthesis in the Nowick laboratory, **2018**, version 1.6.3.



## **Chapter 4**



**Localized supramolecular peptide self-assembly  
directed by enzyme-induced proton-gradients**





## Summary

<b>Context</b> .....	<b>130</b>
4.1. Abstract .....	134
4.2. Introduction .....	135
4.3. Results and discussion .....	136
4.4. Conclusion .....	141
4.5. Additional Figures .....	143
4.6. Experimental section .....	152
4.6.1. Materials .....	152
4.6.2. Preparation of Fmoc-AA-OH .....	153
4.6.3. Multilayer film preparation and hydrogel self-assembly .....	153
4.6.4. Quartz crystal microbalance with dissipation monitoring .....	153
4.6.5. O-dianisidine assay .....	154
4.6.6. Atomic force microscopy .....	154
4.6.7. Infrared spectroscopy .....	154
4.6.8. Scanning electron microscopy and cryo-SEM.....	155
<b>REFERENCES</b> .....	<b>156</b>



## Context

Nine years ago, my host group has introduced a new concept of localized film buildup based on a gradient of catalysts produced from an electrode. This has been illustrated by the reduction of  $\text{Cu}^{2+}$  in  $\text{Cu}^{1+}$  which catalyzes the covalent crosslinking of polymers by click chemistry, leading to a thin polymer nanofilm coated on the electrode (Figure 1 left)<sup>1</sup>. The spatially controlled generation of this catalyst is responsible for the polymer film buildup localization. By analogy with the term used in the biology development field, this catalyst was called “morphogen”. This strategy was extended to other kinds of morphogens: (i) using bis-quinone compounds generated from bis-catechol derivatives oxidized in situ at the surface of an electrode. This leads to a thin polymer film buildup covering the electrode surface by crosslinking polyamines (Figure 1 middle).<sup>2a</sup> (ii) Using  $\text{Fe}^{2+}$  oxidized in  $\text{Fe}^{3+}$  by an anodic current, it is also possible to create an organometallic layer onto the electrode by complexation of  $\text{Fe}^{3+}$  with tannic acid (Figure 1 right).<sup>2b</sup> (iii) Finally, proton generation from an electrode through hydroquinone oxidation has allowed the buildup of polyelectrolyte-based films using charge-shifting polymers.<sup>6</sup>

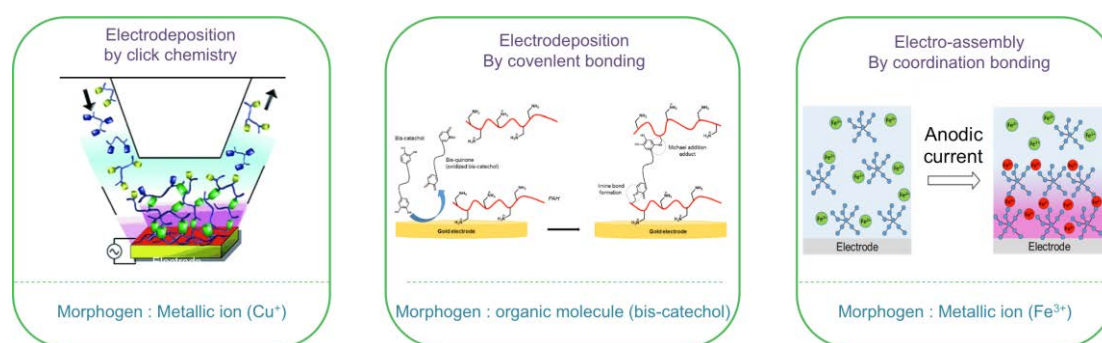


Figure 1: Strategies developed to initiate a localized self-assembly of polymeric film by electrochemistry. Copyright © (left) 2010, (middle) 2015 and (right) 2017, American Chemical Society.

The main drawback to use an electrode to initiate the localization of film self-construction is the requirement of a conductive material to produce the gradient of morphogens. This reduces considerably the scope of applications of this strategy. To overcome the use of conductive surfaces, my goal was to develop an enzymatically-active multilayer film able to generate a gradient of morphogens.

**In chapter four, I will present a convenient way to produce a proton gradient from a non-conductive surface by using an enzymatically-active multilayer film.**

---

- **Published article** - Wiley, *Angewandte Chemie, Int. Ed.* 2017, 56, 15984-15988.

Jennifer Rodon Fores, Miguel Léonardo Martínez Mendez, Xiyu Mao, Déborah Wagner, Marc Schmutz, Morgane Rabineau, Philippe Laval, Pierre Schaaf, Fouzia Boulmedais and Loïc Jierry

---

#### 4.1. Abstract

Electrodes are ideal substrates for surface localized self-assembly processes. Spatiotemporal control over such processes is generally directed through the release of ions generated by redox reactions occurring specifically at the electrode. The so-used gradients of ions proved their effectiveness over the last decade but are in essence limited to material-based electrodes, considerably reducing the scope of applications. Herein is described a strategy to generate enzymatically proton gradients from non-conductive surfaces. In the presence of oxygen, immobilization of glucose oxidase (GOx) on a multilayer film provides a flow of protons through enzymatic oxidation of glucose by GOx. The confined acidic environment located at the solid-liquid interface allows the self-assembly of Fmoc-AA-OH (Fmoc = fluorenylmethyloxycarbonyl and A = alanine) dipeptides into  $\beta$ -sheet nanofibres exclusively from and near the surface. In the absence of oxygen, a multilayer nano-reactor containing GOx and horseradish peroxidase (HRP) induces similarly Fmoc-AA-OH self-assembly.

## 4.2. Introduction

Self-assembly is an easy and powerful way to organize matter from molecular to nanometer scale and beyond.<sup>3</sup> Spatial and temporal control over the self-assembly process has allowed the emergence of materials with original features through the design of nanostructured coatings or materials giving rise to a large scope of applications.<sup>4,5</sup> Currently, several methods describe the directed initiation and growth of supramolecular self-assembly at an interface. Most of them are triggered by a physical external stimulus or due to a template effect coming from a prior surface treatment of the material. Recent investigations based on chemical gradients have demonstrated a great potential (*i*) to localize precisely in space the molecular buildup<sup>6</sup>, (*ii*) to control the assembly evolution over time<sup>7</sup> and (*iii*) to orientate the resulting nanostructure according to the features of one or several gradients.<sup>8</sup> This approach is inspired from reaction-diffusion processes found in Nature and appears as a promising way for further development of more complex chemical systems.<sup>9</sup>

Among the different gradient entities studied, protons are the most used because of their easy generation at a surface electrode. Indeed, oxidizing water or hydroquinone for instance leads to the production of protons that diffuse from the electrode to the surrounding environment, creating a confined acidic region at the interface. In 2010, Cameron's group described the surface-induced self-assembly of Fmoc protected dipeptides leading to the growth of a supramolecular hydrogel resulting in a dense fibre network.<sup>10</sup> Carbazole-protected amino acids have also been investigated for their spatially resolved self-assembly on electrode surfaces.<sup>11</sup> Using patterned electrodes, Payne demonstrated the specific control in space and time of the self-assembly of Fmoc protected phenylalanine by localized application of an electrical signal during a precise duration.<sup>12</sup> A fine electrochemical control of the proton production allowed triggering spatially and temporally resolved multicomponent hydrogels.<sup>13</sup> Surface-assisted self-assembly has also been used to develop efficient biosensors by immobilizing enzymes and bacteria.<sup>14</sup> Thus, the efficiency of this approach is well established but the restriction to use electrodes as surfaces reduces considerably its range of applications. In the domain of surface-assisted self-assembly of low molecular weight hydrogelators (LMWH), only one alternative was described so far, based on the introduction of sulfonic acid groups on a surface catalyzing the in situ formation of the hydrogelator.<sup>15</sup>

### 4.3. Results and discussion

Here, we describe the self-assembly of peptides directed by a continuous gradient of protons produced enzymatically on a non-conductive surface. Our model system is composed of (i) Fmoc-AA-OH (Scheme 1a), a LMWH already described as hydrogelator under acidic conditions in solution<sup>16,17</sup> and (ii) glucose oxidase (GOx), an enzyme producing protons through the transformation of glucose in gluconic acid in the presence of O<sub>2</sub> (Scheme 1b). Surface immobilization of GOx in a multilayer film will permit the production of protons in the presence of glucose. When Fmoc-AA-OH dipeptide diffuses toward the interface, its C-terminal carboxylate group is protonated which should induce spontaneously its self-assembly, solely at the interface (Scheme 1c). The buildup of GOx-coated surfaces and the evolution of the self-assembly process over time were followed both by quartz crystal microbalance (QCM-D) and attenuated total reflectance Fourier transformed infrared spectroscopy (ATR-FTIR). The morphology of the self-assembled architectures was investigated by atomic force microscopy (AFM), scanning electron microscopy (SEM) and *cryo*-SEM.

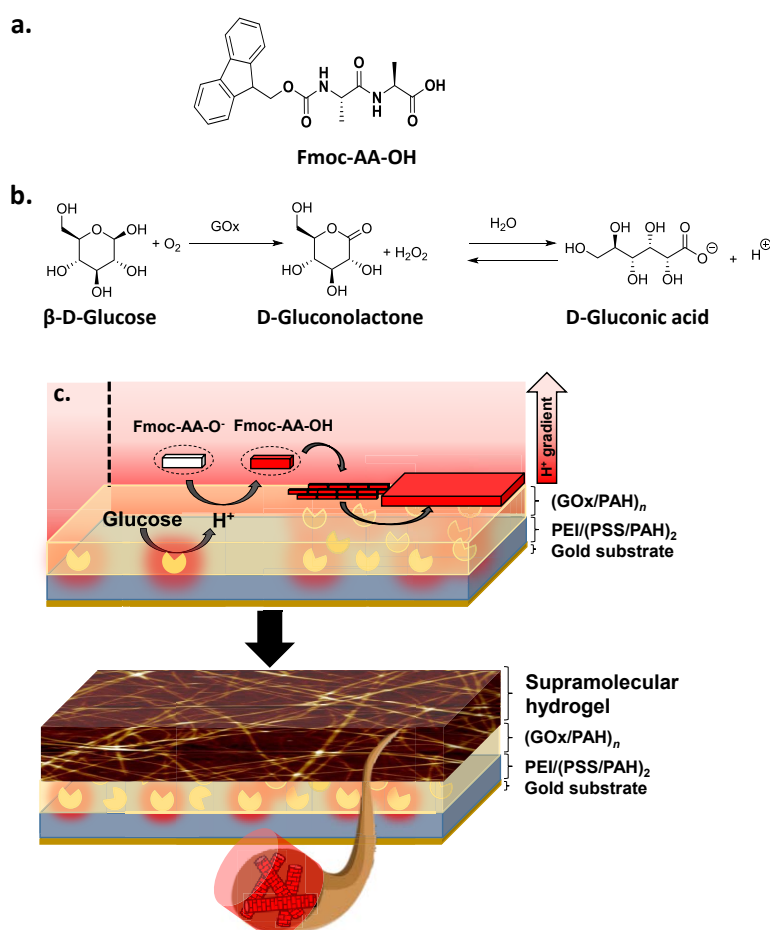


Schéma 1: **a)** Chemical structure of Fmoc-AA-OH dipeptide; **b)** Enzymatic oxidation of glucose by GOx; **c)** Enzymatically-triggered self-assembly of peptides through proton gradient generation from a non-conductive surface onto which is adsorbed GOx.

In solution, upside down vial tests of Fmoc-AA-OH (3.6 mg/mL) at different pH confirmed that gelation occurs in a few minutes at  $\text{pH} \leq 4$  (Figure S1). We have ensured that Fmoc-AA-OH (3.6 mg/mL, pH 5) can effectively lead to hydrogel formation within roughly 10 min in the presence of GOx (6.25  $\mu\text{M}$ ) and glucose (2 mg/mL, 11.10 mM) (Figure 2a). The isoelectric point (IP) of GOx is around 4.2. It can thus be electrostatically adsorbed onto a positively charged surface at pH 7. To immobilize GOx on a surface, we used the layer-by-layer technique based on the alternated deposition of polyanions and polycations on a surface<sup>18</sup>, a strategy already reported to design bioreactors<sup>19</sup>. We first modified the surface by dipping it into a solution of poly(ethylene imine) (PEI) and successively in poly(styrene sulfonate) (PSS) and poly(allylamine hydrochloride) (PAH) solutions to obtain a PEI/(PSS/PAH)<sub>2</sub> precursor multilayer film. GOx was then deposited and capped by a PAH layer to obtain the film PEI/(PSS/PAH)<sub>2</sub>/(GOx/PAH)<sub>1</sub>, named (GOx/PAH)<sub>1</sub> film. Its buildup was followed by QCM-D (Figure S2) and its thickness was evaluated to ~8 nm (ESI, Part 3). Its enzymatic activity was confirmed by spectrophotometric tests (Figure S3).

When a (GOx/PAH)<sub>1</sub> film was put in contact with a Fmoc-AA-OH/glucose solution under a flow rate of 700  $\mu\text{L}/\text{min}$ , an important decrease of the normalized frequency shift was observed by QCM-D over time indicating a deposition of mass (Figure 2c). After 40 min, the solution was replaced by the buffer solution (rinsing step) and the normalized frequency shift increased slightly until it stabilized at around -120 Hz. In addition, the dissipation value at 15 MHz was of the order of  $40 \times 10^{-6}$  in agreement with the formation of a hydrogel (Figure S4). Replacing GOx in the multilayer film by bovine serum albumin (BSA, Mw ~ 66 kDa, IP 4.7 at 25°C) or removing glucose from the Fmoc-AA-OH solution did not lead to any significant changes of the normalized frequency shift (Figure 2c). These control experiments highlight the crucial role of the enzymatic activity of GOx in the multilayer film to direct the localized self-assembly process of Fmoc-AA-OH through the generation of protons. To increase the enzymatic proton production, several layers of GOx alternated with PAH have been incorporated in the multilayer to obtain a PEI/(PSS/PAH)<sub>2</sub>/(GOx/PAH)<sub>n</sub>, film named (GOx/PAH)<sub>n</sub>, with  $n = 2, 3$  and 6. When a Fmoc-AA-OH/glucose solution was put in contact with each of these films, a higher decrease of the normalized frequency shift was observed in comparison to (GOx/PAH)<sub>1</sub> film, indicating more deposited mass (Figure S5 in ESI). After 40 minutes of contact, the thickness reached about ~1.1  $\mu\text{m}$ , ~ 2.3  $\mu\text{m}$ , ~ 3.2  $\mu\text{m}$  and ~ 3.3  $\mu\text{m}$  for self-assemblies induced by (GOx/PAH)<sub>1</sub>, (GOx/PAH)<sub>2</sub>, (GOx/PAH)<sub>3</sub> and (GOx/PAH)<sub>6</sub> films respectively (Figure 3a). These thicknesses were obtained from the QCM data by using the Voinova model (See ESI part 3). Thus, the thickness of the self-assembled hydrogel increases with the number of GOx/PAH layers and levels off for  $n > 3$ . This is probably due to the limited diffusion of glucose into the multilayer for films exceeding 3 bilayers of GOx/PAH on the top.



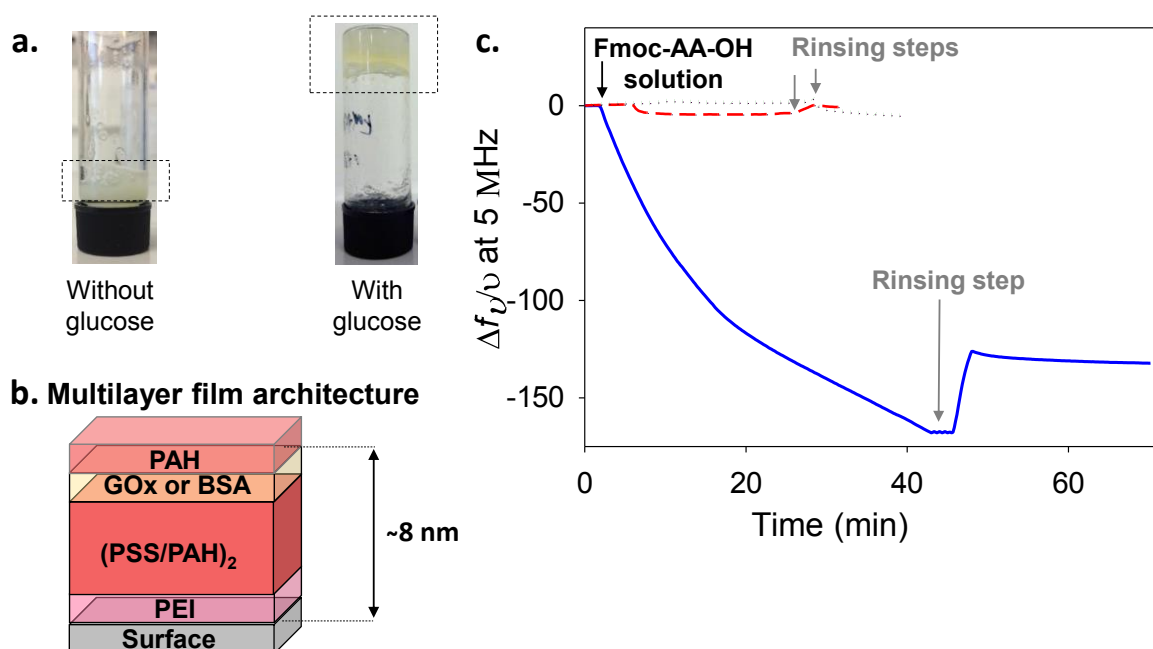


Figure 2: a) Upside down vial gelation tests of Fmoc-AA-OH in the presence of GOx; b) Architecture of (GOx/PAH)<sub>1</sub> and (BSA/PAH)<sub>1</sub> films; c) Evolution of the normalized frequency shift (QCM-D) over time during the contact of Fmoc-AA-OH/glucose solution (500  $\mu$ L/min) with (GOx/PAH)<sub>1</sub> (blue line), with (BSA/PAH)<sub>1</sub> film (red dashed line) and during the contact of Fmoc-AA-OH solution (without glucose) with a (GOx/PAH)<sub>1</sub> film (green dotted line).

Because glucose is the provider of protons through its oxidation by GOx, the influence of its concentration on the self-assembly buildup has also been investigated. In addition to the 2 mg/mL concentration used up to now, we also studied the self-assembly process and gelation that occur in presence of 0.5, 1, 1.5, 3, 4 and 5 mg/mL of glucose, keeping a constant concentration of Fmoc-AA-OH (1 mg/mL). When brought in contact with a (GOx/PAH)<sub>3</sub> multilayer film, QCM-D monitoring shows no significant decrease of the frequency shift for concentrations lower than 2 mg/mL, i.e. 0.5, 1 and 1.5 mg/mL, despite the presence of few fibres as observed by SEM (Figures S7a-c). This means that the self-assembly can occur at these low concentrations of glucose but no gelation starts. In contrast, an important and almost equivalent frequency shift is observed for each of the 3 higher glucose concentrations investigated. It thus appears that a critical concentration, which lies between 1.5 and 2 mg/mL, is necessary to get the formation of a hydrogel layer on the surface (Figure S7c). Higher glucose concentrations do not lead to layers thicker than the  $\sim 3.2 \mu$ m obtained with 2 mg/mL. In addition, we also observed that the diameter of the smaller peptide fibres observed by SEM is roughly 55 nm whatever the glucose concentration used (Figure S7d).

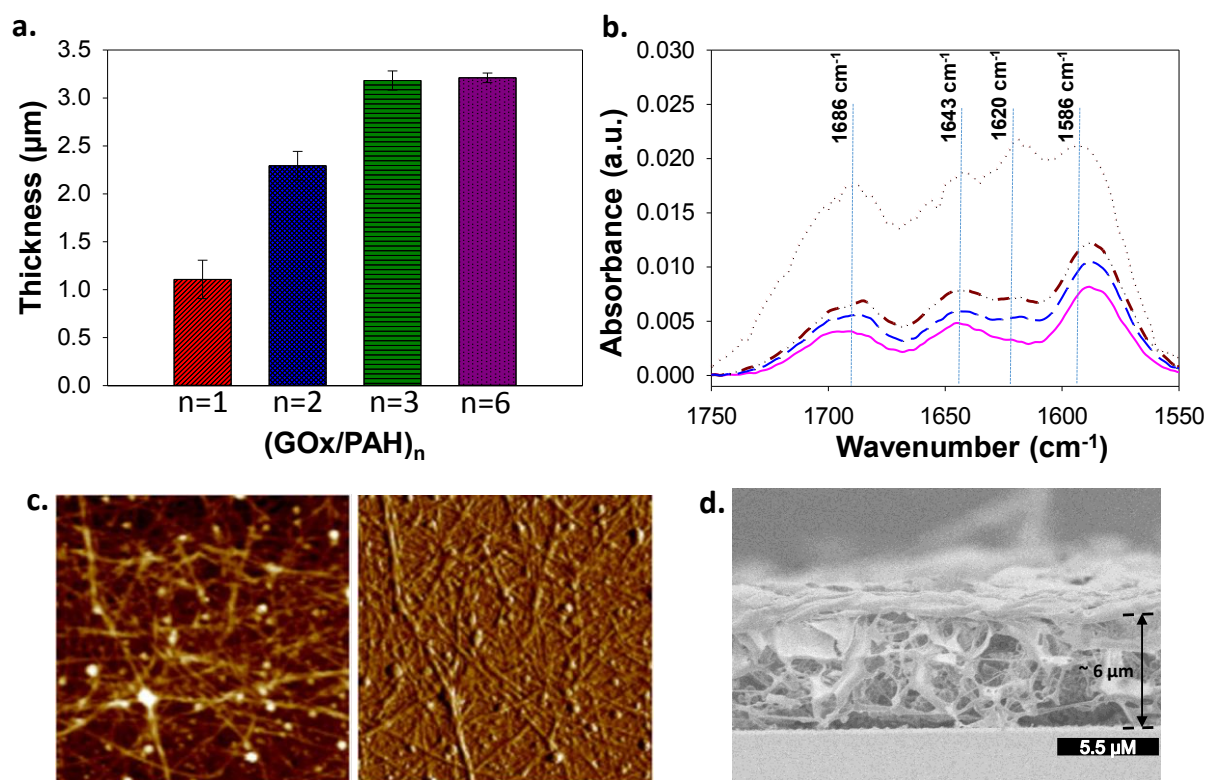


Figure 3: **a)** Thickness values of Fmoc-AA-OH self-assembly formed on  $(\text{GOx/PAH})_1$ ,  $(\text{GOx/PAH})_2$ ,  $(\text{GOx/PAH})_3$  and  $(\text{GOx/PAH})_6$  films. Standard deviations are calculated from three independent experiments; **b)** ATR-FTIR spectra of  $(\text{GOx/PAH})_3$  film in contact with Fmoc-AA-OH/glucose solution after 5 min (pink), 40 min (blue), 1h (green) and 12h (red dotted). These bands are visualized after subtraction of the spectra of  $(\text{GOx/PAH})_3$  film (Figure S6); **c)** Height and phase AFM images ( $5.5 \times 5.5 \mu\text{m}^2$ ) of Fmoc-AA-OH self-assembly (contact mode, dry state, z-scale 84 nm); **d)** Cryo-SEM cross-section image of Fmoc-AA-OH self-assembly in the z-section.

In order to confirm the self-assembly of Fmoc-AA-OH, ATR-FTIR experiments were performed during the contact of Fmoc-AA-OH/glucose solution with  $(\text{GOx/PAH})_3$  films built on a ZnSe crystal. When bringing the peptide/glucose solution in contact with the surface an increase in intensity of the amide I band region over time was observed. In particular three vibration bands at 1686, 1643 and 1620  $\text{cm}^{-1}$  appear (Figure 3b). The band at 1620  $\text{cm}^{-1}$  confirms a  $\beta$ -sheet structure adopted by the self-assembly of Fmoc-AA-OH. In addition, the presence of the band at 1686  $\text{cm}^{-1}$  allows the assignment of the antiparallel  $\beta$ -sheet conformation, which is consistent with observations done on others peptide-based supramolecular hydrogels.<sup>20</sup> The band at 1643  $\text{cm}^{-1}$  is characteristic of an amide band involved in polyproline II (PPII) conformation<sup>16a</sup>. The band located at 1586  $\text{cm}^{-1}$  and the peak area between 1750-1700  $\text{cm}^{-1}$  can be attributed to  $\text{COO}^-$  antisymmetric stretch and C=O stretching of COOH of gluconic acid Fmoc-AA-OH respectively. One observes a steady increase of the intensity of these bands over time during at least 12 hours confirming the gradual buildup of the self-assembled layer. When BSA replaces GOx in the multilayer, no formation of Fmoc-AA-OH hydrogel is observed by ATR-FTIR (Figure S8).

The morphology of the Fmoc-AA-OH self-assembly, obtained from (GOx/PAH)<sub>n</sub> films (n=1,3) after 40 min of contact with Fmoc-AA-OH/glucose solution was imaged by AFM in contact mode in dry state and by SEM. A network of long fibres extending up to several hundred nanometers was observed that underpin the hydrogel structure (Figure S9). This fibrous network is denser than the one obtained from (GOx/PAH)<sub>1</sub> film (Figures 3c and S10). To visualize the internal morphology of the localized self-assembly, a (GOx/PAH)<sub>3</sub> functionalized glass surface was put into contact with a Fmoc-AA-OH/glucose solution for 16 h, rinsed and imaged by cryo-SEM. The cross-section image shows the presence of an architecture of ~ 6 μm in thickness all along the glass surface (Figure 3d) highlighting the full covering of the substrate by the self-assembled hydrogel and showing a regular thickness all along the surface (Figure S11). It can be pointed that QCM and cryo-SEM indicate layer thicknesses exceeding several micrometers even if the absolute values differ by a factor of two. This may be due to the use of the model to treat the QCM data. We also verified that when a (GOx/PAH)<sub>3</sub> film is adsorbed on a specific area of the glass and this substrate is entirely brought in contact with glucose and Fmoc-AA-OH mixture, the resulting hydrogel is formed strictly in the area pre-coated by the multilayer film. Only some peptide-based fibres have spread over several micrometres at the interface between the multilayer area and the naked glass (Figure S12).

It must be noted that a slight flow (700 μL/min) of Fmoc-AA-OH/glucose was necessary for the self-assembly process to occur: only a low QCM signal was observed when the mixture was in contact with (GOx/PAH)<sub>3</sub> film without flow (Figure 4b). This can be explained by the fact that GOx requires a supply in O<sub>2</sub> to be effective, continuously brought by the flow of reactants. When Fmoc-AA-OH/glucose solution was degassed and injected with a similar flow rate, no decrease of the fundamental frequency shift was observed confirming this hypothesis (Figure S13). In order to provide in situ the fuel, i.e. O<sub>2</sub>, to the system without flow of the reactants, a second enzyme, the horseradish peroxidase (HRP), was added onto the multilayer film. This enzyme can transform H<sub>2</sub>O<sub>2</sub>, produced when glucose is reduced by GOx, into O<sub>2</sub> (Figure 4a).<sup>21</sup> With respect to its IP 8.8 the following multilayer has been investigated PEI/(PSS/PAH)<sub>2</sub>/GOx/PAH/PSS/HRP. Unfortunately, when this film was brought in contact with Fmoc-AA-OH and glucose, no self-assembly was observed (Figure S14). The efficiency of this system is sensitive to the spatial distance between the two enzymes: optimal motor can be effectively designed when both enzymes are spatially very close together.<sup>22</sup> Thus HRP was directly adsorbed onto GOx leading to the following multilayer PEI/(PSS/PAH)<sub>2</sub>/(GOx/HRP) named (GOx/HRP). When this film was brought in contact with a Fmoc-AA-OH/glucose without flow, a decrease of the normalized frequency shift was measured showing the self-assembly of Fmoc-AA-OH (Figure 4b) which was confirmed by ATR-FTIR and AFM experiments (Figures S15 and S16).

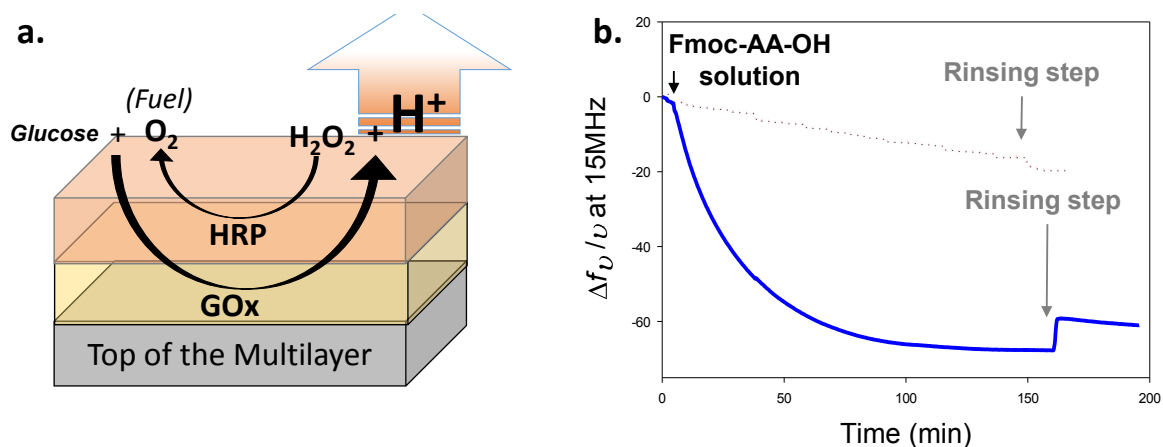


Figure 4: a) Enzymatically-triggered proton gradient generated from  $(\text{GOx}/\text{HRP})_1$  film; b) Evolution of the normalized frequency shift (QCM-D) over time when  $(\text{GOx}/\text{PAH})_3$  film (red dotted line) and  $(\text{GOx}/\text{HRP})$  film (blue line) are brought in contact with Fmoc-AA-OH/glucose without flow.

#### 4.4. Conclusion

In summary, despite recent developments of enzyme-assisted self-assembly strategies no approach has been reported involving enzyme-immobilized surfaces to create a flow of ions at an interface to initiate a self-assembly process. Herein, we present a first enzymatic system based on GOx to produce protons which trigger the self-assembly of a Fmoc-AA-OH peptide network. It requires the presence of  $\text{O}_2$  in solution. We also show that the simultaneous presence of GOx and HRP on top of the multilayer allows circumventing the outside supply of  $\text{O}_2$  through a cascade of reactions. Using this strategy allows getting rid of conductive substrates to realize proton-gradient induced self-assemblies and thus to generalize this type of self-assembly to almost any kind of substrate, whatever its nature and geometry. Such multi-enzymatic systems localized on surfaces lead to molecular motors that can tune (i) the self-assembly process, (ii) its resulting function, (iii) its sensitivity/responsivity to surrounding stimuli and finally (iv) its evolution over space and time. This approach is still in its infancy but represents an exciting perspective for further research.

#### Copyright information

Texts and figures of chapter 4 have been reprinted with permission from [Rodon Fores, J., *et al.*, Localized supramolecular peptide self-assembly directed by enzyme-induced proton gradients, *Wiley Angewandte chemie Int. Ed.*, **2017**, 56, 15984-15988.], Copyright 2019, Published by Wiley-VCH Verlag GmbH & Co.

### Highlights of the chapter

- ✓ It is possible to generate a proton gradient from a non-conductive surface.
- ✓ The system possesses a threshold of glucose amount to be able to produce enough proton to obtain the self-assembly
- ✓ The system presents a limit of enzyme layer, over which no influence on the self-assembly is observed.
- ✓ The main limit of the system is the requirement of oxygen but this drawback can be overcome by the utilization of an enzymatic tandem reaction using Gox with the HRP.

## 4.5. Additional Figures

Inverted tube tests to determine the pH range of the peptide gelation.

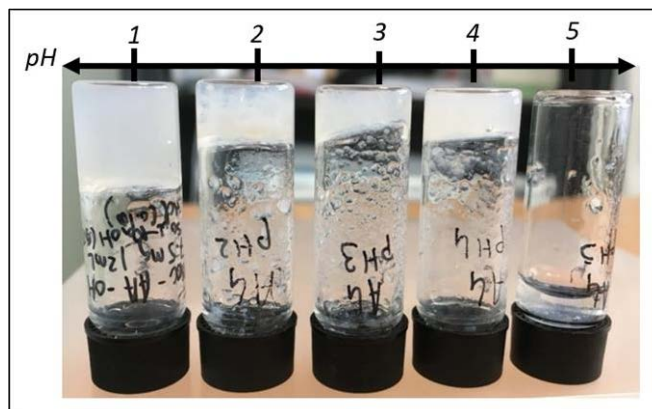


**Figure S1:** Upside down vial tests with Fmoc-AA-OH (0.98 mM) aqueous solutions prepared at different pH. First, 200  $\mu\text{L}$  of NaOH (0.5 M) solution were added to 3.6 mg of Fmoc-AA-OH until complete dissolution of the dipeptide obtained by stirring and/or sonication. Then, 800  $\mu\text{L}$  of ultrapure water were added to obtain 1 mL of dipeptide solution. Then, between 50 and 150  $\mu\text{L}$  of HCl (0.1 M) were added to adjust the pH from 5 to 1, respectively. Vials were turned upside down after 1 min.

QCM monitoring of the multilayer film PEI/(PSS/PAH)<sub>2</sub>/(GOx/PAH)<sub>1</sub> build-up.

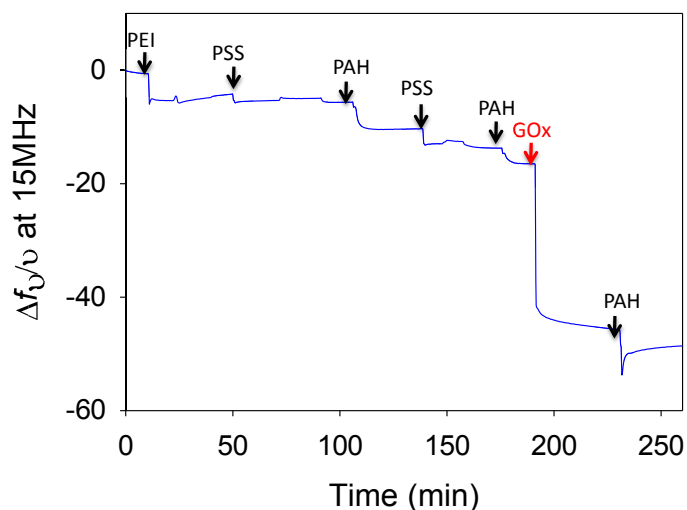


**Figure S2:** Evolution of the normalized frequency, measured at 15 MHz by QCM-D, as a function of time during the buildup of PEI/(PSS/PAH)<sub>2</sub>/(GOx/PAH)<sub>1</sub>.

## UV-Vis monitoring of the couple GOx/HRP activity.

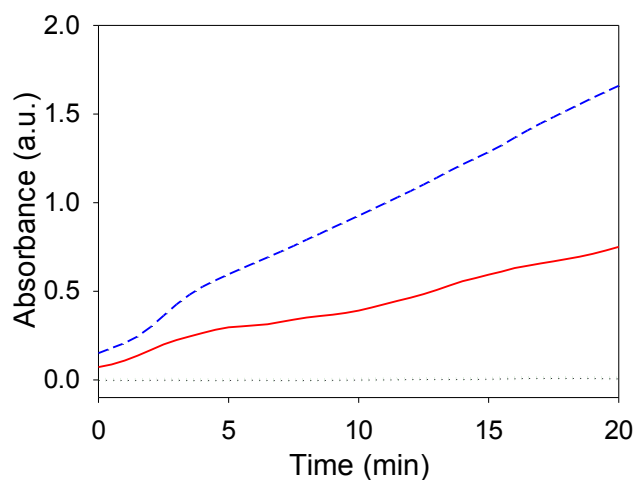


**Figure S3:** Evolution of the absorbance, measured at 440 nm, as a function of time of O-dianisidine/HRP/glucose mixture solution in contact with PEI/(PSS/PAH)<sub>2</sub>/(GOx/PAH)<sub>1</sub>, named (GOx/PAH)<sub>1</sub>, (red line), PEI/(PSS/PAH)<sub>2</sub>/(GOx/PAH)<sub>3</sub>, named (GOx/PAH)<sub>3</sub>, (blue dashed line) and PEI/(PSS/PAH)<sub>2</sub> film (green dotted line). HRP oxidizes colourless o-dianisidine into a brown coloured dye ( $\lambda = 440$  nm) using H<sub>2</sub>O<sub>2</sub> produced by the oxidation of glucose from GOx.

## Dissipation factors monitoring by QCM-D to follow the viscoelasticity of the Fmoc-AA-OH self-assembly.

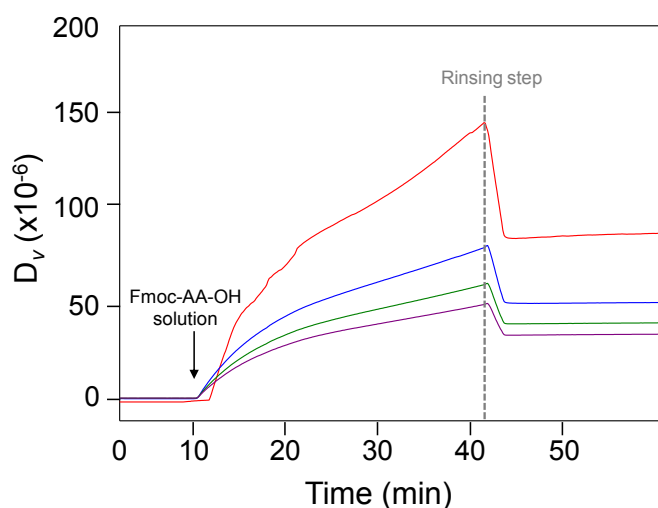


**Figure S4:** Evolution of the dissipation values  $D_v$ , measured by QCM-D, at the fundamental frequency ( $D_1$  at 5 MHz, red line), the third ( $D_3$  at 15 MHz, blue line), fifth ( $D_5$  at 25 MHz, green line) and seventh ( $D_7$  at 35 MHz, purple line) overtones as a function of time when (GOx/PAH)<sub>1</sub> film is brought in contact with Fmoc-AA-OH (1 mg/mL)/glucose (2 mg/mL) mixture solution followed by a rinsing step.

Optimization of the multilayer architecture on the Fmoc-AA-OH self-assembly monitored QCM-D.

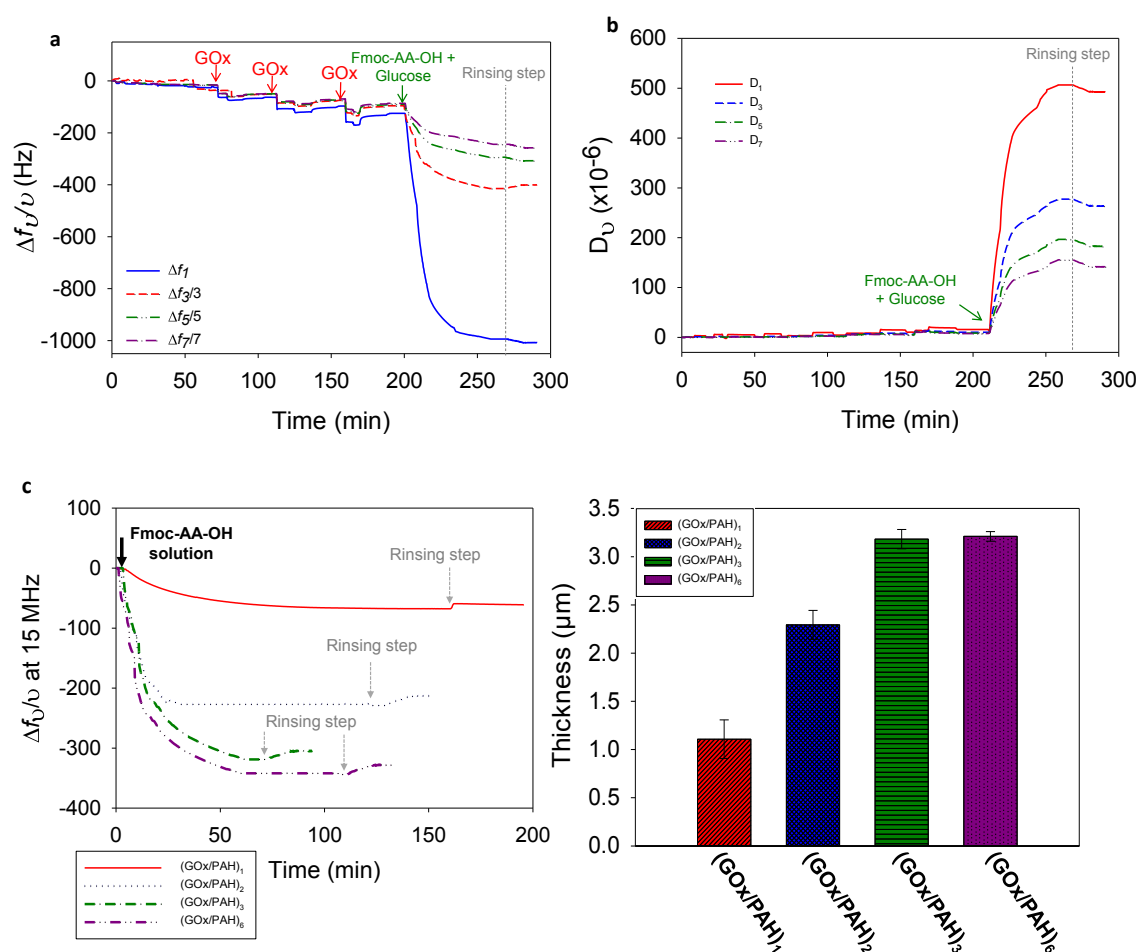


**Figure S5:** a) Evolution of the fundamental frequency shift and its overtones and, b) the corresponding dissipation values  $D_{\nu}$  as a function of time during the buildup of PEI/(PSS/PAH)<sub>2</sub>/(GOx/PAH)<sub>3</sub> named (GOx/PAH)<sub>3</sub>, followed by the contact with Fmoc-AA-OH (1 mg/mL)/glucose (2 mg/mL) mixture solution under a flow rate of 500  $\mu\text{L}/\text{min}$  and a rinsing step; c) (left) Evolution of the normalized frequency shift (15 MHz) when (GOx/PAH)<sub>n</sub> multilayer is brought in contact with Fmoc-AA-OH (1 mg/mL)/glucose (2 mg/mL) mixture solution under a flow rate of 500  $\mu\text{L}/\text{min}$  and a rinsing step. The number of bilayer  $n = 1, 2, 3$  and 6; (right) Thickness values of Fmoc-AA-OH self-assembly formed on (GOx/PAH)<sub>1</sub>, (GOx/PAH)<sub>2</sub>, (GOx/PAH)<sub>3</sub> and (GOx/PAH)<sub>6</sub> films, calculated from QCM data using the Voinova model (QTools software: see Part 3 in ESI). Standard deviations are calculated from three independent experiments



Infrared spectroscopy monitoring over time of the Fmoc-AA-OH self-assembly generated at the solid-liquid interface.

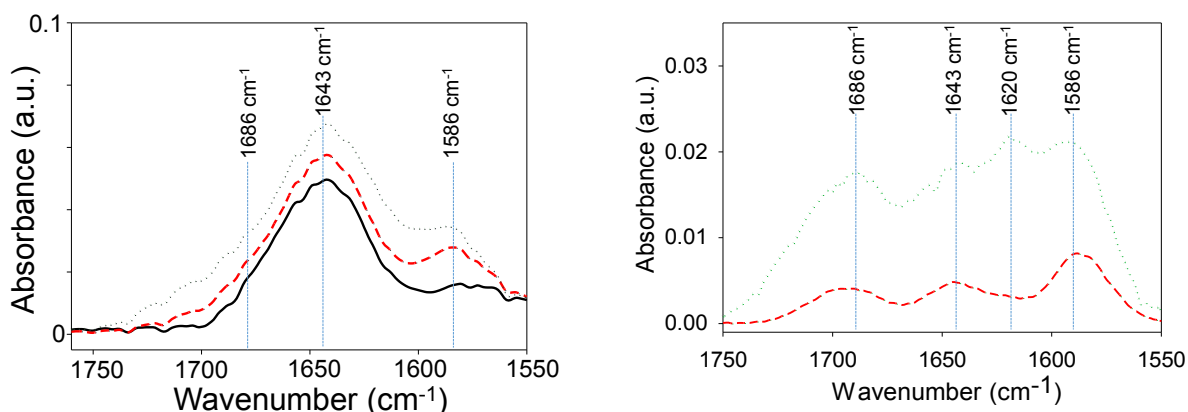
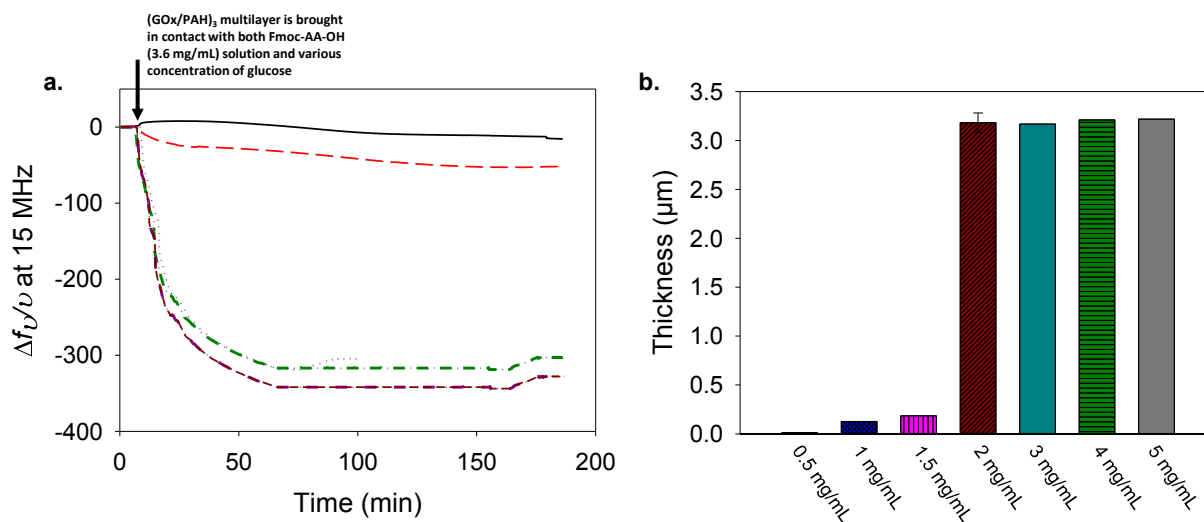
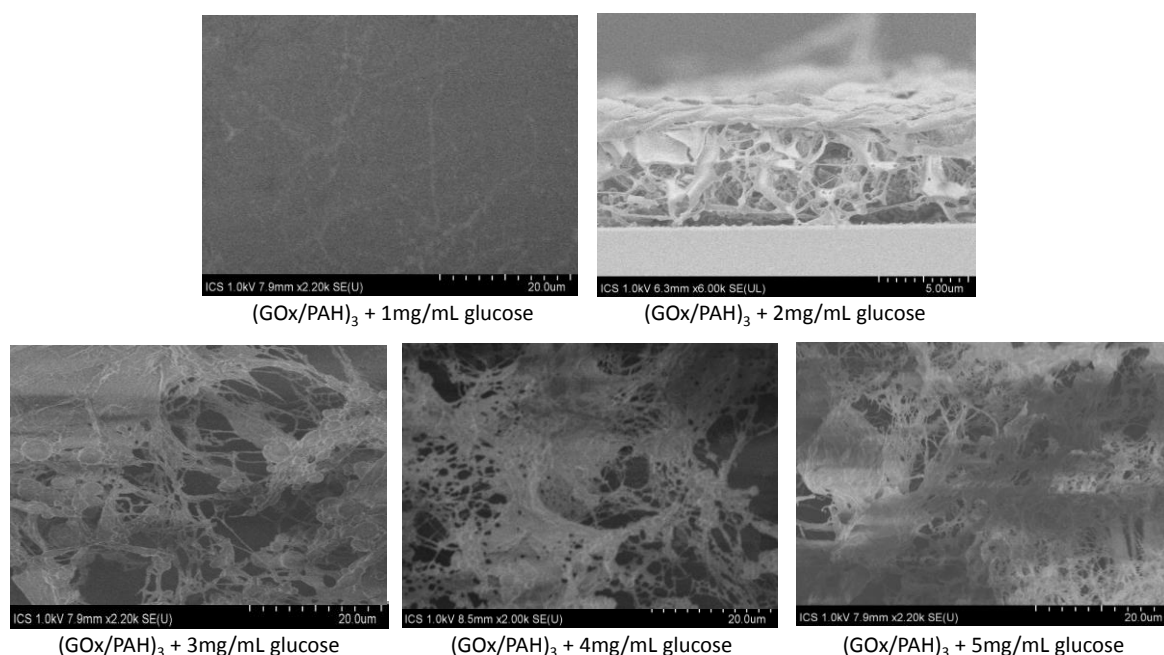


**Figure S6:** (left) ATR-FTIR spectra of  $(GOx/PAH)_3$  film (black line). This film was brought in contact with Fmoc-AA-OH (1 mg/mL)/glucose (2 mg/mL) mixture solution. Then, a first ATR-FTIR spectra  $t_5$  is recorded after 5 minutes (red dashed line) and a second spectra  $t_{12h}$  after 12 hours followed by a rinsing step (green dotted line); (right) to visualize the emergence of the different bands, the spectra of the  $(GOx/PAH)_3$  film was subtracted from  $t_5$  and  $t_{12h}$  spectra leading to the red dashed line (after 5 minutes) and the green dotted line (after 12h) respectively.

Influence of the glucose concentration on the Fmoc-AA-OH self-assembly.



c.



d.

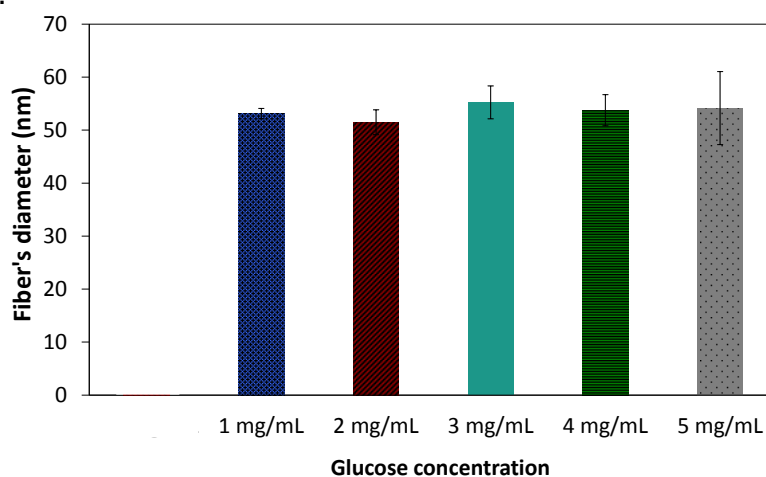


**Figure S7:** a) Evolution of the normalized frequency shift, measured at 15 MHz by QCM-D, as a function of time when  $(GOx/PAH)_3$  film is brought in contact with Fmoc-AA-OH and various concentration of glucose: 0.5 mg/mL, 1.0 mg/mL, 1.5 mg/mL, 2 mg/mL, 3 mg/mL, 4 mg/mL and 5 mg/mL; b) Thickness values of the supramolecular hydrogel formed on  $(GOx/PAH)_3$  multilayer film according to the solution mixture of Fmoc-AA-OH/glucose used, with various concentration of glucose. The thicknesses were calculated using QTools software; c) SEM images obtained from freeze-dried supramolecular hydrogel formed from  $(GOx/PAH)_3$  multilayer when brought in contact with both Fmoc-AA-OH solution (3.6 mg/mL) and various concentration of glucose; d) Diameter of the smaller fiber observed on SEM images in supramolecular hydrogel formed from various concentrations of glucose. Standard deviation are determined from at least three different fibers.

Infrared spectroscopy of the control test using BSA instead of GOx in the multilayer film.

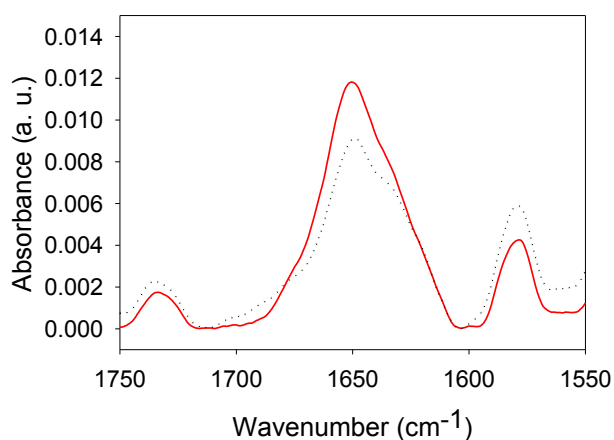


**Figure S8:** FTIR-ATR spectra of  $(\text{BSA/PAH})_1$  film recorded (red line) before and (green dotted line) after 40 min of contact with Fmoc-AA-OH (1 mg/mL)/glucose (2 mg/mL) mixture solution followed by a rinsing step.

Morphology of Fmoc-AA-OH self-assembly grew from the multilayer film (GOx/PAH) and study by AFM and cryo-SEM.

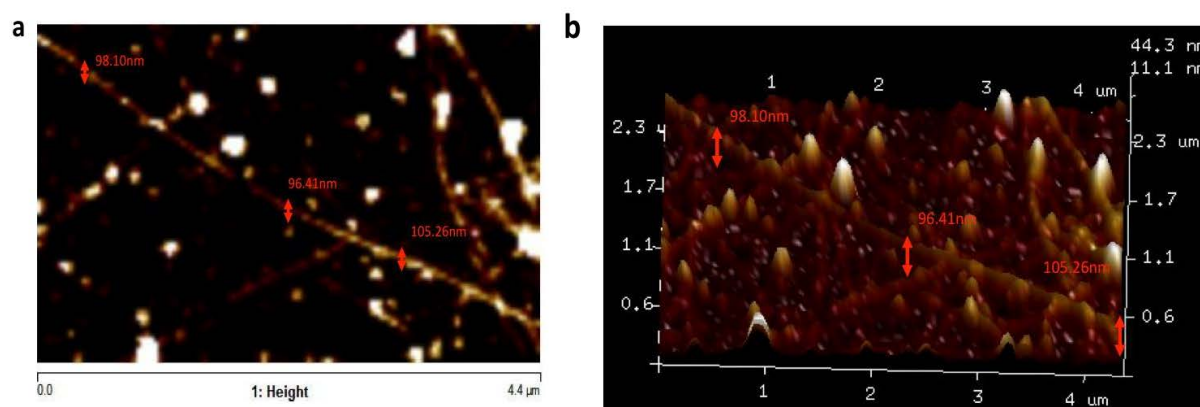


**Figure S9:** a) 2-D and, b) 3-D AFM phase images, obtained in contact mode and in dry state of  $(\text{GOx/PAH})_1$  film after 12 h or contact with Fmoc-AA-OH (1 mg/mL)/glucose (2 mg/mL) mixture solution followed by a rinsing step. These images show an isolated fiber to highlight its diameter.

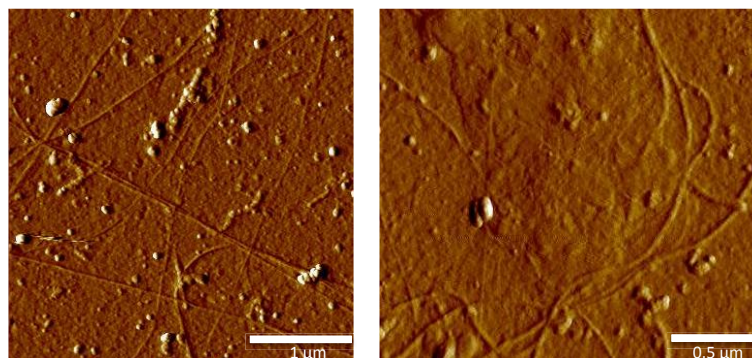


**Figure S10:** AFM phase images obtained in contact mode and in dry state, of  $(GOx/PAH)_1$  film after 12 h of contact with Fmoc-AA-OH (1 mg/mL)/glucose (2 mg/mL) mixture solution followed by a rinsing step.

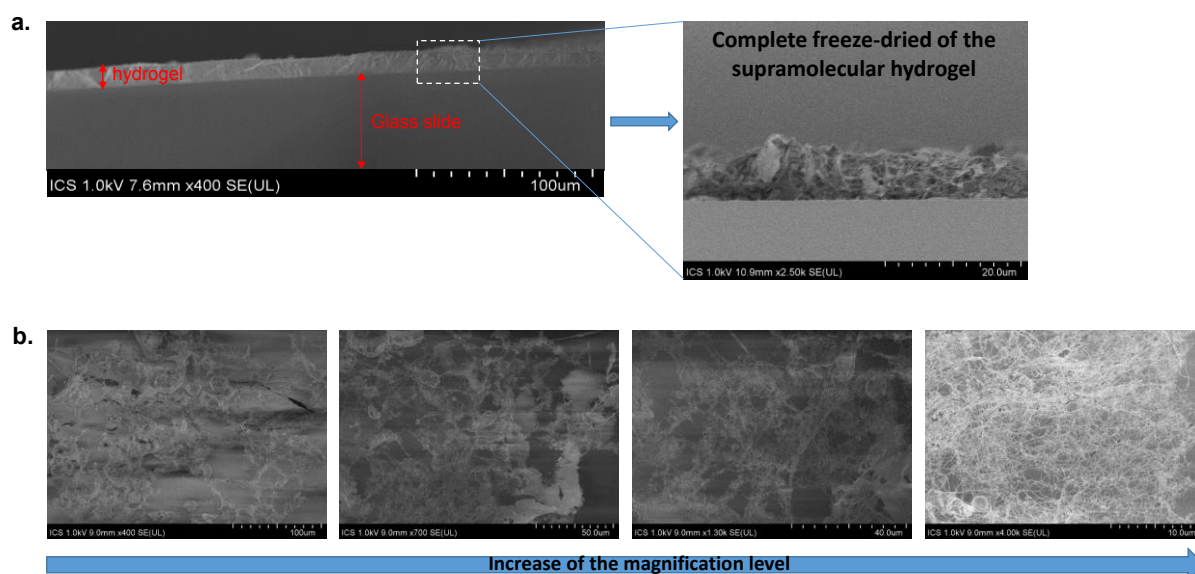


**Figure S11:** **a)** (right) Cryo-SEM image obtained from  $(GOx/PAH)_3$  multilayer after 12h of contact with both glucose (2 mg/mL) and Fmoc-AA-OH (3.6 mg/mL) solution before the freeze-dried process. The supramolecular hydrogel grew from  $(GOx/PAH)_3$  multilayer adsorbed on glass substrate. (left) Cryo-SEM image of the supramolecular hydrogel after a full freeze-dried treatment, **b)** increase of the magnification level to observe the self-assembly.

SEM experiments highlighting the possibility to control the localization of the self-assembly by the presence of the enzymatically-active multilayer film  $(GOx/PAH)_3$ .

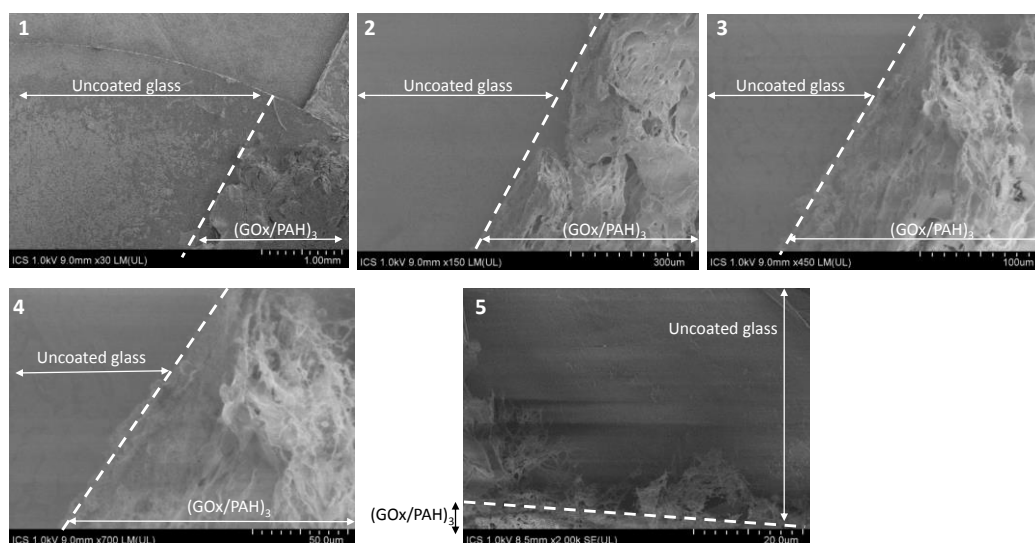


**Figure S12:** SEM images 1, 2, 3, 4 and 5 with increase of the magnification level going from 1 (millimeter scale) to 5 (micrometer scale). A multilayer film  $(GOx/PAH)_3$  has been deposited specifically on one side of a glass substrate (see Material and Methods section for more details) and the entire glass substrate brought in contact with the solution mixture containing Fmoc-AA-OH (3.6 mg/mL) and glucose (5 mg/mL) during 12 and then rinse before freeze-dried process and visualization by SEM.

QCM experiment showing the crucial importance  $O_2$  in the Fmoc-AA-OH self-assembly.

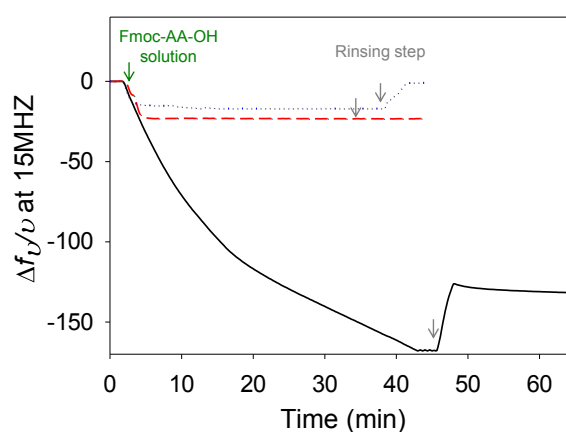


**Figure S13:** Evolution of the normalized frequency shift, measured at 15 MHz by QCM-D, as a function of time when  $(GOx/PAH)_1$  film is put in contact with (blue dotted line) a degassed Fmoc-AA-OH/glucose mixture under a flow rate of 500  $\mu\text{L}/\text{min}$ , (black line) non-degassed Fmoc-AA-OH mixture solution under a flow rate of 500  $\mu\text{L}/\text{min}$  and (red dashed line) without flow, followed by a rinsing step.

Optimization and characterization of the enzymatic tandem reaction.

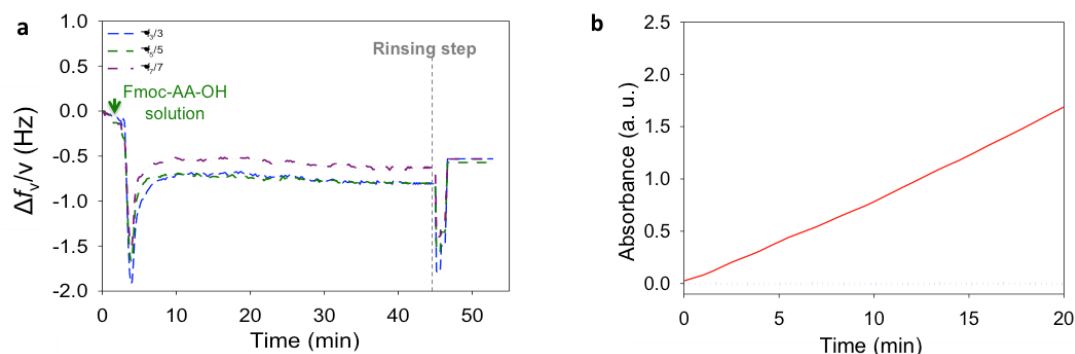


**Figure S14:** a) Evolution of the normalized frequency shifts, measured by QCM, as a function of time when PEI/(PSS/PAH)<sub>2</sub>/GOx/PAH/PSS/HRP film is put in contact with Fmoc-AA-OH (1 mg/mL) /glucose (2 mg/mL) mixture solution without flow rate and, b) Evolution of the absorbance, measured at 440 nm, as a function of time of o-dianisidine/glucose mixture solution in contact with PEI/(PSS/PAH)<sub>2</sub>/GOx/PAH/PSS/HRP film (blue dotted line) and (GOx/HRP)<sub>1</sub> film (red line).

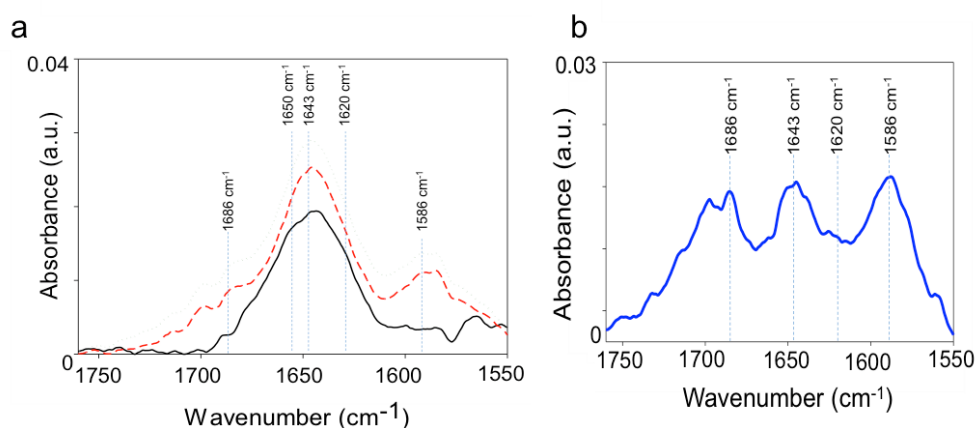


**Figure S15:** ATR-FTIR spectra of (GOx/HRP)<sub>1</sub> film recorded, a) before (black line), after 1 min (red dashed line) and 12 h (green dotted line) of contact with Fmoc-AA-OH (1 mg/mL)/glucose (2 mg/mL) mixture solution without flow and, b) after 40 min of contact after subtraction of the (GOx/HRP)<sub>1</sub> multilayer contribution.

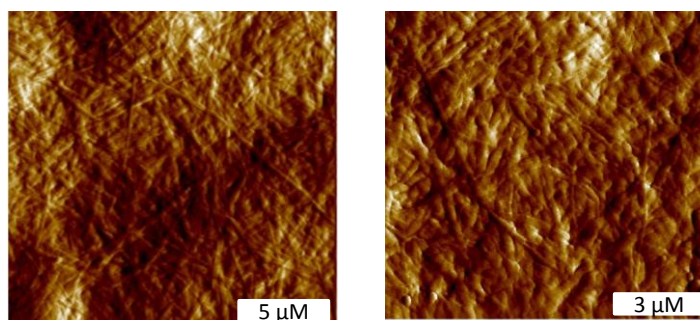


**Figure S16:** AFM phase images, obtained in contact mode and dry-state, of (GOx/HRP)<sub>1</sub> film after 12 h of contact with Fmoc-AA-OH/glucose mixture solution (without flow) followed by a rinsing step.

## 4.6. Experimental section

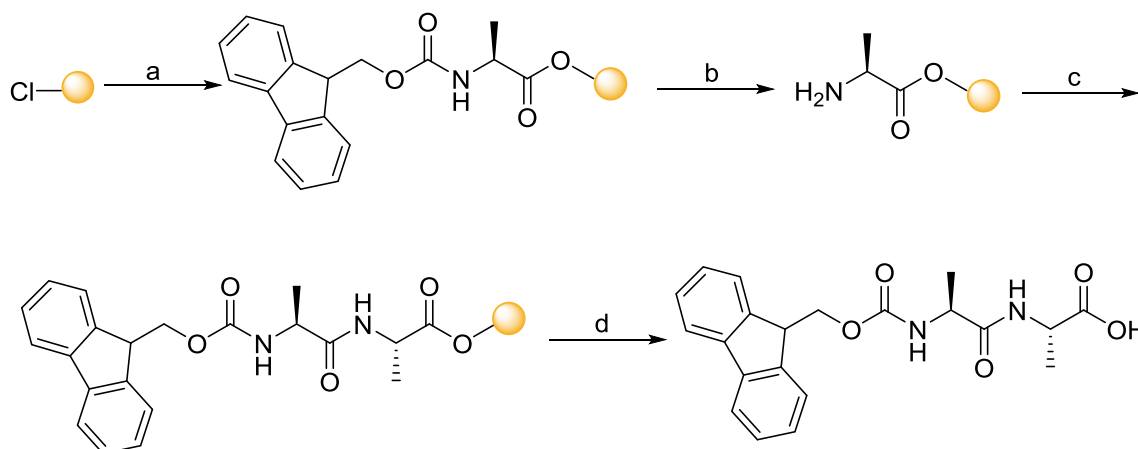
### 4.6.1. Materials

All chemicals used in this work are gathered in the following table. All reagents and solvents were purchased at the top commercial quality and used without further purification.

Name, acronym (abbreviation)	MW (g.mol <sup>-1</sup> )	Supplier	CAS number
Bovine serum albumin (BSA)	66 000	Sigma-Aldrich	9048-46-8
Poly(ethylene imine) (PEI)	750 000	Alfa Aesar	9002-98-6
Poly(allylamine) hydrochloride (PAH)	15 000	Sigma Aldrich	71-550-12
Poly(styrene sulfonate) (PSS)	70 000	Sigma Aldrich	25704-18-1
Deuterated Water (D <sub>2</sub> O)	20.03	Sigma Aldrich	7789-20-0
Dimethylformamide (DMF)	73.09	Acros Organics	68-12-2
Dichloromethane (DCM)	84.93	Acros Organics	75-09-2
Trifluoroacetic acid (TFA)	114.02	Alfa Aesar	76-05-1
Deuterated DMSO (DMSO-d <sub>6</sub> )	84.17	SDS	2206-27-1
N-Ethyl-diisopropylamine (DIEA)	129.25	Alfa Aesar	7087-68-5
Glucose Oxydase from <i>Aspergillus niger</i> (GOx)	160 000	Sigma Aldrich	9001-37-0
Peroxydase from Horseradish (HRP)	40 000	Sigma Aldrich	9003-99-0
D-Glucose	180.16	Sigma Aldrich	50-99-7
Fmoc-alanine (Fmoc-A-OH)	311.33	Iris biotech	35661-39-3
Methylpyrrolidone (NMP)	99.13	Sigma Aldrich	872-50-4
Triisopropylsilane (TIPS)	158.36	Sigma Aldrich	6485-79-6
Resin 2-chlorotriyl chloride (2-CTC)	-	Sigma Aldrich	42074-68-0
1-Hydroxybenzotriazole hydrate (HOBt)	135.12	Sigma Aldrich	123333-53-9
N,N,N',N'-Tetramethyl-o-(1H-benzotriazol-1-yl)uranium hexafluorophosphate (HBTU)	379.24	Alfa Aesar	94790-37-1
Diethyl ether	74.12	Acros Organics	60-29-7

#### 4.6.2. Preparation of Fmoc-AA-OH

Fmoc-AA-OH was prepared according the following synthetic pathway.



a) Fmoc-A-OH, DIEA, DMF; b) 20% piperidine DMF; c) Fmoc-A-OH, DIEA, HBTU, HOBT, DMF; d) 95%TFA, 2.5%H<sub>2</sub>O, 2.5%triisopropylsilane

Characterization of Fmoc-AA-OH was in full agreement with reported data in the literature<sup>25</sup>.

#### 4.6.3. Multilayer film preparation and hydrogel self-assembly

All polyelectrolytes, enzymes and proteins were prepared in ultrapure water (Milli-Q Plus system, Millipore, Billerica, MA) with no adjustment of pH. Different surfaces were used depending on the characterization techniques investigated: Gold coated quartz crystal for QCM-D and AFM experiments, ZnSe crystal for ATR-FTIR experiments and glass slide for Cryo-SEM and colorimetric (in SAFAS instrument) experiments. After the deposition of a PEI (1 mg/mL) precursor layer on the chosen surface by dipping, the multilayer film was performed by alternately exposing the surface to PSS (1 mg/mL) and PAH (1 mg/mL) solutions for 10 min with an intermediate rinsing step with ultrapure water during 5 min. GOx (1 mg/mL), BSA and HRP were adsorbed for 20 min followed by 5 min of rinsing step with ultrapure water.

#### 4.6.4. Quartz crystal microbalance with dissipation monitoring

QCM-D experiments were performed on a Q-Sense E1 apparatus (Q-Sense AB, Göteborg, Sweden) by monitoring the resonance frequencies of gold coated crystals, as well as the dissipation factors at four frequencies: the fundamental frequency at 5 MHz ( $\nu = 1$ ) and the 3<sup>rd</sup>, 5<sup>th</sup>, and 7<sup>th</sup> harmonics ( $u = 3, 5$  and  $7$  at 15, 25, and 35 MHz respectively). The QCM-D results give information on the adsorption process, as well as on viscoelastic properties of the adsorbed film<sup>23</sup>. The Software *QTools*® was used to determine the film thicknesses of multilayer films using the Sauerbrey equation (valid for rigid films)<sup>23</sup> and of the peptide self-assembly using the Vogt-Voinova model (valid for viscoelastic films).<sup>24</sup>

For a thin and rigid film, the mass can be obtained by using the Sauerbrey's equation<sup>23</sup>:

$$\Delta m = -C\Delta f/u$$



where  $C$  is the mass sensitivity constant ( $17.7 \text{ ng.cm}^{-2}.\text{Hz}^{-1}$  at 5 MHz), and  $u$  is the overtone number. The Sauerbrey equation applied when  $\Delta f/v$  is independent of  $v$ . We verified that this was the case in our experiments. As we assumed that the density of the film is close to  $1 \text{ g.cm}^{-3}$ , we can infer the evolution of the film thickness, during the buildup. Thickness is determined thanks to the previous equation:

$$d = -C\Delta f/100 \times v$$

where  $d$  is the thickness in nm.

#### 4.6.5. O-dianisidine assay

Microplate reader UV spectroscopy (FLX-Xenius®, SAFAS, Monaco) using SP<sub>2000</sub>V<sub>7</sub> software was the main device entailed in enzymatic activity measurement. The GOx activity of the enzymatic multilayer films deposited on a glass slide was measured by incubation of the substrate,  $\beta$ -D-glucose. Concentration and volume ensure a large excess of substrates for the enzymatic reaction. Glucose is a colourless GOx substrate.

The GOx's activity was monitored by using a second enzyme, HRP, which will use the  $\text{H}_2\text{O}_2$  produced by the GOx to react with O-dianisidine (colourless) to obtain the o-dianisidine oxidized, which is brown. The reaction was followed at 440 nm. (GOx/PAH)<sub>3</sub> film, (GOx/PAH)<sub>1</sub> film, PEI/(PSS/PAH)<sub>2</sub>, were disposed in a 24 wells plate with 1 mL of a solution containing glucose (2 mg/mL), HRP (1 mg/mL) and o-dianisidine ( $1 \times 10^{-3}$  M). (GOx/HRP)<sub>1</sub> film and (GOx/PAH/PSS/HRP)<sub>1</sub> film were disposed in a 24 wells plate with 1 mL of a solution containing glucose (2 mg/mL) and o-dianisidine ( $1 \times 10^{-3}$  M). All solution were prepared in ultrapure water.

#### 4.6.6. Atomic force microscopy

Atomic force microscopy (AFM) was carried out with a BioScope Catalyst (Bruker corp., Santa Barbara, CA, USA). Micrographs from different interaction stages of Fmoc-AA-OH with the enzymatic film were recorded in contact mode by using silicon tips mounted on nitride levers. All samples were observed in dry state with triangular cantilevers having a spring constant of 0.4 N/m and a nominal tip radius of 2 nm. Selected AFM images were treated with the nanoscope analysis software (Bruker corp., Santa Barbara, CA, USA). All samples analyzed in AFM were prepared on gold-coated quartz crystal. They were air dried before analysis.

#### 4.6.7. Infrared spectroscopy

The Fourier Transform Infrared (FTIR) experiments were performed on a Vertex 70 spectrometer (Bruker, Germany) using DTGS detector. Spectrum were recorded in the Attenuated Total Reflection (ATR) mode using a 45° trapezoidal ZnSe (internal reflection element) crystal (6 reflections, dimensions  $72 \times 10 \times 6 \text{ mm}^3$ ) in ATR cell (GRASEBY-SPECAC, England).

Reference (bare ZnSe crystal in contact with ultrapure water) and sample spectra were taken by collecting 128 interferograms between 800 and 4000  $\text{cm}^{-1}$  at 2  $\text{cm}^{-1}$  resolution, using Blackman-Harris three-term apodization and the standard Bruker OPUS/IR software (version 7.5). Multilayer films were assembled on ZnSe crystal by the dipping method as described above. PEI, PSS, PAH, GOx, HRP, Fmoc-AA-OH solutions were prepared as described previously but in deuterated water to avoid the water signal in the amide I region.

#### **4.6.8. Scanning electron microscopy and cryo-SEM**

To observe cross-sectioned gels, a specific cryo-holder was designed and manufactured by the mechanical facility of the Charles Sadron Institute (see Figure below). The glass slide, covered by enzymatic precursor film and the self-assembled gel, was inserted vertically in the jaws of the vise. The holder with the sample is then rapidly plunged into nitrogen slush in the cryo preparation chamber of the Quorum PT 3010 machine. As the sample is free standing over the holder, during the plunging, the sample is rapidly frozen by direct contact with the nitrogen slush. The sample is then transferred under vacuum into the chamber attached to the microscope and fractured with a razor blade. A slight etching at  $-80^{\circ}\text{C}$  is performed to render the fibers more visible followed by the deposition of a thin Pt layer (metallization step). The sample is then transferred in the FEG-cryoSEM (Hitachi SU8010) and observed at 1kV at  $-170^{\circ}\text{C}$ .



*Picture of the specific cryo-holder designed and built for the preparation of cross-sections. The “cross-section” holder is a vise like holder with two movable jaws. A screw compressing/uncompressing two springs moves the jaws forwards and backwards. By design the center of the holder is invariable as the two jaws can be displaced independently to adjust to the sample thickness by screws and springs. In that way, the sample will be in the optical axis of the SEM after introduction in the microscope and easily found under the beam.*

#### **Experiment illustrated in Figure S12 in supporting information part has been done as following:**

A sellotape was fixed on the half of a circular glass slide and the multilayer (PEI/(PSS/PAH)<sub>2</sub>/(GOx/PAH)<sub>3</sub>, named (GOx/PAH)<sub>3</sub>, was built on the whole substrate by dipping. The multilayer was performed by first the deposition of the PEI layer (1 mg/mL) and then, by alternately dipping the substrate to PSS (1 mg/mL) and PAH (1 mg/mL) solutions for 10 min with an intermediate rinsing step with ultrapure water during 5 min. GOx (1 mg/mL) were adsorbed for 20 min followed by 5 min of rinsing step with ultrapure water. The sellotape is then removed carefully and the substrate displaying an half of its surface with (GOx/PAH)<sub>3</sub> and an half surface uncoated (naked) is dipped in a mixture solution of Fmoc-AA-OH (3.6 mg/mL) and glucose (5 mg/mL) during 12h at room temperature. The substrate was rinsed by dipping into ultrapure water (MilliQ) and then freeze-dried by dipping it into liquid nitrogen and then freeze-dried before imaging.

## REFERENCES

1. a) Rydzek, G., *et al.*, Polymer multilayer films obtained by electrochemically catalyzed click chemistry, *Langmuir*, **2010**, *26*, 2816. b) Rydzek, G., *et al.*, Electrochemically triggered assembly of films: a one-pot morphogen-driven buildup, *Angew. Chem. Int. Ed.*, **2011**, *50*, 4374. c) Rydzek, G., *et al.*, Morphogen-driven self-construction of covalent films built from polyelectrolytes and homobifunctional spacers: buildup and pH response, *Soft Matter*, **2012**, *8*, 10336.
2. a) Maerten, C., *et al.*, Morphogenelectrochemically triggered self-construction of polymeric films based on mussel-inspired chemistry, *Langmuir*, **2015**, *31*, 13385. b) Maerten, C., *et al.*, Electrotriggered confined self-assembly of metal-polyphenol nanocoatings using a morphogenic approach, *Chem. Mater.*, **2017**, *29*, 9668.
3. a) Lehn, J.-M., Supramolecular chemistry: concepts and perspectives, in *Supramolecular Chemistry*, Wiley-VCH, Weinheim, **1995**; b) Whitesides, G., Grzybowski, B., Self-assembly at all scales, *Science*, **2002**, *295*, 2418, c) Aida, T., *et al.*, Functional supramolecular polymers, *Science*, **2012**, *335*, 813.
4. a) Cohen Stuart, M., *et al.*, Emerging applications of stimuli-responsive polymer materials, *Nat. Mater.*, **2010**, *9*, 101, b) Ariga, K., *et al.*, Nanoarchitectonics: a new materials horizon for nanotechnology, *Mater. Horiz.*, **2015**, *2*, 406.
5. a) Komiyama, M., *et al.*, Chemistry can make strict and fuzzy controls for bio-systems: DNA nanoarchitectonics and cell-macromolecular nanoarchitectonics, *Bull. Chem. Soc. Jpn.* **2017**, *90*, 967 b) Singh, N., *et al.*, Peptide-based molecular hydrogels as supramolecular protein mimics, *Chem. Eur. J.*, **2017**, *23*, 981.
6. Dochter, A., *et al.*, Film self-assembly of oppositely charged macromolecules triggered by electrochemistry through a morphogenic approach, *Langmuir*, **2015**, *31*, 10208.
7. Vigier-Carrière, C., *et al.*, Bioactive seed layer for surface-confined self-assembly of peptides, *Angew. Chem., Int. Ed.*, **2015**, *127*, 10336.
8. Capito, R., *et al.*, Self-assembly of large and small molecules into hierarchically ordered sacs and membranes, *Science*, **2008**, *319*, 1812.
9. a) Soh, S., *et al.*, Reaction-diffusion systems in intracellular molecular transport and control, *Angew. Chem., Int. Ed.*, **2010**, *49*, 4170., b) Pandian, G. and Sugiyama, H., Nature-inspired design of smart biomaterials using the chemical biology of nucleic acids, *Bull. Chem. Soc. Jpn.*, **2016**, *89*, 843.
10. Johnson, E., Adams, D., and Cameron, P., Directed self-assembly of dipeptides to form ultrathin hydrogel membranes, *J. Am. Chem. Soc.*, **2010**, *132*, 5130.
11. Kubiak, P., *et al.*, Polymerization of low molecular weight hydrogelators to form electrochromic polymers, *Chem. Commun.*, **2015**, *51*, 10427.
12. Liu, E., *et al.*, Reversible electroaddressing of self-assembling amino-acid conjugates, *Adv. Funct. Mater.*, **2011**, *21*, 1575.
13. Raeburn, J., *et al.*, Electrochemically-triggered spatially and temporally resolved multi-component gels, *Mater. Horizons*, **2014**, *1*, 241.
14. Liu, Y., *et al.*, Biofabrication multifunctional soft matter with enzymes and stimuli-responsive materials, *Adv. Funct. Mater.*, **2012**, *22*, 3004.
15. Olive, A., *et al.*, Spatial and directional control over self-assembly using catalytic micropatterned surfaces, *Angew. Chem., Int. Ed.*, **2014**, *53*, 4132.
16. a) Mu, X., *et al.*, Experimental and computational studies reveal an alternative supramolecular structure for Fmoc-dipeptide self-assembly, *Biomacromolecules*, **2012**, *13*, 3562., b) Jayawarna, V., *et al.*, Nanostructured hydrogels for three-dimensional cell culture through self-assembly of fluorenylmethoxycarbonyl-dipeptides, *Adv. Mater.*, **2006**, *18*, 611., c) Adams, D., Relationship between molecular structure, gelation behavior and gel properties of Fmoc-dipeptides, *Soft Matter*, **2010**, *6*, 1971.
17. Cheng, W., and Li, Y., Peptide hydrogelation triggered by enzymatic induced pH switch, *Sci. China-Phys. Mech. Astron.*, **2016**, *59*, 678711.

18. Decher, G., Fuzzy nanoassemblies: toward layered polymeric multicomposites, *Science*, **1997**, 277, 1232.
19. a) Onda, M., *et al.*, Sequential actions of glucose oxidase and peroxidase in molecular films assembled by layer-by-layer alternate adsorption, *Biotechnol. Bioeng.*, **1996**, 51, 163., b) Onda, M., *et al.*, Sequential reaction and product separation on molecular films of glucoamylase and glucose oxidase assembled on an ultrafilter, *J. Fermentation Bioeng.*, **1996**, 82, 502., c) Zhang, S., *et al.*, Quantitative collection and enzymatic activity of glucose oxidase nanotubes fabricated by templated layer-by-layer assembly, *Biomacromolecules*, **2015**, 16, 2382.
20. Yamada, N., *et al.*, Regulation of  $\beta$ -sheet structures within amyloid  $\beta$ -sheet assemblage from tripeptide derivatives, *J. Am. Chem. Soc.*, **1998**, 120, 12192.
21. Hernandez-Ruiz, J., *et al.*, Catalase-like activity of horseradish peroxidase: relationship to enzyme inactivation by  $H_2O_2$ , *Biochem. J.*, **2001**, 354, 107.
22. Xin, L., *et al.*, Regulation of an enzyme cascade reaction by a DNA machine, *Small*, **2013**, 9, 3088.
23. Sauerbrey, G., Verwendung von schwingquarzen zur wägung dünner schichten und zur mikrowägung, *Z. Phys.*, **1959**, 155, 206.
24. a) Voinova, M., *et al.*, Viscoelastic acoustic response of layered polymer films at fluid-solid interfaces: continuum mechanics approach, *Phys. Scr.*, **1999**, 59, 391., b) Höök, F. *et al.*, Variation in coupled water, viscoelastic properties, and film thickness of a mefp-1 protein film during adsorption and cross-linking: a quartz crystal microbalance with dissipation monitoring, ellipsometry, and surface plasmon resonance study, *Anal. Chem.*, **2001**, 73, 5796.
25. Khattab, S., *et al.*, Cyanoacetamide-based oxime carbonates: an efficient, simple alternative for the introduction of Fmoc with minimal dipeptide formation, *Tetrahedron*, **2012**, 68, 3056., b) Marty, R., *et al.*, Two-fold odd-even effect in self-assembled nanowires from oligopeptide-polymer-substituted perylene bisimides, *J. Am. Chem. Soc.*, **2014**, 136, 3919.





## Chapter 5



**Supported catalytically-active supramolecular  
hydrogels for continuous flow chemistry**

*Towards the design of a self-sustained hydrogel growth*



## Summary

<b>5.1. Supported catalytically-active supramolecular hydrogels for continuous flow chemistry</b> .....	<b>164</b>
5.1.1. Abstract .....	164
5.1.2. Introduction.....	165
5.1.3. Results and discussion.....	166
5.1.4. Conclusion .....	173
<b>5.2. Towards the design of a self-sustained hydrogel growth.....</b>	<b>175</b>
5.2.1. Introduction.....	175
5.2.2. Design of an adequate precursor peptide .....	176
5.2.3. Synthesis of the precursor Fmoc-GFFY( <i>Succ</i> )GHY( <i>Succ</i> ) .....	178
5.2.4. Gelation tests of Fmoc-GFFY( <i>Succ</i> )GHY( <i>Succ</i> ) in vials .....	179
5.2.5. Characterization of the autocatalytic hydrogel by FT-IR and Fluorescence microscopy .	182
5.2.6. Surface-localization of the autocatalytic hydrogel.....	184
5.2.6.1. Monitoring of the mass deposition onto a surface by QCM-D.....	184
5.2.6.2. Morphological characterization of the hydrogel grew from an auto-catalytic process and generated from a surface.....	186
5.2.7. Conclusion .....	187
<b>GENERAL CONCLUSION OF CHAPTER 5 .....</b>	<b>187</b>
<b>5.3. ESI of the part 5.1 of this chapter .....</b>	<b>189</b>
5.3.1. Additional Figures.....	189
5.3.2 Experimental section.....	197
5.3.2.1. Materials .....	197
5.3.2.2. Synthesis and characterization of Fmoc-GFFYGHY, Fmoc-GFFpYGHY, Fmoc-GFFYGHpY and Fmoc-GFFpYGHpY.....	198
5.3.2.3. Preparation of peptide solution and hydrogel formation .....	210
5.3.2.4. Multilayer film preparation and localized hydrogel formation at the liquid-solid interface ..	211
5.3.2.5. Quartz crystal microbalance with dissipation monitoring (QCM-D) .....	211
5.3.2.6. Atomic force microscopy (AFM) .....	212
5.3.2.7. Infrared spectroscopy.....	212
5.3.2.8. Scanning Electron Microscopy (SEM) and <i>cryo</i> -SEM .....	212
5.3.2.9. Transmission Electronic Microscopy (TEM).....	213
5.3.2.10. Analytic High-Performance Liquid Chromatography (HPLC) .....	213
5.3.2.11. Nuclear Magnetic Resonance (NMR) .....	214
5.3.2.12. Circular Dichroism (CD) .....	214
5.3.2.13. High Resolution Mass Spectroscopy (HRMS) .....	214
5.3.2.14. Esterase-like activity assays.....	215
5.3.2.15. Esterase-like activity of the supported-CASH onto a glass substrate.....	216
5.3.2.16. Esterase-like activity and kinetic resolution of the supported CASH in the continuous flow reactor .....	216
5.3.2.17. Determination of the proportion of peptides involved in the catalytic process. ....	217
5.3.2.18. Experimental determination of $K_m$ , $V_{max}$ and $k_{cat}$ using methyl ester 9 and the Michaelis-Menten equation .....	217
5.3.2.19. Molecular simulation.....	219
<b>REFERENCES .....</b>	<b>220</b>





## Context

*LEASA is an approach allowing to anchor a supramolecular hydrogel on a surface where enzymes are beforehand immobilized. What breakthroughs can be expected using LEASA? In the first part of this chapter I will show an example of LEASA application toward the design of reactors for flow chemistry processes. Indeed, supramolecular hydrogel made from LMWH used to be mechanically fragile materials. It thus seems hardly possible to consider them for chemical transformations at large scales. If the supramolecular hydrogel is supported on a more robust material, it becomes easier to handle and this problem can so be circumvented. But in this chapter, I will also investigate another property of supramolecular hydrogels: catalytic properties emerging from the assembly of suitable peptide hydrogelators. This gives rise to a functionality of the resulting material.*

*In the second short part of this chapter, I will show the promising preliminary results obtained toward the design of self-sustained hydrogel growth. This development is based on the achievements from the first part.*

## 5.1. Supported catalytically-active supramolecular hydrogels for continuous flow chemistry

---

- Submitted article - Nature Communications, 2019

Jennifer Rodon Fores, Miryam Criado-Gonzalez, Alain Chaumont, Alain Carvalho, Christian Blanck, Marc Schmutz, Christophe A. Serra, Fouzia Boulmedais, Pierre Schaaf and Loïc Jierry.

---

### 5.1.1. Abstract

Inspired from biology, one current goal in supramolecular chemistry is to control the emergence of new functionalities arising from self-assembly of molecules.<sup>1,2</sup> In many respects, peptides are probably the most interesting class of molecules since their self-assembly can lead to catalytically-active nanofibrous networks able to underpin hydrogels.<sup>3,4</sup> Unfortunately, the mechanical fragility of these materials is incompatible with concrete process developments relaying this exciting field to academic curiosity.<sup>5</sup> Here, we show that this drawback can be circumvented by using enzyme-assisted self-assembly of peptides initiated at the walls of a supporting porous material. We apply this simple strategy to grow an esterase-like catalytically-active supramolecular hydrogel (CASH) in an open-cell polymer foam, filling the whole interior space of it. Our so-supported-CASH is efficient toward inactivated esters and shows kinetic resolution of racemic esters. This resulting hybrid material is robust enough to be used in continuous flow reactors, reusable and stable over months. It allows getting, at large scale, enantiopure carboxylic acid derivatives.

### **5.1.2. Introduction**

To provide mechanical robustness to highly soft materials such as hydrogels, use of polymer foams as internal skeleton that will rigidify the matter is an interesting approach.<sup>6</sup> In case of peptide-based hydrogels, a first technological issue that needs to be resolved is the spatial localization of the hydrogel growth from the surface of the polymer foam in order to link hydrogel and polymer materials. This can be achieved by immobilizing a (bio)catalyst on a planar surface.<sup>7,8,9,10</sup> We use the surface immobilization of an enzyme able to transform non-self-assembling precursors present in solution into self-assembling building blocks.<sup>11</sup> The confinement of these building blocks at the material-water interface induces the growth of nanofibers anchored on the surface and underpinning a hydrogel.<sup>12,13,14</sup>

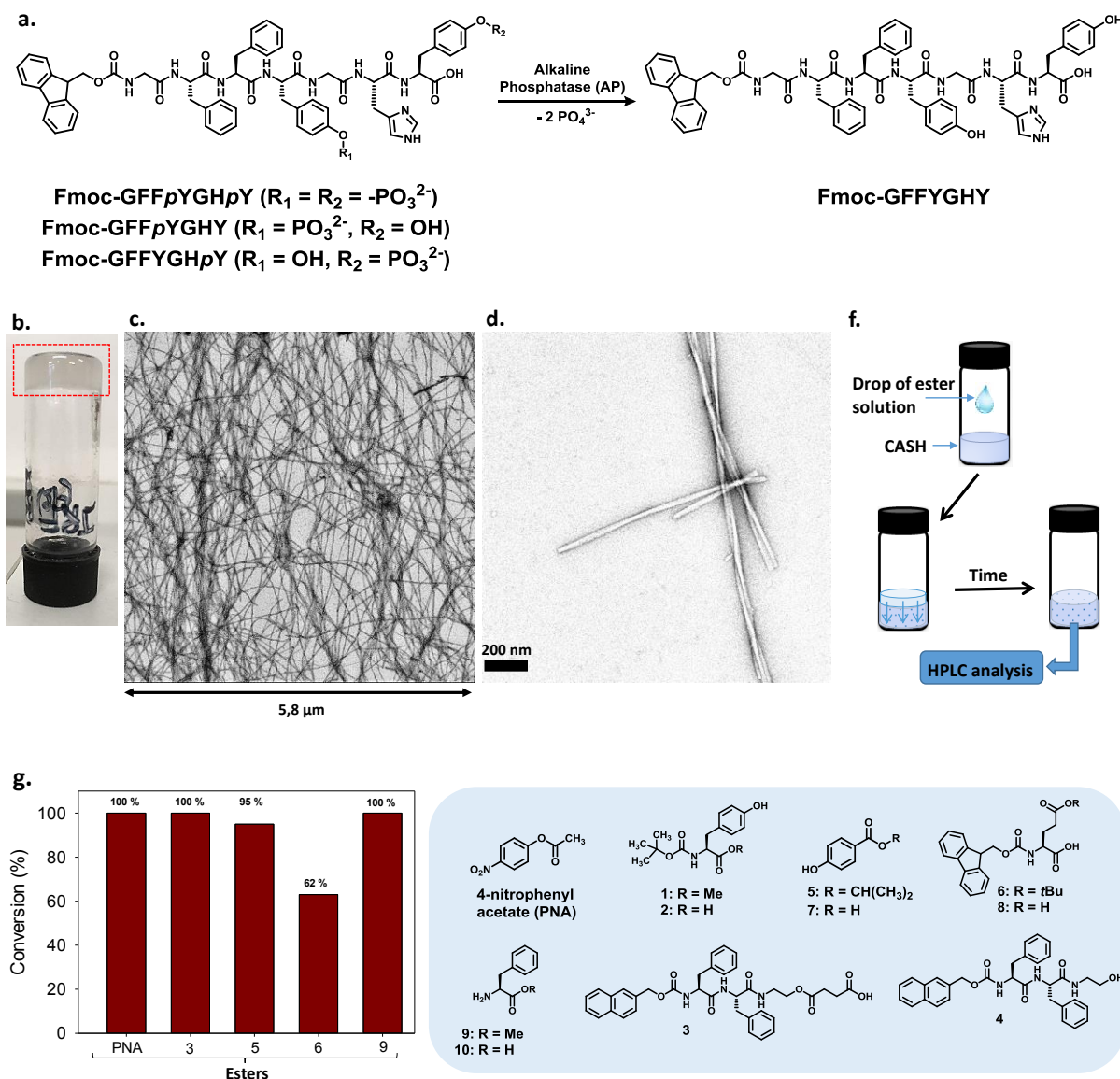
The development of a supported-CASH is based on the appropriate choice of the precursor which has to fulfill two essential conditions: *(i)* generate self-assembling derivatives in the presence of an adequate enzyme and *(ii)* to result in a supramolecular hydrogel exhibiting catalytic activity. Up to now, no such precursor of low molecular weight hydrogelator (LMWH) has been described.

### 5.1.3. Results and discussion

Among the catalytically-active supramolecular hydrogel examples reported in literature,<sup>15</sup> our attention focused on the following peptide sequence *Nap*-GFFYGHY (*Nap*=naphthalene) described by Yang et al.<sup>16</sup> This peptide is not soluble in water at room temperature but when a suspension of this peptide is heated close to 100°C and then cooled slowly, an esterase-like hydrogel is obtained, reactive towards the activated ester 4-nitrophenyl acetate (PNA). The most interesting aspect of this heptapeptide regarding to our goal lays in the presence of two tyrosine residues (Y) in positions 4 and 7: the phosphorylation of the two phenol groups was necessary to obtain a *bis*-phosphorylated heptapeptide Fmoc-GFF $\rho$ YGH $\rho$ Y (Fig. 1a) well soluble in water (ESI section 2). We introduced a Fmoc group instead of the *Nap* in N-terminal position because of the very high propensity of this group to induce self-assembly.<sup>17</sup>

When alkaline phosphatase (AP) is added to a 1% mol. solution of Fmoc-GFF $\rho$ YGH $\rho$ Y, a quasi-translucent hydrogel forms almost instantaneously (Fig. 1b) constituted of 97% of the twice dephosphorylated Fmoc-GFFYGHY (Fig. S1). This resulting peptide produced enzymatically *in situ* leads to an entanglement of several micrometers long fibers observable by transmission electron microscopy (TEM) (Fig. 1c). Magnification of these fibers suggests a ribbon shape of 27 nm in width, having a right-handed twist with roughly 300 nm pitch when two or more ribbons are associated together (Fig. 1d). Infrared and circular dichroism spectroscopies confirm the antiparallel  $\beta$ -sheet association between the peptides, as already reported for other kinds of peptide self-assemblies (Fig. S2).<sup>12,13,18</sup> When the resulting hydrogel is put in contact with a PNA solution (1 mM) as depicted in Fig. 1g (section 14 in ESI), the gel turns spontaneously to yellow due to *para*-nitrophenol production (Fig. S3). But this way to produce carboxylic acid derivatives is not practical: in addition to the mechanical fragility of such supramolecular hydrogel, (i) the time to let the substrate penetrate within the CASH and the low reaction time to get a full conversion due to the substrate diffusion inside the hydrogel are long. More importantly, (ii) the isolation of the formed carboxylic acid derivatives requires the dissolution of the CASH followed by purification steps, sentencing this self-assembled catalytic material to a single run. Therefore this way to realize the catalytic reaction is time consuming, expensive and tedious, motivating our investigations toward supported-CASH developments.

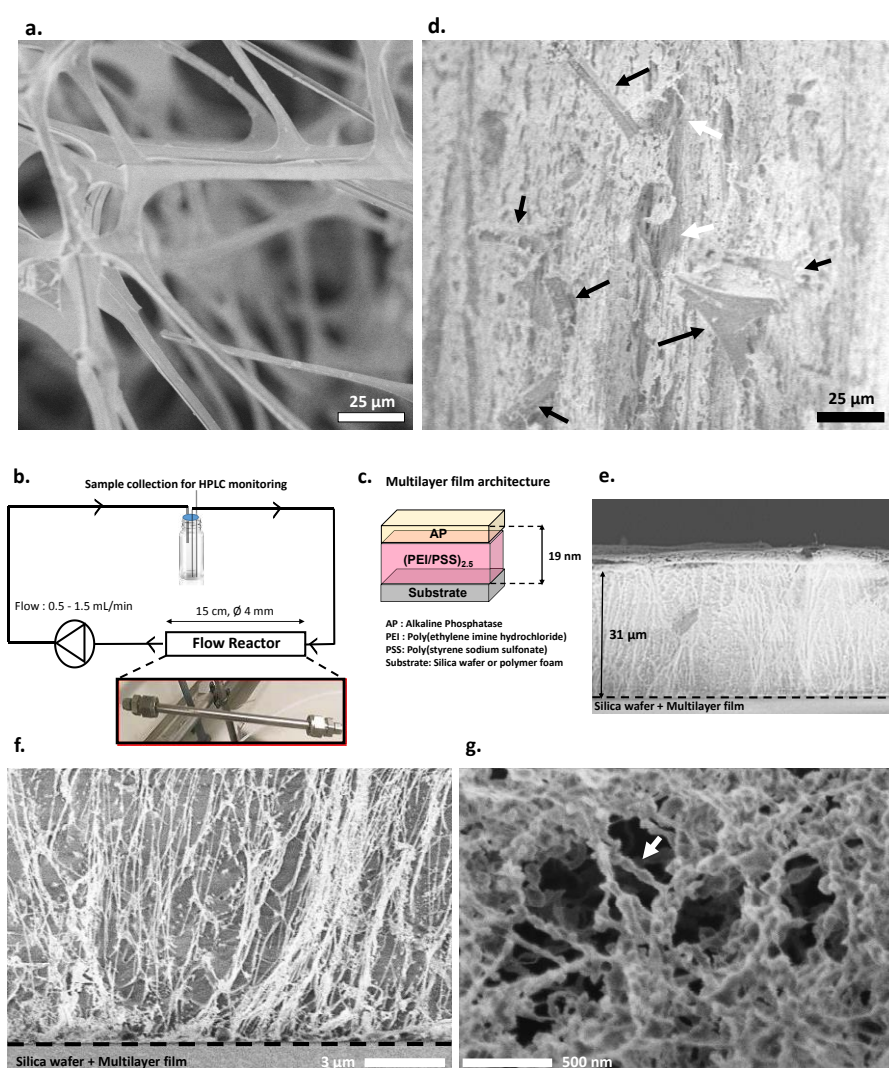
Supported catalytically-active supramolecular hydrogels for continuous flow chemistry  
Towards the design of a self-sustained hydrogel growth



**Figure 1: Self-assembly and catalytic activity.** *a*, Chemical structure of Fmoc-GFFpYGHpY and its enzymatic transformation into Fmoc-GFFYGHY in presence of AP. *b*, Picture of the upside down vial containing the Fmoc-GFFYGHY hydrogel formed. *c*, TEM image of Fmoc-GFFYGHY self-assembly nanofibers. *d*, Magnification of TEM image. *e*, Schematic of the catalytic process based on the ester substrates diffusion within the CASH. *f*, Schematic of the catalytic process based on the ester substrates diffusion within the CASH. *g*, Methyl esters 1, 9, primary ester 3 and secondary ester 5 can be quasi quantitatively converted in 24 hours (2 hours in cases of PNA) in their corresponding carboxylic acids 2, 10, 4 and 7 respectively. This large scope a suitable substrates shows the non-sensitivity of this catalytic system toward functionalized esters. Indeed, chemical reactive groups such as phenol, carboxylic acid or amine, do not affect the catalytic efficiency of our CASH.

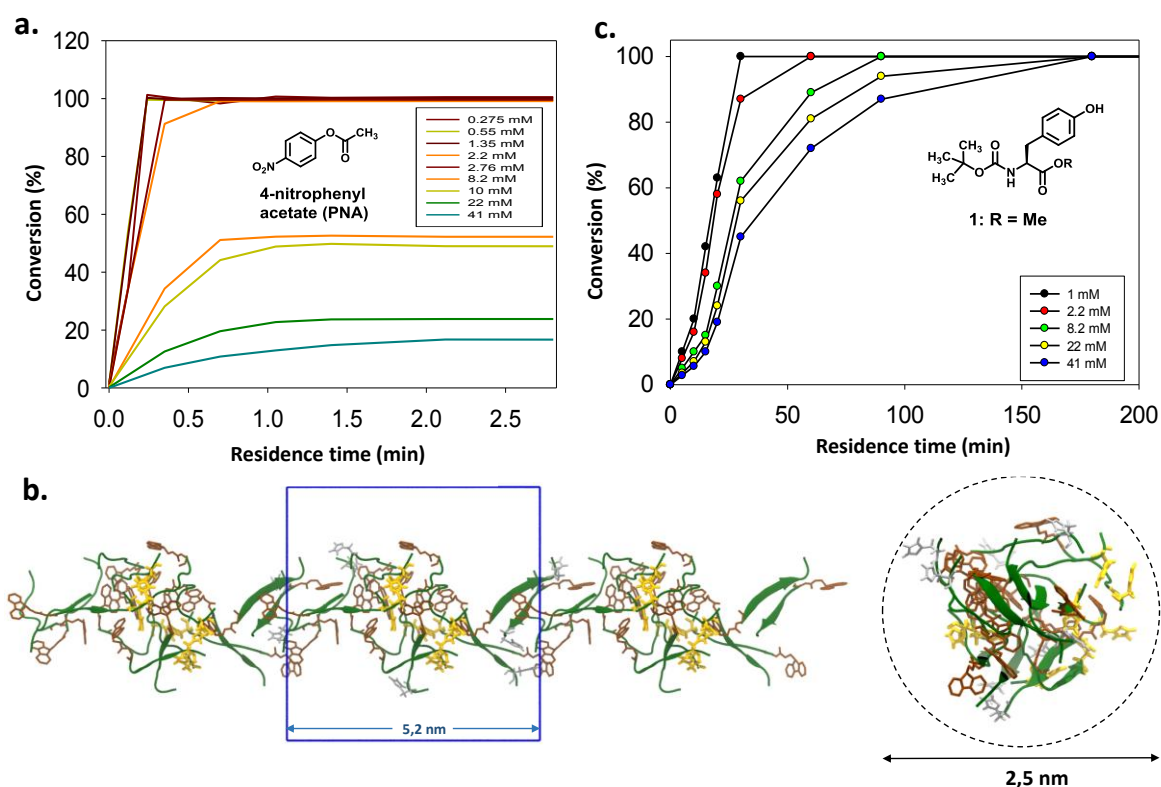
To build our supported-CASH we used as porous catalyst support, a commercial open cell melamine foam displaying diameter cells of roughly 200  $\mu\text{m}$  (Fig. 2a). The foam was designed to get a suitable tubular shape and placed inside a metallic column as shown in Figure 2b (length: 15 cm; diameter: 4 mm). We deposited on the walls of the pores, a polyelectrolyte multilayer constituted of 2,5 PEI/PSS bilayers (PEI: poly(ethylene imine); PSS: poly(styrene sulfonate)) covered by an AP layer by dipping alternately in PEI, PSS and AP solutions (Fig. 2c). We then flowed a Fmoc-FFpYGHpY solution through the functionalized column to form the supported-CASH (details are found in section 16 in ESI). Using Cryo-SEM (at low etching) of this coated foam shows that the supported-CASH is filling the whole space of the polymer foam (Fig. 2d).

In order to further characterize the supported-CASH, and because the use of the multilayer renders the buildup process independent of the substrate, we investigated it on flat surfaces where more characterization techniques are available. We modified the surfaces with an enzymatically-active multilayer similar to that deposited on the foam walls. The buildup of the multilayer was first monitored by quartz crystal microbalance with dissipation (QCM-D) and leads to a 19 nm thick  $(\text{PEI}/\text{PSS})_2/\text{PEI}/\text{AP}$  film (section 5 in ESI). When this so-modified substrate was brought in contact with Fmoc-GFFpYGHpY solution, a spontaneous and huge decrease of all QCM frequencies was observed, characteristic of a highly hydrated mass deposition (Fig. S4).<sup>13,14</sup> AFM, SEM, HPLC composition analysis and fluorescence emission intensity measurements confirm the nanofibrous architecture of the hydrogel made up the hydrogelator Fmoc-GFFYGHY with Fmoc groups stacking the resulting assembly (Fig. S5-7).<sup>13,18</sup>



**Figure 2: Supported-CASH nanofibrous network.** **a**, Melamine open cell foam observed by SEM. **b**, Scheme of the continuous flow reactor. **c**, Multilayer architecture adsorbed on foam or planar substrate to initiate the CASH formation. **d**, Z-section view of CASH supported on melamine open cell foam observed by cryo-SEM. Black arrows indicate the backbone of the polymer foam. White arrows show the fibrous network located everywhere within the interior space of the hydrogel-filled foam. **e**, Cryo-SEM image of the CASH formed all along the enzyme-modified silica wafer substrate, **f**, magnification of the interface glass/CASH (middle) showing the growth of nanofibers orientated from the bottom to the top, and **g**, magnification of these constituting nanofibers highlighting their helical shape (white arrows).

Cryo-SEM analysis was realized on CASH grown up from a silica wafer. The sample was cut in the z-section in order to measure the thickness of the formed hydrogel when the substrate was 12 hours in contact with the Fmoc-GFFpYGHpY solution. The CASH thickness is roughly 31  $\mu\text{m}$ , a regular value all along the sample (Fig. 2e). Strikingly, we noticed a perpendicular orientation of the fibers starting from the surface:<sup>19</sup> a fibrous architecture different to what is observed when the hydrogel is formed in the bulk. Some of the fibers are collapsed to each other but thinner fibers are also present (Fig. 2f). Cryo-SEM images taken to get a closer look allow to measure 70 nm of diameter. As observed by TEM, these nanofibers seem to have a chiral twisted ribbon shape displaying 140 nm width (Fig. 2g). A complete ester hydrolysis was observed in few minutes when this glass-supported hydrogel layer was dipped into PNA solution (Section 14 and Fig. S8 in ESI).





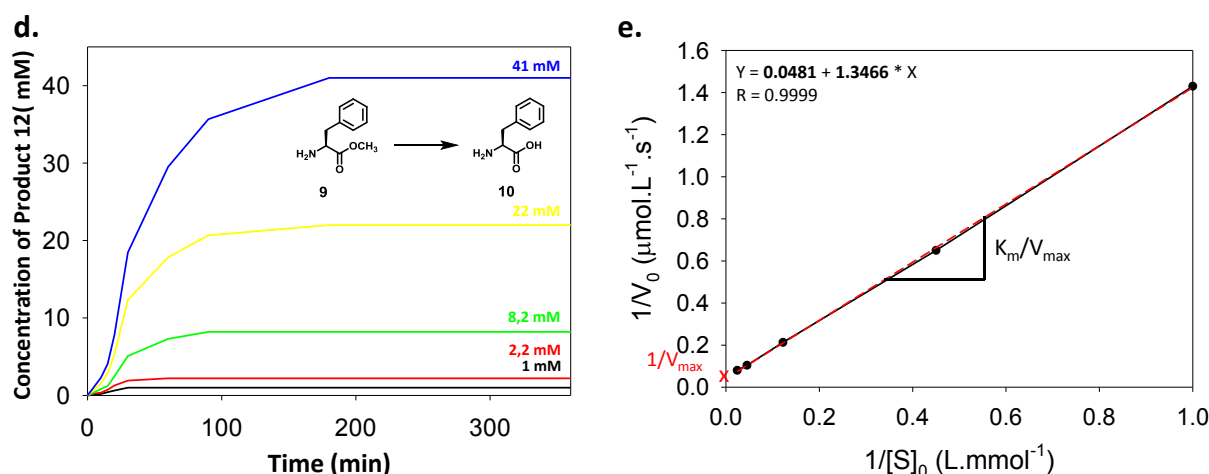


Figure 3: **Supported-CASH kinetic and simulation.** **a.** *Para*-nitrophenol conversion over the residence of time for various concentrations of PNA. **b.** (left) Molecular dynamics of 16 peptides Fmoc-GFFYGHY showing a fiber-like spatial arrangement (blue square represents the unit cubic simulation box to which 3D periodic boundary conditions have been applied). (right) The fiber-like diameter is roughly 2,5 nm. Histidine residues are represented in orange when another histidine is closer than 5 Angstroms and in grey otherwise. **c.** Conversion of ester **9** hydrolysis over residence time for various concentration of **9**. **d.** Production of the acid **10** over time from various concentrations of **9** hydrolyzed through the supported-CASH column. **e.** Determination of  $V_{max}$  and  $K_m$  according to the Lineweaver and Burk model (linear regression in dashed red).

Evaluation of the catalytic activity of this supported-CASH in the flow reactor was first done using PNA as substrate at 1 mM with 1.5 mL/min as flow rate (Fig. 2b): 98% of hydrolysis is obtained in 2.8 minutes. This duration corresponds to the cumulate residence time of the substrate spent when passing through the supported CASH column in a closed loop system. HPLC analysis confirms also that no constituting peptide hydrogel, *i.e.* Fmoc-GFFYGHY, was released from the column, suggesting the preservation of its integrity during the catalytic process. Five successive runs have been realized in identical conditions without loss of catalytic efficiency highlighting the effective recycling of the supported-CASH. Remarkably, this catalytic reactor can be stored (4°C) at least for one month and reused again without losing activity (Fig. S9). Increasing the PNA concentration (from 0.28 mM to 2.20 mM) requires more time to get a full ester hydrolysis. Interestingly, for concentrations higher than 2.20 mM, the conversion in *para*-nitrophenol levels off whatever the concentration of the substrate and the higher amount of PNA converted is constant at 141  $\mu$ moles (Fig. 3a). Actually *para*-nitrophenyl esters are well-known to be powerful acyl agents and particularly to acylate imidazole groups.<sup>20</sup> The imidazole-containing histidine residues present in esterase-like peptide sequences are essential for ester hydrolysis, and thus if they are acylated the desired catalytic transformation is stopped. But the acylation of imidazole is a reversible reaction and washing of the column with adequate amount of water restores entirely its initial catalytic activity (Fig. S10).<sup>21</sup> This PNA's ability to inhibit the catalytic sites of the CASH can be used to determine their number in our dimensioned catalytic flow reactor. Assuming that one PNA inhibits one histidine, we determined that one of eleven peptides is involved in the catalytic process (Section 16 in ESI).

Molecular dynamics show the spatial organization of 16 Fmoc-GFFYGHY (Fig. 3b and S11, section 19 in ESI): all Fmoc groups stack together through  $\pi$ - $\pi$  interactions orientating the heptapeptide chains in antiparallel  $\beta$ -sheet assemblies as observed previously by CD and IR (Fig. S2).

This long fiber organization having 2.5 nm as diameter leads to the spatial confinement of several histidine residues that may constitute the “catalytic pocket”.

Interestingly, we discovered that this CASH is also highly effective to hydrolyze a wide panel of inactivated esters, which is rarely reported, when the substrate has diffused within the catalytic hydrogel (Fig. 1g). Tertiary ester such as **6** requires more time to be fully hydrolyzed (Fig. S12) and complex structures such as **3** can self-assemble when its ester moiety is chemically cleaved<sup>22</sup> giving thus rise to a second self-assembled architecture growing within the CASH (Fig. S13)<sup>23</sup>. This substrate’s versatility is crucial with regard to developments for chemical synthetic tools. Using a flow reactor, the hydrolysis reaction is fast (Fig. S15). For instance, the inactivated methyl ester **9** (1 mM) is entirely hydrolyzed into **10** in less than 40 minutes (25°C, 1.5 ml/min). Increasing the concentration of **9** extends the necessary residence time but without inhibition effect, as expected for this non-acylating substrate (Fig. 3c). A linear dependence of  $1/V_0$  with  $1/[S]$  where  $V_0$  represents the reaction rate at the initial time and  $[S]$  the substrate **9** concentration (Fig. 3d and Section 18 in ESI) was observed showing the Michaelis Menten behavior of our enzyme-like supported-CASH (Fig. S14). We determined the following values of  $K_m = 28$  mM,  $V_{max} = 20.8 \mu\text{mol}\cdot\text{s}^{-1}$  and  $k_{cat} = 3.0 \times 10^3 \text{ s}^{-1}$ . This last  $k_{cat}$  value is at least ten times higher than those reported for others CASH determined on activated *para*-nitrophenol ester derivatives.<sup>24,25</sup>

In the literature, few CASH described enantioselective processes<sup>26,27</sup> and the kinetic resolution of inactivated esters using CASH is still an unsuccessful challenge.<sup>15,24,28</sup> We observed a strong discrimination from the supported-CASH between the *L* and *D* amino-acid *tert*iobutyl esters **6**: indeed, after 30 minutes of residence time, we observed that almost 45% of the natural enantiomer *L*-**6** was hydrolyzed whereas the *D*-**6** was not yet affected (Fig. 4a). By decreasing the flow rate to 0,5 mL/min, it was possible to obtain more than 90% conversion of the *L*-**6** into its corresponding acid derivative *L*-**8** (Fig. 4b). After loading of the flow reactor with 200 mg of racemic *rac*-**6** and using a flow rate of 0,5 mL/min, we stopped the reaction after 30 minutes of running. The reaction medium was slightly basified and extracted with dichloromethane yielding to 95% of a white solid being the chemically pure acid *L*-**8** with 99% of enantiomeric excess (ee) from the aqueous phase (Fig 4c). The non-hydrolyzed ester *D*-**6** was isolated with a chemical yield of 96% and 92% ee from the organic layer. Enantio-enriched *L*-**6** (40% ee) lead quasi-quantitative isolation of both enantiopure *L*-**8** and the ester *D*-**6** (Fig. S16). Racemic amino-acid *tert*iobutyl esters such as the lysine and tyrosine were also tested: in both cases we observed a faster kinetic hydrolysis of the *L* enantiomer (Fig. 4d-e) highlighting the ability of the catalytic pocket to react faster with the natural amino-acids.

Finally, other kinds of racemic esters can be envisioned such as the oxirane of 4-methoxycinnamic methyl ester where the (*R,R*) enantiomer is hydrolyzed faster than the (*S,S*) one (Fig. S17): this compound is a key intermediate in the industrial preparation of the Diltiazem, a drug used to treat high blood pressure, angina and certain heart arrhythmias.

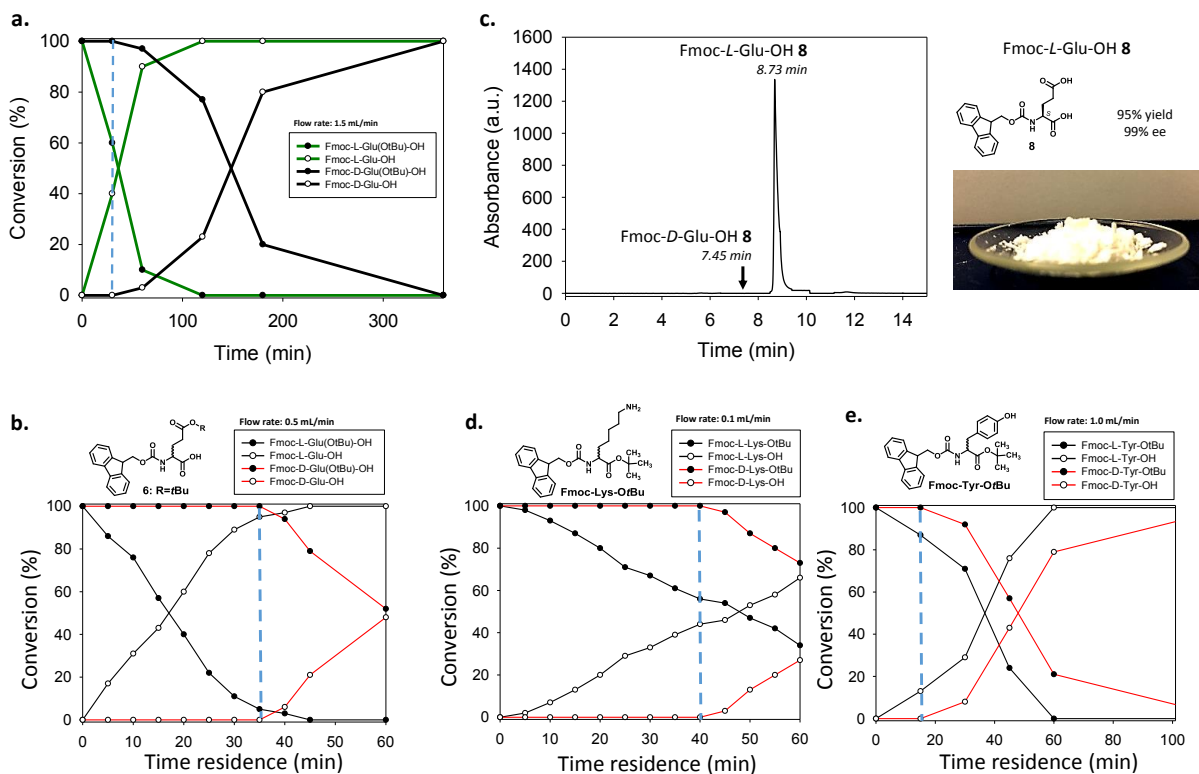


**Figure 4: Kinetic resolution of various racemate. a,** Proportion of L-6, D-6 and their corresponding hydrolyzed derivatives L-8 and D-8 respectively over the residence time using 1.5 ml/min as flow rate or **b,** 0.5 mL/min as flow rate. **c,** (left) ee determination of isolated L-8 by chiral HPLC and (right) quantitative mass of chemically and enantiomerically pure L-8 using supported CASH in a continuous flow process. **d,** Conversion of L and D lysine tertibutyl ester enantiomers and **e,** L and D tyrosine tertibutyl ester enantiomers into their corresponding carboxylic acids at various flow rates over the time residence.

#### **5.1.4. Conclusion**

Continuous flow chemistry appears particularly well adapted for CASH applications since the flow through the catalytic hydrogel compensates the low diffusion rate of substrates under static conditions (decreasing thus the reaction time) and provides also an easy separation way between products and the catalytic phase. These features were not obvious because supramolecular hydrogels are physical gels resulting from the self-assembly of small molecules and thus a gradual delamination of the CASH through the shear stress induced by the flow is a scenario that was not possible to rule out at first sight. Yet supported-CASH proved to be stable with respect to flow and over time and the catalytic process could be repeated several times without any catalytic loss. Our designed supported-CASH gives rise to an efficient esterase-like hydrogel active towards activated esters but also towards a large panel of inactivated substrates such as methyl, primary, secondary and tertiary ester classes, a feature never reported which increases its interest for the chemist's community. Last but not least, our supported CASH shows also kinetic resolution capacity allowing to isolate quantitative amount of enantiopure carboxylic acids from racemic or enantio-enriched inactivated esters. Thus we believe our contribution can find an echo in various communities of chemists going from synthetic chemistry to material science and chemical engineering.



## 5.2. Towards the design of a self-sustained hydrogel growth

### 5.2.1. Introduction

Based on the work described in the first part of this chapter, I will try to use the catalytic property of a supramolecular hydrogel to “catalyze” its own growth through a self-sustained process (Figure 5).

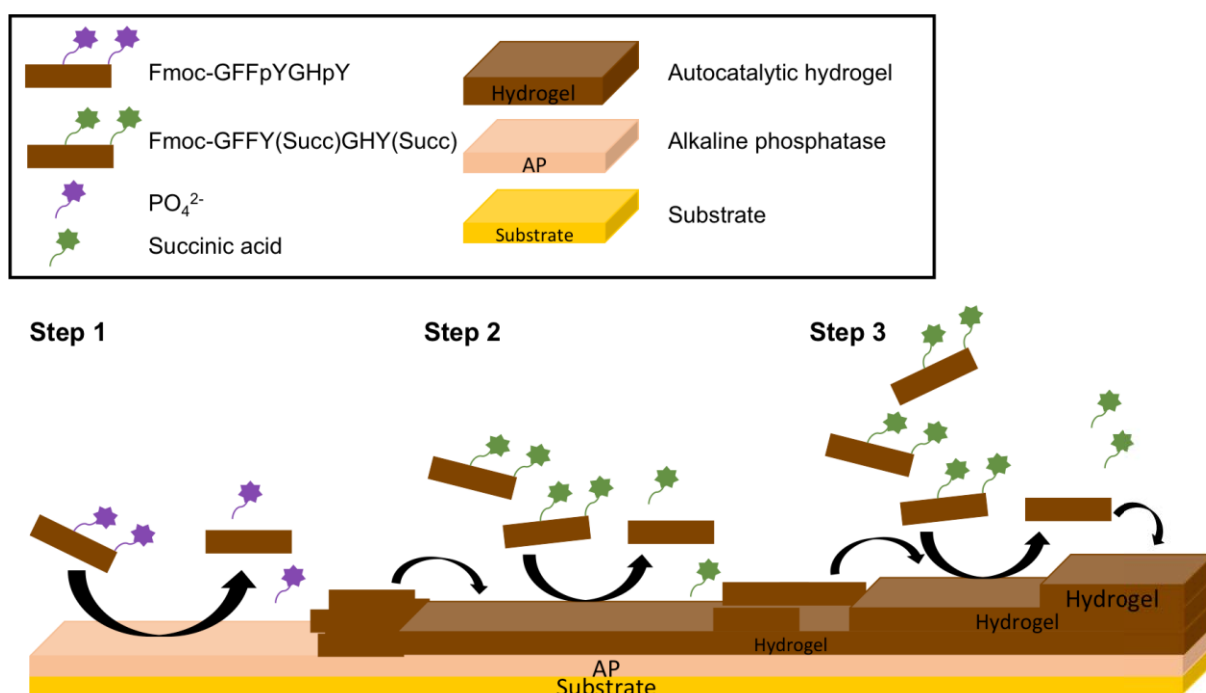


Figure 5: Formation of a localized and self-sustained hydrogel growth in three steps. Step1 corresponds to LEASA of a catalytically-active supramolecular hydrogel. Step 2 corresponds to the peptide precursors transformation in hydrogelators, catalyzed by the hydrogel. In Step 3, more catalytic hydrogel is present ensuring a self-sustaining growth of the material formed.

Preliminary results of this project are gathered as follows: (i) the strategy of synthesis, (ii) preparation and characterization of an adequate peptide precursor, (iii) gelation tests in bulk conditions and highlighting of the self-sustained hydrogel growth and (iv) localization of the catalytically-active self-assembly from a surface using the LEASA approach.

### 5.2.2. Design of an adequate precursor peptide

The CASH described in the first part of this chapter shows an esterase-like activity emerging from the self-assembly of the hydrogelator peptide Fmoc-GFFYGHY. To get a chemical system for which this previous CASH catalyzes the formation of its own constituting building block, *i.e.* Fmoc-GFFYGHY, the peptide precursor that needs to be used must have an equivalent sequence but modified with at least one ester group. The presence of the ester group should ensure the following points: (i) avoid the self-assembly in the bulk in absence of the esterase-like hydrogel, (ii) help to solubilize the precursor peptide in water. Thus, in order to fulfill these two conditions, we have proposed to introduce succinic ester groups onto the phenol of the two tyrosine residues, leading to the so-called peptide Fmoc-GFFY(Succ)GHY(Succ) (Figure 6).

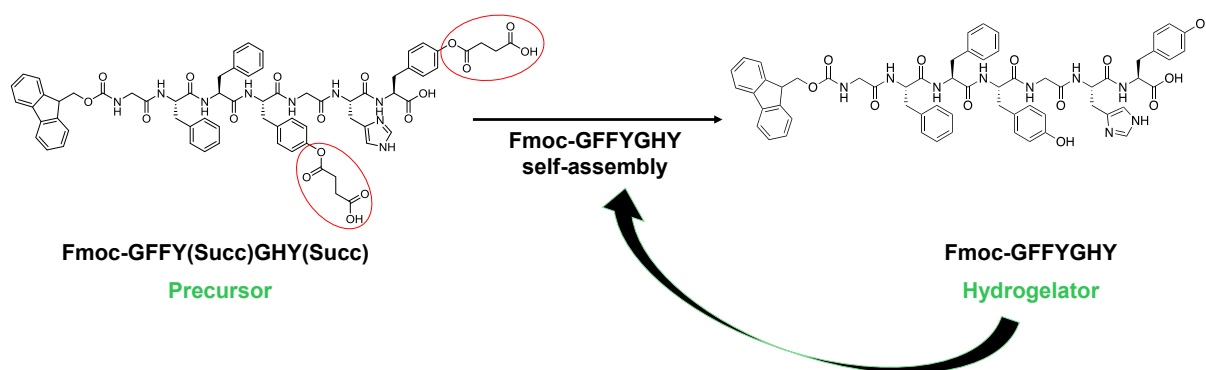


Figure 6: Chemical structure of the peptide precursor, Fmoc-GFFY(Succ)GHY(Succ), proposed to achieve the self-sustained hydrogel growth.

Before considering the synthesis of Fmoc-GFFY(Succ)GHY(Succ), it is necessary to check if the CASH (Fmoc-GFFpYGHpY + AP) is able to catalyze the desired ester hydrolysis. To do this, I have prepared a model substrate which is the Fmoc-tyrosine residue modified with a succinic ester group on the phenol group, called Fmoc-Y(Succ). The ability of the catalytic hydrogel to hydrolyze it was checked through a vial test. The CASH was formed into a vial and a solution of the Fmoc-Y(Succ) (200  $\mu$ L at 1 mg/mL) diffused within the hydrogel. The hydrolysis of the model ester Fmoc-Y(Succ) was then monitored over time by HPLC analysis of the hydrogel composition (Figure 7a). We observed that the catalytic hydrogel is able to fully hydrolyze the succinic ester group in roughly 700 minutes (50% of the model substrate is hydrolyzed in 80 minutes).

To get the suitable precursor peptide Fmoc-GFFY(Succ)GHY(Succ), my synthetic strategy was to isolate first the peptide Fmoc-GFFYGHY from solid support chemistry and then modify the two tyrosine residues in presence of succinic anhydride. But one question remained left: is the imidazole group from the histidine residue of Fmoc-GFFYGHY be modified by succinic anhydride as well? Through HPLC monitoring over time, I have compared the reaction kinetics of residues Fmoc-Y and Fmoc-H in presence of succinic anhydride: in the conditions used, the Fmoc-histidine residue did not react with the succinic anhydride unlike the tyrosine, which is fully converted in less than 1500 minutes (Figure 7b).

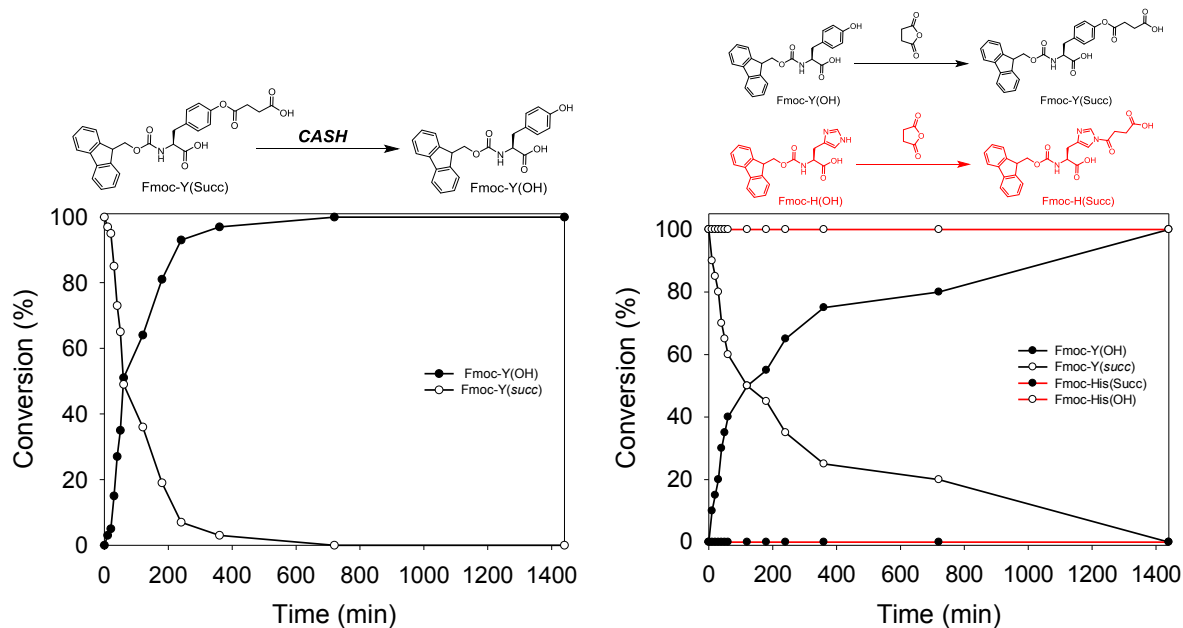


Figure 7: a) Conversion of Fmoc-Y(Succ) into Fmoc-Y as a function of time after the diffusion of Fmoc-Y(Succ) within the catalytic hydrogel. b) Monitoring of the reaction kinetic of Fmoc-Y and Fmoc-H in presence of succinic anhydride as a function of time.

To sum up this part, the CASH hydrolyzes Fmoc-Y(Succ) and only the tyrosine residue reacts with the succinic anhydride. Therefore I set up the synthesis strategy to get Fmoc-GFFY(Succ)GHY(Succ). As described in the following section, the hydrogelator Fmoc-GFFYGHY was prepared and then brought in contact with succinic anhydride to modify both tyrosine residues.



### 5.2.3. Synthesis of the precursor Fmoc-GFFY(Succ)GHY(Succ)

The synthesis of the peptide Fmoc-GFFY(Succ)GHY(Succ) has been performed on a 2-CTC resin (Figure 8). The step **a** refers to the loading of the resin with the first amino acid (aa), Fmoc-Y(OtBu), in presence of DIEA in DMF. The step **b** stands for the Fmoc group deprotection in presence of 10 % of piperidine in DMF, the step **c** stands for the coupling step of the next aa with HOBt and HBTU with DIEA in DMF and the final step **d** corresponds to the cleavage of the peptide from the resin. The deprotection of the lateral chains was realized in 95% of TFA, 2.5 % water and 2.5 % TIPS. The final step of the synthesis is the acylation of both tyrosine in presence of 2.5 eq. of succinic anhydride in DCM at room temperature during 24 h. Several precipitations of residues in cold diethyl ether lead to a white solid. <sup>1</sup>H NMR and high resolution mass analyses confirmed the structure of the desired precursor peptide Fmoc-GFFY(Succ)GHY(Succ). The detailed protocol and characterization of this synthesis is reported in chapter 2.



Figure 8: Peptide synthesis pathway of the precursor peptide Fmoc-GFFY(succ)GHY(succ) realized on solid support.

### 5.2.4. Gelation tests of Fmoc-GFFY(Succ)GHY(Succ) in vials

First of all, the ability of Fmoc-GFFY(Succ)GHY(Succ) to generate an hydrogel once the succinic ester groups are hydrolyzed has to be demonstrated. To catalyze this reaction and start the gelation process at the same time, we have used the CASH formed from Fmoc-GFFpYGHpY, described in the first part of this chapter. This catalytic hydrogel was formed in a vial (300 $\mu$ L at 10 mg/mL of Fmoc-GFFpYGHpY and 20  $\mu$ L of AP at 1 mg/mL) and 200  $\mu$ L solution of Fmoc-GFFY(Succ)GHY(Succ) at 10 mg/mL was deposited on top of the CASH. 24h later ( $t=24$ h), the solution of the precursor has not yet diffused entirely within the CASH. However, still 24h later ( $t=48$ h), there is no more distinction between the precursor solution and the CASH: only a homogeneous and viscous solution is obtained. Which means that the addition of the Fmoc-GFFY(Succ)GHY(Succ) first solubilizes the initial cash. Interestingly, at  $t=72$ h, a unique hydrogel phase is observed when the inverted tube test is realized (Figure 8). HPLC analysis confirmed the unique presence of Fmoc-GFFYGHY in the gel composition. To explain these observations, we expect that Fmoc-GFFY(succ)GHY(succ) intercalates into the self-assembled nanofibers leading to a “dissolution” of the hydrogel, explaining the “sol” state observed. Even if nanofibers are thus free in solution, they are still catalytically-active, ensuring the transformation of the precursor in hydrogelator Fmoc-GFFYGHY. Finally, the re-formation of the “gel” state is in agreement with a self-sustained process: the system catalyzes the generation of its own building blocks.

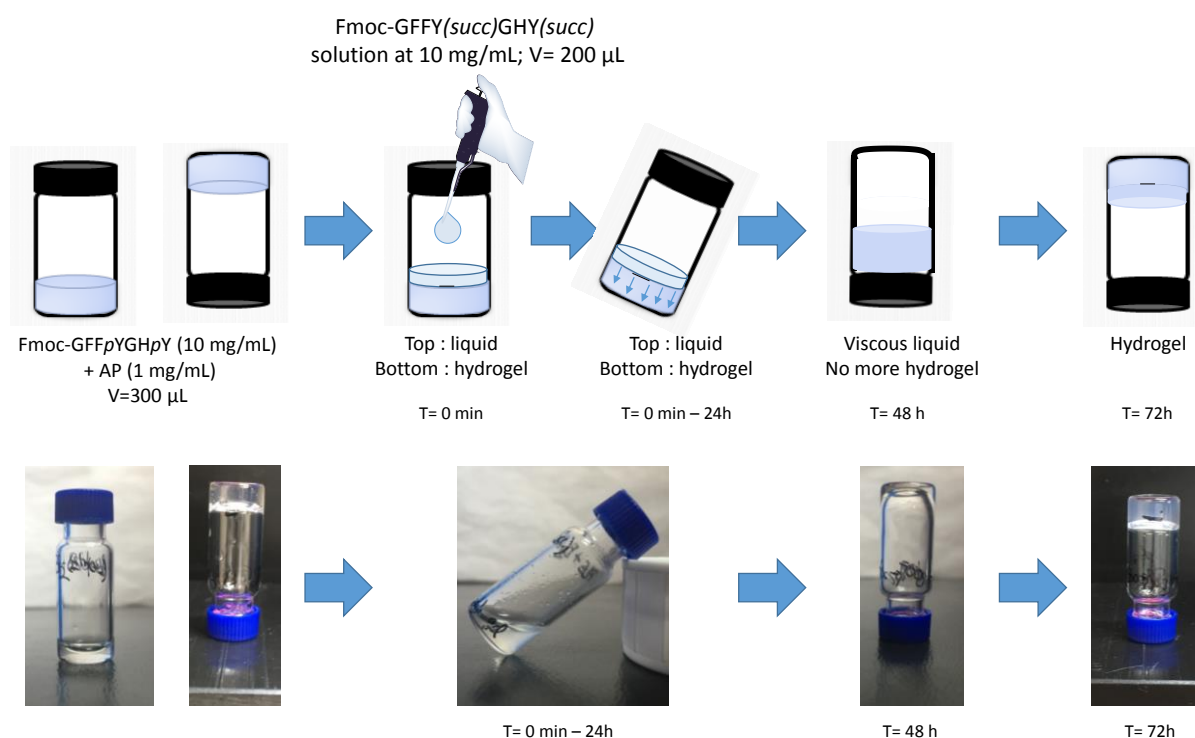


Figure 8: Hydrogelation of Fmoc-GFFY(succ)GHY(succ) in presence of CASH.

The kinetic of Fmoc-GFFY(*succ*)GHY(*succ*) hydrolysis should depend on the amount (volume) of CASH present in the vial. To verify this hypothesis, different volumes of the catalytic hydrogel were prepared: 20, 50, 100 and 200. 200  $\mu\text{L}$  of a Fmoc-GFFY(*succ*)GHY(*succ*) solution (1 mg/mL) was dropped off in the vial, on the catalytic hydrogel. It must be noted that the concentration of precursor peptide is ten times lower than in the previous experiment. As a consequence, the deposition of Fmoc-GFFY(*Succ*)GHY(*Succ*) solution onto the CASH does not lead to a dissolution of the hydrogel (and the CASH does not swell over the time needed for the monitoring). In addition, this low concentration of Fmoc-GFFY(*Succ*)GHY(*Succ*) solution does not allow hydrogelation if it would be transformed into Fmoc-GFFYGHY. The chemical composition of the supernatant and the hydrogel were analyzed by HPLC over 24 hours and results for each volume of CASH are shown in figure 9. In particular, the amount of the hydrogelator Fmoc-GFFYGHY formed into the CASH and the one of the precursor Fmoc-GFFY(*Succ*)GHY(*Succ*) present both in the supernatant and in the CASH are monitored. First of all, we observed that with all volumes of CASH investigated, a complete conversion of the precursor in hydrogelator is observed in roughly the same duration, *i.e.* 700 minutes. This observation is in agreement with an autocatalytic process where the product generated catalyzes its own formation. With 20, 100 and 200  $\mu\text{L}$  of CASH, the proportion of Fmoc-GFFYGHY formed inside the hydrogel increases up to 100 minutes and then its formation accelerates. If we consider an infinite concentration of precursor peptides at  $t=0$ , this acceleration of the kinetic formation of the hydrogelator can be explained by a contribution of the new Fmoc-GFFYGHY peptides formed in the CASH, increasing the number of catalytically self-assembled nanofibers.

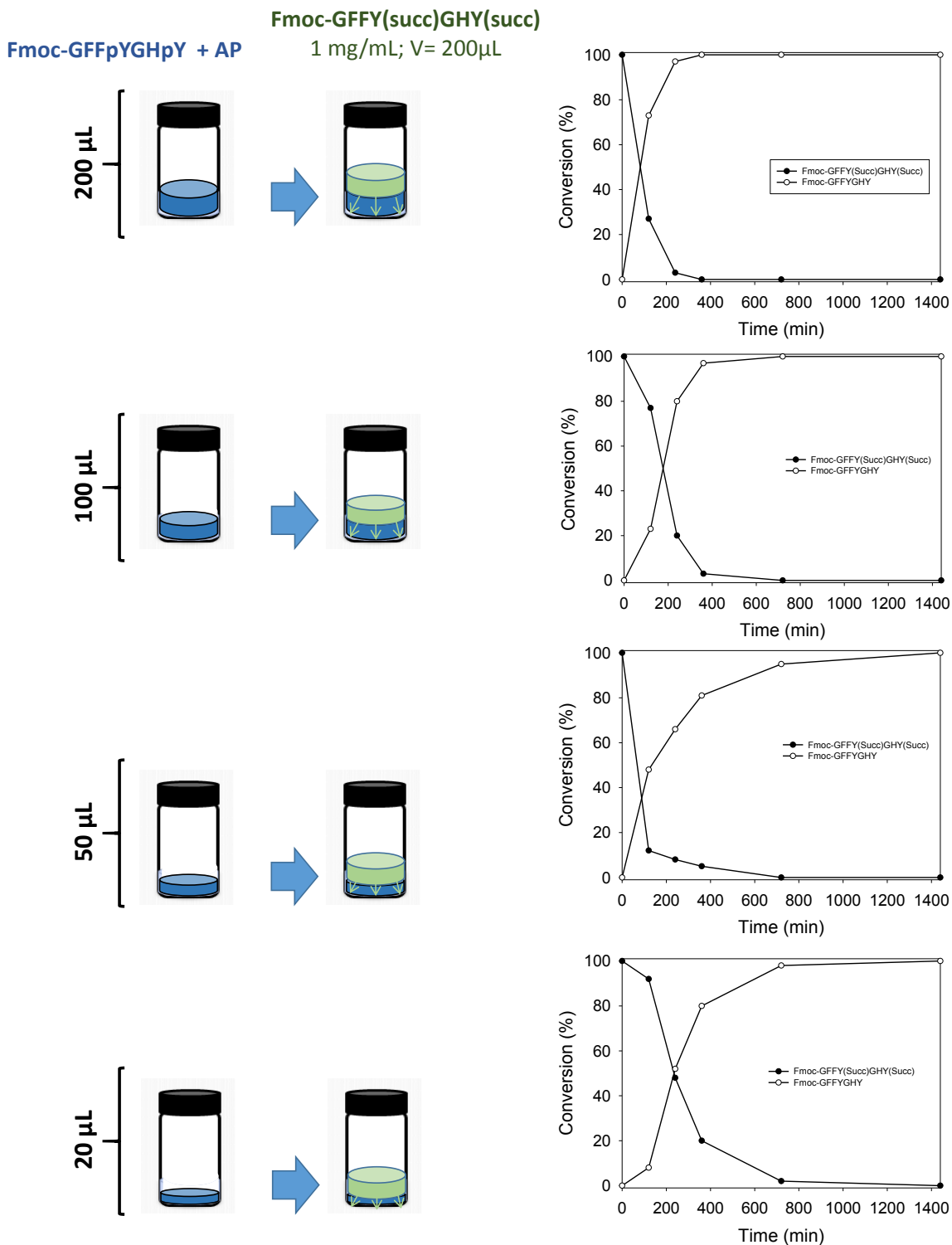


Figure 9: kinetic transformation of the precursor peptide Fmoc-GFFY(Succ)GHY(Succ) (200  $\mu$ L; 5 mg/mL) when diffusing within different volumes of CASH (20, 50, 100 and 200  $\mu$ L). HPLC composition analyses of the CASH and of the supernatant were done over 24h to follow the hydrogelator formation depending on the quantity of the precursor catalytic hydrogel.

Two negative control assays were performed to demonstrate that the chemical transformation of the precursor Fmoc-GFFY(Succ)GHY(Succ) in Fmoc-GFFYGHY is catalyzed by the CASH. First of all, HPLC monitoring of solely precursor (1 mg/mL) was performed over 5 days to determine the contribution of the ester hydrolysis coming from water (Figure 10a). No noteworthy hydrolysis of this peptide was observed (<5%). An assay using a non-catalytically active hydrogel instead of the CASH was used in the presence of the precursor Fmoc-GFFY(Succ)GHY(Succ). When the tripeptide Fmoc-FFpY is mixed with AP, a supramolecular hydrogel resulting from Fmoc-FFY self-assembly is formed, displaying no esterase-like activity. No conversion of the precursor Fmoc-GFFY(Succ)GHY(Succ) in the hydrogelator Fmoc-GFFYGHY was observed by HPLC over 1400 minutes, both in the gel and in the supernatant (Figure 10b).

We also investigated the possibility to form the supramolecular hydrogel from Fmoc-GFFY(Succ)GHY(Succ) using an esterase such as the commercially available Pig Liver Esterase (PLE). This could be interesting for further LEASA developments. Unfortunately, when this reaction was followed by HPLC over 24h (Figure 10c), no formation of the hydrogelator Fmoc-GFFYGHY was observed, which means that the PLE is inactive toward the precursor peptide Fmoc-GFFY(Succ)GHY(Succ).

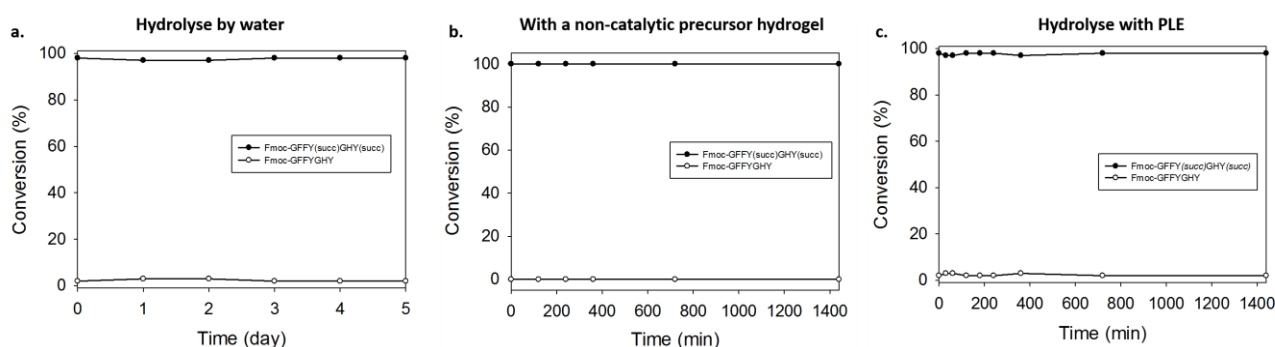


Figure 10: HPLC monitoring over time of three vial test assays: hydrolysis of Fmoc-GFFY(succ)GHY(succ) in a) water, b) in presence of a non-catalytic supramolecular hydrogel and c) in presence of PLE.

### 5.2.5. Characterization of the autocatalytic hydrogel by FT-IR and Fluorescence microscopy

The FT-IR measurements were performed on an ATR diamond. The Fmoc-GFFYGHY hydrogel was formed from the precursor peptide Fmoc-GFFY(Succ)GHY(Succ) solution brought in contact with a CASH hydrogel (generated from Fmoc-GFFYpGHpY and AP) After diffusion within the CASH, a solution is obtained which reforms a gel later (see Figure 8 for a description of the process). The goal of this FT-IR study was to analyze the self-assembly of the resulting hydrogel. Sharper and more intense bands in the amide region are observed compared to both the solution of the precursor Fmoc-GFFY(succ)GHY(succ) and the hydrogel formed using AP (Figure 11a).

We observe bands at 1686 and 1636  $\text{cm}^{-1}$  in the amide I region, which correspond to antiparallel  $\beta$ -sheets conformations. Vibration bands between 1512 and 1437  $\text{cm}^{-1}$  are assigned to the carbamate group.<sup>43</sup>

The fluorescence emission assays has confirmed the densification of the Fmoc-GFFYGHY self-assembly in the hydrogel formed from Fmoc-GFFY(Succ)GHY(Succ) because a significant increase of the fluorescence emission intensity measured at 325 nm ( $\lambda_{\text{ex}} = 290$  nm) (Figure 11b) was measured. This emission is due to more excimer assembly of Fmoc groups. As negative control experiment, we let diffuse the precursor peptide Fmoc-GFFY(Succ)GHY(Succ) within the non-catalytically-active Fmoc-FFY hydrogel and observed a unique emission at 305 nm corresponding to unstacked Fmoc-groups (Figure 11c).

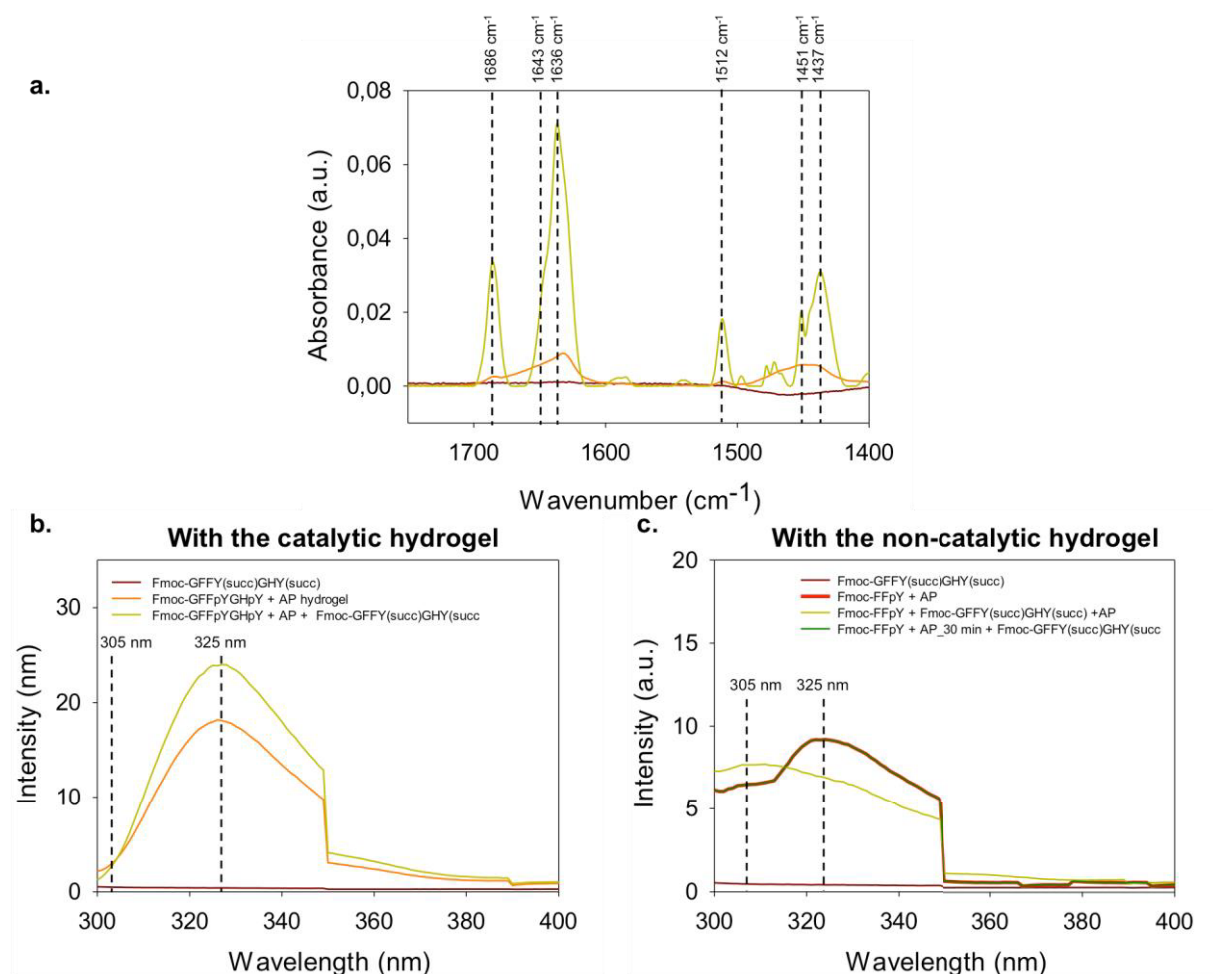


Figure 9: a) FT-IR spectra of the hydrogel with the autocatalytic self-assembly and the catalytic precursor hydrogel (green) and the catalytic precursor hydrogel alone at the same concentration (orange). b) Fluorescence spectra of (right) the Fmoc-GFFY(Succ)GHY(Succ) peptide solution (dark red), the catalytic precursor hydrogel (orange) and the resulting peptide after autocatalysis (green). The negative control with the solution of the Fmoc-GFFY(Succ)GHY(Succ) peptide (dark red), non-catalytic precursor hydrogel (red), the resulting peptide when the solution of Fmoc-GFFY(Succ)GHY(Succ) have diffused at 5 min (green) and 30 min (dark green) (left).

## 5.2.6. Surface-localization of the autocatalytic hydrogel

### 5.2.6.1. Monitoring of the mass deposition onto a surface by QCM-D

The self-assembly formation from the surface in presence of Fmoc-GFFY(Succ)GHY(Succ) was monitored by QCM-D. The QCM-D was chosen because it is a very sensitive technique for characterizing mass deposition on surface.

I have modified the surface of gold QCM substrate with an enzymatically-active multilayer, where AP is the chosen enzyme. The buildup of the multilayer was first monitored and leads to a 19 nm thick for (PEI/PSS)<sub>2</sub>/PEI/AP multilayer film architecture (section 5 in ESI of the part 5.1). When this so-modified substrate was brought in contact with Fmoc-GFFpYGHpY solution, a spontaneous decrease of 200 Hz of the fundamental frequency was observed, characteristic of a highly hydrated mass deposition (Figure 12).<sup>13,14</sup> This hydrogel layer is called pre-hydrogel. Then, when we brought different concentrations of the precursor Fmoc-GFFY(Succ)GHY(Succ) in contact with the pre-hydrogel a spontaneous decrease of all frequency shifts is observed. This decrease is comprised between 200 and 1000 Hz (for the fundamental frequency) depending on the peptide concentration considered (from 0.1 mg/mL to 1.0 mg/mL), is much more important than the decrease observed during the pre-hydrogel formation (Figure 13a).

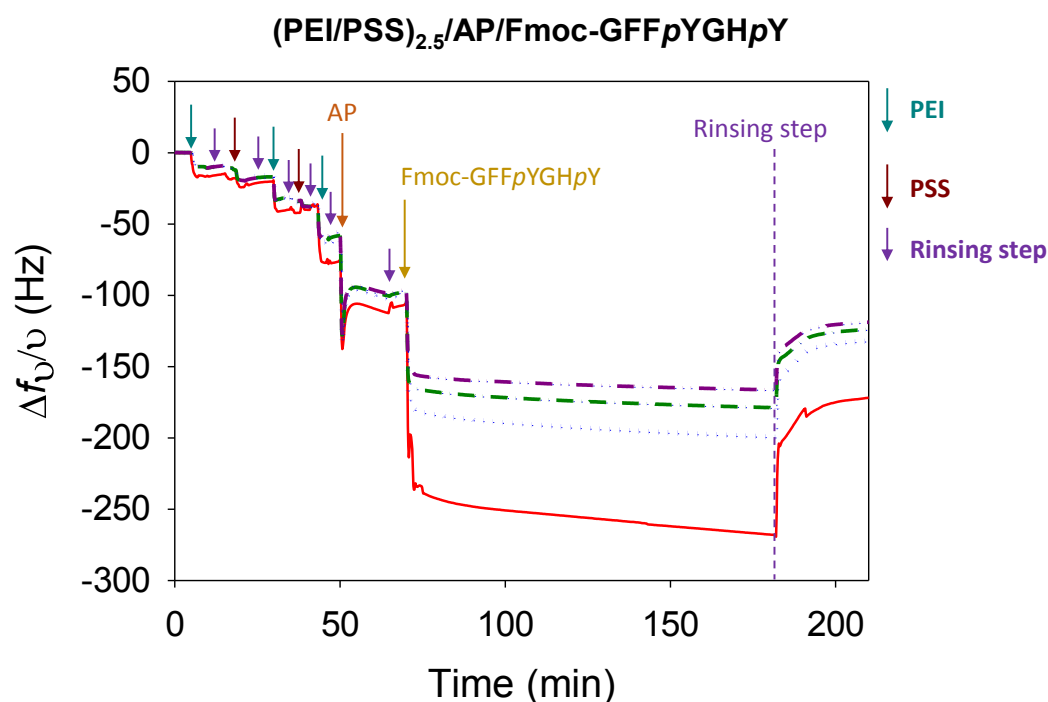


Figure 12: Evolution of the 1<sup>st</sup>, 3<sup>th</sup>, 5<sup>th</sup> and 7<sup>th</sup> frequency shift measured by QCM-D of the pre-hydrogel in presence of Fmoc-GFFY(Succ)GHY(Succ) solution.

Negative control tests were also performed to demonstrate that 1) adsorbed AP does not have any influence on the ester hydrolysis of Fmoc-GFFY(Succ)GHY(Succ) and 2) Fmoc-GFFY(Succ)GHY(Succ) does not only diffuse within the pre-hydrogel, but also intercalate in the self-assembly and thus decrease the frequency shift. To answer to these two points, a first experiment was done using the enzymatically-active multilayer (PEI/PSS)<sub>2.5</sub>/PEI/AP. When brought in contact with Fmoc-GFFY(Succ)GHY(Succ) solution, no decrease of the QCM signals was observed, meaning that AP cannot transform the precursor peptide into the hydrogelator Fmoc-GFFYGHY (Figure 13b). A second QCM experiment was carried out using the non-catalytically active pre-hydrogel formed from AP and Fmoc-FFpY. When Fmoc-GFFY(Succ)GHY(Succ) solution was brought in contact with this pre-hydrogel, no decrease in the QCM-D frequencies were observed (Figure 13c).

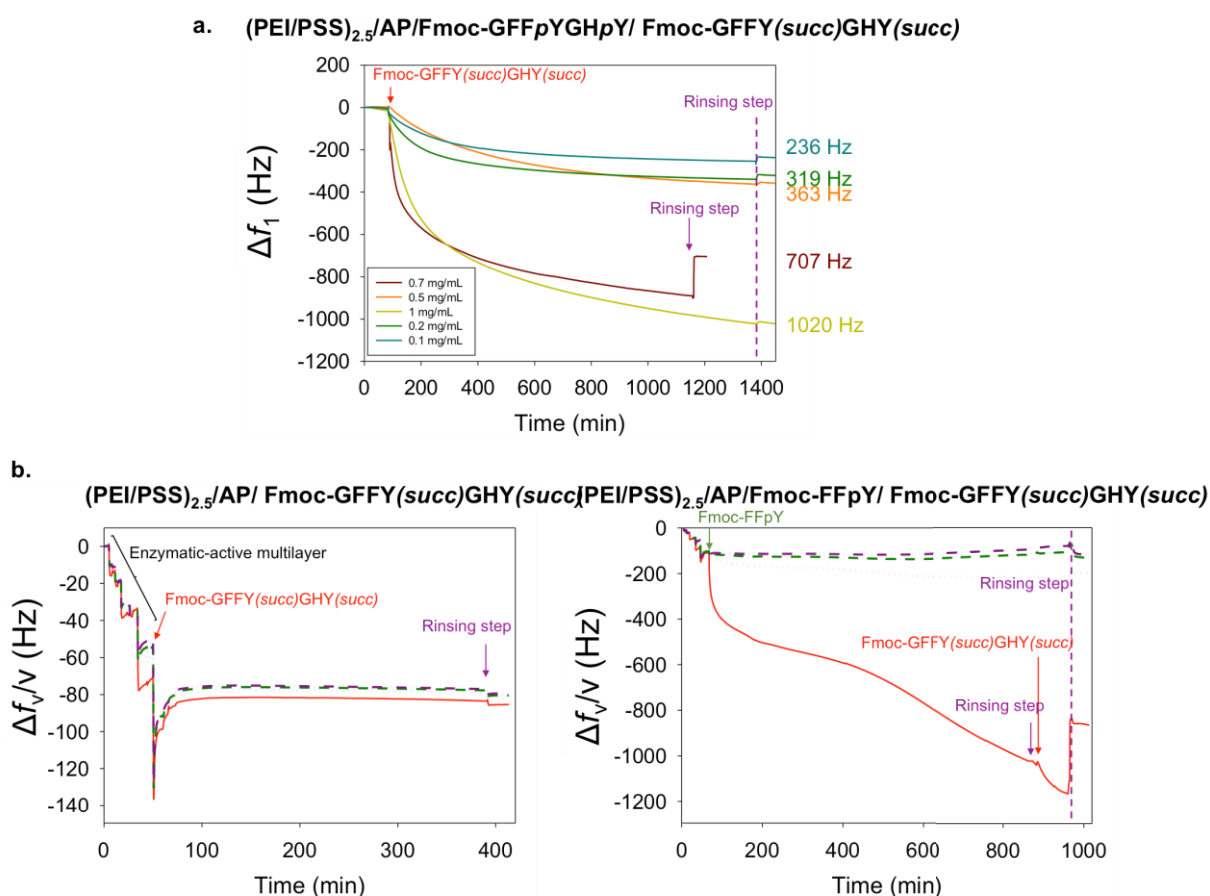


Figure 10: a) QCM-D signal for the fundamental frequency for the different concentration of Fmoc-GFFY(Succ)GHY(Succ) solution brought in contact with the catalytically-active pre-hydrogel and b) the negatives controls tests (left) with only the enzymatic-active multilayer and (right) with the non-catalytically active pre-hydrogel.



### 5.2.6.2. Morphological characterization of the hydrogel grown from an auto-catalytic process and generated from a surface

The internal fibrous architecture of the auto-catalytic hydrogel formed from Fmoc-GFFY(Succ)GHY(Succ) was also studied by cryo-SEM. As described in the previous section 5.2.6.1, a catalytically-active pre-hydrogel was first formed onto a wafer substrate from adsorbed AP and then contacted with Fmoc-GFFpYGHpY solution (1 mg/mL). The esterase-like pre-hydrogel grew during 2 hours, reaching a final thickness of 12  $\mu\text{m}$  (Figures 14d, e and f) and displaying an internal fibrous network of long fibers going from the substrate to the top of the gel. The smaller fiber diameter measured is about 5 nm. Then, a solution of the precursor peptide Fmoc-GFFY(Succ)GHY(Succ) was brought in contact with the pre-hydrogel during 12 h. Cryo-SEM analysis shows a substrate entirely cover with a hydrogel 16  $\mu\text{m}$  thick (Figures 14 a, b and c). The fibrous network is quasi-identical to the one formed from AP and Fmoc-GFFpYGHpY.

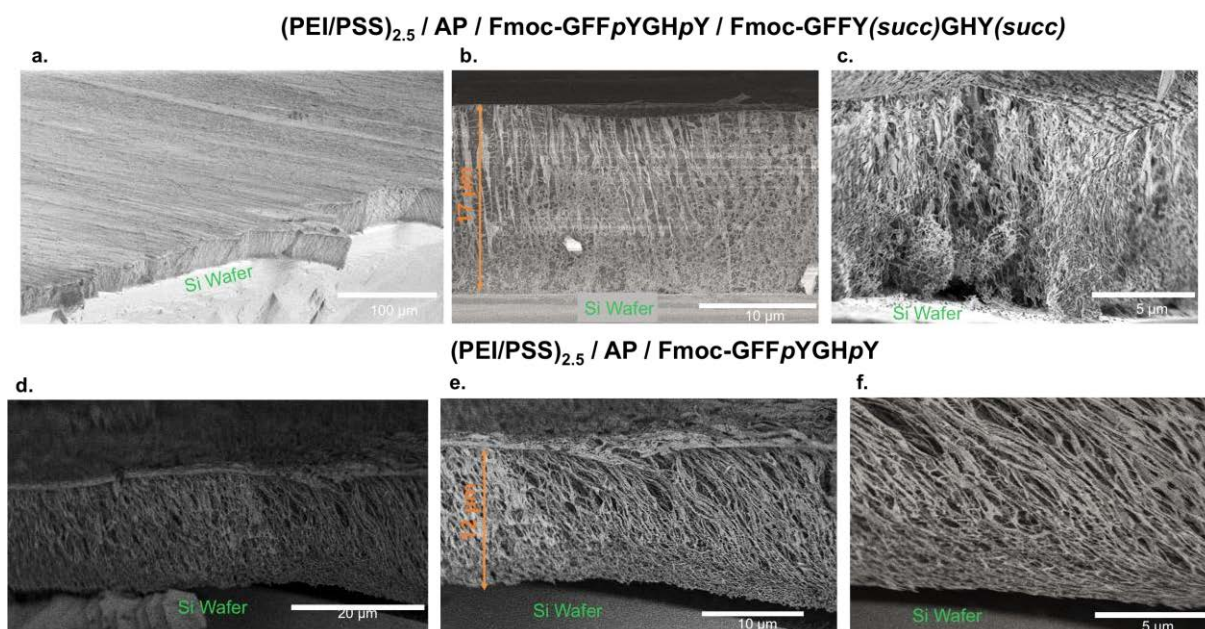


Figure 14: Cryo-SEM pictures of hydrogel generated (i) from a silica wafer modified with AP and then put in contact with Fmoc-GFFpYGHpY (d,e and f), (ii) from the pre-hydrogel put in contact with Fmoc-GFFY(Succ)GHY(Succ) during 12h (a, b and c).

### **5.2.7. Conclusion**

To summarize the second part of this chapter, I succeeded to design and to synthesize an autocatalytic precursor, Fmoc-GFFY(Succ)GHY(Succ). This preliminary study shows that the resulting hydrogel is promising: indeed, I demonstrated its formation in solution when it is initiated by the catalytic prehydrogel but also from a surface through QCM and *cryo*-SEM experiments. I also characterized its supramolecular assembly through FT-IR and fluorescence emission spectroscopy.

The way to initiate the self-assembly and thus observe how the self-sustaining process fall into place, is important. In the near future we would like to use an electrochemical stimulus because this approach would allow to finely control the amount of precursor peptide Fmoc-GFFY(Succ)GHY(Succ) which is hydrolyzed in hydrogelator Fmoc-GFFYGHY.

## **GENERAL CONCLUSION OF CHAPTER 5**

*In this chapter 5, I have described a peptide self-assembly from which emerges an efficient esterase-like activity over all classes of esters. Moreover, this CASH can be supported on different kinds of surfaces and especially on porous polymer supports such as open-cell foams. This allowed to design a reactor containing our supported CASH. This reactor for continuous flow transformations can be re-used for several successive runs without loss of its catalytic activity.*

*This CASH was also the first step to get a hydrogel self-sustained growth. This autocatalytic system is currently still under investigation but this preliminary work shows promising results.*

### Highlights of the chapter

- ✓ The CASH exhibits esterase-like activity for all kinds of esters and can be use for racemic discrimination.
- ✓ The CASH can be supported on different kinds of surfaces, in particular on porous materials.
- ✓ The supported-CASH can be used in flow chemistry, which permits to reuse it several times and isolate it from the substrate and product.
- ✓ The CASH lead to the design of a promising autocatalytic self-assembly hydrogel, which is under investigation

## 5.3. ESI of the part 5.1 of this chapter

### 5.3.1. Additional Figures

Characterization of the self-assembly by HPLC, CD and FT-IR

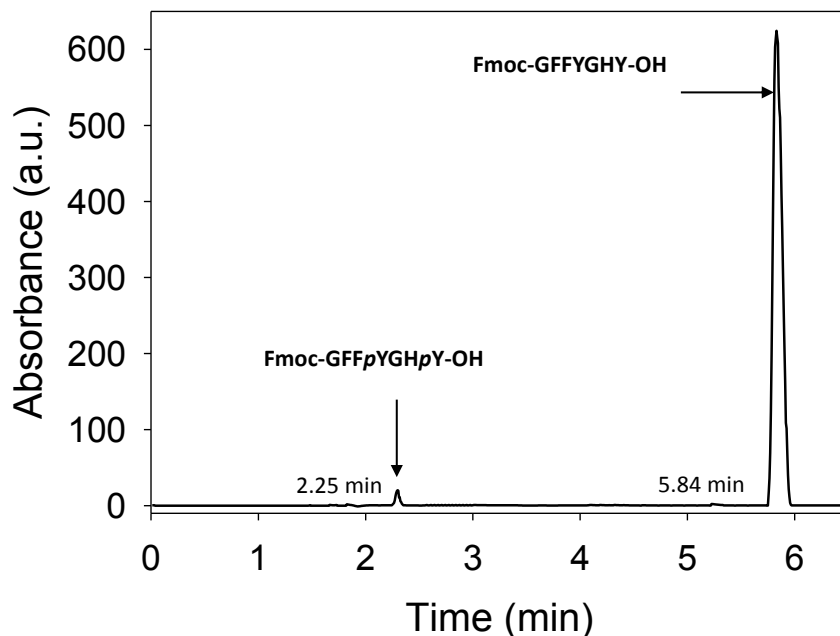


**Figure S1:** HPLC chromatogram showing the chemical composition analysis of Fmoc-GFFYGHY hydrogel.

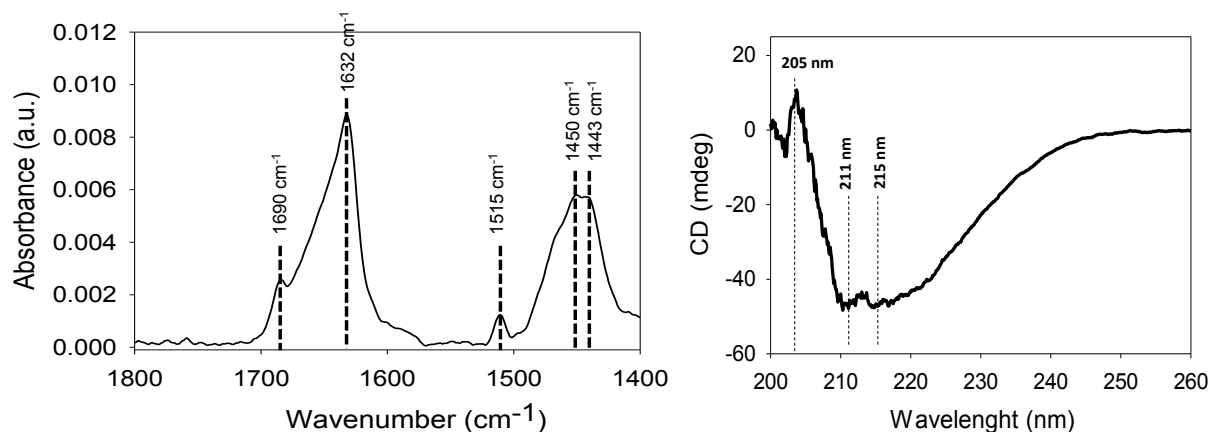


**Figure S2:** IR (left) and CD (right) spectra of the Fmoc-GFFYGHY hydrogel (=CASH). (left) All vibrational bands observed at 1632, 1515, 1450, 1443 cm<sup>-1</sup> and in particular the one located at 1690 cm<sup>-1</sup> are characteristics of the antiparallel  $\beta$ -sheet assemblies.<sup>29</sup> (right) Minima bands at 211 and 215 nm, in addition to the maxima at 205 nm, confirm the presence of  $\beta$ -sheet assembly in the CASH.

### Characterization of the esterase-like catalytic activity of the hydrogel formed in solution (inside the vial)

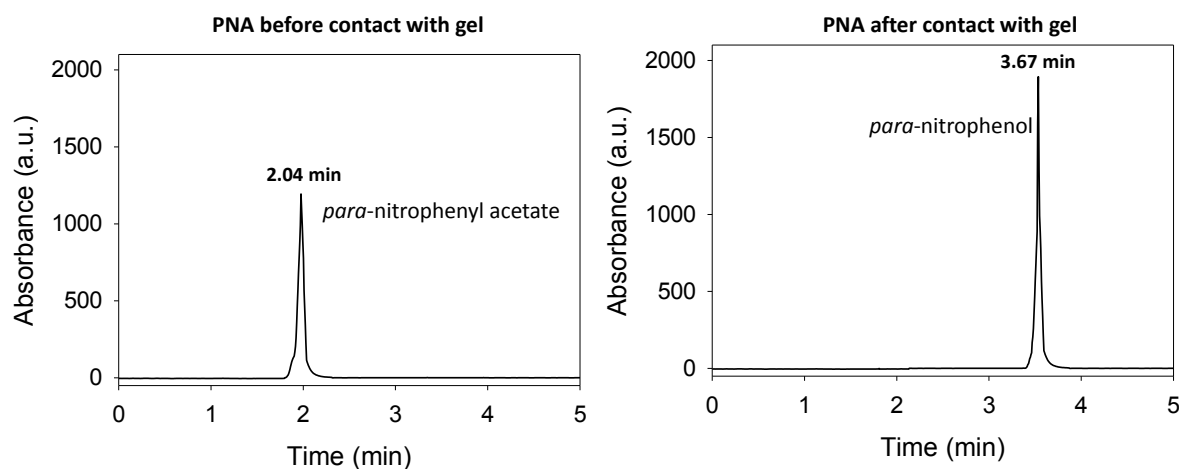


**Figure S3:** HPLC chromatograms of the complete ester hydrolysis of the model substrate PNA in presence of the catalytic hydrogel formed in the bulk (vial test, see ESI section 15). (left) HPLC analysis of the PNA solution deposited onto the CASH in the vial, and (right) HPLC analysis of the CASH 2 hours after the complete diffusion of the PNA solution within the catalytic hydrogel.

### Characterization of the self-assembly formed from the surface by QCM-D, HPLC, AFM and SEM

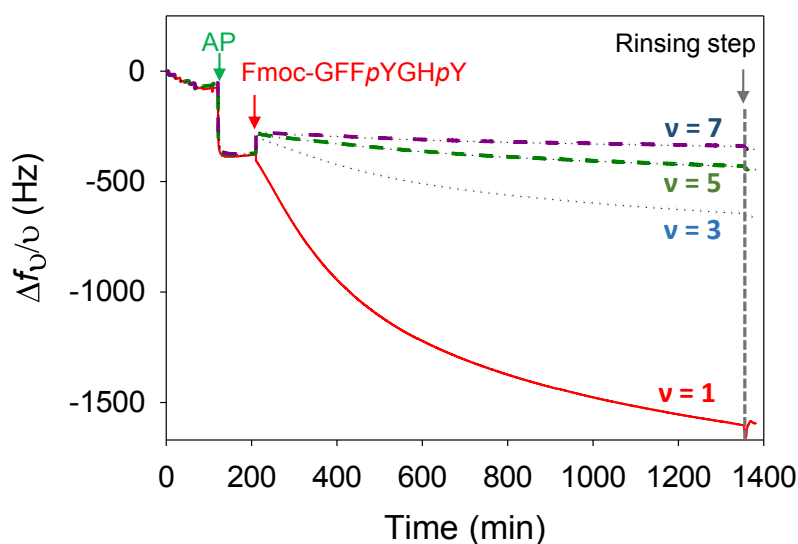


**Figure S4:** QCM frequencies evolution over time when the enzymatic multilayer is brought in contact with Fmoc-GFFpYGHpY solution ( $\nu$  represents the different overtones).

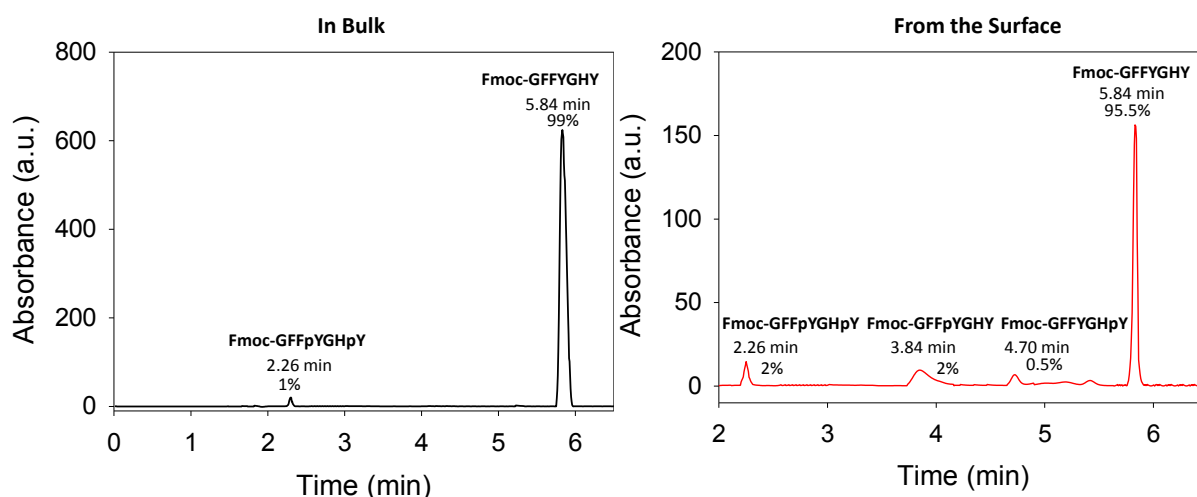


**Figure S5:** HPLC analyses of the CASH hydrogel formed in the bulk (left) with enzyme in solution (equivalent to Fig. 1c in the manuscript) and from enzymes adsorbed on a surface through the multilayer film PEI/(PSS/PEI)<sub>2</sub> (right). HPLC conditions used: column C18 reversed phase SUPELCOSIL ABZ; eluent: 80/20 (acetonitrile/H<sub>2</sub>O); isocratic flow: 1 mL/min; temperature: 22°C.

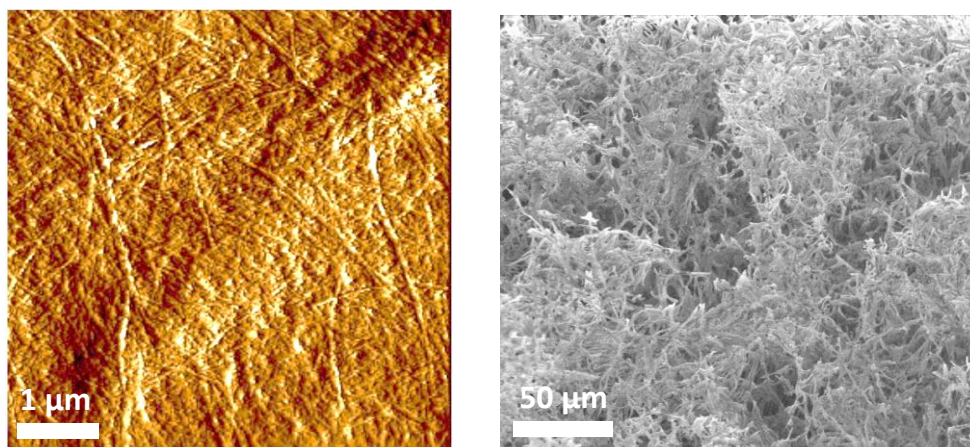


**Figure S6:** (left) AFM phase image and (right) SEM image of the CASH formed from the QCM quartz crystal (flat substrate).

Fluorescence assay to observe the presence of the excimer characteristic of the  $\pi$ - $\pi$  interaction inside the self-assembly

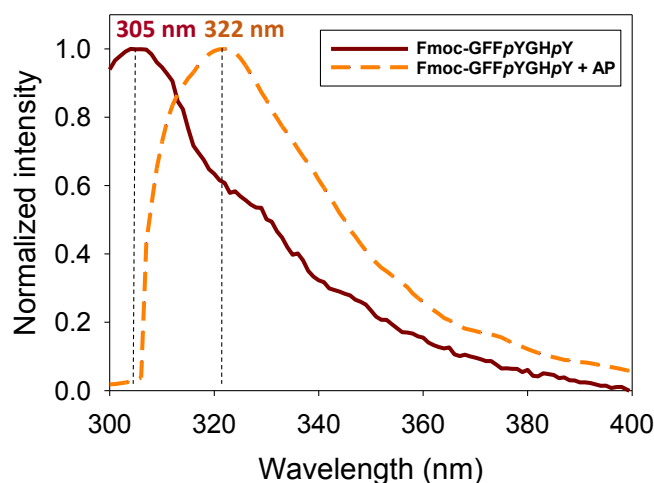


**Figure S7:** Normalized emission fluorescence intensity shift of the CASH formed in presence of alkaline phosphatase (AP) when excited at 290 nm (dashed orange curve) compared to Fmoc-GFFpYGHpY solution (red curve). The maximum emission band shift observed from 305 nm to 322 nm is due to the Fmoc groups' excimer characteristic of the peptide Fmoc-GFFYGHY self-assembly.<sup>30</sup>

Esterase-like catalytic activity assays on the self-assembly generated from the surface

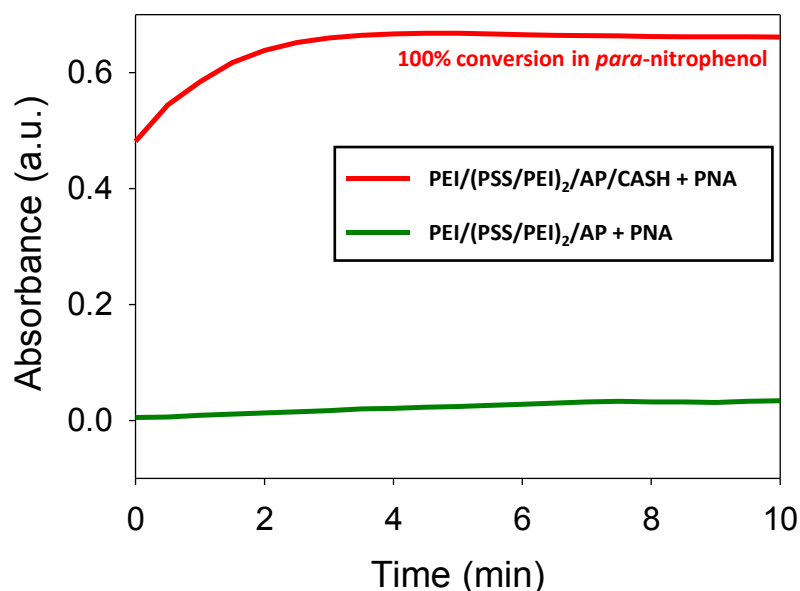


**Figure S8:** *p*-NPA hydrolysis followed over time through the absorbance measured at 405 nm in presence of the multilayer (green) or the glass-supported CASH (red).

Esterase-like catalytic activity assays with the supported-CASH in the reactor

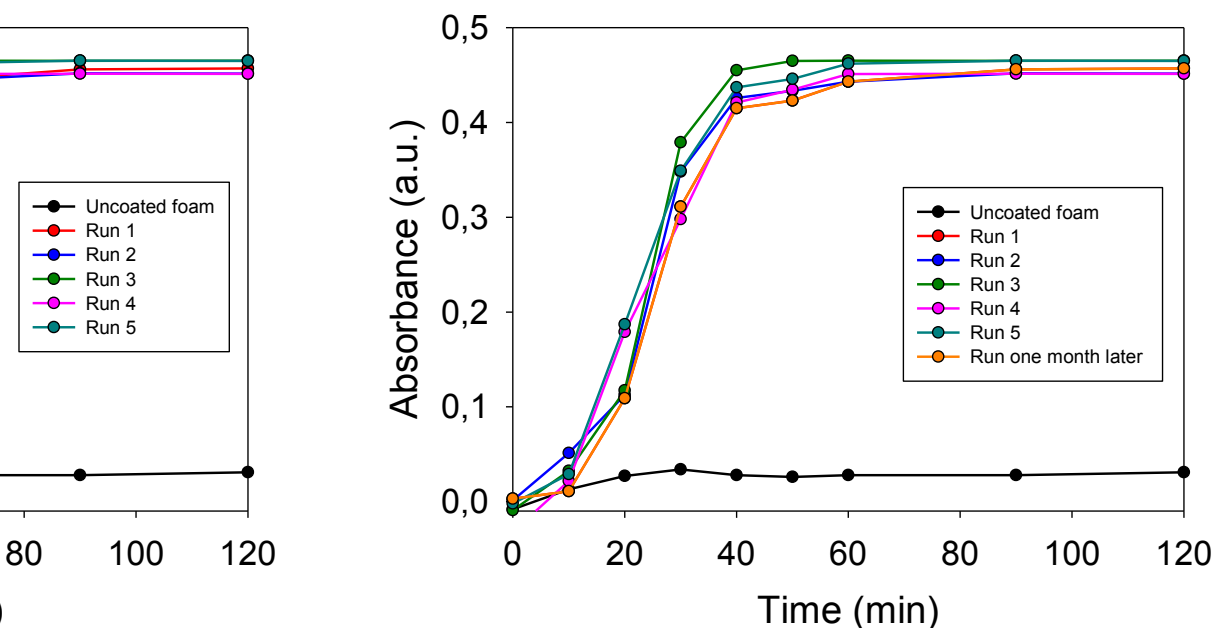


**Figure S9:** (left) Reusability test of a supported-CASH column illustrated through five successive runs of PNA hydrolysis (evolution of the para-nitrophenol formation over residence time) and one run after one month later (right), the supported CASH was sealed and stored at 4°C. A washing step with deionized water is realized between each run to ensure a complete removal of PNA or para-nitrophenol traces from the previous run.

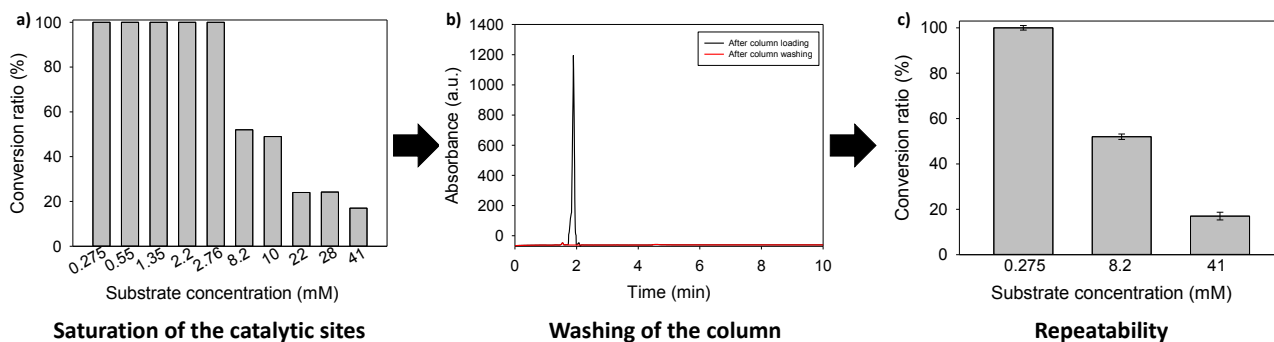


**Figure S10:** a) Saturation of the catalytic site of the supported CASH column by acylation of imidazole group but after b) washing of the column all the para-nitrophenol left the column and the column c) is reusable. Thus we have obtained identical conversion values in a second as those obtained in the first one for equivalent concentrations of PNA. Error bars have been calculated from three independent experiments.



## Modelisation of the interaction between the Fmoc-Group and the laid out of the Histidine group

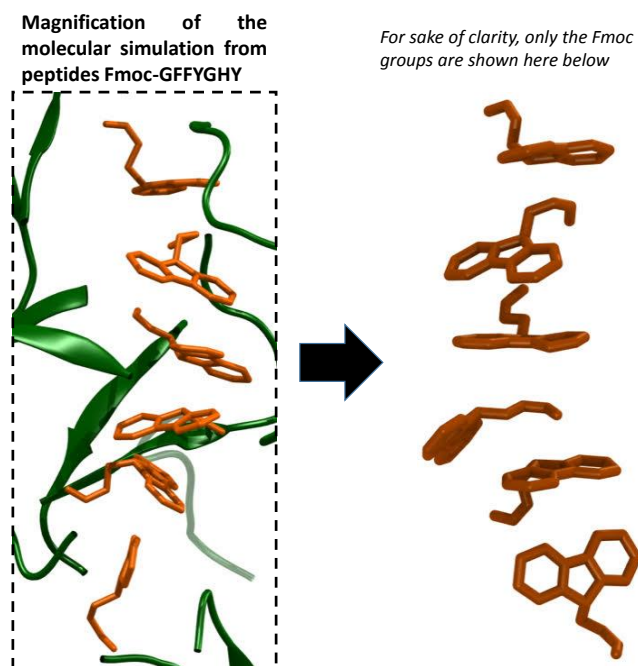


**Figure S11:** Magnifications from the molecular simulation of 16 peptides Fmoc-GFFYGHY (figure 3b in the manuscript) highlighting the  $\pi$ - $\pi$  stacking of the Fmoc groups.

## Esterase-like catalytic assays on the supported-CASH on non activated esters

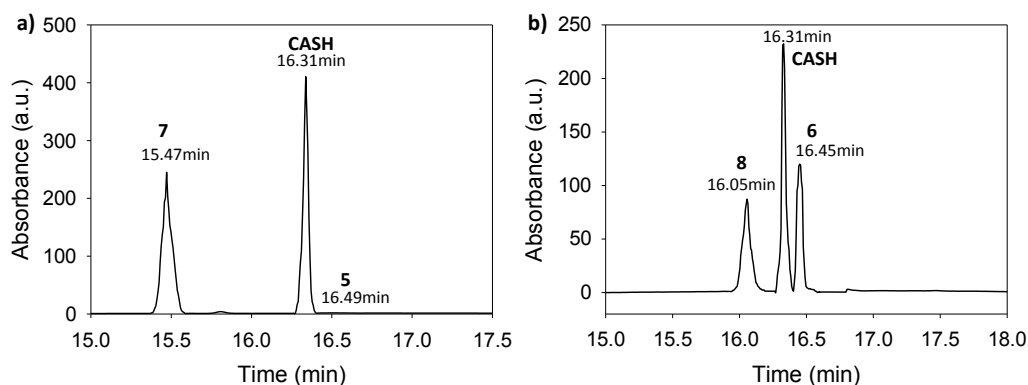


**Figure S12:** HPLC chromatograms of ester hydrolysis of a) substrate 5 in 7 and b) ester substrate 6 in 8 both after 24 h in contact within the catalytic hydrogel formed in the bulk (vial). HPLC conditions used: column C18 reversed phase SUPELCOSIL ABZ+<sub>50/50</sub> (Acetonitrile/H<sub>2</sub>O) isocratic\_flow: 1 mL/min<sub>22</sub>°C. The CASH is vortexed and dissolved in acetonitrile/H<sub>2</sub>O (50/50) mixture before HPLC analysis: that is the reason why there is the presence of the peptide Fmoc-GFFYGHY (called CASH) in the following chromatograms.

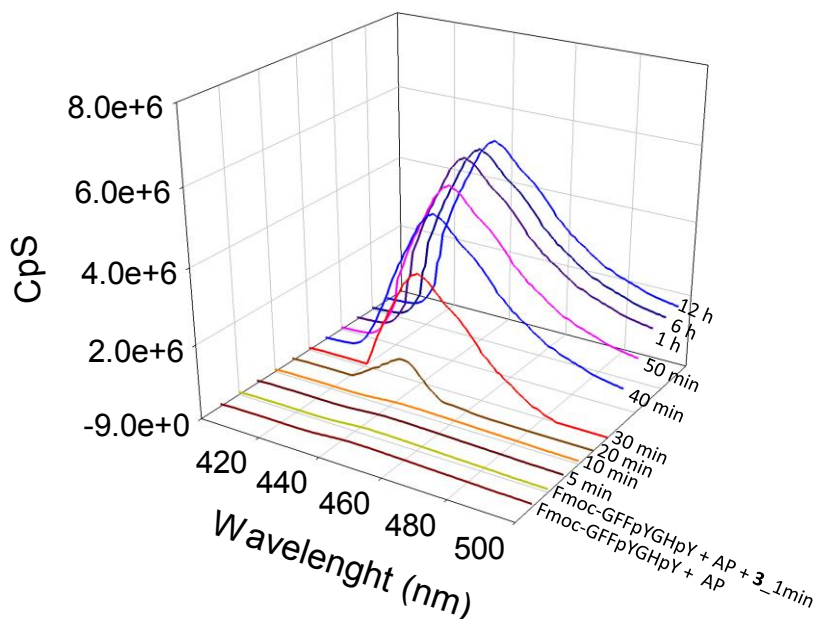


**Figure S13:** Fluorescence emission monitoring over time of the excimer of the naphthalene group ( $\lambda_{ex} = 350 \text{ nm}$ ,  $\lambda_{em} = 435 \text{ nm}$ ) to follow the self-assembly process of derivative **4** when formed from the hydrolysis of ester **3** in situ within the CASH (in the bulk).

t : time residence (s)  
x : conversion  
 $S_0$ : initial concentration (mM)

$$t = \frac{K_m}{V_{max}} \cdot \ln \frac{1}{1-x} + \frac{S_0 \cdot x}{V_{max}} + 600$$

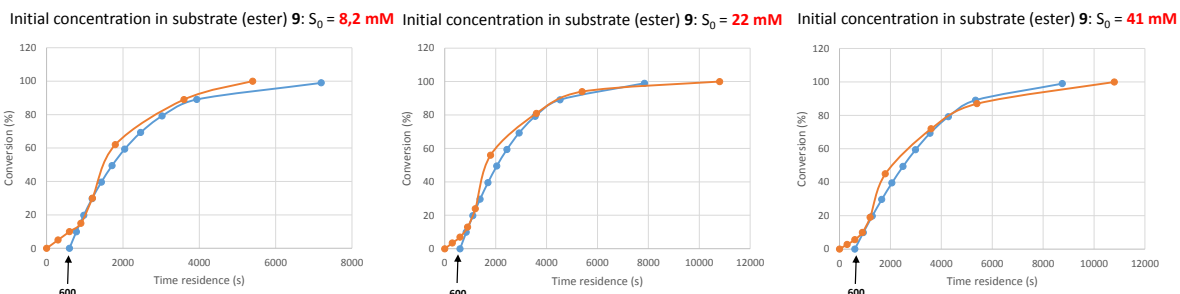


**Figure S14:** Evolution of the conversion of ester **9** in its corresponding carboxylic acid **10** (orange curves) over the time residence realized through the supported-CASH reactor (see figure 2b in the manuscript), for three different concentrations  $S_0$  of **9**: 8.2 mM (left), 22 mM (middle) and 41 mM (right). We consider our CASH flow reactor as a packed bed reactor operating as a plug flow reactor.<sup>31</sup> For such reactor, the Michaelis Menten equation derived for the batch reactor can be applied and leads to the following relation (blue curves).

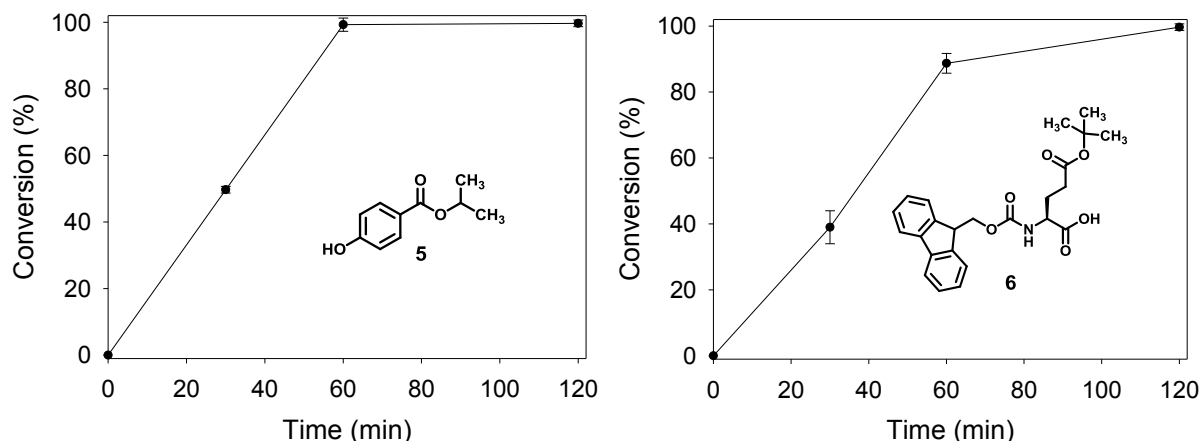


**Figure S15:** Conversion of secondary **5** (left) and tertiary ester **6** (right) in their corresponding carboxylic acids **7** and **8** respectively over time residence through the supported-CASH flow reactor. The error bars have been calculated from three independent runs.

### Racemic discrimination by esterase-like catalytic activity of the supported-CASH

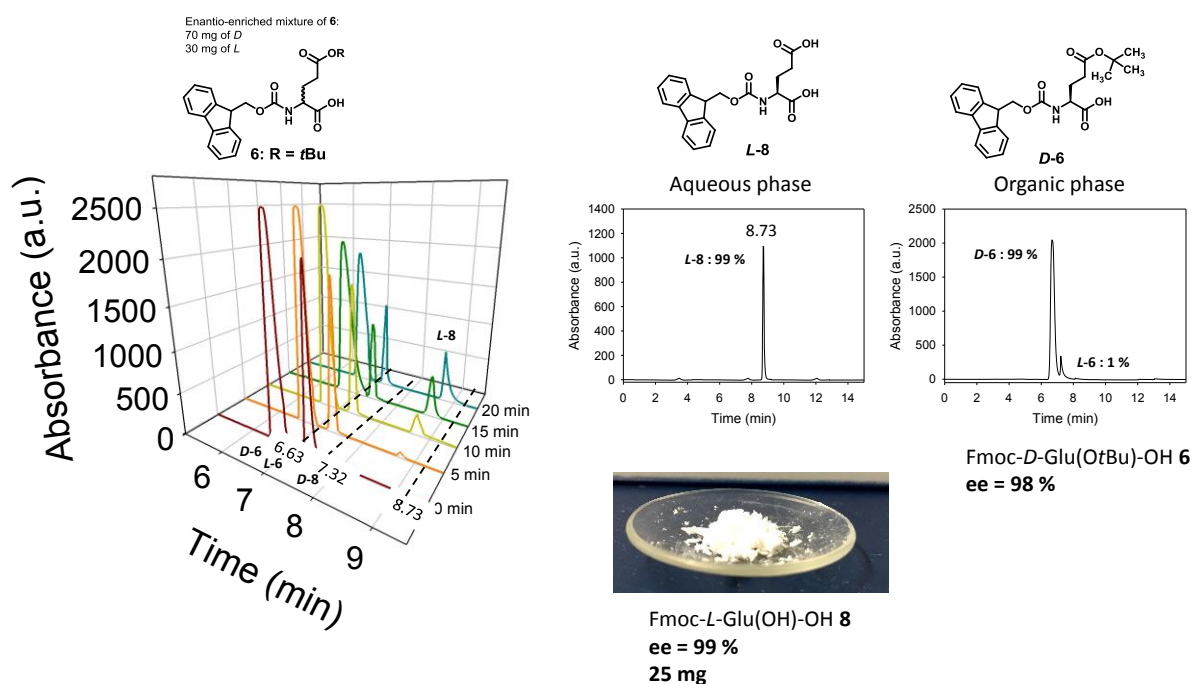
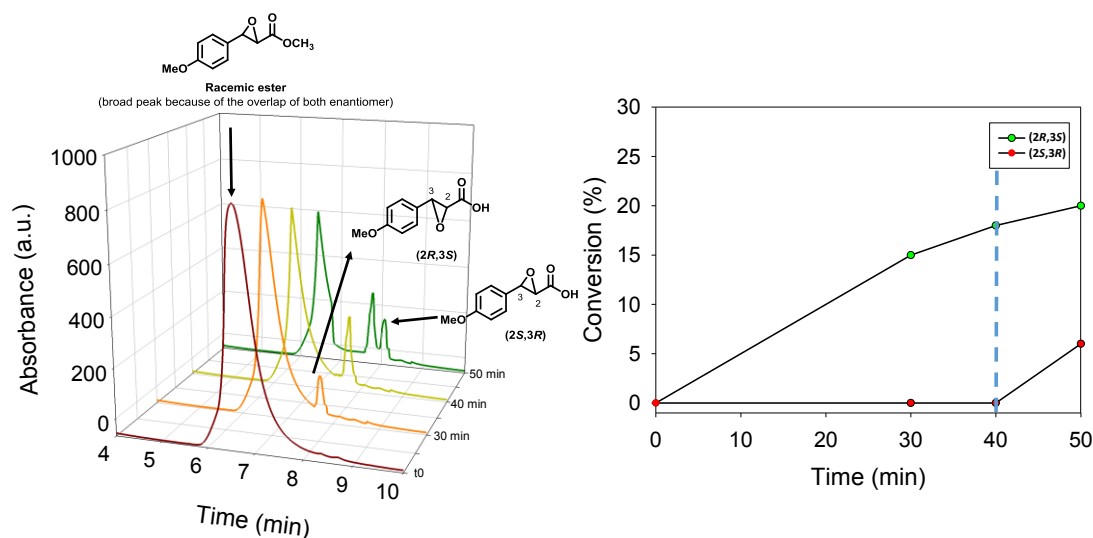


**Figure S16:** Kinetic resolution of 100 mg of enantio-enriched amino acids tertioButyl ester **D-6**, 40% ee. (left) HPLC monitoring of the reaction medium composition over the time residence. (right) HPLC analysis of the residues obtained from the aqueous and organic phase of the extraction.



**Figure**

**S17:** Kinetic resolution of the oxirane of methyl para-methoxycinnamate (racemate, 50 mg) into the corresponding carboxylic acid through the supported-CASH in continuous flow conditions: (left) HPLC monitoring over time of the reaction medium composition using a chiral phase (chiral column Cosmosil 3B with the following dimensions 4.6 mm I.D. x 250 mm. The eluent used for all analyses was *n*-hexane/isopropanol in ratio 97.5/2.5 in isocratic conditions at 1 mL/min); (right) Graph showing the formation of the carboxylic acid enantiomers over residence time.

## 5.3.2 Experimental section

### 5.3.2.1. Materials

All chemicals used in this work are gathered in the following table. They were all used as received, without further purifications.

Name, acronym (abbreviation)	MW (g.mol <sup>-1</sup> )	Supplier	CAS number
Bovine serum albumin (BSA)	66 000	Sigma-Aldrich	9048-46-8
Alkaline Phosphatase from bovine intestinal mucosa (AP)	170 000	Sigma-Aldrich	9001-78-9
Poly(ethylene imine) (PEI)	750 000	Alfa Aesar	9002-98-6
Poly(styrene sulfonate) (PSS)	70 000	Sigma Aldrich	25704-18-1
Deuterated Water (D <sub>2</sub> O)	20.03	Sigma Aldrich	7789-20-0
Dimethylformamide (DMF)	73.09	Acros Organics	68-12-2
Dichloromethane (DCM)	84.93	Acros Organics	75-09-2
Trifluoroacetic acid (TFA)	114.02	Alfa Aesar	76-05-1
Deuterated DMSO (DMSO- <i>d</i> <sub>6</sub> )	84.17	SDS	2206-27-1
N-Ethyl-diisopropylamine (DIEA)	129.25	Alfa Aesar	7087-68-5
Fmoc-L-phenylalanine (Fmoc-F-OH)	387.43	Iris biotech	35661-40-6
Fmoc-L-Tyrosine Phosphate (Fmoc-Y(PO <sub>3</sub> H <sub>2</sub> )-OH)	483.41	Bachem	147762-53-6
Fmoc-L-Glycine (Fmoc-G-OH)	297.31	Iris biotech	29022-11-5
Fmoc-trityl-L-Histidine (Fmoc-H(Trt)-OH)	619.71	Iris biotech	109425-51-6

Triisopropylsilane (TIPS)	158.36	Sigma Aldrich	6485-79-6
Resin 2-chlorotrityl chloride (2-CTC)	-	Sigma Aldrich	42074-68-0
1-Hydroxybenzotriazole hydrate (HOBt)	135.12	Sigma Aldrich	123333-53-9
N,N,N',N'-Tetramethyl-o-(1H-benzotriazol-1-yl)uranium hexafluorophosphate (HBTU)	379.24	Alfa Aesar	94790-37-1
Diethyl ether	74.12	Acros Organics	60-29-7
Polymer Foam (melamine) BASOTCT V3012 white	/	FoamPartner	/
L-Phenylalanine methyl ester hydrochloride	215.68	Sigma Aldrich	7524-50-7
4-Nitrophenyl acetate (PNA)	181.15	Sigma Aldrich	830-03-5
Fmoc-L-glutamic acid 5- <i>tert</i> -butyl ester (Fmoc-L-Glu(OtBu)-OH)	425.47	Sigma Aldrich	71989-18-9
Fmoc-D-glutamic acid 5- <i>tert</i> -butyl ester (Fmoc-D-Glu(OtBu)-OH)	425.47	Sigma Aldrich	104091-08-9
Fmoc-L-aspartic acid 4- <i>tert</i> -butyl ester Fmoc-L-Asp(OtBu)-OH	411.25	Sigma Aldrich	71989-14-5
Fmoc-L-Lysine <i>t</i> -butyl ester hydrochloride (Fmoc-L-Lys-OtBu)	460.98	Iris Biotech GMBH	940941-43-5
Fmoc-D-Lysine <i>t</i> -butyl ester hydrochloride(Fmoc-D-Lys-OtBu)	460.98	Iris Biotech GMBH	2250436-42-9
4-Hydroxybenzoic acid isopropyl ester (Isopropyl 4-hydroxybenzoate)	180.20	Sigma Aldrich	4191-73-5
Boc-L-Tyrosine methyl ester (Boc-L-Tyr-OMe)	295.33	Sigma Aldrich	4326-36-7
Fmoc-L-tyrosine <i>tert</i> -butyl ester (Fmoc-L-Tyr-OtBu)	237.29	Sigma Aldrich	16874-12-7
D-tyrosine <i>tert</i> -butyl ester (H <sub>2</sub> N-D-Tyr-OtBu)	237.29	Alfa Aesar	87553-74-0
Fmoc Chloride	258.70	Sigma Aldrich	28920-43-6

### 5.3.2.2. Synthesis and characterization of Fmoc-GFFYGHY, Fmoc-GFF $\rho$ YGHY, Fmoc-GFFYGH $\rho$ Y and Fmoc-GFF $\rho$ YGH $\rho$ Y

All peptides were prepared using solid support chemistry. The “Fmoc strategy” was used based on 2-CTC resin.<sup>32</sup> The following synthetic pathway is given in the scheme below (next page).

#### General procedure for peptide synthesis on solid support:

- **Step a:** loading of the resin 2-chlorotrityl chloride (2-CTC, called as “resin” or “r” in the rest of this procedure). Addition of 3 eq/r of Fmoc-Tyr(OR)-OH + 6 eq/r of DIEA in 3 mL of DMF for 300 mg of resin. The solution in contact with the resin is stirred at RT for 2 h. Then, the solution is removed and a solution of MeOH is added at RT for 1 h.
- **Step b:** Fmoc group deprotection: 3 mL of a 20% of piperidine in DMF solution is added and stirred at RT for 15 min.

*Supported catalytically-active supramolecular hydrogels for continuous flow chemistry  
Towards the design of a self-sustained hydrogel growth*

---

- **Step c:** Coupling step: 3eq/r of Fmoc-amino acid + 3 eq/r of HOBt + 3 eq/r of HBTU + 6 eq/r of DIEA are added in 3 mL of DMF and let in contact with the resin at RT for 30 min.
- **Step d:** Cleavage of the resin and lateral chains deprotection: addition of 3 mL of a solution containing 95% TFA + 2.5 % H<sub>2</sub>O + 2.5 % triisopropylsilane it's stirred at RT for 2 h. Then the solution is filtered. The solvent is then removed. Finally the product is precipitated by using a small amount of cold ether.

Between each step **a**, **b**, **c** and **d**, a rinsing stage is executed by using 5 times 3 mL of DMF and then a Kaiser test is made to confirm the achievement of the coupling or deprotection steps.

Protocol for Kaiser Test (Ninhydrin Test): one drop of each solution **A**, **B** and **C** described below is added in a test tube containing 10 beads of the resin. The test tube is heated at 100 °C during 3 seconds. When the beads and the solution take a blue coloration, this Kaiser test is positive: this indicates the presence of free amine that means that the Fmoc-deprotection step succeeded or a failed coupling step. When the beads and solution keep their yellow color, the Kaiser test is negative. This indicates that the coupling step is completed or has failed in the case of Fmoc-deprotection. When the Fmoc deprotection or the coupling step failed, those steps are repeated up to get the expected positive or negative Kaiser test.

Solution A:

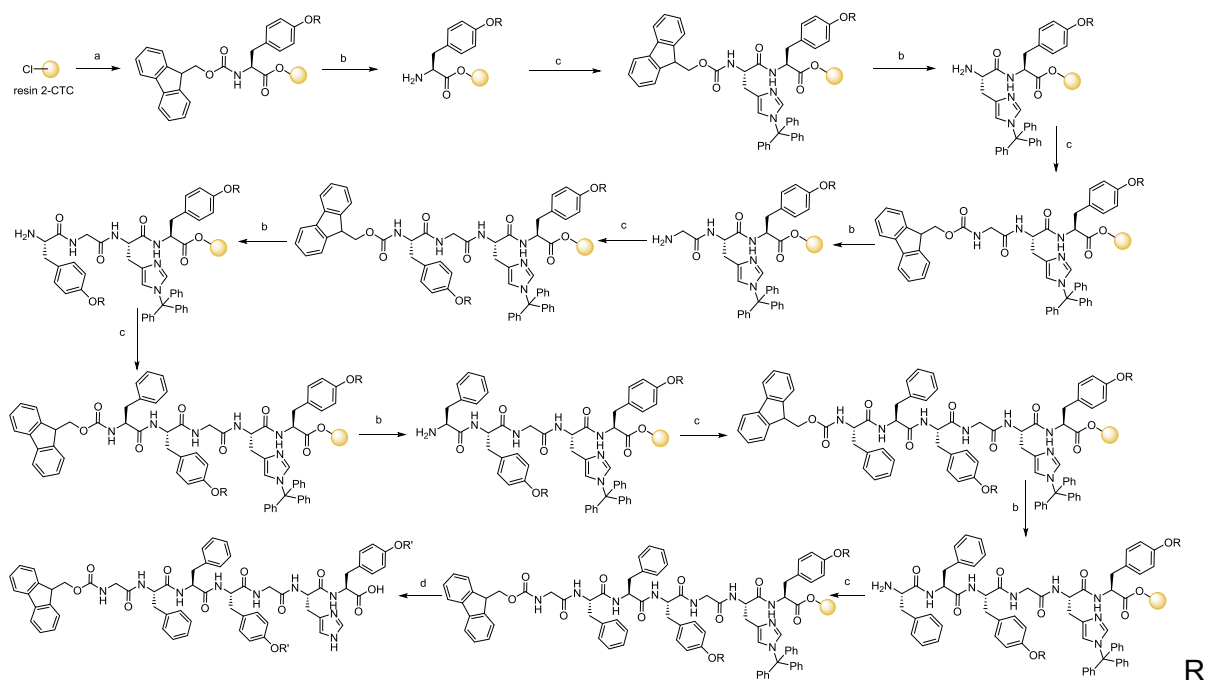
- Dissolve 16.5 mg of KCN in 25 mL of distilled water.
- Dilute 1.0 mL of the previous KCN aqueous solution with 49 mL of pyridine.

Solution B:

- Dissolve 1.0 g of ninhydrin in 20 mL of *n*-butanol.

Solution C:

- Dissolve 40 g of phenol in 20 mL of *n*-butanol.

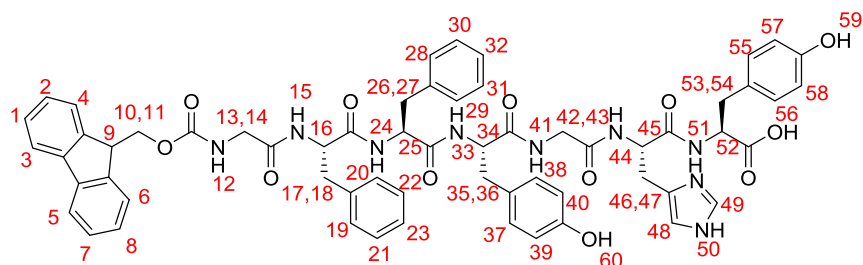


= PO<sub>3</sub>H<sub>2</sub> or *t*Bu

R' = PO<sub>3</sub>H<sub>2</sub> or H

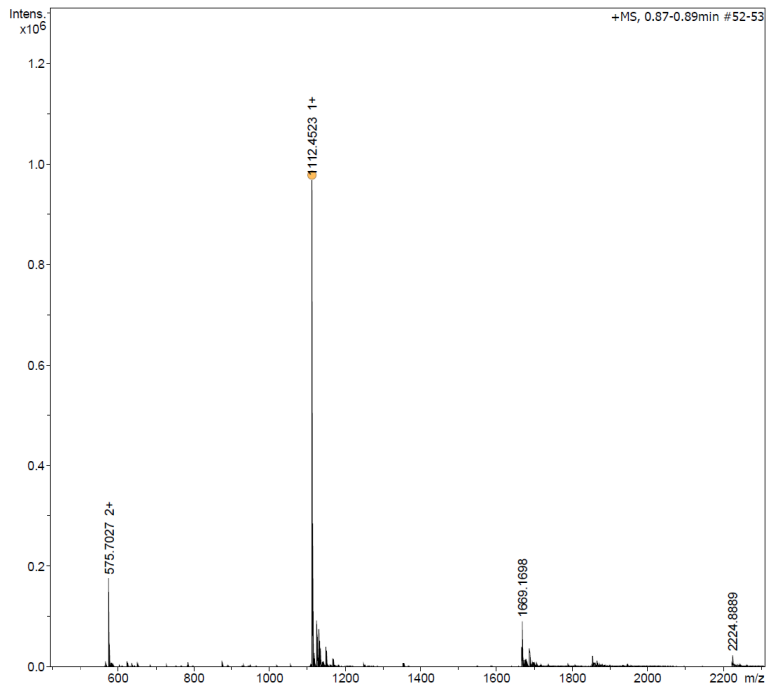
When the amino acid Fmoc-Tyrosine-OH was required in the final sequence, the protection of the phenol group was ensured by a *t*Bu group. When a tyrosine-phosphate is required, the Fmoc-Tyr(OPO<sub>3</sub>H<sub>2</sub>)-OH is directly introduced during the synthesis.

### Fmoc-GFFYGHY:

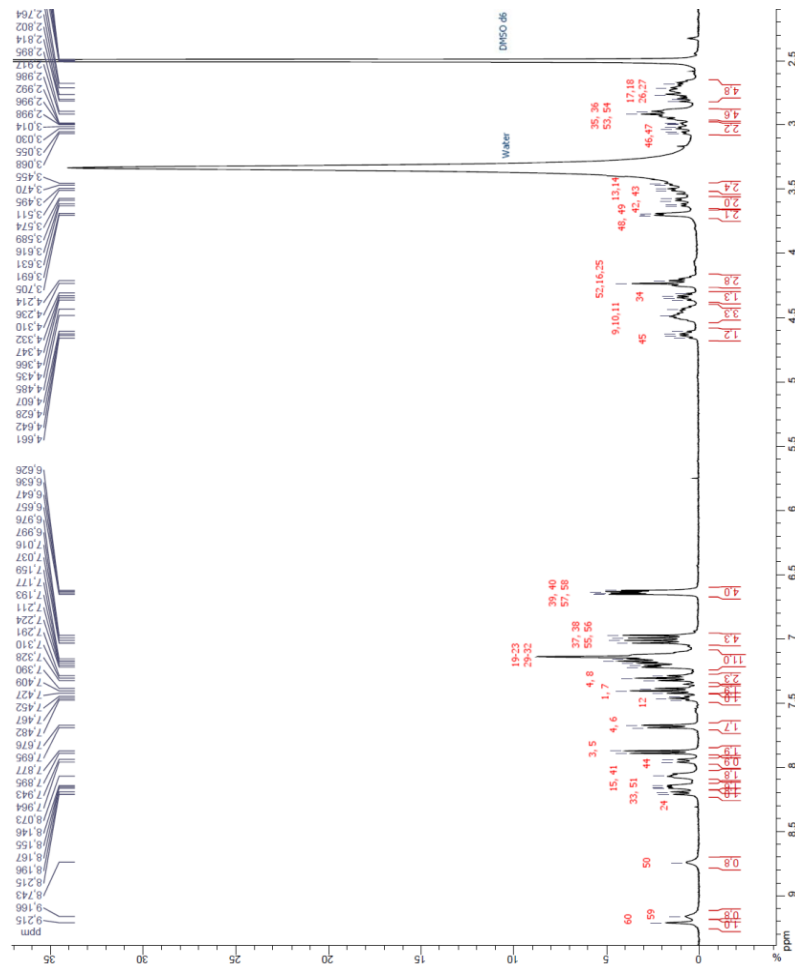


<sup>1</sup>H NMR (400 MHz, DMSO-*d*<sub>6</sub>) δ 2.81-2.68 (m, 4H), 2.92-2.90 (m, 4H), 3.67-2.99 (ddd, 2H, *J*=4.8, 10.6, 18.6 Hz), 3.51-3.46 (dd, 2H, <sup>2</sup>*J* = 7.2, <sup>3</sup>*J* = 16.9 Hz), 3.62-3.57 (dd, 2H, <sup>2</sup>*J* = 7.2, <sup>3</sup>*J* = 16.9 Hz), 3.71-3.69 (d, 2H, <sup>3</sup>*J* = 5.8 Hz), 4.24-4.21 (m, 3H), 4.37-4.31 (m, 1H), 4.49-4.44 (m, 3H), 4.66-4.61 (m, 1H), 6.66-6.63 (dd, 4H, <sup>2</sup>*J* = 4.0, <sup>3</sup>*J* = 8.51 Hz), 7.04-6.98 (dd, 4H, <sup>2</sup>*J* = 8.3, <sup>3</sup>*J* = 16.0 Hz), 7.22-7.16 (m, 11H), 7.33-7.31 (t, 2H, <sup>3</sup>*J* = <sup>3</sup>*J* = 7.5 Hz), 7.43-7.39 (t, 2H, <sup>3</sup>*J* = <sup>3</sup>*J* = 7.5 Hz), 7.48-7.45 (t, 1H, <sup>3</sup>*J* = <sup>3</sup>*J* = 6.4 Hz), 7.70-7.68 (d, 2H, <sup>3</sup>*J* = 7.5 Hz), 7.90-7.88 (d, 2H, <sup>3</sup>*J* = 7.6 Hz), 7.96-7.95 (d, 2H, *J* = 7.6 Hz), 8.11-8.07 (m, 2H), 8.17-8.15 (m, 2H), 8.21-8.20 (d, 1H, *J* = 7.8 Hz), 8.74 (s, 1H), 9.17 (s, 1H), 9.22 (s, 1H) HRMS (ESI/Q-TOF) *m/z*: [M + H]<sup>+</sup> Calcd for C<sub>61</sub>H<sub>62</sub>N<sub>9</sub>O<sub>12</sub> 1112.4522; Found 1112.4523. UV-VIS spectra: max Abs: 288 nm. IR spectra: ν<sub>OH</sub> = 3521 cm<sup>-1</sup>; ν<sub>C=O acid</sub> = 1739 cm<sup>-1</sup>; ν<sub>C=O amide</sub> = 1673 cm<sup>-1</sup>; ν<sub>N-H</sub> = 1517 cm<sup>-1</sup>; ν<sub>C-O</sub> = 1439 cm<sup>-1</sup>. HPLC analytic (Column C18 SUPULCOSIL ABZ +, ACN/H<sub>2</sub>O (80/20)\_isocratic\_10 min\_Flow: 1 mL/min\_22 °C): *rt* = 5.84 min; CD : λ = 200 nm and 270 nm.

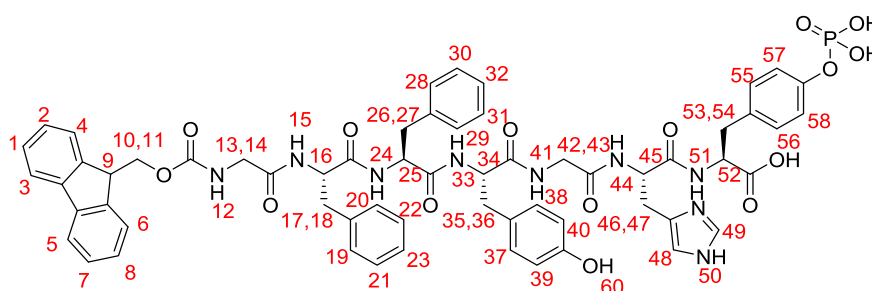
HRMS spectrum of Fmoc-GFFYGHY:



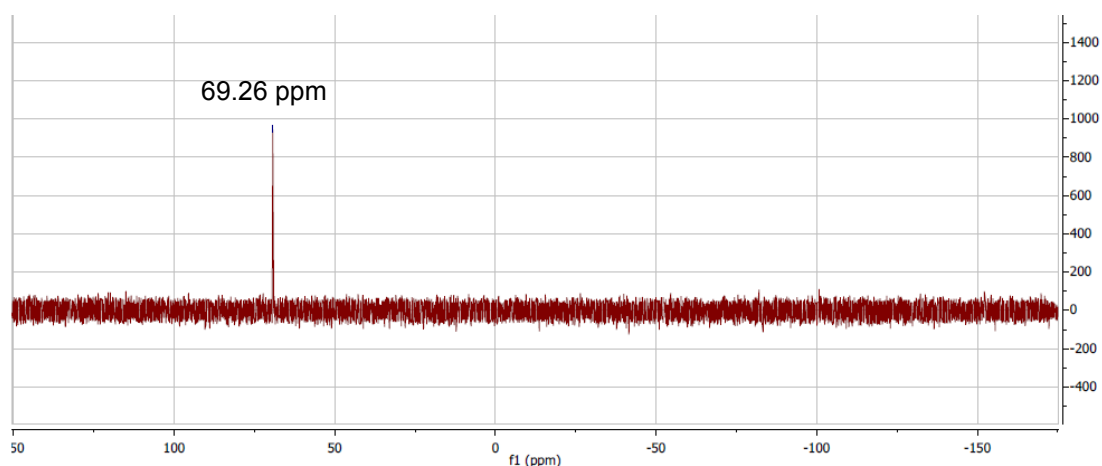
$^1\text{H}$  NMR spectrum of Fmoc-GFFYGHY:



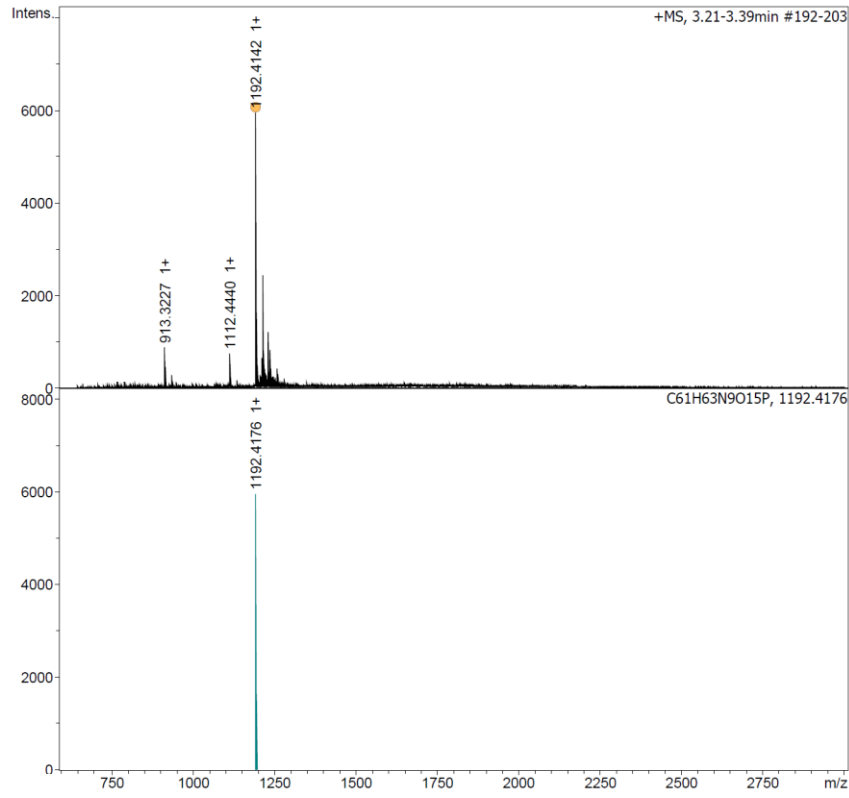


**Fmoc-GFFYGHpY:**

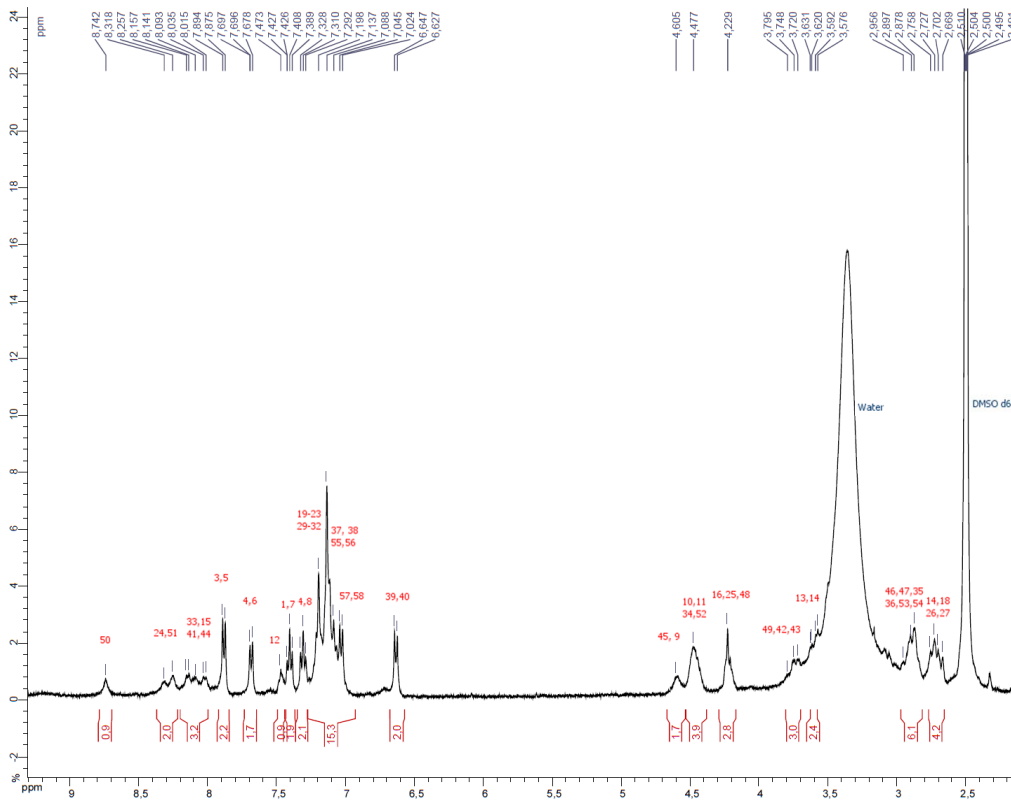
$^1\text{H}$  NMR (400 MHz,  $\text{DMSO-}d_6$ )  $\delta$  2.76-2.67 (m, 4H), 2.96-2.88 (m, 6H), 3.63-3.58 (m, 2H), 3.80-3.72 (m, 3H), 4.23 (m, 3H), 4.48 (m, 4H), 4.61 (m, 2H), 6.65-6.63 (d, 2H,  $^3J = 8.0$  Hz), 7.20-7.02 (m, 15H), 7.33-7.29 (t, 2H,  $^3J = ^3J = 7.5$  Hz), 7.43-7.41 (t, 2H,  $^3J = 7.5$  Hz), 7.47 (m, 1H), 7.70-7.68 (d, 2H,  $^3J = 7.9$  Hz), 7.89-7.88 (d, 2H,  $^3J = 7.5$  Hz), 8.16-8.02 (m, 3H), 8.32-8.26 (m, 2H), 8.74 (m, 1H);  $^{31}\text{P}$  NMR (161,92 MHz,  $\text{DMSO-}d_6$ )  $\delta$  68.37 HRMS (ESI/Q-TOF)  $m/z$ :  $[\text{M} + \text{H}]^+$  Calcd for  $\text{C}_{61}\text{H}_{62}\text{N}_9\text{O}_{12}$  1192.4169; Found 1192.4176. UV-VIS spectra: max Abs: 291 nm. IR spectra:  $\nu_{\text{OH}} = 3520$   $\text{cm}^{-1}$ ;  $\nu_{\text{C=O acid}} = 1739$   $\text{cm}^{-1}$ ;  $\nu_{\text{C=O amide}} = 1674$   $\text{cm}^{-1}$ ;  $\nu_{\text{N-H}} = 1640$   $\text{cm}^{-1}$ ;  $\nu_{\text{C-O}} = 1395$   $\text{cm}^{-1}$  and  $1200$   $\text{cm}^{-1}$ . HPLC analytic (Column C18 SUPULCOSIL ABZ +, ACN/H<sub>2</sub>O (80/20)\_isocratic\_10 min\_Flow: 1 mL/min\_22 °C) : rt : 4.70 min; CD :  $\lambda = 200$  nm and 271 nm

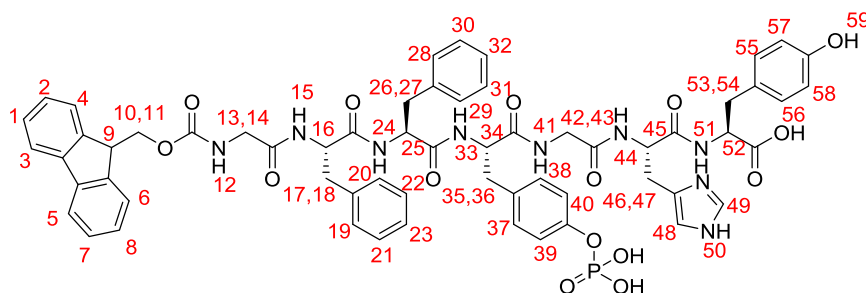
 **$^{31}\text{P}$  NMR spectrum of Fmoc-GFFYGHpY:**

HRMS spectrum of Fmoc-GFFYGHpY:

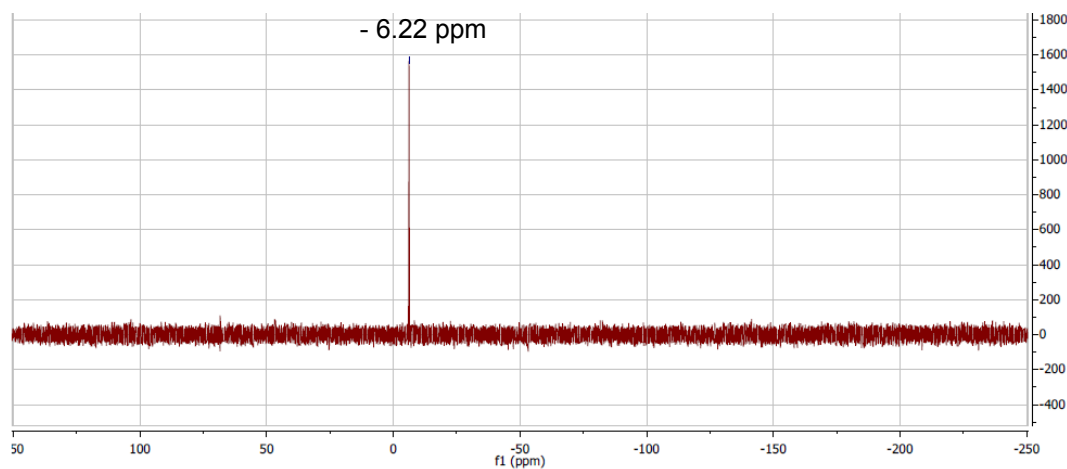


<sup>1</sup>H NMR spectrum of Fmoc-GFFYGHpY:

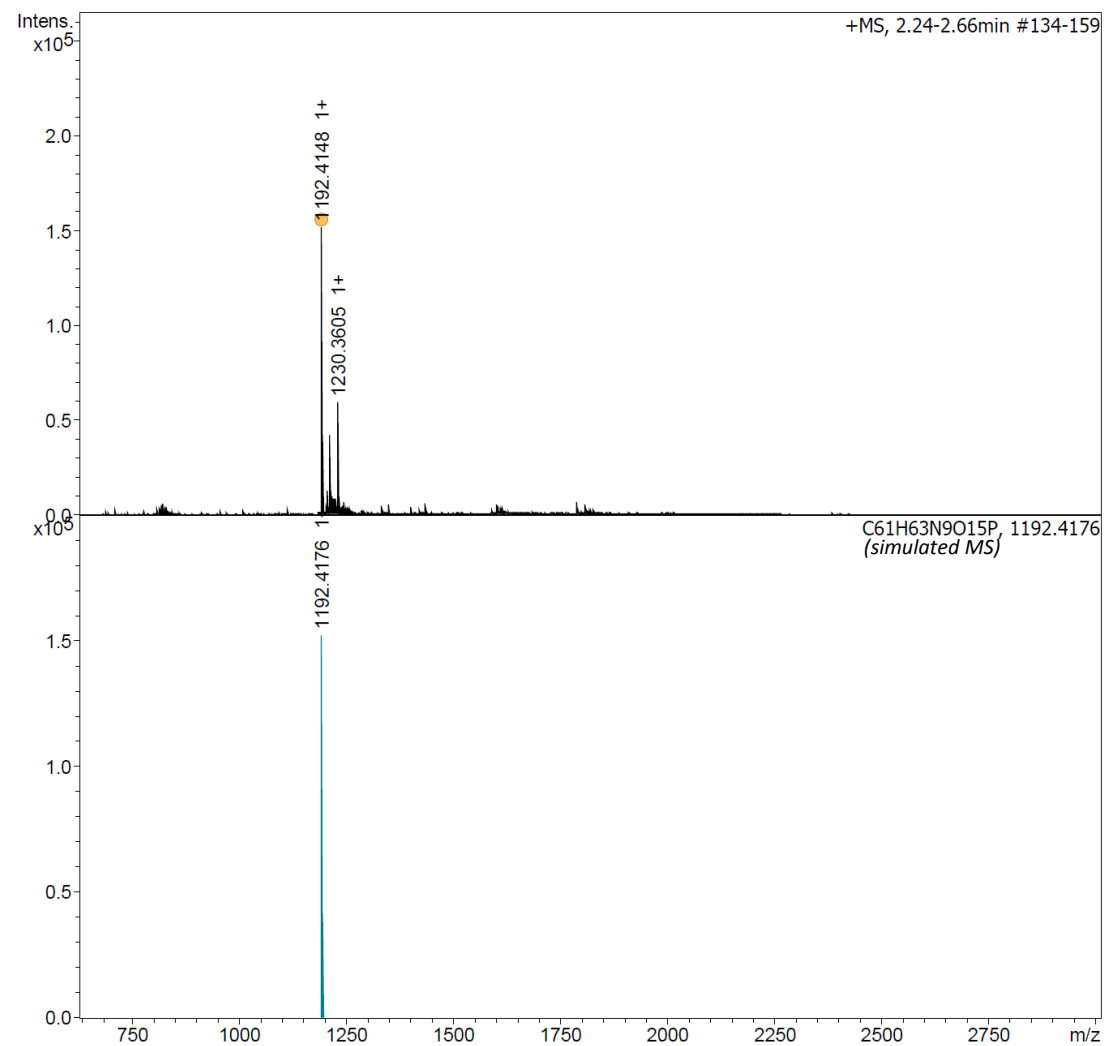


**Fmoc-GFFpYGHY:**

$^1\text{H}$  NMR (400 MHz,  $\text{DMSO}-d_6$ )  $\delta$  2.94-2.67 (m, 8H), 3.02-2.98 (dd, 2H,  $^2J = 5.5$ ,  $^3J = 14.2$  Hz), 3.09-3.04 (dd, 2H,  $^2J = 5.5$ ,  $^3J = 14.2$ , 18.6 Hz), 3.51-3.46 (dd, 2H,  $^2J = 7.5$ ,  $^3J = 15.9$  Hz), 4.26-4.20 (m, 4H), 4.38-4.32 (m, 2H), 4.52-4.49 (m, 3H), 4.70-4.65 (m, 1H), 6.66-6.64 (d, 2H,  $^3J = 8.0$  Hz), 7.00-6.98 (d, 2H,  $^3J = 8.3$  Hz), 7.06-7.04 (d, 2H,  $^3J = 8.0$  Hz), 7.22-7.16 (m, 11H), 7.33-7.29 (m, 3H), 7.46-7.39 (m, 3H), 7.57-7.53 (td, 1H,  $^2J = 1.2$ ,  $^3J = 7.05$  Hz), 7.70-7.68 (d, 2H,  $^3J = 7.5$  Hz), 7.89-7.88 (d, 2H,  $^3J = 7.6$  Hz), 7.99-7.96 (m, 1H), 8.23-8.10 (m, 5H), 8.93 (s, 1H);  $^{31}\text{P}$  NMR (161.92 MHz,  $\text{DMSO}-d_6$ )  $\delta$  -6.22 HRMS (ESI/Q-TOF)  $m/z$ :  $[\text{M} + \text{H}]^+$  Calcd for  $\text{C}_{61}\text{H}_{62}\text{N}_9\text{O}_{12}$  1192.4169; Found 1192.4176; UV-VIS spectra: max Abs: 290 nm. IR spectra:  $\nu_{\text{OH}} = 3520 \text{ cm}^{-1}$ ;  $\nu_{\text{C=O acid}} = 1739 \text{ cm}^{-1}$ ;  $\nu_{\text{C=O amide}} = 1674 \text{ cm}^{-1}$ ;  $\nu_{\text{N-H}} = 1640 \text{ cm}^{-1}$ ;  $\nu_{\text{C-O}} = 1395 \text{ cm}^{-1}$  and  $1200 \text{ cm}^{-1}$ . HPLC analytic (Column C18 SUPULCOSIL ABZ +, ACN/ $\text{H}_2\text{O}$  (80/20)\_isocratic\_10 min\_Flow: 1 mL/min\_22 °C) :  $r_t$  : 3.84 min; CD :  $\lambda = 200 \text{ nm}$  and  $276 \text{ nm}$

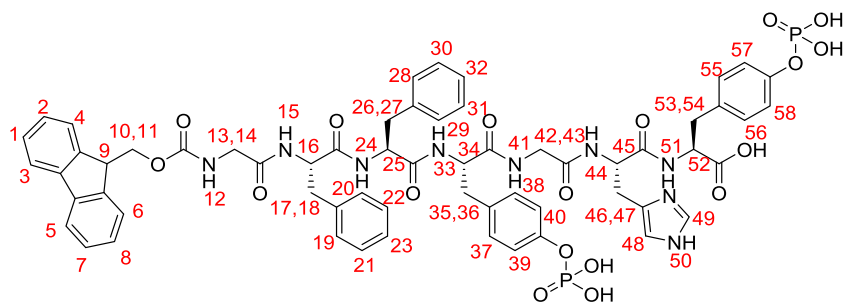
 **$^{31}\text{P}$  NMR spectrum of Fmoc-GFFpYGHY:**

HRMS spectrum of Fmoc-GFFpYGHY:



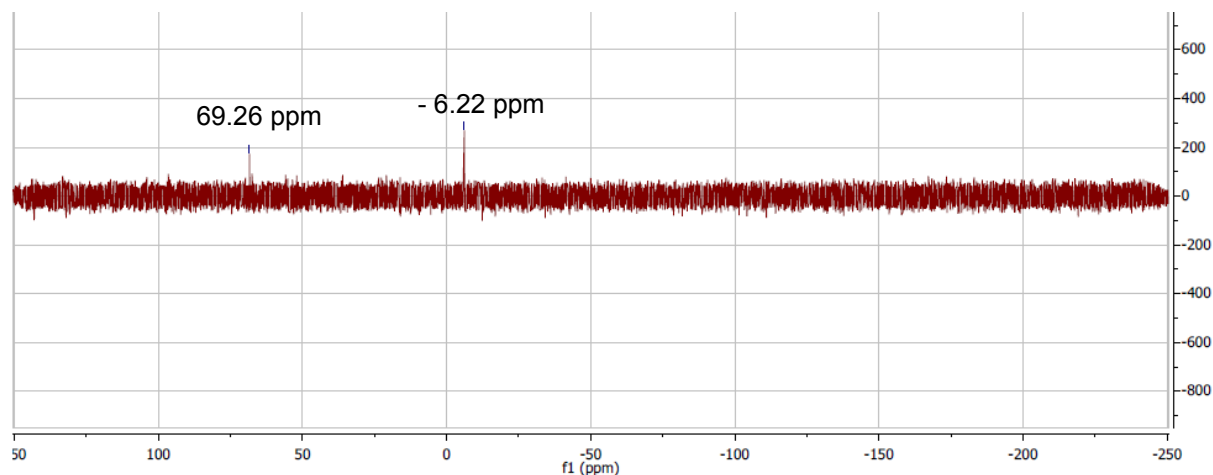


**Fmoc-GFFpYGHpY:**

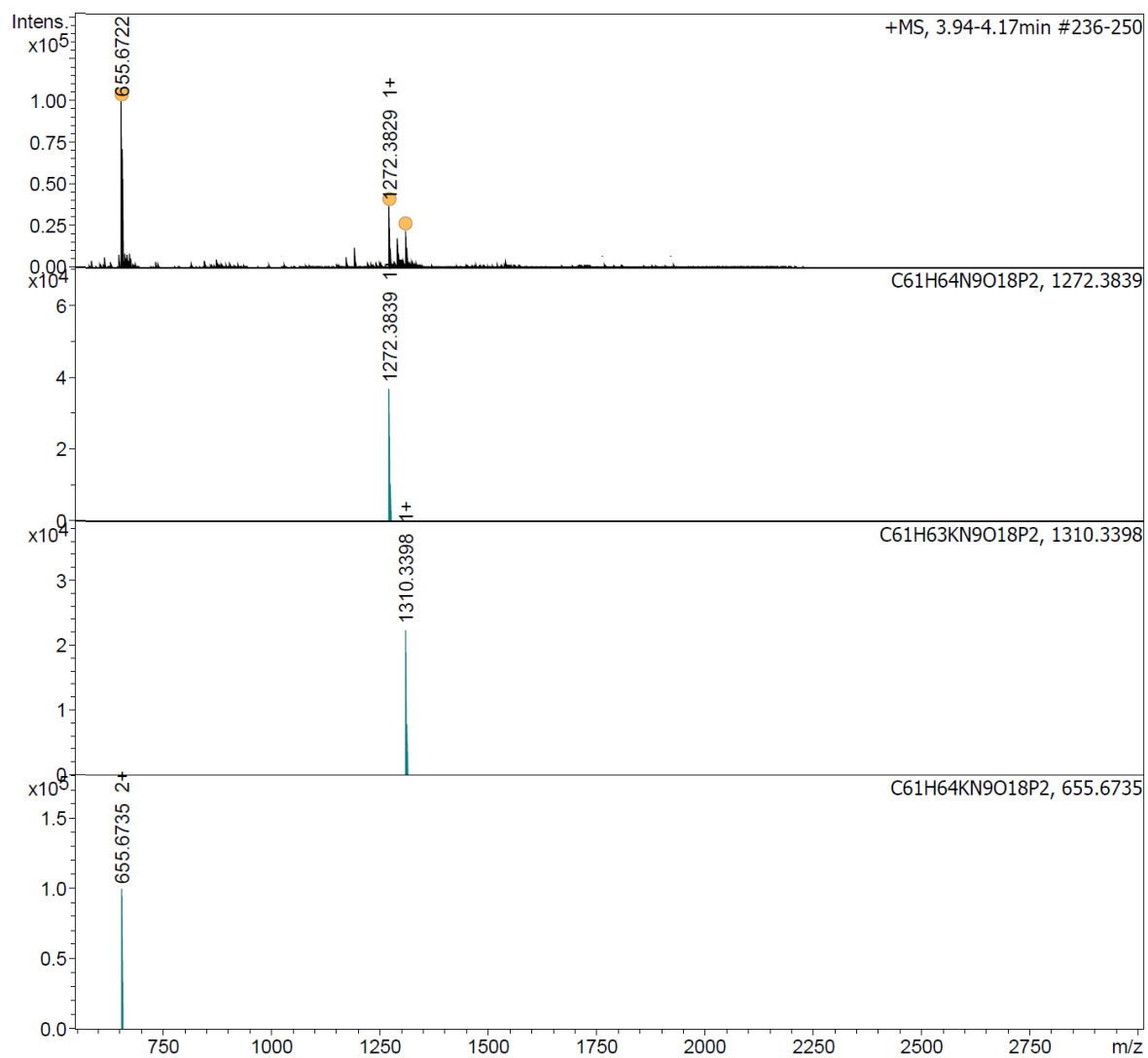


$^1\text{H}$  NMR (400 MHz,  $\text{DMSO-}d_6$ )  $\delta$  2.92-2.89 (m, 4H), 3.04-2.99 (m, 4H), 3.51-3.46 (dd, 3H,  $^3J=5.6, 17.7$  Hz), 3.64-3.57 (m, 4H), 4.25-4.20 (m, 4H), 4.52-4.50 (m, 5H), 4.67-4.64 (m, 1H), 7.28-7.04 (m, 17H), 7.33-7.28 (m, 2H), 7.47-7.39 (m, 3H), 7.57-7.53 (td, 1H,  $^3J=1.2, 7.1$  Hz), 7.70-7.68 (d, 2H,  $^3J=7.5$  Hz), 7.89-7.88 (d, 2H,  $^3J=7.6$  Hz), 7.97 (m, 1H), 8.27-8.07 (m, 5H), 8.92 (s, 1H);  $^{31}\text{P}$  NMR (161.92 MHz,  $\text{DMSO-}d_6$ )  $\delta$  68.37, -6.17 HRMS (ESI/Q-TOF)  $m/z$ :  $[\text{M} + \text{H}]^+$  Calcd for  $\text{C}_{61}\text{H}_{62}\text{N}_9\text{O}_{12}$  1271.38; Found 1271.3839; UV-VIS spectra: max Abs: 292 nm. IR spectra:  $\nu_{\text{OH}}=3520$   $\text{cm}^{-1}$ ;  $\nu_{\text{C=O acid}}=1739$   $\text{cm}^{-1}$ ;  $\nu_{\text{C=O amide}}=1674$   $\text{cm}^{-1}$ ;  $\nu_{\text{N-H}}=1640$   $\text{cm}^{-1}$  and 1547;  $\nu_{\text{C-O}}=1395$   $\text{cm}^{-1}$  and 1200  $\text{cm}^{-1}$ . HPLC analytic (Column C18 SUPULCOSIL ABZ +, ACN/H<sub>2</sub>O (80/20)\_isocratic\_10 min\_flow: 1 mL/min\_22°C) : rt : 2.26 min; CD :  $\lambda=200$  nm and 266 nm

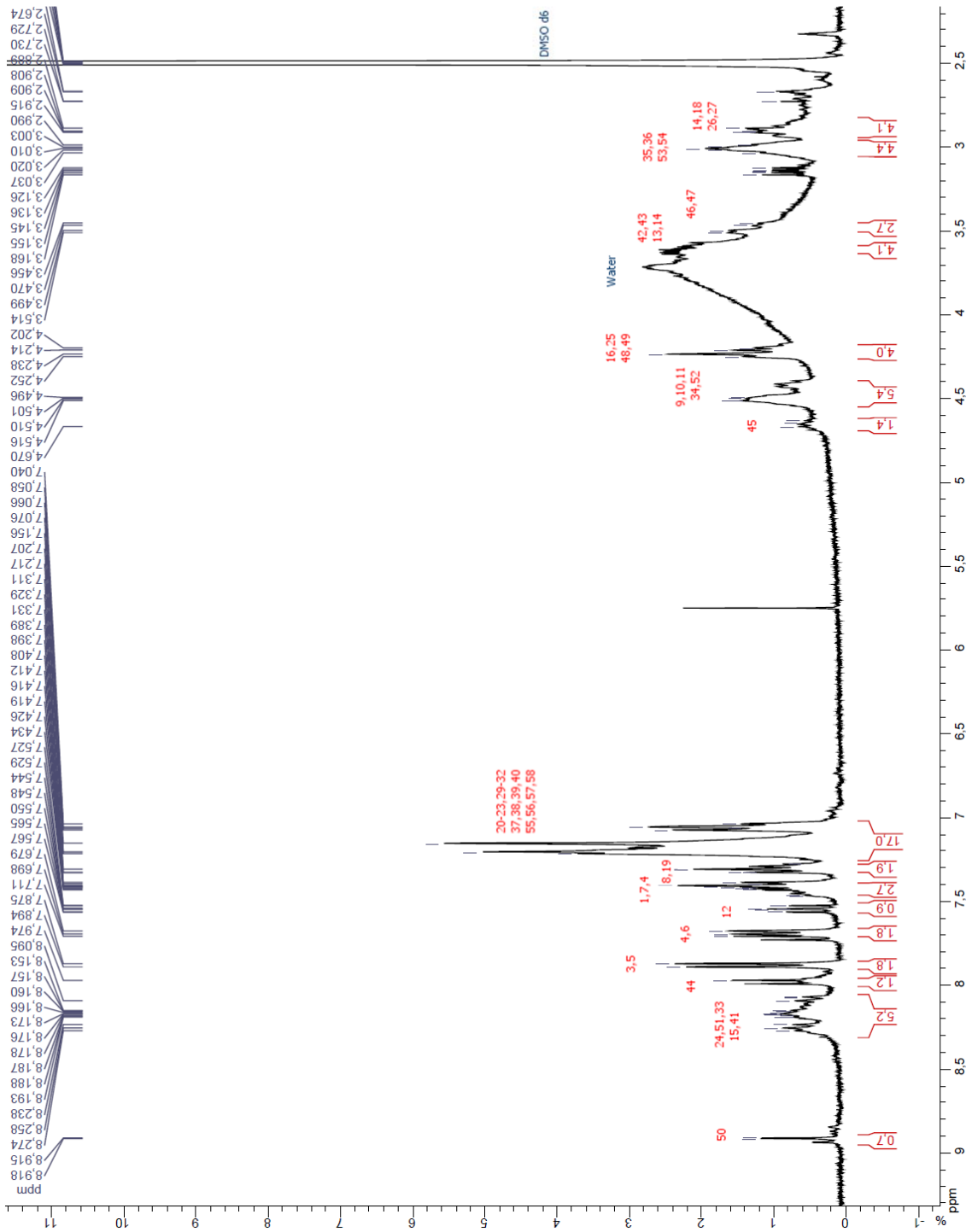
$^{31}\text{P}$  NMR spectrum of Fmoc-GFFpYGHpY:



## HRMS spectrum of Fmoc-GFFpYGHpY:



$^1\text{H}$  NMR spectrum of Fmoc-GFFpYGHpY:





### 5.3.2.3. Preparation of peptide solution and hydrogel formation

All hydrogels were prepared in PBS buffer (pH 7.4). The PBS buffer is prepared the day of the hydrogel preparation.

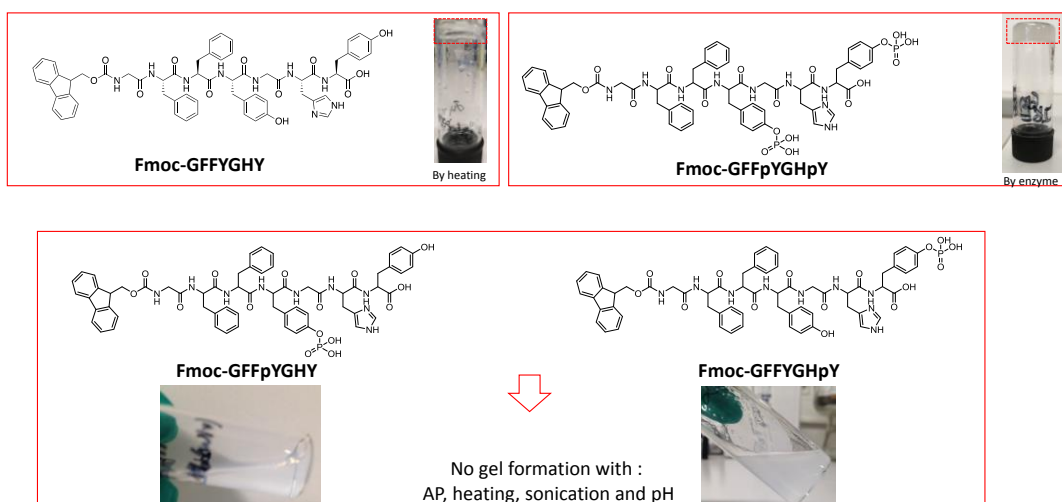
**PBS Buffer (pH 7.4):** one tablet of commercially available PBS (P4417 from Sigma Aldrich) was dissolved in 200 mL of ultrapure water (Milli-Q Plus system, Millipore, Billerica, MA) leading to 0.001 M phosphate buffer, 0.0027 M potassium chloride and 0.137 M sodium chloride. If necessary, the pH of this buffer was adjusted to 7.4 value by addition of few drops of HCl (0.01 M) or NaOH (0.01 M) solution. The pH value was monitored using a pH meter.

**General preparation of peptide solution:** an adequate amount of peptide was dissolved in PBS to get the suitable concentration (usually 1 and 10 mg/mL). This solution was vortexed 2-5 minutes and sonicated in an ultrasound bath during 1 minute. The resulting peptide solution was thus used for all kinds of analyses described in this ESI.

**Fmoc-GFFYGHY hydrogel formation** were obtained by dissolving Fmoc-GFFYGHY (10 mg/mL) in PBS buffer. This solution was vortexed during 2 minutes and then dipped into an ultrasound bath during 1 minute. The solution was heated at around 100 °C to solubilize the peptide. When the solution cooled down the hydrogel formed.

**Fmoc-GFFpYGHpY hydrogel formation** were obtained by dissolving Fmoc-GFFpYGHpY (10 mg/mL) in PBS buffer. This solution was vortexed 2 minutes and then dipped into an ultrasound bath during 1 minute. 1 mg/mL of commercial AP (P7640 from Sigma Aldrich) was added (ratio AP/peptide (1/10)). The resulting mixture was vortexed 10 seconds. The resulting hydrogel was obtained after 5 minutes

**Upside-down vial tests with peptides for the hydrogelation assays:** Hydrogels were obtained from Fmoc-GFFYGHY by heating and cooling and from Fmoc-GFFpYGHpY using AP, as described above. No hydrogels were obtained from mono-phosphorylated peptides Fmoc-GFFYGHpY or Fmoc-GFFpYGHY using heating/cooling, AP or by decreasing the pH, as illustrated below.



#### 5.3.2.4. Multilayer film preparation and localized hydrogel formation at the liquid-solid interface

All polyelectrolytes (1 mg/mL), proteins (AP 1 mg/mL and BSA 1 mg/mL), and peptides or amino acid (1 mg/mL) were prepared in PBS buffer freshly prepared as described in section 5.1.6.3. Different solid substrates were used depending on the characterization technique investigated: gold coated quartz crystal for QCM-D monitoring, ZnSe crystal for ATR-FTIR experiments, Glass slide and Si Wafer for Cryo-SEM analyses, glass slide for fluorescence emission assays (using a multiplate reader (FLX-Xenius®, SAFAS, Monaco)) and melamine foam (from Foam Partner industry) for activity assays in the continuous flow reactor experiments.

The growth of the supramolecular hydrogel from the chosen substrate was done as following: after the deposition of a PEI (1 mg/mL) precursor layer on the chosen surface by dipping (for 10 minutes in the PEI solution), the multilayer film was built up by alternately exposing the surface to PSS (1 mg/mL in PBS buffer) and PEI (1 mg/mL in PBS buffer) solutions for 10 minutes with an intermediate rinsing step with PBS buffer during 5 minutes. AP (1 mg/mL) or BSA (1 mg/mL), all prepared in PBS, were put in contact with the substrate during 20 minutes followed by 5 minutes of rinsing step with PBS buffer. Finally, the peptide Fmoc-GFFpYGHpY solution (1 mg/mL in PBS buffer) was let in contact with the modified surface overnight. The volume of each solution brought in contact with the substrate was 1 mL except for the QCM-D experiment where it was 700  $\mu$ L. All steps were done at RT.

#### 5.3.2.5. Quartz crystal microbalance with dissipation monitoring (QCM-D)

QCM-D experiments were performed on a Q-sense E1 apparatus (Q-Sense AB, Göteborg, Sweden) by monitoring the resonance frequencies of gold coated crystals, as well as the dissipation factors at four frequencies: the fundamental frequency at 5 MHz ( $\nu = 1$ ) and the 3<sup>rd</sup>, 5<sup>th</sup>, and 7<sup>th</sup> harmonics ( $u = 3, 5$  and  $7$  at  $15, 25,$  and  $35$  MHz respectively). The QCM-D results give information on the adsorption process, as well as on viscoelastic properties of the adsorbed film<sup>16</sup>. Preparation of the multilayer film and formation of the hydrogel layer are described in section 4 just above.

The Software *QTools*® was used to determine the film thicknesses of multilayer films using the Sauerbrey equation (valid for rigid films)<sup>33</sup> and of the peptide self-assembly using the Vogt-Voinova model (valid for viscoelastic films).<sup>34</sup>

For a thin and rigid film, the mass can be obtained by using the Sauerbrey's equation:<sup>33</sup>

$$\Delta m = -C\Delta f/u$$

where  $C$  is the mass sensitivity constant ( $17.7 \text{ ng}\cdot\text{cm}^{-2}\cdot\text{Hz}^{-1}$  at 5 MHz), and  $u$  is the overtone number. The Sauerbrey equation was applied when  $\Delta f/u$  is independent of  $u$ . We verified that this was the case in our experiments. As we assumed that the density of the film is close to  $1 \text{ g}\cdot\text{cm}^{-3}$ , we can infer the evolution of the film thickness, during the buildup. Thickness is determined thanks to the previous equation:

$$d = -C\Delta f/100 u$$

where  $d$  is the thickness in nm.

The QCM-D monitoring of the multilayer buildud lead to a  $\Delta f = -108.51$  for  $\vartheta = 1$ . Thus, the calculated thickness  $d$  of this film is:

$$d = \frac{-17.7 \times -108.51}{100 \times 1} = 19.2 \text{ nm}$$

### 5.3.2.6. Atomic force microscopy (AFM)

Atomic force microscopy (AFM) was carried out with a BioScope Catalyst (Bruker corp., Santa Barbara, CA, USA). Micrographs from different interaction stages of Fmoc-GFFpYGHpY with the enzymatic film were recorded in contact mode by using silicon tips mounted on nitride levers. All samples were observed in dry state with triangular cantilevers having a spring constant of 0.4 N/m and a nominal tip radius of 2 nm. Selected AFM images were treated with the nanoscope analysis software (Bruker corp., Santa Barbara, CA, USA). Multilayer films were assembled on gold-coated quartz crystals by the dipping method as described above. PEI, PSS, AP, BSA, or Fmoc-GFFpYGHpY solutions were prepared as described previously (section 4, just above). Samples were air dried before analysis.

### 5.3.2.7. Infrared spectroscopy

The Fourier Transform Infrared (FTIR) experiments were performed on a Vertex 70 spectrometer (Bruker, Germany) using a DTGS detector. Spectra, for the surface analysis, were recorded in the Attenuated Total Reflection (ATR) mode using a 45° trapezoidal ZnSe (internal reflection element) crystal (6 reflections, dimensions 72 × 10 × 6 mm<sup>3</sup>) in ATR cell (GRASEBY-SPECAC, England). Reference (bare ZnSe crystal in contact with ultrapure water) and sample spectra were taken by collecting 128 interferograms between 800 and 4000 cm<sup>-1</sup> at 2 cm<sup>-1</sup> resolution, using Blackman-Harris three-term apodization and the standard Bruker OPUS/IR software (version 7.5). Multilayer films were assembled directly on a ZnSe crystal installed in the FTIR cell. PEI, PSS, AP, BSA, or Fmoc-GFFpYGHpY solutions were prepared as described previously (section 5.3.2.4, just above) but in deuterated PBS buffer to avoid the water signal in the amide I region, and were brought in contact (flow) with the ZnSe substrate.

Spectra of the hydrogels made in solution were recorded in ATR mode using a diamond. All the hydrogels were formed in deuterated PBS buffer.

### 5.3.2.8. Scanning Electron Microscopy (SEM) and cryo-SEM

To observe cross-sectioned gels, a specific cryo-holder was designed and manufactured by the mechanical facility of the Charles Sadron Institute (see Figure below). The glass slide covered by enzymatic precursor film and the self-assembled gel was inserted vertically in the jaws of the vise. The sample was plunged rapidly into liquid ethane and then fixed into the holder, which was previously placed inside nitrogen slush. Finally, the holder with the sample was placed inside the cryo preparation chamber of the Quorum PT 3010 machine. As the sample was free standing over the holder, during the plunging, the sample was rapidly frozen by direct contact with the liquid ethane.

The sample was then transferred under vacuum into the chamber attached to the microscope and fractured with a razor blade. First, a sputtering In case step was realized (10 mA for 30s), then the surface was fractured. A slight etching at -90°C for 2 min was performed to render the fibers more visible followed by the deposition of a thin Pt layer (metallization step, 5 mA for 20s). The sample was then transferred in the FEG-cryoSEM (Hitachi SU8010) and observed at 1kV at -170°C.



*Picture of the specific cryo-holder designed and built for the preparation of cross-sections. The “cross-section” holder is a vise like holder with two movable jaws. A screw compressing/uncompressing two springs moves the jaws forwards and backwards. By design the center of the holder is invariable as the two jaws can be displaced independently to adjust to the sample thickness by screws and springs. In that way, the sample will be in the optical axis of the SEM after introduction in the microscope and easily found under the beam.*

#### **5.3.2.9. Transmission Electronic Microscopy (TEM)**

The TEM images were performed with sample prepared in liquid (diluted solutions (1 mg/mL of Fmoc-GFFpYGHpY and Fmoc-GFFYGHY) or hydrogels (10 mg/mL of Fmoc-GFFpYGHpY or Fmoc-GFFYGHY (prepared as described in section 2 just above))). All the samples were freshly prepared before TEM measurements. To make the observations 20  $\mu$ L of the sample is dropped off on a shelf. Then, the sample is observed by a TEM Tecnai G2 machine in negative staining. To make the observations, 5  $\mu$ L of the different hydrogels are deposited onto a freshly glow discharged carbon-covered grid (400 mesh).

The hydrogel is left for 2 minutes and the grid is negatively stained with 5 microliters uranyl acetate (2% in water) for another minute and finally dried using a filter paper. The grids were observed at 200kV with a Tecnai G2 (FEI) microscope. Images were acquired with a camera Eagle 2k (FEI) ss CD camera.

#### **5.3.2.10. Analytic High-Performance Liquid Chromatography (HPLC)**

Analytic High-Performance Liquid chromatography (HPLC) was carried out with a 1100 Series from Agilent technologies.

**For characterization of the different peptides and the catalytic assays:** the column is a Supelcosil ABZ + Plus with the following dimensions 15 cm  $\times$  4.6 mm, 3  $\mu$ m. The eluent used for all analyses was acetonitrile/deionized water in different ratios depending on the experiment. Ratio 80/10 in isocratic conditions, at 1 mL/min for the first catalytic assays but a ratio 50/50 in isocratic conditions, at 1 mL/min for the peptide characterization.

**For the racemic discrimination assays:** the column is a chiral column is a Cosmosil 3B with the following dimensions 4.6 mm I.D.  $\times$  250 mm. The eluent used for all analyses was n-hexane/ isopropanol in ratio 90/10 in isocratic conditions, at 1 mL/min except for the racemic solution of methyl-3-(4-methoxyphenyl) oxirane-2-carboxylate where the ratio was 97.5/2.5 in isocratic conditions at 1 mL/min.

Chromatograms were recorded by the software OpenLab Agilent 1100. All samples were observed in solution in diluted conditions (ten times under the gelation condition (1 mg/mL of peptides)).

**Esters Samples preparation:** Different concentrations of esters were used: 0.275 mM, 0.55 mM, 1.35 mM, 2.2 mM, 2.76 mM, 2.76 mM, 8.2 mM, 10 mM, 22 mM, 28 mM and 41 mM. Esters were solubilized in ultrapure water. 20  $\mu$ L of the solution is diluted in 300  $\mu$ L of isopropanol and then 50  $\mu$ L of the new solution is added in 450  $\mu$ L of the eluent ratio of n-hexane and isopropanol.

**Note:** Solutions were prepared in the eluent ratio of ACN / water and n-hexane/isopropanol. All solutions were filtrated with a PTFE 0,2  $\mu$ m filter before each injection.

### 5.3.2.11. Nuclear Magnetic Resonance (NMR)

$^1\text{H}$ -NMR spectra were recorded on a Bruker Avance 400 spectrometer at 400 MHz in the specified solvent at 25°C. The spectra were internally referenced to the residual solvent signal. The chemical shifts are given in ppm and coupling constants J are listed in Hz. The following notation is used for the  $^1\text{H}$ -NMR spectral: singlet (s), doublet (d), triplet (t), multiplet (m).

### 5.3.2.12. Circular Dichroism (CD)

Circular dichroism (CD) spectra were recorded using a Jasco J-1100 spectropolarimeter with a data pitch of 1 nm on the light wavelength. The CD spectra show the ellipticity expressed as an angle as a function of the wavelength. Liquid samples were inserted in a quartz cell of path length 1 mm. Solutions were maintained at 25 °C using a Peltier apparatus with an accuracy of  $\pm 0.2$  °C.

**Sample preparation:** Solutions of Fmoc-GFFpYGHpY and Fmoc-GFFpYGHpY + AP are at a concentration of 0.25 mg/mL for Fmoc-GFFpYGHpY and 0.25 mg/mL for AP in a freshly prepared PBS buffer at pH 7.4. All the solution were freshly prepared before the experiment. First the peptide is dissolved in PBS buffer and vortexed 1 minute and then dipped in an ultra-sound bath for 1 minute. Then the enzyme is added and the resolving mixture is vortexed 10 seconds. For the enzyme solution, the enzyme is dissolved in PBS buffer and just vortexed 30 seconds.

### 5.3.2.13. High Resolution Mass Spectroscopy (HRMS)

All the spectra were done by a platform from the Laboratoire de spectrométrie de masse Bio-organique (Département des sciences analytiques, Institut Pluridisciplinaire Hubert Curien, UMR 7178 (CNRS-UdS) ECPM, 25 rue Becquerel F67087-Strasbourg-Cedex 2) For doing the mass analysis they performed them on a microTOF-Q mass spectrometer (Bruker Daltonics GmbH, Bremen, Germany). This instrument was used at a maximum accelerating potential of 20 kV in positive mode and was operated in linear mode at 19 kV. The delay extraction was fixed at 80 ns and the frequency of the laser (nitrogen 337 nm) was set at 5 Hz. Each raw spectrum was opened with flexAnalysis 2.4 build 11 (Bruker Daltonics GmbH, Bremen, Germany) software.

### 5.3.2.14. Esterase-like activity assays

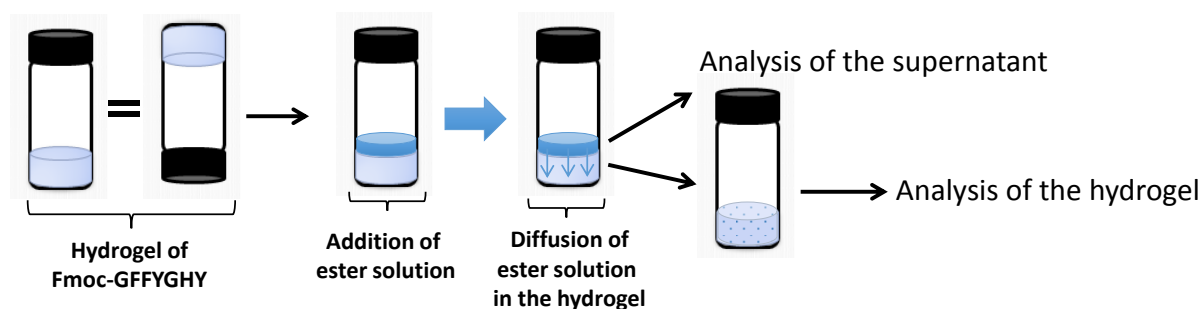
- With *para*-nitrophenyl acetate (PNA):

Microplate reader UV spectroscopy (FLX-Xenius<sup>®</sup>, SAFAS, Monaco) using SP<sub>2000</sub>V<sub>7</sub> software was the main device entailed in esterase-like activity measurement toward PNA. The activity of the Fmoc-GFFYGHY hydrogel (formed by the dephosphorylation of Fmoc-GFFpYGHpY in presence of AP) was measured on three kinds of samples: first one in solution with a self-standing hydrogel; second by generating the hydrogel on a surface on a glass slide coated beforehand with the following multilayer PEI/(PSS/PEI)<sub>2</sub>/AP (protocol described in section 5.3.2.4) and finally by coating on a polymer open-cell foam with the multilayer PEI/(PSS/PEI)<sub>2</sub>/AP. Concentration (1 mM) and volume (1 mL) ensure a large excess of *p*-NPA to monitor the esterase like activity through the absorbance measurements at 405 nm (corresponding to the *para*-nitrophenol maximum absorption).

- With one of the three classes of non-activated esters:

All experiments were followed by HPLC. Esters (1 mM) were dissolved in a freshly prepared PBS buffer at pH 7.4. Then, 50  $\mu$ L of this ester solution were dropped off on the catalytic hydrogel (see figure below).

The hydrogel is formed in the bulk in a 4 mL glass vial, from a PBS buffer solution thanks to the dephosphorylation of Fmoc-GFFpYGHpY (10 mg/mL) in the presence of AP (1 mg/mL). 200  $\mu$ L of this catalytically-active supramolecular hydrogel (CASH) is formed and 50  $\mu$ L of different ester solutions (1 mM) are brought in contact with it. The solution of ester diffuses within the CASH and the monitoring of the ester hydrolysis is monitored as following: (i) the CASH containing the ester solution is vortexed and mixed with 1 mL of deionized water, (ii) 10  $\mu$ L of this solution is mixed with 1 mL of deionized water and (iii) and 5  $\mu$ L is analyzed by HPLC.



Schematic of the catalytic activity assays on non-activated esters.

### 5.3.2.15. Esterase-like activity of the supported-CASH onto a glass substrate

Tests of the esterase-like activity of the supported CASH on a glass substrate were done using PNA as the model substrate. 1 mL solution of 1 mM of PNA was brought in contact with the supported CASH. This system was stirred using an orbital system. The reaction was followed by HPLC or by absorbance recorded at 405 nm. The preparation way of the glass supported CASH and the dimensions of it are given below.

**Preparation of the supported-CASH:** All polyelectrolytes (1 mg/mL), enzyme (AP, 1 mg/mL), and Fmoc-GFFpYGHpY (1 mg/mL) were prepared in PBS buffer freshly prepared as described in section 5.3.2.3.

The preparation of the hydrogel on a planar glass (or silica wafer) substrate (glass disk  $\varnothing = 1$  cm) was done as follows: after the deposition of a PEI (1 mg/mL) precursor layer on the planar surface by dipping, the multilayer film was built up by alternately exposing the surface to PSS (1 mg/mL in PBS buffer) and PEI (1 mg/mL in PBS buffer) solutions for 10 minutes with an intermediate rinsing step with PBS buffer during 5 minutes. AP (1 mg/mL) solution was prepared in PBS and the foam put in contact during 20 minutes followed by 5 minutes of rinsing step with PBS buffer.

Finally, the peptide Fmoc-GFFpYGHpY solution (1 mg/mL in PBS buffer) was let in contact with the modified surface overnight (12 h). The glass (or silica wafer)-supported CASH was removed from the peptide Fmoc-GFFpYGHpY solution and slightly rinsed with PBS buffer.

### 5.3.2.16. Esterase-like activity and kinetic resolution of the supported CASH in the continuous flow reactor

**Enzymatically active multilayer film deposition on foam surface:** all polyelectrolytes (1 mg/mL), enzyme (AP 1 mg/mL), and Fmoc-GFFpYGHpY (1 mg/mL) were freshly prepared in PBS buffer as described in section 5.1.6.3 above. After the first deposition of a PEI (1 mg/mL) precursor layer on the foam surface by dipping, the multilayer film was built up by alternately exposing the foam in PSS (1 mg/mL in PBS buffer) and PEI (1 mg/mL in PBS buffer) solutions for 10 minutes with an intermediate rinsing step with PBS buffer during 5 minutes. AP (1 mg/mL) solution was prepared in PBS, put in contact during 20 minutes followed by 5 minutes of rinsing step with PBS buffer. Finally, the Fmoc-GFFpYGHpY solution (1 mg/mL in PBS buffer) was brought in contact with the modified foam installed already within the reactor (column) through a continuous flow (in a closed circuit) of 0.5 mL/min during 12 h.

**Ester solution:** according to the desired ester concentration, x mg of ester was dissolved in 20 mL of deionized water before flow catalysis.

**Protocol for flow catalysis:** the solution of substrate (ester) was introduced in the reactor at 1.5 mL/min flow in a closed circuit. In open circuit (continuous flow conditions) the flow was adapted (decreased) to the desired residence time. For all substrates (except in case of PNA) the conversion in the corresponding carboxylic acid and the enantiomeric excess were followed by HPLC using an adequate column.

**Washing step of the flow reactor (column):** a solution of 10 mL of deionized water was passed through the flow reactor at 0.5 mL/min flow in an open circuit in the case of PNA and at 1.5 mL/min for all others esters. The resulting solution was checked by HPLC or by UV (in the case of PNA) to be sure that all residual ester or acid have been removed from the reactor.

**Quantitative production and isolation of chemically pure and enantiopure Fmoc-L-Glu(OH)-OH:** when the conversion of Fmoc-L-Glu(OtBu)-OH in Fmoc-L-Glu(OH)-OH reached 80 % after 30 min of time residence (monitored by HPLC / before the hydrolysis of Fmoc-D-Glu(OtBu)-OH in Fmoc-D-Glu(OH)-OH), the reaction is stopped: all the reaction medium is removed from the reactor and this latter is washed with deionized water (see paragraph just above). Then, the reaction medium and the washing solution are gathered and basified up to pH 10 using NaHCO<sub>3</sub> (0.5 M) solution. This aqueous phase is extracted three times with dichloromethane (equivalent volume as the aqueous phase).

The organic phase is dried on magnesium sulfate and the solvent is removed under reduced pressure. The aqueous phase is neutralized using 0.1 HCl and then freeze-dried. The Fmoc-L-Glu(OH)-OH is isolated as a white solid from the aqueous phase and the enantio-enriched mixture of Fmoc-L-Glu(OtBu)-OH and Fmoc-D-Glu(OtBu)-OH is isolated as a colourless oil from the organic phase.

#### **5.3.2.17. Determination of the proportion of peptides involved in the catalytic process.**

The number of peptide Fmoc-GFFYGHY that has been reacted with PNA is estimated from Fig. 3a and is equivalent to 141  $\mu$ moles: this is the amount of PNA converted when 22, 28 and 41 mM of PNA is used. We postulate that one PNA has reacted with one histidine. To determine the ratio of peptides Fmoc-GFFYGHY that have reacted with PNA against peptides present in the CASH within the investigated tubular column (15 cm length and 4 mm diameter, see 4b in the manuscript), the supported hydrogel was entirely dissolved using a flow of acetone. After the removal of this organic solvent under reduced pressure, the residue was first analyzed by <sup>1</sup>H NMR and HPLC to confirm the solely presence of Fmoc-GFFYGHY, and then weight. A mass of 1.66 mg (1.49  $\mu$ moles) was isolated as a white solid. Thus, the ratio  $r$  of peptide involved in the catalytic process against the whole number of peptide Fmoc-GFFYGHY engaged in the CASH is:  $r = 1490 / 141 \approx 11$ .

#### **5.3.2.18. Experimental determination of $K_m$ , $V_{max}$ and $k_{cat}$ using methyl ester 9 and the Michaelis-Menten equation**

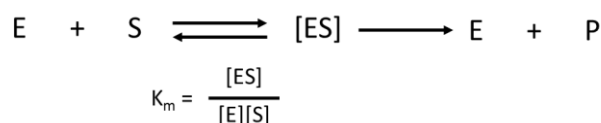
To determine the characteristic values of our catalytic system, two hypotheses were made. As our system of catalysis is a hydrogel supported on porous polymer foam contained in a reactor in a continuous flow system, the first hypothesis made is that the catalysis can be related to a packed bed reactor under continuous flow. The second is that the hydrogel can be considered as a synzyme, which acts as a "Michaelian" enzyme during its steady state.

Due to the catalyst and its confinement inside a reactor, a pre-steady state is observed. To determine the  $K_m$ ,  $V_{max}$  and  $k_{cat}$ , only the steady state is taken in account.

***The Michaelis-Menten equation describes the kinetic curve of  $V_0$ -[S]:***



We consider S as the ester substrate, P as the product formed (carboxylic acid derivative) and E as the catalytic site of our enzyme-like supported CASH. According to the Michaelis-Menten equation, it is considered the following equilibrium:



For low substrate concentration, when  $[S] \ll K_m$ ,  $V = \frac{V_{max} \times [S]}{K_m}$  and the speed is directly proportional to the substrate concentration.

For high substrate concentrations, when  $[S] \gg K_m$ ,  $V = V_{max}$  and the speed is independent of the substrate concentration.

Michaelis-Menten equation: <sup>35</sup>

$$V = V_{max} \frac{[S]}{K_m + [S]}$$

where  $V_{max}$  is the maximal speed of the reaction (mol/min),  $[S]$  is the concentration of substrate (M) and  $K_m$  the Michaelis constant (M).

When  $V = \frac{V_{max}}{2}$ ,  $[S] = K_m$

There are four graphical methods to establish the values of  $K_m$  and  $V_{max}$  under given experimental conditions: Lineweaver-Burk, Eadie-Hofstee, Hanes and Cornish-Bowden-Eisenthal. We used the Lineweaver-Burk graphical method.

To determine  $K_m$  and  $V_{max}$  values, the Lineweaver-Burk graphical method was chosen. In order to plot the  $1/V_0$  in function of  $1/[S]_0$ , the  $V_0$  values of the different concentration of substrate, were graphically determined by the slope present at the beginning of the steady state of the catalysis (after the inflection point) in the graph of the evolution of the product concentration as a function of time.

The advantage of this mathematical transformation is that it allows to draw a graph of  $1/V_0$  versus  $1/[S]_0$ , whose curve is actually a straight line for enzymes obeying the Michaelian relationship between reaction speed and concentration of the substrate.

The ordinate at the origin gives  $1/V_{max}$ . The slope of the straight line determines  $K_m$ , which is  $K_m/V_{max}$ .

So, we obtained:

$$1/V_{max} = 0.0481 \text{ s}/\mu\text{mol} \Rightarrow V_{max} = \mathbf{20.79 \mu\text{mol/s}}$$

$$K_m : K_m/V_{max} = 1.35 \text{ s} \Rightarrow K_m = 1.35 \times 20.79 = \mathbf{28 \text{ mM}}$$

Then, it is possible to determine the  $k_{cat}$  by using the following equation:

$$k_{cat} = \frac{V_{max}}{[enzyme]}$$

The hypothesis is that  $[enzyme] = [\text{"catalytic site"} \text{ of the hydrogel}]$  ( $\mu\text{mol/L}$ ).

$$\text{Then, } k_{cat} = \frac{V_{max}}{[enzyme]} = \frac{V_{max}}{[\text{catalytic site of the hydrogel}]} = \frac{20.79}{0.007} = 3 \times 10^3 \text{ s}^{-1}$$

The concentration of catalytic site called [Enzyme] has been determined as following: the number of peptides involved in the catalytic process and present in our flow reactor (length 15cm; diameter 4 mm) is 141  $\mu\text{mol}$  (see Section 17 page 25). Considering the volume in the flow reactor, it represents a concentration [enzyme]  $\approx 0.007 \text{ moles.L}^{-1}$ .

### 5.3.2.19. Molecular simulation

Classical molecular dynamics “MD” were performed using the AMBER.18 GPU software in which the potential energy  $U$  is empirically described by a sum of bond, angle and dihedral deformation energies and a pair wise additive 1-6-12 potential (electrostatic + van der Waals) between non-bonded atoms.<sup>36</sup> (Eq 1)

$$U = \sum_{\text{bonds}} k_b (r - r_0)^2 + \sum_{\text{angles}} k_\theta (\theta - \theta_0)^2 + \sum_{\text{dihedrals } n} \sum V_n (1 + \cos(n\phi - \gamma)) + \sum_{i < j} \left[ \frac{q_i q_j}{R_{ij}} - 2\varepsilon_{ij} \left( \frac{R_{ij}^*}{R_{ij}} \right)^6 + \varepsilon_{ij} \left( \frac{R_{ij}^*}{R_{ij}} \right)^{12} \right] \quad (\text{Eq 1})$$

The simulated system was composed of 16 Fmoc-GFFYGHY peptides and 3875 water molecules. Furthermore 16  $\text{Na}^+$  ions were added in order to neutralize the system. Force field parameters for the different amino acids were taken from the AMBER ff14SB force field<sup>37</sup> while those for  $\text{Na}^+$  cations stem from the work of Cheatham et al.<sup>38</sup> Water molecules were represented using the TIP3P.<sup>39</sup> Atomic charges of the Fmoc fragment were obtained using the RESP procedure.<sup>40</sup> Cross terms in van der Waals (vdW) interactions were constructed using the Lorentz–Berthelot rules. 1-4 van der Waals and 1-4 electrostatic interactions were scaled by a factor of 2 and 1.2, respectively. Simulations were performed using a cubic box and 3D periodic conditions were applied. An atom-based cutoff of 9 Å for electrostatic and vdW interactions was applied, while long-range electrostatic interactions were calculated using the particle mesh Ewald method. After equilibration an MD simulation of a total of 6  $\mu\text{s}$  in the NVT ensemble was performed. The temperature of the system was maintained at 298.15K using a Berendsen thermostat<sup>41</sup> with a relaxation time of 1.0 ps. A time step of 2 fs was used to integrate the equations of motion via the Verlet leapfrog algorithm. Snapshots along the trajectory were taken using the VMD software.<sup>42</sup>

## REFERENCES

1. Lehn, J.-M., Perspectives in chemistry – Aspects of adaptative chemistry and materials, *Angew. Chem., Int. Ed.*, **2015**, 54, 3276.
2. Whitesides, G. and Grzybowski, B., Self-assembly at all scales, *Science*, **2002**, 295, 2418.
3. Guler, M. and Stupp, S., A self-assembled nanofiber catalyst for ester hydrolysis, *J. Am. Chem. Soc.*, **2007**, 129, 12082.
4. Rodriguez-Llansola, F., *et al.*, Switchable performance of an L-proline-derived basic catalyst controlled by supramolecular gelation, *J. Am. Chem. Soc.*, **2009**, 131, 11478.
5. Weiss, R., The past, present, and future of molecular gels. What is the status of the field, and where is it going?, *J. Am. Chem. Soc.*, **2014**, 136, 7519.
6. Teramoto, N., *et al.*, Polymer foam-reinforced hydrogels inspired by plant body frameworks as high-performance soft matter, *Polymer J.*, **2014**, 46, 592.
7. Olive, A., *et al.*, Spatial and directional control over self-assembly using catalytic micropatterned surfaces, *Angew. Chem., Int. Ed.*, **2014**, 53, 4132.
8. Du, X., *et al.*, Supramolecular hydrogelators and hydrogels: From soft matter to molecular biomaterials, *Chem. Rev.*, **2015**, 115, 13165.
9. Vigier-Carrière, C., *et al.*, Surface-assisted self-assembly strategies leading to supramolecular hydrogels, *Angew. Chem., Int. Ed.*, **2018**, 57, 1448.
10. Yang, B., *et al.*, Surface-mediated supramolecular self-assembly of protein, peptide, and nucleoside derivatives: From surface design to the underlying mechanism and tailored functions, *Langmuir*, **2018**, 34, 15109.
11. Yang, Z., *et al.*, Enzymatic formation of supramolecular hydrogels, *Adv. Mater.*, **2004**, 16, 1440.
12. Williams, R., *et al.*, Enzyme-assisted self-assembly under thermodynamic control, *Nat. Nanotech.*, **2009**, 4, 19.
13. Vigier-Carrière, C., *et al.*, Bioactive seed layer for surface-confined self-assembly of peptides, *Angew. Chem., Int. Ed.*, **2015**, 54, 10198.
14. Rodon Fores, J., *et al.*, Localized supramolecular peptides self-assembly directed by enzyme-induced proton gradients, *Angew. Chem., Int. Ed.*, **2017**, 56, 15984.
15. Zozulia, O., *et al.*, Catalytic peptide assemblies, *Chem. Soc. Rev.*, **2018**, 47, 3621.
16. Yang, C., *et al.*, Molecular hydrogels with esterase-like activity, *Chin. J. Chem.*, **2013**, 31, 494.
17. Tao, K., *et al.*, Fmoc-modified amino acids and short peptides: simple, bio-inspired building blocks for the fabrication of functional materials, *Chem. Soc. Rev.*, **2016**, 45, 3935.
18. Smith, A., *et al.*, Fmoc-diphenylalanine self-assembles to a hydrogel *via* a novel architecture based on  $\pi$ - $\pi$  Interlocked  $\beta$ -Sheets, *Adv. Mater.*, **2008**, 20, 37.
19. Reches, M. and Gazit, E., Controlled patterning of aligned self-assembled peptide nanotubes, *Nat. Nanotech.*, **2006**, 1, 195.
20. Bender, M. and Turnquest, B., The imidazole-catalyzed hydrolysis of *p*-nitrophenyl acetate, *J. Am. Chem. Soc.*, **1957**, 79, 1652.
21. Moroz, Y., *et al.*, New tricks for old proteins: single mutations in a non-enzymatic protein give rise to various enzymatic activities, *J. Am. Chem. Soc.*, **2015**, 137, 14905.
22. Li, J., *et al.*, Enzyme-instructed intracellular molecular self-assembly to boost activity of cisplatin against drug-resistant ovarian cancer cells, *Angew. Chem., Int. Ed.*, **2015**, 54, 13307.
23. Singh, N., *et al.*, Synthesis of a double-network supramolecular hydrogel by having one network catalyse the formation of the second, *Chem. Eur. J.*, **2017**, 23, 2018.
24. Singh, N., *et al.*, Insight into the esterase like activity demonstrated by an imidazole appended self-assembling hydrogelator, *Chem. Commun.*, **2015**, 51, 13213.
25. Krystyna, L. and Ulijn, R., Short peptides in minimalistic biocatalyst design, *Biocatalysis*, **2015**, 1, 67.
26. Rodriguez-Llansola, F., *et al.*, Supramolecular hydrogel as a reusable heterogeneous catalyst for the direct aldol reaction, *Chem. Commun.*, **2009**, 0, 7303.
27. Singh, N., *et al.*, Tandem reactions in self-sorted catalytic molecular hydrogels, *Chem. Sci.*, **2016**, 7, 5568.

28. Som A. and Matile, S., Rigid-rod  $\beta$ -barrel ion channels with internal "cascade blue" cofactors – catalysis of amide, carbonate, and ester hydrolysis, *Eur. J. Org. Chem.*, **2002**, 3874.
29. Yamada, N., *et al.*, Regulation of  $\beta$ -sheet structures within amyloid-like  $\beta$ -sheet assemblage from tripeptide derivatives, *J. Am. Chem. Soc.*, **1998**, 120, 12192.
30. Vigier-Carrière, C., *et al.*, Bioactive seed layer for surface-confined self-assembly of peptides, *Angew. Chem., Int. Ed.*, **2015**, 54, 10198.
31. Fogler H., "Elements of chemical reaction engineering", (3rd Ed.), Prentice Hall, Upper Saddle River, USA, **1999**.
32. Li, R., *et al.*, Facile control over the supramolecular ordering of self-assembled peptide scaffolds by simultaneous assembly with a polysaccharide, *Scientific Report*, **2017**, 7, 4797.
33. Kreuzer, A. and Salveson, P., Standard practices for Fmoc-based solid-phase peptide synthesis in the Nowick laboratory, **2018**, version 1.6.3
34. Sauerbrey, G., Verwendung von schwingquarzen zur wägung dünner schichten und zur mikrowägung, *Z. Phys.*, **1959**, 155, 206.
35. a) Voinova, M., *et al.*, Viscoelastic acoustic response of layered polymer films at fluid-solid interfaces: continuum mechanics approach, *Phys. Scr.*, **1999**, 59, 391; b) Höök, F., *et al.*, Variation in coupled water, viscoelastic properties, and film thickness of a Mefp-1 protein film during adsorption and cross-linking: a quartz crystal microbalance with dissipation monitoring, ellipsometry, and surface plasmon resonance study, *Anal. Chem.*, **2001**, 73, 5796.
36. Pearlman, D., *et al.*, A package of computer programs for applying molecular mechanics, normal mode analysis, molecular dynamics and free energy calculations to simulate the structural and energetic properties of molecules, *Comp. Phys. Commun.*, **1995**, 91, 1.
37. Maier, J., *et al.*, ff14SB: Improving the accuracy of protein side chain and backbone parameters from ff99SB, *J. Chem. Theory Comput.*, **2015**, 11, 3696.
38. Joung, S. and Cheatham, T., Determination of alkali and halide monovalent ion parameters for use in explicitly solvated biomolecular simulations, *J. Phys. Chem. B*, **2008**, 112, 9020.
39. Jorgensen, W., *et al.*, Comparison of simple potential functions for simulating liquid water, *J. Chem. Phys.*, **1983**, 79, 926.
40. Bayly, C., *et al.*, A well-behaved electrostatic potential based method using charge restraints for deriving atomic charges: the RESP model, *J. Phys. Chem.*, **1993**, 97, 10269.
41. Berendsen, H., *et al.*, Molecular dynamics with coupling to an external bath, *J. Chem. Phys.*, **1984**, 81, 3684.
42. Humphrey, W., *et al.*, "VMD - Visual Molecular Dynamics", *J. Molec. Graphics*, **1996**, 14, 33.
43. Li, R., *et al.*, Facile control over the supramolecular ordering of self-assembled peptide scaffolds by simultaneous assembly with a polysaccharide, *Scientific Report*, **2017**, 7, 4797.





## **Chapter 6**



**Morphological, mechanical and biological study of a  
composite hydrogel based on self-assembled  
peptides and hyaluronic acid**

*The sixth chapter of my manuscript presents a study of the interactions between a polysaccharide and an enzyme-assisted self-assembly of peptides. These kinds of supramolecular hydrogels are promising in the biomedical field thanks to the low toxicity of the chemical agents involved (enzyme, peptide) and the nature of the material formed. This study focused on understanding the contribution of hyaluronic acid in the peptide assembly from a physico-chemical, morphological, mechanical and biological point of view.*

## Summary

6.1. Introduction .....	226
6.2. State of the art.....	226
6.3. Results and Discussion.....	228
6.3.1. Preliminary hydrogelation upside-down vial test assays .....	229
6.3.2. Mechanical properties of the composite hydrogels .....	231
6.3.3. Morphological study of the fibrous network composing the composite hydrogels .....	233
6.3.4. Molecular study of the interactions between HA and the self-assembly of Fmoc-FFY .....	238
6.3.5. LEASA of the composite hydrogels on a surface .....	245
6.3.6. Cell culture with NIH 3T3 Fibroblasts .....	249
6.4. Conclusion .....	252
6.5. Experimental section.....	253
6.5.1. Materials .....	253
6.5.2. Synthesis and characterization of Fmoc-FFpY .....	254
6.5.3. Multilayer film preparation and hydrogel self-assembly .....	256
6.5.4. Upside-down hydrogel test in Bulk .....	257
6.5.5. Quartz crystal microbalance with dissipation monitoring .....	257
6.5.6. Atomic force microscopy .....	258
6.5.7. Infrared spectroscopy .....	258
6.5.8. Scanning electron microscopy and cryo-SEM.....	258
6.5.9. Transmission Electronic Microscopy .....	259
6.5.10. Fluorescence emission spectroscopy .....	259
6.5.11. Circular Dichroism .....	260
6.5.12. Rheology.....	260
6.5.13. <sup>1</sup> H and <sup>31</sup> P NMR.....	260
6.5.14. Epifluorescence microscopy and confocal laser scanning microscopy .....	261
6.5.15. Cells assays on Fibroblast NIH 3T3 .....	262
<b>ANNEXES .....</b>	<b>267</b>
<b>REFERENCES .....</b>	<b>270</b>



## 6.1. Introduction

Materials that form spontaneously by self-assembly from natural or synthetic building blocks are promising for a variety of applications. In biomedicine for example, there is significant interest in exploiting self-assembly to mimic the extracellular matrix (ECM) for cell-culture applications. Here, we propose a composite hydrogel combining the properties of a peptide self-assembly and hyaluronic acid (HA), one of the major components of extracellular matrix, which makes it an attractive material. This material is also interesting from a fundamental point of view since both components, hyaluronic acid and the self-assembled peptides are both negatively charged. What kind of interaction between them ensure the material cohesion? The study presented here, will explain the interactions between these two negatively charged molecules and how we obtain a various range of mechanical properties by changing their ratio but also by changing the buffer or media used to get the composite hydrogel.

## 6.2. State of the art

One of the most common applications for low-molecular weight hydrogelators is to use them as support for cells assays or biomedical issues. Their softness, easy way of preparation and their biological adapted composition (amino acids sequence) make them candidates of choice. The group who reported the first case of cell culture using Fmoc-dipeptides is Ulijn' group<sup>1</sup> in 2006. They reported chondrocyte cells in 2D and 3D cell-culture experiments. This study, was then extended by Xu *et al.* in 2007.<sup>2</sup> Ulijn *et al.*, reported afterwards the use of a mixture of peptides, Fmoc-Gly-Gly-OH with Fmoc-Phe-Phe-OH, for the 2D or 3D cell culture.<sup>3</sup> According to the authors, the hydrogels are stable under cell culture conditions and consist of nanofibers that have dimensions similar to those of the fibrous components of the extracellular matrix (ECM).<sup>1,2</sup> After these first reports, the field was extensively investigated and several peptide hydrogels were designed for specific cells lines or specific applications.<sup>4-9</sup>

Beside the design of peptide supramolecular hydrogels with peptides possessing no specificity for cells, Ulijn *et al.* designed a supramolecular hydrogel containing the Fmoc-Arg-Gly-Asp-OH (Fmoc-RGD) along with the peptide forming the fibrous scaffold. The RGD sequence is known to be a binding sequence of the integrin present in cells and is widely used to promote cell adhesion. The authors suggested that the RGD motif plays a dual role: as a structural component that is localized at the surface of the unique, interwoven cylindrical nanofiber structure and as a biological ligand that forms the specific RGD–integrin binding to promote adhesion, spreading, and proliferation of cells.<sup>10</sup>

Using a similar design principle, Hamley *et al.* found that Fmoc-RGD itself forms a self-supporting hydrogel consisting of well-defined amyloid fibrils with  $\beta$ -sheet features. In addition, preliminary cell culture experiments showed that Fmoc-RGD could be used to culture bovine fibroblasts.<sup>11</sup> These results show how it is possible to modulate the hydrogel properties for modulating cell adhesion depending on the cell line and the importance to add specific moieties in the fibrous networks to favor interactions between the hydrogel and the cells. Another peptide supramolecular hydrogel, developed by Hirose *et al.*, is now commercially available and known as PuraMatrix® ((RADA)<sub>16</sub> with R = Arginine, A = Alanine and D = aspartic acid, so-called RADA16).<sup>12-17</sup> Nowadays this hydrogel is one of the most used supramolecular hydrogel for cell culture. The commercial availability of RADA16 allows many research laboratories to evaluate the use of the hydrogel for 3D cell culture.<sup>18-23</sup>

Realizing the merits of multicomponent hydrogels, Collier *et al.* designed and examined multi-peptide co-assembling hydrogels based on peptides RGDS-Q<sub>11</sub> (with Q stands for glutamine and S for serine) and IKVAV-Q<sub>11</sub> (with I = isoleucine, K = lysine, V=valine and A = alanine) consisting of two segments: a nanofiber-forming peptide, Q<sub>11</sub>, which self-assembles to form  $\beta$ -sheets at the C-terminal and a ligand of integrin, RGDS or IKVAV, at the N-terminal.<sup>24,25</sup> Then, many of multi-peptide co-assembling hydrogels were design for cell culture support applications.<sup>26-34</sup>

Stupp *et al.* have reported interesting interactions between biopolymers and charged self-assembling peptides leading to the fabrication of stable membranes by co-assembly a positively charged short peptide molecules and hyaluronic acid (HA), which is negatively charged.<sup>35,36</sup> Similarly, Mata *et al.* designed thin self-supporting bioactive membranes combining positively charged multi-domain self-assembling peptides and HA.<sup>37</sup> By changing the assembly conditions like time and temperature, membranes with various topographical pattern morphologies were fabricated, affecting stem cell adhesion, spreading, and morphology. Recently, such membranes were tailored for tissue regeneration applications by functionalizing the peptides with different bioactive functions, including integrin-binding peptide sequences.<sup>38</sup> All these results demonstrate that using self-assembled composite hydrogels can present great advantages such as the ability to modify the material properties by rationally achieving the desired stiffness, strength, weight and density, as well as resilience and compliance, which are factors of the greatest importance in tissue engineering, regenerative medicine and drug delivery applications.

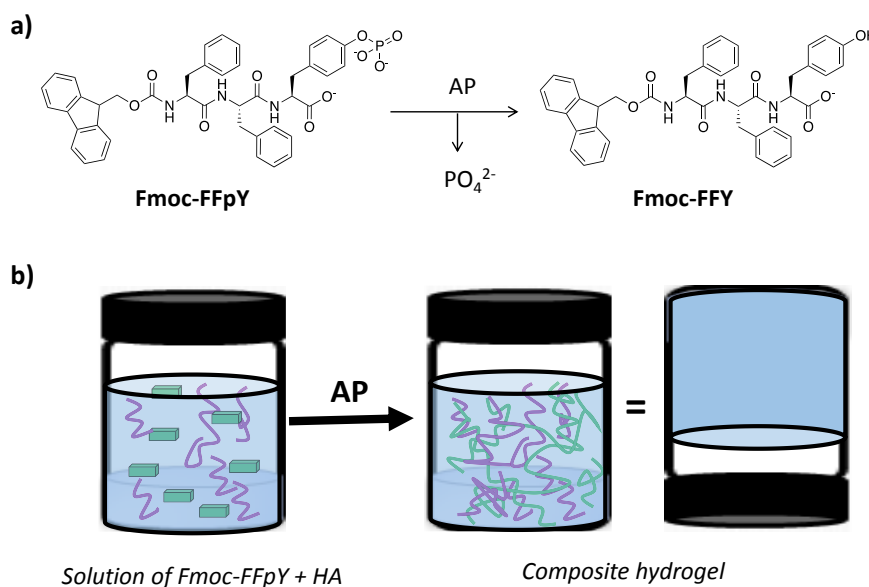
In 2018, Adler-Abramovich *et al.* developed a composite hydrogel composed of a self-assembly of Fmoc-FF and HA. These authors showed that when the two components are mixed in different ratios the mechanical properties of the resulting hydrogel changed. When the amount of HA is higher than the amount of Fmoc-FF the composite hydrogel becomes softer compared to the Fmoc-FF self-assembled hydrogel but still presents a higher hardness compared to the HA alone. The Fmoc-FF network helps to strengthen the HA network which passes from 100 Pa up to 25 kPa and the HA network permits the biocompatibility of the composite hydrogel.

The composite hydrogel also allowed released of curcumin, a hydrophobic polyphenol showing antioxidant, anti-inflammatory, and antitumor activities. The release can be modulated as a function of concentration of Fmoc-FF peptide within the hydrogel matrix.<sup>39</sup>

***The electrostatic interaction between peptide assemblies and polysaccharides has recently been highlighted and seems particularly promising in the development of new biomaterials. In this chapter, the interaction between a polysaccharide negatively charged, hyaluronic acid, and an enzyme-assisted self-assembly of peptides is investigated for cell adhesion tests.***

### 6.3. Results and Discussion

Here, we describe the EASA of a peptide, Fmoc-FFpY, in presence of HA in different buffers and culture media to evaluate the molecular, morphological and mechanical properties of the resulting composite material to determine the best support for cell culture. Our model system is composed of Fmoc-FFpY (Scheme 1), a LMWH already described as hydrogelator under the action of the alkaline phosphatase (AP).<sup>40</sup> When a Fmoc-FFpY tripeptide meets AP in borax buffer (25 mM, pH = 9.5), its phosphate group ( $\text{PO}_4^{2-}$  noted as p in the peptide formula) is removed and the corresponding hydrogelator, Fmoc-FFY, is released and self-assembles. The peptide self-assembly is a soft gel (20 Pa formed in borax pH 9.5 as discussed later). By adding a certain amount of HA<sup>41-43</sup>, which must strengthen the self-assembly, we should obtain a change in the mechanical properties and be able to obtain a range of Young moduli.



Scheme 1: a) Formation of the Fmoc-FFY hydrogelator by the action of AP, b) schematic representation of the composite hydrogel formed in the bulk.

### **6.3.1. Preliminary hydrogelation upside-down vial test assays**

In a first study, tests in solution were realized to determine the conditions to generate a hydrogel from the self-assembly of Fmoc-FFY in presence of HA. In fact, unlike reported by Stupp's group with the formation of the membranes<sup>35,36</sup>, Fmoc-FFpY and HA are both negatively charged as well as the hydrogelator Fmoc-FFY, which may hinder gel formation. When 5 mg/mL (6.44 mM) of Fmoc-FFpY is dissolved in borax buffer (25 mM, pH 9.5) at 20 °C with 1 mg/mL (6.67 μM) of AP, a hydrogel is obtained after 20 min, but when no AP is added, no gelation occurs, even after 48 hours as expected. Then, when 0, 2, 3, 4, 5 and 10 mg/mL of HA (2.12, 4.24, 6.36, 8.47, 10.59 and 21.19 μM respectively) are added to the peptide solution, followed by the addition of AP, hydrogels are obtained with different times of formation (20 min, 25 min, 35 min, 45 min, 45 min and 50 min respectively) but not all hydrogels have a good stability over time, some of them become, after one week, a viscous solution (Figure 1a). This allows us to conclude that HA does not prevent the hydrogel formation.

However, for cells, borax buffer at pH 9.5 is not optimal. Consequently, we tried to form a composite hydrogel in the following media: borax (25 mM, pH 7.4), Phosphate buffered saline (PBS) pH 7.4, Roswell park memorial institute medium (RPMI), RPMI + Fetal bovine serum (FBS), Dubelcco's modified institute medium (DMEM), DMEM + FBS and gelose Mueller-Hinton medium (MH) (Figure 1b). Assays were done for the formation of the hydrogels at 20 °C and evaluation of the stability at 20 °C, formation at 20 °C and stability evaluation at 37 °C (cell culture temperature) and finally formation and stability evaluation at 37 °C. All the stability evaluations were done over one week (Figure 2a). From these experiments, we observed that three media were enabled to keep a gel in all these conditions and with the different ratios of HA. These media are borax pH 9.5, RPMI and MH. For cell culture, cells need to have a medium complemented by Fetal Bovine Serum (FBS) to feed them. Nevertheless, none of the composite hydrogel concentration conditions leads to the formation of a gel stable in time in a medium complemented with FBS (Figure 2a). So, we added medium complemented with FBS on a previously formed composite hydrogel inside a none complemented medium. We observed that for the three selected media, all of the hydrogels formed inside them stayed stable when the complemented medium (RPMI + FBS for RPMI, MH + FBS for MH and RPMI + FBS and MH + FBS for borax pH 9.5) is brought in contact with the hydrogel over one week (Figure 2b).

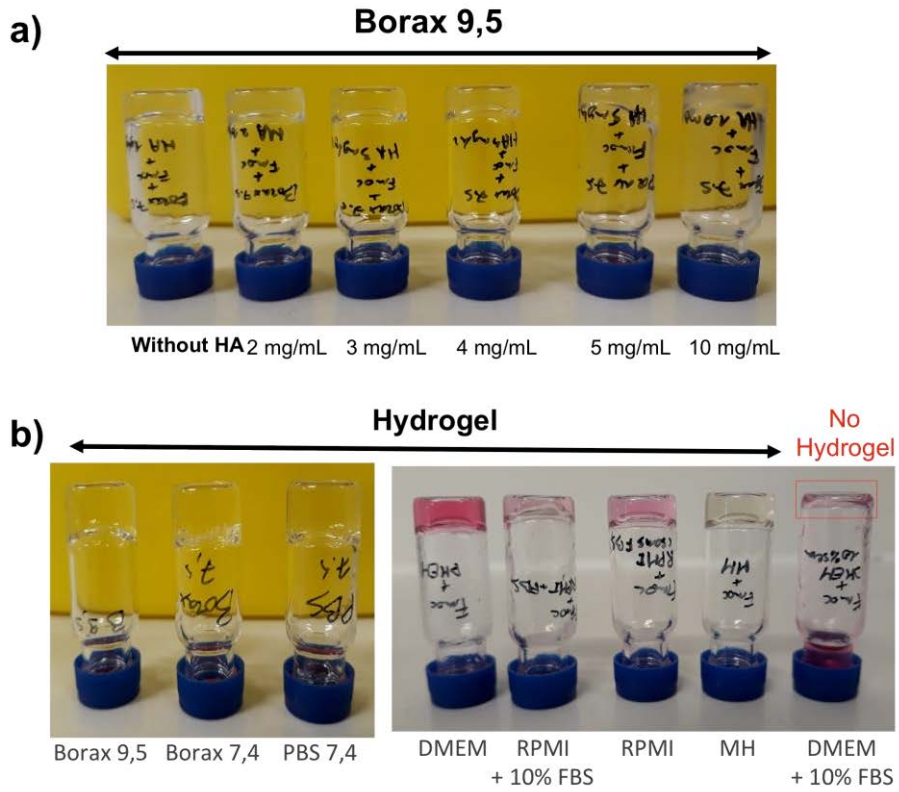
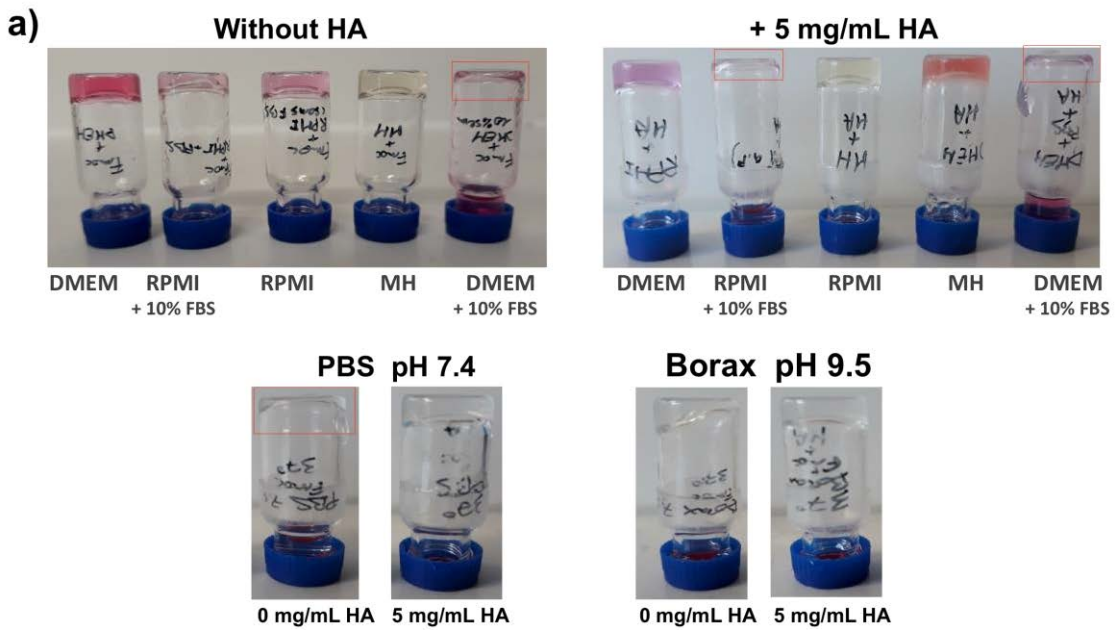


Figure 1: Upside-down vial tests a) in borax (25 mM, pH 9.5) at different concentrations of HA, b) in different buffers and cell culture media.



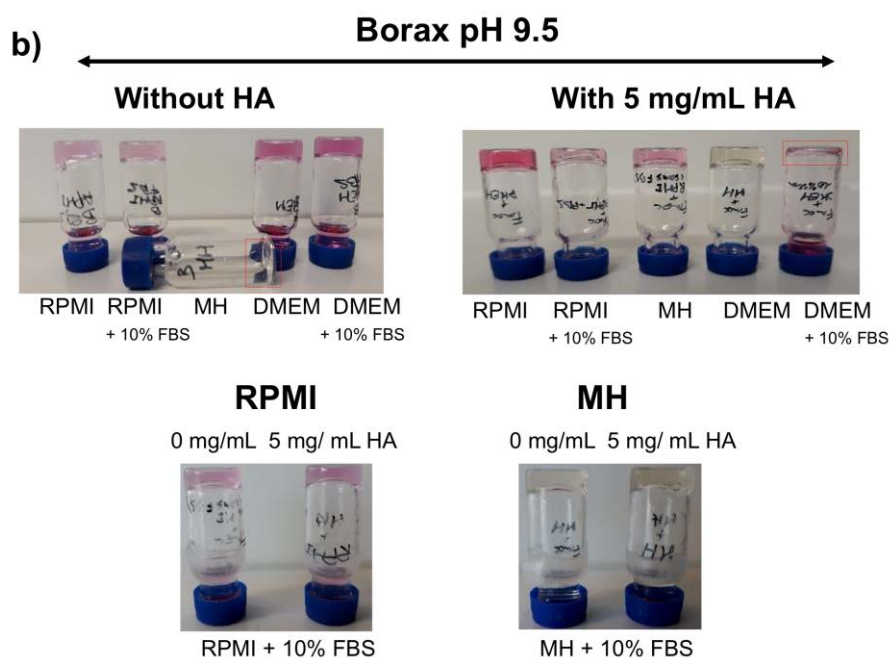


Figure 2: Upside-down vial tests with Fmoc-FFpY (5 mg/mL) + HA (0 or 5 mg/mL) + AP (1 mg/mL) aqueous solutions prepared a) in cell culture media, PBS (pH 7.4) and borax (pH 9.5). Their formation and stability over one week were tested at 20 °C and 37 °C. The Upside-down vial test reported in a) correspond to the results after the different stability test after one week. b) addition of 200  $\mu$ L of complemented cell culture media onto hydrogel prepared in borax buffer pH 9.5 (top) and complemented RPMI onto hydrogel prepared in RPMI medium and complemented MH onto hydrogel prepared in MH medium.

The three best media or buffers to form the hydrogel in solution, regarding the preliminary tests in vial, are borax buffer at pH 9.5, RPMI cell culture medium and MH bacteria culture medium.

For the rest of the study, we selected RPMI medium, to compare the behavior of the composite hydrogels when formed in borax buffer (25 mM, pH 9.5), known to be the best buffer for the peptide self-assembly formation<sup>40</sup>, or in a cell culture medium. MH is a medium for bacteria culture. As we will focus on cell assays in this chapter, this medium will not be investigated further. Yet, bacteriological assays could be realized in the future with the composite hydrogel formed in MH medium to promote bacteria proliferation.

### 6.3.2. Mechanical properties of the composite hydrogels

Mechanical properties were determined by rheological measurements. The storage moduli,  $G'$ , and the loss moduli,  $G''$ , were obtained for the different composite hydrogels formed in borax, in RPMI or formed in borax and exchange 1h with RPMI. The  $G'$  measured for the borax series are about 20 Pa for all HA conditions. These results are 100 times lower than the ones measured in RPMI (between 2000 to 500 Pa). Surprisingly, when the HA concentration increased, the storage modulus decreased, indicating that one obtains a softer material (Figure 3a,b). For the Loss modulus, when the HA concentration increases the modulus increases too (from 2 to 5 Pa) for the borax series, which means that the viscoelasticity of the material increase.

Unlike the hydrogels formed in borax, the one formed in RPMI shows a decrease of the  $G''$  (from 500 to 10 Pa) when the HA concentration increase, meaning that the resulting material is less viscoelastic.

When composite hydrogels are formed in borax buffer and are then brought in contact for one hour with RPMI medium to carry out an exchange of the medium before undertaking the rheological measurements, the mechanical properties observed are in between the results obtained for borax and RPMI series (280 Pa  $>G'$   $>60$  Pa depending of the HA concentration) and the viscoelasticity of the material stays unchanged regarding the Ha concentration (Figure 3c). These three series of measurements show that one can obtain a wide range of mechanical properties in the soft matter range by adjusting the concentrations of HA in the Fmoc-FFY self-assembly but also by changing the medium or buffer used to form the gel. This is exactly what we wanted to obtain: the possibility to obtain a wide range of mechanical properties by simply mixing two different components. This will be very useful for biologist as they will be able to work with only one kind of support to perform cell cultures under various conditions.

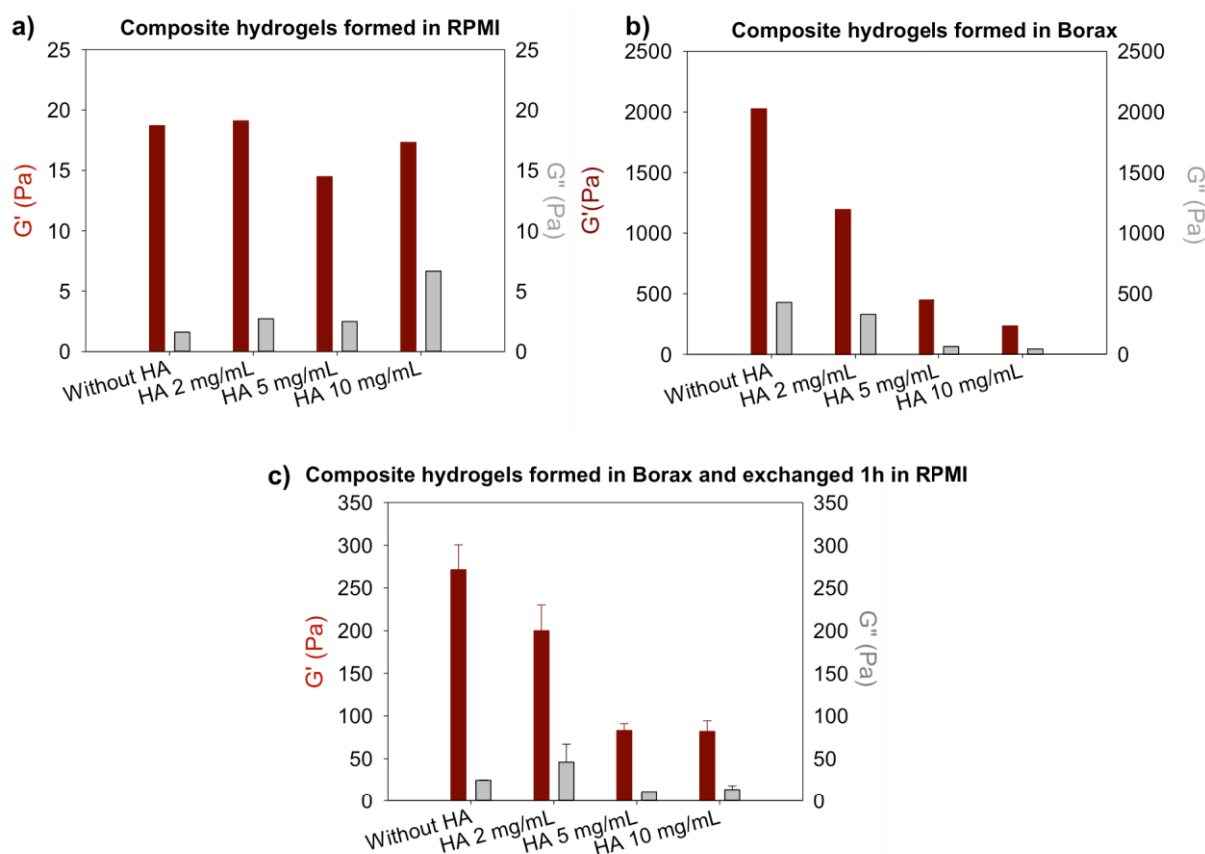


Figure 3: Storage and loss moduli measurements of the composite hydrogels with different concentration of HA in a) RPMI, b) in Borax (25 mM, pH 9.5) and c) formation in Borax followed by 1h exchange in RPMI.

*However, a question arose during these observations: are the fiber morphologies and the interactions at the molecular level between the Fmoc-FFY self-assembly and HA in the two different media (RPMI and borax pH 9.5) used for the composite hydrogel formation comparable?*

### **6.3.3. Morphological study of the fibrous network composing the composite hydrogels**

To gain further insight into the molecular organization of the composite hydrogels, we used transmission electron microscopy (TEM) and confocal laser scanning microscopy (CLSM). We observed that throughout all the samples (different media or different HA concentrations) that the gel is composed of fibers. The elementary fiber has always the same diameter, which is about 5.5 nm (Figure 4a), but the number and size of composite fibers, composed of two or more elementary fibers, increased when the concentration of HA increases and when the formation is performed in borax buffer compared to RPMI medium (Figure 4a,b). These results, observed by TEM, are confirmed in CLSM (Figure 4c,d). HA seems to force elementary fibers to interact one with each other which results in bigger fibers, yet the fibers are less abundant in solution.

This leads to the presence of holes in the gel. These observations can explain why the materials get softer when the HA amount increases. Locally, the rheology measurements will sense more water and some fibers. On the other hand, for smaller HA concentration there are more fibers present, but they are thinner; this leads to a harder material.

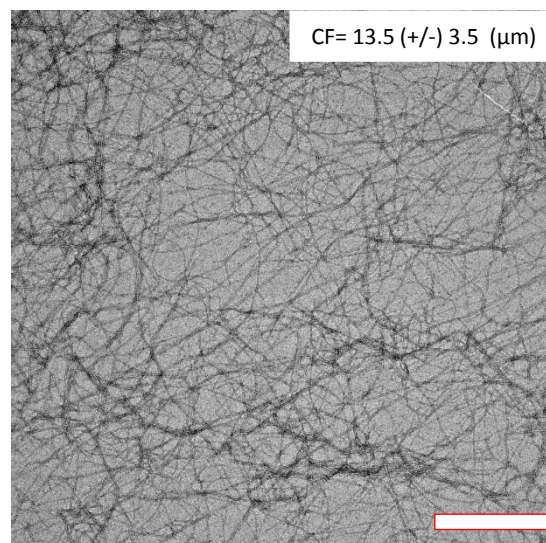
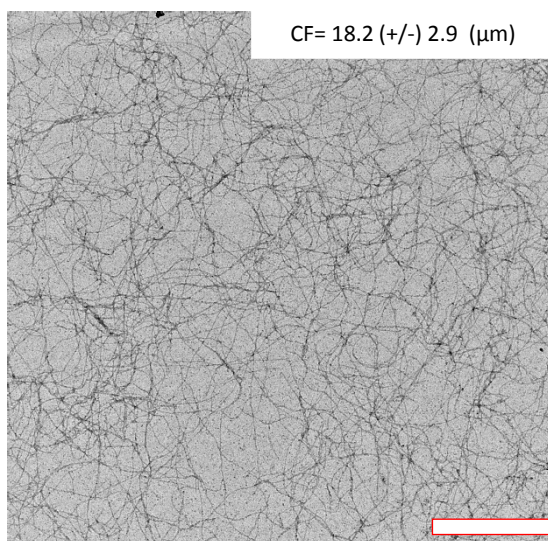


a)

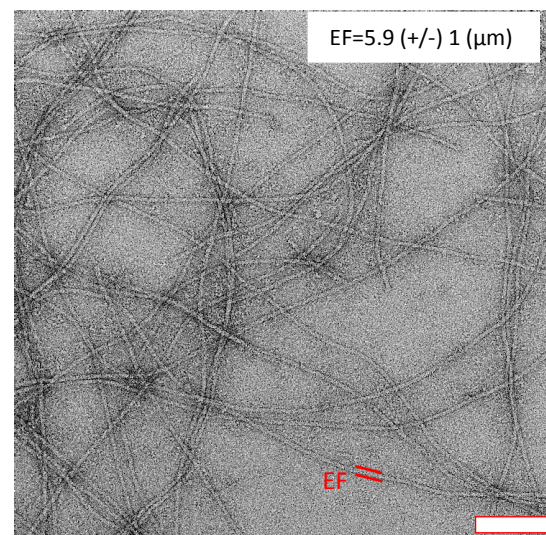
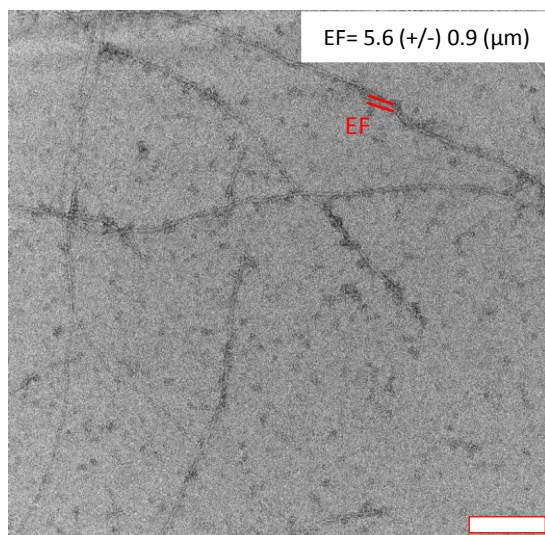
Without HA

2 mg/mL HA

Scale bar : 500 nm



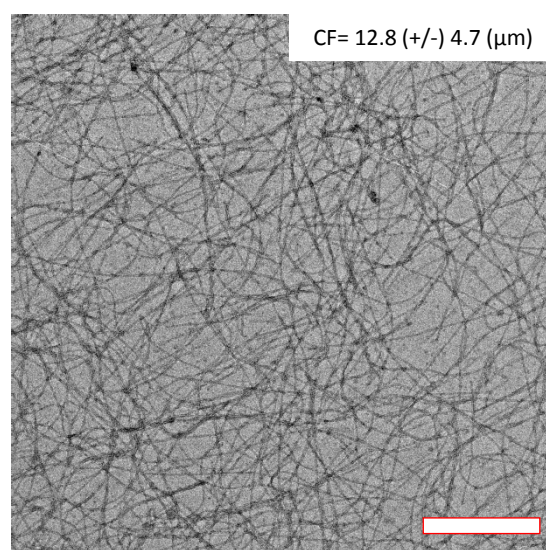
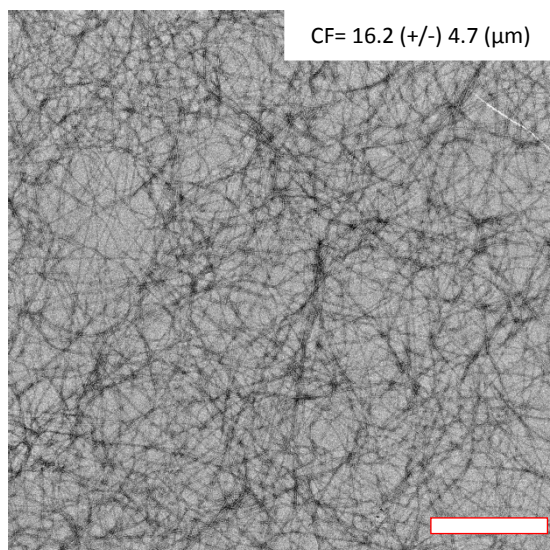
Scale bar : 100 nm



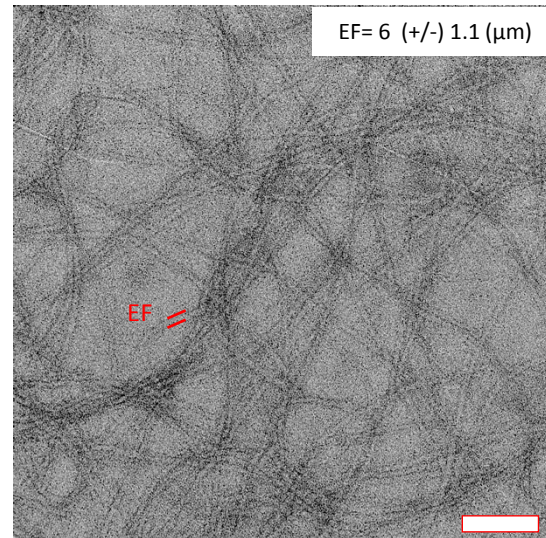
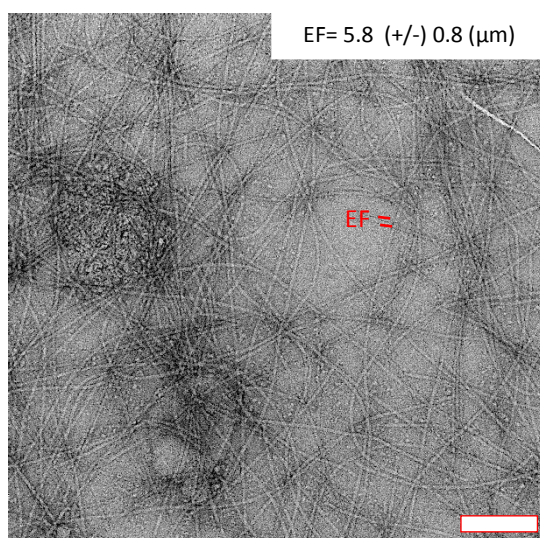
5 mg/mL HA

10 mg/mL HA

Scale bar : 500 nm



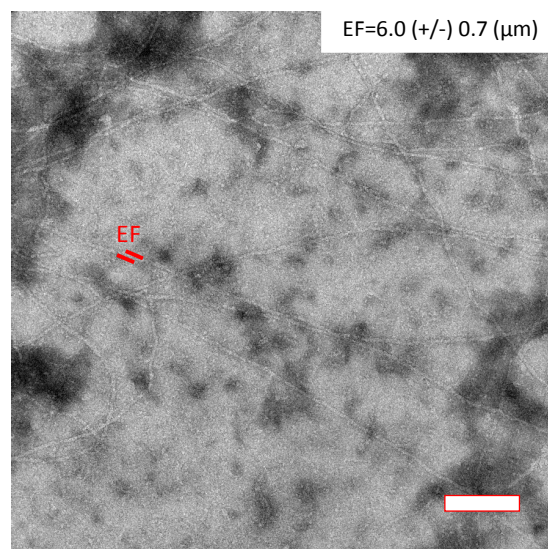
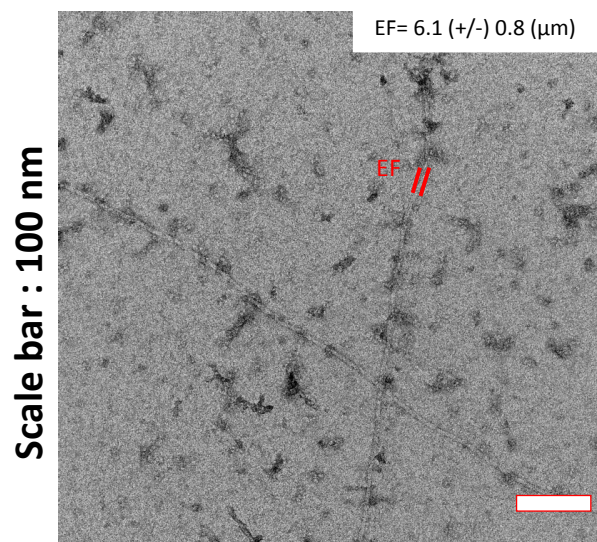
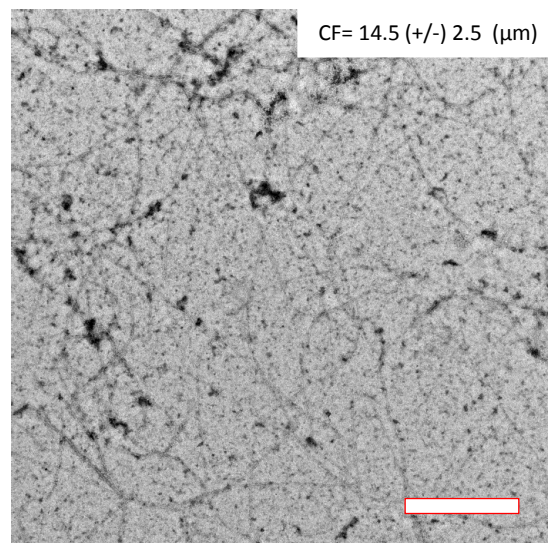
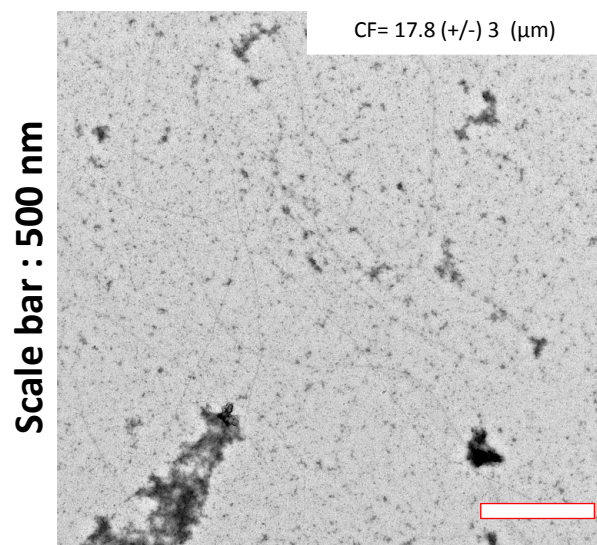
Scale bar : 100 nm



b)

Without HA

5 mg/mL HA



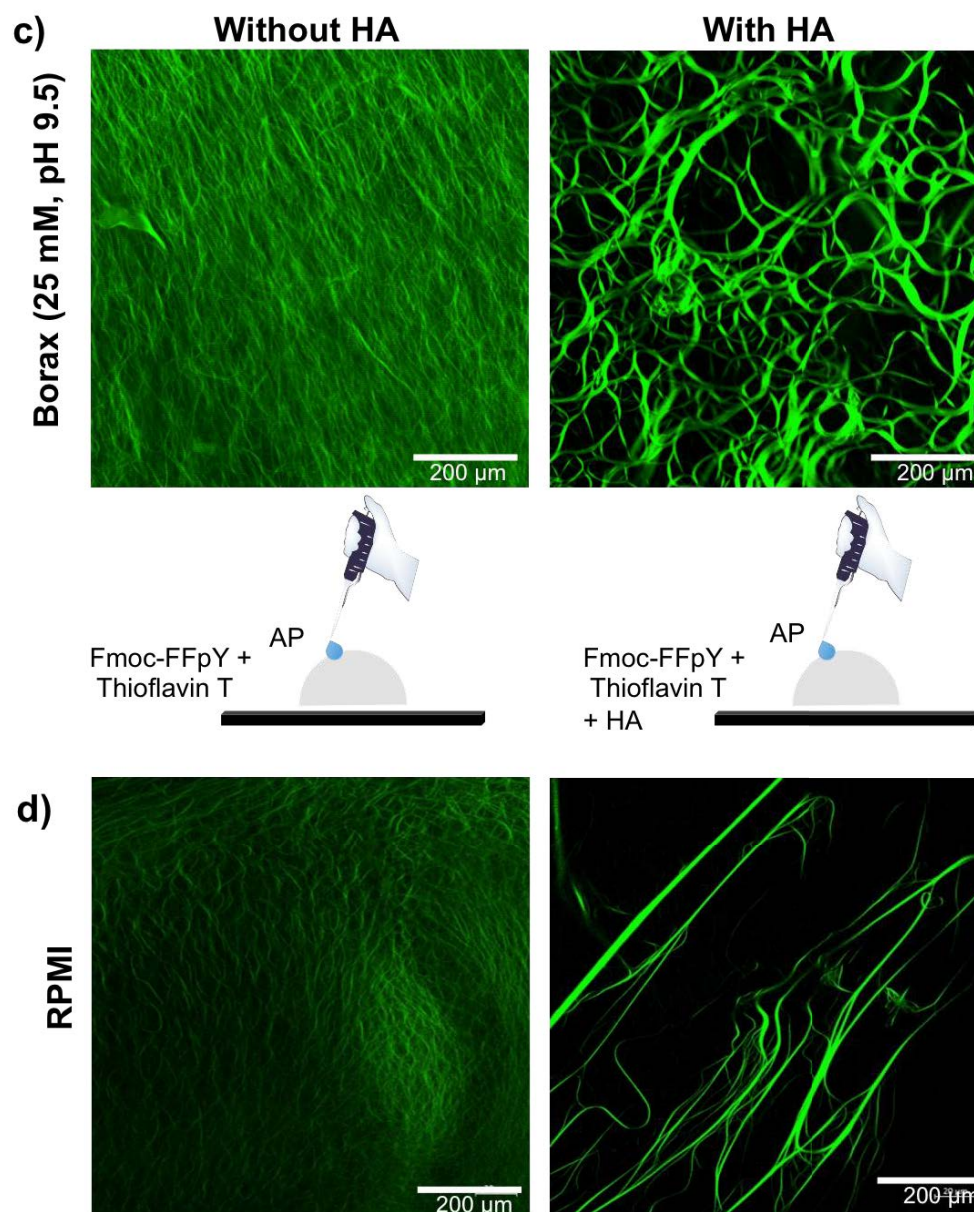


Figure 4: TEM pictures of the composite hydrogels formed a) in borax and b) in RPMI; and CLSM pictures of the composite hydrogels formed in c) borax and d) in RPMI.

### 6.3.4. Molecular study of the interactions between HA and the self-assembly of Fmoc-FFY

To understand the different results presented above, Circular Dichroism (CD), FT-IR and Fluorescence spectroscopy were performed.

#### 6.3.4.1. Circular Dichroism

CD analysis of each composite hydrogel in borax buffer and RPMI were recorded to observe if the hyaluronic acid interacts with the peptide self-assembly at the molecular level. Previous work in the literature with the self-assembly of Fmoc-Phe, Fmoc-Tyr and other Fmoc-amino acid derivatives were performed and from these studies two possible models for monomers orientation and interactions in the context of fibrils were proposed.<sup>44</sup> Peptide supramolecular self-assemblies are known to generally lead to the formation of fibers and at the molecular level, the structures are in parallel or anti-parallel  $\beta$ -sheet conformations. This leads to the following proposed models: “parallel” orientation or “anti-parallel” orientation of amino acids within a fiber<sup>44</sup>. In the first model, the “parallel” orientation, adjacent Fmoc groups interact parallelly and aromatic phenyl groups of the benzyl side-chains are engaged in edge-to-face  $\pi$ - $\pi$  interactions with themselves.<sup>45,46</sup> This orientation facilitates a central hydrogen bond network involving the carbamate functionality along the fiber axis and orients the carboxy terminus on one face of the fibers. This model is supported by characteristic CD spectroscopy absorptions at 270-230 nm (Fmoc-Fmoc  $n$ - $\pi^*$  transitions) and 200-230 nm (side chain benzene  $\pi$ - $\pi^*$  transitions).<sup>44,45</sup> The second model involves aromatic  $\pi$ - $\pi$  interactions occurring between Fmoc groups in an antiparallel way and side-chain benzyl groups with similar CD spectroscopy absorptions.

In RPMI medium, CD spectra shows peaks at 206 nm and 217 nm, which according to Nilsson's group, represent the  $\pi$ - $\pi^*$  phenyl side chain excitation and a hydrogen bond network involving the carbamate functionality. The peaks at 230, 254 and 270 nm represent the  $n$ - $\pi^*$  Fmoc-Fmoc excitation. One can observe that when the concentration of HA increases (spectra at 0, 2, 5 and 10 mg/mL of HA), the signals characteristic of the  $n$ - $\pi^*$  Fmoc-Fmoc excitation disappear and the ones showing the side chain interactions of the peptides and hydrogen bonding decrease in intensity (Figure 5a). Similarly, in borax buffer, CD spectra show peaks at 206, 217 and 230 nm which are attributed to phenyl side chain interactions and hydrogen bonds. However, no peaks are present between 230 and 270 nm corresponding of the Fmoc-Fmoc interactions, but a peak at 300 nm is present, which can be attributed to the interactions between Fmoc groups and phenyl groups of the side chain.<sup>47,48</sup> As for the samples prepared in RPMI, when the HA concentration is increased, the signals decrease and the peak at 300 nm completely disappears, even at the lower HA concentration (Figure 5b).

From these results we can first conclude that in RPMI the self-assembly follows the first model and in borax the second one. Secondly, the addition of HA in the different media leads to a diminution of the chirality of the self-assembly, which is expressed by the intensity decrease of the signals. To further understand the interactions between HA and the self-assembly, which is behind this decrease in chirality, FT-IR spectra were recorded.

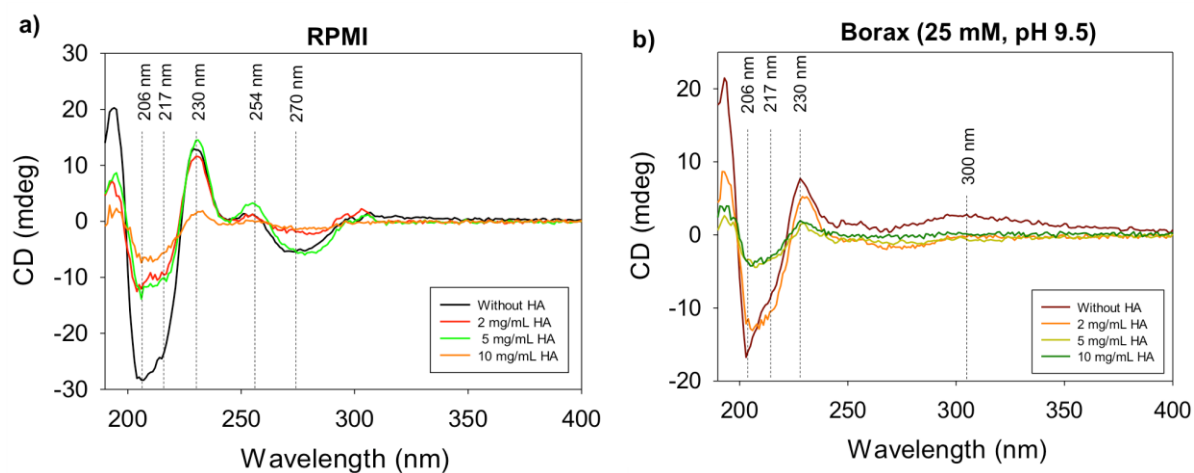


Figure 5: CD spectra of the composite hydrogels formed a) in borax and b) in RPMI

#### 6.3.4.2. Fourier Transformed Infrared

Infrared spectra, both in borax buffer and RPMI medium, shows that the peptides self-assembly form  $\beta$ -sheet conformation confirmed by the presence of a peak at  $1630\text{ cm}^{-1}$ . For borax buffer, the peptides are in anti-parallel  $\beta$ -sheet conformation, determined by the presence of a characteristic peak at  $1689\text{ cm}^{-1}$  while in RPMI medium they form parallel  $\beta$ -sheets as indicated by the absence of this peak. The peak at  $1570\text{ cm}^{-1}$  is attributed to the hydrogen bonds between -NH and -COOH groups. The FT-IR spectrum confirmed the CD results. As for CD spectra, when the HA quantity increases, a diminution of the signals is observed (Figure 6a,b). This could mean that HA interacts with peptides and prevents a strong interaction between them. This explanation is also compatible with the increase of softness of the materials observed in rheology.

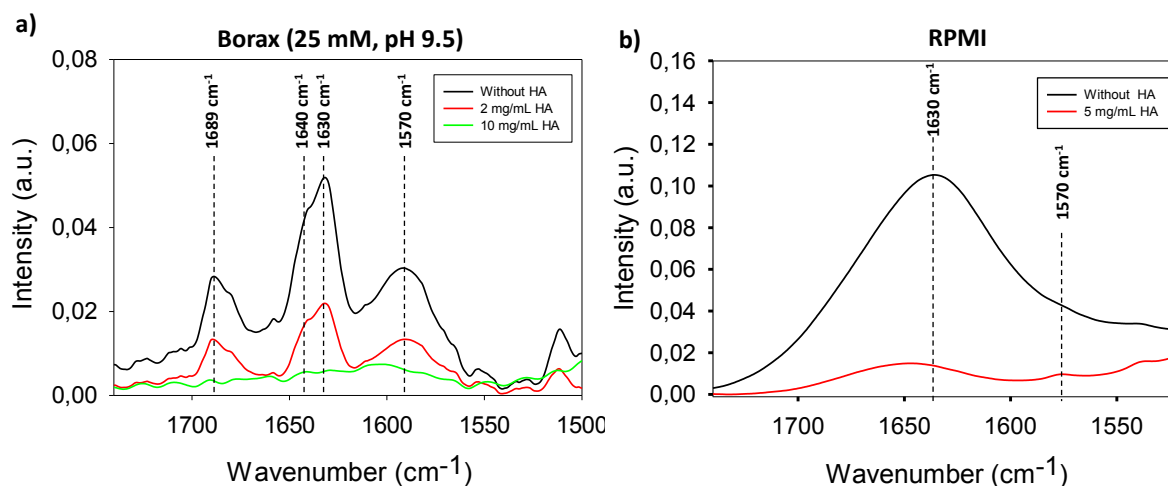
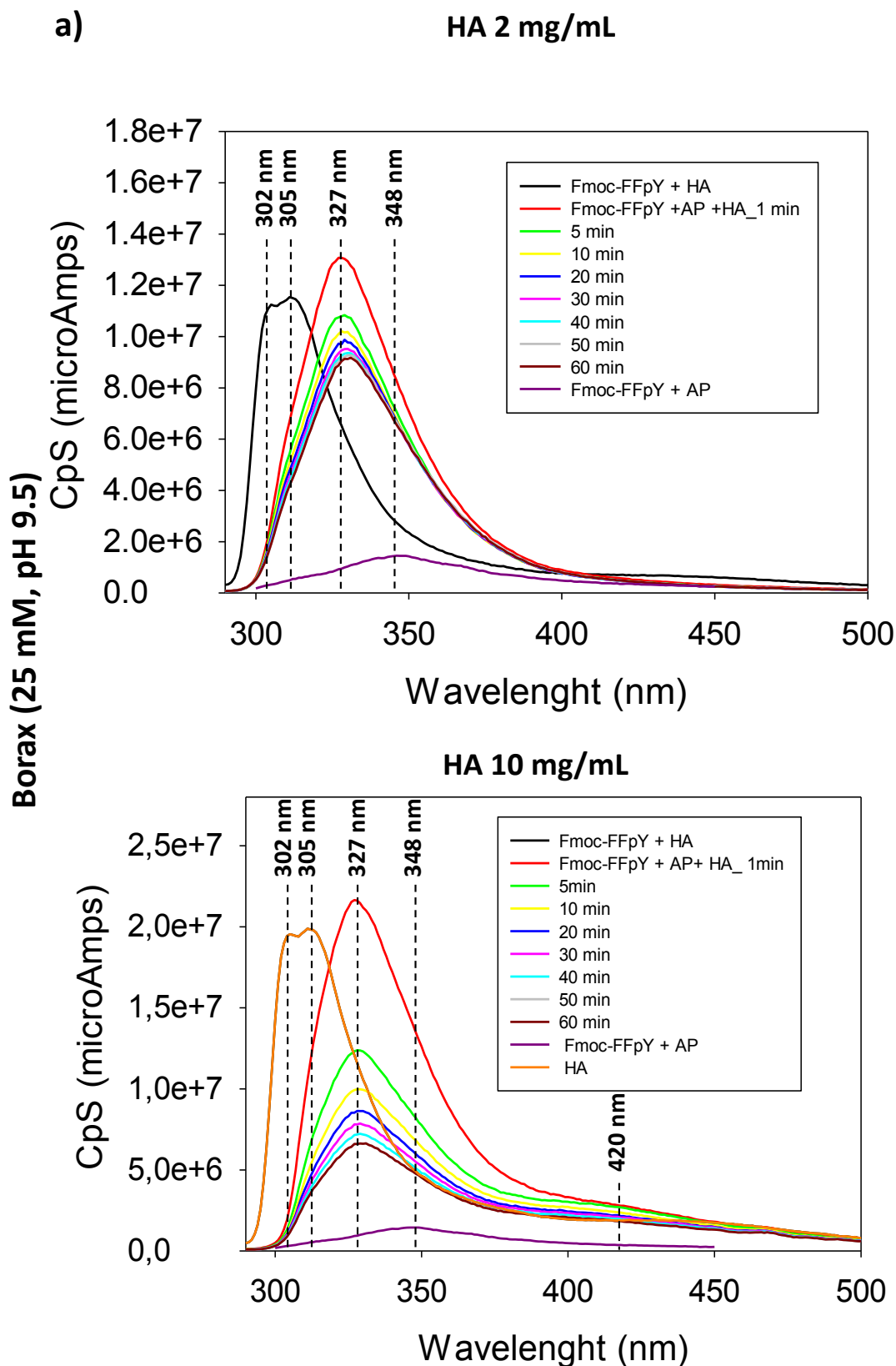


Figure 6: FT-IR spectra of composite hydrogels formed a) in borax and b) in RPMI

### 6.3.4.3. Fluorescence assays

Fluorescence assays of the signals of Fmoc-excimer is observed between the peptide self-assembly in the absence of HA and when HA is added (at 1 mg/mL or 10 mg/mL). This increase takes place over the first minutes of the interaction. Then, this signal shows a decrease of the signal intensity over time but it still remains higher than without HA (Figure 7a). A similar effect takes place with RPMI (Figure 7b). The interaction of HA with the peptide self-assembly seems to be a two steps interaction. First, HA tends to not react with the self-assembly but favors it. Our hypothesis is that HA interacts with water. This leads to an increase of the local concentration of peptides and helps the peptide to reach the critical gelation concentration. Consequently it favor the self-assembly formation. HA changes the osmotic pressure inside the solution.





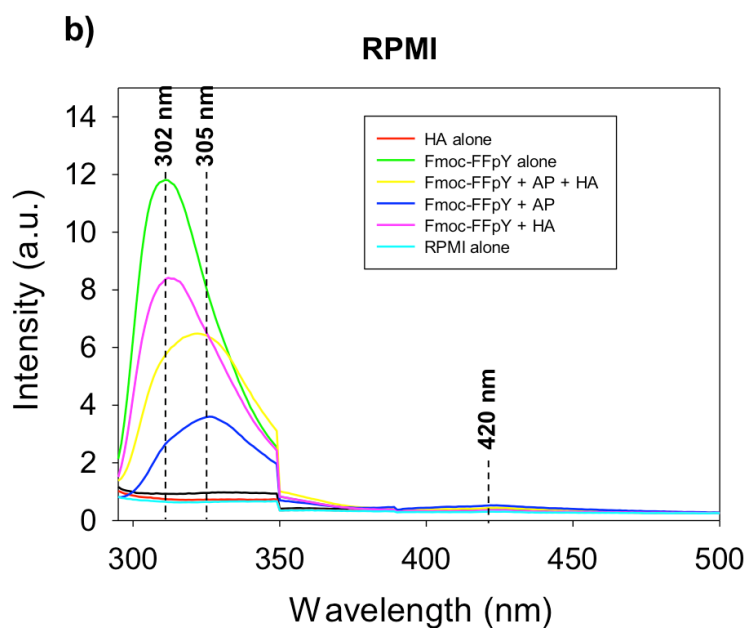


Figure 7: Fluorescence spectra of the composite formed in a) borax at 2 mg/mL (left) and 10 mg/mL HA (right); b) of the composite hydrogel formed in presence or absence of HA in RPMI and the different negative and positive controls.

To confirm this hypothesis, the same experiment was done but instead of using HA, we used a PEG solution, with the same concentration and molecular weight. PEGs are known to change the osmotic pressure of the solution by interacting with water.<sup>49</sup> Similar fluorescence spectra were obtained for PEG and HA (Figure 8). This means that HA has the ability to modify the osmotic pressure, which has a similar effect as an increase of the concentration of Fmoc-FFpY and AP in solution. This must favor the peptide self-assembly and thus the increase the fluorescence intensity of the excimer compared to that without HA or PEG. In a second step, HA starts to react with the self-assembly, inducing a decrease of the number of Fmoc-excimeres.

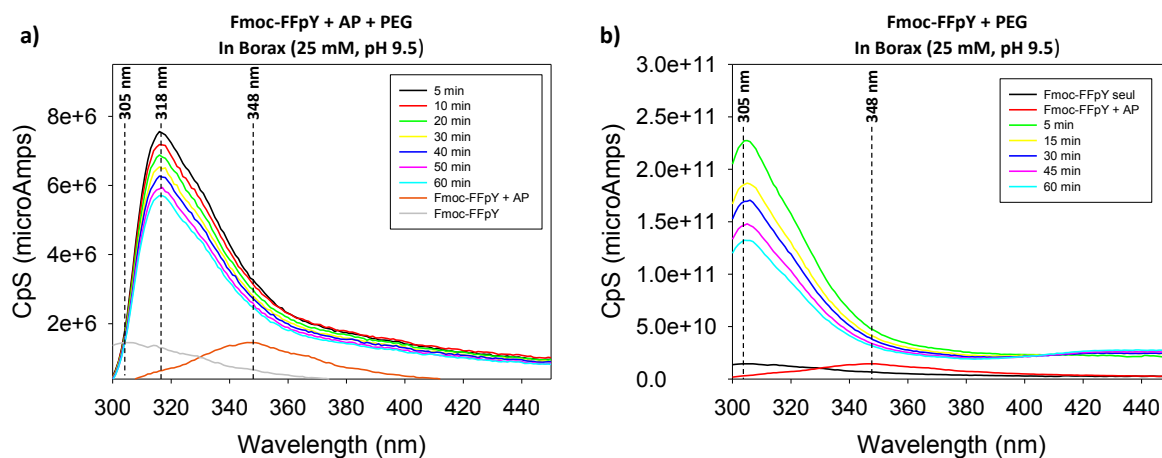


Figure 8: Evolution of the fluorescence spectra of Fmoc-FFpY in presence of PEG (which have roughly the same molecular weight than HA (450 000 Da)) over time a) with AP or b) without AP.

In Figure 9, a proposed interaction model of HA and the self-assembly is postulated. According to Mohs *et al.*, who studied the “impact of structurally modifying hyaluronic acid on CD44 interaction”, they showed that HA interacts with water, which is responsible for the change of the osmotic pressure of the solution.<sup>50</sup> HA is also known to interact through its –OH and –COOH groups by hydrogen bonding with tyrosine (present in CD44). The methyl group interacts with the hydrophobic pocket lined by a tyrosine and an isoleucine, and the carbonyl oxygen binds to a tyrosine with a water mediated hydrogen bond. What we postulate is that, as supposed by the fluorescence assays, the interaction between HA and the peptide self-assembly is done in two steps. First, HA interacts with water, which increase the local concentration and we observe the formation of the self-assembly when the enzyme remove the phosphate group. In a second time, HA starts interacting principally with tyrosine and the C-*ter* carboxylic acid present in the hydrogelator, Fmoc-FFY-COOH, *via* hydrogen bonds. The Fmoc-groups and the phenylalanine from the side chains can have hydrophobic interactions with the methyl groups present in HA in addition of the  $\pi$ - $\pi$  interactions between them.

**Step 1:** HA interacts with water leading to a modification of the osmotic pressure and coerce peptides into self-assemble after dephosphorylation by AP.

**Step 2:** HA interacts with the peptide (**a**) by hydrogen bonds (highlighted by a red circle) and hydrophobic effect involving the methyl of the HA (purple circle in **b**), which leads (**b**) to the destabilization of the peptide self-assembly. This destabilization is expressed by the decrease of the CD, FTIR and fluorescence signals. However, by the interactions between HA and peptides, the cohesion of the hydrogel and the fibrous network is kept but has a different nature.

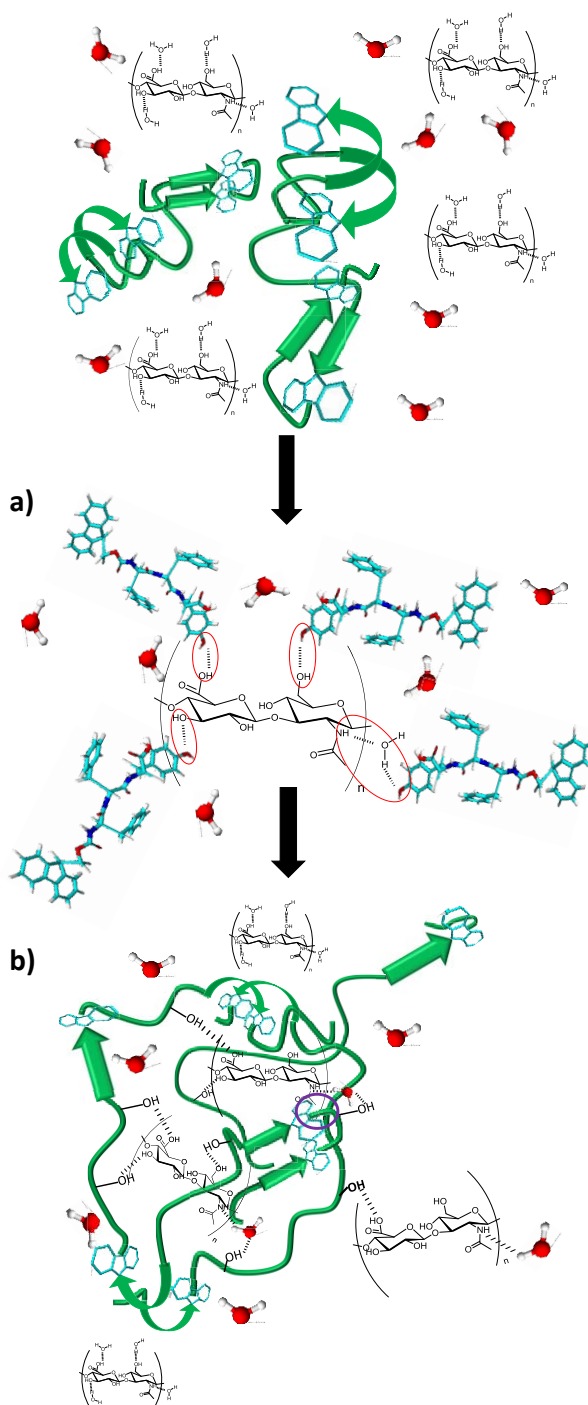


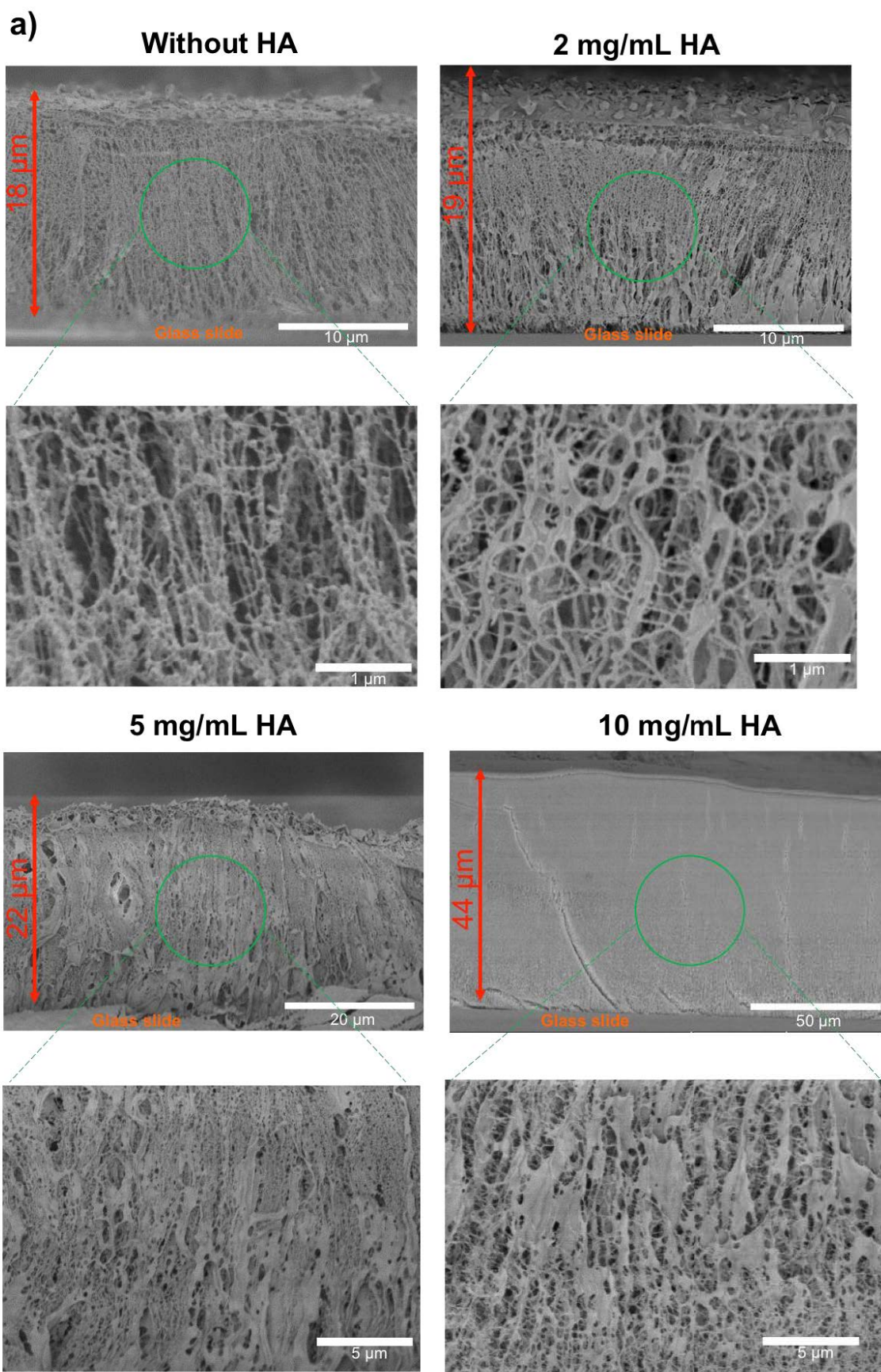
Figure 9: Schematic representation of the proposed mechanism of interaction between HA and Fmoc-FFY.

### **6.3.5. LEASA of the composite hydrogels on a surface**

The composite hydrogels were also generated from a surface to make them easier to handle. This is done by depositing the enzymes on the surface and not having them in the bulk solution. To do so, a multilayer film is build-up on the surface by electrostatic interaction. The selected multilayer film is PEI/(PSS/PAH)<sub>2</sub>. This multilayer then allow us to adsorb an enzyme, alkaline phosphatase, onto the surface, which is now enzymatically-active. As shown with the rheological measurements, our composite hydrogels are very soft, which make them difficult to handle without breaking them. By generating them from a surface, it renders them easier to use by biologists for cell culture. To follow the generation of the composite self-assemblies from a surface we first tried to monitor them by using quartz crystal microbalance coupled to dissipation (QCM-D) and FT-IR on ZnSe surfaces. We were able to observe the formation of the multilayer film, the enzyme deposition and the self-assemblies but when the amount of HA increased, we reached rapidly the limits of the two techniques due to the too large thickness of the generated film (the two techniques are based on the sensing of the substrates by waves whose amplitude decreases exponentially with the distance from the substrate). To observe the formation of the composite self-assembly from the surface, two different techniques were used, the *cryo*-SEM and CLSM microscopy to characterize the hydrogels generated from the surface. For all the following experiments, hydrogels are generated from a surface using the enzymatically-active surface modified by the following build-up: PEI/(PSS/PAH)<sub>2</sub>/AP.

#### **6.3.5.1. Morphology of the composite self-assembly generated from a surface by *cryo*-SEM**

*Cryo*-SEM experiments are done in the Z-section. For the experiments performed in borax buffer, in the absence of HA, we observe the presence of a pearl necklace shape of the fibers, with an orientation of the fibers from the surface to the bulk and a thickness of the film of around 18  $\mu\text{m}$  (Figure 10a). Then, when the HA concentration is increased; the pearl necklace aspect is smoothed and leads to a veiled shape of the fibers and the thickness of the film increases from 18  $\mu\text{m}$  to 44  $\mu\text{m}$  (Figure 10a). When the self-assemblies are generated in RPMI, or after 1h hour exchange in RPMI, the same fibers morphology and thicknesses are observed (Figure 10b,c).



←—————→  
Borax (25 mM, pH 9.5)

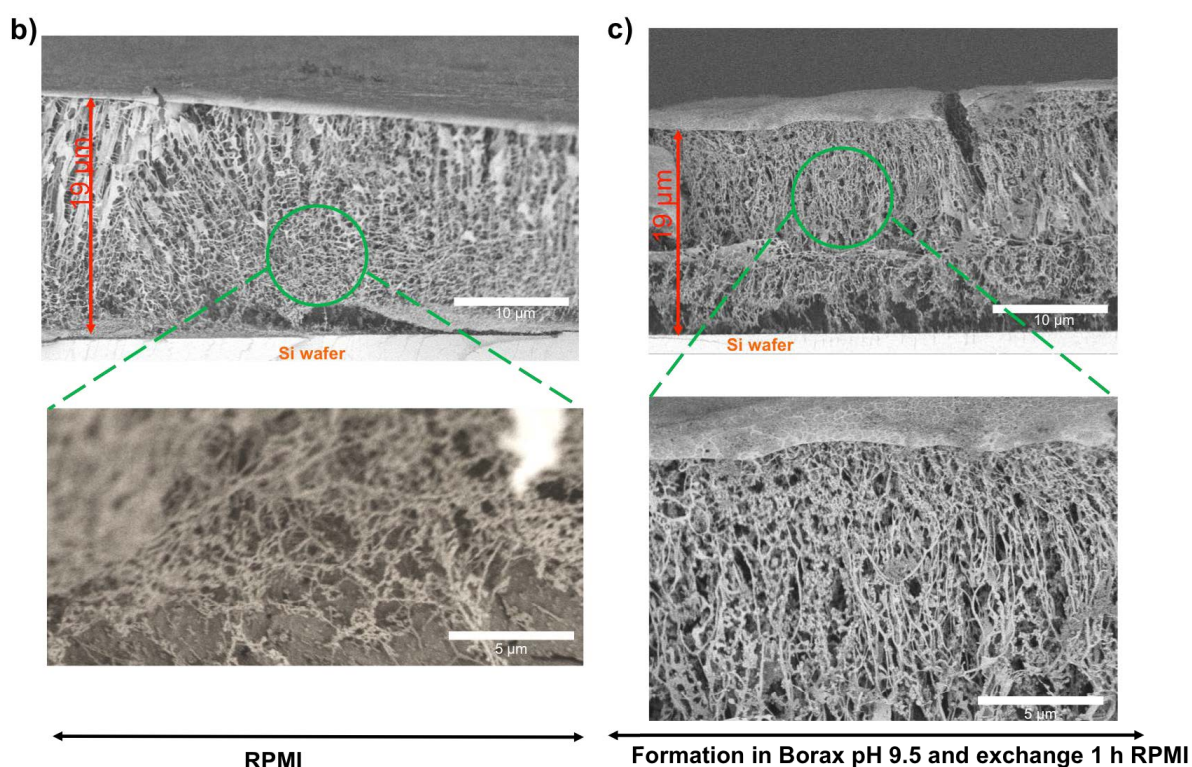


Figure 10: Cryo-SEM pictures of the composite hydrogel formed from a surface a) in borax at different concentrations of HA, b) in RPMI without HA and c) in borax and then exchanged 1h in RPMI, without HA.

### 6.3.5.2. Confocal images of the composite self-assemblies generated from surface

Experiments performed in CLSM gave similar results as the one performed in cryo-SEM. When a solution of HA containing Thioflavine T is brought in contact with the enzymatically-active surface no self-assembly is observed (Figure 11a). In the same way, when a solution of the peptide containing Thioflavine T is brought in contact with a HA layer electrostatically adsorb on the multilayer film without alkaline phosphatase, no fibers are observed (Figure 11a). However, when a solution of Fmoc-FFpY in presence (or in absence) of HA, also containing Thioflavine T, is brought in contact with the enzymatically-active multilayer film, fibers are observed and their diameter are roughly the same, for elementary as well as composed fibers, and are about 5 nm and 15 nm respectively in both RPMI and borax buffer pH 9.5 (Figure 11b,c). This results are similar than the one obtained for the experiments performed in solution with CLSM and TEM (part 6.3.3). We can then conclude that the composite self-assemblies act in the same way in solution and from a surface.

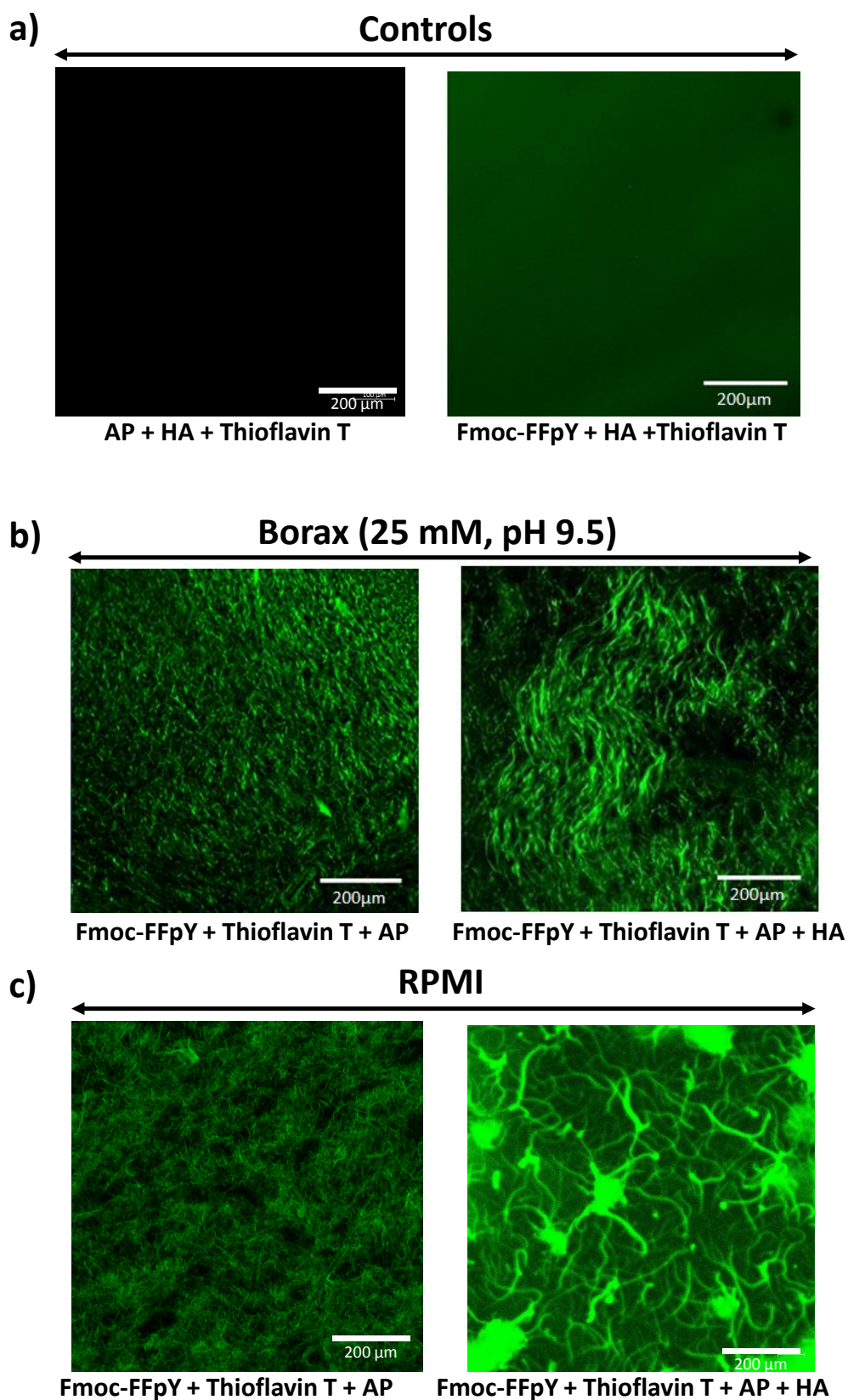


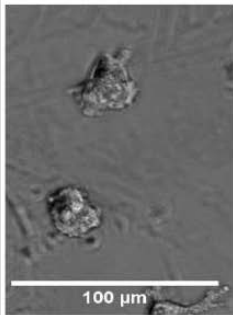
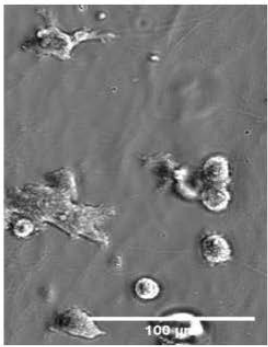
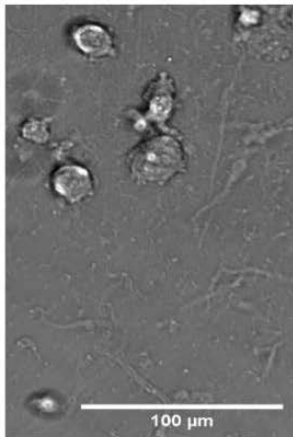
Figure 11: confocal images of a) the negative controls of the multilayer film containing AP and a solution of HA and Thioflavin T deposited on it (left) and a multilayer film without AP, where a solution of Fmoc-FFpY, HA and Thioflavin T was put in contact with it (right). b) Composite hydrogel formed from a glass substrate in absence of HA (left) and in presence of HA (right) b) in Borax buffer (25 mM, pH 9.5) and c) in RPMI.

Now that we demonstrated that it is possible to generate our composite self-assemblies from a surface in different media, we performed cell culture on the composite self-assemblies formed in borax (25 mM, pH 9.5), in RPMI and in borax exchanged during 1h with RPMI, to verify the suitability of the composite hydrogels for biological applications.

### 6.3.6. Cell culture with NIH 3T3 Fibroblasts

NIH 3T3 fibroblasts were used for the viability assays. Fibroblasts (in RPMI + 10% FBS) were let in contact of the composite hydrogels for 4 hours at 37 °C. Then, a Life/dead test was performed to determine the viability of the hydrogels. NIH 3T3 fibroblast cells showed high viability (Figure 12), with a preference for hydrogels containing less amount of HA and formed or exchanged in RPMI medium. As already discussed, borax at pH 9.5 is not the best buffer to performed cell culture and as reported by the rheological measurements, hydrogels are softer when HA concentration increases and when formed in borax. Indeed, NIH 3T3 fibroblast cells are known to prefer hard substrates, which is in agreement with the presented results. Nevertheless, the overall viability for all the experiments is good compared to the positive control done on a naked glass substrate (Figure 12b).

a)

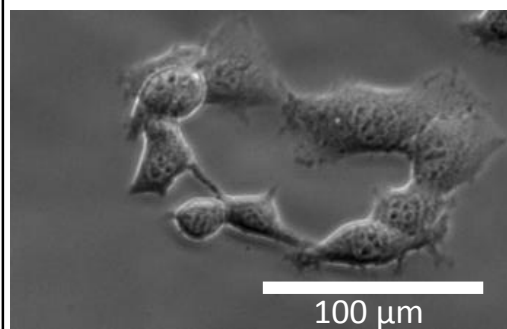
<b>Borax (25 mM, pH 9.5)</b>			
	<b>Without HA</b>	<b>5 mg/mL HA</b>	<b>10 mg/mL HA</b>
Cell viability (%)	93,9(+/- 3) %	95,6 (+/- 3,3) %	81,66 (+/- 11,7) %
Cell adhesion depending on the support			



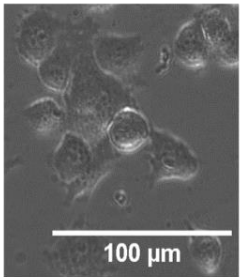
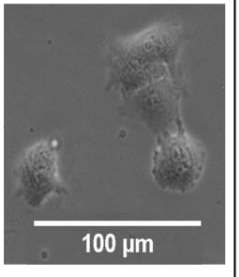
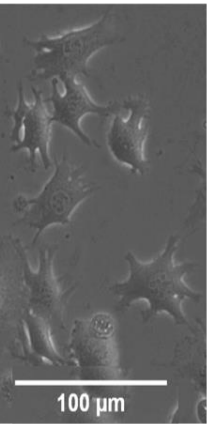
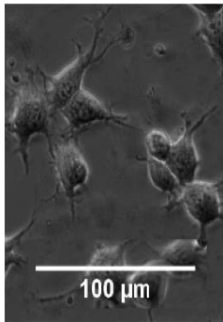
b)

**Positif control : glass slide**

Cell viability : 96,8 (+/- 1,8) %



c)

RPMI				
	Without HA	2 mg/mL HA	5 mg/mL HA	10 mg/mL HA
Cell viability (%)	95,6 (+/- 3)	96,9 (+/- 1,7)	96,8 (+/- 1,9)	88,4 (+/- 2,6)
Cell adhesion depending of the support				

d)

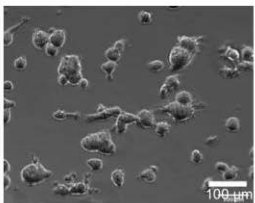
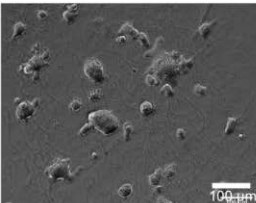
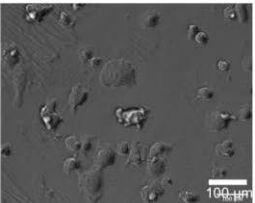
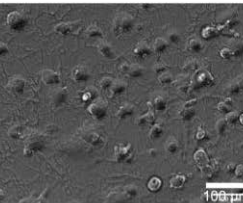
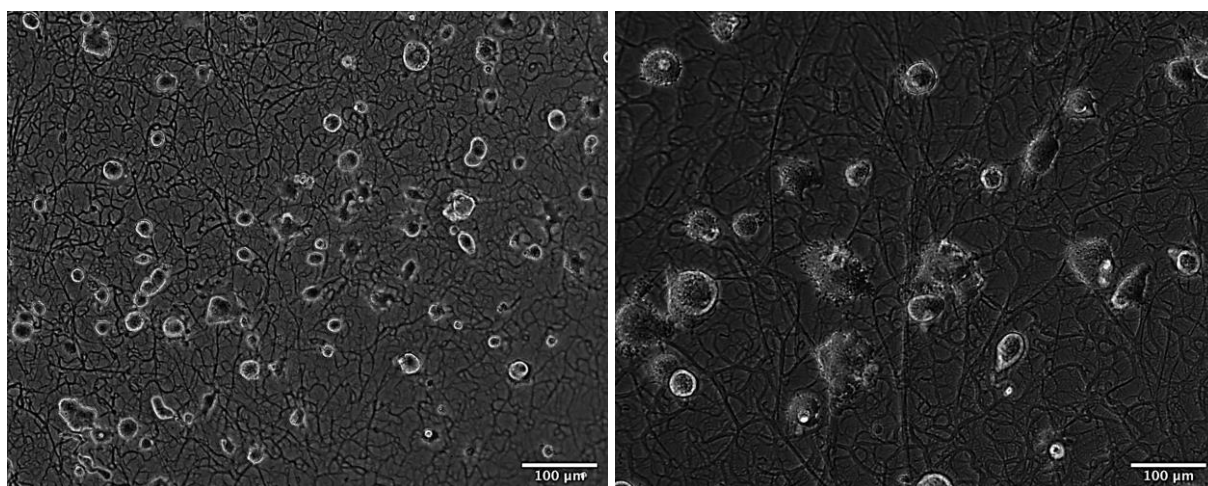
Formation of the support in Borax and exchange 1h with RPMI				
	Without HA	2 mg/mL HA	5 mg/mL HA	10 mg/mL HA
Cell viability (%)	91,4 % (+/- 3)	85,2 % (+/- 5)	75% (+/- 8)	77,7 % (+/- 7)
Cell adhesion depending of the support				

Figure 12: Cell adhesion for the NIH 3T3 fibroblast and cell viability determined for different concentrations of HA a) in borax, b) positive control on glass slide c) in RPMI and d) in borax exchanged 1h with RPMI.

A second observation that can be made is that the cell adhesion changes depending on the HA amounts and in which media the hydrogel is formed (Figure 12). When cells prefer a substrate we can observe that they spread and form long thin arms (Figure 12c for 0-5 mg/mL HA in RPMI), compared to when they do not like the support. In that case they stayed round as observed in borax (Figure 12a).

These results are encouraging for the possibility to differentiate stem cell by using this kind of versatile cell culture support. The medium used is, in that case, of the utmost importance.

A last observation was done with the cells assays. When the HA concentration increases up to 10 mg/mL, is possible to observe by optical microscopy the fibrous network composing the composite hydrogel (Figure 13). This confirmed also that HA induces the formation of bigger fibers by combining elementary fibers one with each other. Nevertheless, more cells assays will be needed to determine if cells preferentially adhere on areas where the fibers are present.



*Figure 13: Optical microscopy images of cells assays on a composite hydrogel generated from a surface with 10 mg/mL of HA. The fibrous network of the hydrogel is clearly visible under the fibroblasts.*

## 6.4. Conclusion

In this final chapter, the study aimed at designing new composite hydrogels by combining a peptide self-assembly with the favorable biological properties of the natural HA to obtain a range of morphological properties suitable for biologists to be used as cell culture substrate and to understand the interactions between the different components. As the HA ratio in the composite hydrogels increases, the hardness of the resulting materials decreases and the NIH 3T3 fibroblast cell viability decreases too. With CD, FT-IR, Fluorescence, confocal and SEM microscopy we demonstrated that the HA interacts with the peptide self-assembly at the molecular level even if both molecules are negatively charged. We figured out also that the medium, in which the composite hydrogels are formed, is of utmost importance for their properties. This statement seems obvious but in most of the publications, hydrogels are formed in one buffer and then cell culture is done with another medium above it. Yet, the undertaking exchange of the media performed during the cell culture is not mentioned even if, as we show, it represents a critical point because it influences properties such as the mechanical properties of the hydrogel. Due to the possibility to finely tune many parameters, and due to the wide-range applications in biomedicine and biotechnology, we believe our contribution can find an echo in various communities of chemists and biologist going from material science to bioengineering.

### Highlights of the chapter

- ✓ It is possible to obtain a wide range of mechanical properties from one composite hydrogel containing only three different molecules.
- ✓ The buffer or media, in which a hydrogel is formed, have an utmost importance for cell culture but also for the mechanical properties of the resulting composite hydrogels.
- ✓ Hyaluronic acid and Fmoc-FFY, two negatively charged molecules, can interact *via* hydrogen bonds and hydrophobic interactions to generate a composite hydrogel with versatile mechanical properties.
- ✓ Composite hydrogels containing a peptide self-assembly and hyaluronic acid are viable for cell culture if formed in a compatible media for cells.

## 6.5. Experimental section

### 6.5.1. Materials

All chemicals used in this work are gathered in the following table. All reagents and solvents were purchased at the top commercial quality and used without further purification.

Name, acronym (abbreviation)	MW (g.mol <sup>-1</sup> )	Supplier	CAS number
Bovine serum albumin (BSA)	66 000	Sigma-Aldrich	9048-46-8
Poly(ethylene imine) (PEI)	750 000	Alfa Aesar	9002-98-6
Poly(allylamine) hydrochloride (PAH)	15 000	Sigma Aldrich	71-550-12
Poly(styrene sulfonate) (PSS)	70 000	Sigma Aldrich	25704-18-1
Deuterated Water (D <sub>2</sub> O)	20.03	Sigma Aldrich	7789-20-0
Dimethylformamide (DMF)	73.09	Acros Organics	68-12-2
Dichloromethane (DCM)	84.93	Acros Organics	75-09-2
Trifluoroacetic acid (TFA)	114.02	Alfa Aesar	76-05-1
Deuterated DMSO (DMSO-d <sub>6</sub> )	84.17	SDS	2206-27-1
N-Ethyl-diisopropylamine (DIEA)	129.25	Alfa Aesar	7087-68-5
Alkaline Phosphatase from bovine intestinal mucosa (ALP)	170 000	Sigma Aldrich	9001-78-9
Fmoc-L-phenylalanine (Fmoc-F-OH)	387.43	Iris biotech	35661-40-6
Fmoc-L-Tyrosine Phosphate (Fmoc-Y(PO <sub>3</sub> H <sub>2</sub> )-OH)	483.41	Bachem	147762-53-6
Triisopropylsilane (TIPS)	158.36	Sigma Aldrich	6485-79-6
Resin 2-chlorotrityl chloride (2-CTC)	-	Sigma Aldrich	42074-68-0
1-Hydroxybenzotriazole hydrate (HOBt)	135.12	Sigma Aldrich	123333-53-9
N,N,N',N'-Tetramethyl-o-(1H-benzotriazol-1-yl)uranium hexafluorophosphate (HBTU)	379.24	Alfa Aesar	94790-37-1
Diethyl ether	74.12	Acros Organics	60-29-7
Hyaluronic acid	472 000 IP = 1,55	Primalhyal 400 So-Prim 400	9004-61-9
Sodium tetraborate, 98%, anhydrous (borax Buffer)	201.22	Acros Organics	1330-43-4
Phosphate buffered saline (PBS buffer)	94.97	Sigma Aldrich	-
Roswell Park Memorial Institute medium (RPMI)	-	Dutscher	12633012

Dulbecco's Modified Eagles Medium (DMEM) (high glucose)	-	Dutscher	Cat: L0103-500
Gelose Mueller-Hinton (MH)	-	Durscher	993881
Foetal bovin serum (FBS)	-	Dutscher	S1810
Polyethylene glycol (PEG)	430,000-480,000	Seebio Biotech	25322-68-3

### 6.5.2. Synthesis and characterization of Fmoc-FFpY

All peptides were prepared using solid support chemistry. The "Fmoc strategy" was used based on 2-CTC resin.<sup>51</sup> The following synthetic pathway is given in the scheme below.

#### General procedure:

**Step a:** loading of the resin. Addition of 3 eq/r of Fmoc-Tyr(OPO<sub>3</sub><sup>2-</sup>)-OH + 6 eq/r of DIEA in 3 mL of DMF for 300 mg of resin. The solution in contact with the resin is stirred at RT for 2 h. Then, the solution is removed and a solution of MeOH is added at RT for 1 h.

**Step b:** Fmoc group deprotection: 3 mL of a 20% of piperidine in DMF solution is added and stirred at RT for 15 min.

**Step c:** Coupling step: 3eq/r of Fmoc-amino acid + 3 eq/r of HOBt + 3 eq/r of HBTU + 6 eq/r of DIEA are added in 3 mL of DMF and let in contact with the resin at RT for 30 min.

**Step d:** Cleavage of the resin and lateral chains deprotection: addition of 3 mL of a solution containing 95% TFA + 2.5 % H<sub>2</sub>O + 2.5 % triisopropylsilane it's stirred at RT for 2 h. Then the solution is filter. The solvent is then removed. Finally the product is precipitate by using a small amount of cold ether.

Between each step **a**, **b**, **c** and **d**, a rinsing stage is executed by using 5 times 3 mL of DMF and then a Kaiser test is made to confirm the achievement of the coupling or deprotection steps.

Protocol Kaiser Test (Ninhydrin Test): one drop of solution A, B and C is added in a test tube containing 10 beads of the resin. The test tube is heated at 100 °C.

#### Solution A:

- Dissolve 16.5 mg of KCN in 25 mL of distilled water.
- Dilute 1.0 mL of above solution with 49 mL of pyridine.
- Pour it into a small reagent bottle and label it "A"

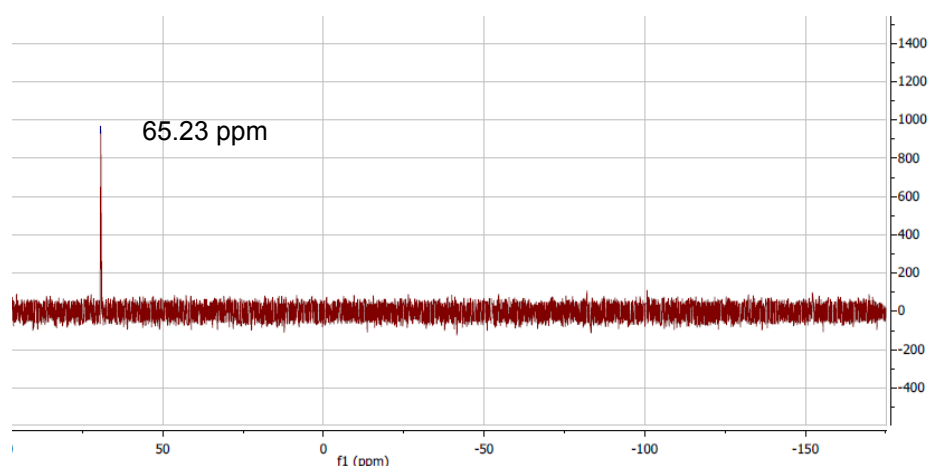
#### Solution B:

- Dissolve 1.0 g of ninhydrin in 20 mL of n-butanol.
- Pour into a small reagent bottle and label it as "B".

#### Solution C:

- Dissolve 40 g of phenol in 20 mL of n-butanol.
- Pour it into a small reagent bottle and label it "C".



**<sup>31</sup>P NMR spectrum****6.5.3. Multilayer film preparation and hydrogel self-assembly**

All polyelectrolytes, enzymes and proteins were prepared in buffer solution or in cell medium.

Buffer solution preparation:

- **Borax buffer (25 mM, pH 9.5):** 1 g of sodium tetraborate anhydrous is added in 200 mL of ultrapure water (Milli-Q Plus system, Millipore, Billerica, MA). The pH is adjusted drop by drop by using a solution of HCl 0.1 M or a solution of NaOH 0.05 M.
- **PBS buffer (pH 7.4):** 1 tablet is added in 200 mL of ultrapure water (Milli-Q Plus system, Millipore, Billerica, MA). The pH is adjusted drop by drop by using a solution of HCl 0.1 M or a solution of NaOH 0.05 M.
- **Cell culture medium:** RPMI, DMEM and MH are solution commercially available, which are used without further steps.
  - RPMI composition (with or without 10% FBS) pH 7.4<sup>53</sup>: Medium for cell culture containing L-glutamine, phenol red, 25 mM HEPES, sodium bicarbonate (2 g/L), L-cystine and L-methionine.
  - DMEM composition (with or without 10% FBS) pH 7.4<sup>54</sup>: Variation of EMEM (Eagles minimal essential medium), is a culture medium rich in nutrients necessary for the maintenance and proliferation of different types of cells. It contains nearly 4 times more amino acids, vitamins and 2 to 4 times more glucose than in EMEM as well as salts and iron. Good medium for longer cell cultures (from 8 h). The one used contain: L-glutamine, sodium pyruvate, phenol red, HEPES (25 mM), sodium bicarbonate (3.7 g/L) and glucose (4.5 g/L).
  - MH composition pH 7.4<sup>55</sup>: In gel form usually, this medium is specific for microbial culture. It consists mainly of infusion of beef, casein peptone, cornstarch and agar. Thus it is often used to perform the standard antibiogram, and test the action of antibiotics on bacteria. The one used for the study contain: peptone (17.5 g/L), beef infusion (2 g/L), amidon (1.5 g/L) and agar (17 g/L).

- FBS composition<sup>52</sup>: Blood liquid, without cell or protein of coagulation, directly from the fetuses of cow. It consists essentially of water, dissolved substances such as proteins (ex: BSA) and various ions (Na<sup>+</sup>, Cl<sup>-</sup>, etc.). This serum is widely used for its protein-rich composition that allows for a suitable environment where cells can grow (detailed composition in Annexe 1).

Different surfaces were used depending on the characterization techniques investigated: Gold coated quartz crystal for QCM-D and AFM experiments, ZnSe crystal for ATR-FTIR experiments and glass slide for Cryo-SEM, SEM, confocal, epifluorescence microscope, SAFAS and biological assays. After the deposition of a PEI (1 mg/mL) precursor layer on the chosen surface by dipping, the multilayer film was performed by alternately exposing the surface to PSS (1 mg/mL) and PAH (1 mg/mL) solutions for 10 min with an intermediate rinsing step with borax buffer. The polyelectrolyte multilayer is always prepared in borax buffer. Then, the AP (1 mg/mL), is adsorbed for 20 min followed by 5 min of rinsing step with borax or RPMI medium. Finally, the solution of Fmoc-FFpY with or without HA is added for 24 h in borax buffer or RPMI medium.

All the solutions (comprising buffer solutions) are always freshly prepared before any experimentation.

#### **6.5.4. Upside-down hydrogel test in Bulk**

All tests were performed in HPLC vial (with a capacity of 1.5 mL).

Four different solutions were usually prepared for preparing the samples. One solution with the enzyme at 3 mg/mL, one solution with Fmoc-FFpY at 15 mg/mL, one solution with three times the desired concentration of HA and finally in case of a sample without HA a solution with only the buffer or cell culture medium. Then, three solutions are mixed by mixing 50  $\mu$ L of each to obtain the desired ratio between all the molecules. For each mixture, all the solutions used to prepare it were freshly prepared in the same buffer or medium.

#### **6.5.5. Quartz crystal microbalance with dissipation monitoring**

QCM-D experiments were performed on a Q-Sense E1 apparatus (Q-Sense AB, Göteborg, Sweden) by monitoring the resonance frequencies of gold coated crystals, as well as the dissipation factors at four frequencies: the fundamental frequency at 5 MHz ( $\nu = 1$ ) and the 3<sup>rd</sup>, 5<sup>th</sup>, and 7<sup>th</sup> harmonics ( $\nu = 3, 5$  and  $7$  at 15, 25, and 35 MHz respectively). The QCM-D results give information on the adsorption process, as well as on viscoelastic properties of the adsorbed film<sup>14</sup>. The Software *QTools*® was used to determine the film thicknesses of multilayer films using the Sauerbrey equation (valid for rigid films)<sup>56</sup> and of the peptide self-assembly using the Vogt-Voinova model (valid for viscoelastic films).<sup>57</sup>

For a thin and rigid film, the mass can be obtained by using the Sauerbrey's equation<sup>56</sup>:

$$\Delta m = -C\Delta f/u$$



where  $C$  is the mass sensitivity constant ( $17.7 \text{ ng}\cdot\text{cm}^{-2}\cdot\text{Hz}^{-1}$  at 5 MHz), and  $\nu$  is the overtone number. The Sauerbrey equation applied when  $\Delta f/\nu$  is independent of  $\nu$ . We verified that this was the case in our experiments. As we assumed that the density of the film is close to  $1 \text{ g}\cdot\text{cm}^{-3}$ , we can infer the evolution of the film thickness, during the buildup. Thickness is determined thanks to the previous equation:

$$d = -C\Delta f/100 \times \nu$$

where  $d$  is the thickness in nm.

### 6.5.6. Atomic force microscopy

Atomic force microscopy (AFM) was carried out with a BioScope Catalyst (Bruker corp., Santa Barbara, CA, USA). Micrographs from different interaction stages of Fmoc-AA-OH with the enzymatic film were recorded in contact mode by using silicon tips mounted on nitride levers. All samples were observed in dry state with triangular cantilevers having a spring constant of  $0.4 \text{ N/m}$  and a nominal tip radius of  $2 \text{ nm}$ . Selected AFM images were treated with the nanoscope analysis software (Bruker corp., Santa Barbara, CA, USA). All samples analyzed in AFM were prepared on gold-coated quartz crystal. They were air dried before analysis.

### 6.5.7. Infrared spectroscopy

The Fourier Transform Infrared (FTIR) experiments were performed on a Vertex 70 spectrometer (Bruker, Germany) using DTGS detector. Spectrum were recorded in the Attenuated Total Reflection (ATR) mode using a  $45^\circ$  trapezoidal ZnSe (internal reflection element) crystal (6 reflections, dimensions  $72 \times 10 \times 6 \text{ mm}^3$ ) in ATR cell (GRASEBY-SPECAC, England). Reference (bare ZnSe crystal in contact with ultrapure water) and sample spectra were taken by collecting 128 interferograms between  $800$  and  $4000 \text{ cm}^{-1}$  at  $2 \text{ cm}^{-1}$  resolution, using Blackman-Harris three-term apodization and the standard Bruker OPUS/IR software (version 7.5). Multilayer films were assembled on ZnSe crystal by the dipping method as described above. PEI, PSS, PAH, AP, Fmoc-FFpY With (or without) HA solutions were prepared as described previously but in deuterated water to avoid the water signal in the amide I region. For the samples with the higher concentration of HA (from  $2 \text{ mg/mL}$  to  $10 \text{ mg/mL}$ ), the measurement were performed on the ATR-diamond in solution.

### 6.5.8. Scanning electron microscopy and cryo-SEM

To observe cross-sectioned gels, a specific cryo-holder was designed and manufactured by the mechanical facility of the Charles Sadron Institute. The glass slide, covered by enzymatic precursor film and the self-assembled gel, was inserted vertically in the jaws of the vise. The holder with the sample is then rapidly plunged into nitrogen slush in the cryo preparation chamber of the Quorum PT 3010 machine. As the sample is free standing over the holder, during the plunging, the sample is rapidly frozen by direct contact with the nitrogen slush. The sample is then transferred under vacuum into the chamber attached to the microscope and fractured with a razor blade.

A slight etching at  $-80^{\circ}\text{C}$  is performed to render the fibers more visible followed by the deposition of a thin Pt layer (metallization step). The sample is then transferred in the FEG-cryoSEM (Hitachi SU8010) and observed at 1kV at  $-170^{\circ}\text{C}$ .

#### **For the cryo-SEM experiments:**

The first set of samples was prepared fully in borax buffer (25 mM, pH 9.5). For the sample called exchanged sample, after preparing all the multilayer + the hydrogel inside borax buffer, the sample is put in contact with 500  $\mu\text{L}$  of RPMI medium for 1h to permit the diffusion of the RPMI medium inside the self-assembly and polyelectrolyte multilayer to observe if there is any changes in the morphology of the self-assembly after performing a modification of the buffer and so in conclusion of the environment of the self-assembly.

The last sample observed in Cryo-SEM is a sample, where the polyelectrolyte multilayer was prepared in borax buffer but from the AP layer till the self-assembly formation is performed in RPMI medium.

**For the SEM experiments:** All the samples were fully prepared in borax buffer.

### **6.5.9. Transmission Electronic Microscopy**

The TEM images were performed with sample prepared in liquid state X 50 or x 500 times diluted in ratio with the gelation conditions in solution. To make the observations 20  $\mu\text{L}$  of the sample is dropped off on a shelf. Then, the sample is observed by a TEM Technai G2 machine in negative coloration. To make the observations, 5 microliters of the different hydrogels are deposited onto a freshly glow discharged carbon-covered grid (400 mesh). The hydrogel is left for 2 minutes and the grid is negatively stained with 5 microliters uranyl acetate (2% in water) for another minute and finally dried using a filter paper. The grids were observed at 200kV with a Tecnai G2 (FEI) microscope. Images were acquired with a camera Eagle 2k (FEI) ssCD camera.

### **6.5.10. Fluorescence emission spectroscopy**

Two different apparatus were used to perform them:

#### **a) The microplate reader UV spectroscopy for samples on surface**

Microplate reader UV spectroscopy (FLX-Xenius®, SAFAS, Monaco) using SP2000V7 software. To follow the  $\pi$ -stacking of the Fmoc group, when the self-assembly is initiated from the surface, we excite our molecule at 280 nm and take our spectrum in the range 300-600 nm. The sample preparation followed the description above in part 6.5.3.

#### **b) The fluorimeter for samples in solution**

The fluorimeter Fluoromax-4 (Horiba jobin Yvon-Edison, NJ USA) using FluorEssence software was the main device entailed in the fluorescence measurement of the  $\pi$ -stacking. For performing the measurement, samples were prepared in quartz cuvette of 1 mm length path.

The fluorescence assays were done for self-assembly in solution in diluted concentration regarding the gelation concentration in solution: Fmoc-FFpY (1 mg/mL), AP (1 mg/mL) and HA (0, 1, 2, 5, 10 mg/mL). Spectra were recorded in the 300-600 nm range with an excitation at 280 nm.

### 6.5.11. Circular Dichroism

Circular dichroism (CD) spectra were recorded using a Jasco J-1100 spectropolarimeter with a data pitch of 1 nm on the light wavelength in the 190-600 nm range. CD spectra show the ellipticity expressed as an angle as a function of the wavelength.

**Samples preparation:** in a mold of 1 cm in diameter is introduced 170  $\mu$ L of Fmoc-FFpY (1 mg) + HA (0, 2, 5 or 10 mg/mL) + 30  $\mu$ L of AP solution at 6 mg/mL. the mixture is homogenized with the tip of a pipette. The solution is let 24h to obtain a gel. Samples were prepared in borax buffer, RPMI medium or borax buffer and then 1h in contact with RPMI medium. Finally, the hydrogel is dropped off between two quartz cover slip with a thickness of 2 mm each. To do the baseline, the two cover slips were put in contact with each other without any solution or sample between them.

Solutions inside the apparatus were maintained at 25°C using a Peltier apparatus with an accuracy of  $\pm 0.2$  °C.

### 6.5.12. Rheology

Rheological properties were measured in a Kinexus Malvern rheometer using plate geometry of 1 mm diameter and a gap of 0.5 mm. Firstly, 380  $\mu$ L of Fmoc-FFpY (7 mg/mL) were mixed with 20  $\mu$ L (6 mg/mL) of AP inside a mold of 1 mm of diameter. The solution is homogenized and the analysis of the hydrogel is done after 24h. To obtain the rheological properties of our samples, strain measurements were carried out from 0.01% to 100% at 0.3Hz and frequency sweeps were performed from 0.01 Hz to 10 Hz at a fixed strain of 0.06%.

Samples were prepared fully in borax buffer, fully in RPMI medium or in borax buffer and then let in contact 1h with RPMI medium.

### 6.5.13. $^1\text{H}$ and $^{31}\text{P}$ NMR

$^1\text{H}$  and  $^{31}\text{P}$  NMR spectra were recorded on a Bruker Avance 400 spectrometer at 400 MHz and 161.92 MHz respectively in the specified solvent at 25°C. The spectra were internally referenced to the residual solvent signal. The chemical shifts are given in ppm and coupling constants J are listed in Hz. The following notation is used for the  $^1\text{H}$ -NMR spectral: singlet (s), doublet (d), triplet (t), multiplet (m).  $^1\text{H}$  and  $^{31}\text{P}$  NMR is used to characterize peptide synthesis

### 6.5.14. Epifluorescence microscopy and confocal laser scanning microscopy

Confocal laser scanning microscopy is an optical technique, which aims at overcoming limitations of traditional wide-field fluorescence microscopes by eliminating out-of-focus light thanks to a spatial pinhole placed at the confocal plane of its objective lens. It is a powerful tool for generating high-resolution images and 3D reconstructions of a studied sample and is thus widely used in biology and materials science.

#### Principle

In traditional fluorescence microscopy, the sample is uniformly illuminated by light by means of a light source (mercury lamp, laser), which emits radiations filtered by an emission filter and reflected toward the sample by a dichroic mirror (figure 14a). The fluorescence emitted from the sample passes then back through this mirror and through an emission filter before being detected. As the plane of focus is not the only plane to be illuminated, an out-of-focus blur appears and damages image contrast and resolution.

In contrast, in confocal microscopy, patented by Minsky in 1988 (US3013467), a laser beam is focused onto a point on the sample through the objective lens (Figure 14b). The light emitted by the fluorescent sample passes through a dichroic mirror and then through a confocal aperture called pinhole, which does not permit rays of light from out-of-focus points to pass through it. The focused light is next filtered by an emission filter and transmitted to a photomultiplier aimed at amplifying the signal before detection. To obtain a full image, the sample is scanned point per point in a defined bi-dimensional area (XY slice) by means of scanning mirrors.

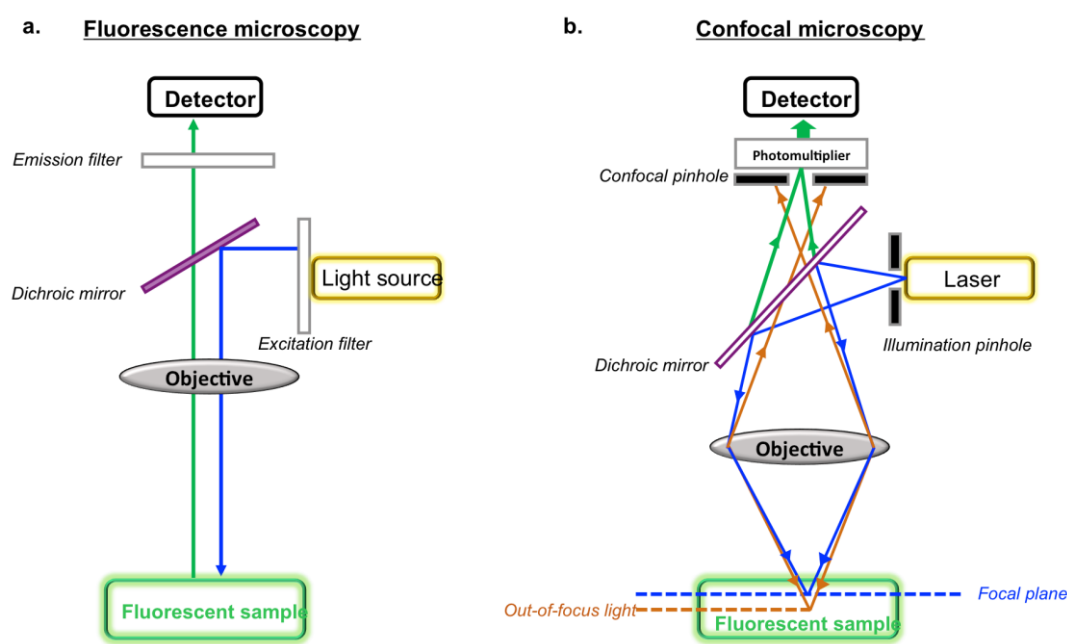


Figure 14: Comparison of fluorescence microscopy principle (a) and confocal microscopy principle (b).

This arrangement of objective, diaphragms and mirrors, which allows for the conjugation of optical points, thus enables to improve the images quality and to circumvent the limitations imposed by standard microscopy. This confocal feature presents many other advantages: as previously announced, it offers for example the possibility of optically sectioning a sample and reconstructing it in 3D by stacking individual XY slices. It also permits to detect different fluorophores at the same time by exciting them sequentially or to quantify the mobility of fluorescent molecules thanks to fluorescence recovery after photo-bleaching (FRAP) experiments. FRAP method<sup>57</sup> consists in bleaching an area of the sample with the laser adjusted at its maximum power and to take images at different post-bleach times to evaluate the fluorescence recovery in the area previously bleached: no fluorescence recovery after a certain period of time means that light-sensitive molecules are immobilized within the sample, whereas the reappearance of fluorescence in the course of time signifies that the molecules are mobile and diffuse within the sample at a certain diffusion rate, which can be calculated.

Confocal laser scanning microscopy was used in this study to characterize self-assembly.

### *Experimental setup*

Observations were carried out with a Zeiss LSM 710 microscope using a x10, x20 and x40 objective (Zeiss, Plan Aplanachromat). To observe the self-assembly, a fluorescent molecule is added to the self-assembly, the Thioflavin T, which have the property to become fluorescent when it changes its conformation by going in the hydrophobic zone of the self-assembly and in particular inside the  $\beta$ -sheets. The Thioflavin T fluorescence (here, related to the FITC) was detected after excitation at  $\lambda = 488$  nm and an emission band pass filter of 505-530 nm (green emission). The images were analyzed by means of the Zen black software from Zeiss and "Image J" software.<sup>58</sup>

Samples are prepared on surface, by the protocol described in the part 4.3.2, and on solution. The concentration in solution are the following: Fmoc-FFpY (5 mg/mL), HA (15 mg/mL), AP (1 mg/mL) and Thioflavin T (0,15 mg/mL), which is solubilized in the peptide solution. Then, on the glass cover slip 50  $\mu$ L of each solution (peptide + Thioflavin T, AP and HA) are mixed for the analysis.

#### **6.5.15. Cells assays on Fibroblast NIH 3T3**

- **Preparation of the samples:**
  - Hydrogel sample as support for the cell culture:

Hydrogel samples are prepare on surface. Glass slide of 14 mm of diameter are cleaned up by UV-Ozone for 15 min then dropped off at the bottom of a 24-wells plate (CORNING brand) for cells culture. Then, as described in the point 4.3.3. the polyelectrolyte multilayer is buildup by dipping of 1 mL of each solutions. After the deposition of a PEI (1 mg/mL) precursor layer for 10 min, the multilayer film was performed by alternately exposing the surface to PSS (1 mg/mL) and PAH (1 mg/mL) solutions for 10 min with an intermediate rinsing step with borax buffer. The polyelectrolyte multilayer is always prepared in borax buffer. Then, the AP (1 mg/mL), is adsorbed for 20 min followed by 5 min of rinsing step with borax or RPMI medium. Finally, the solution of Fmoc-FFpY with or without HA is added for

24 h in borax buffer or RPMI medium. Finally, two rinsing step with the cell culture medium is performed (usually RPMI + 10 % FBS) and then the solution containing the cells are dropped off on the samples.

○ Cells solution:

The cells that will be used for our cell cultures on gels are fibroblasts of line NIH 3T3. Basically they are prepared in DMEM and transferred to RPMI for the purpose of the experiment. After removing the buffer and washing the surface with PBS, the cells are peeled off their petri dish with 3 mL of trypsin and 3 minutes in the oven. Then, 7 mL of DMEM is added to stop the action of trypsin. The solution is recovered and transferred to a centrifuge tube and centrifuged for 10 minutes. The supernatant is gently removed without touching the cells and a small volume of RPMI is added to the tube. This allows us to proceed with the transplanting which consists in taking a 100  $\mu$ L of this solution for injected it into a new culture dish. The solution is supplemented with 10 ml of the appropriate culture medium before being placed in an oven. The last step is the counting of cells using the Neubauer cell. To do this, a 10th dilution (100  $\mu$ L of solution in 900  $\mu$ L of RPMI) is previously performed (otherwise the number of cells is too large to allow counting). The average number of cells per well is  $1 \times 10^5$  cells. From the number of cells counted, it is possible to find the exact volume to be taken from the cell solution (Equation 1).

$$volume\ to\ be\ taken = \frac{V_{total} \times N_{desired}}{N_{count} \times Dilution \times 10^4\ (for\ the\ Neubauer\ cell)} \text{ (Equation 1)}$$

with  $V_{total}$  = desired total volume to dropped off in the different wells,  $N_{desired}$  = desired number of cells,  $N_{count}$  = number of cells counted.

The media slides are moved into a new 24-well plate, and the cell solution at 1 mL is introduced into each well with the slides to be tested. The plate is placed in the oven at 37 ° C throughout the culture period. In our case, all the cells assays were lasting 4h. At the end of these 4 hours, the plate is removed from the oven and the cultures are studied under optical microscopy under an epifluorescence microscope. Then, a cell viability test is carried out (commercial test) and the plate is put back in the oven for an extra 15 min. Finally, a last observation is made at the fifth hour of culture in optical mode and fluorescence.

**Choice of the cells line:**

Fibroblasts are cells belonging to the cell family of the tissue connective. The cartilaginous (or chondrocyte) and bone cells are the other limbs, as well as smooth muscle cells and adipocytes. The fibroblasts, bone cells and chondrocytes have as synth-power properties to etch the extracellular matrix proteins and maintain the cohesion of the body. In addition, depending on the environment but also their type, fibroblasts can differentiate and transform into bone cells, chondrocytes, smooth muscle cells or adipocytes.

The fibroblast NIH 3T3 are mouse fibroblasts, constituting a cell line. Their name means that originally, primary cells, embryo fibroblasts of mice, were subcultured every 3 days at a given concentration,  $3 \times 10^5$  cells in boxes of 20 cm<sup>2</sup>. At the end of about twenty operations, the cells are spontaneously immortalized, which can then be grown and preserved forever. Immortalized cells can divide without limit in time, unlike primary cells for which a barrier, 30 to 50 divisions, cannot be exceeded. In fact, the primary cells, during successive divisions, see the ends of their chromosomes, the telomeres, degrade. the end of a certain number of degradations, the cell becomes unstable, genes of regulation no longer functional. As a guardrail (the cell would lose regulators and could become cancerous), she stops dividing. However, some cells, such as rodent fibroblasts, have their telomeres protected. It's for that they can immortalize spontaneously.

- **Neubauer cell counting:**

Neubauer's chamber is a thick glass plate with the size of a glass slide (30x70x4 mm). The counting region consists of two square shaped ruled areas. There are depressions or the moats on either side or in between the areas on which the squares are marked thus giving an "H" shape (Figure 15a). The ruled area is 3 mm<sup>2</sup> divided into 9 large squares each with a 1 mm<sup>2</sup> area. The large central square (which can be seen in its entirety with the X10 objective), is divided into 25 medium squares with double or triple lines. Each of these 25 squares are again divided into 16 small squares with single lines, so that each of the smallest squares has an area of 1/400 mm<sup>2</sup> (Figure 15b)<sup>59</sup>. The glass cover is a squared glass of width 22 mm. The glass cover is placed on the top of the Neubauer chamber, covering the central area. The ruled area is 0.1 mm lower than the rest of the chamber. So that when a cover slip is kept on the counting region, there is a gap of 0.1 mm between the cover slip and the ruled area (Figure 15c). The counting can be done either in the central large square or in the corner squares, depending on the size of the cells under study (Figure 15d).

- WBC Counting Area:

The four large squares placed at the corners are usually used for white blood cell (WBC) count. Since their concentration is lower than red blood cells (RBC) a larger area is required to perform the cell count.

- RBC Counting Area:

The large center square is used for RBC counts. As already stated, this area is subdivided into 25 medium squares, which in turn are each divided into 16 squares. Of the 25 medium squares, only the four corner squares and the center square within the large center square are used to perform RBC counts.

For our samples, the count of the cells are done in the WBC counting area way.

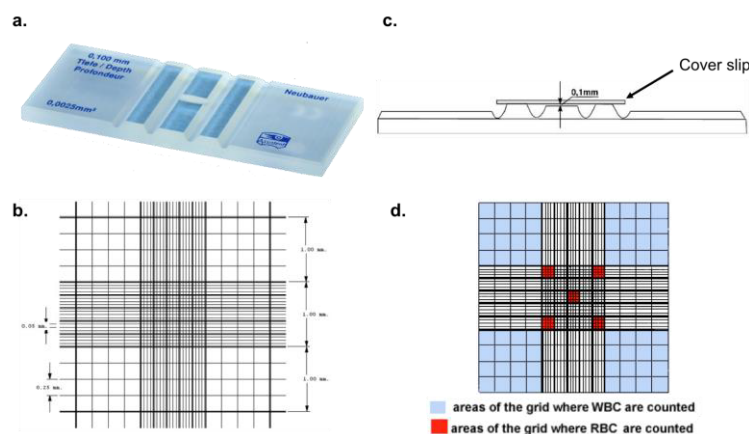


Figure 15: (a) Neubauer's chamber, (b) scheme of the ruled area of the Neubauer's chamber, (c) representative scheme of the cover slip in the Neubauer's chamber showing the disposition of the counting region, (d) scheme of the cell counting areas in Neubauer's chamber<sup>59</sup>

### *Experimental setup*

- Sample preparation:

A rat fibroblast line NIH 3T3 was cultivated in DMEM medium supplemented with 10% fetal bovine serum (FBS), and 1% penicillin/streptomycin. A preparation of a dilution with a suitable concentration should be prepared for cell counting. Typically, the concentration range for a cell count with Neubauer chamber is between 250 000 cells/ml and 2.5 million cells/ml. An appropriate dilution of the mixture with regard to the number of cells to be counted should be used. If the sample is not diluted enough, the cells will be too crowded and difficult to count. If it is too dilute, the sample size will not be enough to make strong inferences about the concentration in the original mixture. In our cells assays, cell culture was done with 250 000 cells/mL. Only 10  $\mu$ L of the solution is introduced in the Neubauer chamber. The precision on the injected volume is important to be able to find the exact number of cells in the whole culture box. The injected solution will then spread over the entire surface of the capillary counting network. It is important to always count the inside of the squares in the same way (example: for each square, consider only the left side, the top one and the inside).

- Calculating the cell counts:

The total number of cells per microliter of sample can be calculated from the number of cell counted and area counted. This is because the ruled areas of the chamber contain an exact volume of diluted sample as said in the previous point (Equation 2).

$$\text{particle per } \mu\text{L volume} = \frac{\text{Counted particles}}{\text{Counted surface (mm}^2\text{)} \times \text{Chamber depth (mm)} \times \text{Dilution}} \quad (\text{Equation 2})$$

Counted surface = 1 mm<sup>2</sup> x 4 = 4 mm<sup>2</sup> (area of the four large corner squares)

Depth = 0.1 mm; Dilution = 1/10

Experiments were carried out on 12 mm diameter glass slide placed into 24 well plates. The film samples were prepared a day before the assay. Prior to the assay, all samples were sterilized with UV exposure for 30 min. To study the influence of the concentration of HA on the resulting composite self-assembly materials on cell viability, we seeded 5x10<sup>4</sup> NIH 3Y3 mouse fibroblasts cells in each well. The cell culture was done at 37°C in an incubator for 4h, in DMEM containing glucose, 10% fetal bovine serum and 1% penicillin-streptomycin. After the 4h, samples are observed in optical microscopy to observe their spreading on the surface and their phenotype. Then, the samples are incubated 1h more with the solution for the life/dead test at 37°C. The life/dead test contains mainly three fluorophores to stain the nuclei (by DAPI), the apoptotic cells (by fluorescein) and the necrotic cells (by phalloidin).

- **Cell viability test:**

Apoptotic/necrotic/healthy cells detection kit, catalog number PK CA707-30018 (Annexe 2).

This test distinguishes living cells from dead cells (by apoptosis or necrosis) from a cell culture. It consists of using three fluorochromes to mark the cells differently (Figure 4). These three substances are mixed together in a special buffer, "Binding Buffer X5" diluted in ultra pure water to obtain an X1 binding buffer. The culture medium of the wells containing our cell cultures is removed. This completed buffer is used to fill the wells. The 24-wells plate is then placed in an incubator at 37 °C for 15 min in the dark. The test buffer is then removed, and the cultures rinsed very gently to avoid removing all dead cells. The microscopic observations are then made in epifluorescence.



To count the cells, a blue fluorescence is observed for the nucleus thanks to Hoechst 33342 fluorochrome. This fluorochrome marks the nucleus of all cells. The second fluorochrome used is FITC-Annexin V which is green fluorescence and only marks the apoptotic cells. And the last fluorochrome is the homodimer, red fluorescence, which marks the necrotic cells (Figure 16). Sometimes a cell is marked with 3 colors, it means that it is a very old apoptotic cell. In our case, the percentage of apoptotic and necrotic cells is not crucial. This test is used to estimate the cell viability of cultures in contact with our gels. The aim of these assays is mainly to try to determine the percentage of living cells on the total number of cells. A dozen images with microscopes were taken for each condition (without HA, 2 mg/mL, 5 mg/mL, etc.). The cells are then counted on all these images and an average is calculated to obtain a representative value.

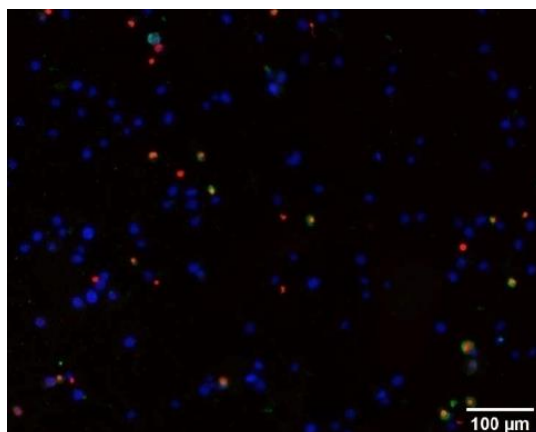


Figure 16: Example of an image obtained for Fmoc-FFpY + AP without HA hydrogel in Epifluorescence microscope after live/death cell test. One can observe the blue, green and red fluorescence, which will permit to determined the cell viability.

## ANNEXES

- Annexe 1:

### Composition of FBS

Component	Average	Range
Endotoxins (ng/ml)	0.35	0.01 - 10.0
Glucose (mg/ml)	1.25	0.85 - 1.81
Protein (mg/ml)	38	32 - 70
Albumin (mg/ml)	23	20 - 36
Hemoglobine ( $\mu\text{g/ml}$ )	113	24 - 181
Bilirubin, total ( $\mu\text{g/ml}$ )	4	3 - 11
Bilirubin, direct ( $\mu\text{g/ml}$ )	2	0 - 5
Urea ( $\mu\text{g/ml}$ )	160	140 - 200
Urate ( $\mu\text{g/ml}$ )	29	13 - 41
Creatinin ( $\mu\text{g/ml}$ )	31	16 - 43
Insulin ( $\mu\text{U/ml}$ )	10	6 - 14
Cortisol (ng/ml)	0.5	0.1 - 23
Growth hormone (ng/ml)	39.0	18.7 - 51.6
Parathormone, PTH (ng/ml)	1.72	0.085 - 6.18
Triiodothyronine, T3 (ng/ml)	1.2	0.56 - 2.23
Thyroxine, T4 (ng/ml)	0.12	0.08 - 0.16
Thyroid-stimulating hormone, TSH (ng/ml)	1.22	0.2 - 4.5
Follicle-stimulating hormone, FSH (pg/ml)	95	20 - 338
Testosterone (pg/ml)	400	210 - 990
Progesterone, P4 (pg/ml)	80	3 - 360
Prolactin = Luteotropic hormone, LTH (pg/ml)	176	20 - 500
Luteinizing hormone, LH ?? (pg/ml)	8	1,2 - 18
Prostaglandin E (ng/ml)	5.9	0.5 - 30.5
Prostaglandin F (ng/ml)	12.3	3.8 - 42.0
Vitamine A (ng/ml)	90	10 - 350
Vitamine E (ng/ml)	1.1	1 - 4.2
Cholesterol ( $\mu\text{g/ml}$ )	310	120 - 630
Lactate-dehydrogenase, LDH (mU/ml)	864	260 - 1,215
Alkaline Phosphatase (mU/ml)	255	110 - 352
Aspartate-Aminotransferase, ASAT (mU/ml)	130	20 - 200
Sodium, $\text{Na}^+$ ( $\mu\text{eq/ml}$ )	137	125 - 143
Potassium, $\text{K}^+$ ( $\mu\text{eq/ml}$ )	11.2	10.0 - 14.0
Calcium, $\text{Ca}^{2+}$ ( $\mu\text{eq/ml}$ )	6.75	6.30 - 7.15
Chloride, $\text{Cl}^-$ ( $\mu\text{eq/ml}$ )	103	98 - 108
Phosphate, $\text{P}_i$ ( $\mu\text{g/ml}$ )	98	43 - 114
Selen ( $\mu\text{g/ml}$ )	0.026	0.014 - 0.038
pH	7.40	7.20 - 7.60

- Annexe 2:

## Apoptotic/Necrotic/Healthy Cells Detection Kit



### Instruction Manual

Product Name	Size	Catalog Number
Apoptotic/Necrotic/Healthy Cells Detection Kit	50 assays	PK-CA707-30018

### Introduction

Apoptosis and necrosis are the two major processes leading to cell death. Apoptosis is an active, genetically regulated "Cell suicide" induced by diverse factors. This disassembly of the cell from within creates multiple events and is associated e.g. with changes in the phospholipid content of the outer leaflet of the cytoplasmic membrane. Phosphatidylserine (PS) is translocated from the inner to the outer surface of the cell for phagocytic cell recognition.

Apoptotic cells can be easily and reliably identified with Annexin V, a 35 kD  $\text{Ca}^{2+}$ -dependent phospholipid protein with a high affinity for PS, that binds specifically to PS exposed on the outer membrane leaflet of apoptotic cells. When Annexin V is labeled e.g. with fluorescein (FITC;  $\lambda_{\text{exc}}/\lambda_{\text{em}} = 492/514$  nm) apoptotic cells are stained brightly green.

Necrosis normally results from a severe cellular insult. Since both internal organelle and plasma membrane integrity are lost, this results in spilling of cytosolic and organellar contents into the surrounding environment. Ethidium homodimer III (EthD-III) is a highly positively charged nucleic acid probe, which is impermeant to live or apoptotic cells, but stains necrotic cells intensively with red fluorescence ( $\lambda_{\text{exc}}/\lambda_{\text{em}} = 528/617$  nm). Due to its significantly higher affinity for DNA and higher fluorescence quantum yield, EthD-III is a superior alternative to propidium iodide (PI) or ethidium homodimer I (EthD-I) commonly used in some other cell staining kits.

Membrane-permeable Hoechst 33342 is a minor groove-binding DNA stain that emits bright blue fluorescence upon binding to DNA ( $\lambda_{\text{exc}}/\lambda_{\text{em}} = 350/461$  nm). It is used for blue-fluorescent staining of the entire cell population.

The Apoptotic/Necrotic/Healthy Cells Detection Kit provides a convenient assay for quantifying apoptotic (green), necrotic (red) cells and healthy (blue only) within the same cell population by flow cytometry or fluorescence microscopy. Membrane permeable Hoechst 33342 stains the nuclei of both apoptotic and necrotic cells. However, healthy cells are stained by Hoechst only, not by FITC-Annexin V or EthD-III. Late apoptotic cells (entering into secondary necrosis) are stained both green and blue. Necrotic cells are stained both red and blue. Cells stained with triple colors blue, green and red are dead cells progressing from apoptotic cell population.

### Kit Contents

FITC-Annexin V in TE buffer containing 0.1% BSA and 0.1%  $\text{NaN}_3$  (pH 7.5), 250  $\mu\text{l}$

Ethidium Homodimer III (EthD-III) in PBS, 250  $\mu\text{l}$

5X Binding Buffer, 15 ml

Hoechst 33342 in PBS, 250  $\mu\text{l}$

**Caution:** Sodium azide and ethidium homodimer III are hazardous substances. Handle with care and dispose properly.

### Storage and Stability

Store the kit at 4°C and protect FITC-Annexin V, EthD-III and Hoechst 33342 from light. Do not freeze!

### Intended Use

For in vitro research use only. Not for diagnostic or therapeutic procedures.



## Experimental Procedures

### Suspension cells

1. Induce apoptosis in cells by a desired method.
  2. Prepare 1X Binding Buffer by diluting 5X Binding Buffer 1:5 in distilled water.
  3. Wash cells with PBS once and resuspend cells at  $2-3 \times 10^6$  cells /ml in 1X Binding Buffer.
  4. Pipet 100  $\mu$ l cell suspension in a microcentrifuge tube.
  5. Add 5  $\mu$ l of FITC-Annexin V, 5  $\mu$ l of Ethidium Homodimer III and 5  $\mu$ l Hoechst 33342 solutions to each tube.
- Note:** We recommend including two control samples, for staining with each of the probes (FITC-Annexin V, EthD-III, Hoechst 33342) separately.
6. Incubate at room temperature for 15 minutes in the dark.
  7. For flow cytometry analysis, add 400  $\mu$ l 1X Binding Buffer to each tube and measure fluorescence in FITC, propidium iodide and DAPI channels within 1 hour of staining.
  8. For fluorescence microscopy analysis, wash cells with 1X Binding Buffer, resuspend cells in 1X Binding Buffer, and observe fluorescence using FITC, Texas Red and DAPI filter sets.

### Adherent cells for microscope viewing

1. Induce apoptosis in cells by a desired method (Note: You may also grow cells directly on a coverslip).
2. Prepare 1X Binding Buffer by diluting 5X Binding Buffer 1:5 in distilled water.
3. Wash cells twice with 1X Binding Buffer.
4. Prepare staining solution by adding 5  $\mu$ l of FITC-Annexin V, 5  $\mu$ l of Ethidium Homodimer III and 5  $\mu$ l of Hoechst 33342 to 100  $\mu$ l 1X Binding Buffer. Prepare enough staining solution to cover cells.  
Note: reducing the concentration of EthD-III may result in better signal:background ratio for some cell types.
5. Incubate samples with the staining solution for 15 minutes at RT, protected from light.
6. Wash cells with 1X binding Buffer 1-2 times.
7. Cover cells with 1X Binding Buffer and observe fluorescence using FITC, Texas Red and DAPI filter sets.
8. When staining cells on coverslips: Mount coverslip onto a slide with 1X Binding Buffer, aspirate residual 1X binding Buffer and seal coverslip with nail polish or (recommended for permanent preservation of slides) mount coverslip onto a slide with a drop PromoFluor Antifade Reagent (PK-PF-AFR1), remove excess liquid and wait until the mounting medium slowly solidifies.

### Adherent cells for flow cytometry

1. Detach cells from cell culture plate or well using trypsin or other cell dissociation methods.
2. Pellet cells and discard supernatant.
3. Follow staining protocol for suspension cells.

Optional: Formaldehyde fixation may be performed for long term preservation of cell staining. Annexin V binding to PS requires calcium, therefore buffers used for washing and fixation should contain 1.25 mM calcium chloride ( $\text{CaCl}_2$ ). Fixation may increase background staining by Ethidium Homodimer III. Cells should be washed thoroughly prior to fixation to remove unbound dye.

### Expected Results

Green fluorescent plasma membrane staining identifies apoptotic cells, while necrotic cells are identified by red fluorescent nuclear staining. Late apoptotic cells may show green and red staining. All cell nuclei will be stained with blue fluorescence. Dead cells may stain more intensely with Hoechst 33342 than live cells.

## References

1. Boersma A.W., et al. Quantification of apoptotic cells with fluorescein isothiocyanate-labeled annexin V in chinese hamster ovary cell cultures treated with cisplatin. *Cytometry*. 1996 Jun 1; 24(2):123-30.
2. Martin S.J., et al. Early redistribution of plasma membrane phosphatidylserine is a general feature of apoptosis regardless of the initiating stimulus: inhibition by overexpression of Bcl-2 and Abl. *J Exp Med*. 1995 Nov 1; 182(5):1545-56.

## REFERENCES

1. Jayawarna, V., *et al.*, Nanostructured hydrogels for three-dimensional cell culture through self-assembly of fluorenylmethoxycarbonyl-dipeptides, *Ad. Mater.*, **2006**, *18*, 611.
2. Yang, Z., *et al.*, Enzymatic control of the self-assembly of small molecules: a new way to generate supramolecular hydrogels, *Soft Matter*, **2007**, *3*, 515.
3. Jayawarna, V., *et al.*, Three-dimensional cell culture of chondrocytes on modified diphenylalanine scaffolds, *Biochem. Soc. Trans.*, **2007**, *35*, 535.
4. Truong, W. T., *et al.*, Dissolution and degradation of Fmoc-diphenylalanine self-assembled gels results in necrosis at high concentrations in vitro, *Biomater. Sci.*, **2015**, *3*, 298.
5. Zhang, Y., *et al.*, Versatile small-molecule motifs for self-assembly in water and the formation of biofunctional supramolecular hydrogels, *Langmuir*, **2011**, *27*, 529.
6. Liebmann, T., *et al.*, Self-assembling Fmoc dipeptide hydrogel for in situ 3d cell culturing, *BMC Biotechnol.*, **2007**, *7*, 88.
7. Jayawarna, V., *et al.*, Introducing chemical functionality in Fmoc-peptide gels for cell culture, *Acta Biomater.*, **2009**, *5*, 934.
8. Jayawarna, V., *et al.*, Self-assembling peptide hydrogels: directing cells behaviour by chemical composition, *Tissue Eng. A*, **2008**, *14*, 908.
9. Zhou, J., *et al.*, Molecular hydrogel-stabilized enzyme with facilitated electron transfer for determination of H<sub>2</sub>O<sub>2</sub> released from live cells, *Anal. Chem.*, **2014**, *86*, 4395.
10. Zhou, M., *et al.*, Self-assembled peptide-based hydrogels as scaffolds for anchorage-dependent cells, *Biomaterials*, **2009**, *30*, 2523.
11. Cheng, G., *et al.*, Hydrogelation of self-assembling RGD-based peptides, *Soft Matter*, **2011**, *7*, 1326.
12. Yokoi, H., *et al.*, Dynamic reassembly of peptide Rada16 nanofiber scaffold, *Proc. Natl. Acad. Sci. U. S. A.*, **2005**, *102*, 8414.
13. Owczarz, M., *et al.*, Sol-Gel transition of charged fibrils composed of a model amphiphilic peptide, *J. Colloid Interface Sci.*, **2015**, *437*, 244.
14. Soler-Botija, C., *et al.*, Engineered 3D bioimplants using elastomeric scaffold, self-assembling peptide hydrogel, and adipose tissue-derived progenitor cells for cardiac regeneration, *Am. J. Transl. Res.*, **2014**, *6*, 291.
15. Zou, Z., *et al.*, Biocompatibility of functionalized designer self-assembling nanofiber scaffolds containing FRM motif for neural stem cells, *J. Biomed. Mater. Res., Part A*, **2014**, *102*, 1286.
16. Liang, P., *et al.*, Recombinant self-assembling 16-residue peptide nanofiber scaffolds for neuronal axonal outgrowth, *Eng. Life Sci.*, **2015**, *15*, 152.
17. Wang, J., *et al.*, FGL-Functionalized self-assembling nanofiber hydrogel as a scaffold for spinal cord-derived neural stem cells, *Mater. Sci. Eng. C*, **2015**, *46*, 140.
18. Hamada, K., *et al.*, Spatial distribution of mineralized bone matrix produced by marrow mesenchymal stem cells in self-assembling peptide hydrogel scaffold, *J. Biomed. Mater. Res., Part A*, **2008**, *84A*, 128.
19. Li, Z., *et al.*, Bone marrow enriched graft, modified by self-assembly peptide, repairs critically-sized femur defects in goats, *Int. Orthop.*, **2014**, *38*, 2391.
20. Kakiuchi, Y., *et al.*, The macroscopic structure of Rada16 peptide hydrogel stimulates monocyte/macrophage differentiation in HL60 cells *via* cholesterol synthesis, *Biochem. Biophys. Res. Commun.*, **2013**, *433*, 298.
21. Mie, M., *et al.*, Hydrogel scaffolds composed of genetically synthesized self-assembling peptides for three-dimensional cell culture, *Polym. J.*, **2013**, *45*, 504.
22. Liu, X., *et al.*, Functionalized self-assembling peptide nanofiber hydrogels mimic stem cell niche to control human adipose stem cell behavior in vitro, *Acta Biomater.*, **2013**, *9*, 6798.
23. Mi, K., *et al.*, Self-assembling peptide Rada16 nanofibre scaffold for a cancer cell three-dimensional culture, *Iran. Polym. J.*, **2009**, *18*, 801.
24. Jung, J. P., *et al.*, Co-assembling peptides as defined matrices for endothelial cells, *Biomaterials*, **2009**, *30*, 2400.
25. Tian, Y., *et al.*, Fibrillized peptide microgels for cell encapsulation and 3d cell culture, *Soft Matter*, **2011**, *7*, 6005.

26. Silva, G., *et al.*, Selective differentiation of neural progenitor cells by high-epitope density nanofibers, *Science*, **2004**, 303, 1352.
27. Beniash, E., *et al.*, Self-assembling peptide amphiphile nanofiber matrices for cell entrapment, *Acta Biomater.*, **2005**, 1, 387.
28. Tysseling-Mattiace, V., *et al.*, Self-assembling nanofibers inhibit glial scar formation and promote axon elongation after spinal cord injury, *J. Neurosci.*, **2008**, 28, 3814.
29. Matson, J., and Stupp, S., Self-assembling peptide scaffolds for regenerative medicine, *Chem. Commun.*, **2012**, 48, 26.
30. Muraoka, T., *et al.*, Light-triggered bioactivity in three dimensions, *Angew. Chem., Int. Ed.*, **2009**, 48, 5946.
31. Sur, S., *et al.*, Photodynamic control of bioactivity in a nanofiber matrix, *ACS Nano*, **2012**, 6, 10776.
32. Song, Y., *et al.*, Neural progenitor cells survival and neuronal differentiation in peptide-based hydrogels, *J. Biomater. Sci., Polym. Ed.*, **2011**, 22, 475.
33. Song, Y., *et al.*, Two-dimensional effects of hydrogel self-organized from IKVAV-containing peptides on growth and differentiation of NSCS, *J. Wuhan Univ. Technol., Mater. Sci. Ed.*, **2009**, 24, 186.
34. Song, Y., *et al.*, Cytocompatibility of self-assembled hydrogel from IKVAV-containing peptide amphiphile with neural stem cells, *J. Wuhan Univ. Technol., Mater. Sci. Ed.*, **2009**, 24, 753.
35. Capito, R., *et al.*, Self-assembly of large and small molecules into hierarchically ordered sacs and membranes, *Science*, **2008**, 319, 1812.
36. Mata, A., *et al.*, Bone regeneration mediated by biomimetic mineralization of a nanofiber matrix, *Biomaterials*, **2010**, 31, 6004.
37. Mendes, A., *et al.*, Co-assembled and microfabricated bioactive membranes, *Adv. Funct. Mater.*, **2013**, 23, 430.
38. Ribeiro, S., *et al.*, Nanostructured interfacial self-assembled peptide-polymer membranes for enhanced mineralization and cell adhesion, *Nanoscale*, **2017**, 9, 13670.
39. Aviv, M., *et al.*, Improving the mechanical rigidity of hyaluronic acid by integration of a supramolecular peptide matrix, *ACS Appl. Mat. Interf.*, **2018**, 10, 41883.
40. Vigier-Carrière, C., *et al.*, Bioactive seed layer for surface-confined self-assembly of peptides, *Angew. Chem., Int. Ed.*, **2015**, 54, 10198.
41. Highley, C., *et al.*, Recent Advances in Hyaluronic Acid Hydrogels for Biomedical Applications, *Curr. Opin. Biotechnol.*, **2016**, 40, 35.
42. Burdick, J., *et al.*, Hyaluronic Acid Hydrogels for Biomedical Applications, *Adv. Mater.*, **2011**, 23, H41.
43. Slaughter, B., *et al.*, Hydrogels in Regenerative Medicine, *Adv. Mater.*, **2009**, 21, 3307.
44. Ryan, D., *et al.*, The influence of side-chain halogenation on the self-assembly and hydrogelation of Fmoc-phenylalanine derivatives., *Soft Matter*, **2010**, 6, 3220.
45. Yang, Z., Enzymatic formation of supramolecular hydrogels, *Adv. Mater.*, 2004, 16, 1440.
46. Ryan, D., *et al.*, Self-assembly and hydrogelation promoted by F<sub>5</sub>-phenylalanine, *Soft Matter*, **2010**, 6, 475.
47. Smith, A., *et al.*, Fmoc-diphenylalanine self assembles to a hydrogel via a novel architecture based on  $\pi$ - $\pi$  Interlocked  $\beta$ -sheets, *Adv. Mater.*, **2008**, 20, 37.
48. Guilbaud-Chéreau, C., *et al.*, Protected amino acid-based hydrogels incorporating carbon nanomaterials for near-infrared irradiation-triggered drug release, *ACS Appl. Mater. Interfaces*, **2019**, DOI : 10.1021/acsami.9b02482.
49. Parsegian, V., *et al.*, Lessons from the direct measurement of forces between biomolecules. *Physics of Complex and Supramolecular Fluids* (S.A. Safran and N.A. Clark, eds.), John Wiley & Sons, New York, **1987**, 115.
50. Bhattacharya, D., *et al.*, Impact of structurally modifying hyaluronic acid on CD44 interaction, *J. Mater. Chem. B.*, **2017**, 5, 8183.
51. Khattab, S., *et al.*, Cyanoacetamide-based oxime carbonates: an efficient, simple alternative for the introduction of Fmoc with minimal dipeptide formation, *Tetrahedron*, **2012**, 68, 3056., b)  
Marty, R., *et al.*, Two-fold odd-even effect in self-assembled nanowires from oligopeptide-polymer-substituted perylene bisimides, *J. Am. Chem. Soc.*, **2014**, 136, 3919.
52. Lindl, T. (2002): "Zell- und Gewebekultur". 5th ed. Spektrum Akademischer Verlag, Heidelberg

53. Sigma-Aldrich. RPMI-1640 Media Formulation. Available from: <https://www.sigmaaldrich.com/life-science/cell-culture/learning-center/media-formulations/rpmi-1640.html>.
54. Sigma-Aldrich. Dulbecco's Modified Eagle's Medium (DME) Formulation. Available from: <https://www.sigmaaldrich.com/life-science/cell-culture/learning-center/media-formulations/dme.html>.
55. Microbiologie-medical. GELOSE MUELLER-HINTON (MH). Available from: <http://www.microbiologie-medicale.fr/milieudisolement/nonselectifs/mh.htm>.
56. Sauerbrey, G., Verwendung von schwingquarzen zur wägung dünner schichten und zur mikrowägung, *Z. Phys.*, **1959**, 155, 206.
57. a) Voinova, M., *et al.*, Viscoelastic acoustic response of layered polymer films at fluid-solid interfaces: continuum mechanics approach, *Phys. Scr.*, **1999**, 59, 391., b) Höök, F. *et al.*, Variation in coupled water, viscoelastic properties, and film thickness of a mefp-1 protein film during adsorption and cross-linking: a quartz crystal microbalance with dissipation monitoring, ellipsometry, and surface plasmon resonance study, *Anal. Chem.*, **2001**, 73, 5796.
58. Axelrod, D., *et al.*, Mobility measurement by analysis of fluorescence photobleaching recovery kinetics, *Biophys. J.*, **1976**, 16, 1055.
59. Schneider, A., *et al.*, Polyelectrolyte multilayers with a tunable young's modulus: influence of film stiffness on cell adhesion, *Langmuir*, **2006**, 22, 1193.

# **General Conclusion & Outlooks**







The localized self-assembly triggered by enzymes is a recent research field which has started in 2009 with the pioneer work from Ulijn's group.<sup>1</sup> Nowadays we count more than 40 articles about the self-assembly directed from planar surfaces and 23 of them were published in the last three years according to the Web of Science, highlighting the growth of the research development of this field. Potential applications have already been published mainly in biology, biomaterials, sensors and surfaces coating and many of them rose during the time of my Ph.D. as presented in the introductory chapter of this manuscript.

My investment in my doctoral project has started in 2016 for which I benefited from the work of a previous Ph.D. student of my host group (Dr. Cécile Vigier-Carrière, 2013 – 2016), who has shown the potentiality of adsorbed enzymes on multilayer films to initiate the growth of supramolecular hydrogels from defined surfaces. She also established the rules governing the structural features of the resulting self-assembled networks.

My contribution over the last three years to this field can be divided in the four following axes:

✓ **Supported supramolecular hydrogels based on the LEASA concept for applications in catalytic flow reactor and biological substrate design.**

Thanks to the spatial localization of the EASA process, the supporting of supramolecular hydrogels allows to manipulate them which is a *sine qua non* condition to foresee further developments: (i) grown from an open-cell polymer foam, a supported catalytically-active hydrogel has been designed, displaying efficient esterase like activity towards all classes of esters and excellent kinetic resolution as well. Applications in catalytic cartridge design for continuous flow reactor is currently under consideration to be patented by an office of technology transfer (SATT Conectus Alsace); (ii) grown from glass slides, the resulting hydrogel is a very soft biological substrate (20 – 2000 Pa) for biological studies about the relation between the elasticity of the material and cell adhesion, cell fate and motility. Thanks to the embedding of hyaluronic acid during the self-assembly process, it is possible to tune the resulting elastic modulus of the so-generated composite hydrogel. The interaction between a polyanion and a negatively charged self-assembled architecture is barely observed and its nature is not yet elucidated.

✓ **Towards the autocatalytic growth of a peptide self-assembly using LEASA's concept.**

The catalytic self-assembly described just above was the first step on the path to the design of another one which can catalyze its own formation. I have designed and

---

<sup>1</sup> Williams, R., *et al.*, Enzyme-assisted self-assembly under thermodynamic control, *Nat. Nanotechnol.*, **2009**, 4, 19.

synthesized a promising precursor peptide sensitive to the esterase-like supramolecular hydrogel discussed just above. This peptide precursor is transformed in hydrogelator when in contact with the catalytic hydrogel. I have proved that this hydrogel layer formed on a surface can catalyze its own growth.

✓ **Demonstration of an alternative way to electrochemical protons production to direct peptide self-assembly and hydrogel coating formation through an enzymatically-active multilayer film.**

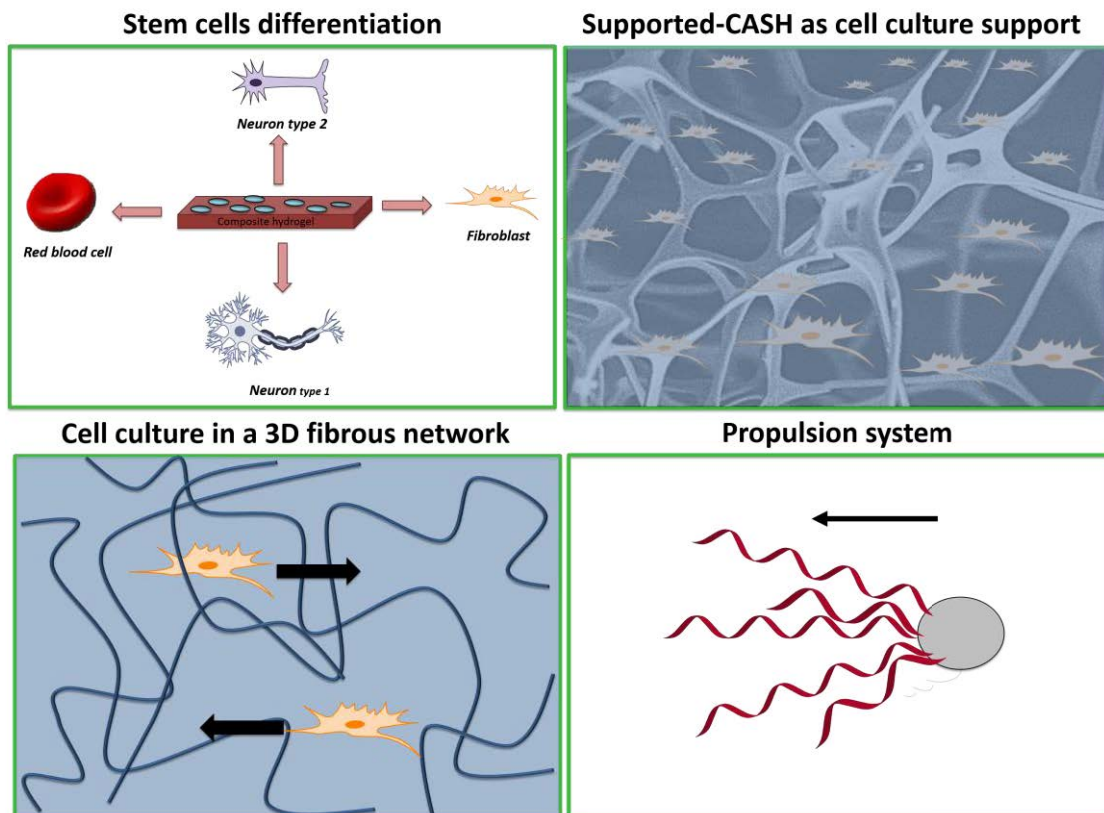
I designed the first non-conductive surface able to produce a proton gradient to localize supramolecular hydrogel formation by modifying it with an enzymatically active multilayer using two enzymes, one is GOx, producing protons from glucose oxidation. I optimized the production of proton and overcame the necessity of oxygen by introducing a second enzyme, horseradish peroxidase. This enzyme is able to produce the O<sub>2</sub> needed by the GOx, from the H<sub>2</sub>O<sub>2</sub> released by the GOx, leading to a self-sustaining system. The efficiency of the enzymatic tandem reactions were achieved by adapting the position between the two enzymes in the multilayer. This coating can be formed on any kind of surface, which opens the scope of applications of this kind of materials.

✓ **Proteins lacking catalytic activity can trigger the localized supramolecular hydrogelation.**

This discovery was an incidental finding and thus not scheduled initially in my Ph.D. work program. I have shown that proteins -lacking catalytic activity play the role of nucleation point mainly through electrostatic interactions between proteins and precursor peptides. This is a crucial finding in the elaboration of the peptide self-assembly nanostructures. Thanks to a dynamic equilibrium between the precursor and its corresponding hydrogelator, this nucleation step induces an equilibrium displacement leading to the full consumption of hydrogelators leading to the precursor form towards the hydrogelator specie leading to the self-assembled nanofibers growth. This discovery is a change of paradigm in the EASA definition since the self-assembly initiation no longer requires enzymatic transformation of the precursor into the hydrogelator.

From these different projects emerged new questions that have to be answered in more or less short-term outlooks. In the design of new biomaterials for cell culture applications of EASA and LEASA, it would be of interest to 1) use composite hydrogels as a tool for controlling stem cell differentiation for regenerative medicine. 2) Performing cell culture and being able to keep cells in a porous material coated by an appropriate hydrogel, as in chapter 5, will be of utmost interest for big clinical issues in the regenerative medicine to repair severe damage of bones for example. Despite their innate regenerative capacity, bones can only cover the gap of

small defects (gap thickness less than 2 mm)<sup>2</sup>. If a biocompatible porous materials containing osteoblasts can be attached in large osseous defects, it can help the bones to completely heal by favoring the osteogenesis in a medium often render hostile to it by damage to the surrounding soft tissues and vasculature<sup>3</sup>. 3) Still in the field of biomedicine, inserting cells inside of a biocompatible hydrogel and being able to form the hydrogel in presence of the cells will allow to inject the material containing the cells in damage to the body. As the material is a physical hydrogel, cells could have the possibility to move inside it without damaging the hydrogel in an irreversible manner. The hydrogel will be able to connect the borders of the damage and favor the healing, as the fibrous networks of hydrogels mimics the fibrous nature of the extracellular matrix or by delivering drugs too<sup>4</sup> (Outlook 1).



Outlook 1: Applications for EASA and LEASA

To achieve the different outlooks in applicative fields, it is important to characterize more in depth the surfaces covered by enzymes (surface concentration, enzyme distribution on the surface and enzymatic activity of the surface) to understand how the self-assembled structures interacts with the surface, the mechanisms behind the self-assembly formation. In the objective to design for example propulsion system<sup>5</sup> by initiating movement in one side of Janus nanoparticles, as the actin filament on the cell membrane leading to the cell motility, which can leads to engineering applications.

<sup>2</sup> Mahamutha, A., *et al.*, Healing mechanism in bone fracture, *J. Pharma. Sci. & research*, **2018**, 7, 44

<sup>3</sup> Verrier, S., *et al.*, Tissue engineering and regenerative approaches to improving the healing of large bone defects, *Eur. Cell Mater.*, **2016**, 32, 87.

<sup>4</sup> Williams, R., *et al.*, The in vivo performance of an enzyme-assisted self-assembled peptide/protein hydrogel, *Biomaterials*, **2011**, 32, 5304.

<sup>5</sup> Gao, W., *et al.*, Organized self-assembly of janus micromotors with hydrophobic hemispheres, *J. Am. Chem. Soc.*, **2013**, 135, 998





# **ANNEXES**





During my Ph.D., I had the opportunity to collaborate with a post doctorate, Miryam Criado-Gonzalez, on several projects aiming on the generation of peptide self-assemblies initiated at nanoparticles or in host gels. In all these projects, I participated by producing the peptides needed, in the discussions and interpretations of the results.

The first publication of Criado *et al.* demonstrated the use of LEASA by embedding enzymes in a host hydrogel (PEG hydrogel)<sup>1</sup>. Alkaline phosphatase is dispersed in the host hydrogel and a solution of the precursor, Fmoc-FFpY, is dropped off onto it. When precursors meet AP, the hydrogelator, Fmoc-FFY, is generated and self-assembles, leading to the formation of an interpenetrated fibrous network (Figure 30). We also tried to embed the precursors inside the host hydrogel and dropping a solution of AP onto it. This experiment leads to the same results. The resulting material possesses a higher Young modulus compared to the host hydrogel alone. The originality of these works relies in the possibility to initiate the formation of a second self-assembled network just by entrapping enzymes within a material, which allows to control the mechanical properties of this material.

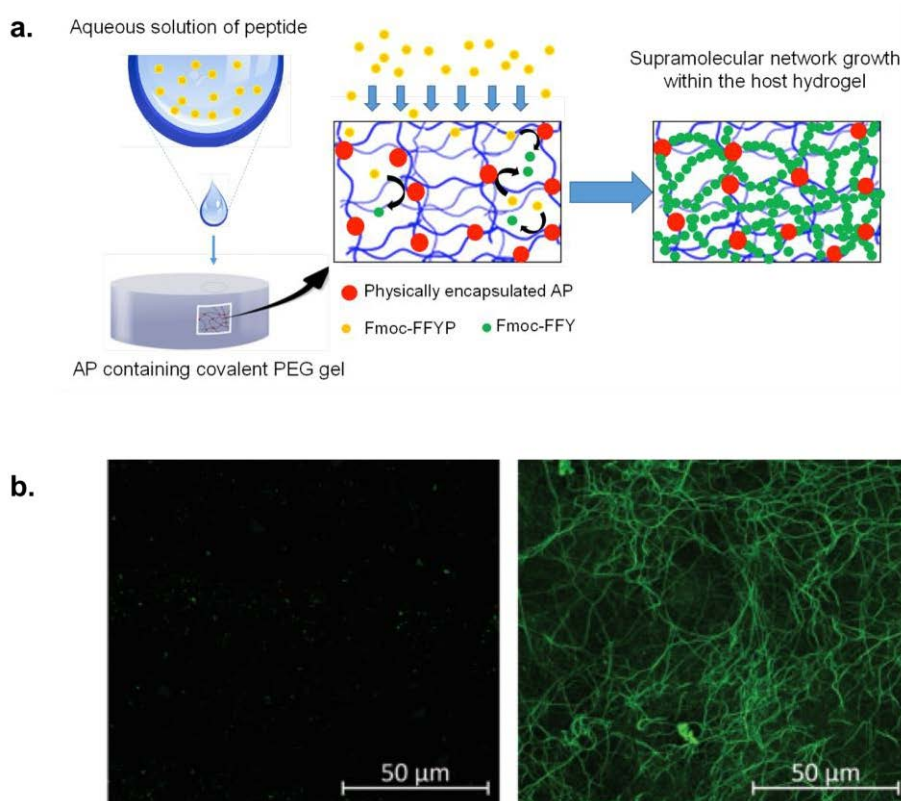


**Figure 1:** a) Schematic representation of the interpenetrated network design through peptide diffusion within the AP-entrapped host hydrogel and b) confocal images of the AP-PEG hydrogel containing thioflavine T (left) before and (right) after diffusion of the precursor fmoc-FFpY<sup>108</sup>. Copyright © Ref 108 reproduced by permission of The Royal Society of Chemistry.

<sup>1</sup> Criado, M., *et al.*, Enzyme-assisted self-assembly within a hydrogel induced by peptide diffusion, *Chem. Commun.*, **2019**, 55, 1156.



The second article of Criado *et al.* reports a system in which Nanoparticles (NPs) were used as the surface onto which AP was covalently bond to allow the localization of the self-assembly of the Fmoc-FFY hydrogelator after dephosphorylation of its precursor, Fmoc-FFpY<sup>2</sup>. The resulting self-assembly leads to a fibrous network starting from the NP surfaces. The NPs are then entrapped in the hydrogel and serve as anchoring points for fibers of the gel. We find that when this gel is formed, it undertakes a phase change. This phase change takes place after several days, a time laps that depends upon the NP and the peptide concentrations. No change is observed when the enzymes are not covalently linked to the NPs but only added into the NP solution. The phase change leads to the appearance of a dense phase that is concentrated in both NPs and self-assembled peptide fibers and to a dilute phase that is more dilute in both compounds but not devoid of them (Figure 29). This shows that the phase change is not a syneresis process as could be thought at first sight. We postulate that the appearance of a dense phase is due to the attraction between NPs themselves and to the fact that fibers are strongly anchored onto the enzymes covalently bound to the NPs. This observation is an important step since it represents a new behavior of such gels and will be of importance for future applications.

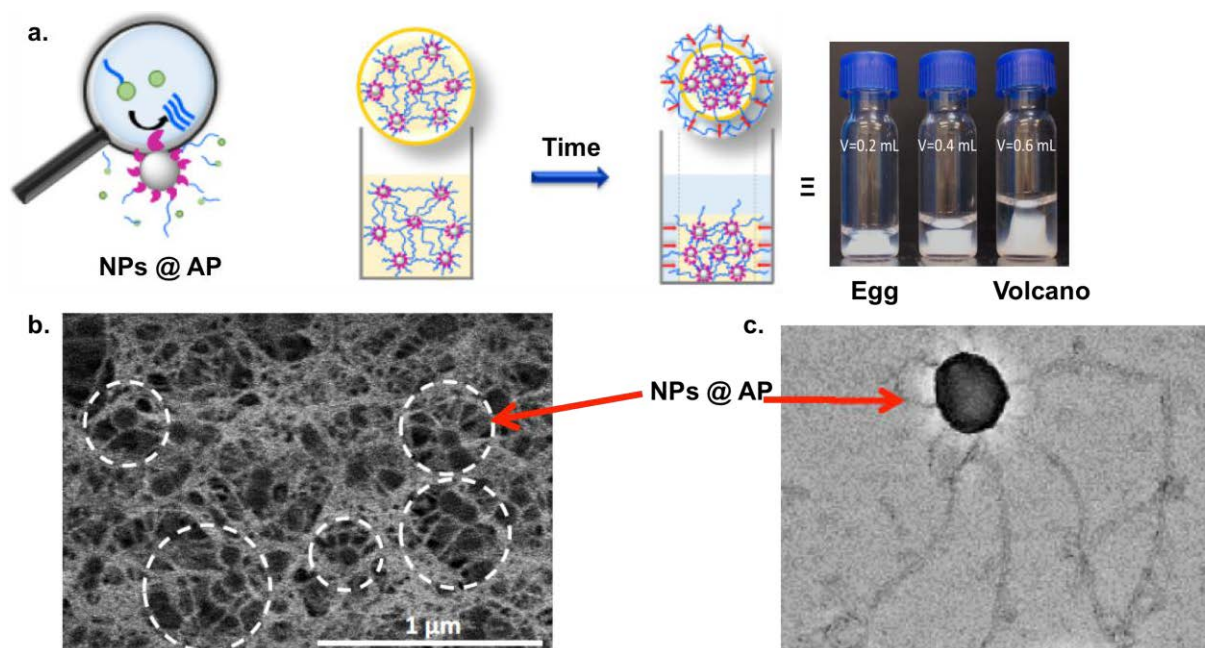


**Figure 2:** a) Scheme of the LEASA from NPs surface and the contraction effect of the resulting hydrogel giving rise to two different shapes, the "egg" and "volcano" shape. Highlights of the nanofibers that grow in all directions from NPs @ AP by b) Cryo-SEM and c) by TEM.

<sup>2</sup> Criado, M., *et al.*, Phase separation in supramolecular hydrogels based on peptide self-assembly from enzyme-coated nanoparticles, *Langmuir*, **2019**,



## Enzyme-assisted self-assembly within a hydrogel induced by peptide diffusion†

Cite this: *Chem. Commun.*, 2019, 55, 1156

Received 27th November 2018,  
Accepted 19th December 2018

DOI: 10.1039/c8cc09437c

rsc.li/chemcomm

Miryam Criado-Gonzalez,<sup>id abc</sup> Jennifer Rodon Fores,<sup>a</sup> Déborah Wagner,<sup>a</sup> André Pierre Schröder,<sup>a</sup> Alain Carvalho,<sup>a</sup> Marc Schmutz,<sup>id a</sup> Eva Harth,<sup>id d</sup> Pierre Schaaf,<sup>\*abc</sup> Loïc Jierry<sup>id \*a</sup> and Fouzia Boulmedais<sup>id \*a</sup>

**The diffusion of adequate peptide through an enzyme-embedded host hydrogel leads to the *in situ* start-up and growth of an interpenetrated fibrous network. Based on the enzyme-assisted self-assembly concept, both chemistry and mechanical features of the hybrid hydrogel can be tuned.**

Hydrogels have been used for decades as substrates for cell growth and tissue engineering.<sup>1</sup> Historically, they are based on cross-linked polymer networks and referred to as chemical gels or on polymer chains interacting through ionic or hydrogen bonds. The latter are referred to as physical gels. More recently, hydrogels were developed based on low molecular weight hydrogelators (LMWHs) capable of self-assembling into entangled fibrils through H bonding, van der Waals forces,  $\pi$ - $\pi$  interactions or metal-ligand bonds.<sup>2</sup> Over the last few years, it has become increasingly apparent that fine tuning of the mechanical and chemical properties of the substrate is of paramount importance in guiding cell fate.<sup>3</sup> In addition, tissues are also highly structured, presenting morphological, biochemical and mechanical gradients.<sup>4</sup> Thus, these features have led to the development of new types of hydrogels trying to mimic some of these properties. Among them, double networks using LMWHs are of great interest.<sup>5</sup> Generally this kind of hydrogel is composed of a polymer network interpenetrated with a supramolecular one both formed simultaneously in the bulk.<sup>6</sup> Such double networks can present mechanical properties that can closely match those of living tissues such as cartilage.<sup>7</sup> Of particular interest is their

enhanced mechanical damage resistance due to the energy dissipation under stress related to the weakness of the inter-molecular bonds and their reversible character. The self-assembled network of amino acids in a physical gel also allows control of the release of small molecules.<sup>7</sup> The next goal to achieve in this field is to design biomaterials in which the interpenetrated network could be started-up and grown when desired at specific and precise spatial locations in the host hydrogel (local or gradual positions), and with a fine control of the self-assembly evolution over time (growth, disassembly, periodicity). Indeed the control of spatio-temporal interaction between molecular entities in complex chemical environments is a *sine qua non* challenge to overpass toward the design of artificial biological tissues or organs.<sup>8</sup> One emerging way to this end is the use of reaction-diffusion processes in organic materials.<sup>9</sup> Up to now, only a few examples have highlighted the strength of the diffusion-reaction approach for spatial organization.<sup>10</sup> In particular, Eelkema, van Esch and coworkers have shown the possibility of the diffusion of hydrogelator precursors within a host material from defined positions.<sup>11</sup> Thanks to proton catalysis, precursors transform into hydrogelators that self-assemble, leading to macroscale objects with a control of their shape, size and chemical functionalities.

Herein, we demonstrated the possibility of using the diffusion of non-self-assembling compounds into an enzyme-embedded material to initiate the growth of a nanofibrous network specifically within the host material, thus changing both its chemical composition and mechanical properties. The enzyme located inside the host hydrogel spontaneously transforms the diffusing compound into a self-assembling building block, an approach called enzyme-assisted self-assembly (EASA), pioneered by Xu in 2004<sup>12</sup> and extended by Ulijn<sup>13</sup> and others.<sup>14</sup> More specifically, thanks to the diffusion of the tripeptide Fmoc-FFpY (Scheme 1a) into a poly(ethylene glycol) (PEG) hydrogel containing alkaline-phosphatase (AP), Fmoc-FFY is generated *in situ* through enzymatic dephosphorylation, which then self-assembles. Indeed, AP has been shown to transform Fmoc-FFpY into Fmoc-FFY efficiently, which self-assembles through  $\pi$ - $\pi$  stacking between the aromatic rings and H-bonding.<sup>14b</sup>

<sup>a</sup> Université de Strasbourg, CNRS, Institut Charles Sadron UPR 22,

67034 Strasbourg, France. E-mail: schaaf@unistra.fr,

Loic.Jierry@ics-cnrs.unistra.fr, fouzia.boulmedais@ics-cnrs.unistra.fr

<sup>b</sup> Institut National de la Santé et de la Recherche Médicale, UMR-S 1121,

“Biomatériaux et Bioingénierie”, 67087 Strasbourg, France

<sup>c</sup> Université de Strasbourg, Faculté de Chirurgie Dentaire, Fédération de Médecine

Translationnelle de Strasbourg and Fédération des Matériaux et Nanoscience

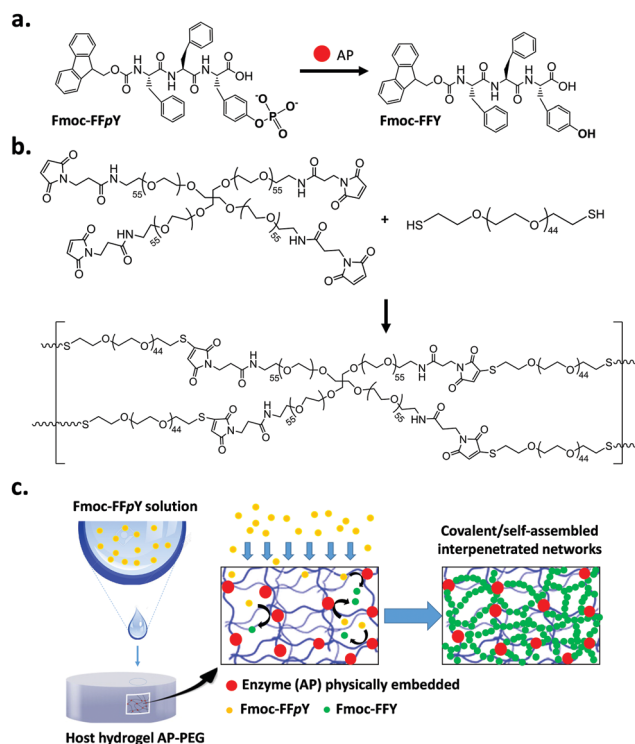
d’Alsace, 67000 Strasbourg, France

<sup>d</sup> Department of Chemistry, Center of Excellence in Polymer Chemistry,

University of Houston, Houston, Texas 77030, USA

† Electronic supplementary information (ESI) available. See DOI: 10.1039/c8cc09437c

## Communication



**Scheme 1** (a) Fmoc-FFpY dephosphorylation by AP yielding Fmoc-FFY; (b) covalent network of the PEG hydrogel through the thiol-ene click reaction between HS-PEG44-SH and 4-arm-PEG55 maleimide; (c) schematic representation of the hybrid covalent/self-assembled network designed through peptide diffusion within the AP-embedded host hydrogel.

The covalent PEG hydrogel was prepared through thiol-ene click chemistry by mixing a homobifunctional PEG thiol ( $M_w = 2$  kDa) and a 4-arm-PEG maleimide ( $M_w = 10$  kDa) in water (Scheme 1b).<sup>15</sup> An enzymatically active PEG gel, named AP-PEG, was obtained by physically trapping AP during PEG gel formation. Drops of Fmoc-FFpY solution can be deposited onto the surface of the enzymatically active covalent hydrogel AP-PEG. The diffusion of this solution occurs in a few minutes into the host gel (Scheme 1c).

First of all, AP was mixed in the PEG precursor solution before the covalent hydrogelation process (see the Material and methods section in the ESI†). Once the AP-PEG gel was obtained, we checked that the enzymatic activity of AP was maintained. *para*-Nitrophenyl phosphate (PNP) was used as the model substrate and a few drops of it were added on the AP-PEG gel. Thus, the enzymatic phosphate hydrolysis of PNP leading to the release of *para*-nitrophenol was monitored easily by UV spectrophotometry (Fig. S1 in the ESI†). One observes that AP remains active within the PEG gel. 25  $\mu\text{L}$  of Fmoc-FFpY solution (2.5  $\text{mg mL}^{-1}$ ) was then deposited on the top of the AP-PEG gel. The diffusion of Fmoc-FFpY within the enzymatically active host PEG gel takes place in a few minutes. The integrity of the host gel is maintained even after 24 hours, and its transparency as well, without a noticeable swelling effect (Fig. S2 in the ESI†).

The *in situ* formation of Fmoc-FFY and its resulting self-assembly were first evidenced by Fourier transformed infrared (FTIR)

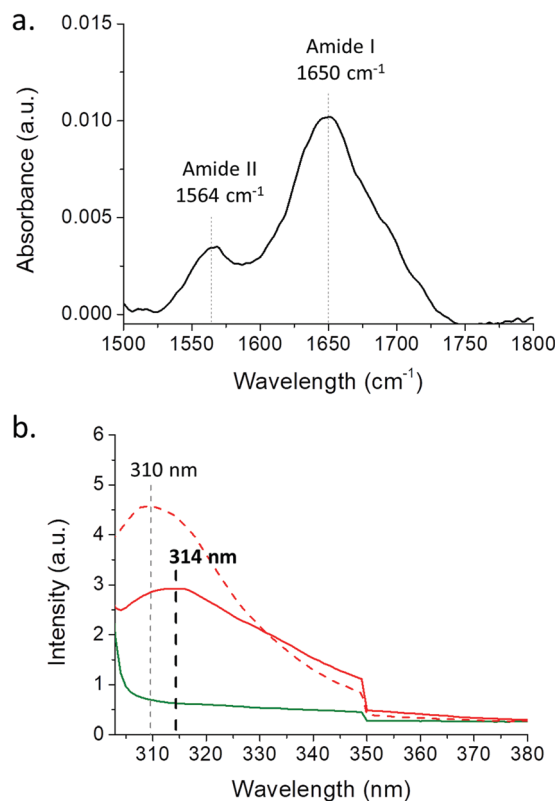


**Fig. 1** (a) FTIR spectrum of the AP-PEG hydrogel 24 h after the diffusion of Fmoc-FFpY (2.5  $\text{mg mL}^{-1}$ ) and (b) fluorescence emission spectra ( $\lambda_{\text{ex}} = 290$  nm) of the AP-PEG gel (solid green line), 1 h (dashed red line) and 24 h (solid red line) after the Fmoc-FFpY diffusion.

spectroscopy in the attenuated total reflection mode in deuterated water. FTIR spectra of the AP-PEG gel were recorded before and 24 h after the deposition of the Fmoc-FFpY solution. One observes a band at 1650  $\text{cm}^{-1}$  assigned to the carbonyl groups of the amide involved in the antiparallel  $\beta$ -sheet assemblies (Fig. 1a).<sup>14b,16</sup> Fluorescence emission spectroscopy was also performed to confirm the presence of the Fmoc excimer signature as usually observed in peptide-based self-assemblies generated in water.<sup>14b,17</sup> The Fmoc-FFpY solution exhibits a fluorescence emission at 310 nm when excited at 290 nm due to the presence of the Fmoc group. In the presence of AP, Fmoc-FFY self-assembly occurs and a shift of the fluorescence emission towards 314 nm is observed due to the Fmoc excimer formation (Fig. S3 in the ESI†). When 25  $\mu\text{L}$  of Fmoc-FFpY solution (2.5  $\text{mg mL}^{-1}$ ) is deposited onto the AP-PEG gel, a shift of the fluorescence emission from 310 nm at  $t = 0$  up to 314 nm at  $t = 24$  h is measured (Fig. 1b), similar to that observed in solution. No shifts were observed for Fmoc-FFpY diffusing within the PEG gel embedding no AP or when Fmoc-G, a non-self-assembling amino acid (G: glycine), was deposited onto the AP-PEG hydrogel (Fig. S3 in the ESI†). These control experiments show the physical presence of Fmoc-FFY self-assembly inside the host material and its specific generation in the presence of AP.

The formation of the supramolecular self-assembly of Fmoc-FFY within the AP-PEG gel was visualized by confocal laser

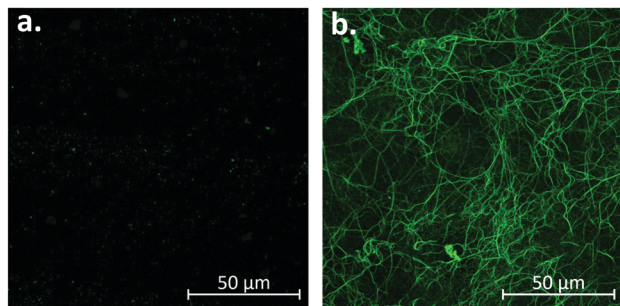


**Fig. 2** Confocal images of the AP-PEG gel containing ThT (a) before and (b) 24 h after the diffusion of 25  $\mu\text{L}$  of Fmoc-FFpY ( $2.5 \text{ mg mL}^{-1}$ ). The absence of fluorescence emission originating from ThT oligomerization is confirmed by (a).

scanning microscopy using Thioflavin T (ThT), a dye that reveals  $\beta$ -sheet secondary structures through a green emission of fluorescence intensity. First of all, it must be noted that the presence of ThT in the AP-PEG gel does not lead to fluorescence emission, thus excluding the potential artefact coming from the oligomerization of ThT (Fig. 2a). The diffusion of Fmoc-FFpY within the AP-PEG gel (containing ThT) results in a full green fluorescence emission in the whole material that did not allow observation of any structuration. This might be due to a highly dense stacking of the  $\beta$ -sheet moieties. However, the use of a lower concentration of ThT allows the observation of the formation of the network composed of several hundred micrometres long fibres (Fig. 2b and Fig. S4 in the ESI<sup>†</sup>). This entanglement of fibres having a homogeneous fluorescent fibrillary structure in the presence of ThT has spread throughout the gel according to the images taken at several micrometers depth (Fig. S5, ESI<sup>†</sup>). It must be noted that no fibrous network was observed at all in the absence of AP embedded in the host PEG gel (Fig. 2a) or when Fmoc-G diffused within the AP-PEG gel instead of Fmoc-FFpY (Fig. S8 in the ESI<sup>†</sup>). Because of the absorbance of AP-PEG in the spectral region from 190 to 240 nm, circular dichroism monitoring of the self-assembly process was not an adapted analytical method.

The morphology of the internal architecture of the hybrid covalent/self-assembled network was visualized by cryo scanning electron microscopy (Cryo-SEM). 24 h after the diffusion of Fmoc-FFpY within the AP-PEG gel, a highly dense fibrous network was observed (Fig. 3), similar to the one observed when AP and Fmoc-FFpY were mixed (Fig. S7 in the ESI<sup>†</sup>). Two levels of organization appear with micrometer fibers highly

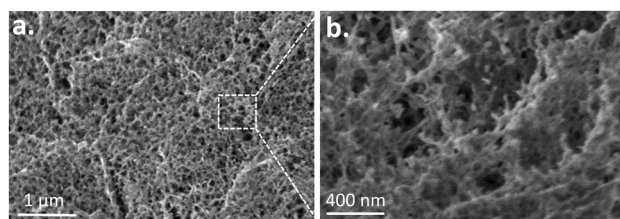


**Fig. 3** (a) Cryo-SEM images and (b) magnification of the AP-PEG hydrogel 24 h after the diffusion of 25  $\mu\text{L}$  of Fmoc-FFpY ( $2.5 \text{ mg mL}^{-1}$ ).

stacked together but also with isolated nanofibers showing diameters less than 100 nm. In contrast, it was not possible to image AP-PEG by cryo-SEM due to the difficulty in obtaining good freezing conditions, avoiding water crystallization. This could be explained by the weak crosslinking density of the organic matter in the AP-PEG gel. Thus, both fluorescence and cryo-SEM investigations have confirmed that the growth of nano and microstructures can be initiated and then grown within a host hydrogel using the enzyme-assisted self-assembly approach. As far as we know, the use of this strategy has never been reported.

Because the diffusion of a peptide inside the AP-PEG hydrogel can trigger a change in both the chemical composition and the internal morphology of the host gel, we can expect that its mechanical properties will also be affected. This was determined through dynamic oscillatory rheology as a function of frequency and strain providing information of the storage ( $G'$ ) and the loss moduli ( $G''$ ).  $G'$  is employed as an indicator of the elastic behaviour of the material by measuring the ability to store deformation energy, which can be recovered after removing the applied load.  $G''$  measures the deformation energy that is dissipated as heat and friction during the shearing process.<sup>18</sup> The AP-PEG gel shows a little frequency dependence at 0.06% strain up to 1 Hz. At a frequency of 1 Hz,  $G'$  (resp.  $G''$ ) takes a value of  $317 \pm 15 \text{ Pa}$  (resp.  $15 \pm 0.1 \text{ Pa}$ ). 24 hours after the diffusion of 25  $\mu\text{L}$  of Fmoc-FFpY solution ( $2.5 \text{ mg mL}^{-1}$ ) within the AP-PEG hydrogel, the  $G'$  value (resp.  $G''$ ) reaches  $436 \pm 35 \text{ Pa}$  (resp.  $33 \pm 6 \text{ Pa}$ ) (Fig. 4 and Fig. S8, Table S1 in the ESI<sup>†</sup>). When a lower concentration of Fmoc-FFpY ( $1 \text{ mg mL}^{-1}$ ) or a solution of a non-self-assembling compound such as Fmoc-G ( $2.5 \text{ mg mL}^{-1}$ ) was used, almost no variation of both  $G'$  and  $G''$  was observed. The generation of the self-assembled system within the host material increases the global network density, thus explaining the increase of the storage modulus after the diffusion of Fmoc-FFpY within the AP-PEG hydrogel. In addition, the doubling of the  $G''$  value compared to that of the AP-PEG hydrogel must be related to the ability of the peptide self-assembled network to dissipate energy under stress due to its non-covalent character (Fig. 4 and Fig. S9 in the ESI<sup>†</sup>).

In conclusion, we have shown that a tripeptide generated *in situ* within an enzymatically active chemical hydrogel can

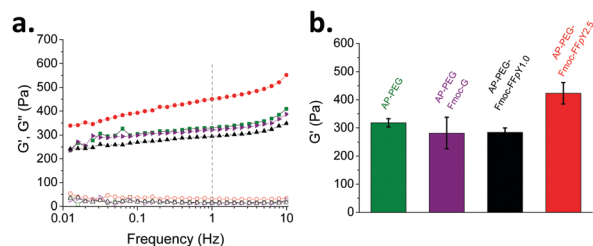


**Fig. 4** (a) Storage modulus ( $G'$  – solid symbols) and loss modulus ( $G''$  – hollow symbols) as a function of the frequency of the AP-PEG gel (■) before and after contact with (▲)  $1 \text{ mg mL}^{-1}$  Fmoc-FFpY, (●)  $2.5 \text{ mg mL}^{-1}$  Fmoc-FFpY or (▶)  $2.5 \text{ mg mL}^{-1}$  of Fmoc-G solutions for 24 h. (b) Storage modulus ( $G'$ ) at 1 Hz for the four samples studied. The results are shown as mean  $\pm$  sd ( $n = 3$ ).

self-assemble, giving rise to the formation of a supramolecular network inside the covalent host material. This interpenetrated network results from the local start-up and growth of the tripeptide-based nano and microfibers that change both the chemical constitution and the internal morphology of the material and also enhances the mechanical properties through the increase of the storage and loss moduli as well. The originality of this work relies on the possibility of initiating the formation of a secondary self-assembled network through an enzymatic trigger embedded within a material, an approach never reported so far. The control of the enzyme localization into a host 3D environment opens the gate to the spatial tuning of both the chemistry and the mechanical properties of the considered material. We believe that the locally controlled diffusion of chemicals leading to spatially defined architectures represents a powerful tool for complex chemical system development, the design of artificial cells or living tissues and thus can find applications in the field of tissue engineering and in mechanotransduction investigations.

M. C.-G. acknowledges the IDEX of the Université de Strasbourg for granting a post-doctoral fellowship. J. R. F. and D. W. acknowledge the International Center for Frontier Research in Chemistry (Labex CSC, PSC-016 and PSC-005) for PhD and Master funding, respectively. E. H. is grateful to the Région Alsace, Département du Bas-Rhin and the Communauté Urbaine de Strasbourg for the award of a Gutenberg Excellence Chair. The ICS microscopy platform is acknowledged for the use of the SEM instrument. We gratefully acknowledge the financial support from the Agence Nationale de la Recherche (EASA, ANR-18-CE06-0025-03) and the Institut Carnot-MICA.

## Conflicts of interest

There are no conflicts to declare.

## Notes and references

- 1 *Biomedical Applications of Hydrogels Handbook*, ed. R. M. Ottenbrite, K. Park and T. Okano, Springer, 2010.
- 2 N. M. Sangeetha and U. Maitra, *Chem. Soc. Rev.*, 2005, **34**, 821–836.
- 3 J. H. Wen, L. G. Vincent, A. Fuhrmann, Y. S. Choi, K. C. Hribar, H. Taylor-Weiner, S. Chen and A. J. Engler, *Nat. Mater.*, 2014, **13**, 979–987.

- 4 A. Seidi, M. Ramalingam, I. Elloumi-Hannachi, S. Ostrovidov and A. Khademhosseini, *Acta Biomater.*, 2011, **4**, 1441–1451.
- 5 E. R. Draper, E. G. B. Eden, T. O. McDonald and D. J. Adams, *Nat. Chem.*, 2015, **7**, 848–852; J. Wang, Z. Wang, J. Gao, L. Wang, Z. Yang, D. Kong and Z. Yang, *J. Mater. Chem.*, 2009, **19**, 7892–7896; J. Wang, X. Miao, Q. Fengzhao, C. Ren, Z. Yang and L. Wang, *RSC Adv.*, 2013, **3**, 16739–16746.
- 6 D. J. Cornwell and D. K. Smith, *Mater. Horiz.*, 2015, **2**, 279–293.
- 7 W. X. Sun, B. Xue, Y. Li, M. Qin, J. Y. Wu, K. Lu, J. H. Wu, Y. Cao, Q. Jiang and W. Wang, *Adv. Funct. Mater.*, 2016, **26**, 9044–9052.
- 8 K. Powell, *Nature*, 2018, **563**, 172–175.
- 9 S. Kondo and T. Miura, *Science*, 2010, **329**, 1616–1620; S. Soh, M. Byrska, K. Kandere-Grzybowska and B. Grzybowski, *Angew. Chem., Int. Ed.*, 2010, **49**, 4170–4198.
- 10 I. Ziemecka, G. J. M. Koper, A. G. L. Olive and J. H. van Esch, *Soft Matter*, 2013, **9**, 1556–1561; T. S. Shim, S. M. Yang and S. H. Kim, *Nat. Commun.*, 2015, **6**, 6584.
- 11 M. Lovrak, W. E. J. Hendriksen, C. Maity, S. Mytnyk, V. van Steijn, R. Eelkema and J. H. van Esch, *Nat. Commun.*, 2017, **8**, 15317.
- 12 Z. Yang, H. Gu, D. Fu, P. Gao, J. K. Lam and B. Xu, *Adv. Mater.*, 2004, **16**, 1440–1444.
- 13 R. J. Williams, A. M. Smith, R. Collins, N. Hodson, A. K. Das and R. V. Ulijn, *Nat. Nanotechnol.*, 2008, **4**, 19–24.
- 14 (a) J. R. Fores, M. L. M. Mendez, X. Y. Mao, D. Wagner, M. Schmutz, M. Rabineau, P. Lavalle, P. Schaaf, F. Boulmedais and L. Jierry, *Angew. Chem., Int. Ed.*, 2017, **56**, 15984–15988; (b) C. Vigier-Carriere, T. Garnier, D. Wagner, P. Lavalle, M. Rabineau, J. Hemmerlé, B. Senger, P. Schaaf, F. Boulmedais and L. Jierry, *Angew. Chem., Int. Ed.*, 2015, **54**, 10198–10201; (c) J. Gao, H. M. Wang, L. Wang, J. Y. Wang, D. L. Kong and Z. M. Yang, *J. Am. Chem. Soc.*, 2009, **131**, 11286–11287; (d) W. Wang, J. Qian, A. Tang, L. An, K. Zhong and G. Liang, *Anal. Chem.*, 2014, **86**, 5955–5961; (e) R. J. Williams, J. Gardiner, A. B. Sorensen, S. Marchesan, R. J. Mulder, K. M. McLean and P. G. Hartley, *Aust. J. Chem.*, 2013, **66**, 572–578; (f) S. C. Bremmer, J. Chen, A. J. McNeil and M. B. Soellner, *Chem. Commun.*, 2012, **48**, 5482–5484; (g) X. Qin, W. Xie, S. Tian, J. Cai, H. Yuan, Z. Yu, G. L. Butterfoss, A. C. Khuong and R. A. Gross, *Chem. Commun.*, 2013, **49**, 4839–4841; (h) L. Chropoulou, S. Lorenzoni, G. Masci, M. Dentini, A. R. Togna, G. Togna, F. Bondi and C. Palocci, *Soft Matter*, 2010, **6**, 2525–2532; (i) Y. Liu, V. Javvaji, S. R. Raghavan, W. E. Bentley and G. F. Payne, *J. Agric. Food Chem.*, 2012, **60**, 8963–8967; (j) S. Sakai, K. Komatani and M. Taya, *RSC Adv.*, 2012, **2**, 1502–1507.
- 15 J. Yu, X. Xu, F. Yao, Z. Luo, L. Jin, B. Xie, S. Shi, H. Ma, X. Li and H. Chen, *Int. J. Pharm.*, 2014, **470**, 151–157.
- 16 N. Yamada, K. Ariga, M. Naito, K. Matsubara and E. Koyama, *J. Am. Chem. Soc.*, 1998, **120**, 12192–12199.
- 17 A. M. Smith, R. J. Williams, C. Tang, P. Coppo, R. F. Collins, M. L. Turner, A. Saiani and R. V. Ulijn, *Adv. Mater.*, 2008, **20**, 37–41.
- 18 M. A. Meyers and K. K. Chawla, *Mechanical Behavior of Materials*, Prentice Hall, Englewood Cliffs, NJ, 1998; J. M. Anderson, A. Andukuri, D. J. Lim and H.-W. Jun, *ACS Nano*, 2009, **3**, 3447–3454.

# Phase Separation in Supramolecular Hydrogels Based on Peptide Self-Assembly from Enzyme-Coated Nanoparticles

Miryam Criado-Gonzalez,<sup>†,‡,§</sup> Jennifer Rodon Fores,<sup>†</sup> Alain Carvalho,<sup>†</sup> Christian Blanck,<sup>†</sup> Marc Schmutz,<sup>†</sup> Leyla Kocgozlu,<sup>‡,§</sup> Pierre Schaaf,<sup>\*,†,‡,§</sup> Loïc JERRY,<sup>\*,†</sup> and Fouzia Boulmedais<sup>†</sup>

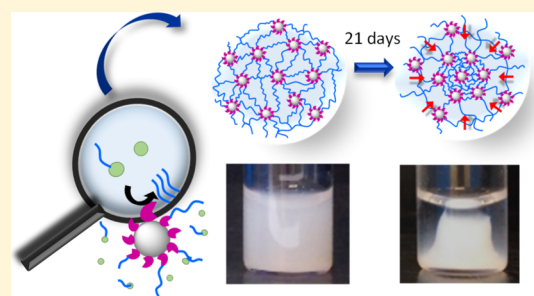
<sup>†</sup>Université de Strasbourg, CNRS, Institut Charles Sadron UPR 22, 67034 Strasbourg, France

<sup>‡</sup>Institut National de la Santé et de la Recherche Médicale, UMR-S 1121, “Biomatériaux et Bioingénierie”, 67087 Strasbourg, France

<sup>§</sup>Université de Strasbourg, Faculté de Chirurgie Dentaire, Fédération de Médecine Translationnelle de Strasbourg and Fédération des Matériaux et Nanoscience d’Alsace, 67000 Strasbourg, France

## Supporting Information

**ABSTRACT:** Spatial localization of biocatalysts, such as enzymes, has recently proven to be an effective process to direct supramolecular self-assemblies in a spatiotemporal way. In this work, silica nanoparticles (NPs) functionalized covalently by alkaline phosphatase (NPs@AP) induce the localized growth of self-assembled peptide nanofibers from NPs by dephosphorylation of Fmoc–FFpY peptides (Fmoc: fluorenylmethyloxycarbonyl; F: phenylalanine; Y: tyrosine; p: phosphate group). The fibrillary nanoarchitecture around NPs@AP underpins a homogeneous hydrogel, which unexpectedly undergoes a macroscopic shape change over time. This macroscopic change is due to a phase separation leading to a dense phase (in NPs and nanofibers) in the center of the vial and surrounded by a dilute one, which still contains NPs and peptide self-assemblies. We thus hypothesize that the phase separation is not a syneresis process. Such a change is only observed when the enzymes are localized on the NPs. The dense phase contracts with time until reaching a constant volume after several days. For a given phosphorylated peptide concentration, the dense phase contracts faster when the NPs@AP concentration is increased. For a given NPs@AP concentration, it condenses faster when the peptide concentration increases. We hypothesize that the appearance of a dense phase is not only due to attractive interactions between NPs@AP but also to the strong interactions of self-assembled peptide nanofibers with the enzymes, covalently fixed on the NPs.



## INTRODUCTION

In a highly simplified vision, living organisms can be considered as assemblies of multi-stimuli responsive systems able to adapt to surrounding environmental changes. Stimulated by the ambition to create artificial living matter,<sup>1–8</sup> the research community has focused its investigations toward the design of materials sensitive to external stimuli.<sup>9</sup> Mainly through bioinspired strategies, this engagement has given rise to the so-called class of smart materials. Currently, one main challenge is to control this responsiveness in space and over time.<sup>10–15</sup> Along this route, spatial localization of (bio)-catalysts has recently proven to be an effective process to direct supramolecular self-assemblies in a spatiotemporal way.<sup>16–20</sup> Localization of (bio)catalysts in space allows inducing the chemical switch from non-self-assembling entities into self-assembling ones, leading to a spontaneous self-assembly process occurring exclusively and specifically near the (bio)-catalyst localization. Ulijn and co-workers have first shown that the immobilization of thermolysin on a glass substrate followed by the contact with a mixture of fluorenylmethyloxycarbonyl (Fmoc)–L and LL dipeptide (L = leucine) allows the self-assembly nucleation of Fmoc–L<sub>n</sub> spatially controlled from the

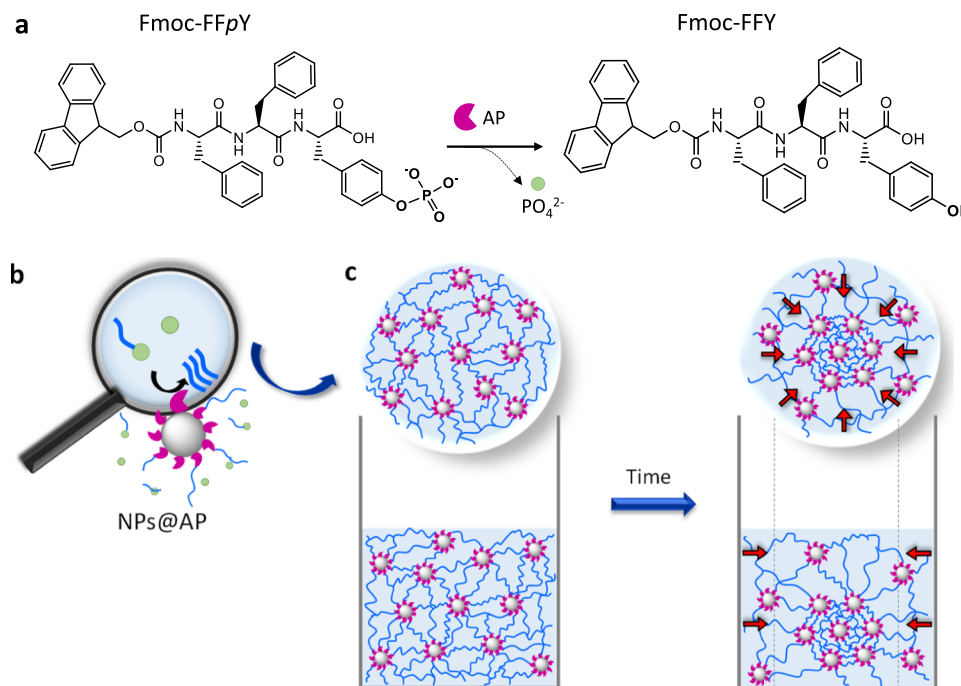
enzymatically active surface.<sup>21</sup> This approach has been successfully used to entrap laminin inside a localized hydrogel for therapeutic applications.<sup>22</sup> Recent works using different enzyme/peptide systems showed that by adsorbing the enzymes on multilayer films, the resulting self-assembled nanoarchitecture can be tuned by playing on various parameters such as the enzyme density,<sup>23</sup> the presence of a seeding layer,<sup>24</sup> or the glucose concentration for instance.<sup>25</sup> In 2018, the group of van Esch showed that the growth of supramolecular fibers can be spatially localized at the nanoscale by using negatively charged polystyrene nanoparticles (NPs) facilitating the acid-catalyzed formation of hydrogelators.<sup>26</sup> The properties of the resulting gel (gelation time, mechanical properties, and network morphology) have been modified by the presence of NPs. Wang et al. described the development of core–shell nanogels using the self-assembly of a suitable peptide on silica NPs previously functionalized by enzymes.<sup>27</sup> Conte et al. reported also the covalent grafting of enzymes

Received: May 13, 2019

Revised: July 23, 2019

Published: July 23, 2019

**Scheme 1. (a) Fmoc–FFpY Dephosphorylation by AP Leading to the Gelator Fmoc–FFY: Schematic Representations of (b) Fmoc–FFY Nanofibers (in Blue) Self-Assembled from NPs@AP by Dephosphorylation of Fmoc–FFpY Leading to (c) a Hybrid Supramolecular Hydrogel Undergoing a Phase Separation Over Time**



onto magnetic NPs, allowing the nucleation of self-assembled nanofibers from the surface of NPs using a suitable hydrogelator precursor.<sup>28</sup> The resulting hydrogel could be macroscopically deformed through the simple external use of a magnet placed near the vial containing the hydrogel. A permanent new shape was obtained after 1 month of interaction with a magnetic field, resulting in a squeezing of the initial NP-based hydrogel, separating it from water.

Here, we report the design of a hybrid supramolecular hydrogel prepared from the Fmoc–FFpY tripeptide (F: phenylalanine, Y: tyrosine, p: phosphate group) and silica NPs functionalized covalently by alkaline phosphatase (AP). AP transforms Fmoc–FFpY into Fmoc–FFY, an efficient hydrogelator, able to self-assemble spontaneously and exclusively from the surface of NPs, leading to the formation of a homogeneous nanofibrous network (Scheme 1). Unexpectedly, the hybrid supramolecular hydrogel undergoes a macroscopic change over time because of a phase separation leading to one phase, in the center of the vial, denser in NPs and in peptide fibers than the other surrounding phase.

## MATERIALS AND METHODS

**Materials.** Tetraethyl orthosilicate (TEOS), (3-glycidioxypropyl)trimethoxysilane (GPMS), phosphatase alkaline from bovine intestinal mucosa (AP) (10 DEA units/mg protein), and the *p*-nitrophenyl phosphate (PNP) liquid substrate system were provided by Sigma-Aldrich. Sodium tetraborate anhydrous (borax) and dry toluene were supplied by Acros Organics. Fmoc–FFpY was purchased from PepMic, ammonium hydroxide from Carlo Erba, and ethanol from VWR.

**Synthesis and Functionalization of Silica NPs.** Silica NPs were synthesized following the procedure described elsewhere.<sup>29,30</sup> Briefly, 80 mL of ethanol, 4.85 mL of Milli-Q water, and 3.6 mL of NH<sub>4</sub>OH were mixed in a two-neck flask under mechanical stirring (400 rpm) and heated up to 55 °C. When the temperature is reached, 8 mL of ethanol and 3.1 mL of TEOS, mixed in a separated vial, were added

quickly to the previous solution and kept under stirring for 5 h. In a second step, in order to obtain larger NPs from the first synthesis (~80 nm), 10 mL of the NP colloidal suspension was mixed with 70 mL of ethanol, 13 mL of Milli-Q water, and 7.5 mL of NH<sub>4</sub>OH in a two-neck flask and heated again up to 55 °C under mechanical stirring (400 rpm). When the temperature was reached, a mixture of 10 mL of ethanol and 1 mL of TEOS was added dropwise to the solution and kept under stirring for 5 h. Subsequently, the solution was centrifuged (6000 rpm, 20 min) and the precipitate of NPs was washed three times with ethanol by centrifugation (6000 rpm, 20 min). For the covalent immobilization of AP, 2.5 mL of NPs was dried at 100 °C under argon atmosphere for 2 h in a 50 mL flask. Then, 10 mL of 5% v/v GPMS in dry toluene was added to dry NPs. The suspension was sonicated for 10 min to avoid aggregates and kept shaking at 720 rpm overnight at room temperature. The obtained epoxy-functionalized NPs were centrifuged and the precipitate was first washed three times with toluene to remove unbound GPMS and subsequently, three times with ethanol to remove toluene. The final NPs were dispersed in 1 mL of ethanol and subsequently added dropwise to an aqueous solution of AP [1 mg mL<sup>-1</sup> in borax buffer (25 mM, pH = 9.5)] and kept shaking for 24 h at 4 °C. Then, the NPs were centrifuged and washed five times with borax buffer (25 mM, pH = 9.5) to remove the unbound enzyme. NPs@AP showed an activity equivalent to 30 units mL<sup>-1</sup> with a solid content of 5% (w/v). Finally, NPs@AP were re-dispersed in 1 mL of borax buffer (25 mM, pH = 9.5) and stored at 4 °C until needed.

**Dynamic Light Scattering.** Dynamic light scattering (DLS) experiments were carried out in a Malvern Nanosizer ZS with a measurement angle of 173° and collecting five spectra per sample at 25 °C. To determine the hydrodynamic diameter of NPs, 7 μL of as-prepared NPs (5% w/v) were diluted in 1.4 mL of ethanol. Kinetic measurements were carried out by placing first in a plastic cuvette 7 μL of NPs@AP (5% w/v) diluted in 400 μL borax buffer (25 mM, pH = 9.5) and then, 1 mL of Fmoc–FFpY [0.1 and 1 mg mL<sup>-1</sup> in borax buffer (25 mM, pH = 9.5)]. Spectra were recorded at different time intervals. The autocorrelation function was converted into an intensity particle size distribution using ZetaSizer Software 7.10 version. To obtain the average hydrodynamic diameter values using the Stokes–Einstein equation, it was assumed that the particles were spherical.

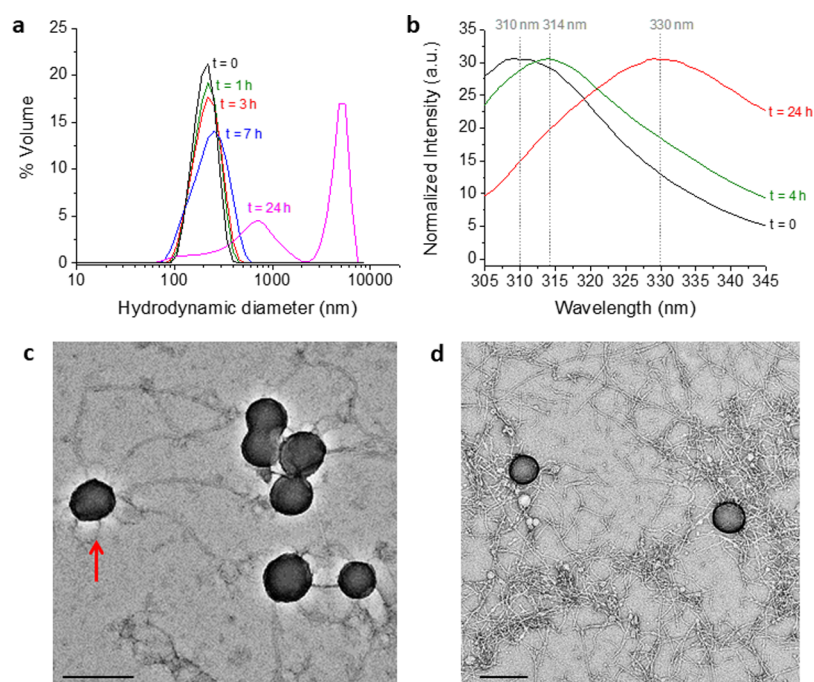


**Figure 1.** (a) Evolution of the hydrodynamic diameter, measured by DLS, as a function of time of NPs@AP (0.03% w/v, equiv [AP] = 0.2 units  $\text{mL}^{-1}$ ) in contact with  $0.1 \text{ mg mL}^{-1}$  Fmoc-FFpY. (b) Fluorescence emission spectra ( $\lambda_{\text{ex}} = 290 \text{ nm}$ ) of Fmoc-FFpY in the absence (black line) and in the presence of NPs@AP (1.25% w/v, equiv [AP] = 7.5 units  $\text{mL}^{-1}$ ) after 4 h (green line) and 24 h (red line). (c) TEM images of Fmoc-FFY fibers formed from NPs@AP after 1 h and (d) 4 h. The scale bars represent 200 nm. The arrow in (c) highlights the nanofibers that grow in all directions from NPs@AP.

**Transmission Electron Microscopy.** Transmission electron microscopy (TEM) images were taken in a Technai G2 machine in negative coloration. To determine the average size of NPs,  $10 \mu\text{L}$  of a diluted solution of NPs in ethanol was placed over a carbon-coated copper grid. To observe the peptide fibers,  $5 \mu\text{L}$  of NPs@AP (0.03% w/v) was dropped on the grid followed by the addition of  $5 \mu\text{L}$  of Fmoc-FFpY  $0.1 \text{ mg mL}^{-1}$  in borax buffer (25 mM, pH = 9.5) for 30 min before observation.

**Infrared Spectroscopy.** The Fourier transform infrared (FTIR) experiments were performed on a Vertex 70 spectrometer (Bruker, Germany) using a DTGS detector. Spectra were recorded in attenuated total reflection (ATR) mode by collecting 128 interferograms between 600 and  $4000 \text{ cm}^{-1}$  at a  $2 \text{ cm}^{-1}$  resolution, using Blackman-Harris three-term apodization and the standard Bruker OPUS/IR software (version 7.5). For NPs and NPs@AP,  $200 \mu\text{L}$  of each solution was dried before recording the spectra. In the case of the Fmoc-FFpY solution ( $10 \text{ mg mL}^{-1}$ ) and the Fmoc-FFY hydrogel, obtained from a mixture of 1.25% w/v NPs@AP (equiv [AP] = 7.5 units  $\text{mL}^{-1}$ ) and  $1 \text{ mg mL}^{-1}$  Fmoc-FFpY, samples were prepared in deuterated water.

**UV Spectroscopy.** The enzymatic activity of NPs@AP was determined by measuring the absorbance at  $\lambda = 405 \text{ nm}$  as a function of time using a microplate reader UV spectroscopy (FLX-Xenius, SAFAS, Monaco). PNP is a colorless substrate, which, by sequential enzymatic hydrolysis of the phosphate substituent of PNP in the presence of AP, yields a yellow absorbance at  $\lambda = 405 \text{ nm}$ . Incubation of  $150 \mu\text{L}$  (at 1 mM in borax buffer) of PNP was performed for different concentrations of AP in solution to determine the calibration curve, i.e., slope of the absorbance versus time as a function of AP concentration. The slope obtained for the NPs@AP solution in contact with PNP allows to determine the concentration in AP. The concentration and volume used ensure a large excess of substrate for the enzymatic reaction.

**Fluorescence Spectroscopy.** All fluorescence spectra were recorded between 305 and 345 nm using the microreader fluorescence spectroscope (FLX-Xenius, SAFAS, Monaco) at an excitation wavelength of 290 nm and a specific 96 well-plate. NPs@

AP ( $50 \mu\text{L}$ , 5% w/v) was put in contact with  $150 \mu\text{L}$  of  $1 \text{ mg mL}^{-1}$  Fmoc-FFpY solution to allow the formation of the Fmoc excimer because of the Fmoc-FFY self-assembly.

**Hydrogel Formation.** All solutions were prepared in borax buffer (25 mM, pH = 9.5). Fmoc-FFpY ( $150 \mu\text{L}$ ) was mixed with  $50 \mu\text{L}$  of one of the following compounds: AP, NPs, or NPs@AP in vials. After 24, 48, and 72 h, inverted tube tests were carried out to determine the hydrogel formation. Fmoc-G was used as control.

**Scanning Electron Microscopy and Cryo-SEM.** To observe the morphology of the gels, a specific cryo-holder and a cryo-preparation chamber were designed and manufactured by the mechanical facility of the Charles Sadron Institute.<sup>23</sup> A piece of the gel was placed on the cryo-holder to be quickly plunged into an ethane slush. As the sample is free-standing over the holder, the sample is rapidly frozen during the plunging by direct contact with the liquid ethane. Subsequently, the sample is transferred into the Quorum PT 3010 chamber attached to the microscope. There, the frozen sample is fractured with a razor blade. A slight etching at  $-90 \text{ }^\circ\text{C}$  may be performed to render the fibers more visible. The sample is eventually transferred to the FEG-cryo scanning electron microscope (Hitachi SU8010) and observed at 1 kV at  $-150 \text{ }^\circ\text{C}$ .

**Analytic High-Performance Liquid Chromatography.** High-performance liquid chromatography (HPLC) was carried out with 1100 Series from Agilent Technologies. The column is a Supelcosil ABZ + Plus with the following dimensions  $15 \text{ cm} \times 4.6 \text{ mm}$ ,  $3 \mu\text{m}$ . The eluent used for all analyses was acetonitrile/deionized water in a ratio of 90/10 in isocratic conditions, at  $1 \text{ mL min}^{-1}$  with a run time of 25 min. Chromatograms were recorded by the software OpenLab Agilent 1100. The preparation of the samples was carried out by diluting  $90 \mu\text{L}$  of the corresponding phase of the “volcano”-like gels, phase A or phase B, in  $310 \mu\text{L}$  of acetonitrile. The resulting solution was filtered using a PTFE  $0.2 \mu\text{m}$  filter before injection.

**Circular Dichroism.** Circular dichroism (CD) spectra were recorded using a Jasco J-1100 spectropolarimeter with a data pitch of 1 nm on the light wavelength. For measurements,  $40 \mu\text{L}$  of phase A or phase B from the contracted “volcano”-like hydrogels, formed by contact of Fmoc-FFpY ( $1.0 \text{ mg mL}^{-1}$ ) with NPs@AP (1.25% w/v,



equiv [AP] = 2.5 units mL<sup>-1</sup>), was placed between two quartz slides of 1 mm thickness.

## RESULTS AND DISCUSSION

**Self-Assembly of Peptide on NPs@AP in Diluted Solution.** We first synthesized silica NPs with an average size of  $117.5 \pm 6.1$  nm and a hydrodynamic diameter of  $\sim 155$  nm following a reported procedure<sup>12</sup> (Figure S1 in the Supporting Information). Subsequently, AP was covalently grafted on the surface of the silica NPs using an epoxy silane coupling agent, giving rise to NPs@AP. The presence of AP on the silica NPs was first confirmed by FTIR spectroscopy (Figure S2 in the Supporting Information) showing a band centered at 1633 cm<sup>-1</sup> corresponding to the amine I band of AP. The catalytic activity of NPs@AP was checked using PNP as a model substrate. After establishing the calibration curve of the enzyme free in solution (catalytic activity vs AP concentration), the concentration of active AP grafted on NPs was determined before and after several rinsing steps with the buffer (Figure S3 in the Supporting Information). Several rinsing steps ensured that all the enzymes were firmly fixed on the NPs. After five rinsing steps based on centrifugation and resuspension cycles in the buffer, the supernatant showed no detectable enzymatic activity. NPs@AP suspension with a solid content of 5% (w/v) was obtained with an equivalent activity in AP between 10 and 30 units mL<sup>-1</sup>, depending on the batch. Once the enzyme was localized on the surface of the NPs, these were employed as catalytic supports for the localized growth of peptide supramolecular hydrogels. For that purpose, the low-molecular-weight hydrogelator Fmoc-FFpY was generated in situ by enzymatic dephosphorylation of Fmoc-FFpY in the presence of NPs@AP (Scheme 1a). All experiments were performed at room temperature (20 °C).

The formation of self-assembled peptide networks over time around the NPs@AP was first followed by DLS using an NPs@AP solution diluted at 0.03% w/v (equiv [AP] = 0.2 units mL<sup>-1</sup>) and two different concentrations of Fmoc-FFpY, 0.1 mg mL<sup>-1</sup> (Figure 1a) and 1 mg mL<sup>-1</sup> (Figure S4 in the Supporting Information). These two peptide concentrations did not lead to a gel formation allowing DLS measurements. At 0.1 mg mL<sup>-1</sup> of Fmoc-FFpY, the hydrodynamic diameter of NPs@AP increased roughly from 220 nm up to 260 nm after 7 h (Figure 1a). After 24 h, two different peaks were observed, one centered at 705 nm and the other at 5  $\mu$ m. The initial increase of the hydrodynamic diameter from 220 to 260 nm in 7 h should be due to the formation and growth of the nanofiber networks around the NPs leading to the peak centered at 705 nm after 24 h. The peak centered at 5  $\mu$ m could be due to the formation of nanogels constituted of several NPs surrounded by their fibrous peptide networks. This effect is more pronounced in the case of a higher concentration of Fmoc-FFpY, 1 mg mL<sup>-1</sup> showing a faster increase of the hydrodynamic diameter of NPs@AP after the contact with Fmoc-FFpY and a faster appearance of the second peak (Figure S4a in the Supporting Information). It must be noticed that the given sizes are obtained by applying the model of a Brownian sphere and thus should not be taken as representing rigorously the size of the scattering object but only reflecting their average hydrodynamic size. They nevertheless show a trend: the self-assembly leads to a continuous increase of size of the particles, indicating the formation of a network around the NPs.

The in situ formation of Fmoc-FFY and its resulting self-assembly was evidenced by the presence of the Fmoc excimer signature, usually observed in peptide-based self-assemblies in water using fluorescence emission spectroscopy (Figure 1b).<sup>24,31</sup> The Fmoc-FFpY solution ( $t = 0$ ) exhibits an emission of fluorescence centered at 310 nm when excited at 290 nm because of the presence of the aromatic Fmoc group. In the presence of NPs@AP (1.25% w/v, equiv [AP] = 7.5 units mL<sup>-1</sup>), a shift of the fluorescence emission takes place over time, 314 nm after 4 h and 330 nm after 24 h, because of the Fmoc excimer formation, indicating Fmoc-FFY self-assembly. Using the same AP concentration in solution (7.5 units mL<sup>-1</sup>), the Fmoc excimer formation is faster when AP is located on the surface of the silica NPs than when free in solution (Figure S5 in the Supporting Information). In the latter case, a slight shift up to 317 nm is observed after 24 h and it is necessary to wait until 48 h to observe the shift at 330 nm. This can be due to a local enhancement of the enzyme concentration when adsorbed on NPs, in agreement with previous reported work.<sup>28</sup>

The formation of the self-assembled peptide fibers from NPs@AP was also characterized by TEM to observe the growth of the nanofibers from AP-coated NPs. A diluted concentration of NPs@AP, i.e. 0.03% w/v (equiv [AP] = 0.2 units mL<sup>-1</sup>), was put in contact on a TEM grid followed by a drop of Fmoc-FFpY (1 mg mL<sup>-1</sup>). After 1 and 4 h, the sample was dried before measurement. Several micrometer-long fibers (10 nm in diameter) were observed, often originating from the surfaces of the NPs (Figure 1c,d). An increase in the density of fibers is observed with time, giving rise to a denser network. No fibers were observed in areas without NPs, supporting the idea that fibers are formed only from AP-coated NPs.

**Hybrid Supramolecular Hydrogel Obtained from the NPs@AP Concentrated Solution.** The formation of Fmoc-FFY self-assembled hydrogels from NPs@AP was then studied by varying the quantity of NPs@AP between 0.12 and 2.5% w/v (equiv AP concentration between 1 and 15 units mL<sup>-1</sup>) while keeping constant the peptide concentration at 1 mg mL<sup>-1</sup>. Hydrogelation tests were performed in glass vials. After 24 h of contact between NPs@AP and Fmoc-FFpY at room temperature, the inverted vial test was performed (Figure 2).

No gelation was observed below 0.12% w/v of NPs@AP, whereas gels were formed above 0.25% w/v. To prove that gelation comes from the dephosphorylation of Fmoc-FFpY in the presence of AP located on the surface of the silica NPs, two

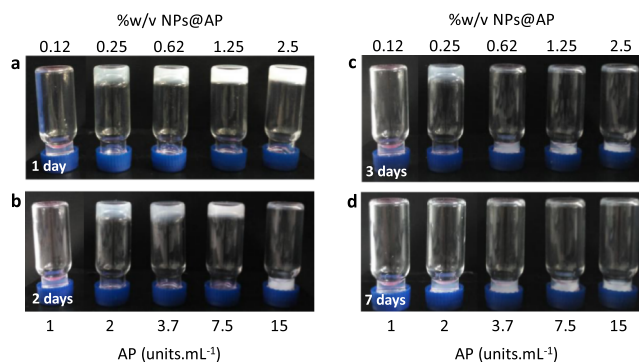


**Figure 2.** Inverted tube tests of Fmoc-FFpY (1 mg mL<sup>-1</sup>) in contact with different concentrations of NPs@AP, with the equivalent in AP concentration, after (a) 1 day, (b) 2 days, (c) 3 days, and (d) 7 days.

experiments were carried out. Fmoc-FFpY (1 mg mL<sup>-1</sup>) was put in contact with non-functionalized NPs (1.25% w/v), i.e., in the absence of grafted enzymes. Fmoc-G (G: glycine), a peptide which does not self-assemble in the presence of AP, was brought in contact with NPs@AP (1.25% w/v, equiv 7.5 units mL<sup>-1</sup>). After 24 h, in both cases, no gelation was observed (Figure S6 in the Supporting Information) and NPs sedimented on the bottom of the vial. FTIR spectra of short peptides are sensitive to their secondary structure, especially in the amide I region (1600–1700 cm<sup>-1</sup>).<sup>32</sup> In solution, the Fmoc-FFpY spectrum shows a broad amide I band (CO-NH) centered around 1645 cm<sup>-1</sup>, which is commonly assigned to disordered amide groups. A broad carboxylate (COO<sup>-</sup>) vibrational band is also visible at 1590 cm<sup>-1</sup> related to the deprotonated form of the terminal carboxylic acid groups (Figure S7 in the Supporting Information). The peak at 1685 cm<sup>-1</sup> is assigned to carbamate moiety. In the case of the Fmoc-FFY hydrogel formed with NPs@AP, we observed a shift of the amide I band to a lower frequency (1632 cm<sup>-1</sup>), which is the signature of aggregation via intermolecular hydrogen bonding, i.e.,  $\beta$ -sheet structure.<sup>33</sup> At the same time, the carboxylate and carbamate peaks are shifted to higher frequencies, 1595 and 1687 cm<sup>-1</sup>, respectively.

Unexpectedly, the hybrid hydrogels dropped down when the vials were inverted after few days (Figure 2), happening faster when the NPs@AP concentration is increased. For example, the falling down is observed after 7 days at 0.25% w/v NPs@AP and only 2 days at 2.5% w/v suspension. This phenomenon is due to a phase separation in the vial, which takes place over time, leading to two phases: one phase appears highly opaque, white, and centered in the vial (phase A) and the other is transparent and colorless (phase B), surrounding phase A (Figure 3).

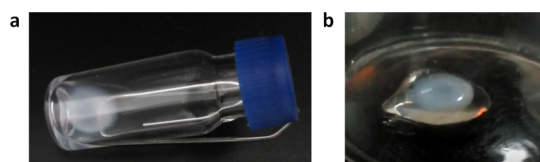


**Figure 3.** Hydrogel, obtained from a mixture of 1.25% w/v NPs@AP (equiv [AP] = 7.5 units mL<sup>-1</sup>) and 1 mg mL<sup>-1</sup> Fmoc-FFpY, which underwent a phase separation after 2 days (a) observed in a vial and (b) observed after its transfer in a Petri dish.

As can be seen on Movie V1 in Supporting Information, phases A and B look like the yellow and the white part of an “egg”, the opaque and dense phase A being embedded in the transparent and viscous phase B. Phase B behaves as the white part of an egg when manipulated with a spatula. This phase separation leads to less adhesion between the initially (bulky) formed hydrogel and the walls of the vial, resulting in its falling down when the vial is inverted. It must be noted that in the absence of NPs, a transparent hydrogel stable over 2 weeks is obtained using Fmoc-FFpY (1 mg mL<sup>-1</sup>) and AP in solution (Figure S8 in the Supporting Information).

The morphology of the gel obtained using 1.25% w/v of NPs@AP (equiv [AP] = 7.5 units mL<sup>-1</sup>) was visualized by cryo-SEM (Figures 4a and S9–10 in the Supporting Information). After 24 h, a homogeneous density of the fiber-network in the whole gel is observed. Thinner fibers have a diameter of around 30 nm. Magnification of the image allowed to distinguish isolated NPs in dark gray color with a

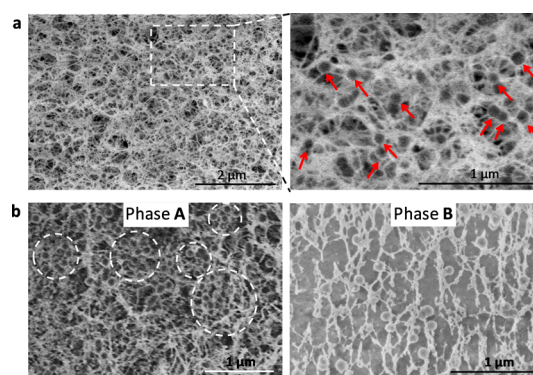


**Figure 4.** Cryo-SEM images of the Fmoc-FFY hydrogel, obtained from a mixture of 1.25% w/v NPs@AP (equiv [AP] = 7.5 units mL<sup>-1</sup>) and 1 mg mL<sup>-1</sup> Fmoc-FFpY, observed after (a) 24 h (left) and zoom-in highlighting single NPs with red arrows (right) and (b) 2 days with the phase A (left) and phase B (right) of the “egg”-like phase separation over time.

perfectly circular shape (Figure 4a right), similar to the size of isolated NPs@AP (Figure S11 in the Supporting Information). NPs play the role of cross-linking points within the 3D fibrous network and are present in the entanglements in the whole hydrogel network. For comparison, a cryo-SEM image of a gel obtained without NPs, that is, by mixing 5 mg mL<sup>-1</sup> of Fmoc-FFpY and AP (10 units mL<sup>-1</sup>), shows a homogeneous fibrillary structure with noncircular holes (Figure S12 in the Supporting Information). After 3 days of allowing the phase separation, the morphologies of phases A and B obtained from the “egg”-like gel were also observed (Figures 4b and S10 in the Supporting Information).

Phase A shows a higher density in Fmoc-FFY fibers and in NPs@AP with the presence of more NP aggregates in comparison to the bulky gel observed after 24 h. Phase B is characterized by a much lower density of both nanofibers and NPs@AP, the density difference being even larger when compared to the dense phase A. This is expected because of conservation of matter. These observations justify the term “dense” and “dilute” to describe phases A and B. This is schematically represented in Scheme 1c.

Keeping the NPs@AP concentration fixed at 1.25% w/v (equiv [AP] = 7.5 units mL<sup>-1</sup>), a faster phase separation is obtained by decreasing the peptide concentration from 2.5 to 0.5 mg mL<sup>-1</sup> (Figure 5).

Two different batches of NPs@AP, with an enzymatic activity of 30 and 10 units mL<sup>-1</sup> for a suspension of 5% w/v, were used to follow the phase separation over time (Figures S13 and S14 in the Supporting Information). The volume of the dense phase shrank, reaching a final shape after several days or weeks, depending upon the NP batch used. For both NPs@AP activity, different shapes of phase A were observed, depending upon the volume of the solution of Fmoc-FFpY and NPs@AP in the vial (Figure 6). An “egg-like” shape is observed for smaller gel volumes (200  $\mu$ L) and a “volcano-like” shape for larger ones (>200  $\mu$ L). By looking carefully to both shapes, the “egg-like” structure is similar to the bottom part of a “volcano-like” structure. For small volumes, a “volcano-like” shape cannot be formed probably because of the meniscus of the liquid/air interface.

To be more quantitative, we determined the ratio of the volume of phase A ( $V_t$ ) with respect to the total volume ( $V_0$ ) of the solution as a function of time (Figure 7). Using the

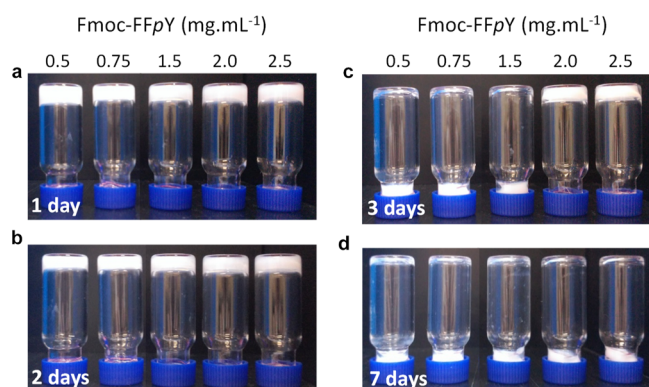


**Figure 5.** Inverted tube tests of NPs@AP (1.25% w/v, equiv [AP] = 7.5 units mL<sup>-1</sup>) in contact with different concentrations of Fmoc-FFpY after (a) 1 day, (b) 2 days, (c) 3 days, and (d) 7 days.

photographic pictures obtained from 600  $\mu\text{L}$  as the initial volume obtained in Figures S13 and S14 (in the Supporting Information), the area of phase A was divided into thin slits of truncated cones, characterized by two characteristic radii. Assuming a symmetrical shape of phase A, the volume of each truncated cone was determined using the adequate mathematical formulae and then were added them up to obtain the volume of phase A (for more details see the Supporting Information). Hydrogels, obtained from 1 mg mL<sup>-1</sup> Fmoc-FFpY mixed with NPs@AP at 2.5% w/v (equiv [AP] = 15 units mL<sup>-1</sup>) and 1.25% w/v (equiv [AP] = 2.5 units mL<sup>-1</sup>), contracted to 40% of their initial volume after 10 and 20 days, respectively.

To determine if the phase separation is only observed when the enzyme is grafted on the surface of NPs, we performed experiments with gels obtained in the presence of non-functionalized NPs with Fmoc-FFpY and AP (Figure S15 in the Supporting Information). Fmoc-FFpY at 1 mg mL<sup>-1</sup> and non-functionalized NPs at 1.25% w/v were added to the AP solution at 7.5 units mL<sup>-1</sup>. NP sedimentation is observed after 2 days, which probably originates from NP aggregation in a gel, which is not dense enough to avoid the sedimentation of these aggregates. We thus performed experiments by increasing the enzyme concentration at 500 units mL<sup>-1</sup>. The obtained gel remains stable over weeks without any indication of a phase

separation. This indicates that the observed phase separation is intimately related to the fact that the enzymes are covalently linked to the NPs and not just to the presence of the NPs.

What could be the origin of this phase separation? One can only speculate at this point about it. First of all, one can ask if the observed phase separation is a syneresis process. Syneresis is the contraction of a gel with expulsion of solvent (here water).<sup>34</sup> It originates from the fact that the solvent is not a good solvent for the gel material, which leads to an increase of the density of chain/chain interactions in the gel. Syneresis was already observed on peptides of self-assembled hydrogels.<sup>35,36</sup> In our case, the “dilute” phase (phase B) is not only constituted of water, as it should be for syneresis, but also of supramolecular peptide self-assemblies and NPs. This is seen by the highly viscous nature of phase B of the “egg”-like structure (see the Video the Supporting Information) and its characterization by cryo-SEM, revealing the presence of NPs and fibers (Figure 4b left). Fibers linked to NPs were also observed in phase B of the “volcano-like” structure (Figure S16 in the Supporting Information). We further verified the presence of Fmoc-FFpY peptides in the “dense” (phase A) and the “dilute” (phase B) phases of the “volcano-like” structure using HPLC. The peptides are present in both phases, with a much smaller concentration in phase B (Figure S17 in the Supporting Information). The ratio of the peptide concentration found in phase B over phase A is of the order of 6% (Table S1 in the Supporting Information). The NPs cannot be detected by HPLC because they were retained by the column. Finally, by performing CD experiments on the “dilute” and “dense” phases, we observed a similar CD signal in both phases, with a much smaller intensity for phase B (Figure S18a in the Supporting Information). There are two intense bands, a negative one at 203 nm and a positive one at 228 nm, both attributed to  $\pi$ - $\pi$  interactions between phenyl side chains.<sup>37</sup> Supramolecular hydrogels are dynamic entities where self-assembly and disassembly of the peptide fibers take place constantly. Moreover, NPs have a tendency to attract each other, thanks to van der Waals forces, and to aggregate over time when left in solution even inside a gel.<sup>38</sup> One can thus assume that such attraction between NPs takes also place in the gel with time. Now, it is known that the peptide fibers also interact with the enzymes<sup>39</sup> and thus with the NPs covered by enzymes. These favorable interactions between the NPs and

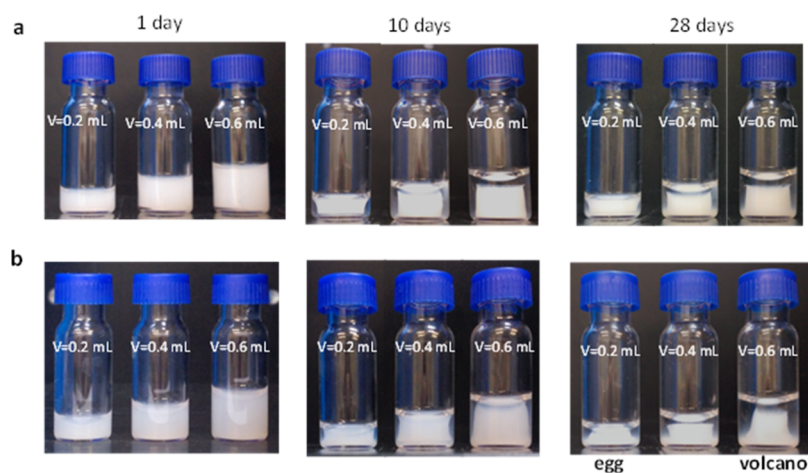


**Figure 6.** Phase separation observed over time, when the vials are not inverted, of the NPs@AP and 1 mg mL<sup>-1</sup> Fmoc-FFpY mixture with (a) NPs@AP (2.5% w/v, equiv [AP] = 15 units mL<sup>-1</sup>) and (b) NPs@AP (1.25% w/v, equiv [AP] = 2.5 units mL<sup>-1</sup>).

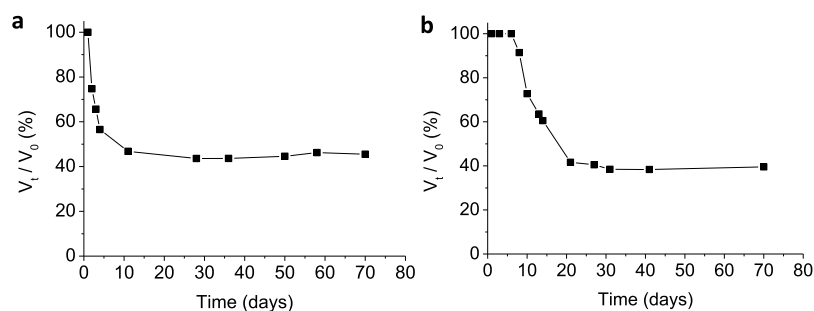


**Figure 7.** Evolution of the volume contraction of the hydrogels obtained in 600  $\mu\text{L}$  of mixture with (a) NPs@AP (2.5% w/v, equiv [AP] = 15 units  $\text{mL}^{-1}$ ) mixed with 1  $\text{mg mL}^{-1}$  Fmoc-FFpY and (b) NPs@AP (1.25% w/v, equiv [AP] = 2.5 units  $\text{mL}^{-1}$ ) mixed with 1  $\text{mg mL}^{-1}$  Fmoc-FFpY. The volume contraction was calculated as the ratio of the volume of phase A ( $V_t$ ) with respect to the total volume of the solution ( $V_0$ ).

the fibers should also favor a fiber network densification. This densification process of both the NPs and the peptide fibers is then accompanied by a reduction of the peptide density at the periphery of the dense part (phase A), leading to the appearance of a dilute phase B. Moreover, the NPs at the periphery of phase A have fewer neighbors than those inside phase A and are thus less attracted by other particles. These particles then diffuse to and from phase B. Such a phase separation is not observed when the enzymes are not covalently fixed on the NPs, indicating that a strong interaction between the fibers and the NPs (through the enzymes here) is required for this phase separation to take place. All these hypotheses have to be addressed in further studies in greater detail.

## CONCLUSIONS

We investigated peptide supramolecular hydrogels initiated at the surface of AP-coated silica NPs through localized enzyme-assisted self-assembly processes. Using DLS and TEM, we confirmed the nucleation of self-assembled peptide nanofibers from the NPs surface. At adequate concentrations of peptides Fmoc-FFpY and NPs@AP, the self-assembly process leads to the formation of a hydrogel in the bulk. Such a supramolecular hydrogel evolves over time, leading to a phase separation different from syneresis: a core phase composed of high densities of peptide nanofibers and aggregated NPs and an outer phase, with the consistency of a gel, with more diluted peptide nanofibers and NPs. Such a phase separation requires the attachment of the enzymes on the NPs. It is hypothesized that attraction between the NPs is at the origin of the phase change, but further studies are needed to get a clear picture of this morphological evolution, so far, to our knowledge, never observed. The understanding and the control of both the spatial localization of molecular self-assembly processes and their evolution over time leading to the design of a chemical system from the nanometer up to the macroscopic scale is a *sine qua none* condition toward the development of highly complex materials such as artificial living matter. That is why we expect that our contribution will interest a large part of the research community.

## ASSOCIATED CONTENT

### Supporting Information

The Supporting Information is available free of charge on the ACS Publications website at DOI: 10.1021/acs.langmuir.9b01420.

TEM image and histogram of NPs, DLS spectrum of NPs, ATR-FTIR spectra of NPs and NPs@AP,

calibration curve of AP in solution and activity of NPs@AP, DLS spectra of NPs@AP in the presence of Fmoc-FFpY, fluorescence spectra of AP and Fmoc-FFpY, inverted tube tests of NPs mixed with Fmoc-FFpY and NPs@AP mixed with Fmoc-G, inverted tube tests of AP at different concentrations mixed with Fmoc-FFpY, FTIR spectra of Fmoc-FFpY and NPs@AP, cryo-SEM images of the NPs@AP/Fmoc-FFY hydrogel after 1 and 2 days and the AP/Fmoc-FFY hydrogel, pictures of phase transition evolution over time of NPs@AP mixed with Fmoc-FFpY and non-functionalized NPs mixed with AP and Fmoc-FFpY in solution, HPLC and CD spectra of phases A and B, and volume calculation of phase A (PDF)

Hydrogel of supramolecular peptide self-assemblies obtained by mixing 150  $\mu\text{L}$  of a 1  $\text{mg mL}^{-1}$  of Fmoc-FFpY with 50  $\mu\text{L}$  of a NP@AP (7.5 units  $\text{mL}^{-1}$ ) leading to egg-like structure. Both the dense and the dilute phase appear to behave in gel-like manner (MP4)

## AUTHOR INFORMATION

### Corresponding Authors

\*E-mail: [schaaf@unistra.fr](mailto:schaaf@unistra.fr) (P.S.).

\*E-mail: [loic.jierry@ics-cnrs.unistra.fr](mailto:loic.jierry@ics-cnrs.unistra.fr) (L.J.).

### ORCID

Pierre Schaaf: 0000-0001-7423-5492

Fouzia Boulmedais: 0000-0002-4934-9276

### Notes

The authors declare no competing financial interest.

## ACKNOWLEDGMENTS

M.C.-G. acknowledges the IDEX of Université de Strasbourg for granting a postdoctoral fellowship. J.R.F. acknowledges the International Center for Frontier Research in Chemistry (Labex CSC, PSC-016 and PSC-005) for a PhD fellowship. ICS microscopy platform and ICS characterization platform are acknowledged for the use of the SEM and DLS instruments, respectively. We gratefully acknowledge the financial support from Agence Nationale de la Recherche (EASA, ANR-18-CE06-0025-03) and Institut Carnot-MICA (DIAART).

## REFERENCES

- (1) Lehn, J.-M. Perspectives in Chemistry—Aspects of Adaptive Chemistry and Materials. *Angew. Chem., Int. Ed. Engl.* **2015**, *54*, 3276–3289.

- (2) Grzybowski, B. A.; Huck, W. T. S. The Nanotechnology of Life-Inspired Systems. *Nat. Nanotechnol.* **2016**, *11*, 585–592.
- (3) Leira-Iglesias, J.; Tassoni, A.; Adachi, T.; Stich, M.; Hermans, T. M. Oscillations, Travelling Fronts and Patterns in a Supramolecular System. *Nat. Nanotechnol.* **2018**, *13*, 1021–1027.
- (4) Marchetti, M. C.; Joanny, J. F.; Ramaswamy, S.; Liverpool, T. B.; Prost, J.; Rao, M.; Simha, R. A. Hydrodynamics of Soft Active Matter. *Rev. Mod. Phys.* **2013**, *85*, 1143–1189.
- (5) Boekhoven, J.; Hendriksen, W. E.; Koper, G. J. M.; Eelkema, R.; van Esch, J. H. Transient Assembly of Active Materials Fueled by a Chemical Reaction. *Science* **2015**, *349*, 1075–1079.
- (6) Mann, S. Life as a Nanoscale Phenomenon. *Angew. Chem., Int. Ed. Engl.* **2008**, *47*, 5306–5320.
- (7) Komiyama, M.; Yoshimoto, K.; Sisido, M.; Ariga, K. Chemistry Can Make Strict and Fuzzy Controls for Bio-Systems: DNA Nanoarchitectonics and Cell-Macromolecular Nanoarchitectonics. *Bull. Chem. Soc. Jpn.* **2017**, *90*, 967–1004.
- (8) Ariga, K.; Leong, D. T.; Mori, T. Nanoarchitectonics for Hybrid and Related Materials for Bio-Oriented Applications. *Adv. Funct. Mater.* **2018**, *28*, 1702905.
- (9) Stuart, M. A. C.; Huck, W. T. S.; Genzer, J.; Müller, M.; Ober, C.; Stamm, M.; Sukhorukov, G. B.; Szleifer, I.; Tsukruk, V. V.; Urban, M.; Winnik, F.; Zauscher, S.; Luzinov, I.; Minko, S. Emerging Applications of Stimuli-Responsive Polymer Materials. *Nat. Mater.* **2010**, *9*, 101–113.
- (10) Ziemecka, I.; Koper, G. J. M.; Olive, A. G. L.; van Esch, J. H. Chemical-Gradient Directed Self-Assembly of Hydrogel Fibers. *Soft Matter* **2013**, *9*, 1556–1561.
- (11) Valignat, M.-P.; Theodoly, O.; Crocker, J. C.; Russel, W. B.; Chaikin, P. M. Reversible Self-Assembly and Directed Assembly of DNA-Linked Micrometer-Sized Colloids. *Proc. Natl. Acad. Sci. U.S.A.* **2005**, *102*, 4225–4229.
- (12) Capito, R. M.; Azevedo, H. S.; Velichko, Y. S.; Mata, A.; Stupp, S. I. Self-Assembly of Large and Small Molecules into Hierarchically Ordered Sacs and Membranes. *Science* **2008**, *319*, 1812–1816.
- (13) Winkleman, A.; Gates, B. D.; McCarty, L. S.; Whitesides, G. M. Directed Self-Assembly of Spherical Particles on Patterned Electrodes by an Applied Electric Field. *Adv. Mater.* **2005**, *17*, 1507–1511.
- (14) Sone, E. D.; Zubarev, E. R.; Stupp, S. I. Semiconductor Nanohelices Templated by Supramolecular Ribbons. *Angew. Chem., Int. Ed. Engl.* **2002**, *41*, 1705–1709.
- (15) Qing, G.; Xiong, H.; Seela, F.; Sun, T. Spatially Controlled DNA Nanopatterns by “Click” Chemistry Using Oligonucleotides with Different Anchoring Sites. *J. Am. Chem. Soc.* **2010**, *132*, 15228–15232.
- (16) Du, X.; Zhou, J.; Shi, J.; Xu, B. Supramolecular Hydrogelators and Hydrogels: From Soft Matter to Molecular Biomaterials. *Chem. Rev.* **2015**, *115*, 13165–13307.
- (17) Vigier-Carrière, C.; Boulmedais, F.; Schaaf, P.; Jierry, L. Surface-Assisted Self-Assembly Strategies Leading to Supramolecular Hydrogels. *Angew. Chem., Int. Ed. Engl.* **2018**, *57*, 1448–1456.
- (18) Yang, B.; Adams, D. J.; Marlow, M.; Zelzer, M. Surface-Mediated Supramolecular Self-Assembly of Protein, Peptide, and Nucleoside Derivatives: From Surface Design to the Underlying Mechanism and Tailored Functions. *Langmuir* **2018**, *34*, 15109–15125.
- (19) Olive, A. G. L.; Abdullah, N. H.; Ziemecka, I.; Mendes, E.; Eelkema, R.; van Esch, J. H. Spatial and Directional Control over Self-Assembly Using Catalytic Micropatterned Surfaces. *Angew. Chem., Int. Ed. Engl.* **2014**, *53*, 4132–4136.
- (20) Criado-Gonzalez, M.; Rodon Fores, J.; Wagner, D.; Schröder, A. P.; Carvalho, A.; Schmutz, M.; Harth, E.; Schaaf, P.; Jierry, L.; Boulmedais, F. Enzyme-Assisted Self-Assembly within a Hydrogel Induced by Peptide Diffusion. *Chem. Commun.* **2019**, *55*, 1156–1159.
- (21) Williams, R. J.; Smith, A. M.; Collins, R.; Hodson, N.; Das, A. K.; Ulijn, R. V. Enzyme-Assisted Self-Assembly under Thermodynamic Control. *Nat. Nanotechnol.* **2008**, *4*, 19–24.
- (22) Williams, R. J.; Hall, T. E.; Glattauer, V.; White, J.; Pasic, P. J.; Sorensen, A. B.; Waddington, L.; McLean, K. M.; Currie, P. D.; Hartley, P. G. The in Vivo Performance of an Enzyme-Assisted Self-Assembled Peptide/Protein Hydrogel. *Biomaterials* **2011**, *32*, 5304–5310.
- (23) Vigier-Carrière, C.; Wagner, D.; Chaumont, A.; Durr, B.; Lupattelli, P.; Lambour, C.; Schmutz, M.; Hemmerlé, J.; Senger, B.; Schaaf, P.; Boulmedais, F.; Jierry, L. Control of Surface-Localized, Enzyme-Assisted Self-Assembly of Peptides through Catalyzed Oligomerization. *Langmuir* **2017**, *33*, 8267–8276.
- (24) Vigier-Carrière, C.; Garnier, T.; Wagner, D.; Lavalle, P.; Rabineau, M.; Hemmerlé, J.; Senger, B.; Schaaf, P.; Boulmedais, F.; Jierry, L. Bioactive Seed Layer for Surface-Confined Self-Assembly of Peptides. *Angew. Chem., Int. Ed. Engl.* **2015**, *54*, 10198–10201.
- (25) Rodon Fores, J.; Mendez, M. L. M.; Mao, X.; Wagner, D.; Schmutz, M.; Rabineau, M.; Lavalle, P.; Schaaf, P.; Boulmedais, F.; Jierry, L. Localized Supramolecular Peptide Self-Assembly Directed by Enzyme-Induced Proton Gradients. *Angew. Chem., Int. Ed. Engl.* **2017**, *56*, 15984–15988.
- (26) Wang, Y.; Versluis, F.; Oldenhof, S.; Lakshminarayanan, V.; Zhang, K.; Wang, Y.; Wang, J.; Eelkema, R.; Guo, X.; van Esch, J. H. Directed Nanoscale Self-Assembly of Low Molecular Weight Hydrogelators Using Catalytic Nanoparticles. *Adv. Mater.* **2018**, *30*, 1707408.
- (27) Wu, C.; Hu, W.; Wei, Q.; Qiao, L.; Gao, Y.; Lv, Y.; Liu, M.; Li, C.; Wang, X.; Wang, Q. Controllable Growth of Core-Shell Nanogels Via Esterase-Induced Self-Assembly of Peptides for Drug Delivery. *J. Biomed. Nanotechnol.* **2018**, *14*, 354–361.
- (28) Conte, M. P.; Sahoo, J. K.; Abul-Haija, Y. M.; Lau, K. H. A.; Ulijn, R. V. Biocatalytic Self-Assembly on Magnetic Nanoparticles. *ACS Appl. Mater. Interfaces* **2018**, *10*, 3069–3075.
- (29) Chang, S. M.; Lee, M.; Kim, W.-S. Preparation of Large Monodispersed Spherical Silica Particles Using Seed Particle Growth. *J. Colloid Interface Sci.* **2005**, *286*, 536–542.
- (30) Wu, Y.; Chen, C.; Liu, S. Enzyme-Functionalized Silica Nanoparticles as Sensitive Labels in Biosensing. *Anal. Chem.* **2009**, *81*, 1600–1607.
- (31) Smith, A. M.; Williams, R. J.; Tang, C.; Coppo, P.; Collins, R. F.; Turner, M. L.; Saiani, A.; Ulijn, R. V. Fmoc-Diphenylalanine Self Assembles to a Hydrogel Via a Novel Architecture Based on II–II Interlocked B-Sheets. *Adv. Mater.* **2008**, *20*, 37–41.
- (32) Fleming, S.; Frederix, P. W. J. M.; Ramos Sasselli, I.; Hunt, N. T.; Ulijn, R. V.; Tuttle, T. Assessing the Utility of Infrared Spectroscopy as a Structural Diagnostic Tool for B-Sheets in Self-Assembling Aromatic Peptide Amphiphiles. *Langmuir* **2013**, *29*, 9510–9515.
- (33) Tang, C.; Smith, A. M.; Collins, R. F.; Ulijn, R. V.; Saiani, A. Fmoc-Diphenylalanine Self-Assembly Mechanism Induces Apparent Pka Shifts. *Langmuir* **2009**, *25*, 9447–9453.
- (34) Castilla, A. M.; Wallace, M.; Mears, L. L. E.; Draper, E. R.; Doutch, J.; Rogers, S.; Adams, D. J. On the Syneresis of an Opv Functionalised Dipeptide Hydrogel. *Soft Matter* **2016**, *12*, 7848–7854.
- (35) Adams, D. J.; Mullen, L. M.; Berta, M.; Chen, L.; Frith, W. J. Relationship between Molecular Structure, Gelation Behaviour and Gel Properties of Fmoc-Dipeptides. *Soft Matter* **2010**, *6*, 1971–1980.
- (36) Conte, M. P.; Singh, N.; Sasselli, I. R.; Escuder, B.; Ulijn, R. V. Metastable Hydrogels from Aromatic Dipeptides. *Chem. Commun.* **2016**, *52*, 13889–13892.
- (37) Ryan, D. M.; Anderson, S. B.; Senguen, F. T.; Youngman, R. E.; Nilsson, B. L. Self-Assembly and Hydrogelation Promoted by F5-Phenylalanine. *Soft Matter* **2010**, *6*, 475–479.
- (38) Chakrabarti, A.; Chaudhury, M. K. Surface Folding-Induced Attraction and Motion of Particles in a Soft Elastic Gel: Cooperative Effects of Surface Tension, Elasticity, and Gravity. *Langmuir* **2013**, *29*, 15543–15550.
- (39) Fores, J. R.; Criado-Gonzalez, M.; Schmutz, M.; Blanck, C.; Schaaf, P.; Boulmedais, F.; Jierry, L. Protein-Induced Low Molecular Weight Hydrogelator Self-Assembly through a Self-Sustaining Process. *Chem. Sci.* **2019**, *10*, 4761–4766.



# Auto-assemblages localisés assistés par des protéines : du mécanisme aux applications

## Résumé

La cellule est un système chimique complexe qui a bénéficié de milliards d'années d'évolution pour se perfectionner, et représente une machinerie très bien organisée ne laissant rien au hasard. Pour assurer son rôle, elle contrôle un ensemble de processus d'auto-assemblage où des composants isolés interagissent spontanément entre eux pour conduire à la formation de structures organisées et fonctionnelles telles que les microtubules, le collagène ou les fibres d'actine. En m'inspirant de l'organisation cellulaire, mon projet doctoral consiste en la conception de systèmes chimiques artificiels basés sur l'auto-assemblage de peptides originaux. Ces édifices donnent naissance à des hydrogels supramoléculaires d'intérêts dans le domaine des biomatériaux. Je m'intéresse à la fois à des aspect fondamentaux concernant la compréhension de l'initiation des processus d'auto-assemblage en présence de biomacromolécules, mais aussi à des problématiques plus appliquées consistant à élaborer des stratégies pour contrôler le lieu mais aussi le moment où ces édifices moléculaires auto-assemblés prennent naissance. Enfin, je m'intéresse à l'émergence des différentes propriétés apparaissant lors de la formation de certains auto-assemblages comme la catalyse ou l'auto-catalyse.

**Mots clés :** *Auto-assemblage, peptides, protéines, hydrogels, modification de surface, catalyse, auto-catalyse, couche par couche, polyélectrolytes.*

## Abstract

The cell is a complex chemical system that has benefited from billions of years of evolution to perfect itself, and represents a very well organized machinery leaving nothing to chance. To ensure its role, it controls a set of self-assembly processes where isolated components interact spontaneously with each other to lead to the formation of organized and functional structures such as microtubules, collagen or actin fibers. Inspired by cellular organization, my doctoral project involves the design of artificial chemical systems based on the self-assembly of original peptides. These buildings give rise to supramolecular hydrogels of interest in the field of biomaterials. I am interested at the same time in fundamental aspects concerning the comprehension of the initiation of the processes of self-assembly in the presence of biomacromolecules, but also with more applied problems of elaborating strategies to control the place but also the moment where these self-assembled molecular structures originate. Finally, I am interested in the emergence of the different properties appearing during the formation of certain self-assemblies such as catalysis and auto-catalysis.

**Keywords:** *Self-assembly, peptides, proteins, hydrogels, surface modification, catalysis, auto-catalysis, layer-by-layer, polyelectrolytes.*